

**Nanoscience & Nanotechnology Series**

---

# **Sustainable Nanotechnology**

Edited by Zibiao Li, Jie Zheng and Enyi Ye

# Sustainable Nanotechnology

## Nanoscience & Nanotechnology Series

### *Editor-in-chief:*

Nguyễn T. K. Thanh, *University College London, UK*

### *Series editors:*

Gabriel Caruntu, *Central Michigan University, USA*

Shinya Maenosono, *Japan Advanced Institute of Science and Technology, Japan*

Neerish Revaprasadu, *University of Zululand, South Africa*

### *Titles in the series:*

- 1: Nanotubes and Nanowires
- 2: Fullerenes: Principles and Applications
- 3: Nanocharacterisation
- 4: Atom Resolved Surface Reactions: Nanocatalysis
- 5: Biomimetic Nanoceramics in Clinical Use: From Materials to Applications
- 6: Nanofluidics: Nanoscience and Nanotechnology
- 7: Bionanodesign: Following Nature's Touch
- 8: Nano-Society: Pushing the Boundaries of Technology
- 9: Polymer-based Nanostructures: Medical Applications
- 10: Metallic and Molecular Interactions in Nanometer Layers, Pores and Particles: New Findings at the Yoctolitre Level
- 11: Nanocasting: A Versatile Strategy for Creating Nanostructured Porous Materials
- 12: Titanate and Titania Nanotubes: Synthesis, Properties and Applications
- 13: Raman Spectroscopy, Fullerenes and Nanotechnology
- 14: Nanotechnologies in Food
- 15: Unravelling Single Cell Genomics: Micro and Nanotools
- 16: Polymer Nanocomposites by Emulsion and Suspension
- 17: Phage Nanobiotechnology
- 18: Nanotubes and Nanowires, 2nd Edition
- 19: Nanostructured Catalysts: Transition Metal Oxides
- 20: Fullerenes: Principles and Applications, 2nd Edition
- 21: Biological Interactions with Surface Charge Biomaterials
- 22: Nanoporous Gold: From an Ancient Technology to a High-Tech Material
- 23: Nanoparticles in Anti-Microbial Materials: Use and Characterisation
- 24: Manipulation of Nanoscale Materials: An Introduction to Nanoarchitectonics
- 25: Towards Efficient Designing of Safe Nanomaterials: Innovative Merge of Computational Approaches and Experimental Techniques
- 26: Polymer-Graphene Nanocomposites
- 27: Carbon Nanotube-Polymer Composites
- 28: Nanoscience for the Conservation of Works of Art
- 29: Polymer Nanofibers: Building Blocks for Nanotechnology
- 30: Artificial Cilia

- 31: Nanodiamond
- 32: Nanofabrication and its Application in Renewable Energy
- 33: Semiconductor Quantum Dots: Organometallic and Inorganic Synthesis
- 34: Soft Nanoparticles for Biomedical Applications
- 35: Hierarchical Nanostructures for Energy Devices
- 36: Microfluidics for Medical Applications
- 37: Nanocharacterisation, 2<sup>nd</sup> Edition
- 38: Thermometry at the Nanoscale: Techniques and Selected Applications
- 39: Nanoceramics in Clinical Use: From Materials to Applications, 2<sup>nd</sup> Edition
- 40: Near-infrared Nanomaterials: Preparation, Bioimaging and Therapy Applications
- 41: Nanofluidics, 2nd Edition
- 42: Nanotechnologies in Food, 2nd Edition
- 43: ZnO Nanostructures: Fabrication and Applications
- 44: Diatom Nanotechnology: Progress and Emerging Applications
- 45: Nanostructured Materials for Type III Photovoltaics
- 46: Chemically Derived Graphene: Functionalization, Properties and Applications
- 47: Graphene-based Membranes for Mass Transport Applications
- 48: Carbon Nanostructures for Biomedical Applications
- 49: Surface Chemistry of Colloidal Nanocrystals
- 50: Reducing Agents in Colloidal Nanoparticle Synthesis
- 51: Carbon Nitride Nanostructures for Sustainable Energy Production and Environmental Remediation
- 52: Nanotubes and Nanowires, 3rd Edition
- 53: Bionanodesign: Old Forms for New Functions, 2nd Edition
- 54: Photothermal Nanomaterials
- 55: Concepts and Design of Materials Nanoarchitectonics
- 56: Anticorrosive Nanomaterials: Future Perspectives
- 57: Sustainable Nanotechnology

*How to obtain future titles on publication:*

A standing order plan is available for this series. A standing order will bring delivery of each new volume immediately on publication.

*For further information please contact:*

Book Sales Department, Royal Society of Chemistry, Thomas Graham House, Science Park, Milton Road, Cambridge, CB4 0WF, UK

Telephone: +44 (0)1223 420066, Fax: +44 (0)1223 420247

Email: [booksales@rsc.org](mailto:booksales@rsc.org)

Visit our website at [www.rsc.org/books](http://www.rsc.org/books)



# *Sustainable Nanotechnology*

Edited by

**Zibiao Li**

*A\*STAR, Singapore*

*Email: lizb@imre.a-star.edu.sg*

**Jie Zheng**

*A\*STAR, Singapore*

*Email: zheng\_jie@imre.a-star.edu.sg*

and

**Enyi Ye**

*A\*STAR, Singapore*

*Email: yeey@imre.a-star.edu.sg*

Nanoscience & Nanotechnology Series No. 57

Print ISBN: 978-1-83916-255-8

PDF ISBN: 978-1-83916-577-1

EPUB ISBN: 978-1-83916-578-8

Print ISSN: 1757-7136

Electronic ISSN: 1757-7144

A catalogue record for this book is available from the British Library

© The Royal Society of Chemistry 2022

*All rights reserved*

*Apart from fair dealing for the purposes of research for non-commercial purposes or for private study, criticism or review, as permitted under the Copyright, Designs and Patents Act 1988 and the Copyright and Related Rights Regulations 2003, this publication may not be reproduced, stored or transmitted, in any form or by any means, without the prior permission in writing of The Royal Society of Chemistry or the copyright owner, or in the case of reproduction in accordance with the terms of licences issued by the Copyright Licensing Agency in the UK, or in accordance with the terms of the licences issued by the appropriate Reproduction Rights Organization outside the UK. Enquiries concerning reproduction outside the terms stated here should be sent to The Royal Society of Chemistry at the address printed on this page.*

*Whilst this material has been produced with all due care, The Royal Society of Chemistry cannot be held responsible or liable for its accuracy and completeness, nor for any consequences arising from any errors or the use of the information contained in this publication. The publication of advertisements does not constitute any endorsement by The Royal Society of Chemistry or Authors of any products advertised. The views and opinions advanced by contributors do not necessarily reflect those of The Royal Society of Chemistry which shall not be liable for any resulting loss or damage arising as a result of reliance upon this material.*

The Royal Society of Chemistry is a charity, registered in England and Wales, Number 207890, and a company incorporated in England by Royal Charter (Registered No. RC000524), registered office: Burlington House, Piccadilly, London W1J 0BA, UK, Telephone: +44 (0) 20 7437 8656.

For further information see our web site at [www.rsc.org](http://www.rsc.org)

Printed in the United Kingdom by CPI Group (UK) Ltd, Croydon, CR0 4YY, UK

# *Preface*

With the increasing awareness of the global sustainability challenges, how to accomplish environmental conservation and energy production without the depletion of natural sources has attracted great attention. Through fabricating materials at the nanometer scale, nanotechnology has facilitated an efficient and economically and environmentally acceptable solution for waste treatment and energy production. This book is devoted to illustrating the subject of sustainable nanotechnology being used to promote more efficient environmental sustainability, including environmental remediation and energy optimization. First, a comprehensive discussion of the latest advances in using green nanotechnology to address the global challenges in water purification, CO<sub>2</sub> management, plastic waste remediation, food waste valorization, toxic chemical pollution, and energy efficiency will be provided, followed by new opportunities that green nanotechnology has created in the production of alternative renewable energy under the premise of low natural resource consumption and minuscule toxicity production. The perspectives and future research directions of green nanotechnology to achieve more environmental sustainability will also be presented in the proposed chapters. This book offers an important reference for the research community to understand more about green nanotechnology and its application in sustainable development and circular economy, as well as the perspectives for future R&D directions.

Zibiao Li  
Jie Zheng  
Enyi Ye





# Contents

<b>Chapter 1</b>	<b>Introduction of Nanotechnology and Sustainability</b>	<b>1</b>
	<i>P. L. Chee, W. L. Toh, P. Y. Yew, S. Peng and D. Kai</i>	
1.1	Introduction	1
1.2	Types of Nanostructures	2
1.2.1	Nanoparticles	2
1.2.2	Nanofibers	5
1.2.3	Nanotubes	6
1.2.4	Nanoplates	6
1.3	Green Chemistry and Synthetic Approaches	7
1.3.1	Mechanochemistry	7
1.3.2	Microwave Irradiation	9
1.3.3	Photochemistry and Photocatalysis	9
1.3.4	Electrochemistry and Electrocatalysis	10
1.3.5	Flow Chemistry	11
1.3.6	Biological Synthesis	12
1.4	Green and Sustainable Resources	13
1.4.1	Renewable Resources – Biomass and Biomolecules	13
1.4.2	Renewable Resources – Waste	14
1.5	Environmental Impact and Life Cycle of Nanotechnology	17
1.5.1	Sustainable Evaluation of Nanotechnology	18
1.5.2	Impact on the Environment and Human Health	22
1.6	Perspectives and Conclusion	23
	References	23

---

Nanoscience & Nanotechnology Series No. 57

Sustainable Nanotechnology

Edited by Zibiao Li, Jie Zheng and Enyi Ye

© The Royal Society of Chemistry 2022

Published by the Royal Society of Chemistry, [www.rsc.org](http://www.rsc.org)

<b>Chapter 2</b>	<b>Green Nanotechnology for High-performance Impurity Detection and Water Treatment</b>	<b>33</b>
	<i>Bofan Li, Nannan Wang, Jie Zheng, Houjuan Zhu, Sheng Wang, Enyi Ye and Zibiao Li</i>	
2.1	Introduction	33
2.2	Biosensors and Nanoparticles for Impurity Detection	35
2.2.1	Electrochemical Biosensors	35
2.2.2	Nanoparticles	40
2.3	Nanomaterials for Adsorbing and Degrading Pollutants in Water	44
2.3.1	Nanosorbents	45
2.3.2	Nanophotocatalysts	47
2.4	Nanofibrous Sorbents, Membranes, and Aerogels for Removing Oil From Water	49
2.4.1	Nanofibrous Sorbents	49
2.4.2	Nanofibrous Membranes	50
2.4.3	Nanofibrous Aerogel	52
2.5	Thin-film Nanocomposite Membranes for Energy-efficient Water Purification	52
2.5.1	Zero-dimensional Materials: Nanoparticles and Quantum Dots	53
2.5.2	One-dimensional Materials: Nanotubes	55
2.5.3	Two-dimensional Materials: Nanosheets	55
2.5.4	Three-dimensional Materials: Metal–Organic Frameworks and Organic Cages	56
2.6	Conclusions and Outlook	58
	References	58
<b>Chapter 3</b>	<b>Nanotechnology for CO<sub>2</sub> Capture, Storage, and Conversion</b>	<b>65</b>
	<i>X. Zhang, N. Qin, E. Ye, G. Guan, M. Y. Han and Z. Li</i>	
3.1	Introduction	65
3.2	Capture of CO <sub>2</sub> by Nanostructured Materials	68
3.2.1	Adsorbing of CO <sub>2</sub> on Nanostructured Materials	68
3.2.2	Separation of CO <sub>2</sub> by Using Nanotechnology	71
3.2.3	Fixation of CO <sub>2</sub> Over Nanomaterials	73
3.3	Photocatalytic CO <sub>2</sub> Reduction Over Nanostructures	74
3.3.1	Metals and Alloys	74
3.3.2	Metal Oxides and Their Nanohybrids	77
3.3.3	Other Metal Compounds and Their Hybrids	82

3.3.4	Two-dimensional Carbon-containing Materials	84
3.3.5	Metal–Organic Frameworks	91
3.4	Electrochemical Reduction of CO <sub>2</sub> With Nanostructured Materials	94
3.4.1	Nanostructured Monometal Electrocatalysts	94
3.4.2	Hybridization of Different Metals	99
3.4.3	Metal Oxides and Their Hybrids	103
3.4.4	Other Interesting Electrocatalytic Systems	107
3.5	Summary and Outlook	109
	References	110
<b>Chapter 4</b>	<b>Nanotechnology for the Remediation of Plastic Wastes</b>	<b>117</b>
	<i>Y. Zheng, C. Mao, Z. Zhang, R. Liu and B. Yan</i>	
4.1	Introduction	117
4.2	Biodegradable Plastics	120
4.2.1	Nanomaterials for Improving the Performance of Plastics	124
4.2.2	Biodegradability of Plastics	125
4.3	Nanotechnologies for the Remediation of Plastics	127
4.3.1	Nanofiller	127
4.3.2	Photodegradation of Plastics	129
4.3.3	Nanotechnology in Flexible Plastics	131
4.3.4	Nanotechnology in the Carbonization of Plastics	131
4.3.5	Nanotechnology for the Transformation of Plastics to High-value Products	133
4.4	Conclusion and Outlook	137
	References	138
<b>Chapter 5</b>	<b>Sustainable Nanomaterials for Pollutant Treatment</b>	<b>144</b>
	<i>Van-Phuc Dinh, Zibiao Li and Enyi Ye</i>	
5.1	Introduction	144
5.2	Heavy Metals in Wastewater	146
5.3	Mechanisms of the Adsorption of Contaminants From Wastewater Using Nanomaterials	147
5.3.1	Isotherm Adsorption Models	147
5.3.2	Kinetic Adsorption Models	148
5.3.3	Data Analysis	149
5.3.4	Spectroscopy Methods	149

5.4	Metal Oxide Nanomaterials	152
5.4.1	MnO <sub>2</sub> Nanomaterials	153
5.4.2	Iron Oxide Nanomaterials	155
5.4.3	Zinc Oxide Nanomaterials	156
5.5	Conclusions	157
	References	157
<b>Chapter 6</b>	<b>The Application of Nanomaterials in the Built Environment</b>	<b>163</b>
	<i>Pin Jin Ong, Ming Hui Chua, Soo Xiang Yun Debbie and Qiang Zhu</i>	
6.1	Introduction	163
6.2	Nanomaterial in Building Components	165
6.2.1	Glass	165
6.2.2	Brick	166
6.2.3	Stone	170
6.2.4	Indoor Air Treatment	173
6.2.5	Wood	176
6.3	Risk of Nanomaterials	178
6.4	Conclusion	180
	References	180
<b>Chapter 7</b>	<b>Nanotechnology for Energy Storage and Efficiency</b>	<b>185</b>
	<i>Jie Xuan, Guijian Guan, Yong Yu, Enyi Ye and Zibiao Li</i>	
7.1	Introduction	185
7.2	Engineering Core Size, Surface Property, Composition, and Photoluminescence of Thiolate-coated Au or Ag NCs	189
7.2.1	Synthesis Strategies for Size Control	190
7.2.2	Surface Control	196
7.2.3	Composition Control	197
7.2.4	Photoluminescence Control	201
7.3	Energy Conversion Applications	206
7.3.1	Solar Cells	206
7.3.2	Water Splitting	207
7.3.3	CO <sub>2</sub> Fixation	209
7.3.4	Fuel Cells	210
7.3.5	Lithium-ion Batteries	211
7.3.6	Light-driven Emitting Diodes	212
7.4	Summary	214
	References	215

<i>Contents</i>	xiii
<b>Chapter 8 Nanocatalysis With Sustainability</b>	<b>220</b>
<i>Lili Zhou, Jie Zheng, Enyi Ye, Zibiao Li and Chaobin He</i>	
8.1 Introduction	220
8.2 Nanocatalysis Materials	222
8.2.1 Metallic Nanoparticles	222
8.2.2 Magnetically Recyclable Nanocatalysts	224
8.2.3 Nanocarbon Materials	227
8.2.4 Nanostructured Porous Materials	232
8.3 Nanocatalysis With Sustainability	237
8.3.1 Photocatalysis	237
8.3.2 Environmental Remediation	239
8.3.3 Production of High-value Fuels	240
8.3.4 Production of High-value Chemicals	241
8.4 Conclusion	243
References	244
<b>Chapter 9 Bio-refining Through Nanotechnology</b>	<b>255</b>
<i>Feng Liu, Yi Ren, Ming Hui Chua and Hui Zhou</i>	
9.1 Introduction	255
9.2 First Generation Bio-refineries Based on Nano-catalysts	257
9.2.1 Biodiesel Production	257
9.2.2 High-value Chemicals from Glycerol	260
9.2.3 Conversion of Starch-rich Biomass to Bio-ethanol	261
9.3 Second Generation Bio-refineries Based on Nano-catalysts	262
9.3.1 Bio-ethanol Derived From Lignocellulosic Biomass	262
9.3.2 Lactic Acid and Chemicals Derived From Glucose	264
9.3.3 Chemicals Derived From Cellulose	264
9.3.4 Pyrolysis of Lignocellulosic Biomass	265
9.3.5 Bio-oil Upgrading	268
9.3.6 Other Applications	269
9.4 Prospects and Outlook	270
References	271

<b>Chapter 10 Nanotechnology Research for Alternative Renewable Energy</b>	<b>277</b>
<i>Jie Zheng, Claris Jie Ee Wong, Enyi Ye and Zibiao Li</i>	
10.1 Introduction	277
10.2 Solar Energy	278
10.2.1 Concentrated Solar Power	279
10.2.2 Photovoltaic	284
10.3 Wind Energy	284
10.4 Geothermal Energy	287
10.5 Hydrogen Energy	287
10.6 Conclusions and Perspectives	291
References	292
<b>Subject Index</b>	<b>299</b>

## CHAPTER 1

# *Introduction of Nanotechnology and Sustainability*

P. L. CHEE,<sup>a</sup> W. L. TOH,<sup>b</sup> P. Y. YEW,<sup>a</sup> S. PENG<sup>c</sup> AND D. KAI<sup>\*a</sup>

<sup>a</sup> Institute of Materials Research and Engineering (IMRE), A\*STAR, 2 Fusionopolis Way, Innovis, no. 08-03, Singapore 138634, Singapore;

<sup>b</sup> Department of Chemistry, Massachusetts Institute of Technology, Cambridge, Massachusetts 02139, United States; <sup>c</sup> Jiangsu Key Laboratory of Electrochemical Energy Storage Technologies, College of Materials Science and Technology, Nanjing University of Aeronautics and Astronautics, Nanjing, 210016 China

\*Emails: pengshengjie@nuaa.edu.cn; kaid@imre.a-star.edu.sg

## 1.1 Introduction

The importance of sustainability has never been felt so greatly before, especially with the recent occurrences of extreme weather, stronger storms, global warming, *etc.* The depletion of resources, rising sea water levels and ozone layer depletion are also signs of concern, as they could threaten the survivability of future generations. Yet, the current efforts that aim to promote sustainable development, such as the implementation of carbon tax, are not very fruitful. This could be accounted to the relatively heavier emphasis on result efficiency in this fast-paced world, which merely results in the shift of the companies to countries with less stringent regulations. Furthermore, cost and inefficient processes also contribute to unsuccessful attempts.

Nanotechnology is defined by the National Nanotechnology Initiative (NNI) as “the understanding and control of matter at the nanoscale, at dimensions between approximately 1 and 100 nanometers, where unique phenomena

---

Nanoscience & Nanotechnology Series No. 57

Sustainable Nanotechnology

Edited by Zibiao Li, Jie Zheng and Enyi Ye

© The Royal Society of Chemistry 2022

Published by the Royal Society of Chemistry, www.rsc.org



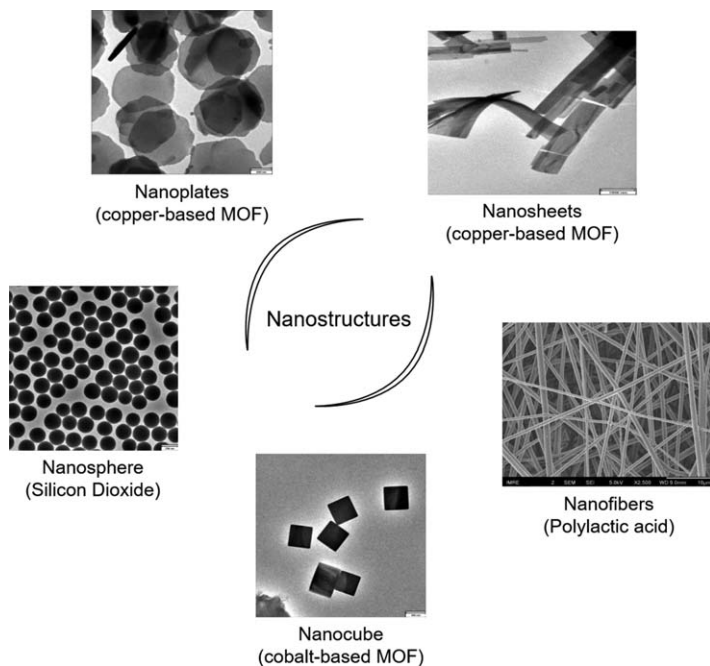
enable novel applications”.<sup>1</sup> The ability to control matter at the nanoscale presents new possibilities, such as more efficient processes and accessibility to remote regions, which would be advantageous for new development. At the nanoscale, the surface area of the material is greatly increased, enabling higher reactivity. A smaller scale also suggests that less energy is required for operation, thereby leaning toward sustainability. Granted with small size, nanoscale materials could reach regions that were once impossible to reach, which is beneficial to the clinical field, where human anatomy is the limitation for treatment. Furthermore, materials in the range of nanoscale are found to possess different sets of properties from the bulk material itself. For example, the material in bulk form could be non-toxic but could become toxic when reduced to the nanoform.<sup>2</sup> A possible explanation for the change could be attributed to the enhanced reactivity arising from the increased surface area. Besides the divergence in properties between bulk and nanoscale materials, property variation among the nanomaterials itself is not uncommon. For instance, nanoparticles (NPs) consisting of the same material but of different sizes were shown to possess different absorption wavelengths.<sup>3</sup> The size of the NPs was also found to be a parameter that affects absorption performance.<sup>4</sup> Additionally, the morphology of the NPs determines their reactivity and other properties.<sup>5</sup> This divergence in the properties according to the morphology and size of the NPs could potentially be adopted as a controlling element for new unique applications. With the broad spectrum of properties exhibited by nanomaterials in magnetic, electrical, mechanical and catalytic domains, nanotechnology is no doubt indispensable in various sectors, ranging from transport, energy and agriculture to healthcare and information and communication<sup>6</sup> to achieve both new development and sustainability. For instance, nanocapsules are useful for drug delivery and pharmaceutical purposes, whereas quantum dots are sought after for biosensors and cell imaging.<sup>5</sup> Nanobased technology is also identified with the potential to promote sustainability in agriculture and food systems through various means but not limited to nanobased fertilizers and nanobased water treatment for agricultural fields.<sup>7</sup>

## 1.2 Types of Nanostructures

Nanomaterials exist in various forms and dimensions, such as NPs, nanofibers, nanotubes and nanoplates (Figure 1.1). Their properties are heavily dependent on the structure, size and shape, and therefore, different forms of nanomaterials are suited for distinct applications. More details of each type of nanomaterial will be delved into in the following sections.

### 1.2.1 Nanoparticles

NPs are defined as “particulate dispersions or solid particles with a size in the range of 10–1000 nm”.<sup>8</sup> Their synthesis could be categorized into two main branches, namely, the bottom-up and the top-down approach. In the former approach, NPs are formed through the building up of atoms and



**Figure 1.1** Different types of nanostructures. MOF: metal–organic framework.

molecules, whereas in the latter, NPs are obtained through the breaking down of bulk material. The bottom-up approach is more efficient as it enables large-scale and fast synthesis with a more homogeneous structure and lower defect rate. Some of the commonly used processes are green synthesis, the sol–gel process, spinning and the biochemical process.<sup>5</sup> In contrast, the top-down approach is more destructive as it involves etching out existing crystal plates that are present on the substrate. Inevitably, the derived NPs are not as consistent.<sup>5</sup> NPs could be further divided into three major clusters based on their material type – inorganic, organic and carbon-based – and the different types of NPs will be discussed in the subsequent sections.

### 1.2.1.1 Inorganic NPs

Gold, silver and copper are some of the more established elements in this category, populated by metal and metal oxides. The reason for the attention garnered by these materials could be narrowed down to the tunability of optoelectronic properties, achievable through the manipulation of size and shape of the inorganic NPs. Within the group, gold NPs are considered one of the most highly regarded materials. Their biocompatible nature appeals greatly to biomedical usage, and their presence in this field could be perceived in various forms, such as carriers for drugs<sup>9</sup> and genes,<sup>10,11</sup> tracers for bioimaging<sup>12,13</sup> and agents for cancer therapy.<sup>14</sup> While other inorganic NPs

have also been examined for similar functions, toxicity and poor degradability remain a persisting concern,<sup>15,16</sup> which would have to be resolved before inorganic NPs could be utilized in the aforementioned applications. In response to the concern, numerous studies have emerged over the years with different techniques to improve the biocompatibility of inorganic NPs.<sup>17</sup> At present, researchers have identified surface modification as a probable means to overcome the incompatible status.<sup>18</sup> Specifically, PEGylation appears to be a good strategy to improve the compatibility of NPs by concealing their foreign identity and, ideally, avoiding evoking the immune response.<sup>18</sup> In the circumstance that toxicity is caused by non-specific accumulation, selective biodegradable NP<sup>19</sup> carriers could be used such that they would not remain in the system for an excessively long duration. Alternatively, means to promote renal excretion<sup>19,20</sup> would be relevant in circumventing the non-specific accumulation and the consequent toxicity. The methods to produce these inorganic NPs fall under three big branches – physical, chemical and biological. Microwave irradiation,<sup>21</sup> laser ablation<sup>22</sup> and hydrothermal process<sup>23</sup> are examples of the physical methods that have been used to obtain the NPs. In terms of chemical techniques, there are the sol-gel and phase-transfer methods.<sup>24</sup> Recently, copper oxide NPs were successfully synthesized using *Aspergillus terreus*,<sup>25</sup> in which a biological means is exploited to generate inorganic NPs. With the continuous development in the field, inorganic NPs would remain relevant and no doubt an invaluable asset to further the frontier of existing technology.

### 1.2.1.2 Organic NPs

Organic NPs are solid particles with diameters in the range of 10 nm to 1  $\mu\text{m}$  that are made up of organic compounds.<sup>26</sup> Considering the work performed on inorganic NPs, the studies conducted on their organic counterpart seem to pale in comparison. For example, existing persistent luminescence agents still mainly rely on inorganic NPs.<sup>27-29</sup> The fewer explorations could be attributed to complicated preparation procedures and poor solubility of the organic compounds, which inevitably cause it to be less efficacious than intended.<sup>15</sup> Yet, research in this area is of paramount importance as organic NPs possess high potential waiting to be unleashed. Their inherent biocompatibility is highly relevant to biomedical applications. In addition, organic NPs, with the flexibility to be modified into different structures and sizes<sup>30</sup> and be equipped with unique functions,<sup>31</sup> have unlimited possibilities. In fact, recent research has seen a surge in the development of organic NPs. Dong and coworkers designed an organic NPs by introducing triphenylamine to diketopyrrolopyrrole molecule functionalized with thiophene group.<sup>32</sup> As a result, these organic NPs demonstrated improved intersystem crossing ability through the heavy atom effect and they also had refined charge transport capacity and bathochromic shift absorption.<sup>32</sup> Researchers have also attempted to streamline the synthesis process. In their study, Wei and their team successfully simplified the synthesis reaction and attained amphiphilic luminescent

polymers through a “one-pot” mercaptoacetic acid locking imine reaction.<sup>33</sup> At present, some of the techniques that have been developed to synthesize organic NPs are nanoprecipitation,<sup>27</sup> microemulsion,<sup>34</sup> self-assembly,<sup>35,36</sup> electrospraying<sup>37</sup> and photoablation of aggregation-induced enhanced emission luminophores.<sup>38</sup> Among the new functionalities introduced to the organic NPs, the organelle-targeting function seems to have become popular in recent years. Studies have succeeded at targeting organic NPs to selected regions such as lysosomes,<sup>39</sup> mitochondria<sup>40</sup> and kidney.<sup>30</sup> With the developments to date, it would not be surprising to encounter the extensive use of organic NPs in the fields of drug delivery, bioimaging and photodynamic/photothermal therapy in the near future.

### 1.2.1.3 Carbon-based NPs

Among the different types of carbon-based nanostructures, carbon nanoparticles (CNPs) seem to be the most attractive. Being endowed with good electrical conductivity, high sensitivity, large specific surface area and impressive electrochemical activity, CNPs have infiltrated and transformed the electrochemical sensing platform. CNP-modified electrodes, which combine CNPs and electrochemical techniques, have been shown to be capable of determining a broad range of analytes ranging from chemicals<sup>41,42</sup> to bacteria.<sup>43</sup> Higher efficiency was also detected for these CNP-modified electrodes.<sup>41</sup> Besides the revolutionary impact in the electrochemical sensing field, the presence of CNPs is also apparent in the biomedical field. Their biocompatible and non-toxic nature is the main factor that has seen the expansion of its scope of applications to the biomedical field.<sup>44</sup> Their bright fluorescence and tunable photoluminescence characteristics appeal to biosensing,<sup>45</sup> photodynamic therapy,<sup>46,47</sup> drug delivery<sup>48</sup> and bioimaging purposes.<sup>49,50</sup> With their dimensions in the nanoscale range, CNPs easily traverse cell membranes, which is not impeded even by binding with drug molecules,<sup>51</sup> proteins<sup>52</sup> or genes.<sup>53</sup> This advantage, coupled with their biocompatible properties, makes CNPs well suited as carriers. In addition, it is not surprising to find the presence of CNPs in the photo-/electrocatalysis arena.<sup>54,55</sup> The adjustable band gap that arises from the introduction of CNPs empowers us to tap into the visible light<sup>54</sup> and near-infrared<sup>56</sup> range of solar energy to promote the catalysis process. Techniques that have been explored for the synthesis of CNPs include but are not limited to microwave irradiation,<sup>57</sup> pulsed laser irradiation,<sup>58</sup> hydrothermal<sup>59,60</sup> and ultrasonic treatment.<sup>61</sup>

### 1.2.2 Nanofibers

Nanomaterial can exist in the form of nanofibers, which is made possible by progress in the arena of electrospinning. Particularly, the thickness of the fibers is found to vary along with numerous parameters, which include but are not limited to the distance between the nozzle and the collector, flow rate of fluid, surface tension of fluid and dielectric permittivity.<sup>62</sup> Through

careful manipulation of these variables, nanofibers could be achieved. This process utilizes electrostatic force to direct the charged polymer solution across the charged field to the collector. According to the requirement in the fiber orientation, the collector may be a flat surface or a rotating drum. These nanofibers demonstrate the potential to be implemented in diverse applications ranging from filters,<sup>63</sup> food packaging<sup>64</sup> and electrocatalysts<sup>65</sup> to carriers for therapeutic agents<sup>66</sup> and wound-healing applications.<sup>67</sup>

### 1.2.3 Nanotubes

With a high length-to-diameter ratio, nanotubes are regarded as one-dimensional structures. Briefly, nanotubes are formed *via* rolling sheets into tubes, and this group of materials could be further classified according to the layers of sheets utilized to wrap into the cylindrical structure. When a single sheet is used, the obtained structure is known as a single-walled nanotube (SWNT), whereas multi-walled nanotubes (MWNTs) are attained by wrapping layers of concentric single-walled nanotubes into a cylinder. Owing to the difference in the layers of sheets that contribute to the formation of nanotubes, these structures consequently possess distinct properties. For instance, MWNT was revealed to exhibit better fluorescence quenching ability than SWNT, whereas the latter demonstrates higher sensitivity to the base sequences of Fluor-ssDNA.<sup>68</sup> In comparison with the SWNT arrays, MWNT arrays were found to experience higher friction and adhesive force.<sup>69</sup> As such, nanotubes appeal to a broad range of applications ranging from sensors,<sup>70</sup> electrodes<sup>71</sup> and filters<sup>72,73</sup> to biomaterials<sup>74</sup> and energy-harvesting applications.<sup>75</sup> Carbon nanotubes in particular are extremely alluring within this group of materials. Apart from having desirable mechanical properties, carbon nanotubes also possess good electrical conductivity and thermal stability, which are prerequisites for applications such as electrodes and sensors. Recently, carbon nanotubes were investigated for use in tissue engineering. Promising results were attained as osteogenic differentiation of the mesenchymal stem cells was shown to be stimulated.<sup>74</sup>

### 1.2.4 Nanoplates

Nanoplates can be considered two-dimensional structures, given that the third dimension is in the nanometer range. As a higher-order nanostructure, there are numerous approaches to modify its structure. For instance, the morphology of the nanostructure could be lamellar, fragmented or compact.<sup>76</sup> Intercalation and exfoliation are also two of the commonly used techniques to vary nanoplates. Specifically, the manipulation of temperature for exfoliation can lead to several changes in the morphology of the nanoplates. It was shown that a higher temperature used for the treatment generally reduced the Langmuir surface area and average pore diameter of graphene nanoplates.<sup>77</sup> The pore volume and mesopore volume in the graphene nanoplates were found to increase with temperature for up to 300 °C,

and beyond this temperature, a decline was observed.<sup>77</sup> Besides the thermal exfoliation, many other methods have been developed to generate the nanoplates, such as seed-mediated growth,<sup>78</sup> template-assisted self-assembly<sup>79</sup> and chemical vapor deposition.<sup>80</sup> With a large specific surface area, these materials are widely investigated for use in sensors due to their high sensitivity. To date, nanoplate-based sensors have been shown to be capable of detecting a large spectrum of analytes, ranging from glucose<sup>81</sup> and DNA<sup>82</sup> to cancer biomarkers<sup>83</sup> and gas.<sup>84</sup> This technology has also been explored as an alternative drug delivery system.<sup>85</sup> Recently, it was reported that silver nanoplates with a very narrow gap were successfully constructed and this development will improve future analysis performed using surface-enhanced Raman scattering.<sup>78</sup>

## 1.3 Green Chemistry and Synthetic Approaches

In recent years, efforts have been devoted to discovering and optimizing greener synthetic methods that follow one or more of the Twelve Principles of Green Chemistry. Existing methods that have been developed with green chemistry in mind can be extrapolated to nanotechnology development in terms of synthetic methodologies and green manufacturing processes (Table 1.1).

### 1.3.1 Mechanochemistry

Mechanochemistry is the use of mechanical force to break and make new chemical bonds. It has been employed not only in inorganic solid-state syntheses and phase transformations<sup>86</sup> but also increasingly in organic syntheses, such as in forming and breaking carbon-carbon, carbon-heteroatom and metal-ligand coordination bonds.<sup>87</sup> The synthesis of high-surface-area carbon<sup>88</sup> as well as metal-organic frameworks<sup>89</sup> has also been shown to be possible.

Mechanochemical transformations are usually carried out *via* ball milling, with ball bearings commonly made of hard ceramics such as yttria-stabilized zirconia (YSZ), alumina or stainless steel, but other types of mills such as planetary mills, vibration mills and rolling mills also exist.<sup>86</sup> Small amounts of solvent are sometimes added to reduce friction and improve the degree of mixing of solids.<sup>86</sup> Sonochemistry can be considered a subcategory of mechanochemistry and involves the use of ultrasound energy for chemical reactions.<sup>90</sup>

Mechanochemical synthesis is advantageous in that it can be performed in the absence of a solvent, which is usually a significant source of chemical waste, and requires relatively unsophisticated equipment. More interestingly, new modes of reactivity have been unlocked using sonochemical methods. For example, force-responsive polyadderene has been shown to undergo a cascade-type “unzipping” reaction to form polyacetylene upon sonication.<sup>91</sup>

**Table 1.1** Summary of green chemistry synthesis methods.

Methods	Products	Advantages	Limitations
Mechanochemistry	Ceramics, polymers, metal–organic frameworks, organic compounds	<ul style="list-style-type: none"> <li>– Facile and requires simple equipment</li> <li>– May be performed with limited/no solvent</li> </ul>	<ul style="list-style-type: none"> <li>– Undesirable temperature increase may arise during process</li> <li>– Metal contamination from ball bearings</li> </ul>
Microwave Irradiation	Metal nanoparticles, metal–organic frameworks, organic compounds	<ul style="list-style-type: none"> <li>– Rapid and uniform heating in high dielectric solvents</li> </ul>	<ul style="list-style-type: none"> <li>– Additional susceptor component required for heating low-dielectric solvents</li> </ul>
Photochemistry and Photocatalysis	Organic compounds, silver and gold nanoparticles	<ul style="list-style-type: none"> <li>– Light as a reaction component leaves no side products</li> <li>– Solar light in particular does not leave a carbon footprint</li> </ul>	<ul style="list-style-type: none"> <li>– Requires reactants or catalysts that are photoactive</li> </ul>
Electrochemistry and Electrocatalysis	Organic compounds, inorganic compounds/ceramics, metal nanoparticles	<ul style="list-style-type: none"> <li>– Unlocks new modes of reactivity and selectivity</li> <li>– Ability to precisely tune driving force (through applied potential) and reaction rates (through applied current) affords excellent control over size and morphology of metal nanoparticles</li> <li>– Potentially safer reactions as compared to thermal methods</li> </ul>	<ul style="list-style-type: none"> <li>– Additional electrolyte required for solution conductivity</li> <li>– Product must be separated from electrolyte</li> </ul>
Flow Chemistry	Organic compounds, colloidal nanocrystals	<ul style="list-style-type: none"> <li>– Good control over mass and heat transfer</li> <li>– Scale-up can be done by increasing the number of reactors (<i>numbering up</i>) or increasing the duration of flow (<i>scaling out</i>)</li> <li>– Complementary handle to thermal, photochemical and electrochemical methods</li> </ul>	<ul style="list-style-type: none"> <li>– Not amenable to heterogeneous reaction mixtures that can clog tubing</li> </ul>
Biological Synthesis	Metal nanoparticles	<ul style="list-style-type: none"> <li>– Avoids the need for harmful solvents and reactants</li> <li>– Control over morphology and size distribution of nanoparticles can be achieved by choice of microbe/plant species</li> </ul>	<ul style="list-style-type: none"> <li>– Resources and infrastructure to support growth of host organism required (<i>e.g.</i> culture media for microbes, potting soil or hydroponics for plants)</li> </ul>

The side effects unique to a mechanochemical approach must also be taken into consideration.<sup>86</sup> For example, the temperature within the reactor can rise over the course of milling, up to 200 °C or higher. Contamination originating from the wear and tear of the mill or ball bearings or residue from previous reactions can be an issue for applications requiring high purity. Finally, milling has also been known to lead to the deformation and loss of faceting of crystallites, as well as the aggregation of particles, both of which are processes that can have adverse effects on nanoparticulate products.

### 1.3.2 Microwave Irradiation

Microwave irradiation involves the application of electromagnetic radiation of between 0.3 and 300 GHz in frequency to a sample and is an alternative to traditional convective heating.<sup>92,93</sup> It works on the principle of *dielectric heating*, whereby dipoles in the molecules of the solvent or reactant align with the electric field component of incoming microwaves, causing molecular rotational velocities to increase and producing heat *via* molecular friction between rotating molecules.<sup>93</sup> Heating throughout the bulk of the sample then occurs *via* conduction or radiation. As microwaves are non-ionizing and are not in the energy range to break chemical bonds, any induced chemical transformations are purely a result of temperature increases.<sup>93</sup>

Microwave heating has the advantage of being fast compared to conventional heating.<sup>93</sup> Since microwave heating onsets throughout the bulk rather than the edges (volumetric heating), thermal gradients are also gentler and heating is more uniform, suppressing local temperature fluctuations and unwanted side reactions and engendering greater reproducibility in general. Simple microwave reactions can be performed in home microwave ovens, but more sophisticated models that include features such as stirring and temperature and pressure monitoring exist.<sup>93</sup>

However, microwave heating is limited to solvents that possess a net permanent dipole moment, such as water, ethanol, acetone and dimethylsulfoxide (DMSO). Solvents such as carbon tetrachloride and benzene lack a dipole moment and are essentially microwave transparent. In the case where the bulk solvent is not a microwave absorber, an additional component that is capable of microwave heating (*e.g.* inert metal oxides, carbides) known as a *susceptor* can be added as a heating element.<sup>92</sup>

Microwave synthesis has been broadly applied to both inorganic and organic syntheses.<sup>93,94</sup> Of note is the successful demonstration of its application to metallic NPs.<sup>95</sup> Due to more homogeneous thermal profiles compared to conventional heating, microwave irradiation has allowed the synthesis of NPs at smaller sizes, lower polydispersities, and a greater degree of crystallinity than conventional heating.

### 1.3.3 Photochemistry and Photocatalysis

Photochemistry commonly refers to the use of electromagnetic radiation in the visible or ultraviolet spectrum to drive chemical reactions.<sup>96,97</sup> Light is perhaps



one of the ‘cleanest’ reagents available, since it leaves no side products and, in the case of solar light, is readily available and does not leave a carbon footprint.<sup>96</sup> Photochemistry’s role in discussions of sustainability has traditionally been in renewable solar power generation,<sup>98,99</sup> but the development of direct photochemical synthesis and photoredox catalysts to drive organic transformation has made significant progress in recent years.<sup>100,101</sup> Direct photochemistry involves reactant molecules absorbing photons and entering a more reactive high-energy excited state,<sup>102</sup> whereas, in photoredox catalysis, photons are absorbed by catalysts, which are then activated and able to oxidize or reduce reactant molecules.<sup>101</sup> The development of photoredox catalysts was motivated by the drive to make use of freely available sunlight, since most organic molecules do not absorb light within the solar spectrum, but transition metal-based catalysts, such as tris(bipyridine)ruthenium(II) chloride, do.<sup>100</sup> Examples of photoredox catalysis include reductive dehalogenation and the  $\alpha$ -trifluoromethylation of aldehydes.<sup>103</sup>

In the context of nanotechnology, photochemical methods have most commonly been employed for silver NP synthesis due to the well-known photoreduction of  $\text{Ag}^+$  ions.<sup>104,105</sup> Gold nanorods of controllable aspect ratios have also been synthesized using  $\text{Ag}^+$  ions as photomediators.<sup>106</sup>

### 1.3.4 Electrochemistry and Electrocatalysis

Electrochemistry generally refers to the use of electricity to make and break chemical bonds.<sup>107</sup> Electrocatalysis refers to the use of a catalyst that is reduced or oxidized by the electrode prior to interaction with the substrate and may be either an extraneous species that is attached to the electrode or dissolved in an electrolyte solution or the electrode surface itself.<sup>107</sup> At the heart of much of modern electrochemical research is meeting sustainable development goals, whether that is in the form of higher-capacity, longer-lasting batteries for practical electric vehicle or grid storage applications or efficient electrolyzers capable of splitting water to produce hydrogen to use as renewable and clean fuel.<sup>108</sup>

Electrochemical methods have seen extensive use in manufacturing. The Hall–Héroult process for aluminum production and adiponitrile synthesis are perhaps the two most well-known and largest processes by production volume.<sup>109</sup> In the context of materials production, the electrodeposition of metals and compounds such as metal oxides is well known and exploited in industrial processes such as electroplating and electrowinning.<sup>107</sup>

However, a recent trend has been the general application of electrochemical methods to organic synthesis in the field that has come to be known as *organic electrosynthesis*, which involves the use of electrodes to supply oxidizing or reducing equivalents to substrate molecules in place of chemical agents.<sup>110–112</sup> Using electrochemistry to drive organic transformations has the advantages of avoiding hazardous redox reagents and their associated waste products, being able to generate reactive intermediates *in situ* and accessing new reactivities.<sup>110</sup> For example, a safer electrochemical

analog to the Birch reduction has been developed with excellent chemoselectivity and functional group tolerance.<sup>113</sup>

Electrochemistry has also been widely explored for nanomaterial synthesis. Nanostructures of metals such as copper, palladium, platinum, gold and metal oxides such as cerium oxide and tin oxide have been made with varying morphologies.<sup>114–117</sup> The electrosynthesis of nanostructured polymers has also been demonstrated but has been limited to electronically conductive polymers such as poly(3,4-ethylenedioxythiophene) (PEDOT), poly(aniline) (PANI), poly(pyrrole) (PPy) and poly(thiophene) (PT).<sup>118</sup> Resultant polymer morphologies (nanospheres, nanowires, nanotubes, nanosheets, *etc.*) can be controlled *via* monomer concentration, applied potential, applied current density or the use of templates.<sup>118</sup> Here, the green advantage offered by electrosynthesis is the substitution of harmful redox reagents with electrodes that can be polarized to different potentials to provide matching driving forces. In some cases, the discovery of new reactivity may also pave the way toward safer reactions compared to traditional chemistry.

### 1.3.5 Flow Chemistry

Flow chemistry refers to the use of continuously flowing streams of liquid in place of batch reactors to perform reactions.<sup>119,120</sup> Flow reactions are often performed in microreactors that contain microchannels with diameters of 1 mm and below and accommodate the use of small volumes of solvents and reagents. Due to the array of advantages afforded, flow methods have seen a rise in both academic and industrial interest in recent years. To begin, the narrow channels in flow microreactors in combination with flow rate and channel geometry control enable the implementation of well-defined flow regimes such as laminar, slug and annular flow, as opposed to the turbulent flow present in most, if not all, batch reactors.<sup>119</sup> This allows more precise control of heat transfer and reactant mixing times and is beneficial for reproducible and fine optimization of chemical reactions. For instance, side reactions in general and the thermal runaway of exothermic reactions in particular are suppressed due to more homogeneous thermal profiles. The larger surface-area-to-volume ratio in flow reactors also greatly increases phase transfer and reaction rates in multi-phasic systems involving gas–gas, gas–liquid and liquid–liquid systems, for example.<sup>119</sup> The scale-up of flow processes is easily achievable by either increasing the number of reactors running in parallel (*numbering up*) or simply running a process continuously for the needed duration (*scaling out*).<sup>119</sup>

Flow methods also work hand in hand with the other synthetic approaches outlined here, such as photochemistry and electrochemistry. In photochemistry, the yield is strongly dependent on the irradiation efficiency, which is dependent on the path length  $l$  according to the Beer–Lambert Law,  $A = \epsilon cl$ , where  $A$  is absorbance and  $\epsilon$  the molar extinction coefficient. Hence, flow reactors with narrow channels maximize the irradiation efficiency by exposing a greater proportion of reactants to incident light.<sup>121</sup>

In electrochemistry, energy losses can occur *via* resistive heating between the two electrodes due to solution resistance, which necessitates the addition of a supporting electrolyte to increase conductivity. Since this solution resistance  $R_{\text{solution}}$  is a strong function of distance ( $R_{\text{solution}} = d/\kappa$ , where  $d$  is the distance between driving electrodes and  $\kappa$  the solution conductivity), the short lateral distance across a flow microchannel is again beneficial for minimizing energy losses and can even accommodate forgoing the use of supporting electrolytes in this case.<sup>122</sup>

The precise control of reaction conditions afforded by flow chemistry is particularly advantageous for NP synthesis.<sup>123</sup> The bottom-up synthesis of NPs often requires the hot injection method, wherein organometallic reagents are added to a solvent after it has been heated up in order to favor homogeneous nucleation and produce monodisperse particles. However, this method is not amenable to scaling up using batch methods. The more precise heat and mass transfer control that flow chemistry offers allows better control over nucleation kinetics, enabling high-quality NP synthesis. In addition, the separation and purification of NPs can be streamlined by coupling the continuous flow process with a diafiltration setup, where the product stream is pumped through a nanoporous membrane, simplifying the recovery process and minimizing solvent use.<sup>124</sup> Unfortunately, despite its many advantages, flow chemistry is not without its drawbacks: heterogeneous reaction media, for example, can severely clog tubing.<sup>125</sup>

### 1.3.6 Biological Synthesis

Biological synthesis, or biosynthesis, entails the use of living organisms, often plants or microbes, as reactors for generating chemical products.<sup>126,127</sup> Biosynthesis using plants, for example, can be carried out *in vivo*, whereby the plant absorbs and processes reactant ions, or *in vitro*, whereby plant extract is used as the reaction medium.<sup>126</sup>

The biosynthesis of NPs has been shown to be possible in a variety of eukaryotic (fungi, algae and plants) and prokaryotic (bacteria) organisms and has been a burgeoning field.<sup>128</sup> To date, the biosynthesis of NPs of gold, silver, palladium and platinum, as well as an assortment of metal oxides such as cupric oxide, zinc oxide, and iron oxide, has been demonstrated.<sup>128</sup> The properties of biosynthesized NPs such as size, size distribution and shape can be tuned by controlling the organism type (which in turn influences the enzymes involved) and reaction conditions. An advantage of biosynthesis is the avoidance of harmful chemicals, which is an advantage in terms of waste avoidance and the safety profile of resultant NPs. Reducing agents such as sodium borohydride are substituted with naturally derived compounds such as polyphenols and catechins, and the use of organic solvents is avoided.<sup>128</sup> Different classes of organisms also pose different advantages and disadvantages: for instance, plant-based *in vivo* NP biosynthesis has been observed to occur at faster rates than in microbes, and using plants circumvents the need for culture media.<sup>126</sup> However, research is

still ongoing to better understand the mechanisms of NP formation and growth, especially using *in vivo* methods, and to improve control over the polydispersity of biosynthesized NPs.

## 1.4 Green and Sustainable Resources

Many of today's industrial processes were developed in the previous century, meaning that the choice behind many feedstocks and chemicals was driven by economic pragmatism. As a key example, the chemical industry heavily relies on crude petroleum not just as fuel but also as feedstock, with 96% of all organic chemicals made being derived from petroleum.<sup>129</sup> This is problematic for two reasons: the first being the continual net emission of greenhouse gases such as carbon dioxide from the incineration of carbon-containing waste exacerbating the climate change issue, and the second being the non-renewable nature of fossil fuels. Both reasons sound the death knell on the long-term sustainability of using crude petroleum as feedstock and indicate the urgent need to find sustainable and greener alternatives.

### 1.4.1 Renewable Resources – Biomass and Biomolecules

Biomass has and will continue to play a major role as an alternative source of chemical feedstock. Biomass can be a source of renewable and new precursors<sup>130</sup> that are nominally carbon neutral due to the carbon present having originally been sourced from the atmosphere *via* the photosynthetic process in plants.<sup>126</sup> It is hence inherently compatible with green chemistry, since it already adheres to a number of its principles: biomass is, by definition, biodegradable and does not leave persistent contaminants in the environment; it is far less likely to be toxic in general compared to the man-made chemicals used in many of today's processes; it is renewable within timescales relevant for human societies.

Polysaccharides are comprised of a group of macromolecules called carbohydrates that consist of repeating monosaccharides. Naturally occurring polysaccharides, such as cellulose, pectin, alginate and chitin, are structural building blocks derived from plants, animals or microbes. It was reported that the interest in polysaccharides has increased significantly with the goal of designing and developing novel renewable materials for future applications. Polysaccharides possess several advantages, such as low cost, hydrophilicity, stability, safety, biodegradability and non-toxicity. The presence of several functional groups such as hydroxyl, carboxyl and amino groups on polysaccharides allows for easy chemical modifications resulting in many types of polysaccharide derivatives. In recent years, nanomaterials derived from natural polysaccharides have received significant interest from academic and industrial research laboratories.

Lignin constitutes about 15–35% of lignocellulosic biomass obtained from the processes of wood and paper processing industries, and it is the second most abundant natural material on earth. It consists of cross-linked

polyphenolic structures, which provide structural support for plants, and it plays an important role in the formation of cell walls. Lignin has been long known to be environmentally friendly and possesses antioxidant and anti-UV properties, as well as good antimicrobial activities. This makes lignin exceptionally interesting and a strong candidate for the development of new and sustainable nanomaterials.

Polynucleotides and polypeptides are also important and abundant biomacromolecules in nature. Proteins, composed of amino acids, are the most versatile macromolecules in the body and possess many functionalities. One of the unique characteristics of polypeptides is their self-organization behavior, where the polymer chains can self-assemble into secondary, tertiary or quaternary structures due to the amphiphilic characteristics of various functional groups on the polymer backbone. On the other hand, nucleic acids are the most important biological macromolecules found in living organisms. The functions of nucleic acids are mainly encoding, transmitting and expressing genetic information in living systems. They include DNA (deoxyribonucleic acid) and RNA (ribonucleic acid). DNAs can also be self-assembled *via* bottom-up construction to serve as scaffolds for many inorganic molecules and biopolymers.

## 1.4.2 Renewable Resources – Waste

In the context of sustainable development, the massive and increasing volumes of waste modern industrial societies generate a genuine cause for concern.<sup>131</sup> Improper disposal of waste can lead to its persistence in the natural environment for prolonged periods of time, having potentially devastating effects. The pollution of oceans by plastic waste and its repercussions on wildlife is a sobering reminder of this. Incineration, another popular tactic, is also an inherently unsustainable method of waste management, since it can release toxic compounds into the environment and is a significant contributor to carbon emissions.<sup>132</sup> Hence, efforts to achieve sustainable development must reconcile with the status quo of waste generation. The exploitation of waste as a resource for the chemical industry is a tremendous opportunity for reassimilating waste products into supply chains and making progress toward a more sustainable circular economy model.<sup>131</sup>

### 1.4.2.1 Carbon Dioxide

Carbon dioxide has increasingly been viewed as an attractive feedstock for carbon-containing products as it is the terminal product of carbon oxidation and its incorporation theoretically mitigates the carbon footprint of the product (barring considerations of energy input).<sup>133</sup> Carbon dioxide has been used as a reagent for the production of bicarbonate and carbonate salts, as well as in the electrocarboxylation of organic compounds such as halides.<sup>133</sup> In addition, the synthesis of copolymers incorporating carbon dioxide such as polycarbonates and polyurethanes has been shown to be

possible with the use of reactive monomers such as cyclohexene oxide, hence overcoming the thermodynamic stability of carbon dioxide.<sup>133</sup> Supercritical carbon dioxide has also found use as an environmentally friendly, non-toxic solvent with good solvating properties and has been used for decaffeination and in dry cleaning.

Though exciting, the abovementioned developments represent specialized applications that represent a small market share of all carbon-derived chemicals. In terms of upending the current petroleum-dependent, net carbon-emitting paradigm, the valorization of carbon dioxide into higher-order hydrocarbons has been gaining significant traction.<sup>134,135</sup> The electrochemical conversion of carbon dioxide allows the process to be coupled with renewable sources of electricity (such as solar and wind) and avoids the need for fossil fuel-derived energy.<sup>136,137</sup> There is promise for the production of carbon monoxide (a component of the industrially useful syngas), ethylene (useful for plastic production), and various alcohols and longer alkanes (useful as solvents and fuels) from carbon dioxide, but challenging issues such as product selectivity (especially for higher-order products) and the ability to make energy-efficient electrolyzers that can run at practical current densities remain.<sup>138</sup>

#### 1.4.2.2 Plastic Recycling

*Plastic* is a blanket term for a wide-ranging assortment of versatile polymer-based materials, such as poly(vinyl chloride), poly(styrene) and poly(ethylene) of varying densities. Traditionally, plastic waste has been managed in one of three ways: mechanical recycling, whereby plastics are shredded, melted and reconstituted; feedstock recycling, whereby plastics are converted into hydrocarbons and hydrogen gas; and energy recovery, whereby plastics are incinerated at power plants to generate electricity.<sup>139</sup> Incineration is increasingly becoming an unviable option due to its high carbon footprint and concerns regarding the release of toxins such as dioxins, furans, mercury and polychlorinated biphenyls.<sup>140</sup> Mechanical recycling is on paper an attractive option, but due to the variety of plastics tailor made with different thermal, chemical and mechanical properties for different applications, there is a need to sort plastics by type prior to their disintegration and remolding, as mixing different polymers leads to inferior mechanical properties.<sup>141</sup> Even so, the properties of recycled plastics are still compromised after several cycles. This makes mechanical recycling inherently labor intensive and inefficient, disincentivizing the process.<sup>142</sup>

Feedstock recycling entails the pyrolysis of plastics to produce hydrocarbons and hydrogen gas<sup>143,144</sup> but requires high temperatures (500–800 °C) and emits significant quantities of carbon dioxide,<sup>145</sup> leaving the viability of the process in question for now. Recently, there has been promising research on the solar-driven reforming of various plastics using a photocatalyst at ambient temperature and pressure as a more sustainable alternative.<sup>146</sup>

Chemical recycling is an emerging concept that involves chemically degrading plastic polymers into their constituent monomers, which can then be used as the starting material to produce pristine, high-quality products.<sup>139</sup> However, this method is only amenable to condensation polymers with reactive linkages, such as polyesters and polyurethanes, and is not applicable to most addition polymers such as poly(styrene) and poly(ethylene). The urgent need for a sustainable plastics program worldwide has spurred campaigns for designing new types of chemically recyclable plastics to overhaul existing ones.<sup>142</sup> Design strategies have been inspired by dynamic covalent chemistry, which features linkages that can be reversibly broken and formed, such as imines, Diels–Alder adducts and hemiaminals; self-immolative polymers that undergo a cascade reaction and completely disintegrate into their constituent polymers when exposed to a trigger, such as heat or light; and vitrimer networks, which are able to respond to stimuli without depolymerizing.<sup>142</sup> Assuringly, there has also been progress in the development of catalysts for the chemical recycling of challenging existing plastics such as polyethylene.<sup>147</sup>

### 1.4.2.3 Electronics Recycling

With an annual growth rate of 3–5%, electronic waste or *e-waste* represents the fastest-growing type of municipal waste worldwide.<sup>148</sup> This trend is likely to continue with the current pace of technological advancement in consumer devices such as smartphones and computers. Unfortunately, effective and large-scale recycling programs do not exist even in developed nations, and recycling rates are low, with only 17% of all *e-waste* recycled in 2019.<sup>149</sup> Instead, *e-waste* is often exported to developing countries, where it is simply incinerated in open air or recycled in premises ill equipped to handle the toxic chemicals released, compromising the health and safety of the residents of that community.<sup>149</sup> For example, circuit boards are often crudely recycled by burning to recover copper, but this also releases toxic mercury and cadmium vapors.<sup>149</sup>

Due to the large cumulative quantities of precious metals such as gold hidden within used electronics, *e-waste* has been labeled an “urban mine”, and it is estimated that around US\$10 billion worth of precious metals is currently buried within the global *e-waste* stream.<sup>149</sup> However, *e-waste* recycling is fraught with difficulty. For one, the valuable precious metals (gold, palladium, platinum and ruthenium) are found at minute ppm-level quantities within the bulk material of the appliance, which is often composed mostly of plastic, copper, aluminum and iron.<sup>150</sup> Sorting through and dismantling electronics is also time- and labor-intensive, and the need to provide facilities that are able to handle the toxic vapors generated adds to the overall cost.<sup>149</sup> Hence, *e-waste* recycling businesses require sufficiently large economies of scale to turn a profit.

Current methods to recover metals in *e-waste* recycling are also problematic. Hydro- and pyrometallurgy represent the current paradigm, but

these are highly energy-intensive processes that also generate significant amounts of toxic liquid and gaseous waste.<sup>151</sup> Fortunately, there has been significant progress in developing greener alternative methods, such as bioleaching, the use of supercritical carbon dioxide as extraction solvent, and electrochemistry.<sup>151</sup> An example is the use of electrochemistry to recover rare earth metals such as europium, neodymium, gadolinium and scandium using carbon nanotubes *via* their selective electrodeposition at different applied potentials.<sup>152</sup>

Needless to say, the precious and rare earth metals present in e-waste are highly relevant for nanotechnological applications, and improvements in e-waste recycling create downstream benefits in securing a reliable stream of raw materials for sustainable nanotechnology.

## 1.5 Environmental Impact and Life Cycle of Nanotechnology

Nanotechnology can be considered the golden child of scientific advancements in our modern era. The major breakthroughs in this research field have revolutionized the understandings of science and laid the foundations for new possibilities. Thereafter, a plethora of research areas and applications of nanotechnology skyrocketed. Its potential role in progressing science and economic prosperity attracted not only commercial but also political attention. Widespread efforts to create a positive impact through nanotechnology undeniably raise concerns regarding its consequences and adverse effects, thus raising the question of, is it really the better choice?

The presence of nanotechnology is ubiquitous in our daily life, albeit unnoticeable. In approximately half a century, this emerging technology has rooted itself in various industrial applications and established advanced solutions. The extent of its reach comprises a diversity of fields, including cosmetic, electronic, medical, food packaging, automotive and sensing. Nanotechnology boasts many advantages to each unique application. For example, silver NPs (AgNPs) are an active constituent found in many consumer products due to their wide coverage of antifungal, antimicrobial and antiviral properties.<sup>153,154</sup> In the medical field, NPs are combined with insoluble drugs to facilitate drug delivery in the body.<sup>155</sup> In the early 2000s, nanomaterials were manufactured in hundreds of thousands of tonnes, and the global market of them was estimated to reach an optimistic value of 5 million tonnes in 2025.<sup>156</sup>

According to the European Commission (EC), an estimated US\$67 billion has been invested in nanotechnology by governments around the world since then. In the Framework Programmes 7 (a research funding initiative supported by the EC), nanotechnology makes up the largest fraction, with an estimated value of €896 million (2007–2011).<sup>157</sup> It is no surprise that companies are investing in nanoscience and securing this as a competitive edge over others. Despite its significance, a recent survey conducted in five selected European countries found that the general awareness of



nanotechnology and its effect on our daily lives is relatively low.<sup>158,159</sup> This can be similarly observed in other parts of the world, where a large percentage of citizens know very little about nanotechnology.<sup>160-162</sup> On the other hand, countries such as China and Singapore demonstrated relatively high awareness of nanotechnology.<sup>163,164</sup> Public sentiments toward nanotechnology are generally positive and cautious.

It is imperative to bring awareness of nanotechnology to the community and ensure members of the public can make informed decisions about their choices. Nanotechnology is commonly defined as the control of matter in the nanoscale range of approximately 1–100 nm.<sup>165</sup> With the rapid development of nanotechnology, the rate of utilization seems to have outpaced the necessary evaluations and regulations required to monitor their usage and effects.

### 1.5.1 Sustainable Evaluation of Nanotechnology

As part of the key enabling technologies under Horizon 2020, Europe actively sees this domain as an important field that would play a crucial role in the European industries for the many years to come.<sup>166</sup> Sustainability is quickly becoming the key strategic priority for the government and private stakeholders. The conscious assessment of industrial processes from the extraction of raw materials to their end life provides crucial information to conceptualize a sustainable future. Nanotechnology itself is considered by many in the industry a promising solution toward a green future. This can be attributed to the size of the nanoscale materials, which would naturally tackle the issues of limited resources, space and costs. However, this field has yet to fully mature and the implications of such use are yet to be known.

Manufacturing nanoproducts involves either a top-down or bottom-up approach.<sup>167</sup> It is commonly believed that top-down methods such as carving, lithography and etching would generate more waste. The bottom-up approach is still in its infancy but with good promises to minimize waste. To ensure the sustainability potential of nanotechnology, various studies have been made to evaluate the manufacturing considerations and the adverse impacts on the environment and human health.

#### 1.5.1.1 Industrial Ecology

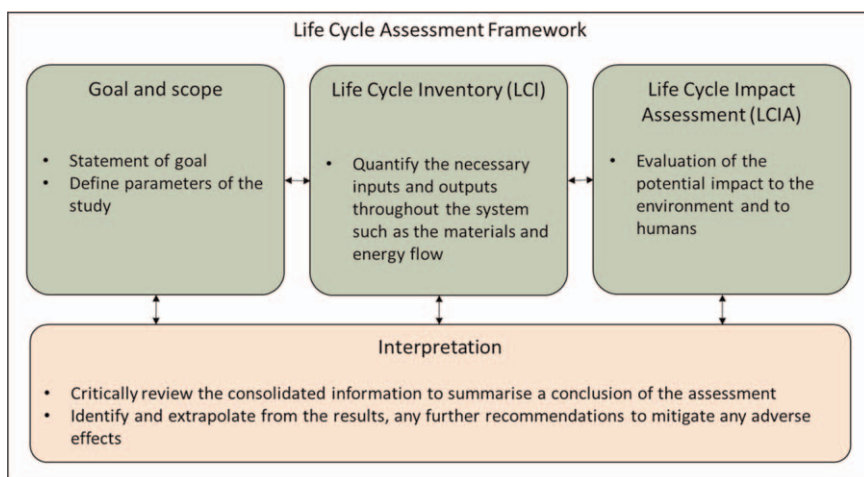
The systems-based approach of industrial ecology (IE) covers multidisciplinary fields and takes the engineering sciences, economic values and environmental studies into concern. It provides an overview of the relationship between industrial systems and the environment. This method focuses on developing a circular system where one aims to optimize the output while maximizing recycling of the by-products and minimizing waste materials.<sup>167-169</sup> Suffice to say, this approach addresses the issues of sustainability by studying the industry through multiple perspectives. IE attempts to evaluate the processes and flows in order to ensure a sustainable and green industry.<sup>167</sup> A defining characteristic of IE is the use of systems to

categorize the different aspects in the industry and identify the relationships in between. Ideally, all waste outputs from a process can be inputs for other processes, thus resulting in a closed-loop system. The concept of a circular economy originates from the idea of IE and industrial metabolism.<sup>170</sup> IE comprises many tools to help with the evaluation of a particular industry, including but not limited to life cycle assessment (LCA), material flow analysis (MFA), substance flow analysis (SFA) and technology assessment (TA). These methods are generally complementary to each other to comprehensively assess the industry.

### 1.5.1.2 Life Cycle Assessment

A notable methodology is LCA, which is often deployed to evaluate the environmental impact of a product or technology from the extraction of raw materials to its end life. The most holistic assessment is the cradle-to-grave assessment, which takes into account the entire life cycle of a product as opposed to other variants of LCAs.<sup>171</sup> It is tremendously challenging to establish a well-rounded framework applicable to all products of nanotechnology due to their diverse applications. Manufacturing nanotechnology in the industry can be classified into two groups: nanotechnology as a singular product and nanotechnology as a supporting role in a product. By definition, only an intentionally produced material with at least 50% of it made up of NPs that have one or more external dimensions in the nanoscale range of 1–100 nm is considered a manufactured nanomaterial.<sup>172</sup>

There are four main phases of an LCA in accordance with the existing standards ISO 14040 and 14044, as indicated in Figure 1.2.<sup>173–175</sup> The International Organization for Standardization (ISO) uphold standards that are considered the benchmark of standardized procedures to accurately



**Figure 1.2** A summarized LCA framework involving the four main phases of the assessment.

assess the life cycle of a product. The most critical aspect is to determine the functional unit and the system boundaries at the goal and scope phase.<sup>176</sup> In the second phase, the units are expanded to quantitatively identify the necessary value of materials, energy and products in the process flow. Subsequently, in the Life Cycle Impact Assessment (LCIA) phase, potential toxicology impact on the ecosystem and human health is identified and derived from the Life Cycle Inventory (LCI). Finally, the last phase interlinks all other three phases to summarize and conclude all findings. The system boundaries should clearly be defined in phase 1 to understand the extent of the assessment. The structured methodology builds on a relative approach where all inputs and outputs are critical to the function of the product.

However, conducting a comprehensive cradle-to-grave assessment is challenging as there are too many uncertainties and variables to the technology.<sup>177</sup> Table 1.2 summarizes a number of recent LCA studies in various fields of nanotechnology. The study of an LCA commonly involves a few key databases to model the potential impacts on the environment, such as Ecoinvent 3, European reference Life Cycle Database (ELCD) and the US Life Cycle Inventory (USLCI).<sup>178</sup> The Cumulative Energy Demand (CED) and the Tool for the Reduction and Assessment of Chemical and Other Environmental Impacts (TRACI 2.1) contribute to the impact assessment phase.<sup>178</sup>

There are a few shortcomings that can be constantly highlighted from these studies, for example, the uncertainties in the end-of-life (EOL) phase. The release of NPs to the environment during their use or the EOL phase is a pressing concern. Large assumptions have been made in LCA studies, such as that these NPs are released as unadulterated particles. However, in reality, NPs may undergo further processes that can transform their properties and interactions with the surroundings.<sup>186</sup> There is also very little understanding of the waste management process and release of NPs.<sup>186,187</sup> Despite its limitations, LCA provides a comprehensive analysis to identify environmental hotspots and a platform for comparison to other technologies.

**Table 1.2** LCA studies on various fields of nanotechnology.

S/N	Research group, year	Technology	System boundary	Ref.
1	Llyod <i>et al.</i> , 2005	Nanofabrication of platinum-group metals	Cradle to gate	179
2	Anctil <i>et al.</i> , 2010	Fullerene for solar cells	Cradle to grave	180
3	Pizza <i>et al.</i> , 2014	Graphite nanoplatelets (GNP) production	Cradle to grave	181
4	Arvidsson <i>et al.</i> , 2014	Graphene production	Cradle to gate	182
5	Yasin <i>et al.</i> , 2019	Silver nanoparticles in the textile industry	Gate to grave	183
6	Moro <i>et al.</i> , 2020	Titanium dioxide nanoparticles in natural or recycled mortars	Cradle to gate	184
7	Weyell <i>et al.</i> , 2020	Laser-induced production of oxidic nanoparticles	Cradle to gate	185
8	Temizel-Sekeryan <i>et al.</i> , 2020	Silver nanoparticles production	Cradle to gate	178

### 1.5.1.3 Material and Substance Flow Analysis

MFA and SFA are both important methods to assess the sustainability characteristics of an industry. Both types of assessments are based on the mass balance principle.<sup>188</sup> SFA is utilized to quantify the input and output flow of a particular substance in production. It focuses on the usage effect of the necessary substance in a region or its entire life cycle and thus is able to identify hidden hotspots of unexpected flow.<sup>189</sup> This is significantly useful for waste management systems to account for the movement of hazardous compounds. The roles of MFA and SFA can significantly strengthen and complement other analyses to develop a holistic evaluation.<sup>190</sup> According to Udo de Haes *et al.*, MFA is a broader concept covering both SFA and bulk flow of materials.<sup>191</sup>

In a study by Arvidsson *et al.*, it was found that different uses of titanium dioxide (TiO<sub>2</sub>) NPs in paint, sunscreen and self-cleaning cement result in different analysis outcomes.<sup>192</sup> The emission of TiO<sub>2</sub> NPs is the highest from sunscreen despite the higher mass flows in the other applications.<sup>192</sup> Wang *et al.* modeled the flow of nanometal oxides and quantum dots (QDs) to the environment and quickly discovered that different waste management techniques between countries was a limitation to the assessment.<sup>193</sup> As highlighted by the authors, there are existing gaps in the current knowledge of NPs. However, through modeling the flow of NPs in an industry, the study can be a foundation to build on for further assessments and to support crucial policy-making.

### 1.5.1.4 Technology Assessment

This assessment aims to evaluate new technology to forecast potential futures and repercussions that it might face. This will provide information on critical decision making concerning the technology and implementing it in society.<sup>194,195</sup> Through the combinations of research assessments, TA is able to convey the consequences of the technology and provide knowledge to better design strategies. Often it has been regarded as a significant step to shape the technology's acceptance in the societal aspect, for example, regulations and public sentiments.<sup>194,196</sup> In emerging technologies such as nanotechnology, this assessment plays a major role in its future.

The TA development has grown over the years, with various modifications being made to this assessment and adopting TA for sustainability assessments.<sup>197,198</sup> A prominent example of the further development of TA is the constructive technology assessment (CTA) and the real-time technology assessment (RTTA).<sup>197,198</sup> Retèl *et al.* assessed the introduction of nanotechnology in oncology through a modified TA:CTA.<sup>199</sup> In order to study the dynamics and impact of nanotechnology, it is recommended to start during the early development phase. This projects potential roadblocks in the system and facilitates decision making.

### 1.5.2 Impact on the Environment and Human Health

The exponential growth of nanotechnology has led to various benefits and solved multiple limitations. However, its fast-expanding reach brings about complications and uncertainties to its impact on the environment and human health. This is especially critical when it comes to selected industries such as healthcare, agriculture and food and beverage. The risks and hazards of these NPs are an immense challenge to identify in the ecosystem and the biological system.<sup>200,201</sup> Ironically, the desirable small nature of nanotechnology creates many uncertainties in its behavior at the EOL phase. Little is known about the toxicity and exposure of NPs to the environment or to humans.

Various modeling studies have been made to understand the direction and flow of the particles. However, these studies are with assumptions that the NPs maintain the same chemical state as that during the production.<sup>186</sup> Their physicochemical properties may undergo transformations and form interactions that may contribute to their toxicity. According to Oberdörster *et al.*, the properties of NPs may modify chemical responses and cellular interactions in the biological systems.<sup>202</sup> In addition, exposure to NPs can involve many different channels such as inhalation, ingestion and skin contact.<sup>203</sup> The risks of short-term and long-term exposure to NPs remain in the dark due to the limited data. Conventional methods to monitor exposure typically utilize the mass and bulk chemistry but this may not be accurate for NPs.

Hence, studies have been made to understand the direct impact of nanotechnology on the environment. According to Ottoni *et al.*, increasing concentrations of AgNP had harmful side effects on the germination of rice seedlings.<sup>204</sup> The effects of NPs on soil have also been investigated by Kumar *et al.* Unfortunately, all manufactured silver, silica and copper NPs had a certain degree of toxic impact on Arctic soil.<sup>205</sup> Similar studies were also conducted on animals and it was found that the increase in doses of AgNP greatly affected the oxygen consumption in zebrafish.<sup>204</sup> Suffice to say, studies have shown that there is a detrimental direct impact of NPs to the environment. However, the effect of manufactured NPs in reality is difficult to comprehend. Their impact on human health is exceedingly critical due to the direct application of NPs on people.

Rushton *et al.* have developed a new approach to predicting toxicity through the analysis of *in vitro* and *in vivo* studies.<sup>206</sup> Here, the results demonstrated the ability of NPs (copper-, titanium dioxide – and gold-based NPs) to produce reactive species (ROS) that would lead to oxidative stress in the biological environment.<sup>206</sup> In the human body, the translocation of the NPs is largely unknown and would be in low quantities. However, accumulation over time may change and affect the internal organs. The combination of properties in NPs such as particle size, surface area and ROS generation are the main suspects for inducing lung damage.<sup>207</sup> Another concern of nanotoxicity is dermal exposure and penetration, especially in the current application of AgNP and titanium dioxide NPs (TiO<sub>2</sub>) in cosmetics and consumer care. *In vitro* studies on the penetration of AgNP have demonstrated

localization of these particles at the *stratum corneum*.<sup>208,209</sup> Furthermore, the surface charge of AgNP was not found to drastically affect this migration on skin samples.<sup>210</sup> Several studies have concluded that damaged and wounded skin will facilitate the penetration of AgNP, but it will not interfere with the healing rate of the skin.<sup>211,212</sup> However, a theoretical study by Watkinson *et al.* showed that NPs are not large enough to pass the skin barrier by passive diffusion or absorption.<sup>213</sup> The behavior of NPs varies depending on their characteristics. Therefore, standardized protocols would be a step forward to understand and manage the impact of NPs on the body.

## 1.6 Perspectives and Conclusion

At present, there is plenty of research about nanotechnology and its possible applications. It appears researchers believe that nanotechnology has not been fully exploited as they continue to push the frontier of science and technology with further development in the field. In view of the government's efforts to address the issue of sustainability, nanotechnology can contribute to the protection of the environment. For instance, the enhanced sensitivity and reactivity that comes with the small scale would be useful for monitoring and treating pollution. Additionally, it would be a big leap if nanotechnology could transform the current manufacturing processes to be leaner with fewer pollutants and more effective processes. While nanotechnology seems very promising, it is also necessary for us to acquire further knowledge of its interaction with the environment to ensure that the implementation is safe.

Also there have been various studies to address the importance of nanotechnology and its impact on our economy, our environment and our health. Although there are still gaps and assumptions made in the research, the emphasis is on understanding and the motivation to uncover the unknown sets us in the correct direction. Long-term studies on the exposure and effect of nanotechnology on the surroundings are one way we can shed light on this aspect. Further scientific studies and classification of NPs are crucial to compare their physicochemical properties across different applications. With a sustainable future in mind, it is ideal to develop a roadmap to identify the positive and negative contributions of nanotechnology. This would contribute to decision making and policy developments at national levels.

## References

1. B. Karn and S. S. Wong, in *Sustainable Nanotechnology and The Environment: Advances and Achievements*, ACS Publications, 2013, pp. 1–10.
2. C. Recordati, M. De Maglie, S. Bianchessi, S. Argenti, C. Cella, S. Mattiello, F. Cubadda, F. Aureli, M. D'Amato and A. Raggi, *Part. Fibre Toxicol.*, 2015, **13**, 12.
3. M. Chen, Y. He, Q. Ye, X. Wang and Y. Hu, *Sol. Energy*, 2019, **182**, 340–347.

4. Y. Liu, G. Sun, D. Wu and S. Dong, *J. Nanopart. Res.*, 2019, **21**, 161.
5. S. Ahmed and W. Ali, *Green Nanomaterials: Processing, Properties, and Applications*, Springer Nature, 2020.
6. S. Ahmed and C. M. Hussain, *Green and Sustainable Advanced Materials: Applications*, John Wiley & Sons, 2018.
7. G. Das, J. K. Patra, S. Paramithiotis and H.-S. Shin, *Int. J. Environ. Res. Public Health*, 2019, **16**, 4848.
8. V. Mohanraj and Y. Chen, *Trop. J. Pharm. Res.*, 2006, **5**, 561–573.
9. J. Cheng, Y.-J. Gu, S. H. Cheng and W.-T. Wong, *J. Biomed. Nanotechnol.*, 2013, **9**, 1362–1369.
10. Z. Xiong, C. S. Alves, J. Wang, A. Li, J. Liu, M. Shen, J. Rodrigues, H. Tomás and X. Shi, *Acta Biomater.*, 2019, **99**, 320–329.
11. B. Du, X. Gu, X. Han, G. Ding, Y. Wang, D. Li, E. Wang and J. Wang, *ChemMedChem*, 2017, **12**, 1768–1775.
12. J.-A. Park, H.-K. Kim, J.-H. Kim, S.-W. Jeong, J.-C. Jung, G.-H. Lee, J. Lee, Y. Chang and T.-J. Kim, *Bioorg. Med. Chem. Lett.*, 2010, **20**, 2287–2291.
13. R. Kotcherlakota, S. Nimushakavi, A. Roy, H. C. Yadavalli, S. Mukherjee, S. Haque and C. R. Patra, *ACS Biomater. Sci. Eng.*, 2019, **5**, 5439–5452.
14. K. Sztandera, M. Gorzkiewicz and B. Klajnert-Maculewicz, *Mol. Pharm.*, 2018, **16**, 1–23.
15. Y. Shi, R. Jiang, M. Liu, L. Fu, G. Zeng, Q. Wan, L. Mao, F. Deng, X. Zhang and Y. Wei, *Mater. Sci. Eng. C*, 2017, **77**, 972–977.
16. X. Zhang, K. Wang, M. Liu, X. Zhang, L. Tao, Y. Chen and Y. Wei, *Nanoscale*, 2015, **7**, 11486–11508.
17. K. Tamarov, S. Näkki, W. Xu and V.-P. Lehto, *J. Mater. Chem. B.*, 2018, **6**, 3632–3649.
18. S. Naahidi, M. Jafari, F. Edalat, K. Raymond, A. Khademhosseini and P. Chen, *J. Control. Release*, 2013, **166**, 182–194.
19. E. B. Ehlerding, F. Chen and W. Cai, *Adv. Sci.*, 2016, **3**, 1500223.
20. J. Liu, M. Yu, C. Zhou and J. Zheng, *Mater. Today*, 2013, **16**, 477–486.
21. Y.-H. Chiang, C.-K. Shih, A.-S. Sie, M.-H. Li, C.-C. Peng, P.-S. Shen, Y.-P. Wang, T.-F. Guo and P. Chen, *J. Mater. Chem. A*, 2017, **5**, 25485–25493.
22. A. Menazea, *Radiat. Phys. Chem.*, 2020, **168**, 108616.
23. A. Betke and G. Kickelbick, *Inorganics*, 2014, **2**, 1–15.
24. C. Rao, H. R. Matte, R. Voggu and A. Govindaraj, *Dalton Trans.*, 2012, **41**, 5089–5120.
25. A. M. Mousa, O. A. A. Aziz, O. E. Al-Hagar, M. A. Gizawy, K. F. Allan and M. F. Attallah, *Appl. Radiat. Isot.*, 2020, **166**, 109389.
26. R. Kumar and S. Lal, *J. Nanomater. Mol. Nanotechnol.*, 2014, **11**, 2.
27. X. Zhen, Y. Tao, Z. An, P. Chen, C. Xu, R. Chen, W. Huang and K. Pu, *Adv. Mater.*, 2017, **29**, 1606665.
28. B. B. Srivastava, S. K. Gupta and Y. Mao, *CrystEngComm*, 2020, **22**, 2491–2501.
29. R. Kang, X. Dou, H. Lian and Y. Li, *J. Am. Ceram. Soc.*, 2020, **103**, 258–265.

30. Y. Huang, K. Jiang, X. Zhang and E. J. Chung, *Bioeng. Transl. Med.*, 2020, **5**, e10173.
31. Z. Long, M. Liu, K. Wang, F. Deng, D. Xu, L. Liu, Y. Wan, X. Zhang and Y. Wei, *Mater. Sci. Eng. C*, 2016, **66**, 215–220.
32. Y. Cai, P. Liang, Q. Tang, X. Yang, W. Si, W. Huang, Q. Zhang and X. Dong, *ACS Nano*, 2017, **11**, 1054–1063.
33. Z. Long, M. Liu, R. Jiang, Q. Wan, L. Mao, Y. Wan, F. Deng, X. Zhang and Y. Wei, *Chem. Eng. J.*, 2017, **308**, 527–534.
34. F. Debuigne, L. Jeunieu, M. Wiame and J. B. Nagy, *Langmuir*, 2000, **16**, 7605–7611.
35. F. Wu, L. Chen, L. Yue, K. Wang, K. Cheng, J. Chen, X. Luo and T. Zhang, *ACS Appl. Mater. Interfaces*, 2019, **11**, 21408–21416.
36. R. Jiang, M. Liu, T. Chen, H. Huang, Q. Huang, J. Tian, Y. Wen, Q.-Y. Cao, X. Zhang and Y. Wei, *Dyes Pigm.*, 2018, **148**, 52–60.
37. H. Valo, L. Peltonen, S. Vehviläinen, M. Karjalainen, R. Kostiaainen, T. Laaksonen and J. Hirvonen, *Small*, 2009, **5**, 1791–1798.
38. C. K. Lim, A. A. Popov, G. Tselikov, J. Heo, A. Pliss, S. Kim, A. V. Kabashin and P. N. Prasad, *Adv. Opt. Mater.*, 2018, **6**, 1800164.
39. M. Gangopadhyay, S. K. Mukhopadhyay, S. Gayathri, S. Biswas, S. Barman, S. Dey and N. P. Singh, *J. Mater. Chem. B.*, 2016, **4**, 1862–1868.
40. C. Li, W. Zhang, S. Liu, X. Hu and Z. Xie, *ACS Appl. Mater. Interfaces*, 2020, **12**, 30077–30084.
41. S. Shahrokhian, L. Naderi and M. Ghalkhani, *Electroanalysis*, 2015, **27**, 2637–2644.
42. N. Soltani, N. Tavakkoli, Z. S. Mosavimanesh and F. Davar, *C. R. Chim.*, 2018, **21**, 54–60.
43. S. Ranjbar and S. Shahrokhian, *Bioelectrochemistry*, 2018, **123**, 70–76.
44. E. Asadian, M. Ghalkhani and S. Shahrokhian, *Sens. Actuators, B*, 2019, **293**, 183–209.
45. X. Ouyang, J. Liu, J. Li and R. Yang, *Chem. Commun.*, 2012, **48**, 88–90.
46. D. Lu, R. Tao and Z. Wang, *Front. Chem. Sci. Eng.*, 2019, **13**, 310–323.
47. D.-W. Zheng, B. Li, C.-X. Li, J.-X. Fan, Q. Lei, C. Li, Z. Xu and X.-Z. Zhang, *ACS Nano*, 2016, **10**, 8715–8722.
48. M. Ajmal, U. Yunus, A. Matin and N. U. Haq, *J. Photochem. Photobiol., B*, 2015, **153**, 111–120.
49. A. Molkenova, A. Toleshova, S.-J. Song, M. S. Kang, A. Abduraimova, D.-W. Han and T. S. Atabaev, *Mater. Lett.*, 2020, **261**, 127012.
50. S. K. Bhunia, A. Saha, A. R. Maity, S. C. Ray and N. R. Jana, *Sci. Rep.*, 2013, **3**, 1–7.
51. S. Bayda, M. Hadla, S. Palazzolo, V. Kumar, I. Caligiuri, E. Ambrosi, E. Pontoglio, M. Agostini, T. Tuccinardi and A. Benedetti, *J. Control. Release*, 2017, **248**, 144–152.
52. G. Zuo, A. Xie, X. Pan, T. Su, J. Li and W. Dong, *ACS Appl. Nano Mater.*, 2018, **1**, 2376–2385.



53. C. Liu, P. Zhang, X. Zhai, F. Tian, W. Li, J. Yang, Y. Liu, H. Wang, W. Wang and W. Liu, *Biomaterials*, 2012, **33**, 3604–3613.
54. Y. K. Kim, S. M. Sharkar, I. In and S. Y. Park, *Carbon*, 2016, **103**, 412–420.
55. P. Yang, J. Zhao, J. Wang, B. Cao, L. Li and Z. Zhu, *J. Mater. Chem. A*, 2015, **3**, 136–138.
56. M. C. Ortega-Liébana, J. L. Hueso, S. Ferdousi, K. L. Yeung and J. Santamaria, *Diamond Relat. Mater.*, 2016, **65**, 176–182.
57. S. Chandra, P. Das, S. Bag, D. Laha and P. Pramanik, *Nanoscale*, 2011, **3**, 1533–1540.
58. F. Kazemzadeh, R. Malekfar and P. Parvin, *J. Phys. Chem. Solids*, 2017, **104**, 252–256.
59. W. Lu, X. Qin, S. Liu, G. Chang, Y. Zhang, Y. Luo, A. M. Asiri, A. O. Al-Youbi and X. Sun, *Anal. Chem.*, 2012, **84**, 5351–5357.
60. Y. Yang, J. Cui, M. Zheng, C. Hu, S. Tan, Y. Xiao, Q. Yang and Y. Liu, *Chem. Commun.*, 2012, **48**, 380–382.
61. H. Li, X. He, Y. Liu, H. Huang, S. Lian, S.-T. Lee and Z. Kang, *Carbon*, 2011, **49**, 605–609.
62. B. Cramariuc, R. Cramariuc, R. Scarlet, L. R. Manea, I. G. Lupu and O. Cramariuc, *J. Electrostat.*, 2013, **71**, 189–198.
63. Y. Bian, S. Wang, L. Zhang and C. Chen, *Build. Environ.*, 2020, **170**, 106628.
64. C. Zhang, Y. Li, P. Wang and H. Zhang, *Compr. Rev. Food Sci. Food Saf.*, 2020, **19**, 479–502.
65. Y. Lei, Q. Wang, S. Peng, S. Ramakrishna, D. Zhang and K. Zhou, *Adv. Energy Mater.*, 2020, **10**, 1902115.
66. X. Feng, J. Li, X. Zhang, T. Liu, J. Ding and X. Chen, *J. Control. Release*, 2019, **302**, 19–41.
67. A. Wali, M. Gorain, S. Inamdar, G. Kundu and M. Badiger, *ACS Appl. Bio Mater.*, 2019, **2**, 4324–4334.
68. S. Oura and K. Umemura, *Jpn. J. Appl. Phys.*, 2018, **57**, 03EK04.
69. B. Bhushan, B. Galasso, C. Bignardi, C. V. Nguyen, L. Dai and L. Qu, *Nanotechnology*, 2008, **19**, 125702.
70. Y. Li, B. Zhou, G. Zheng, X. Liu, T. Li, C. Yan, C. Cheng, K. Dai, C. Liu and C. Shen, *J. Mater. Chem. C*, 2018, **6**, 2258–2269.
71. Y. H. Kwon, K. Minnici, J. J. Park, S. R. Lee, G. Zhang, E. S. Takeuchi, K. J. Takeuchi, A. C. Marschilok and E. Reichmanis, *J. Am. Chem. Soc.*, 2018, **140**, 5666–5669.
72. A. A. Alshahrani, H. Al-Zoubi, L. D. Nghiem and M. in het Panhuis, *Desalination*, 2017, **418**, 60–70.
73. A. A. Alshahrani, M. S. Algamdi, I. H. Alsohaimi, L. D. Nghiem, K. L. Tu, A. E. Al-Rawajfeh and M. in het Panhuis, *Sep. Purif. Technol.*, 2020, **234**, 116088.
74. H. Mori, Y. Ogura, K. Enomoto, M. Hara, G. Maurstad, B. T. Stokke and S. Kitamura, *PLoS One*, 2020, **15**, e0225589.
75. H. Kim, J. W. Park, J. S. Hyeon, H. J. Sim, Y. Jang, Y. Shim, C. Huynh, R. H. Baughman and S. J. Kim, *Biosens. Bioelectron.*, 2020, **164**, 112318.

76. M. T. Müller, K. Hilarius, M. Liebscher, D. Lellinger, I. Alig and P. Pötschke, *Materials*, 2017, **10**, 545.
77. L.-Y. Meng and S.-J. Park, *J. Colloid Interface Sci.*, 2012, **386**, 285–290.
78. T. Jiang, G. Chen, X. Tian, S. Tang, J. Zhou, Y. Feng and H. Chen, *J. Am. Chem. Soc.*, 2018, **140**, 15560–15563.
79. Y. Wan, C. Wu, G. Xiong, G. Zuo, J. Jin, K. Ren, Y. Zhu, Z. Wang and H. Luo, *J. Mech. Behav. Biomed. Mater.*, 2015, **47**, 29–37.
80. C. Dai, B. Li, J. Li, B. Zhao, R. Wu, H. Ma and X. Duan, *Nano Res.*, 2020, **13**, 2506–2511.
81. Y. Zhang, G. Chang, S. Liu, W. Lu, J. Tian and X. Sun, *Biosens. Bioelectron.*, 2011, **28**, 344–348.
82. M. H. Abouzar, A. Poghosian, A. G. Cherstvy, A. M. Pedraza, S. Ingebrandt and M. J. Schöning, *Phys. Status Solidi A*, 2012, **209**, 925–934.
83. H. Wang, H. Li, Y. Zhang, Q. Wei, H. Ma, D. Wu, Y. Li, Y. Zhang and B. Du, *Biosens. Bioelectron.*, 2014, **53**, 305–309.
84. Y. J. Ahn, Y.-G. Gil, Y. J. Lee, H. Jang and G.-J. Lee, *Microchem. J.*, 2020, **155**, 104724.
85. G. Bharath, K. Rambabu, F. Banat, S. Anwer, S. Lee, N. BinSaleh, S. Latha and N. Ponpandian, *Mater. Res. Express*, 2019, **6**, 085409.
86. P. Baláž, M. Achimovičová, M. Baláž, P. Billik, Z. Cherkezova-Zheleva, J. M. Criado, F. Delogu, E. Dutková, E. Gaffet, F. J. Gotor, R. Kumar, I. Mitov, T. Rojac, M. Senna, A. Streletskii and K. Wiczorek-Ciurawa, *Chem. Soc. Rev.*, 2013, **42**, 7571–7637.
87. G.-W. Wang, *Chem. Soc. Rev.*, 2013, **42**, 7668–7700.
88. X. Lin, Y. Liang, Z. Lu, H. Lou, X. Zhang, S. Liu, B. Zheng, R. Liu, R. Fu and D. Wu, *ACS Sustainable Chem. Eng.*, 2017, **5**, 8535–8540.
89. B. Karadeniz, A. J. Howarth, T. Stolar, T. Islamoglu, I. Dejanović, M. Tireli, M. C. Wasson, S.-Y. Moon, O. K. Farha, T. Friščić and K. Užarević, *ACS Sustainable Chem. Eng.*, 2018, **6**, 15841–15849.
90. K. S. Suslick, *Faraday Discuss.*, 2014, **170**, 411–422.
91. Z. Chen, J. A. M. Mercer, X. Zhu, J. A. H. Romaniuk, R. Pfattner, L. Cegelski, T. J. Martinez, N. Z. Burns and Y. Xia, *Science*, 2017, **357**, 475.
92. A. de la Hoz, A. Díaz-Ortiz and A. Moreno, *Chem. Soc. Rev.*, 2005, **34**, 164–178.
93. C. O. Kappe, D. Dallinger and S. Murphree, *Practical Microwave Synthesis for Organic Chemists*, 2009, pp. I–X.
94. O. V. Kharissova, B. I. Kharisov, C. M. Oliva González, Y. P. Méndez and I. López, *R. Soc. Open Sci.*, 2019, **6**, 191378.
95. M. N. Nadagouda, T. F. Speth and R. S. Varma, *Acc. Chem. Res.*, 2011, **44**, 469–478.
96. A. Albinì and M. Fagnoni, *Green Chem.*, 2004, **6**, 1–6.
97. R. Ballini and A. Palmieri, *Adv. Synth. Catal.*, 2018, **360**, 2240–2266.
98. V. Balzani, A. Credi and M. Venturi, *ChemSusChem*, 2008, **1**, 26–58.
99. T. R. Cook, D. K. Dogutan, S. Y. Reece, Y. Surendranath, T. S. Teets and D. G. Nocera, *Chem. Rev.*, 2010, **110**, 6474–6502.
100. T. P. Yoon, M. A. Ischay and J. Du, *Nat. Chem.*, 2010, **2**, 527–532.

101. G. E. M. Crisenza and P. Melchiorre, *Nat. Commun.*, 2020, **11**, 803.
102. M. Silvi and P. Melchiorre, *Nature*, 2018, **554**, 41–49.
103. K. Zeitler, *Angew. Chem., Int. Ed. Engl.*, 2009, **48**, 9785–9789.
104. G. A. Bhaduri, R. Little, R. B. Khomane, S. U. Lokhande, B. D. Kulkarni, B. G. Mendis and L. Šiller, *J. Photochem. Photobiol., A*, 2013, **258**, 1–9.
105. S. Saha, A. Pal, S. Kundu, S. Basu and T. Pal, *Langmuir*, 2010, **26**, 2885–2893.
106. F. Kim, J. H. Song and P. Yang, *J. Am. Chem. Soc.*, 2002, **124**, 14316–14317.
107. E. Gileadi, *Physical Electrochemistry: Fundamentals, Techniques and Applications*, Wiley-VCH, Weinheim, 2011.
108. P. J. Kenis, *Electrochem. Soc. Interface*, 2020, **29**, 41–42.
109. G. Botte, *Interface Mag.*, 2014, **23**, 49–55.
110. B. A. Frontana-Uribe, R. D. Little, J. G. Ibanez, A. Palma and R. Vasquez-Medrano, *Green Chem.*, 2010, **12**, 2099–2119.
111. D. S. P. Cardoso, B. Šljukić, D. M. F. Santos and C. A. C. Sequeira, *Org. Process Res. Dev.*, 2017, **21**, 1213–1226.
112. D. Pletcher, *Electrochem. Commun.*, 2018, **88**, 1–4.
113. B. K. Peters, K. X. Rodriguez, S. H. Reisberg, S. B. Beil, D. P. Hickey, Y. Kawamata, M. Collins, J. Starr, L. Chen, S. Udyavara, K. Klunder, T. J. Gorey, S. L. Anderson, M. Neurock, S. D. Minter and P. S. Baran, *Science*, 2019, **363**, 838–845.
114. J. Yu, T. Fujita, A. Inoue, T. Sakurai and M. Chen, *Nanotechnology*, 2010, **21**, 085601.
115. O. A. Petrii, *Russ. Chem. Rev.*, 2015, **84**, 159–193.
116. R. Inguanta, S. Piazza and C. Sunseri, *Nanotechnology*, 2007, **18**, 485605.
117. M. Lai, J. H. Lim, S. Mubeen, Y. Rheem, A. Mulchandani, M. A. Deshusses and N. V. Myung, *Nanotechnology*, 2009, **20**, 185602.
118. C. Li, H. Bai and G. Shi, *Chem. Soc. Rev.*, 2009, **38**, 2397–2409.
119. M. B. Plutschack, B. Pieber, K. Gilmore and P. H. Seeberger, *Chem. Rev.*, 2017, **117**, 11796–11893.
120. J. Wegner, S. Ceylan and A. Kirschning, *Adv. Synth. Catal.*, 2012, **354**, 17–57.
121. K. Gilmore and P. H. Seeberger, *Chem. Rec.*, 2014, **14**, 410–418.
122. T. Noël, Y. Cao and G. Laudadio, *Acc. Chem. Res.*, 2019, **52**, 2858–2869.
123. S. Falsini, U. Bardi, A. Abou-Hassan and S. Ristori, *Green Chem.*, 2018, **20**, 3897–3907.
124. S. F. Sweeney, G. H. Woehrle and J. E. Hutchison, *J. Am. Chem. Soc.*, 2006, **128**, 3190–3197.
125. N. Anderson, K. V. Gernaey, T. F. Jamison, M. Kircher, C. Wiles, N. E. Leadbeater, G. Sandford and P. Richardson, *Future Med. Chem.*, 2012, **4**, 1779–1789.
126. S. Ahmed and W. Ali, *Green Nanomaterials: Processing, Properties, and Applications*, Springer Singapore, Singapore, 1st edn., 2020.

127. S. Wallace and E. P. Balskus, *Curr. Opin. Biotechnol.*, 2014, **30**, 1–8.
128. R. K. Das, V. L. Pachapur, L. Lonappan, M. Naghdi, R. Pulicharla, S. Maiti, M. Cledon, L. M. A. Dalila, S. J. Sarma and S. K. Brar, *Nanotechnol. Environ. Eng.*, 2017, **2**, 18.
129. L. A. Pfaltzgraff and J. H. Clark, in *An Overview*, Elsevier Ltd, 2014, pp. 3–33.
130. D. Esposito and M. Antonietti, *Chem. Soc. Rev.*, 2015, **44**, 5821–5835.
131. R. A. Sheldon, *Green Chem.*, 2016, **18**, 3180–3183.
132. W. P. Linak and J. O. L. Wendt, *Prog. Energy Combust. Sci.*, 1993, **19**, 145–185.
133. M. Aresta and I. Wiley, *Carbon Dioxide as Chemical Feedstock*, Wiley-VCH, Chichester; Weinheim, 1st edn., 2010.
134. A. A. Olajire, *J. CO<sub>2</sub> Util.*, 2013, **3–4**, 74–92.
135. O. S. Bushuyev, P. De Luna, C. T. Dinh, L. Tao, G. Saur, J. van de Lagemaat, S. O. Kelley and E. H. Sargent, *Joule*, 2018, **2**, 825–832.
136. S. C. Roy, O. K. Varghese, M. Paulose and C. A. Grimes, *ACS Nano*, 2010, **4**, 1259–1278.
137. M. Burkhardt and G. Busch, *Appl. Energy*, 2013, **111**, 74–79.
138. P. De Luna, C. Hahn, D. Higgins, S. A. Jaffer, T. F. Jaramillo and E. H. Sargent, *Science*, 2019, **364**, 80.
139. J. Aguado, D. P. Serrano and C. Royal Society of, *Feedstock Recycling of Plastic Wastes*, Royal Society of Chemistry, Cambridge, UK, 1999.
140. R. Verma, K. S. Vinoda, M. Papireddy and A. N. S. Gowda, *Procedia Environ. Sci.*, 2016, **35**, 701–708.
141. K. Ragaert, L. Delva and K. Van Geem, *Waste Manage.*, 2017, **69**, 24–58.
142. A. Rahimi and J. M. García, *Nat. Rev. Chem.*, 2017, **1**, 0046.
143. S. Czernik and R. J. French, *Energy Fuels*, 2006, **20**, 754–758.
144. A. Angyal, N. Miskolczi and L. Bartha, *J. Anal. Appl. Pyrolysis*, 2007, **79**, 409–414.
145. I. Barbarias, G. Lopez, J. Alvarez, M. Artetxe, A. Arregi, J. Bilbao and M. Olazar, *Chem. Eng. J.*, 2016, **296**, 191–198.
146. T. Uekert, M. F. Kuehnel, D. W. Wakerley and E. Reisner, *Energy Environ. Sci.*, 2018, **11**, 2853–2857.
147. X. Jia, C. Qin, T. Friedberger, Z. Guan and Z. Huang, *Sci. Adv.*, 2016, **2**, e1501591.
148. A. Tuncuk, V. Stazi, A. Akcil, E. Y. Yazici and H. Deveci, *Miner. Eng.*, 2012, **25**, 28–37.
149. V. Forti, C. Baldé, R. Kuehr and G. Bel, *The Global E-waste Monitor 2020. Quantities, Flows, and The Circular Economy Potential*, 2020.
150. C. Hagelüken and C. W. Corti, *Gold Bull.*, 2010, **43**, 209–220.
151. T. G. Ambaye, M. Vaccari, F. D. Castro, S. Prasad and S. Rtimi, *Environ. Sci. Pollut. Res. Int.*, 2020, **27**, 36052–36074.
152. M. P. O'Connor, R. M. Coulthard and D. L. Plata, *Environ. Sci.: Water Res. Technol.*, 2018, **4**, 58–66.
153. B. Calderón-Jiménez, M. E. Johnson, A. R. Montoro Bustos, K. E. Murphy, M. R. Winchester and J. R. Vega Baudrit, *Front. Chem.*, 2017, **5**, 1–26.

154. N. S. Tulve, A. B. Stefaniak, M. E. Vance, K. Rogers, S. Mwilu, R. F. LeBouf, D. Schwegler-Berry, R. Willis, T. A. Thomas and L. C. Marr, *Int. J. Hyg. Environ. Health*, 2015, **218**, 345–357.
155. S. Kalepu and V. Nekkanti, *Acta Pharm. Sin. B*, 2015, **5**, 442–453.
156. J. Pulit-Prociak and M. Banach, *Open Chem.*, 2016, **14**, 76–91.
157. J. Hamanová, M. Tengler, T. Novotný, S. Popelková, J. Holomek, V. Kováčová, F. Oliva, J. Trávníčková, D. Bašić and K. Dibusz, *Understanding Public Perception of Nanomaterials and Their Safety in The EU*, European Chemicals Agency, 2020.
158. G. Gaskell, T. T. Eyck, J. Jackson and G. Veltri, *Public Underst. Sci.*, 2005, **14**, 81–90.
159. I. A. Joubert, M. Geppert, S. Ess, R. Nestelbacher, G. Gadermaier, A. Duschl, A. C. Bathke and M. Himly, *NanoImpact*, 2020, **17**, 100201.
160. E. Goddard, V. Muringai and A. Boaitay, *J. Food Qual.*, 2018, **2018**, 2163526.
161. P. Farshchi, S. K. Sadrnezhaad, N. Nejad, M. Mahmoud and L. Abadi, *J. Nanopart. Res.*, 2011, **13**, 3511–3519.
162. N. A. Kamarulzaman, K. E. Lee, K. S. Siow and M. Mokhtar, *J. Nanopart. Res.*, 2019, **21**, 164.
163. S. George, G. Kaptan, J. Lee and L. Frewer, *J. Nanopart. Res.*, 2014, **16**, 2751.
164. J. Zhang, G. Wang and D. Lin, *Sci. Public Policy*, 2015, **43**, 115–127.
165. W. Ahmed, A. Elhissi and K. Subramani, in *Nanobiomaterials in Clinical Dentistry*, ed. K. Subramani, W. Ahmed and J. K. Hartsfield, William Andrew Publishing, 2013, pp. 3–16.
166. U. Backman, K. Savolainen, D. Brouwer, B. Fadeel, T. Fernandes, T. Kuhlbusch, R. Landsiedel, I. Lynch and L. Pylkkänen, *Nanosafety in Europe 2015-2025: Towards Safe and Sustainable Nanomaterials and Nanotechnology Innovations*, European Commission, Finnish Institute of Occupational Health, 2013.
167. R. Dhingra, S. Naidu, G. Upreti and R. Sawhney, *Sustainability*, 2010, **2**, 3323–3338.
168. G. A. K. Andy Garner, *An Introduction; National Pollution Prevention Center for Higher Education*., University of Michigan, 1995.
169. F. Duchin and S. H. Levine, in *Encyclopedia of Ecology*, ed. S. E. Jørgensen and B. D. Fath, Academic Press, Oxford, 2008, pp. 1968–1975.
170. S. Logakanthi, R. Yukesh Kannah and J. Rajesh Banu, in *Food Waste to Valuable Resources*, ed. J. R. Banu, G. Kumar, M. Gunasekaran and S. Kavitha, Academic Press, 2020, pp. 389–400.
171. I. V. Muralikrishna and V. Manickam, in *Environmental Management*, ed. I. V. Muralikrishna and V. Manickam, Butterworth-Heinemann, 2017, pp. 57–75.
172. European Commission, *Off. J. Eur. Union*, 2011, 38–40.
173. IOF Standardization, *Environmental Management: Life Cycle Assessment; Requirements and Guidelines*, ISO Geneva, Switzerland, 2006.

174. M. Finkbeiner, A. Inaba, R. Tan, K. Christiansen and H.-J. Klüppel, *Int. J. Life Cycle Assess.*, 2006, **11**, 80–85.
175. W. Klöpffer, R. Heijungs, A. Koehler, S. Olsen, P. Frankl and M. Curran, *Nanotechnology and Life Cycle Assessment: A Systems Approach to Nanotechnology and the Environment*, 2007.
176. C. Bauer, J. Buchgeister, R. Hischier, W. R. Poganietz, L. Schebek and J. Warsen, *J. Cleaner Prod.*, 2008, **16**, 910–926.
177. S. Gavankar, S. Suh and A. F. Keller, *Int. J. Life Cycle Assess.*, 2012, **17**, 295–303.
178. S. Temizel-Sekeryan and A. L. Hicks, *Resour., Conserv. Recycl.*, 2020, **156**, 104676.
179. S. M. Lloyd, L. B. Lave and H. S. Matthews, *Environ. Sci. Technol.*, 2005, **39**, 1384–1392.
180. A. Anctil, C. Babbitt, B. Landi and R. P. Raffaele, *35th IEEE Photovoltaic Specialists Conference*, 2010, 000742–000747.
181. A. Pizza, R. Metz, M. Hassanzadeh and J.-L. Bantignies, *Int. J. Life Cycle Assess.*, 2014, **19**, 1226–1237.
182. R. Arvidsson, D. Kushnir, B. A. Sandén and S. Molander, *Environ. Sci. Technol.*, 2014, **48**, 4529–4536.
183. S. Yasin and D. Sun, *J. Cleaner Prod.*, 2019, **233**, 1451–1464.
184. C. Moro, V. Francioso, M. Schrage and M. Velay-Lizancos, *Environ. Impact Assess. Rev.*, 2020, **84**, 106430.
185. P. Weyell, H. D. Kurland, T. Hülser, J. Grabow, F. A. Müller and D. Kralisch, *Green Chem.*, 2020, **22**, 814–827.
186. B. Salieri, D. A. Turner, B. Nowack and R. Hischier, *NanoImpact*, 2018, **10**, 108–120.
187. F. Part, G. Zecha, T. Causon, E.-K. Ehmoser and M. Huber-Humer, *Waste Manage.*, 2015, **43**, 407–420.
188. N. Stanisavljevic and P. H. Brunner, *Waste Manage. Res.*, 2014, **32**, 733–744.
189. B. Neto, C. Kroeze, L. Hordijk and C. Costa, *Selecting Industrial Ecology Tools: Strengths and Weaknesses for Use in a Decision Support Tool*, 2009.
190. C.-L. Huang, J. Vause, H.-W. Ma and C.-P. Yu, *Resour., Conserv. Recycl.*, 2012, **68**, 104–116.
191. R. U. Ayres and L. Ayres, *A Handbook of Industrial Ecology*, Edward Elgar Publishing, 2002.
192. R. Arvidsson, S. Molander and B. A. Sandén, *J. Ind. Ecol.*, 2012, **16**, 343–351.
193. Y. Wang and B. Nowack, *Environ. Pollut.*, 2018, **235**, 589–601.
194. T. Fleischer and A. Grunwald, *J. Cleaner Prod.*, 2008, **16**, 889–898.
195. L. M. Decker Micheal, *Bridges Between Science, Society and Policy*, Springer-Verlag Berlin Heidelberg, 2004.
196. D. Banta, *Int. J. Technol. Assess. Health Care*, 2009, **25**, 7–9.
197. D. H. Guston and D. Sarewitz, *Technol. Soc.*, 2002, **24**, 93–109.
198. J. Schot and A. Rip, *Technol. Forecast. Soc.*, 1997, **54**, 251–268.
199. V. P. Retèl, M. J. M. Hummel and W. H. Van Harten, *Tumori J.*, 2008, **94**, 284–291.
200. K. L. Dreher, *Toxicol. Sci.*, 2004, **77**, 3–5.

201. A. M. Fan and G. Alexeeff, *J. Nanosci. Nanotechnol.*, 2010, **10**, 8646–8657.
202. G. Oberdörster, E. Oberdörster and J. Oberdörster, *Environ. Health Perspect.*, 2005, **113**, 823–839.
203. H. Shi, R. Magaye, V. Castranova and J. Zhao, *Part. Fibre Toxicol.*, 2013, **10**, 15.
204. C. A. Ottoni, M. C. Lima Neto, P. Léo, B. D. Ortolan, E. Barbieri and A. O. De Souza, *Chemosphere*, 2020, **239**, 124698.
205. N. Kumar, V. Shah and V. K. Walker, *J. Hazard. Mater.*, 2011, **190**, 816–822.
206. E. K. Rushton, J. Jiang, S. S. Leonard, S. Eberly, V. Castranova, P. Biswas, A. Elder, X. Han, R. Gelein, J. Finkelstein and G. Oberdörster, *J. Toxicol. Environ. Health, Part A*, 2010, **73**, 445–461.
207. A. Nel, T. Xia, L. Mädler and N. Li, *Science*, 2006, **311**, 622–627.
208. G. Raju, N. Katiyar, S. Vadukumpully and S. A. Shankarappa, *J. Dermatol. Sci.*, 2018, **89**, 146–154.
209. S. Nafisi and H. I. Maibach, in *Emerging Nanotechnologies in Immunology*, ed. R. Shegokar and E. B. Souto, Elsevier, Boston, 2018, pp. 47–88.
210. M. E. K. Kraeling, V. D. Topping, Z. M. Keltner, K. R. Belgrave, K. D. Bailey, X. Gao and J. J. Yourick, *Regul. Toxicol. Pharmacol.*, 2018, **95**, 314–322.
211. S. Kokura, O. Handa, T. Takagi, T. Ishikawa, Y. Naito and T. Yoshikawa, *Nanomed.: Nanotechnol. Biol. Med.*, 2010, **6**, 570–574.
212. C. Rigo, L. Ferroni, I. Tocco, M. Roman, I. Munivrana, C. Gardin, W. R. L. Cairns, V. Vindigni, B. Azzena, C. Barbante and B. Zavan, *Int. J. Mol. Sci.*, 2013, **14**, 4817–4840.
213. A. C. Watkinson, A. L. Bunge, J. Hadgraft and M. E. Lane, *Pharm. Res.*, 2013, **30**, 1943–1946.

## CHAPTER 2

# *Green Nanotechnology for High-performance Impurity Detection and Water Treatment*

BOFAN LI,<sup>\*a,b</sup> NANNAN WANG,<sup>a,b</sup> JIE ZHENG,<sup>a,b</sup> HOUJUAN ZHU,<sup>a</sup> SHENG WANG,<sup>a,b</sup> ENYI YE<sup>a,b</sup> AND ZIBIAO LI<sup>\*a,b,c</sup>

<sup>a</sup> Institute of Materials Research and Engineering, Agency for Science, Technology and Research (A\*STAR), 2 Fusionopolis Way, Innovis #08-03, Singapore 138634, Singapore; <sup>b</sup> Institute of Sustainability for Chemicals, Energy and Environment, Agency for Science, Technology and Research (A\*STAR), 1 Pesek Road, Jurong Island, Singapore 627833; <sup>c</sup> Department of Materials Science and Engineering, National University of Singapore, Singapore 117575, Singapore

\*Emails: li\_bofan@imre.a-star.edu.sg; lizb@imre.a-star.edu.sg

## 2.1 Introduction

With the rapid growth of the world's population and economy, water scarcity is an imperative issue around the world. It is reported that two-thirds of the global population (4 billion people) are experiencing severe water scarcity at least 1 month of the year.<sup>1</sup> This number is continuously increasing due to the global warming and water contamination caused by the accelerated industrialization progress. Moreover, water contamination can result in environmental pollution and life-threatening diseases to humans and animals.<sup>2</sup> Producing freshwater is thus vital to everyone, especially people in



water-scarce areas. There are many technologies to purify and desalinate water, such as distillation, oxidation, adsorption, and membrane filtration.<sup>3</sup> Distillation is an energy-intensive process that requires high energy input to evaporate water. Oxidation can kill bacteria and degrade organic matters in water using chemicals, but the oxidative agents are mostly environmentally hazardous. Adsorption and membrane filtration are physical separation processes that are preferred due to their low energy consumption and small environmental impact.<sup>4,5</sup> They are capable of removing many types of pollutants from water, such as oil, heavy metals, ions, and organic solutes.

Green nanotechnology has been developed and applied in state-of-the-art impurity detection and water treatment technologies.<sup>6</sup> Nanotechnology provides the opportunities to apply nanomaterials to develop cost-effective and high-performance detection and purification methods for water treatment.<sup>7,8</sup> Nanomaterials possess high specific surface areas and various functionalities, making them highly suitable for detecting, adsorbing, and degrading contaminants in water.<sup>9</sup> They can be applied individually or assembled with other materials to function as sensors, sorbents, photocatalysts, and filters.<sup>10</sup> For example, metal nanoparticles (NPs) can be used to detect water contaminants and they can also be incorporated into nanofibers or membranes to enhance the absorption and separation performance.

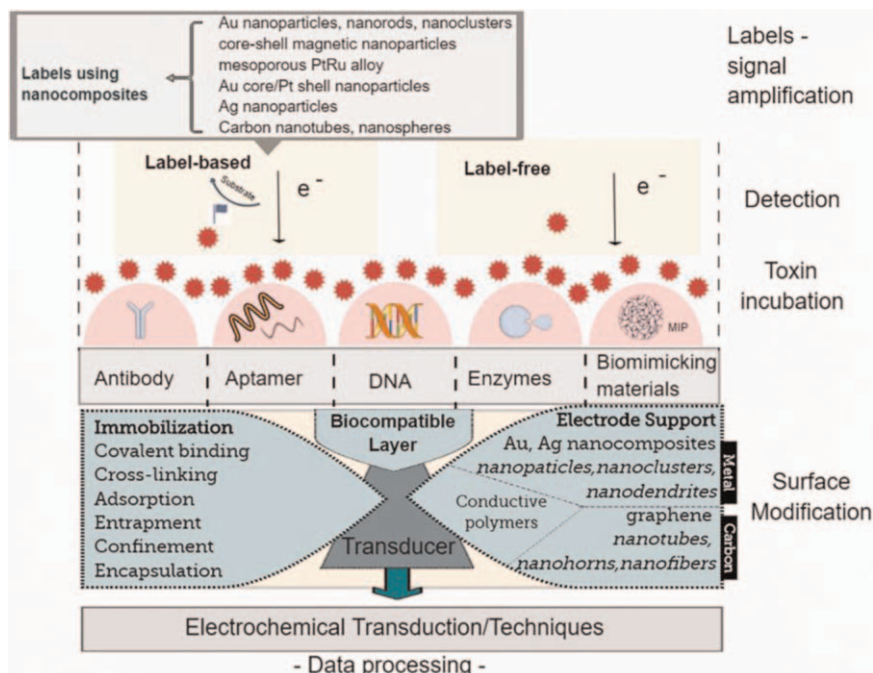
Nanomaterials consist of many types, such as clusters of atoms, particles that are less than 100 nm in size, fibers that are less than 100 nm in diameter, films that are less than 100 nm in thickness, and nanocomposites that combine at least two of them. They are usually be classified by the shape or dimension of the nanomaterials.<sup>11,12</sup> Zero-dimensional nanomaterials are clusters of atoms, such as quantum dots (QDs) and nanodots. They possess the highest surface-to-volume ratio, which is advantageous for sensors and catalysts.<sup>13</sup> One-dimensional nanomaterials are nanorods and nanofibers that possess a high length-to-diameter ratio. Two-dimensional nanomaterials are nanosheets such as graphene and graphene oxide (GO). They have been receiving much attention in recent years in electronics and catalyst areas.<sup>14</sup> Three-dimensional nanomaterials are nanomaterials with certain porous structures, such as the representative metal-organic framework (MOF). Three-dimensional nanomaterials possess a unique and porous structure, which can be utilized for molecular sensing and sieving applications.<sup>15</sup> Nanomaterials are usually synthesized by the “bottom-up” approach or “top-down” approach. For the “bottom-up” approach, nanomaterials are fabricated from atoms or molecules in a regulated manner using advanced control techniques or self-assembling techniques.<sup>16</sup> Alternatively, they can also be fabricated from bulk materials by splitting them into nanoscale pieces using mechanical forces or laser.<sup>17</sup>

In this chapter, nanotechnologies applied in water remediation will be introduced and elaborated on, such as sensors, nanosorbents, photocatalysts, nanofibrous materials, and thin-film nanocomposite (TFN) membranes. Their synthesis and fabrication methods, as well as their applications in detection and purification for water treatment, will be discussed in detail.

## 2.2 Biosensors and Nanoparticles for Impurity Detection

### 2.2.1 Electrochemical Biosensors

The biosensor contains a biometric element that can specifically react with the target of interest (Figure 2.1).<sup>18</sup> Biological events occur at the interface between the bulk solution of the sample and the surface of the sensor, where the sensor converts the event into a measurable signal. Electrochemical biosensors use electrodes as transducers to convert biological changes into electrical signals, voltages, or currents. Sensors (electrochemical technology) and signal processors collect, amplify, and display signals. The electrochemical biosensor combines the sensitivity of electrochemistry and the high specificity of biological reactions so that it can effectively detect small target compounds. Electrochemical biosensors have important characteristics, such as a dynamic concentration range, rapid response within a few seconds to a few minutes, adaptation to miniaturization, and compensation for drift caused by temperature, pH, or other environmental factors. Electrochemical biosensors have the advantages of high reliability, accuracy, and practicality. An ideal biosensor has minimal training and power requirements and portability (*i.e.* handheld and lightweight), and



**Figure 2.1** Schematic description of components and operation principle for electrochemical biosensors used in the detection of cyanotoxins. Reproduced from ref. 18 with permission from American Chemical Society, Copyright 2019.

most importantly, it can obtain meaningful results with little sample volume and reagents. Compared with other detection systems, the electrochemical micro-system integrated with the new sensor and interface design provides an excellent analytical method for the detection of toxins in water. For example, new types of sensors include metal or carbon-based composite materials to enhance electrode response (commonly referred to as electrode support). In fact, due to the selective binding or reaction of biometric elements with target analytes, biosensors can reach low detection limits. The combination of biochemistry and nanotechnology to electrochemical biosensors has been reported to enhance signal transduction to reach femtomolar concentrations.<sup>19,20</sup>

Electrochemical biosensors can be divided into biocatalytic devices and affinity sensors according to the nature and detection mechanism of the biomolecular elements.<sup>21</sup> Immunosensors, nucleic acid sensors, and DNA sensors are subcategories of electrochemical affinity biosensors. In addition, the combination of signal transduction mode and bioreceptor can describe an electrochemical affinity sensor. For example, when electrochemical biosensors involve impedance spectroscopy and antibodies, these biosensors are often referred to as impedance immunosensors. Finally, affinity sensors can use tags to improve detection, usually described as tag-based detection and tag-based label-free detection.

### 2.2.1.1 Label-based Immunosensors

A label-based immunosensor is a common device used for the electrochemical biosensing of cyanotoxin (Table 2.1).<sup>18</sup> The general format of cyanotoxin detection is competitive (direct or indirect) transduction, and sandwich transduction is rarely employed. The advantage of enzyme labeling is the amplification of the signal through the production of the enzyme product present in the substrate. Horseradish peroxidase (HRP) is the most used enzyme in electrochemical microcystin (MC) detection. The use of

**Table 2.1** Summary of toxicity mechanisms and health effects of cyanotoxins. Reproduced from ref. 18 with permission from American Chemical Society, Copyright 2019.

Cyanotoxin	Mechanism of toxicity	Health effects
Microcystins	Phosphatase 1 and 2A inhibition Apoptosis induction	Gastroenteritis, liver damage, tumor promotion
Cylindrospermopsin	Protein synthesis inhibition Overall, unknown	Gastroenteritis, liver and kidney damage, headache, fatigue
Anatoxin-a	Nicotinic cholinergic agonist	Muscle spasm, fatigue, paralysis, respiratory arrest and death
Homoanatoxin-a	Resistant to cholinesterase degradation	
Anatoxin-a(s)	Acetylcholinesterase inhibitor	Tremors, convulsion, salivation, respiratory failure, death
Saxitoxins (paralytic shellfish poisons)	Blocks voltage-gated sodium channel	Nausea, vomiting, diarrhea, paralysis, death

nanotechnology on the electrode holder or label can further amplify the electrical signal to achieve ultrasensitive detection. Hou *et al.* developed a successful direct competition detection method that used  $\text{H}_2\text{O}_2$  and HRP to carry out a biocatalytic precipitation reaction on the substrate.<sup>22</sup> After the immobilization of R1-leucine and R2-arginine (MC-LR) and MC-LR in the analyte, the mAb-HRP conjugate was used to accelerate the oxidation of 4-chloro-1-naphthol (substrate) into a precipitated form. The impedance detection of MC-LR was based on the mass load deposited on the electrode. As the MC-LR concentration decreased, the enzyme precipitation and the impedance signal increased. This biosensor had high sensitivity to MC-LR, with a limit of detection (LOD) of  $4 \text{ pg mL}^{-1}$  and high specificity; however, specificity studies were limited to MC-LR and microcystin-RR (MC-RR) variants. A similar LOD ( $4 \text{ pg mL}^{-1}$ ) was achieved by Gan *et al.*<sup>23</sup> Double amplification uses CNTs on the cosilicate as the carrier, and the HRP secondary antibody conjugate based on the magnetic core-shell nanocomposite was used as the label. The latter was composed of iron(II) and iron(III) oxide ( $\text{Fe}_3\text{O}_4$ ) nanoclusters/polydopamine/gold NPs. Another HRP-based detection method was to use differential pulse voltammograms (DPV) detection and  $\text{MoS}_2$  with Au NRs as the electrode support, with an LOD of  $5 \text{ pg mL}^{-1}$ .<sup>24</sup> He *et al.* reported a successful enzyme-labeled competitive immunosensor with an indium tin oxide modified electrode using nanomaterials, antibodies, and DNA molecules for MC-LR detection with an LOD of  $7 \text{ pg mL}^{-1}$ .<sup>25</sup> The magnetic graphene increased the electrode surface area, and the conjugated gold nanorods with circular DNA (replicated by rolling the circular shape) helped to increase the impedance signal. After adding 2 mM  $\text{H}_2\text{O}_2$  to the 1 mM hydroquinone solution, a calibration curve was established based on the CV measurement. In addition, a DPV biosensor for MC-LR was developed, which used chitosan on a glassy carbon electrode immobilized graphene sheets and conjugated carbon nanospheres with monoclonal antibodies for signal amplification. Optimization steps (incubation time,  $\text{H}_2\text{O}_2$  concentration, and  $\text{H}_2\text{O}_2$ -to-Ab ratio) were important for using a highly sensitive indirect competitive immunosensor to achieve an LOD of  $16 \text{ pg mL}^{-1}$ .<sup>26</sup> Indirect competition detection was based on HRP- $\text{H}_2\text{O}_2$  reaction and DPV monitoring of product precipitation concentration. The tapered tip of single-walled carbon nanohorns (SWNHs) enhanced the immobilization ability of MC-LR, and the minimum detection volume was  $30 \text{ pg mL}^{-1}$ . The reproducibility of the production was verified by analysis; however, the relative standard deviation variability was 5.7–7% for dopamine (DA) self-polymerization on GO and hydrothermal reaction to prepare nitrogen-doped graphene hydrogel solid-phase extraction carrier.<sup>27</sup> Using thiopurine (TH) as the electronic medium, the captured gold NPs were combined with HRP and a secondary antibody on the mesoporous carbon nanospheres. The detection limit of the dual-amplification biosensor was  $9.7 \text{ pg mL}^{-1}$ .<sup>28</sup> The use of gold nanocomposite materials for signal amplification has realized electron transfer. Two successful MC-LR biosensor amplification strategies have been reported. Using DPV labeling competition analysis, the LOD of

MC-LR was  $0.3 \text{ pg mL}^{-1}$ .<sup>29</sup> The competitive immunosensor used carbon nanofibers and Au NPs-modified GC electrodes as signal labels. The LOD was  $1.68 \text{ pg mL}^{-1}$ , and the MC-LR concentration had a wide linear range ( $0.0025\text{--}5 \text{ ng mL}^{-1}$ ) when the signal-to-noise ratio ( $S/N$ ) was 3.<sup>30</sup> At the same time, the LOD of the two methods was very low.

DNAzyme and its conjugates can replace HRP for the enzyme-free electrochemical immunoassay of MC-LR. Tian *et al.* developed a similar enzyme-based detection method that used horseradish peroxidase to semisimulate DNAzyme on CNTs.<sup>31</sup> The detection label was to label MCLR and DNAzyme on the CNTs. The sensor was based on the catalytic reduction of  $\text{H}_2\text{O}_2$ , and its LOD was  $2.31 \text{ pg mL}^{-1}$ . Gan *et al.* introduced another enzyme-free method.<sup>32</sup> The DNAzyme tandem was composed of methylene blue (MB) and DNA strands inserted into silica. G-quadruplex/hemin mimicked the activity of HRP, where MB was an electronic mediator. The  $\pi\text{--}\pi$  superposition between hemin/g-quadruplex and MB-DNA enhanced the catalytic activity of DNAzyme. Because gold nanodendrites had the potential of multiple detection and binding sites in the dendritic structure, the biosensor platform was made using gold nanodendrites. Nanodendrites had a special morphology of repeating long, dense, and sharp branched nanocomposites. DPV electrochemical measurement showed that MC-LR had high specificity in clean water and had broad application prospects. For purified water, the LOD was as low as  $0.3 \text{ pg mL}^{-1}$ , but the performance of the biosensor in real water samples was not tested. In addition, Wei *et al.* developed an enzyme-free biosensor using nanomaterial antibody coupling in a sandwich test.<sup>33</sup> They used a graphene-loaded electrode with fixed Ab to detect by labeling conjugated secondary Ab and PtRu NPs responsible for the electrooxidation of  $\text{H}_2\text{O}_2$ . The biosensor was characterized by impedance. Over time, the detection limit of amperometric measurement was  $9.63 \text{ pg mL}^{-1}$ .

Instead of enzymatic amplification, QDs have been tested for indirect MC-LR detection in electrochemical immunosensors. In the prepared microtiter plate, after antibody-QD was combined with MC-LR of different concentrations, the cadmium ions in QD were released. The semiconductor nanocrystal had a CdSe core encapsulated in a ZnS and polymer shell. A gold electrode and square wave stripping voltammetry were used to measure the acid dissolution of  $\text{Cd}^{2+}$ . The optimized LOD was  $99 \text{ pg mL}^{-1}$ .<sup>34</sup>

### 2.2.1.2 Electrochemical Biocatalytic Biosensors

Enzyme activity inhibition is widely used in colorimetry,<sup>35</sup> the fluorescence<sup>36</sup> method, and electrochemical biocatalysis as a detection tool for cyanobacterial toxins. Campas *et al.* introduced the application of protein phosphatase inhibition in electrochemical biosensor applications.<sup>37</sup> Subsequently, the same team used the time-ampere method to translate the protein phosphatase 2 (PP2A) enzyme inhibition into a current intensity signal so that the LOD reached  $37 \text{ ng mL}^{-1}$  (PP2A inhibited 35%).<sup>38</sup> In 2008, PP2A and NADH oxidase respectively dephosphorylated and recycled nonelectroactive aminobenzene

phosphate, thereby successfully increasing the sensitivity and significantly reducing the detection limit by 775 times.<sup>39</sup> Catanante *et al.* applied PP1 activity to an electrochemical DPV biosensor for MC-LR detection, and the LOD was  $0.93 \text{ ng mL}^{-1}$ .<sup>40</sup> In addition, the LOD measured by using MC-LR chronopotentiometry based on enzyme inhibition was  $0.5 \text{ ng mL}^{-1}$ .<sup>41</sup> Due to the unsuccessful LOD ( $1 \text{ ng mL}^{-1}$ ), the inhibition of acetylcholinesterase activity was used in electrochemical biosensors to detect ATX-a (S).<sup>42</sup>

### 2.2.1.3 Artificial Receptors-based “Biosensors”

Artificial recognition elements or biomimicking materials are of growing interest for several applications. They are considered the low-cost alternatives to antibodies and some researchers name them artificial antibodies.<sup>43</sup> Artificial biosensors have been developed with the sensing layer consisting of imprinted sol-gel materials capable of establishing surface interactions with MC-LR.<sup>44</sup> A special tailoring of molecularly imprinted materials highly specific to MC-LR using CNTs was performed by Queiros *et al.*<sup>45</sup> They used ion-selective electrodes and the sensing membrane of the biosensor consisted of ionophore, polyvinyl chloride, and plasticizer, where ionophore was varied between molecularly imprinted CNTs and nonimprinted CNTs. Artificial antibodies (imprinted polymers) displayed good LOD in a potentiometric sensor application for MC-LR, below the guideline value established by World Health Organization (WHO).

### 2.2.1.4 Future Trends

Overall, the implementation of biosensors in real samples and the detection of cyanotoxins in picomolar or femtomolar concentrations require more effort. Validated low femtomolar LODs (if achieved) can certainly help because using diluted samples can minimize the matrix effect during detection or avoid complex pretreatment procedures. Certainly, low LODs need reevaluation in real water samples to accomplish accurate and precise quantification of cyanotoxins. Reaching low detection limits in real water samples remains a big challenge in electrochemical biosensors. Undoubtedly, the field of electrochemical biosensors for cyanotoxins is growing rapidly. Currently, researchers are testing complex samples and that will probably add complications, such as causing sensor fouling and lowering sensitivity and selectivity. Estimation of LODs in real water samples needs extensive research. This has yet to be determined. Uniformity in the methodology used for LOD determination would be tremendously beneficial for the sensor community. Excellent sources on procedures and methods for the determination of LOD in clean water or a specific matrix are the suggested procedures. Application of these methods in the determination of LOD would tremendously improve the quality assurance of a sensor.

Certainly, electrochemical biosensors show similar capabilities to enzyme-linked immunosorbent assay (ELISA). After optimization in water samples,

they may be used as a routine quantitative screening and point-of-use water monitoring, mainly because of their high portability. Yet, MS-based methodologies are the only recognized analytical techniques that can distinguish between variants or transformation products. The quantification of MC variants in low concentrations using electrochemical biosensors is the biggest challenge to overcome. Ultimately, the selection of aptamers or other high-affinity biomolecules for specific MC variants is expected to be developed. When combined with innovative signal transduction technology and micro- and nanosystems with multimicrofluidic channels, electrochemical biosensors may finally achieve specific variant detection at low concentrations. The interdisciplinary field of electrochemical biosensors is developing rapidly, and new sensor applications/technologies on multi-cyanotoxin analysis are expected to emerge to properly assist the assessment of toxicity in real time. The breakthrough in electrochemical biosensors based on nanotechnology will surely help to quickly detect cyanobacterial toxins and efficiently control the quality of drinking water, providing people with clean and safe drinking water.

## 2.2.2 Nanoparticles

### 2.2.2.1 Quantum Dots

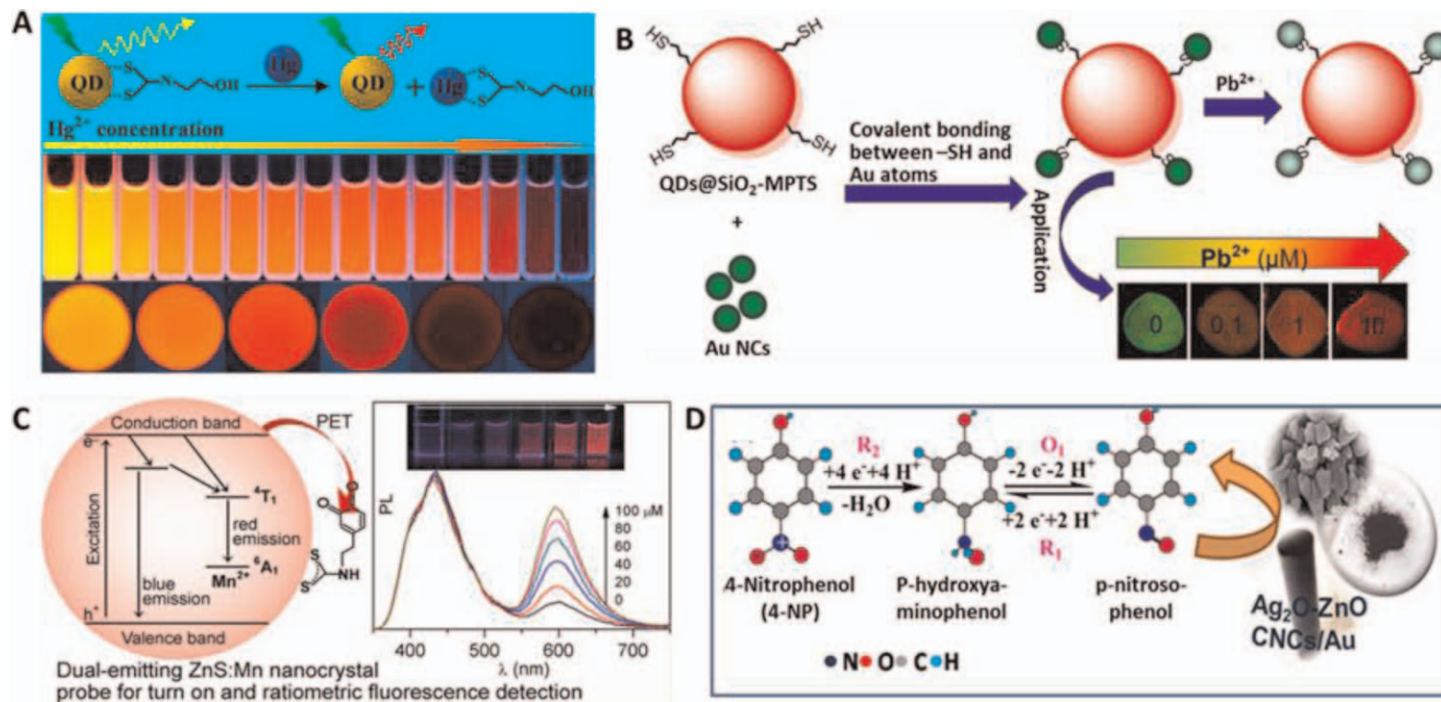
QDs have extensively attracted increasing numbers of researchers' attention in the past years by virtue of their excellent optical features, such as high brightness, large Stokes shift, resistance to photobleaching, narrow emission peak, fluorescence lifetime, and a high absorption coefficient across a broad excitation spectrum. Especially in comparison with the traditional fluorescent organic dyes, QDs with different sizes not only possess high fluorescent quantum yield but also can emit different colored fluorescence under a single excitation, enabling the feasibility to build superior QD-based nanosystems applied in various fields, including biomedical labeling, light-emitting diodes (LEDs), solar cells, and wastewater treatment. To the best of our knowledge, a diversity of QDs has been largely developed in the past few decades. They can be mainly divided into a few classifications, such as cadmium-based QDs (CdSe, CdTe, and CdS QDs), zinc-based QDs including ZnS d-dots, silica-based QDs, transition metal dichalcogenide (TMD)-based QDs (TMD QDs), and carbon-based QDs like carbon dots (CDs), graphene QDs (GQDs), and polymer dots (PDs). By virtue of owning inherent optical properties, most of these QDs have been widely used for the fluorescent identification of chemical or biological agents in water.

As a typical and most common QD, cadmium-based QDs have been successfully investigated in detecting chemical or biological agents in water. Wang's group designed a series of QD-based sensors for the sensitive, selective, and visual detection of heavy metal ions ( $\text{Hg}^{2+}$ ,  $\text{Cu}^{2+}$ ,  $\text{Pb}^{2+}$ ) and other pollutants in real water. Such sensors included single-emissive nanoplates and ratiometric emissive nanoplates. In single emissive

models, novel water-soluble CdSe–ZnS QDs were functionalized with a bidentate ligand of 2-hydroxyethylthiocarbamate (HDTC) for the visual detection of aqueous  $\text{Hg}^{2+}$  in real water with a detection limit of 1 ppb (Figure 2.2A).<sup>46</sup> The fluorescence color of such QDs could be efficiently and selectively quenched by  $\text{Hg}^{2+}$  based on a surface chelating reaction between HDTC and  $\text{Hg}^{2+}$ . An increasing concentration of  $\text{Hg}^{2+}$  led to the gradual change of fluorescence color. Such a phenomenon was applied to build a paper-based sensor for visually detecting  $\text{Hg}^{2+}$  in real water with an LOD of 0.2 ppm, affording the feasibility of mercuric detection. Besides, to enhance sensitivity and selectivity, ratiometric modality with two independent emissive bands as the signal was constructed for the rapid visual identification of analytes in real water.<sup>47</sup> Dual-emission QDs with green and red fluorescence were hybridized for  $\text{Cu}^{2+}$  identification with an LOD of 1.1 nM by covalently linking the green emissive QDs on the surface of red-emitting QDs–embedded silica NPs.<sup>48</sup> In the ratiometric nanohybrid, green fluorescence could respond to  $\text{Cu}^{2+}$ , whereas the red fluorescence of the embedded QDs was insensitive to  $\text{Cu}^{2+}$ . Such variation resulted in continuous color changes from green to red, which was further utilized to determine  $\text{Cu}^{2+}$  in lake water and mineral water samples. In another design, a ratiometric fluorescence nanohybrid was fabricated by covalently linking the green gold nanoclusters (Au NCs) to the surface of red QDs–embedded silica NPs for the on-site visual determination of  $\text{Pb}^{2+}$  with an LOD of 3.5 nM (Figure 2.2B).<sup>49</sup> In such nanohybrid, the phenomena that green fluorescence could be selectively quenched by  $\text{Pb}^{2+}$  whereas red fluorescence was inert to  $\text{Pb}^{2+}$  as internal reference induced a continuous fluorescence color change from green to yellow as observed by the naked eye. Such nanohybrid sensors were applied to detect  $\text{Pb}^{2+}$  in tap water, mineral water, groundwater, and seawater. Also, a nanohybrid doped film was built with fluorescent test strips for the on-site visual identification of  $\text{Pb}^{2+}$  with a visual LOD of 0.1  $\mu\text{M}$ . In light of the design concept of dual-emissive modality, a similar ratiometric nanohybrid was constructed by red QDs and fluorescent GO to visually detect and discriminate  $\text{Fe}^{2+}$  and  $\text{Fe}^{3+}$  in real water.<sup>50</sup>

Besides, zinc-based QDs were also constructed to be applied in environmental detection. For example, as shown in Figure 2.2C, Mn-doped ZnS QDs were synthesized to exhibit dual emission that afforded the visual determination of organophosphate (diethylphosphorothioate, DEP) in real water through turn-on and ratiometric fluorescence.<sup>51</sup> Particularly, dual emission from QDs modified by dopamine dithiocarbamate could be modulated by a photoinduced electron transfer process, in which red fluorescence was ascribed to the doping of  $\text{Mn}^{2+}$  in QDs as the responsive part and blue emission was attributed to an inherent defect in QDs as internal reference. With the addition of DEP, the red fluorescence could be improved by blocking the electron transfer process while blue fluorescence kept stable, leading to color changes from dark blue to red, realizing the visual and quantitative detection of DEP in water. Furthermore,





**Figure 2.2** (A) Schematic illustration of preparing aqueous 2-hydroxyethylthiocarbamate (HTC)-modified CdSe-ZnS QDs and designing QDs-based test paper strips for the visual detection of  $\text{Hg}^{2+}$ . Reproduced from ref. 46 with permission from American Chemical Society, Copyright 2012. (B) Illustrative description of QDs-based ratiometric probe structure and such QDs-integrated ratiometric PVA-film sensor for the visual detection principle for  $\text{Pb}^{2+}$ . Reproduced from ref. 49 with permission from American Chemical Society, Copyright 2014. (C) Illustration of the mechanism of Mn-doped Mn-ZnS QDs for the fluorescence turn-on and ratiometric identification of  $\text{Pb}^{2+}$ . Reproduced from ref. 51 with permission from American Chemical Society, Copyright 2014. (D) Scheme for the possible redox reactions of  $\text{Ag}_2\text{O-ZnO CNCs/Au}$  in the electrochemical determination of 4-NP. Reproduced from ref. 60 with permission from Elsevier, Copyright 2021.

such QDs were applied to build paper-based test strips for the rapid, on-site, and visual identification of DEP residues in real water, including tap water and lake water. In another paradigm, zinc selenide QDs (ZnSe QDs) have been employed to recognize nitroaromatic compounds, that is, traces of 2,4,6-trinitrophenol (TNP, picric acid) in river water by quenched fluorescence based on the inner filter effect.<sup>52</sup> Additionally, carbon quantum dots (CQDs) and boronic acid-functionalized MoS<sub>2</sub> QDs were respectively developed to selectively and sensitively determinate the trace amounts of chromium(VI), chromium(III), and Hg<sup>2+</sup> in real water using quenched fluorescence.<sup>53,54</sup> In another paradigm, graphene quantum dots (GQDs) were built to detect Hg<sup>2+</sup> and cysteine (Cys) in spiked water samples based on the quenched fluorescence of GQDs by Hg<sup>2+</sup> through fluorescence charge transfer.<sup>55</sup>

Except for the fluorescence method, other strategies of QDs were also applied for sensing chemical or biological agents in water, such as the colorimetric method.<sup>56</sup> In 2019, a dual-CQDs-based sensing system with absorbance in the blue region and fluorescence in the red region was fabricated for the selective and sensitive detection of multiple heavy metals including Co<sup>2+</sup>, Fe<sup>3+</sup>, Hg<sup>2+</sup>, and Pb<sup>2+</sup> in real water.<sup>57</sup> On the one hand, the absorbance feature of CQDs varied with different metallic cations in solution and the absorbance pattern also shifted with increasing metal cations concentration, leading to different color changes. Also, the red fluorescence of CQDs could be quenched by metal cations owing to the interaction between the metal cations and the fluorescent surface states from CQDs. Combining the application of fluorescence assay with the colorimetric method, novel sensors for more sensitive and rapid determination were developed to detect Co<sup>2+</sup>, Fe<sup>3+</sup>, Hg<sup>2+</sup>, and Pb<sup>2+</sup> with an LOD of 96.8, 61.7, 39.5, and 37.1 nM, respectively. Besides these methods, QDs-based electrogenerated chemiluminescence (ECL) has been developed to identify chemical agents in water as a novel and effective sensing strategy due to the rapid analysis, low background signal, high sensitivity, and selectivity in environmental sensors. In a simple but effective paradigm, GQD nanocomposites have recently been fabricated to improve the ECL signals in a tris(2,2'-bipyridyl)ruthenium(II)/tripropylamine (Ru(bpy)<sub>3</sub><sup>2+</sup>/TPA) assay for specific *Escherichia coli* analysis in water.<sup>58</sup> Simultaneously, inspired by this ECL sensing mechanism, a portable smartphone-based system was further designed for *E. coli* detection by applying a universal serial bus interface as a voltage excitation source and employing a camera for capturing luminescence. In particular, GQD nanocomposites were used as luminescence enhancers, and *E. coli* antibody was immobilized on the electrode surface. Various concentrations of *E. coli* caused different degrees of enhancement of luminescence signals, which could be captured by a smartphone camera and further processed by a smartphone-based image analysis application (app). Thus, such a sensor integrated QDs with portable analytical devices, affording the opportunity for the real-time and low-cost electrochemical analysis of impurities in water.

### 2.2.2.2 Metal Oxide Nanoparticles

In addition to QDs, metal oxide NPs have also been developed as an attractive sensor system against identifying chemical or biological agents in water due to their unique integration of redox chemistry, semiconductor, electrol, and optical properties.<sup>59</sup> In a simple but effective paradigm, silver oxide (Ag<sub>2</sub>O)/zinc oxide (ZnO) composite nanocones (CNCs) were synthesized using a microwave-assisted cost-effective strategy for the simultaneous electrochemical monitoring and photodegradation of 4-nitrophenol (4-NP) in water that was one of the major toxic water pollutants, as shown in Figure 2.2D.<sup>60</sup> Especially, Ag<sub>2</sub>O–ZnO CNCs were utilized to functionalize the gold electrode for the electrochemical identification of 4-NP with an LOD of 23 nM, a sensitivity of 1.6  $\mu\text{A } \mu\text{M}^{-1} \text{cm}^{-2}$ , as well as an excellent selectivity in real water samples. Additionally, Ag<sub>2</sub>O–ZnO CNCs also had an outstanding photocatalytic performance for degrading 4-NP and organic water pollutant dye, MB, due to the formation of the p–n nanoheterojunction, which respectively referred to p-type Ag<sub>2</sub>O and n-type ZnO semiconductor NPs. Such a system provided the potential to detect and remove 4-NP in industrial applications. Similarly, CoMnO<sub>3</sub> nanosheets (CMO NSs) were prepared *via* the oxalic acid–assisted coprecipitation method for highly sensitive and cost-effective 4-NP in environmental water samples with an LOD of 10 nM and an excellent sensitivity of 2.458  $\mu\text{A } \mu\text{M}^{-1} \text{cm}^{-2}$ .<sup>61</sup> Several Fe<sub>3</sub>O<sub>4</sub>-based sensors were developed for electrochemical determination of 4-NP with high sensitivity and selectivity and low LOD in various water samples, including tap water.<sup>59,62,63</sup> In addition to 4-NP, other chemical compounds, including benzene, toluene, and xylene, were also measured using tin oxide (SnO<sub>2</sub>) or tungsten oxide (WO<sub>3</sub>) NPs decorated graphene based on electrochemical method with a high sensitivity.<sup>64</sup> According to redox and optical features of metal oxide NPs, CuO and ZnO NPs were synthesized by using leaf extract of *Camellia japonica* for optical sensing Li<sup>+</sup> and Ag<sup>+</sup> contaminants in marine water samples.<sup>65</sup> Such sensors mainly relied on the optical changes of NPs induced by the aggregation of NPs through their natural interaction with metal ions.

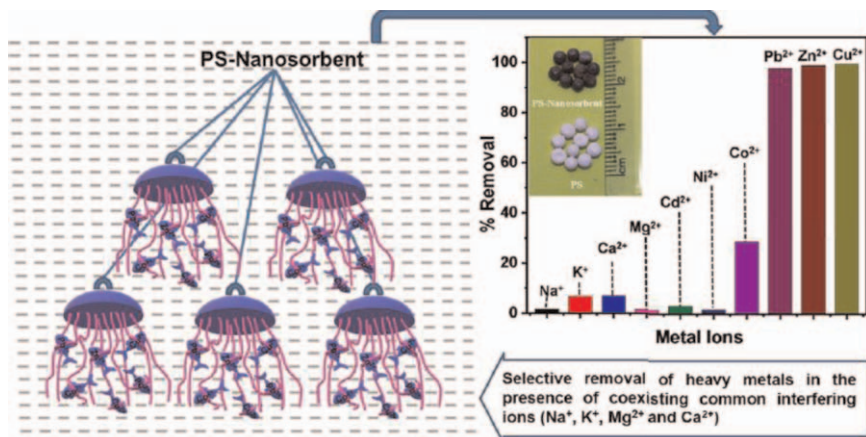
## 2.3 Nanomaterials for Adsorbing and Degrading Pollutants in Water

Water, being one of the most precious presents received from nature, is an essential part of human life and all social activities.<sup>66,67</sup> However, with the rapid development of modern society, severe water pollution is inevitably caused, which in turn retards the development of society and, more importantly, influences the health of human beings. Therefore, the development of new techniques to purify wastewater is a key step for the development of a sustainable society. Nanomaterials with a high surface area have drawn great attention to be used as nanosorbents or pollutant killers in water treatment.

### 2.3.1 Nanosorbents

Organic dyes are extensively employed in various commodities. However, they are also one of the most widespread pollutants in water. Due to their high toxicity, detrimental sanitary effects, and carcinogenic properties, even a level of a few ppm of organic dyes can severely impact people's health. Among all organic dyes, MB is one of the most widely applied basic dyes in water. In addition to the adverse effects on the ecosystem caused by MB, it severely influences people's health, including causing nausea, skin and eye irritations, gastritis, difficulty in breathing, and so on.<sup>68</sup> In 2018, based on a central composite design, Dichiara and coworkers fabricated the modified wood filters by impregnating basswood with graphene to realize the adsorption and desorption of MB in a dynamic system.<sup>69</sup> During a vacuum impregnation process, graphene was well dispersed and immobilized on the basswood. Even at a relatively low MB feed concentration, the resultant modified wood filters exhibited an advanced adsorbing performance with an uptake capacity of up to  $46 \text{ mg g}^{-1}$ . It was noteworthy that the spent filters could be recovered through solvent (such as acetone and acetonitrile) exchanging to reuse for five sorption cycles with less than 20% regeneration efficiency (RE) degeneration. Recently, an alternative method to remove MB with high efficiency was developed by Rakass and coworkers.<sup>70</sup> They utilized nickel molybdate ( $\alpha\text{-NiMoO}_4$ ) as an adsorbent to adsorb MB in aqueous solutions. By varying a series of parameters, including solution pH, temperature, contact time, adsorbent dose, and initial dye concentration, they found that both the adsorbent dose and solution pH would significantly impact the MB removal ability. The best result, in which MB removal reached a 99% level, was obtained at an initial MB solution concentration of lower than 160 ppm at pH 11. It was interesting that, unlike other adsorbents, which displayed greater efficiency with a larger adsorbent dose, in this system, a lower amount of adsorbent dose showed higher MB removal capability owing to the performance of particle interaction with higher MB doses. While pH had little effect on the adsorbent site, it affected the structure of the MB. At lower pH, extra proton ions in the solution coexisted with the basic dye cations on the removal sites of  $\alpha\text{-NiMoO}_4$ , thus lowering its performance. The reaction process was endothermic following the pseudo-second-order model and dye was removed more quickly at higher temperatures. The adsorbent still showed exceptional performance after multiple rounds of recycling, indicating a high RE.

Gupta and coworkers looked at a different aspect of industrial waste, focusing their studies on the selective removal of heavy metal pollutants (Figure 2.3).<sup>71</sup> They prepared a magnesium-doped lithium manganese oxide nanosorbent *via* a one-step solid-state approach. The synthesized nanosorbent showed a specific selective heavy metal absorption in the order of  $\text{Ni}^{2+} < \text{Co}^{2+} < \text{Cd}^{2+} < \text{Pb}^{2+} < \text{Zn}^{2+} < \text{Cu}^{2+}$ , even in the presence of common interfering ions (*i.e.*  $\text{Na}^+$ ,  $\text{K}^+$ ,  $\text{Mg}^{2+}$ , and  $\text{Ca}^{2+}$ ). However, more has to be



**Figure 2.3** The illustration of PS-nanosorbent and its high selectivity in Heavy Metal Removal. Reproduced from ref. 71 with permission from American Chemical Society, Copyright 2018.

done to improve the recyclability of the adsorbents. Moreover, a polysulfone-nanosorbent (PS-nanosorbent) composite was also developed to facilitate the implementation in real applications, exhibiting great reusability and high selectivity in heavy metal removal. Mahmoud and coworkers adopted a different method to deal with the heavy metal ions in water.<sup>72</sup> They prepared nontoxic copper oxide NPs (termed CuO NPs) using a green synthesis approach in the absence of any hazardous chemicals. Exploiting the extracts from mint leaves and orange peels, two NPs (*i.e.* CuO NPs-1 and CuO NPs-2) were synthesized. The obtained NPs were effective in the removal of heavy metal ions, and the affinity of adsorption to CuO NPs was in the order of  $Pb^{2+} > Ni^{2+} > Cd^{2+}$ . The material synthesizing procedure is simple, cost effective, and chemically safe. Unfortunately, there has yet to be an in-depth analysis of the sustainability of its regeneration and reusability. Nonetheless, this result provides a powerful example in piloting the green and clean synthesis of chemicals.

Glyphosate (GLY) has been the world's best-selling herbicide for agricultural and nonagricultural applications for decades, known for killing crops that are not genetically modified to be resistant to it.<sup>73,74</sup> However, the leeching of GLY into the earth causes a rising concern due to its severe harmful effect on humans and our ecosystems. Since it contains three functional groups (amine, carboxylate, and phosphonate), the removal of GLY is highly dependent on pH. In 2021, Soares and coworkers came up with a solution to remove GLY from aqueous solution.<sup>75</sup> Magnetic nanosorbents consisting of magnetite ( $Fe_3O_4$ ) cores coated with trimethyl chitosan-silica hybrid shells were synthesized, and their adsorption abilities were studied. Results indicated that the nanosorbents were able to successfully decrease realistic environmental concentrations of GLY in aqueous solution while still

maintaining good performance after multiple recycling, optimally at pH 5–8. Although this method shows incredible potential, more can be done to improve the sustainability of the recycling method, which is currently performed with ethanol.

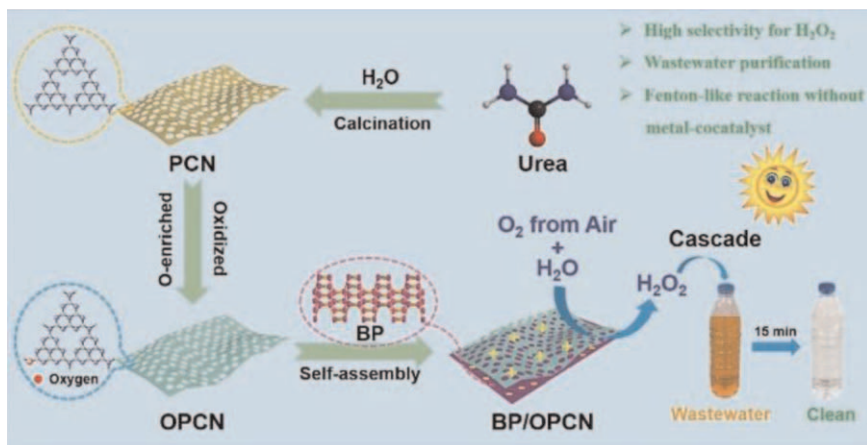
### 2.3.2 Nanophotocatalysts

Photocatalysts are a group of materials that capitalize on the absorption of light to speed up a chemical process by bringing it to a higher energy level and providing more energy for a reaction to occur.<sup>66,67,76</sup> They are gaining popularity in the water purification industry for their high efficiency at an affordable price.

Once again, the removal of a GLY, specifically *N*-(phosphonomethyl)glycine (PMG), was studied by Wu and coworkers in 2021, where they expanded the application of photocatalysis with CeO<sub>2</sub> NPs to work well under both UV and visible light and in aqueous solutions of varying pH.<sup>77</sup> This was a breakthrough as it broadened the applications of CeO<sub>2</sub> NPs in purifying contaminated water in natural environments. Citric acid was utilized as a capping agent to stabilize the growth of CeO<sub>2</sub> NPs with rich oxygen defects through a precipitation reaction. FTIR confirmed the grafting of citric acid onto the surface of CeO<sub>2</sub> NPs and it was seen that an increased pH led to a decrease in activity. This is possibly due to the lowered surface charge of PMG and CeO<sub>2</sub> NPs and a decreased adsorption on the surface of CeO<sub>2</sub> NPs. Nevertheless, this provides a powerful tool in advancing traditional contamination treatment methods.

Amoxicillin (AMX) is a common antibiotic widely used to treat both human and animal diseases.<sup>78–80</sup> As it is not digestible, it is excreted unchanged and leeches into environmental water bodies. Bacteria are faced with unnatural selection factors and develop a resistance to it. Additionally, AMX can be stored in the tissue of aquatic organisms and it has slowly made its way up the food chain. This poses a threat to both humans and the natural ecosystem. In 2021, Le and coworkers used a simple heating reflux method to prepare the implantation of CdS QDs into the laminar ultrathin NH<sub>4</sub>V<sub>4</sub>O<sub>10</sub> nanobelts.<sup>81</sup> FTIR was used to confirm the adsorption due to the formation of hydrogen bonds between NH<sup>4+</sup> and AMX. Testing the effectiveness of the photocatalyst was done under sunlight and it was revealed that the optimum composite ratio was 6-CdS/NH<sub>4</sub>V<sub>4</sub>O<sub>10</sub> with the photodegradation rate of AMX recorded at 90.6% within 120 min of illumination. Beyond that, the photodegradation rate of AMX was decreased due to the accumulation of excess CdS QD. At this ratio, XRD showed the maintenance of the crystal structure. Furthermore, 6-CdS/NH<sub>4</sub>V<sub>4</sub>O<sub>10</sub> has good reusability with a negligible decrease in catalytic activity for at least five cycles.

Tong and coworkers studied *E. coli* disinfection and organic pollutant, *i.e.* rhodamine B (RhB) and acetaminophen (ACTP), degradation using covalent organic frameworks (COFs) in 2020.<sup>82</sup> A solvothermal method followed by



**Figure 2.4** The illustration of the self-assembly of 2D/2D BP/OPCN heterostructures and  $\text{H}_2\text{O}_2$  production for wastewater remediation. Reproduced from ref. 83 with permission from the Royal Society of Chemistry.

the coprecipitation of AgI on the surface of COF-PD was used to prepare the modified COF, *i.e.* COD-PD/AgI. The sample successfully disinfected an aqueous sample of *E. coli* and removed RhB and ACTP *via* visible light-driven (VLD) photocatalysis. Moreover, it maintained its stability for four successive reused cycles, proving its potential as a sustainable water purification solution.

Lastly, Li and coworkers took a more unique approach to purify contaminated water by directly using solar energy to convert  $\text{H}_2\text{O}_2$  into active free radicals.<sup>83</sup> They synthesized a metal-free 2D/2D heterojunction by assembling oxygen-enriched porous g- $\text{C}_3\text{N}_4$  nanosheets (OPCNs) and black phosphorus (BP) nanosheets. The catalyst was highly selective and resolved the limitations that originally faced the traditional Fenton reactions, such as low sunlight utilization and poor selectivity and the requirement for additional metal-based catalysts. The photocatalyst converted the *in situ*-formed  $\text{H}_2\text{O}_2$  at room temperature into free radicals, which subsequently degraded organic pollutants, purifying water, as depicted in Figure 2.4. The photocatalyst also showed high stability and recyclability. This is highly advantageous as it has prospects of using metal-based catalysts as a sustainable and long-term method to remove organic pollutants in the natural environment.

In the past decade, nanomaterials have displayed great advantages in wastewater purification, including eco-friendly approaches and high efficiency; yet further efforts are still necessitated to reduce the energy consumption as well as the overall investment during contaminated water treatment. For instance, optimizing the existing technique/equipment/condition and/or seeking new nanomaterials with an excellent surface area can increase the efficiency of wastewater treatment with high economic viability.

## 2.4 Nanofibrous Sorbents, Membranes, and Aerogels for Removing Oil From Water

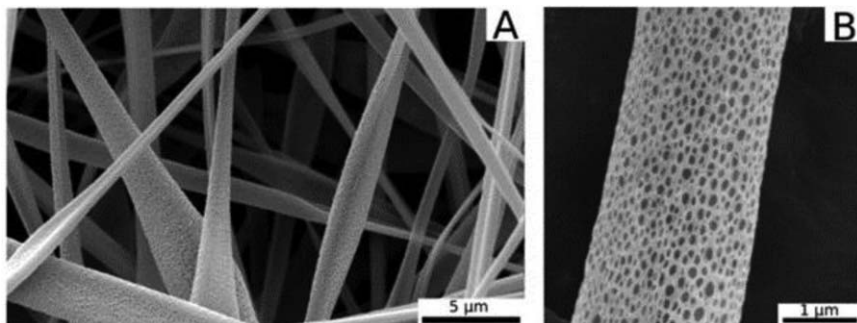
Nanofiber materials refer to fiber materials with a diameter of less than 1000 nm, which can be prepared by methods such as electrospinning, stretching, template synthesis, self-assembly, and microphase separation.<sup>84</sup> Due to their characteristics of high porosity, good flexibility, large surface area, adjustable wettability, good connectivity, and easy synthesis from various materials (polymers, carbon materials, ceramics, *etc.*), nanofibers have the huge potential for applications in the environmental field, including the separation of oil and water.<sup>85–90</sup> Nanofiber materials can be divided into three types, namely, nanofibrous sorbents, nanofibrous membranes, and nanofibrous aerogels.<sup>91</sup> In this section, the applications of nanofiber materials in oil–water separation will be described and summarized based on these three categories.

### 2.4.1 Nanofibrous Sorbents

The use of sorbents to clean up spilled oil is one of the most economical and effective methods.<sup>92,93</sup> The principle of sorbents is to concentrate petroleum and convert it into solid or semisolid, which needs the sorbents to possess high porosity, high capacity, lipophilic and hydrophobic properties, and excellent repeatability. Nanofibrous materials have the abovementioned characteristics and show great potential as oil-absorbing sorbents.<sup>94</sup> Nanofibrous sorbents mainly can be divided into polymer-based and carbon-based nanofibrous sorbents based on the source of the original materials. The polymer-based nanofibrous sorbents are hydrophobic and lipophilic polymer materials, such as polyethylene, polypropylene, polystyrene, poly(vinyl chloride), polysiloxanes, and poly(vinylidene fluoride). Their hybrids are also ideal raw materials for preparing high-performance nanofibrous sorbents.<sup>95,96</sup> For example, Eichhorn *et al.* used cellulose acetate butyrate (CAB) as the raw material to prepare nanofibrous material with nanopores, high surface roughness, and high surface area (Figure 2.5) *via* one-step electrospinning in very high humidity conditions.<sup>97</sup> These characteristics endowed the CAB-based nanofibrous sorbents with excellent oil absorption capacity, reaching  $60 \text{ g g}^{-1}$ , which was much higher than that of commercial polypropylene. Its repeatability was excellent: it still maintained 80% of the adsorption capacity even after five cycles of adsorption.

The addition of suitable fillers can further increase the surface roughness of the polymer-based nanofibrous sorbents, thereby improving the oil absorption capacity. Li *et al.* incorporated modified poly(3-hydroxybutyrate) (PHB) rubber filler into poly(lactic acid) (PLA) using ring-opening polymerization (Figure 2.6a) and prepared PLA/PHB-filler nanofibers with 400–700 nm diameters using electrospinning (Figure 2.6b and c).<sup>98</sup> The incorporation of the PHB filler offered nanofibers high surface roughness and surface area and an excellent oleophilic–hydrophobic surface, leading to the ability to absorb oil





**Figure 2.5** SEM images of the porous CAB-based nanofibrous sorbent at different magnifications: (A) 10 000 $\times$  (B) 60 000 $\times$ . Adapted from ref. 97 with permission from Elsevier, Copyright 2019.

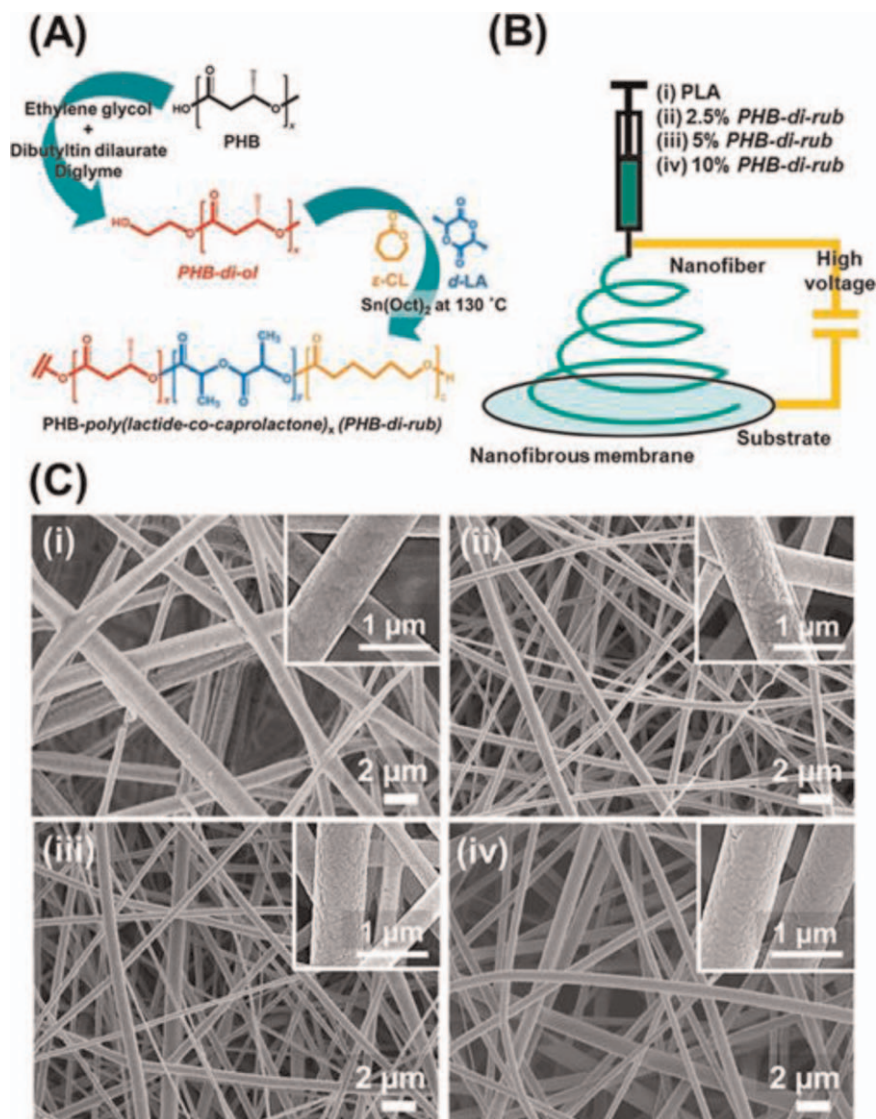
15 times their own weight. At the same time, the nanofibers also showed excellent biodegradability and repetitive applicability, providing new ideas for the green and repeatable design of nanofiber sorbents.

Although the polymer nanofiber sorbent shows great oil–water separation potential, the organic nanofiber sorbent may swell or even dissolve when it is washed and recycled by organic solvents, compromising its performance. The use of carbon nanofibrous can solve this problem. Liu *et al.* developed a sublimation method to prepare macroporous carbon nanofibrous sorbents, which showed excellent oil absorption performance with the maximum adsorption capacity for silicone oil reaching 138.4 g g<sup>-1</sup>.<sup>99</sup> At the same time, the fiber could be reused after being cleaned by an organic solvent, showing an application prospect in cleaning up oil spills.

#### 2.4.2 Nanofibrous Membranes

Membrane separation technology is considered to be one of the most promising methods for oil–water separation, which has the advantages of easy preparation, flexible operation, and high efficiency.<sup>100,101</sup> Among various membranes, nanofibrous membranes have the advantages of high specific surface area, reasonable pore structure, high selectivity, and good compatibility. They can achieve low energy consumption and high permeability, so they are widely applied in the oil–water separation field.<sup>102</sup>

So far, researchers have developed three different types of oil–water separation nanofibrous membranes. First is the superhydrophobic nanofibrous membrane used for oil removal from water. It usually has two structures that can be designed: (1) superhydrophobic nanofibrous membranes with a large pore structure and suitable pore diameter and (2) superhydrophobic nanofibrous membranes with a layered surface structure. The first membrane structure can well separate oil from a water-in-oil emulsion or heavy oil/water mixture, but it is prone to encounter serious and difficult cleaning dirt problems; in contrast, the second membrane structure usually has poor separation capabilities but have better antifouling capabilities.<sup>86,103</sup>



**Figure 2.6** (A) Synthetic route of PHB rubber filler/PLA copolymer by ring-opening polymerization. (B) Schematic diagram of copolymer electrospinning. (C) SEM images of nanofibrous sorbents with different magnifications and different PHB rub filler contents. Adapted from ref. 98 with permission from American Chemical Society, Copyright 2020.

The second is the superhydrophilic nanofibrous membrane for water separation, which is usually manufactured through a series of complex procedures.<sup>104,105</sup> Compared with the superhydrophobic nanofiber membrane, the superhydrophilic nanofiber membrane has a relatively low risk of clogging. The third are intelligent nanofibrous membranes, such as Janus

nanofiber membranes<sup>106,107</sup> and responsive nanofiber membranes<sup>108,109</sup> with adjustable surface wettability, which can achieve a good balance between permeability and antifouling properties. Taking an example of responsive nanofibrous membranes, under external stimuli (such as temperature, UV, pH, *etc.*), the responsive nanofiber membrane can achieve a reversible transition between superhydrophobic and superhydrophilic states by changing the structural or chemical properties, thereby achieving controllable oil–water separation.<sup>110</sup> Chen *et al.* also carried out related work.<sup>111</sup> They used an amphiphilic copolymer containing poly(hexadecyl acrylate) and poly(2-vinylpyridine) blocks to modify the surface of three-dimensional porous graphene and obtained pH-responsive nanofibrous membrane with variable surface wettability, leading to the excellent and controllable oil–water separation ability.

### 2.4.3 Nanofibrous Aerogel

Compared to nanofibrous membranes, nanofibrous aerogels present the unique characteristics of being ultralight, with high elasticity, large internal surface area, and good compressibility,<sup>112–114</sup> leading to a huge application potential in the field of oil–water separation.<sup>115–117</sup> Generally, nanofibrous aerogels for oil–water separation need to be designed in consideration of three aspects: (1) the three-dimensional open-cell honeycomb structure, (2) the mechanical strength and compression resistance, (3) the ability to demulsify and separate water-in-oil emulsions.<sup>91</sup>

Based on these criteria, Wang *et al.* used PVA-*co*-PE masterbatch and CAB as raw materials to obtain PVA-*co*-PE nanofibers with 100–300 nm diameter through the method of melt-extrusion-phase-separation and then prepared two polymer nanofibrous aerogels (NFA) and hydrophobic–lipophilic nanofibrous aerogel (HNFA) with high porosity *via* the direct freeze-drying method.<sup>118</sup> Among them, the HNFAs showed excellent oil–water separation ability and reusability, realizing the high-efficiency separation of water–oil emulsions.

In summary, nanofibers have been widely used in the field of oil–water separation due to their easy large-scale preparation, high porosity, good flexibility, large specific surface area, adjustable wettability, and good connectivity. Especially in these years, considerable progress has been made in oil–water separation efficiency and reusability, making it one of the most promising materials for effective oil–water separation. However, most of the nanofibrous materials used for oil–water separation are still in the laboratory stage, and the fine surface structure is easily destroyed. Continuous efforts are needed to develop and promote related research and industrialization.

## 2.5 Thin-film Nanocomposite Membranes for Energy-efficient Water Purification

Membranes have been developed and widely applied for water purification over the past 40 years.<sup>119</sup> Membrane-based separations have been recognized

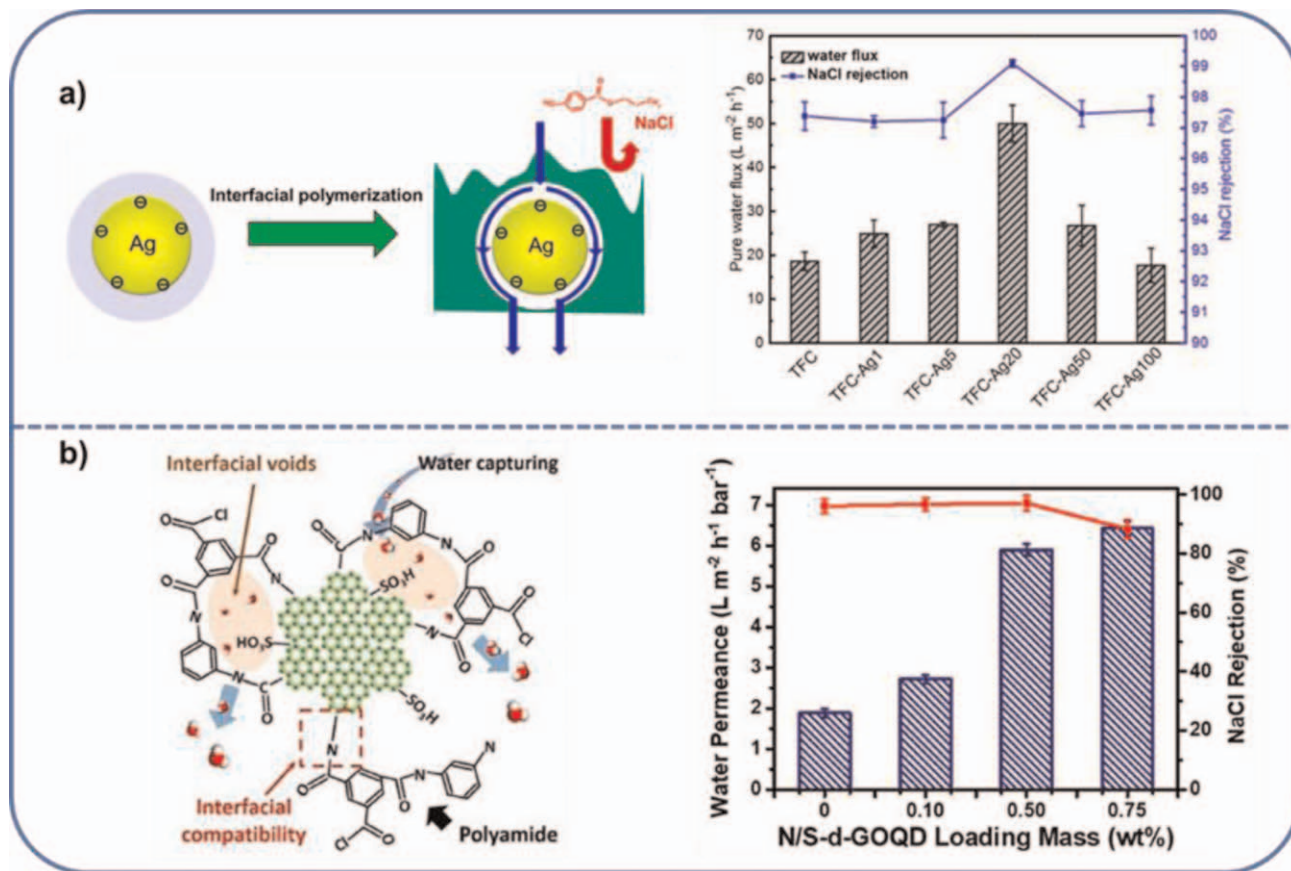
as energy-efficient separations as they can save 90% energy consumption compared to the traditional separation processes.<sup>120</sup> According to the pore size, water filtration membranes can be classified into microfiltration (MF), ultrafiltration (UF), nanofiltration (NF), and reverse osmosis (RO).<sup>121</sup> In MF and UF, substances with sizes larger than 2 nm can be removed, such as suspended particles, bacteria, viruses, proteins, and oils. In comparison, NF and RO separate small molecules with a molecular weight below 1000 g mol<sup>-1</sup> and a size less than 2 nm, like ions and small organic solutes. The difference between NF and RO lies in the pore size, where RO membranes possess a much denser layer that can remove monovalent ions from water compared to NF membranes that can only reject divalent ions.

The state-of-the-art RO membranes are thin-film composite (TFC) membranes, where an ultrathin selective layer with a thickness of 100–300 nm is formed on a porous support layer.<sup>122</sup> The selective layer is commonly formed *via* interfacial polymerization between a diamine dissolved in the aqueous phase and an aryl chloride in the oil phase. The generated polyamide network is dense enough to reject ions, but the water flux is usually low ( $\sim 1 \text{ L m}^{-2} \text{ h}^{-1} \text{ bar}^{-1}$ ), which makes the membrane less economically favored. In order to improve the water flux, various nanomaterials, from zero dimension to three dimensions, have been incorporated into the polyamide selective layer to fabricate TFN membranes.<sup>123,124</sup> This section will summarize and discuss the recent developments in nanomaterials in TFN membranes for water purification.

### 2.5.1 Zero-dimensional Materials: Nanoparticles and Quantum Dots

NPs, such as noble metals, metal oxide NPs, and zeolite, have been extensively applied to fabricate TFN membranes. The very first attempt was made by adding NaA zeolite into the oil phase *via* the interfacial polymerization process.<sup>123</sup> The pure water permeability (PWP) of the pore-opened TFN membrane was higher than the pore-filled TFN membrane due to the increased porosity. Interestingly, the pore-filled zeolite TFN membrane also possessed higher PWP than the pure polyamide TFC membrane. The increment in PWP was also reported in other works even though the NPs were nonporous noble metal and metal oxide. Recently, a study postulated that nanochannels were formed around the silver (Ag) NPs (Figure 2.7a), which could be attributed to the hydrolysis of trimesoyl chloride.<sup>125</sup> The rejections toward NaCl, boron, and small organic solutes were slightly increased due to the improved size exclusion and Donnan exclusion effect.

QDs, such as CQDs, GQDs, and graphene oxide quantum dots (GOQDs), have been employed to develop TFN membranes with high flux and anti-fouling properties in recent years. They possess excellent hydrophilicity that can facilitate fast water transport through the membrane. To avoid the nanodefects between the fillers and the polyamide selective layer, a GOQD decorated with ammonia/sulfonic groups was synthesized and incorporated,



**Figure 2.7** (a) Nanochannels created around the Ag NPs due to the hydrolysis of trimesoyl chloride and the separation performance. Adapted from ref. 125 with permission from American Chemical Society, Copyright 2019. (b) Schematic diagram of the interaction between GOQD and the polyamide layer and separation performance with GOQD loading. Adapted from ref. 126 with permission from American Chemical Society, Copyright 2020.

as shown in Figure 2.7b.<sup>126</sup> The water permeance was increased by three times, attributed to (1) the formation of interfacial voids as water transport channels, (2) the enhanced internal polarity with improved hydrophilicity, and (3) the enlarged surface area. At the same time, the NaCl rejection was slightly increased due to (1) the covalent bond formed between modified GOQDs and polyamide network and (2) the enhanced Donnan effect resulting from negatively charged GOQDs.

### 2.5.2 One-dimensional Materials: Nanotubes

Nanotubes, *e.g.* CNTs, titania nanotubes, and halloysite nanotubes, are one-dimensional structured materials with a high surface-to-volume ratio. They have been incorporated into the thin selective layer to increase the porosity and create transport channels.<sup>127–129</sup> However, the low affinity between the nanotubes and the polyamide layer may generate interfacial nanodefects, resulting in low selectivity. Thus, modifying nanotubes with functional groups is a feasible approach to increase the affinity and minimize the defects. A recent work reported that the aromatic amine-functionalized CNTs could be incorporated into TFN membranes with higher chlorine and acid resistance, better desalination performance, and arsenate rejection compared to the typical amine-functionalized CNTs.<sup>127</sup>

### 2.5.3 Two-dimensional Materials: Nanosheets

Nanosheets have been utilized to form a laminar structure to function as a membrane with intrinsic pores and extrinsic flow channels. Due to the high porosity and size-sieving property, nanosheets such as GO, 2D MOF, and layered double hydroxide (LDH) nanosheets have been incorporated into the polyamide layer to improve the performance. GO is derived from graphene with oxygen-containing functional groups, which enable GO to be dispersed homogeneously in water. Thus, many researchers have added GO into the aqueous solution to fabricate TFN membranes. Due to the hydrophilic property of GO, the TFN membrane can be designed with antifouling properties. In a recent study, a GO-modified TFN membrane was fabricated with enhanced water flux and antifouling properties for forward osmosis.<sup>130</sup> The TFN membranes were applied for sewage filtration for 41 h and 90% water flux could be recovered with an in-line water cleaning-in-place process for 15 min, demonstrating its strong antifouling ability. Another research group synthesized 2D MOF particles, Cu-tetrahydroxy-1,4-quinone, which was incorporated into the polyamide layer by spray deposition prior to interfacial polymerization.<sup>131</sup> The 2D MOF TFN membrane exhibited an increased water permeability up to 2.4 times with a slight increase in salt rejection compared to the pristine TFC membrane in a brackish water RO test. LDH is a hydrotalcite-like 2D material with positively charged metal hydroxide layers intercalated with anions of suitable choices. A Co–Al LDH with a size in the range of 50–100 nm and an interlayer spacing of 3.2 nm was synthesized and

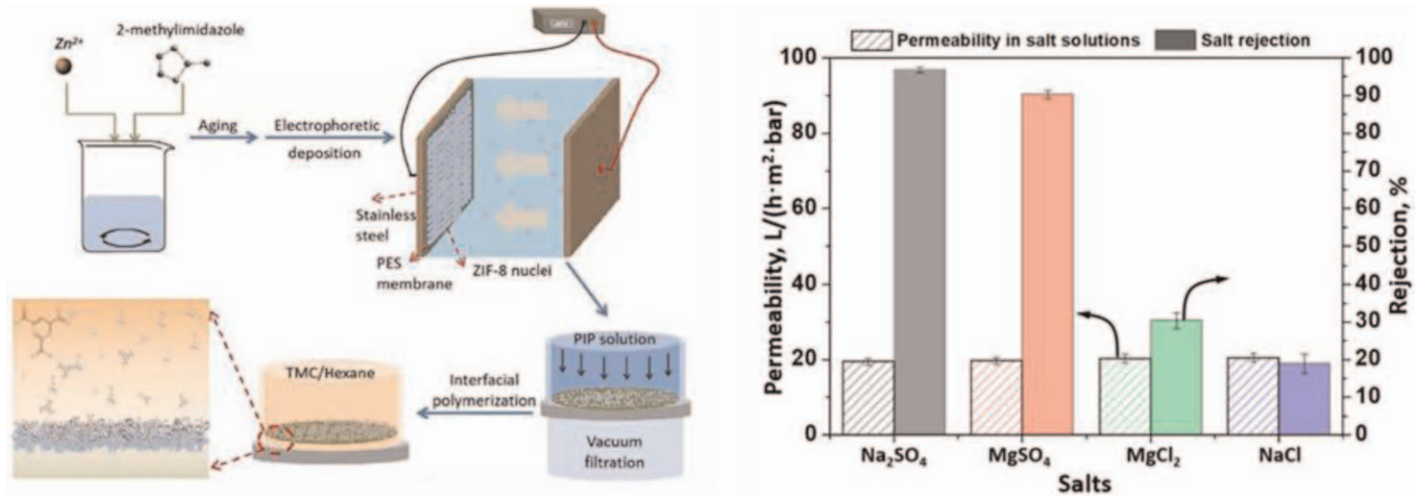
added in the organic phase during the interfacial polymerization.<sup>132</sup> With the improved hydrophilicity and surface roughness, the optimized TFN membrane exhibited a water permeance of  $2.75 \text{ L m}^{-2} \text{ h}^{-1} \text{ bar}^{-1}$  with a 99% rejection in a 2000 ppm NaCl solution.

#### 2.5.4 Three-dimensional Materials: Metal–Organic Frameworks and Organic Cages

Three-dimensional materials, such as MOFs and porous organic materials (POMs), are porous materials that contain intrinsic pores. They usually possess high porosity and relatively rigid structure so that they can increase the porosity and permeability of the polyamide network. In addition, the intrinsic pores can enhance the size-sieving effect of the membrane, leading to the breakthrough in permeability and selectivity trade-off.

MOFs have been extensively employed in TFN membranes due to their high porosity and good chemical stability. However, due to the low affinity, the MOFs tend to agglomerate in the polyamide layer by simply adding them into the aqueous or oil phase. To solve this problem, researchers have attempted to (1) modify the MOFs to have a higher affinity with the polyamide layer and (2) fabricate an MOF interlayer between the polyamide network and substrate. Chung *et al.* fabricated TFN membranes by spray-coating a tannic acid-modified UiO-66-NH<sub>2</sub> onto the substrate prior to forming the polyamide layer *via* interfacial polymerization.<sup>133</sup> The spray-coating facilitated the uniform dispersion of UiO-66-NH<sub>2</sub> on the substrate and the tannic acid might react with the acyl chloride to increase the affinity with the polyamide layer. In addition, the UiO-66-NH<sub>2</sub> contained intrinsic pores of 5.1 Å, which could selectively allow water to pass through while rejecting Na<sup>+</sup> and Cl<sup>-</sup>. Due to the enhanced hydrophilicity and size-sieving effect, the developed TFN membranes exhibited higher water permeance and NaCl rejection in reverse osmosis desalination compared to the pristine TFC membrane. Another work utilized electrophoretic deposition to synthesize a thin layer of ZIF-8 onto the substrate and fabricated the polyamide layer by vacuum-assisted interfacial polymerization.<sup>134</sup> The membrane substrate was mounted to a stainless steel as cathode and immersed in a ZIF-8 solution with another bare stainless steel as anode, as shown in Figure 2.8. By applying a small direct current ( $0.72 \text{ mA cm}^{-2}$ ) for a short period (0.5–2 min), the ZIF-8 could be uniformly deposited on the membrane substrate without aggregation.

POMs are porous materials built with organic skeletons, including polymers of intrinsic microporosity (PIMs), COFs, and porous organic cages (POCs). As POMs contain organic functional groups, they often have good compatibility with the polyamide networks. Xu *et al.* incorporated COF nanosheets into the polyamide layer and applied the developed membrane for reverse osmosis desalination.<sup>135</sup> The COF nanosheets could enhance the porosity and surface wettability of the polyamide layer, leading to an increase in water permeance ( $0.7$  to  $2.2 \text{ L m}^{-2} \text{ h}^{-1} \text{ bar}^{-1}$ ). The rejection toward NaCl was also slightly improved from 96.3 to 97.7%. POCs have also been



**Figure 2.8** Fabrication process of ZIF-8 interlayer *via* electrophoretic deposition and vacuum filtration–assisted interfacial process. The separation performance of the optimized membrane in  $Na_2SO_4$ ,  $MgSO_4$ ,  $MgCl_2$ , and  $NaCl$  salt solutions. Adapted from ref. 134 with permission from Elsevier, Copyright 2021.



applied as nanofillers for TFN membranes. One POC named Noria was synthesized by the condensation reaction of resorcinol and 1,5-pentanediol and it was coated as an interlayer by codeposition with polyethyleneimine.<sup>136</sup> A polyamide layer was then fabricated on the top of this interlayer, where its thickness was decreased due to the host-guest heterogeneous interaction between Noria and amine monomer. The optimized membrane exhibited a high water permeance of  $28 \text{ L m}^{-2} \text{ h}^{-1} \text{ bar}^{-1}$  with over 96% rejection toward divalent salts.

## 2.6 Conclusions and Outlook

This chapter introduces and summarizes the recent developments in nanotechnology for impurity detection and water treatment. Biosensors and NPs can detect impurities in water within a short time, making them good for on-site detection and real-time monitoring of water quality. However, one biosensor or NP can only detect one or a few types of impurities, making them less cost effective. Future work may focus on developing sensors that can detect several types of impurities at one time. Nanosorbents and nanofibrous materials are applied to absorb contaminants in water, so they are designed with high porosity and tortuous microstructure. Nanophotocatalysts have advantages in terms of high conversion rates to degrade organic pollutants in water, but they cannot remove inorganic pollutants like heavy metal ions and salts. TFN membranes can remove most of the contaminants in water with the external pressure required. Future studies may combine these water treatment techniques to achieve an amplified effect. For example, photocatalysts have the potential to be incorporated into TFN membranes to enhance the self-cleaning ability of the membranes. Other nanotechnology-based water treatment methods are expected and have the potential to be designed and investigated.

## References

1. M. M. Mekonnen and A. Y. Hoekstra, *Sci. Adv.*, 2016, **2**, e1500323.
2. V. A. Tzanakakis, N. V. Paranychianakis and A. N. Angelakis, *Water*, 2020, **12**, 2347.
3. L. Ye, H. You, J. Yao and H. Su, *Desalination*, 2012, **298**, 1–12.
4. C. Teodosiu, A.-F. Gilca, G. Barjoveanu and S. Fiore, *J. Cleaner Prod.*, 2018, **197**, 1210–1221.
5. O. M. Rodriguez-Narvaez, J. M. Peralta-Hernandez, A. Goonetilleke and E. R. Bandala, *Chem. Eng. J.*, 2017, **323**, 361–380.
6. M. Nasrollahzadeh, M. Sajjadi, S. Irvani and R. S. Varma, *J. Hazard. Mater.*, 2021, **401**, 123401.
7. P. Westerhoff, P. Alvarez, Q. Li, J. Gardea-Torresdey and J. Zimmerman, *Environ. Sci.: Nano*, 2016, **3**, 1241–1253.
8. D. Jassby, T. Y. Cath and H. Buisson, *Nat. Nanotechnol.*, 2018, **13**, 670–672.
9. S. Cheriyaundath and S. L. Vavilala, *Water Environ. J.*, 2021, **35**, 123–132.

10. C. Santhosh, V. Velmurugan, G. Jacob, S. K. Jeong, A. N. Grace and A. Bhatnagar, *Chem. Eng. J.*, 2016, **306**, 1116–1137.
11. T. A. Saleh, *Environ. Technol. Innov.*, 2020, **20**, 101067.
12. J. N. Tiwari, R. N. Tiwari and K. S. Kim, *Prog. Mater. Sci.*, 2012, **57**, 724–803.
13. Z. Wang, T. Hu, R. Liang and M. Wei, *Front. Chem.*, 2020, **8**, 320.
14. C. Tan, X. Cao, X.-J. Wu, Q. He, J. Yang, X. Zhang, J. Chen, W. Zhao, S. Han, G.-H. Nam, M. Sindoro and H. Zhang, *Chem. Rev.*, 2017, **117**, 6225–6331.
15. S. Das, P. Heasman, T. Ben and S. Qiu, *Chem. Rev.*, 2017, **117**, 1515–1563.
16. R. Li, L. Zhang and P. Wang, *Nanoscale*, 2015, **7**, 17167–17194.
17. K. Gregorczyk and M. Knez, *Prog. Mater. Sci.*, 2016, **75**, 1–37.
18. V. Vogiazzi, A. de la Cruz, S. Mishra, V. Shanov, W. R. Heineman and D. D. Dionysiou, *ACS Sens.*, 2019, **4**, 1151–1173.
19. L. Ruiyi, X. Qianfang, L. Zaijun, S. Xiulan and L. Junkang, *Biosens. Bioelectron.*, 2013, **44**, 235–240.
20. S. Loyprasert, P. Thavarungkul, P. Asawatreratanakul, B. Wongkittisuksa, C. Limsakul and P. Kanatharana, *Biosens. Bioelectron.*, 2008, **24**, 78–86.
21. N. J. Ronkainen, H. B. Halsall and W. R. Heineman, *Chem. Soc. Rev.*, 2010, **39**, 1747–1763.
22. L. Hou, Y. Ding, L. Zhang, Y. Guo, M. Li, Z. Chen and X. Wu, *Sens. Actuators, B*, 2016, **233**, 63–70.
23. C. Gan, L. Ling, Z. He, H. Lei and Y. Liu, *Biosens. Bioelectron.*, 2016, **78**, 381–389.
24. Y. Zhang, M. Chen, H. Li, F. Yan, P. Pang, H. Wang, Z. Wu and W. Yang, *Sens. Actuators, B*, 2017, **244**, 606–615.
25. Z. He, J. Wei, C. Gan, W. Liu and Y. Liu, *RSC Adv.*, 2017, **7**, 39906–39913.
26. H. Zhao, J. Tian and X. Quan, *Colloids Surf., B*, 2013, **103**, 38–44.
27. J. Zhang, J. Lei, C. Xu, L. Ding and H. Ju, *Anal. Chem.*, 2010, **82**, 1117–1122.
28. C. Gan, Z. Sun, L. Ling, Z. He, H. Lei and Y. Liu, *RSC Adv.*, 2016, **6**, 51662–51669.
29. P. Pang, X. Teng, M. Chen, Y. Zhang, H. Wang, C. Yang, W. Yang and C. J. Barrow, *Sens. Actuators, B*, 2018, **266**, 400–407.
30. J. Zhang, Y. Sun, H. Dong, X. Zhang, W. Wang and Z. Chen, *Sens. Actuators B Chem.*, 2016, **233**, 624–632.
31. J. Tian, H. Zhao, F. Yuan, X. Quan and S. Chen, *Int. J. Environ. Anal. Chem.*, 2014, **94**, 988–1000.
32. C. Gan, B. Wang, J. Huang, A. Qileng, Z. He, H. Lei, W. Liu and Y. Liu, *Biosens. Bioelectron.*, 2017, **98**, 126–133.
33. Q. Wei, Y. Zhao, B. Du, D. Wu, Y. Cai, K. Mao, H. Li and C. Xu, *Adv. Funct. Mater.*, 2011, **21**, 4193–4198.
34. H.-W. Yu, J. Lee, S. Kim, G. H. Nguyen and I. S. Kim, *Anal. Bioanal. Chem.*, 2009, **394**, 2173–2181.
35. A. Sassolas, G. Catanante, A. Hayat and J.-L. Marty, *Anal. Chim. Acta*, 2011, **702**, 262–268.
36. O. I. Fontal, M. R. Vieytes, J. M. V. Baptista de Sousa, M. C. Louzao and L. M. Botana, *Anal. Biochem.*, 1999, **269**, 289–296.

37. M. Campàs, D. Szydłowska, M. Trojanowicz and J.-L. Marty, *Biosens. Bioelectron.*, 2005, **20**, 1520–1530.
38. M. Campàs, D. Szydłowska, M. Trojanowicz and J.-L. Marty, *Talanta*, 2007, **72**, 179–186.
39. M. Campàs, M. G. Olteanu and J.-L. Marty, *Sens. Actuators, B*, 2008, **129**, 263–267.
40. G. Catanante, L. Espin and J.-L. Marty, *Biosens. Bioelectron.*, 2015, **67**, 700–707.
41. N. Yu, J. Ding, W. Wang, X. Wang and W. Qin, *Sens. Actuators, B*, 2016, **230**, 785–790.
42. E. Devic, D. Li, A. Dauta, P. Henriksen, A. Codd Geoffrey, J.-L. Marty and D. Fournier, *Appl. Environ. Microbiol.*, 2002, **68**, 4102–4106.
43. N. Idil and B. Mattiasson, *Sensors*, 2017, **17**, 1375.
44. R. B. Queirós, J. P. Noronha, P. V. S. Marques, J. S. Fernandes and M. G. F. Sales, *Analyst*, 2012, **137**, 2437–2444.
45. R. B. Queirós, A. Guedes, P. V. S. Marques, J. P. Noronha and M. G. F. Sales, *Sens. Actuators, B*, 2013, **189**, 21–29.
46. C. Yuan, K. Zhang, Z. Zhang and S. Wang, *Anal. Chem.*, 2012, **84**, 9792–9801.
47. K. Zhang, H. Zhou, Q. Mei, S. Wang, G. Guan, R. Liu, J. Zhang and Z. Zhang, *J. Am. Chem. Soc.*, 2011, **133**, 8424–8427.
48. J. Yao, K. Zhang, H. Zhu, F. Ma, M. Sun, H. Yu, J. Sun and S. Wang, *Anal. Chem.*, 2013, **85**, 6461–6468.
49. H. Zhu, T. Yu, H. Xu, K. Zhang, H. Jiang, Z. Zhang, Z. Wang and S. Wang, *ACS Appl. Mater. Interfaces*, 2014, **6**, 21461–21467.
50. H. Zhu, W. Zhang, K. Zhang and S. Wang, *Nanotechnology*, 2012, **23**, 315502.
51. K. Zhang, T. Yu, F. Liu, M. Sun, H. Yu, B. Liu, Z. Zhang, H. Jiang and S. Wang, *Anal. Chem.*, 2014, **86**, 11727–11733.
52. V. Sharma and M. S. Mehata, *Spectrochim. Acta, Part A*, 2021, **260**, 119937.
53. S. Feng, Z. Gao, H. Liu, J. Huang, X. Li and Y. Yang, *Spectrochim. Acta, Part A*, 2019, **212**, 286–292.
54. X. Guo, J. Huang, Y. Wei, Q. Zeng and L. Wang, *J. Hazard. Mater.*, 2020, **381**, 120969.
55. Z. Li, Y. Wang, Y. Ni and S. Kokot, *Sens. Actuators, B*, 2015, **207**, 490–497.
56. Y. Yan, H. Yu, K. Zhang, M. Sun, Y. Zhang, X. Wang and S. Wang, *Nano Res.*, 2016, **9**, 2088–2096.
57. J. Yang, Y. Zhang, L. Zhang, H. Wang, J. Nie, Z. Qin, J. Li and W. Xiao, *Chem. Commun.*, 2017, **53**, 7477–7480.
58. S. Li, J. Liu, Z. Chen, Y. Lu, S. S. Low, L. Zhu, C. Cheng, Y. He, Q. Chen, B. Su and Q. Liu, *Sens. Actuators, B*, 2019, **297**, 126811.
59. Y. Cheng, Y. Li, D. Li, B. Zhang, R. Hao and S. Sang, *Int. J. Electrochem. Sci.*, 2017, **12**, 7754–7764.
60. U. Chakraborty, G. Bhanjana, Kannu, N. Kaur, R. Sharma, G. Kaur, A. Kaushik and G. R. Chaudhary, *J. Hazard. Mater.*, 2021, **416**, 125771.

61. P. Balasubramanian, T. S. T. Balamurugan, S. M. Chen and T. W. Chen, *J. Hazard. Mater.*, 2019, **361**, 123–133.
62. A. S. Saleemi, M. Hafeez, A. Munawar, N. Akhtar, W. Abbas, M. W. Mazhar, Z. Shafiq, A. P. Davis and S. Lee, *J. Mater. Chem. C*, 2020, **8**, 12984.
63. Y. Su, X. Zheng, H. Cheng, M. Rao, K. Chen, J. Xia, L. Lin and H. Zhu, *J. Hazard. Mater.*, 2021, **409**, 124926.
64. S. Behi, N. Bohli, J. Casanova-Chafer, E. Llobet and A. Abdelghani, *Sensors*, 2020, **20**, 3413.
65. M. Maruthupandy, Y. Zuo, J. Chen, J. Song, H. Niu, C. Mao, S. Zhang and Y. Shen, *Appl. Surf. Sci.*, 2017, **397**, 167–174.
66. A. A. Yaqoob, T. Parveen, K. Umar and M. N. Mohamad Ibrahim, *Water*, 2020, **12**, 495.
67. N. Nouri, P. Khorram, O. Duman, T. Sibel and S. Hassan, *Trends Environ. Anal. Chem.*, 2020, **25**, e00081.
68. D. Seripa, V. Solfrizzi, B. P. Imbimbo, A. Daniele, A. Santamato, M. Lozupone, G. Zuliani, A. Greco, G. Logroscino and F. Panza, *Expert Rev. Neurother.*, 2016, **16**, 259–277.
69. S. M. Goodman, R. Bura and A. B. Dichiarara, *ACS Appl. Nano Mater.*, 2018, **1**, 5682–5690.
70. S. Rakass, H. Oudghiri Hassani, A. Mohmoud, F. Kooli, M. Abboudi, E. Assirey and F. Al Wadaani, *Molecules*, 2021, **26**, 1378.
71. H. Saravaia, H. Gupta, P. Popat, P. Sodha and V. Kulshrestha, *ACS Appl. Mater. Interfaces*, 2018, **10**, 44059–44070.
72. A. E. D. Mahmoud, K. M. Al-Qahtani, S. O. Alflajj, S. F. Al-Qahtani and F. A. Alsamhan, *Sci. Rep.*, 2021, **11**, 12547.
73. T. Poiger, I. J. Buerge, A. Bächli, M. D. Müller and M. E. Balmer, *Environ. Sci. Pollut. Res.*, 2017, **24**, 1588–1596.
74. J. E. Casida and K. A. Durkin, *Chem. Res. Toxicol.*, 2017, **30**, 94–104.
75. S. F. Soares, C. O. Amorim, J. S. Amaral, T. Trindade and A. L. Daniela-Silva, *J. Environ. Chem. Eng.*, 2021, **9**, 105189.
76. Y. Yang, Q. Deng, W. Yan, C. Jing and Y. Zhang, *Chem. Eng. J.*, 2018, **352**, 581–589.
77. H. Wu, Q. Sun, J. Chen, G.-Y. Wang, D. Wang, X.-F. Zeng and J.-X. Wang, *Chem. Eng. J.*, 2021, **425**, 130640.
78. M. Dou, J. Wang, B. Gao, Z. Ma and X. Huang, *Chem. Eng. J.*, 2020, **394**, 124899.
79. I. F. Silva, I. F. Teixeira, R. D. F. Rios, G. M. do Nascimento, I. Binatti, H. F. V. Victória, K. Krambrock, L. A. Cury, A. P. C. Teixeira and H. O. Stumpf, *J. Hazard. Mater.*, 2021, **401**, 123713.
80. M. Dou, J. Wang, B. Gao, C. Xu and F. Yang, *Chem. Eng. J.*, 2020, **383**, 123134.
81. S. Le, Y. Ma, D. He, X. Wang and Y. Guo, *Chem. Eng. J.*, 2021, **426**, 130354.
82. F. Liu, C. Nie, Q. Dong, Z. Ma, W. Liu and M. Tong, *J. Hazard. Mater.*, 2020, **398**, 122865.

83. J. Hu, C. Chen, T. Hu, J. Li, H. Lu, Y. Zheng, X. Yang, C. Guo and C. M. Li, *J. Mater. Chem. A*, 2020, **8**, 19484–19492.
84. Kenry and C. T. Lim, *Prog. Polym. Sci.*, 2017, **70**, 1–17.
85. K. S. Ogueri and C. T. Laurencin, *ACS Nano*, 2020, **14**, 9347–9363.
86. J. Cui, F. Li, Y. Wang, Q. Zhang, W. Ma and C. Huang, *Sep. Purif. Technol.*, 2020, **250**, 117116.
87. M. Liu, N. Deng, J. Ju, L. Fan, L. Wang, Z. Li, H. Zhao, G. Yang, W. Kang, J. Yan and B. Cheng, *Adv. Funct. Mater.*, 2019, **29**, 1905467.
88. B. Yang, L. Wang, M. Zhang, J. Luo, Z. Lu and X. Ding, *Adv. Funct. Mater.*, 2020, **30**, 2000186.
89. M. Liu, P. Zhang, Z. Qu, Y. Yan, C. Lai, T. Liu and S. Zhang, *Nat. Commun.*, 2019, **10**, 3917.
90. Y. He, H. Guo, S. Hwang, X. Yang, Z. He, J. Braaten, S. Karakalos, W. Shan, M. Wang, H. Zhou, Z. Feng, K. L. More, G. Wang, D. Su, D. A. Cullen, L. Fei, S. Litster and G. Wu, *Adv. Mater.*, 2020, **32**, 2003577.
91. X. Wang, J. Yu, G. Sun and B. Ding, *Mater. Today*, 2016, **19**, 403–414.
92. Z. Jiang, L. D. Tijjing, A. Amarjargal, C. H. Park, K.-J. An, H. K. Shon and C. S. Kim, *Composites, Part B*, 2015, **77**, 311–318.
93. J. Saleem, M. Adil Riaz and M. Gordon, *J. Hazard. Mater.*, 2018, **341**, 424–437.
94. F. Topuz, M. A. Abdulhamid, S. P. Nunes and G. Szekely, *Environ. Sci.: Nano*, 2020, **7**, 1365–1372.
95. H. Zhang, Q. Zhen, Y. Yan, X. Guan, R. Liu and Y. Liu, *Mater. Lett.*, 2020, **261**, 127009.
96. H. Li, W. Wu, M. M. Bubakir, H. Chen, X. Zhong, Z. Liu, Y. Ding and W. Yang, *J. Appl. Polym. Sci.*, 2014, **131**, 40080.
97. A. Tanvir, V. P. Ting and S. J. Eichhorn, *Mater. Lett.*, 2020, **261**, 127116.
98. J. C. C. Yeo, D. Kai, C. P. Teng, E. M. J. R. Lin, B. H. Tan, Z. Li and C. He, *ACS Appl. Polym. Mater.*, 2020, **2**, 4825–4835.
99. H. Liu, C.-Y. Cao, F.-F. Wei, P.-P. Huang, Y.-B. Sun, L. Jiang and W.-G. Song, *J. Mater. Chem. A*, 2014, **2**, 3557–3562.
100. Y. Zhu, D. Wang, L. Jiang and J. Jin, *NPG Asia Mater.*, 2014, **6**, e101.
101. N. F. D. Junaidi, N. H. Othman, N. S. Fuzil, M. S. Mat Shayuti, N. H. Alias, M. Z. Shahrudin, F. Marpani, W. J. Lau, A. F. Ismail and N. D. Aba, *Sep. Purif. Technol.*, 2021, **258**, 118000.
102. R. Su, S. Li, W. Wu, C. Song, G. Liu and Y. Yu, *Sep. Purif. Technol.*, 2021, **256**, 117790.
103. W. Ma, M. Zhang, Z. Liu, M. Kang, C. Huang and G. Fu, *J. Membr. Sci.*, 2019, **570–571**, 303–313.
104. N. H. Ismail, W. N. W. Salleh, A. F. Ismail, H. Hasbullah, N. Yusof, F. Aziz and J. Jaafar, *Sep. Purif. Technol.*, 2020, **233**, 116007.
105. M. Shakiba, S. R. Nabavi, H. Emadi and M. Faraji, *Polym. Adv. Technol.*, 2021, **32**, 1301–1316.
106. H.-C. Yang, Y. Xie, J. Hou, A. K. Cheetham, V. Chen and S. B. Darling, *Adv. Mater.*, 2018, **30**, 1801495.

107. L. Yan, X. Yang, J. Long, X. Cheng, D. Pan, Y. Huang and L. Shao, *Chem. Commun.*, 2020, **56**, 478–481.
108. C.-T. Liu and Y.-L. Liu, *J. Mater. Chem. A*, 2016, **4**, 13543–13548.
109. H. Che, M. Huo, L. Peng, T. Fang, N. Liu, L. Feng, Y. Wei and J. Yuan, *Angew. Chem., Int. Ed.*, 2015, **54**, 8934–8938.
110. J. Schoeller, F. Itel, K. Wuertz-Kozak, G. Fortunato and R. M. Rossi, *Polym. Rev.*, 2021, 1–49.
111. H. Zhu, D. Chen, N. Li, Q. Xu, H. Li, J. He and J. Lu, *Adv. Funct. Mater.*, 2015, **25**, 597–605.
112. Y. Si, X. Wang, L. Dou, J. Yu and B. Ding, *Sci. Adv.*, 2018, **4**, eaas8925.
113. Y. Si, X. Wang, C. Yan, L. Yang, J. Yu and B. Ding, *Adv. Mater.*, 2016, **28**, 9512–9518.
114. F. Wang, J. Dai, L. Huang, Y. Si, J. Yu and B. Ding, *ACS Nano*, 2020, **14**, 8975–8984.
115. Y. Shen, D. Li, L. Wang, Y. Zhou, F. Liu, H. Wu, B. Deng and Q. Liu, *ACS Appl. Mater. Interfaces*, 2021, **13**, 20489–20500.
116. M. Zhang, S. Jiang, F. Han, M. Li, N. Wang and L. Liu, *Carbohydr. Polym.*, 2021, **264**, 118033.
117. G. Jiang, J. Ge, Y. Jia, X. Ye, L. Jin, J. Zhang, Z. Zhao, G. Yang, L. Xue and S. Xie, *Sep. Purif. Technol.*, 2021, **270**, 118740.
118. Q. Liu, J. Chen, T. Mei, X. He, W. Zhong, K. Liu, W. Wang, Y. Wang, M. Li and D. Wang, *J. Mater. Chem. A*, 2018, **6**, 3692–3704.
119. S. P. Nunes, P. Z. Culfaz-Emecen, G. Z. Ramon, T. Visser, G. H. Koops, W. Jin and M. Ulbricht, *J. Membr. Sci.*, 2020, **598**, 117761.
120. D. S. Sholl and R. P. Lively, *Nature*, 2016, **532**, 435–437.
121. R. W. Baker, *Membrane Technology and Applications*, John Wiley and Sons Ltd, United Kingdom, 3rd edn, 2012.
122. S. Hermans, H. Mariën, C. Van Goethem and I. F. J. Vankelecom, *Curr. Opin. Chem. Eng.*, 2015, **8**, 45–54.
123. B.-H. Jeong, E. M. V. Hoek, Y. Yan, A. Subramani, X. Huang, G. Hurwitz, A. K. Ghosh and A. Jawor, *J. Membr. Sci.*, 2007, **294**, 1–7.
124. W. J. Lau, S. Gray, T. Matsuura, D. Emadzadeh, J. Paul Chen and A. F. Ismail, *Water Res.*, 2015, **80**, 306–324.
125. Z. Yang, H. Guo, Z.-K. Yao, Y. Mei and C. Y. Tang, *Environ. Sci. Technol.*, 2019, **53**, 5301–5308.
126. Q. Shen, Y. Lin, Y. Kawabata, Y. Jia, P. Zhang, N. Akther, K. Guan, T. Yoshioka, H. Shon and H. Matsuyama, *ACS Appl. Mater. Interfaces*, 2020, **12**, 38662–38673.
127. S. Gholami, J. López, A. Rezvani, V. Vatanpour and J. L. Cortina, *Chem. Eng. J.*, 2020, **384**, 123348.
128. M. Ghanbari, D. Emadzadeh, W. J. Lau, S. O. Lai, T. Matsuura and A. F. Ismail, *Desalination*, 2015, **358**, 33–41.
129. I. Wan Azelee, P. S. Goh, W. J. Lau and A. F. Ismail, *J. Cleaner Prod.*, 2018, **181**, 517–526.
130. X. Wu, J. Tanner, D. Ng, D. Acharya and Z. Xie, *Chem. Eng. J.*, 2021, **420**, 127718.

131. F. Li, T. D. Liu, S. Xie, J. Guan and S. Zhang, *ChemSusChem*, 2021, **14**, 2452–2460.
132. Y. Mutharasi, Y. Zhang, M. Weber, C. Maletzko and T. S. Chung, *Desalination*, 2021, **498**, 114740.
133. D. L. Zhao, Q. Zhao and T. S. Chung, *Desalination*, 2021, **516**, 115230.
134. J. Li, R. Liu, J. Zhu, X. Li, S. Yuan, M. Tian, J. Wang, P. Luis, B. V. der Bruggen and J. Lin, *Desalination*, 2021, **512**, 115125.
135. L. Xu, B. Shan, C. Gao and J. Xu, *J. Membr. Sci.*, 2020, **593**, 117398.
136. Z. Zhai, C. Jiang, N. Zhao, W. Dong, H. Lan, M. Wang and Q. J. Niu, *J. Mater. Chem. A*, 2018, **6**, 21207–21215.

# *Nanotechnology for CO<sub>2</sub> Capture, Storage, and Conversion*

X. ZHANG,<sup>a</sup> N. QIN,<sup>a</sup> E. YE,<sup>b</sup> G. GUAN,<sup>\*a</sup> M. Y. HAN<sup>\*a,b</sup> AND Z. LI<sup>b,c</sup>

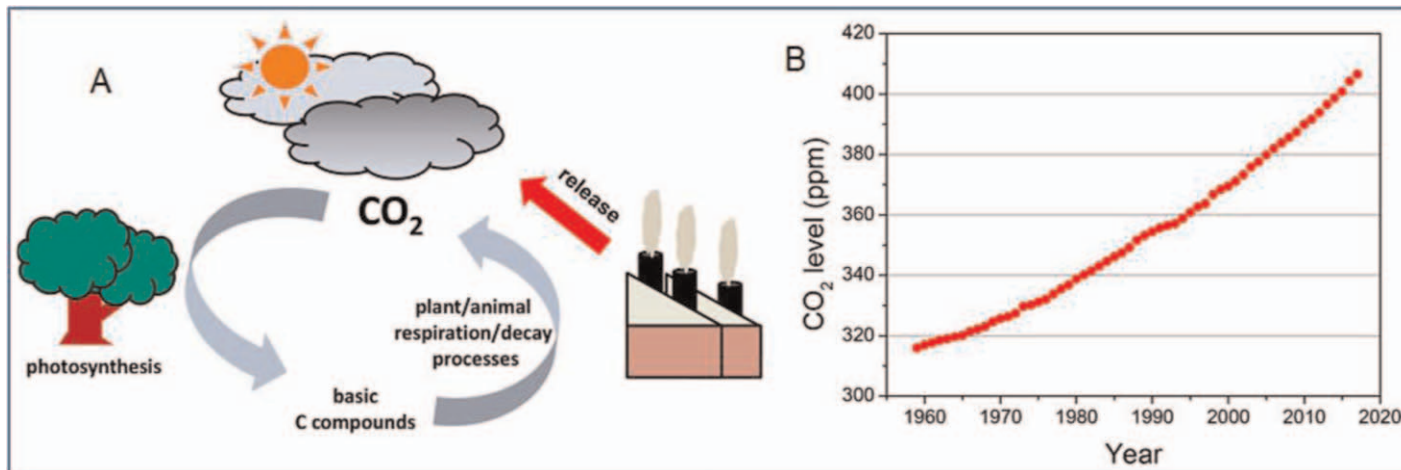
<sup>a</sup> Institute of Molecular Plus, Tianjin University, Tianjin 300072, P.R. China;

<sup>b</sup> Institute of Materials Research and Engineering, Agency for Science, Technology and Research (A\*STAR), 2 Fusionopolis Way, Innovis #08-03, Singapore 138634, Singapore; <sup>c</sup> Department of Materials Science and Engineering, National University of Singapore, Singapore 117575, Singapore  
\*Emails: guijianguan@tju.edu.cn; han\_mingyong@tju.edu.cn

## 3.1 Introduction

Resulting from the rapidly growing population and increasing industrial processes, carbon dioxide (CO<sub>2</sub>) has been released more excessively into the air atmosphere from human activities, power plants, and other industries.<sup>1</sup> Due to the fact that the existing green vegetation cannot completely absorb and convert that much CO<sub>2</sub> gas *via* photosynthesis (see Figure 3.1A), the CO<sub>2</sub> level has been gradually increasing year after year to move up the global temperature with the greenhouse effect (see Figure 3.1B), which seriously influences the global climate and Earth's life cycle through various abnormal variances such as melting of polar ice and ocean acidification.<sup>2,3</sup> In the aspect of environmental safety and human sustainability, the upper limit for atmospheric CO<sub>2</sub> was recognized to be 350 ppm; however, the atmospheric CO<sub>2</sub> value was as high as 410.45 ppm as of June 2019.<sup>4,5</sup> Therefore, lots of research work has recently been performed to decrease the CO<sub>2</sub> concentration to combat global warming.<sup>6</sup> On the one hand, we should use low-carbon or even noncarbon



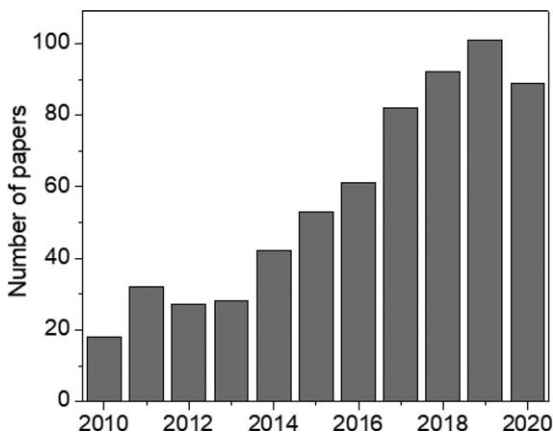


**Figure 3.1** (A) Production of CO<sub>2</sub> into the atmosphere and its cycling by natural photosynthesis. (B) Rapid increment of CO<sub>2</sub> levels in the past several decades. Reproduced from ref. 1 with permission from American Chemical Society, Copyright 2018.

energy to replace fossil fuels for controlling CO<sub>2</sub> production/emission.<sup>7</sup> On the other hand, effective strategies can be developed for CO<sub>2</sub> capture, storage and utilization.<sup>8</sup> To date, it is practically impossible to prevent CO<sub>2</sub> emissions from the human lifestyle, so the postcontrolling technologies are more promising for decreasing CO<sub>2</sub> concentration in the atmosphere. Particularly, the conversion of CO<sub>2</sub> to useful chemicals or fuels could potentially provide clean energy as well as CO<sub>2</sub> reduction for combating the climatic warming and energy shortage.<sup>9,10</sup> Because CO<sub>2</sub> is a thermodynamically stable molecule with the highest carbon valence state of +4, it is very challenging to mimic the natural photosynthesis process *via* artificial approaches, which will be critically determined by the superb properties of used catalytic materials.<sup>11</sup> Thus, it is extremely urgent to rationally design highly effective, stable, and scalable catalysts for substantial improvement in CO<sub>2</sub> reduction.<sup>5</sup>

Aiming at the above requirement for new materials, nanotechnology has frequently been employed for CO<sub>2</sub> capture, storage, and conversion through facilely producing diversified nanostructured materials possessing unique morphological, physical, and chemical features, which have offered unprecedented opportunities for reducing CO<sub>2</sub> concentration in the atmosphere.<sup>12,13</sup> Compared to the bulk counterpart, nanostructured systems possess a larger surface area for adsorbing CO<sub>2</sub> and more reactive sites to catalytically convert CO<sub>2</sub>.<sup>9</sup> As catalysts, nanomaterials exhibited more rapid photogenerated carrier kinetics, greater light absorption, and higher reaction efficiencies owing to their small size. Moreover, their well-defined morphology is beneficial for feasible installation onto other substrates, and surface modification/hybridization further improves their stability and performances.<sup>14</sup> In the future, the efficient implementation of CO<sub>2</sub> removal lies in the application of nanotechnology with a better condition for the environment and economic outlooks.<sup>15</sup> For example, novel porous nanomaterials as adsorbents are currently providing the most promising results because of their excellent physical stability and increased porosity.<sup>16</sup> Core-shell nanostructures have been demonstrated to be promising for electrochemical CO<sub>2</sub> reduction benefiting from their remarkable synergistic process between different electronic structures.<sup>17</sup> Resulting from the strong localized surface plasmon resonance (LSPR), noble metal nanostructured materials exhibit a great enhancement in the photocatalysis of CO<sub>2</sub> degradation.<sup>18,19</sup> In addition, hierarchical photocatalysts have demonstrated lots of merits in the photocatalytic conversion of CO<sub>2</sub>, such as high adsorption capacity and light-absorbing ability, fast separation and transfer of carriers, improved molecular diffusion and boosted surface process.<sup>20,21</sup> Very recently, nanostructured electrocatalysts with atomic precision have been believed to be capable of combining the advantages of heterogeneous and homogeneous catalysts for boosting the catalytic performance toward CO<sub>2</sub> reduction.<sup>7,22</sup>

With large surface area and more active sites, nanostructured materials have become the main focus of many researchers for tackling CO<sub>2</sub> to meet the safety needs, mild reaction conditions, efficiency, selectivity, and cost-effectiveness.<sup>14</sup> As seen from Figure 3.2, there is a gradual increment in the number of research



**Figure 3.2** The number of published papers involving the topic of “nanotechnology” and “CO<sub>2</sub>” in the past 10 years (resulting from the Web of Science database).

works reporting the utilization of nanotechnology for preparing novel adsorbing nanomaterials and efficient nanocatalysts in the reduction of CO<sub>2</sub> concentration. Herein, the related breakthroughs reported after 2015 are overviewed to emphasize the outstanding functions and promising applications of nanomaterials in CO<sub>2</sub> capture, storage, and catalytic reduction, including porous nanomaterials, metals, alloys, metal oxides and their nanohybrids. Based on these important advances, further trends and possible challenges are discussed rationally to guide the developments of next-generation nanotechnology for their better performance in CO<sub>2</sub> reduction.

## 3.2 Capture of CO<sub>2</sub> by Nanostructured Materials

To retard the persistent increase in atmospheric CO<sub>2</sub>, technologies for capturing CO<sub>2</sub> have been developed through using special ligands and/or designing unique morphologies and structures of adsorbents.<sup>15</sup> In recent years, some research has been carried out for developing more applicable approaches to capture CO<sub>2</sub> in postcombustion stages.<sup>23</sup> With a large surface area, designed crystalline surface, and porous structure, a series of novel nanomaterials were confirmed to have a high capability to adsorb CO<sub>2</sub> under mild conditions.<sup>16</sup> In this section, we aim to demonstrate the recent advances in various novel nanostructured materials for capturing CO<sub>2</sub> with high capacity; meanwhile, some examples of separation and fixation of CO<sub>2</sub> over nanomaterials are also demonstrated.

### 3.2.1 Adsorbing of CO<sub>2</sub> on Nanostructured Materials

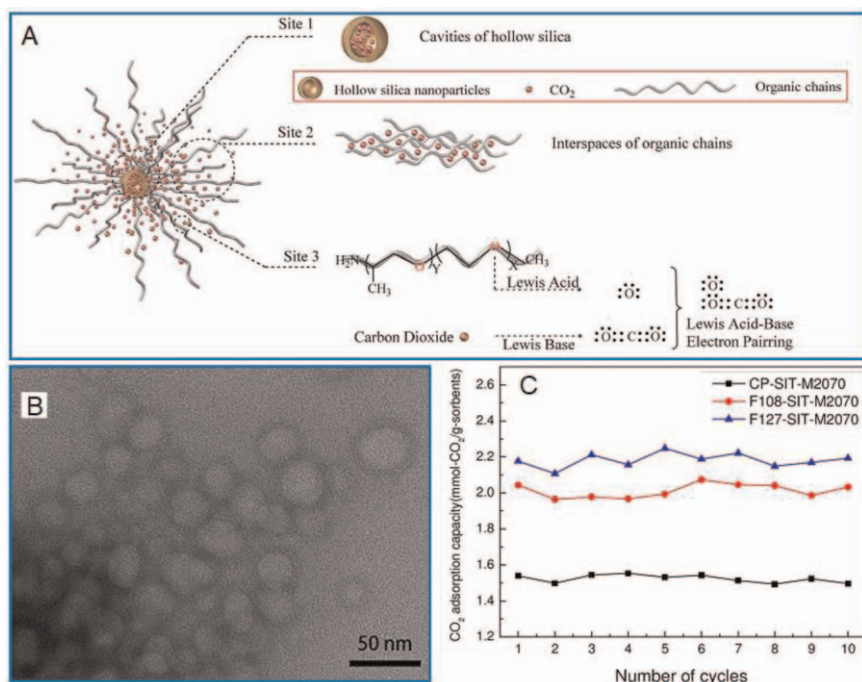
Being one important type of nanomaterial, modified carbon nanotubes and their hybrids have been successfully employed for CO<sub>2</sub> capture. As reported, the modification of multiwalled carbon nanotubes (MWCNTs) with diamine

can greatly improve the CO<sub>2</sub> adsorption capacity, because amine groups attached to the carbonaceous surfaces cause the formation of CO<sub>2</sub>-adsorption sites on MWCNTs.<sup>24</sup> In the experiment, MWCNTs were first treated with a mixture of diluted sulfuric and nitric acid to etch catalytic metal particles and oxidize MWCNTs, which were functionalized with 1,3-diaminopropane (DAP) to introduce the surface modification of diamine groups and improve the performance of MWCNTs in the CO<sub>2</sub> adsorption. At 303 K and a pressure of 17.3 bar, 92.71 mg g<sup>-1</sup> of CO<sub>2</sub> was adsorbed on MWCNT/DAP, which was higher by two times than that with raw MWCNTs. In Keshavarz's study,<sup>25</sup> functionalized MWCNTs and Fe<sub>3</sub>O<sub>4</sub> nanoparticles were dispersed in the absorbent as nanofluids in order to study their effects on the absorption rate of CO<sub>2</sub> and equilibrium amount of absorption using a high-pressure vessel equipped with a magnetic stirrer. The presence of both nanoparticles, namely, MWCNTs and Fe<sub>3</sub>O<sub>4</sub> nanoparticles, enhanced the rate of absorption and the equilibrium solubility to a maximum amount of 46.7% and 23.2%, respectively. Alternatively, hierarchical TiO<sub>2</sub>:Cu<sub>2</sub>O nanostructures were introduced onto the surface of quartz crystal microbalance sensors for significantly improving sensitivity to CO<sub>2</sub> with a fivefold increment as compared to gold.<sup>26</sup> At ambient CO<sub>2</sub> concentrations, the hierarchical nanostructures exhibited excellent reversibility, while at higher pressures, the CO<sub>2</sub> desorption rate decreased to suggest a possible application for CO<sub>2</sub> sequestration under these conditions. Recently, the nanocomposite of layered double hydroxides (LDHs)/oxidized carbon nanotube was synthesized to systematically investigate the influence of the preparation method and chemical composition on the CO<sub>2</sub> capture performance.<sup>27</sup> Regardless of whether "electrostatic self-assembly" or "direct coprecipitation" was used, both the adsorption capacity for CO<sub>2</sub> and the multicycle stability of LDH were improved by the introduction of CNTs. Particularly, the CO<sub>2</sub> binding amount by Mg-Al-NO<sub>3</sub> LDH was increased more than twice by adding 9.1 wt% CNT. Singh's group performed *ab initio* calculations to investigate the CO<sub>2</sub> separation and capture ability of monolayered group III-nitrides (XN) and -phosphides (XP) (X = Al, Ga, In), which was larger than that of graphene and hexagonal boron nitride.<sup>28</sup> As revealed, N<sub>2</sub> showed significantly weaker interaction with the surfaces of XN/XP as compared to CO<sub>2</sub>, indicating high selectivity of sheets toward CO<sub>2</sub> capture.

With the wide investigation of porous nanomaterials, their utilization for the high-capacity capture of CO<sub>2</sub> has also been reported in recent years. Typically, the resin of melamine formaldehyde and mesoporous silica were used as precursor and template to synthesize a series of mesoporous carbon adsorbents containing nitrogen at a high ratio by increasing the carbonization temperature.<sup>29</sup> With the increment of carbonization temperature, their nitrogen content decreased, but the surface area and porosity were enlarged. By using 700 °C as carbonization temperature, the synthesized adsorbent exhibited the largest surface area and greatly enhanced the CO<sub>2</sub> adsorbing ability. Moreover, the adsorption process for CO<sub>2</sub> was reversible for being reused for four cycles with stable adsorbing ability. Alternatively,

the condensation of 2,4,6-tris(4-hydroxyphenyl)triazine and formaldehyde was utilized to synthesize a triazine–formaldehyde phenolic resin as a nitrogen-containing resol, which was then employed as a source of carbon and nitrogen to directly synthesize N-doped mesoporous carbons by mixing it with a diblock copolymer as the soft template.<sup>30</sup> After removing the soft template at 700 °C, the resultant N-doped mesoporous carbons possessed high N atom contents (up to 13 wt%) and displayed gyroid and cylinder nanostructures, which exhibited excellent CO<sub>2</sub> uptake capacities (up to 72 mg g<sup>-1</sup> at 298 K and 150 mg g<sup>-1</sup> at 273 K). In another work reporting porous liquids, Yao *et al.* demonstrated that pore size had a significant impact on their adsorbing amount for gas.<sup>31</sup> Under similar conditions, the porous liquid with a bigger pore size possessed a larger CO<sub>2</sub> adsorbing amount of 2.182 mmol g<sup>-1</sup> (see Figure 3.3).

In recent research, Sargazi *et al.* presented an ultrasound-assisted route for preparing a novel Ta(v)-based metal–organic framework (MOF) with a large surface area of 2100 m<sup>2</sup> g<sup>-1</sup> and high monodispersity.<sup>32</sup> The resultant MOFs were successfully employed in CO<sub>2</sub> adsorption with a better CO<sub>2</sub> capturing

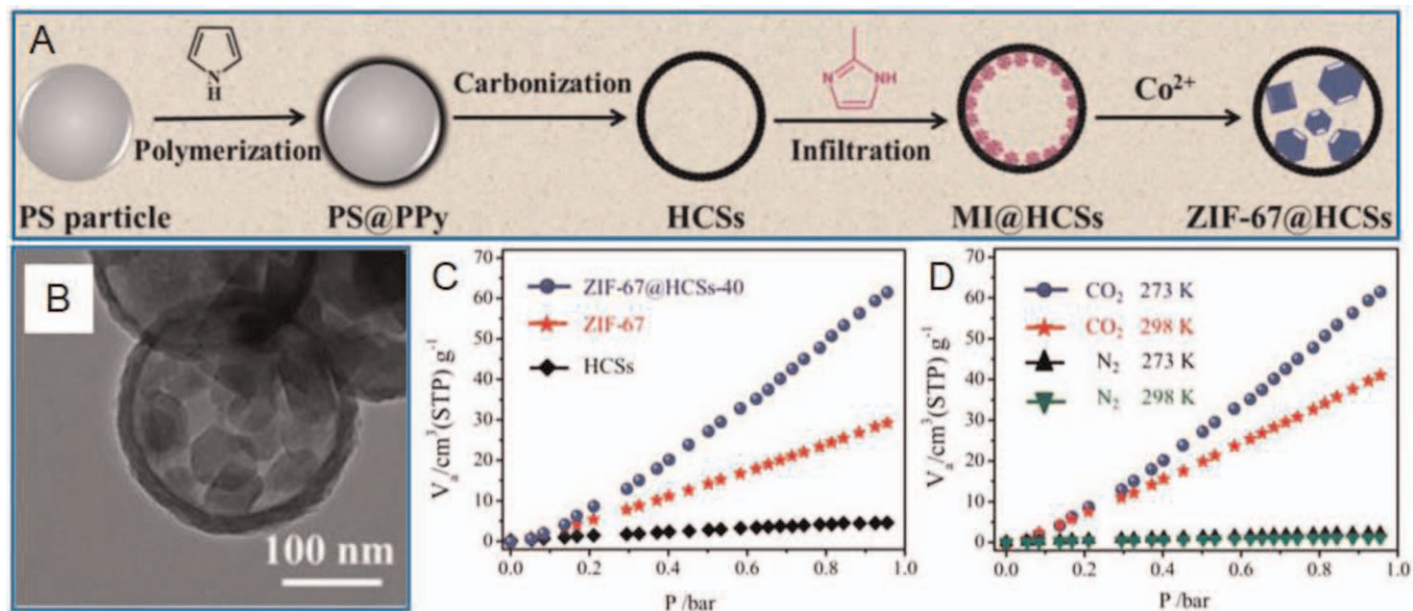


**Figure 3.3** (A) Schematic for adsorbing CO<sub>2</sub> on porous liquids. (B) TEM image of F127-SIT-M2070. (C) Recyclability of porous liquids on CO<sub>2</sub> adsorption (the grafting concentrations of organic chains in CPSIT-M2070, F108-SIT-M2070, and F127-SIT-M2070 are 0.32, 0.37, and 0.39, respectively). Reproduced from ref. 31 with permission from John Wiley & Sons, Copyright © 2018 Wiley-VCH Verlag GmbH & Co. KGaA, Weinheim.

capacity as compared to Co-, In-, Cu-, Mn-, and Fe-MOFs. Similarly, Yan's group demonstrated the production of size-controlled ZIF-67 particles in hollow carbon spheres (HCSs) (see Figure 3.4).<sup>33</sup> Benefiting from the large pore volume of nanostructured ZIF-67 particles, the produced ZIF-67@HCSs exhibited excellent adsorbing ability for CO<sub>2</sub>.

### 3.2.2 Separation of CO<sub>2</sub> by Using Nanotechnology

Through the selective capture of CO<sub>2</sub>, CO<sub>2</sub> gas can be successfully separated by using nanotechnology for further utilization. Typically, continuous assembly of polymers (CAP) was developed to construct a mixed membrane with a cross-linked surface nanolayer with uniform thicknesses (~100 nm) by using the atom transfer radical polymerization (ATRP) of polyethylene glycol (PEG)-based cross-linkers on top of a highly permeable polydimethylsiloxane (PDMS) initiator layer that was precoated onto a microporous polyacrylonitrile (PAN) substrate, which was of potential technological significance for CO<sub>2</sub> capture, benefiting from the CO<sub>2</sub> permeance of up to 1260 GPU and a selectivity for CO<sub>2</sub>/N<sub>2</sub> more than 40 for potential CO<sub>2</sub> capture.<sup>34</sup> Similarly using CAP nanotechnology, iron dopamine nanoparticles were incorporated into a nanoscale-thick PEG matrix to form ultrathin film composite mixed matrix membranes (UTFC-MMMs).<sup>35</sup> The resulting 45 nm thick membranes exhibited an outstanding gas separation application having a CO<sub>2</sub> permeation of ~1200 GPU and a high CO<sub>2</sub>/N<sub>2</sub> selectivity of up to 35. In Zimmermann's work,<sup>36</sup> a freeze-drying method was used for mixing oxidized fibrillated cellulose (OFC) with polyethylenimine (PEI) to fabricate an adsorbing agent for CO<sub>2</sub>, which displayed a plate-like morphology with a porosity of >97% and a large surface area of 2.7 – 8.3 m<sup>2</sup> g<sup>-1</sup>. At a mixed PEI content of 44 wt%, the amount of CO<sub>2</sub> adsorbed was measured as 2.22 mmol g<sup>-1</sup> with an adsorption half time of 10.6 min, and the adsorbent can be recycled at least five times. In another interesting work, efficient CO<sub>2</sub> capture membranes were prepared using a hybrid of the poly(styrene-*b*-butadiene-*b*-styrene)-poly(oxyethylene methacrylate) (SBS-POEM) nanostructural copolymer and ionic liquid (IL) 1-ethyl-3-methylimidazolium dicyanamide, which exhibited a permeability for CO<sub>2</sub> as high as 514 Barrer and selectivity for CO<sub>2</sub>/N<sub>2</sub> as high as 21.6, due to the high CO<sub>2</sub> affinity of the polar POEM side chains,<sup>37</sup> while the SBS membranes exhibited a permeability for CO<sub>2</sub> as high as 372 Barrer and selectivity for CO<sub>2</sub>/N<sub>2</sub> as high as 16.4. In Chung's work,<sup>38</sup> polybenzimidazole (PBI) thin films were chemically crosslinked using 1,3,5-tris(bromomethyl)benzene (TBB) to manipulate the microstructure of polymer chains and to achieve a high sieving ability for the separation of H<sub>2</sub> and CO<sub>2</sub>. The increment of cross-linked density in membranes led to a decrease in fractional free volume (FFV), indicating a tightening effect of TBB crosslinking reaction on PBI films. The membrane with the highest crosslinking density and the lowest FFV possessed the best performance for separating H<sub>2</sub>/CO<sub>2</sub> with a permeability for H<sub>2</sub> as low as 9.6 Barrer and remarkable selectivity for H<sub>2</sub>/CO<sub>2</sub> as high as 24, indicating its promise for CO<sub>2</sub> capture at elevated temperatures.



**Figure 3.4** (A) Preparation method for obtaining ZIF-67 particles in hollow carbon microspheres (ZIF-67@HCSs) via nanospace confined process. (B) TEM image of ZIF-67@HCSs. (C) The CO<sub>2</sub> adsorbing isotherm for ZIF-67, HCSs, and ZIF-67@HCSs at 273 K. (D) The CO<sub>2</sub> and N<sub>2</sub> adsorbing isotherm for ZIF-67@HCSs-40. Reproduced from ref. 33 with permission John Wiley & Sons, Copyright © 2019 WILEY-VCH Verlag GmbH & Co. KGaA, Weinheim.

With gas permeating ability, polyelectrolytes were successfully used for capturing CO<sub>2</sub>. Typically, a mixed membrane of [Bmim][BF<sub>4</sub>] and Nafion was developed to capture CO<sub>2</sub> *via* the existing IL channels in the hybrid polymer.<sup>39</sup> When 40 wt% [Bmim][BF<sub>4</sub>] was contained, the resultant membrane exhibited a high permeability for CO<sub>2</sub> of 390 Barrer and selectivity for CO<sub>2</sub>/N<sub>2</sub> of ~30. Membranes that permeate H<sub>2</sub> and reject CO<sub>2</sub> are cost-effective for purifying H<sub>2</sub> and capturing CO<sub>2</sub>. Poly[2,2-(*m*-phenylene)-5,5-bisbenzimidazole] (PBI) is a leading polymer for this separating process with high physical stability and excellent gas selectivity. In Lin's work,<sup>40</sup> the cross-linkage of PPBI greatly increased H<sub>2</sub>/CO<sub>2</sub> selectivity from 15 to 23 as the H<sub>2</sub> permeability reduced from 45 to 39 Barrer, signifying its promising performance in the purification of H<sub>2</sub> and capture of CO<sub>2</sub>.

### 3.2.3 Fixation of CO<sub>2</sub> Over Nanomaterials

Besides the physical capture of CO<sub>2</sub> on nanomaterials, the chemical bond-based linkage of CO<sub>2</sub> with other compounds was also utilized for fixing or storing CO<sub>2</sub> in nanostructured materials. For example, calcium looping (CaL)-based fixation of CO<sub>2</sub> has been widely utilized in postcombustion carbon capture at high temperatures. For overcoming the drawbacks of CaO sorbents such as fast deactivations and low CO<sub>2</sub> uptake, Benitez-Guerrero *et al.* synthesized two types of Al composites with different ratios of Al<sub>2</sub>O<sub>3</sub>/CaO by mixing nanoalumina and natural limestone in powder forms.<sup>41</sup> Particularly, the CaL-CO<sub>2</sub> reaction condition led to the production of crystalline-phase Ca<sub>3</sub>Al<sub>2</sub>O<sub>6</sub>. Similarly, Jiang *et al.* employed nanosized silica synthesized from coal fly ash to increase the adsorbing rate on CaO nanoparticles and the cyclic stability of uptaking CO<sub>2</sub>, which resulted in a CO<sub>2</sub> sorption of 0.20 g(CO<sub>2</sub>)/g(sorbent)<sup>-1</sup> with a marked increment of 155% compared to conventional CaO.<sup>42</sup> After the second run, most of the CO<sub>2</sub> was captured (90%) in ~20 s, indicating an ultrafast adsorbing speed from the abundant reactive small pores on silica nanomaterials. In Zhang's work,<sup>43</sup> a novel CO<sub>2</sub> storage material (CO<sub>2</sub>SM) was used to mix with Ca(OH)<sub>2</sub> saturated limpid solution for controlling the morphology of CaCO<sub>3</sub> microspheres with a layered nanostructure surface and pure crystalline phase of vaterite during the hydrothermal reaction. Morphologies of the as-prepared CaCO<sub>3</sub> crystals could be tuned using the CO<sub>2</sub>SM concentration, reaction temperature, or crystallization time. After the precipitation of CaCO<sub>3</sub> crystals, the filtered solution could be employed not only to absorb CO<sub>2</sub> but also to produce CaCO<sub>3</sub> microspheres *via* adding the Ca(OH)<sub>2</sub> solution.

The chemical fixation of CO<sub>2</sub> in fine molecules is an ideal alternative to tackle CO<sub>2</sub> as a C1 building block. In one exploitation, nanocrystalline MgO was synthesized by using the simple precipitation method followed by calcination at 450 °C, which had mesoscopic void space and excellent catalytic ability for producing organic carbonate molecules through the chemical fixation of CO<sub>2</sub> on a wide range of epoxides under atmospheric pressure and low temperature within a short reaction time, which resulted in maximum product yields of up to 99% for the cyclic carbonates.<sup>44</sup> This nanocrystalline MgO



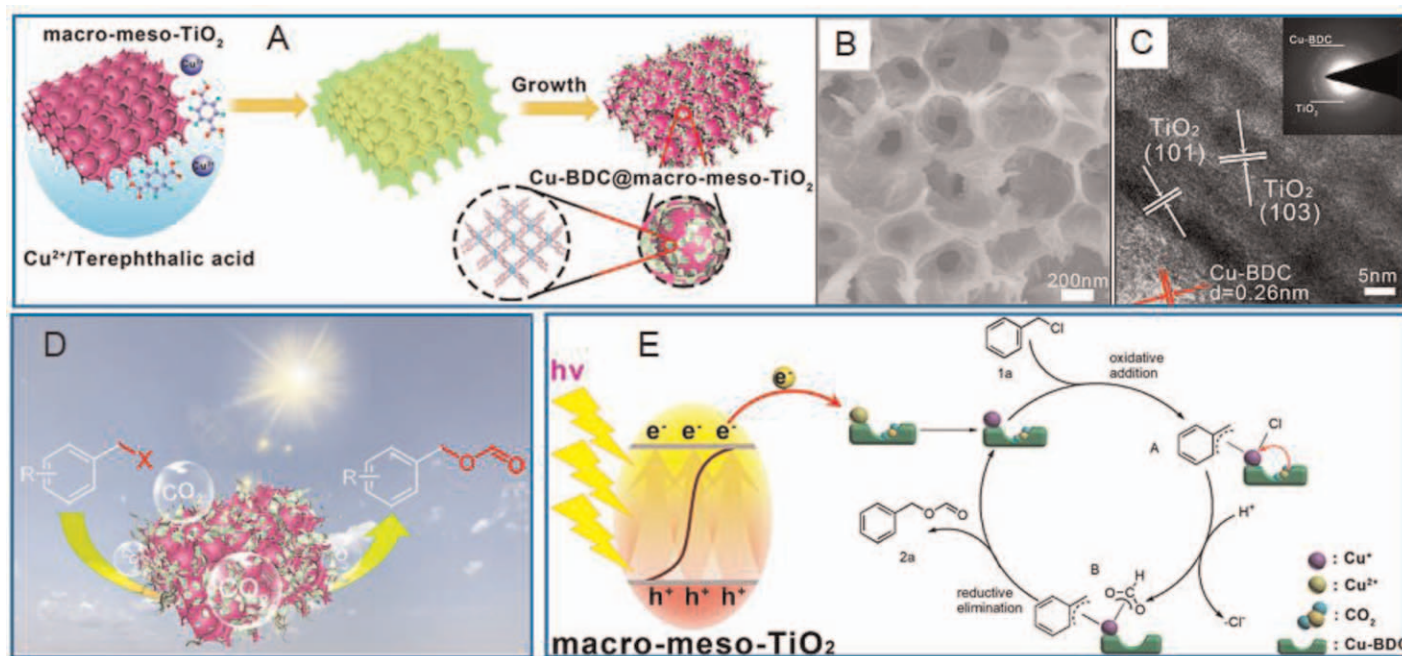
material showed high recycling efficiency for the cycloaddition of CO<sub>2</sub> onto the epoxides. Similarly, basicity-controlled MgCo<sub>2</sub>O<sub>4</sub> spinel oxides were used as promising catalysts for the fixation of CO<sub>2</sub> into epoxides at atmospheric pressure, in which the different interlayer anions (chloride, nitrate, acetate, sulfate) strongly altered their basicity and played a stimulating role in their catalytic efficiency.<sup>45</sup> Particularly, [MgCo<sub>2</sub>O<sub>4</sub>]-[Cl<sup>-</sup>] nanostructures showed porous flower morphology with a high pore diameter and highly exposed basic sites, which exhibited 95% conversion of styrene oxide and 96% selectivity toward styrene carbonate at atmospheric pressure. As revealed, the activation of epoxide and CO<sub>2</sub> by the unique cooperation of active Lewis acidic and basic sites were presented in [MgCo<sub>2</sub>O<sub>4</sub>]-[Cl<sup>-</sup>] for the formation of cyclic carbonates at atmospheric pressure. In Li's work,<sup>46</sup> the organic reaction of CO<sub>2</sub> with benzyl halogen for chemical CO<sub>2</sub> fixation with irradiation with UV light was successfully catalyzed by Cu-BDC nanosheet@macroporous-mesoporous-TiO<sub>2</sub> (Cu-BDC@macro-meso-TiO<sub>2</sub>) (see Figure 3.5). The prepared nanohybrid possessed a three-scale porous structure, including macropores, mesopores, and micropores, and the microporous Cu-BDC nanosheet was confined in the macropore of macro-meso-TiO<sub>2</sub> while the ordered mesoporous structure was in the macroporous walls. Benefiting from the multilevel porous distribution, the active surface areas and mass transfer efficiency were significantly improved for photocatalytic chemical CO<sub>2</sub> fixation.

### 3.3 Photocatalytic CO<sub>2</sub> Reduction Over Nanostructures

For the capture technologies for CO<sub>2</sub>, there is still a danger of CO<sub>2</sub> leaking after adsorption. In comparison, the migration of CO<sub>2</sub> into fuels or other molecules is considered a more compelling strategy for tackling climatic warming and the fuel crisis.<sup>6</sup> The supposition of simulating the photosynthesis in green plants for cycling CO<sub>2</sub> has been attracting remarkable research interest in recent decades.<sup>47-50</sup> Among them, photocatalytic reduction of CO<sub>2</sub> is to use H<sub>2</sub>O and CO<sub>2</sub> for producing O<sub>2</sub> and carbohydrates under irradiation by sunlight.<sup>51</sup> However, the extreme inertness of CO<sub>2</sub> and easy recombination of photoproduct carriers seriously decrease the reduction rate of CO<sub>2</sub> in photocatalysis, which determines that superb photocatalysts are critically important in this intriguing technique.<sup>20</sup> Recent advances in nanotechnology have offered unprecedented opportunities for the photocatalysis of CO<sub>2</sub>, which can promote the separation of photo-generated electrons from holes so as to achieve better catalytic performances for photoreducing CO<sub>2</sub>.<sup>52</sup> In this section, the recent developments in exploiting nanostructured photocatalysts are systematically demonstrated for rapid CO<sub>2</sub> reduction, which are classified by different materials' systems.

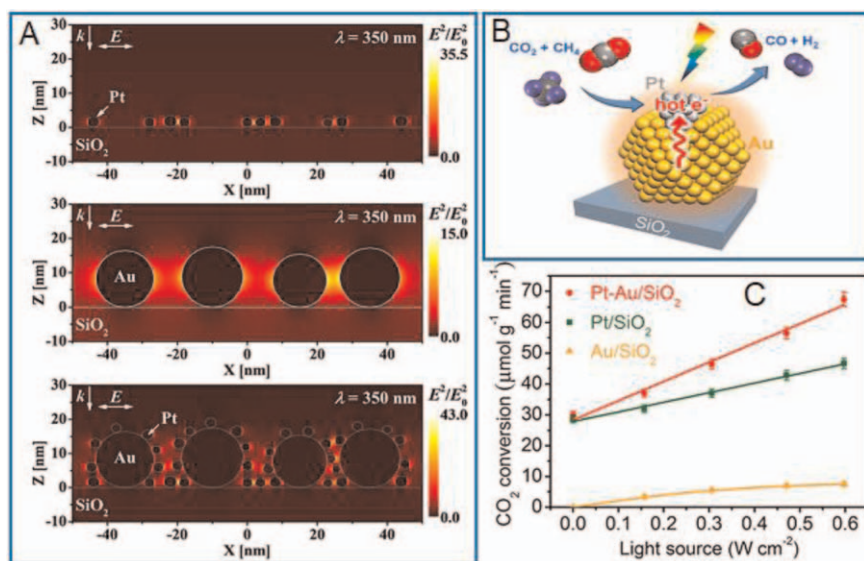
#### 3.3.1 Metals and Alloys

With their superb catalytic ability and strong LSPR, the utilization of metals and alloys is a good alternative for the photocatalytic reduction of CO<sub>2</sub>.



**Figure 3.5** (A) Schematic for synthesizing Cu-BDC@macro-meso-TiO<sub>2</sub>. (B) SEM and (C) TEM images of the synthesized Cu-BDC@macro-meso-TiO<sub>2</sub>. (D) Photocatalytic chemical fixation of CO<sub>2</sub> over Cu-BDC@macro-meso-TiO<sub>2</sub>. (E) Mechanism for the carboxylation of benzyl halide with CO<sub>2</sub>. Reproduced from ref. 46 with permission from American Chemical Society, Copyright 2019.

Typically, the plasmonic coupling effect from Pt and Au nanostructures significantly enhanced the performance of reducing  $\text{CO}_2$  *via* the dry reforming reaction of methane ( $\text{CH}_4$ ) under light, which decreased the photoactivation energy for reducing  $\text{CO}_2$  by  $\sim 30\%$  below thermal activation energy and allowed achieving a 2.4-times higher reduction speed as compared to thermocatalytic conversion (see Figure 3.6).<sup>53</sup> As revealed, the strong coupling effect of LSPR generated a large local electric field and excited lots of hot electrons for activating the reactants and intermediate products, reducing their activated energy, and increasing the reduction speed. In Bai's work,<sup>54</sup> the synergetic effect of surface strain and interfacial polarization was demonstrated in Pd@Au nanoparticles to optimize the reduction of  $\text{CO}_2$  to CO, which benefited from the mismatched lattice structures of Pd cores with the Au shells. In addition, the different electronegativity in Pd cores and Au shells induced charge polarization, which significantly accelerated the transferring of interfacial charges and increased the concentration of electrons at the Au surface. When a three atom-layered Au shell was synthesized, the overall efficiency for converting  $\text{CO}_2$  into CO was significantly boosted to exhibit a great ability of  $166.3 \text{ mmol g}_{\text{cat}}^{-1} \text{ h}^{-1}$  and a high selectivity up to 90.6%.



**Figure 3.6** (A) Spatial distribution of electric field intensity at an excitation wavelength of 350 nm from finite difference time domain (FDTD) simulation on Pt/SiO<sub>2</sub>, Au/SiO<sub>2</sub>, and Pt-Au/SiO<sub>2</sub>. (B) Schematic diagram for light-enhanced  $\text{CO}_2$  activation and reduction by strong plasmonic coupling of Pt and Au particles. (C)  $\text{CO}_2$  conversion efficiencies on different samples with an increment of light intensity. Reproduced from ref. 53 with permission from American Chemical Society, Copyright 2018.

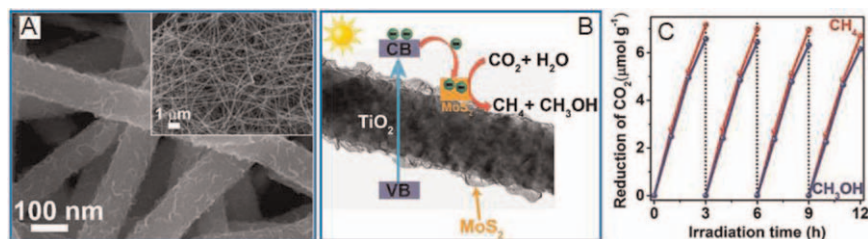
### 3.3.2 Metal Oxides and Their Nanohybrids

**TiO<sub>2</sub>-based Photocatalysts:** Having a wider bandgap at  $\sim 3.2$  eV in the ultraviolet (UV) range, TiO<sub>2</sub> crystals can effectively utilize UV energy and exhibit high photocatalytic capability for CO<sub>2</sub> reduction, which can further be improved *via* morphological engineering and surface functionalization. For example, one-dimensional (1D) TiO<sub>2</sub> tubes and rods were easily prepared through a one-step hydrothermal reaction and exhibited a large specific surface area, increased absorption for visible light, and accelerated electron transportation.<sup>55</sup> Under 9 h irradiation with 420 nm light, the maximum yields of CH<sub>4</sub> by using TiO<sub>2</sub> tubes and rods were 19.16 and 12.71  $\mu\text{mol}_{\text{cat}}^{-1}$ , respectively, approximately higher by 2.33- and 1.48-fold than TiO<sub>2</sub> particles. Moreover, a higher catalytic ability of nanotubes compared to nanorods was observed, owing to their unique hollow structure with a larger surface area. In Cheng's work,<sup>56</sup> a thin film of Cu<sup>2+</sup>-doped TiO<sub>2</sub> rods was prepared by combining hydrothermal reaction and subsequent cation adsorption under ultrasonic conditions, which was an effective photocatalyst for the UV-driven conversion of CO<sub>2</sub> in optofluidic planar reactors. At the concentration of Cu<sup>2+</sup> of 0.02 M, the yield of products after reaction can reach the highest value, and the produced methanol and ethanol were as high as 36.18 and 79.13  $\mu\text{mol}_{\text{cat}}^{-1} \text{h}^{-1}$ , respectively. The result signified that the doping of Cu<sup>2+</sup> ions and 1D structure significantly optimized the transferring of photons.

In hybrid nanosystems containing TiO<sub>2</sub> and plasmonic metals, metals can not only catch the photoproducted electrons from TiO<sub>2</sub> crystals for improving charge separation and accelerating reaction kinetics due to the presence of highly active sites, but they can also serve as a light-absorbing antenna for extending the light-absorbing range by injecting plasmonic hot electrons into the TiO<sub>2</sub> crystals. Based on the coating of Au with TiO<sub>2</sub> nanoparticles with different exposed planes, Bai's group reported that the Au/TiO<sub>2</sub>(101) interfaces lowered the height of the Schottky barrier as compared to Au/TiO<sub>2</sub>(001), which enhanced the transferring of electrons in the conduction band of TiO<sub>2</sub> into Au nanocrystals upon irradiation with UV light and promoted the injection of hot electrons from Au crystals to the conduction band of TiO<sub>2</sub> owing to the excitation of Au with visible light.<sup>57</sup> The more rapid interfacial charge migration/separation led to the participation of more electrons in the reduction of CO<sub>2</sub> to CO and CH<sub>4</sub>. Therefore, the Au-TiO<sub>2</sub> hybrid having exclusive Au/TiO<sub>2</sub>(101) interfaces greatly ameliorated the photocatalytic ability for producing CO and CH<sub>4</sub> compared to products with Au/TiO<sub>2</sub>(001) interfaces. In Strunk's work,<sup>58</sup> Au@TiO<sub>2</sub> nanohybrids with varied geometrical structures were synthesized to investigate the effect of morphology and structural features on the photocatalytic conversion of CO<sub>2</sub>. As reported, the best products were core-shell particles having Au spheres coated on the outer surface of the TiO<sub>2</sub> shell, which benefited from electronic interactions between Au cores, TiO<sub>2</sub> shells, and outer Au spheres. For increasing the conversion of light energy, a combination of photo- and thermocatalysis was demonstrated for reducing CO<sub>2</sub> by using Pd particle-coated TiO<sub>2</sub>.<sup>59</sup> The highest yield of CO was measured as 11.05  $\mu\text{mol}_{\text{g}}^{-1} \text{h}^{-1}$ , which was 8.27 times higher

than the value obtained from P25. As revealed, the hybrid system can increase light conversion *via* a red-shifted absorbing region and visible light absorption from LSPR, and the photoproduced electron and hole can be separated more effectively. Additionally, Pd spheres promoted  $\text{CO}_2$  adsorption to produce  $\text{Pd-CO}_2^-$  and  $\text{Pd-CO}_2^- \cdot \text{V}_\text{O}$  at the defective surface, which can increase CO yield *via* a photothermal coupling effect.

Besides metal nanoparticles, metal oxides and sulfides were also hybridized with  $\text{TiO}_2$  nanostructures for enhancing photocatalysis in the reduction of  $\text{CO}_2$ . Typically, a scalable preparation method was developed to synthesize CuO-containing  $\text{TiO}_2$  hollow nanoparticles with large pores in the shells, which provided a great number of active sites at the material's surface to adsorb and activate the reactant and enabled rapid mass transport of species in the porous channels.<sup>60</sup> Furthermore, the hollow nanostructures comprised of macroporous cores and mesoporous shells favored light scattering/reflection in multiply paths, leading to an increased harvesting property for excitation light. As a result, the CuO-containing  $\text{TiO}_2$  hollow microspheres demonstrated a much higher catalytic ability for the photoreduction of  $\text{CO}_2$  with  $\text{H}_2\text{O}$  into  $\text{CH}_4$ . For realizing an effective photoreduction of  $\text{CO}_2$  with visible light,  $\text{Cu}^{2+}$  ions and CdS quantum dots (QDs) were coated on  $\text{TiO}_2$  nanorod arrays using the ultrasonic-assisted sequential cation adsorption and subsequent adsorption of ionic film and reaction, respectively.<sup>61</sup> The loading amount of CdS QDs was regulated by controlling the times of deposition cycles. When the number of deposition cycles was two, the yield of products reached the maximum value, and the yielded ethanol was measured as  $109.12 \mu\text{mol g}_{\text{cat}}^{-1} \text{h}^{-1}$ . The high-efficiency photocatalysis by the CdS- $\text{Cu}^{2+}/\text{TiO}_2$  array film was attributed to the combination of the 1D nanostructure with decorating  $\text{Cu}^{2+}$  ions and CdS QDs, which accelerated the separation of the photogenerated electrons from holes and broadened the photoresponse in the visible range. In Xu's work,<sup>62</sup>  $\text{TiO}_2$  nanofibers were deposited with  $\text{MoS}_2$  sheets to fabricate a novel 1D/2D  $\text{TiO}_2/\text{MoS}_2$  nanostructure using the hydrothermal transformation approach. As shown in Figure 3.7, the nanoarrays of  $\text{MoS}_2$  sheets with a lateral



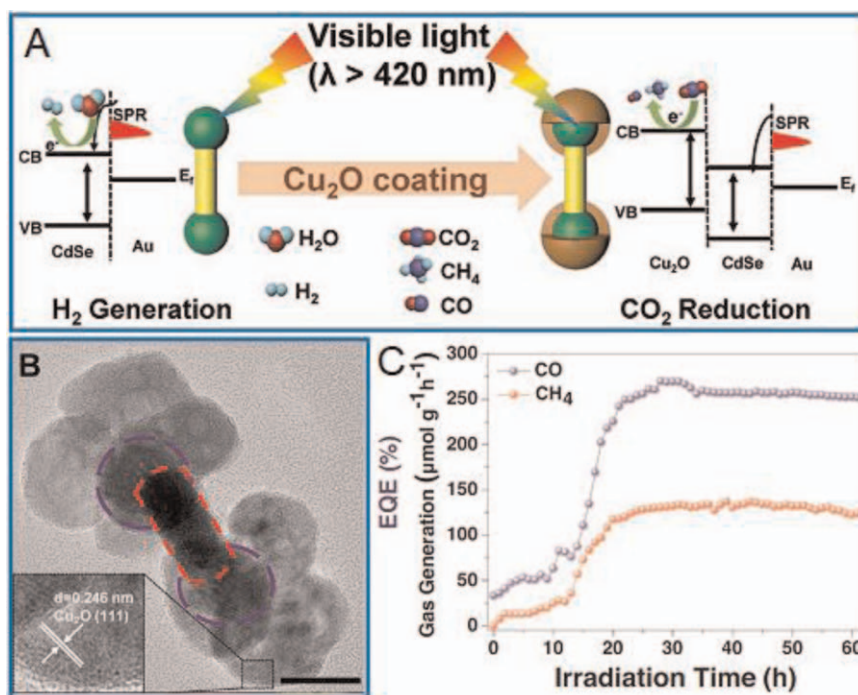
**Figure 3.7** (A) SEM images of 1D/2D  $\text{TiO}_2/\text{MoS}_2$  hybrid nanosystems. (B) TEM image of  $\text{TiO}_2/\text{MoS}_2$  nanohybrid and schematic for charge transfer and separation on heterojunction for  $\text{CO}_2$  conversion. (C) The recyclability for photocatalytic  $\text{CO}_2$  conversion. Reproduced from ref. 62 with permission from John Wiley & Sons, Copyright © 2018 WILEY-VCH Verlag GmbH & Co. KGaA, Weinheim.

size of 80 nm and thickness of 2 nm stand on the TiO<sub>2</sub> nanofibers in vertical and uniform forms. The strong chemical bonds between MoS<sub>2</sub> sheets and TiO<sub>2</sub> nanofibers after hybridization facilitated the separation of photoproduced electron–hole pairs. Moreover, the hierarchical structure showed an increased optical absorbance and CO<sub>2</sub> adsorption; therefore, an excellent photocatalytic performance was obtained to reduce CO<sub>2</sub> for producing CH<sub>4</sub> and methanol.

Graphene has been demonstrated to have the ability to effectively absorb visible light and promote charge migration owing to its high conductivity. For improving the absorbing activity of TiO<sub>2</sub> under visible light, Zubair's group developed an interesting nanostructure by sensitizing TiO<sub>2</sub> nanotube arrays with graphene quantum dots (GQDs), which significantly optimized the photocatalysis of the resulted nanofilms.<sup>63</sup> Under solar light, the optimal samples promoted the photodegradation speed of CO<sub>2</sub> into CH<sub>4</sub> to 1.98 ppm cm<sup>-2</sup> h<sup>-1</sup>. In Amin's work,<sup>64</sup> the photocatalysis of montmorillonite (MMT)-functionalized TiO<sub>2</sub> composites was investigated for catalytically reducing CO<sub>2</sub> with CH<sub>4</sub> by using a continuous monolith reactor. The TiO<sub>2</sub>–MMT composites were dip-coated on monolith channels to produce an anatase phase of TiO<sub>2</sub> with a crystallite size of 13 nm, whose photocatalytic activity was 2.52 times higher than bare TiO<sub>2</sub>. As reported, CO was the major reduction product and its production rate was up to 237.5 mmol g<sub>cat</sub><sup>-1</sup> h<sup>-1</sup> when 10 wt% MMT-modified TiO<sub>2</sub> was used at 100 °C and the feed ratio of CO<sub>2</sub>/CH<sub>4</sub> was set as 1.0.

**Cu<sub>2</sub>O-based Hybrid Photocatalysts:** Besides TiO<sub>2</sub>, another popular metal oxide is cuprous oxide (Cu<sub>2</sub>O), which can prevent the excessive production of hydrogen *via* a competitive hydrogen evolution process. For overcoming its limitations to enhance chemical stability and catalytic activity and suppressing self-corrosion *via* the generation of holes upon light irradiation, the preparation of Cu<sub>2</sub>O-loaded ZnO rods was carried out to show much better catalytic property than pristine ZnO, owing to the improved behavior of charge generation, separation, and transport due to the existence of p–n junctions between the Cu<sub>2</sub>O tips and ZnO rods.<sup>65</sup> The photoreduction of CO<sub>2</sub> under irradiation by UV–visible light showed that CO was the major product, and the CO yield increased with the increment of the Cu<sub>2</sub>O ratio in the heteromaterials. Li *et al.* constructed hollow nanoparticles with Cu<sub>2</sub>O/MnO<sub>x</sub> mesoporous shells to improve the stability and photocatalytic performance of Cu<sub>2</sub>O-involved catalysts.<sup>66</sup> The thin shell shortened the transfer distance of charge carriers and the oxidized cocatalyst MnO<sub>x</sub> effectively attracted holes so that the photoproduced holes can rapidly leave from Cu<sub>2</sub>O and react with the reactants. Meanwhile, the hollow hybrid can also exhibit increased efficiency for separating charges, prolonging the path of light scattering and reflection, and enlarging surface area with active sites, which resulted in an enhancement in catalytic activity by 7.1 times and in stability by 11.2 times as compared with original Cu<sub>2</sub>O particles. In Zhang's work,<sup>67</sup> plasmonic Au/CdSe dumbbell-like rods were used to increase the light-absorbing capability and form a plasmon-enhanced charge-rich area while the additive Cu<sub>2</sub>O particles provided more active points for CO<sub>2</sub> photoreduction and

suppressed the hydrogen generation to increase the selectivity of carbon products. As shown in Figure 3.8, the middle CdSe crystals served as a bridge to migrate the photogenerated charge carriers and efficiently separated the photoproduced electron-hole pairs, resulting in a CO selectivity of up to 100% by synthesizing these Au/CdSe-Cu<sub>2</sub>O hierarchical structures. The extreme selectivity indicated that the Au/CdSe-Cu<sub>2</sub>O hierarchical structures completely suppress the H<sub>2</sub> evolution process under irradiation by visible light ( $\lambda > 420$  nm). Further, the  $2e^-/2H^+$  products of CO can be converted into some  $8e^-/8H^+$  products like CH<sub>4</sub> at a sufficient CO concentration and in the presence of protons. At the optimized conditions, the Au/CdSe-Cu<sub>2</sub>O hybrid displayed high photocatalytic capability and good chemical stability, in which the gas yield speeds were 254 and 123  $\mu\text{mol g}^{-1} \text{h}^{-1}$  for CO and CH<sub>4</sub>, respectively, within a period of 60 h. Recently, Halas *et al.* reported the incorporation of earth-abundant aluminum into Cu<sub>2</sub>O to fabricate antenna-reactor hybrid structures, which were operated more effectively and selectively in the reverse water gas conversion reaction from CO<sub>2</sub> to CO upon visible light irradiation than the common thermal catalysis.<sup>68</sup>

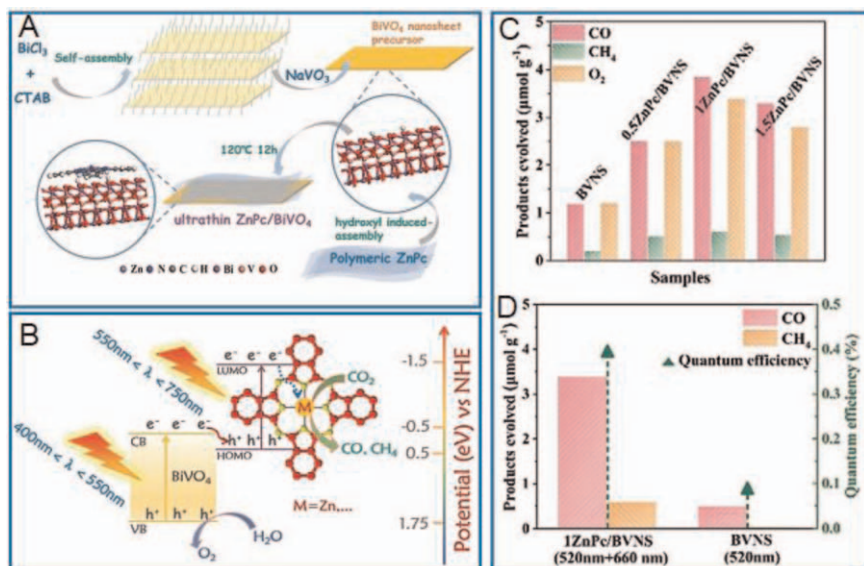


**Figure 3.8** (A) Schematic for varied photocatalytic reactions under visible light irradiation over different samples: H<sub>2</sub> formation on Au/CdSe and CO<sub>2</sub> reduction on Au/CdSe-Cu<sub>2</sub>O samples. (B) HRTEM images of Au/CdSe-Cu<sub>2</sub>O hybrids. (C) Long-term stability of Au/CdSe-Cu<sub>2</sub>O hybrids under irradiation. Reproduced from ref. 67 with permission from John Wiley & Sons, Copyright © 2020 WILEY-VCH Verlag GmbH & Co. KGaA, Weinheim.

**Other Metal Oxides-involved Photocatalysts:** As reported, the reverse water gas shift reaction (RWGS) was activated in a photothermal manner by Nb<sub>2</sub>O<sub>5</sub> nanorod-supported Pd nanocrystals. Through the photothermal effect, visible and near-infrared (NIR) light-active Pd@Nb<sub>2</sub>O<sub>5</sub> hybrid photocatalysts were successfully used to hydrogenate CO<sub>2</sub> to CO at rates up to 1.8 mmol g<sub>cat</sub><sup>-1</sup> h<sup>-1</sup>.<sup>69</sup> In the reaction on Nb<sub>2</sub>O<sub>5</sub> nanorod-supported Pd nanocrystals, this photothermal process involved H<sub>2</sub> dissociation over Pd crystals and then the spillover of H to the Nb<sub>2</sub>O<sub>5</sub> rods for adsorbing and hydrogenating CO<sub>2</sub> into CO. To achieve the precisely tuned micro-/nanos-structured nanosystems, hollow structures with multishells were successfully synthesized by introducing lattice distortion in hollow systems at the nanoscale interface of SnS<sub>2</sub>/SnO<sub>2</sub>, which provided more active points for enhancing the photocatalytic ability under irradiation with visible light and improving the separation of photoproduced electron-hole pairs.<sup>70</sup> As a result, an excellent photocatalytic performance was realized in the solid-gas system for CO<sub>2</sub> conversion, with an exceptional stability and 100% CO selectivity in the absence of any sensitizers and noble metals. In Jain's work,<sup>71</sup> cobalt(II) phthalocyanine (CoPc) was grafted onto the core-shell Ni/NiO semiconductor to synthesize an inorganic nanocomposite for the photoreduction of CO<sub>2</sub> into methanol under irradiation with visible light with triethylamine as a sacrificial donor. Compared to the semiconductor Ni/NiO and CoPc, the synthesized photocatalyst exhibited a remarkable increment in the yield of methanol for CO<sub>2</sub> conversion under identical conditions, which led to the maximum yield of methanol of 3641.2 μmol g<sup>-1</sup> and the conversion speed of 151.7 μmol g<sup>-1</sup> h<sup>-1</sup>. Moreover, the composite photocatalyst showed consistent recyclability for four cycles without any measured decrease in catalytic capability.

Recently, bimetal oxides and their hybrids have been developed for photocatalytically reducing CO<sub>2</sub> in an efficient manner. For example, flower-like ZnMn<sub>2</sub>O<sub>4</sub> particles were produced by the self-assembly of curved nanoplates during the calcination of ZnMn<sub>2</sub>-ptcda (perylene-3,4,9,10-tetracarboxylic dianhydride) MOF precursors, in which the curved nanoplates consisted of small particles with controlled particle size and which increased the band gap of ZnMn<sub>2</sub>O<sub>4</sub> microspheres up to 2.1–2.6 eV.<sup>72</sup> With enlarged specific surface area/porosity, decreased particle size, and a self-assembled mesoporous nanostructure, the photocatalytic activity for the reduction of CO<sub>2</sub> to CO was enhanced significantly to suggest that the ZnMn<sub>2</sub>O<sub>4</sub> flower-like microsphere can be regarded as an ideal photocatalyst in photoreduction, photodegradation, and photosynthesis. More interestingly, a Z-scheme hybrid containing ultrathin Bi<sub>2</sub>WO<sub>6</sub> nanoplates and CdS nanoparticles was fabricated to photocatalytically reduce CO<sub>2</sub> to CH<sub>4</sub> in the environment of water gas, in which Au nanoparticles were used as an effective electron mediator for forming a fast speed channel of carrier transfer and ensuring the rapid separation of photoproduced electron-hole pairs.<sup>73</sup> The photoproduced electrons in the conduction band of Bi<sub>2</sub>WO<sub>6</sub> were transferred into the Au nanocrystal and then moved into the valence band of CdS to annihilate after combining the holes of CdS. This combining process of electron-hole allowed the electrons being





**Figure 3.9** (A) Schematic for synthesizing the ultrathin ZnPc/BVNS heterojunction. (B) Cascade Z-scheme transfer of photoproduced charges on MPC-loaded BVNS. (C) Photocatalytic activities of *x*ZnPc/BVNS and BVNS for CO<sub>2</sub> reduction at visible light for 4 h. (D) Photocatalytic activities and the corresponding quantum efficiency under monochromatic beam for 1ZnPc/BVNS and BVNS. Reproduced from ref. 74 with permission from John Wiley & Sons, Copyright © 2019 Wiley-VCH Verlag GmbH & Co. KGaA, Weinheim.

active in the conduction band of CdS and holes in the valence band of Bi<sub>2</sub>WO<sub>6</sub> to exhibit strong reduction and oxidation ability, respectively, which led to an enhanced stability of CdS against photocorrosion and higher photocatalytic ability of Bi<sub>2</sub>WO<sub>6</sub>/Au/CdS, compared to the individual nanocrystals and binary hybrids. Similarly, the cascade charge migration was also built through an H-bond linkage in a zinc phthalocyanine/BiVO<sub>4</sub> nanosheet (ZnPc/BVNS) nanocomposite (see Figure 3.9), which worked as an efficient photocatalyst in a wide visible range for catalytically reducing CO<sub>2</sub> into CO and CH<sub>4</sub>.<sup>74</sup> The optimized ZnPc/BVNS hybrids exhibited a 16-fold increment in the photocatalytic efficiency compared to the previous BiVO<sub>4</sub> particles under irradiation at 520 nm with the assistance of 660 nm photons. The extraordinary photocatalysis benefited from the fast charge separation by a cascade Z-scheme charge-transferring process in the dimension-matched ultrathin heterostructured nanosystems. And, the central Zn<sup>2+</sup> in ZnPc can accept the excited electrons from the ligand and thus provide a catalytic reaction for reducing CO<sub>2</sub>. Further, this Z-scheme hybrid material was also applicable for combining other metal phthalocyanines like FePc and CoPc on BVNS.

### 3.3.3 Other Metal Compounds and Their Hybrids

Owing to their excellent optical response and suitable band structures, CdS-based photocatalysts have also been studied for CO<sub>2</sub> reduction under solar

light. Considering that the surface electron density significantly determines the photocatalytic activity, Zhou's group proposed a modulation of surface electron density at the Au-loaded CdS to trigger a multielectron participation in the photocatalytic CO<sub>2</sub> reduction reaction.<sup>75</sup> When electrons accumulated near vacancies rather than single Au atoms, the adsorbing types of CO<sub>2</sub> changed from physical adsorption to chemical linkage. The surface electron density was controlled *via* manipulating the size of Au nanocrystals. With Au size down to a single Au atom, the strongest hybridization of Au 5d and S 2p orbitals accelerated the photoreduced electrons transfer onto the surface, leading to the production of more electrons for CO<sub>2</sub> reduction. In consequence, the product yield of Au/Cd<sub>1-x</sub>S manifested an amazing increment of at least 113-fold compared to bare Cd<sub>1-x</sub>S. In Kim's work,<sup>76</sup> Pt nanoparticles were photodeposited onto a core-shell structure of CdS/ZnS as a durable photocatalyst for reducing CO<sub>2</sub>. These nanohybrid materials enhanced photoabsorption and accelerated the separation of photoproduced charge carriers. The photocatalysis involved in the reduction of CO<sub>2</sub> to produce CO and CH<sub>4</sub> with the assistance of triethanolamine as a hole scavenger. The CO and CH<sub>4</sub> production rates of the optimized CdS/ZnS/Pt photocatalyst were ~50 times higher than those with bare CdS, while the photocatalyst maintained its stability for more than 42 h. The production of H<sub>2</sub> and CH<sub>4</sub> became reduced under a long-time run with CdS/ZnS/Pt, which selectively produced CO as the major compound. Similar to CdS, a flowered MoS<sub>2</sub>-involved hybrid catalyst with high activity was developed by an engineering process on the morphological and electronic structure.<sup>77</sup> In the experiment, nanostructural modulation was utilized to synthesize MoS<sub>2</sub> into flowered sheets with large activated surfaces. Subsequently, MoS<sub>2</sub> was hybridized on SnO<sub>2</sub> that has a matched conduction-band edge with MoS<sub>2</sub> and further loaded with Ag nanocrystals with suitable work function to form a unique electronic structure of cascade band alignment for facilitating photodriven charge transfer. The optimized composite of SnO<sub>2</sub>/Ag/MoS<sub>2</sub> exhibited remarkable catalytic activities in the visible range for converting CO<sub>2</sub> into CH<sub>4</sub>, with at least a 10-times increment compared to bare MoS<sub>2</sub>. The increased photocatalysis benefited from the larger specific surface area and improved band alignments for rapidly transferring charges and effectively suppressing the direct annihilation of electron-hole pairs.

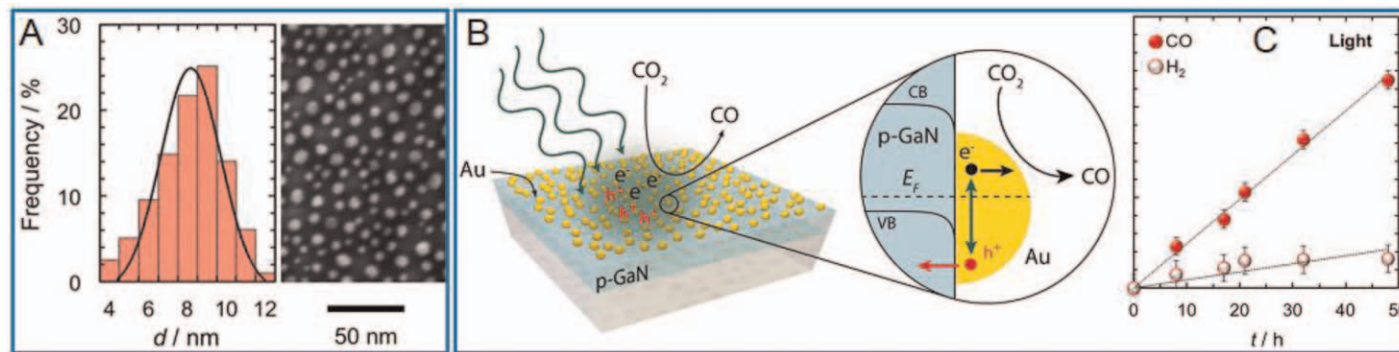
As an intriguing property, plasmonic metal nanocrystals can uniquely harvest nonequilibrium hot carriers such as hot electrons and holes for offering exceptional function to drive photocatalytic reactions. In recent years, there have been some research works to report the hot electron-involved catalytic reaction; in comparison, a few works are demonstrated to realize the harvesting of hot holes in metal nanocrystals. For that, Atwater's group fabricated a Schottky junction of gold/p-type gallium nitride (Au/p-GaN) to investigate the harvesting and utilization of plasmon-produced hot holes in the photoelectrocatalytic degradation of CO<sub>2</sub>.<sup>78</sup> As revealed, there was an interfacial Schottky barrier of >1 eV that existed between the Au/p-GaN junction, however, The Au/p-GaN hybrid films as photocathode exhibited

photoelectrocatalytic activity due to surface plasmon resonance effects, with the vast majority of thermal holes generated through interband transitions in Au being hot enough to be injected above the 1.1 eV interfacial Schottky barrier of the Au/p-GaN heterojunction. (see Figure 3.10). In the hybrid system, most of the holes produced by interband transitions in Au crystals were adequately hot across the interfacial Schottky barrier of 1.1 eV between the Au/p-GaN junctions. Therefore, the Au/p-GaN photocathode was utilized in plasmon-enhanced photoelectrochemical CO<sub>2</sub> conversion with an increased selectivity for producing CO over H<sub>2</sub> generation. In Kuang's work,<sup>79</sup> Au nanoparticles were coupled with CsPbBr<sub>3</sub> nanocrystal for resolving the severe annihilation of charge carriers and the narrow light-absorbing range of CsPbBr<sub>3</sub>. The CsPbBr<sub>3</sub>-Au nanocomposite was fabricated and further employed as a concept system to investigate the electronic interaction between perovskite nanocrystal and Au, which revealed the excitation wavelength-dependent carrier transfer behavior. Upon illumination with visible light ( $\lambda > 420$  nm), photogenerated electrons in CsPbBr<sub>3</sub> can inject into Au with an electron injection rate and efficiency of  $2.84 \times 10^9$  s<sup>-1</sup> and 78%, respectively. The boosted charge separation further translated into a 3.2-fold enhancement in CO<sub>2</sub> photocatalytic reduction activity. When solely exciting Au with a longer-wavelength light ( $\lambda > 580$  nm), the LSPR-induced hot electrons in Au nanoparticles can transfer to CsPbBr<sub>3</sub> and further participate in the photocatalytic reaction toward CO<sub>2</sub> reduction.

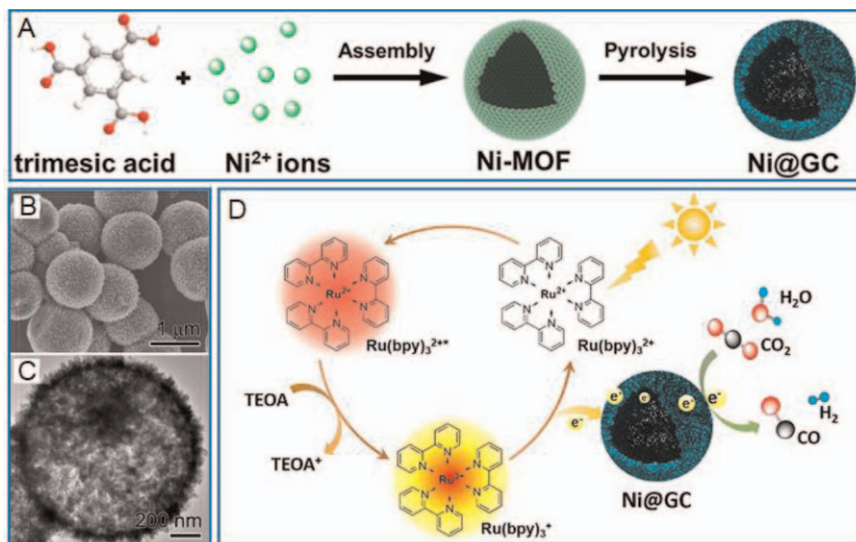
### 3.3.4 Two-dimensional Carbon-containing Materials

**Graphene and Its Derivatives:** Two-dimensional (2D) nanomaterials have usually been utilized as advanced catalysts for boosting their photocatalytic functions. Particularly, the utilization of 2D carbon-based nanosheets was demonstrated as a highly favorable one owing to their extraordinary physicochemical and electrical features.<sup>80</sup> For exploiting efficient, robust, and easily recyclable catalysts, metallic Ni nanoparticles were surrounded by few-layered graphitic carbon (GC) to form Ni@GC magnetic hollow spheres by thermally annealing a Ni-MOF under N<sub>2</sub> gas, which was used for photocatalytically reducing CO<sub>2</sub> with good performance (see Figure 3.11).<sup>81</sup> The synthesized Ni@GC hollow spheres had a large specific surface area and a high-density porous structure and efficiently accelerated the transfer and activation of photogenerated charges as well as improved CO<sub>2</sub> capture in the presence of Ni-C bonding. After incorporating a ruthenium photosensitizer, the Ni@GC nanocatalyst exhibited a high capability for CO<sub>2</sub>-to-CO reduction under irradiation by visible light, resulting in a superb CO production rate of 27  $\mu\text{mol h}^{-1}$ . Moreover, the Ni@GC nanocatalyst was highly stable and can be separated conveniently by using a magnetic field for recycled use.

For achieving an ideal photocatalytic system, Shen *et al.* synthesized various TiO<sub>2</sub>/reduced graphene oxide composite aerogels (TiO<sub>2</sub>-rGO) *via* a one-step hydrothermal and freeze-drying method.<sup>82</sup> The prepared composite aerogel presented a large specific surface area of 287.3 m<sup>2</sup> g<sup>-1</sup> and a pore



**Figure 3.10** (A) SEM image with a size-distribution histogram of Au particles on the p-GaN substrate. (B) Hot hole collection and photo- and electrochemical CO<sub>2</sub> conversion on plasmonic Au/p-GaN cathodes. (C) Gas evolution from plasmonic Au/p-GaN photocathode under plasmon excitation. Reproduced from ref. 78 with permission from American Chemical Society, Copyright 2018.



**Figure 3.11** (A) Illustration for preparing magnetic Ni@GC hollow microspheres. (B) SEM and (C) TEM images of Ni@GC hollow microspheres. (D) Photosensitized CO<sub>2</sub> reduction over the Ni@GC nanocatalyst. Reproduced from ref. 81 with permission from American Chemical Society, Copyright 2019.

volume of  $0.72 \text{ cm}^3 \text{ g}^{-1}$ , contributing to the remarkable absorption capability of reactants and fast intraparticle molecular transfer. In the three-dimensional (3D) structure of the rGO aerogel, TiO<sub>2</sub> nanorods were uniformly interspersed. Through applying the composite catalytic aerogel, CO<sub>2</sub> was efficiently converted to MeOH, CH<sub>4</sub>, EtOH, *etc.* The total yield of carbon generated by TiO<sub>2</sub>-rGO with 25 mmol Ti<sup>4+</sup> was found to be 15.7 times higher compared with the pure P25, owing to two reasons: the introduction of 3D rGO to TiO<sub>2</sub> promoting its light absorption efficiency and the specific chemical-bonding sites and the strong O=C-O-Ti group between rGO and TiO<sub>2</sub> effectively mitigating the annihilation of photoproduced electron-hole pairs. Similarly, a unique hybrid structure of GO-wrapped TiO<sub>2</sub> tubes was developed for the photocatalytic reduction of CO<sub>2</sub>, in which the TiO<sub>2</sub> tubes were synthesized *via* electrochemical anodization and wrapped with GO/rGO layers *via* the formation of interconnected linkage between the adjacent tubes.<sup>83</sup> Such a novel structure accelerated the separation of photoproduced electron-hole pairs with better charge transportation to catalytically reduce captured CO<sub>2</sub> molecules. In the first 20 min, the rGO/TiO<sub>2</sub> multileg tubes had exhibited the highest catalytic ability to produce a maximum yield of CO of  $\sim 1348 \mu\text{mol g}^{-1}$ , which stabilized to  $\sim 760 \mu\text{mol g}^{-1}$  upon irradiation under UV-A light for 2 h. Moreover, the CO production speed was an order of magnitude higher than that with graphene-loaded TiO<sub>2</sub> nanoparticles.

Recently, Z-scheme hybrid nanostructures have been fabricated for photocatalytically reducing CO<sub>2</sub> in the atmosphere of H<sub>2</sub>O gas, in which CdS and

TiO<sub>2</sub> nanocrystals were used as photocatalysts, and rGO was used as an electron mediator.<sup>84</sup> In the Z-scheme nanosystem, the photoproduced electrons from the conduction band of TiO<sub>2</sub> transferred to rGO and subsequently recombined with the existing holes of CdS, resulting in the enriching of photoexcited electrons on the CdS and holes on the TiO<sub>2</sub>. Through the Z-scheme process, the photocatalytic efficiency of CdS/rGO/TiO<sub>2</sub> exhibited extraordinary increment compared with bare CdS, CdS/TiO<sub>2</sub>, and CdS/rGO. Similarly, Oh's group reported the development of a WSe<sub>2</sub>-graphene-TiO<sub>2</sub> ternary nanocomposite using ultrasonic techniques, which exhibited a bandgap of 1.62 eV for UV/visible light utilization.<sup>85</sup> The WSe<sub>2</sub>-graphene-TiO<sub>2</sub> with an optimum loading of graphene of 8 wt% showed high photoactivity, gaining a total CH<sub>3</sub>OH yield of 6.3262 μmol g<sup>-1</sup> h<sup>-1</sup> after 48 h. The excellent photoreduction ability was due to the progressive synergistic relation between WSe<sub>2</sub>/TiO<sub>2</sub> and graphene components in the heterogeneous system.

**Graphitic Carbon Nitride (g-C<sub>3</sub>N<sub>4</sub>):** With a similar layered structure like graphene but an applicable band gap in the visible range, g-C<sub>3</sub>N<sub>4</sub> have exhibited various outstanding performances as visible light-responsive nanocatalysts for CO<sub>2</sub> conversion; however, it faces some disadvantages such as the low ability for charge separation and poor CO<sub>2</sub> adsorbing ability. Structural engineering of g-C<sub>3</sub>N<sub>4</sub> and its surface modification can be employed for overcoming the aforementioned demerits. For example, spine-like 3D g-C<sub>3</sub>N<sub>4</sub> nanostructures were created using three-step reaction processes, in which self-assembly of layered precursor and H<sup>+</sup> intercalation resulted from acid playing a critical function in forming the unique 3D structure.<sup>86</sup> The spine-like g-C<sub>3</sub>N<sub>4</sub> structures showed an improved photocatalytic ability for reducing CO<sub>2</sub> into CH<sub>4</sub> (0.71 μmol g<sup>-1</sup> h<sup>-1</sup>) compared to the small photocatalytic ability of common 2D g-C<sub>3</sub>N<sub>4</sub>. Alternatively, Xu *et al.* reported a supramolecular self-assembly method for preparing porous nitrogen-doped g-C<sub>3</sub>N<sub>4</sub> tubes with Lewis basicity and a large surface area, which were favorable for the capture of CO<sub>2</sub> and its photocatalytic reduction.<sup>87</sup> The porous nitrogen-doped g-C<sub>3</sub>N<sub>4</sub> tubes exhibited an excellent visible light-driven degradation of CO<sub>2</sub> to CO with a conversion rate of 103.6 μmol g<sup>-1</sup> h<sup>-1</sup>, which was 17 and 15 times higher than the values from bulk g-C<sub>3</sub>N<sub>4</sub> and P25, respectively. Similarly, hierarchical O-incorporated g-C<sub>3</sub>N<sub>4</sub> tubes (OCN-tubes) were fabricated using successive exfoliation *via* thermal oxidation and curling condensation of g-C<sub>3</sub>N<sub>4</sub>, which exhibited a hierarchical porous structure consisting of interconnected multiwalled nanochannels with uniform diameters of 20~30 nm.<sup>88</sup> The resultant OCN-tube showed outstanding photocatalytic activity for CO<sub>2</sub> conversion under visible light, with the methanol production rate being 0.88 μmol g<sup>-1</sup> h<sup>-1</sup>, which was five times higher than bulky g-C<sub>3</sub>N<sub>4</sub>. As revealed, the hierarchical tube structure endowed the OCN-tube materials with a larger specific surface area, higher efficiency for utilizing light, and promoted molecular diffusion speed. Meanwhile, the O-containing structure optimized the bandgap of g-C<sub>3</sub>N<sub>4</sub>, leading to a narrower bandgap, stronger CO<sub>2</sub> affinity, and larger capture capacity, as well as higher separation efficiency of photoproduced charge

carriers. In Wang's work,<sup>89</sup> conjugated g-C<sub>3</sub>N<sub>4</sub> sheets functionalized with barbituric acid were obtained through the chemical condensation of urea, which strongly alternated the physical and chemical functions of g-C<sub>3</sub>N<sub>4</sub> by increasing optical absorption and forming surface molecular heterojunctions that accelerated charge separation and improved photocatalysis. At the optimized reaction conditions, the best system could successfully catalyze the CO<sub>2</sub>-to-CO reduction reaction with 15-fold enhancement, relative to the unmodified g-C<sub>3</sub>N<sub>4</sub> obtained from urea.

More usually, g-C<sub>3</sub>N<sub>4</sub>-based nano hybrids were developed for achieving excellent photocatalytic performances by combining other functional nanostructured materials. Typically, the introduction of Pt clusters as cocatalysts into spine-like g-C<sub>3</sub>N<sub>4</sub> nanostructures substantially enhanced the CH<sub>4</sub> generation rate by four times, which benefited from the 3D nanostructures with high defects and the relative band gap variation (relatively negative values for both valence and conduction bands) of the spindle-like 3D g-C<sub>3</sub>N<sub>4</sub> nanostructures.<sup>86</sup> Alternatively, Pt nanoparticles 2.5 nm in size were loaded on the g-C<sub>3</sub>N<sub>4</sub> sheets *via* the chemical reaction in ethylene glycol, which showed a remarkable enhancement for the photocatalytic reduction of CO<sub>2</sub> to CH<sub>4</sub> in a water gas atmosphere after being irradiated by visible light.<sup>90</sup> 2 wt% Pt-incorporated g-C<sub>3</sub>N<sub>4</sub> composites resulted in the most CH<sub>4</sub> production of 13.02 μmol g<sub>cat</sub><sup>-1</sup> through light irradiation for 10 h, which was 5.1-fold higher than bare g-C<sub>3</sub>N<sub>4</sub> nanosheets. The outstanding photocatalytic performances from Pt/g-C<sub>3</sub>N<sub>4</sub> nanosystems for producing CH<sub>4</sub> were attributed to the increased absorbing capability for visible light and more rapid interfacial transfer of photoproduced electrons from g-C<sub>3</sub>N<sub>4</sub> to Pt because of the lower Fermi level of Pt in the Pt/CN hybridized heterostructures. Through the multielectron transferring processes, the electrons in Pt nanocrystals at a high density were beneficial for the photocatalytic conversion of CO<sub>2</sub> to CH<sub>4</sub>, which was ascribed to rapid charge separation after effectively inhibiting the recombination of electron-hole pairs. In Li's work,<sup>91</sup> g-C<sub>3</sub>N<sub>4</sub> sheets decorated using hierarchical TiO<sub>2</sub> flowers were constructed *via* an acid hydrothermal method. After the ongoing chemical exfoliation and etching, the surface area of g-C<sub>3</sub>N<sub>4</sub> nanosheets was significantly increased, along with the formation of porous structure and C vacancies. Interestingly, such TiO<sub>2</sub>/g-C<sub>3</sub>N<sub>4</sub> micronano-heteroarchitectures exhibited remarkably enhanced visible light-responsive catalytic properties for antibiotic degradation and CO<sub>2</sub> reduction, mainly being ascribed to the enlarged surface areas and pore volumes, increased adsorption/active sites and light-absorbing capacity, and higher separation efficiency of photoproduced charge carriers. In a similar work, hollow g-C<sub>3</sub>N<sub>4</sub>@CeO<sub>2</sub> nanocatalysts containing abundant oxygen vacancies were fabricated, in which the synergetic effect from g-C<sub>3</sub>N<sub>4</sub> and CeO<sub>2</sub> and the presence of oxygen vacancies played the critical function in the photocatalytic conversion of CO<sub>2</sub>, resulting in a much earlier and larger amount of CH<sub>4</sub> production than those of the individual g-C<sub>3</sub>N<sub>4</sub> and CeO<sub>2</sub>.<sup>92</sup> Meanwhile, the unique hollow structure can make multiple reflections of light in the hollow space, correspondingly

enhancing the conversion efficiency of light. Furthermore, the L-cysteine offered amine groups to be modified at the surface of g-C<sub>3</sub>N<sub>4</sub> during the preparation of C<sub>3</sub>N<sub>4</sub>, which also contributed significantly to the enhancement of CO<sub>2</sub> adsorbing capability. Experimentally, the g-C<sub>3</sub>N<sub>4</sub>@CeO<sub>2</sub> hybrid heterostructures showed the largest productions for CH<sub>4</sub> (3.5 μmol g<sup>-1</sup>), CH<sub>3</sub>OH (5.2 μmol g<sup>-1</sup>), and CO (16.8 μmol g<sup>-1</sup>). Alternatively, Bi<sub>2</sub>S<sub>3</sub> QDs/g-C<sub>3</sub>N<sub>4</sub> nanocomposites with varied contents of Bi<sub>2</sub>S<sub>3</sub> QDs were fabricated *via* the hydrothermal reaction strategy and utilized in the photocatalytic reduction of CO<sub>2</sub> with a remarkable activity (four times higher CO yield).<sup>93</sup> Bi<sub>2</sub>S<sub>3</sub> QDs uniformly loaded on the nanocatalysts could highly efficiently enhance the absorbing capability for visible light and promote the separation of photoproduced charge carriers, therefore decreasing the annihilation rate of photoproduced electron-hole pairs and improving the performances of photocatalysis. In Liu's work,<sup>94</sup> g-C<sub>3</sub>N<sub>4</sub> tubes were synthesized to enhance the light-harvesting capability and the redox potentials as well as accelerate the charge separating efficiency. Further, the resultant tubular g-C<sub>3</sub>N<sub>4</sub> was modified by a certain amount of zeolitic imidazolate framework-8 (ZIF-8) nanocrystals to greatly increase CO<sub>2</sub> absorbing capacity. Benefiting from the cooperative effects of structural engineering and surface modification, the optimized g-C<sub>3</sub>N<sub>4</sub>/ZIF-8 hybrid catalysts exhibited a remarkable increment in the catalytic generation of CH<sub>3</sub>OH.

In a recent work, GO was used as a structure-manipulating material for forming a novel 2D interface in sandwiched graphene-g-C<sub>3</sub>N<sub>4</sub> structures to enhance visible light-responsive reduction of CO<sub>2</sub> into CH<sub>4</sub>.<sup>95</sup> Experimentally, a one-pot impregnation-thermal reaction strategy was employed when urea and GO were used as two types of precursors. The linkage of C-O-C bonds between graphene and g-C<sub>3</sub>N<sub>4</sub> sheets led to a redshift of the light-absorbing edge and thus the hybridized nanosystems exhibited higher visible light-responsive activity for reducing CO<sub>2</sub> at mild conditions because of the effective inhibition of electron-hole pair annihilation and great increment of the charge migration, showing a 2.3-fold increment than individual g-C<sub>3</sub>N<sub>4</sub> sheets. Similarly, Ong *et al.* demonstrated a 2D/2D hybridized heterostructured photocatalytic materials with unique interfacial contact by incorporating rGO and protonated g-C<sub>3</sub>N<sub>4</sub> (pCN) *via* combining ultrasonic dispersion, electrostatic self-assembly, and subsequent NaBH<sub>4</sub>-based reduction.<sup>96</sup> The intimate contact interface in rGO/pCN heterostructures led to an efficient charge transfer across the heterojunctions to inhibit the annihilation of electron-hole pairs and thus exhibited an outstanding enhancement in the reduction of CO<sub>2</sub> to CH<sub>4</sub> after the participation of H<sub>2</sub>O gas. The best 15 wt% rGO/pCN achieved the highest CH<sub>4</sub> production of 13.93 mmol g<sub>cat</sub><sup>-1</sup> with a quantum yield of 0.560% for light conversion, which was a 5.4- and 1.7-fold improvement from using pCN and rGO/CN materials, respectively. Moreover, the rGO/pCN hybrid exhibited an acceptable stability, and no obvious decrease was measured in the generation of CH<sub>4</sub> from CO<sub>2</sub> reduction after being used for three cycles. In addition, a heterojunction was fabricated by the *in situ* synthesis of thin Bi<sub>12</sub>O<sub>17</sub>C<sub>12</sub>



(BOC) layers on g-C<sub>3</sub>N<sub>4</sub> sheets, which effectively shortened the migration path of charges and thus promoted interfacial charge separation.<sup>97</sup> Under the driving of built-in electric fields, the charge carriers are transferred through a step-like pathway with an enhanced photocatalytic performance.

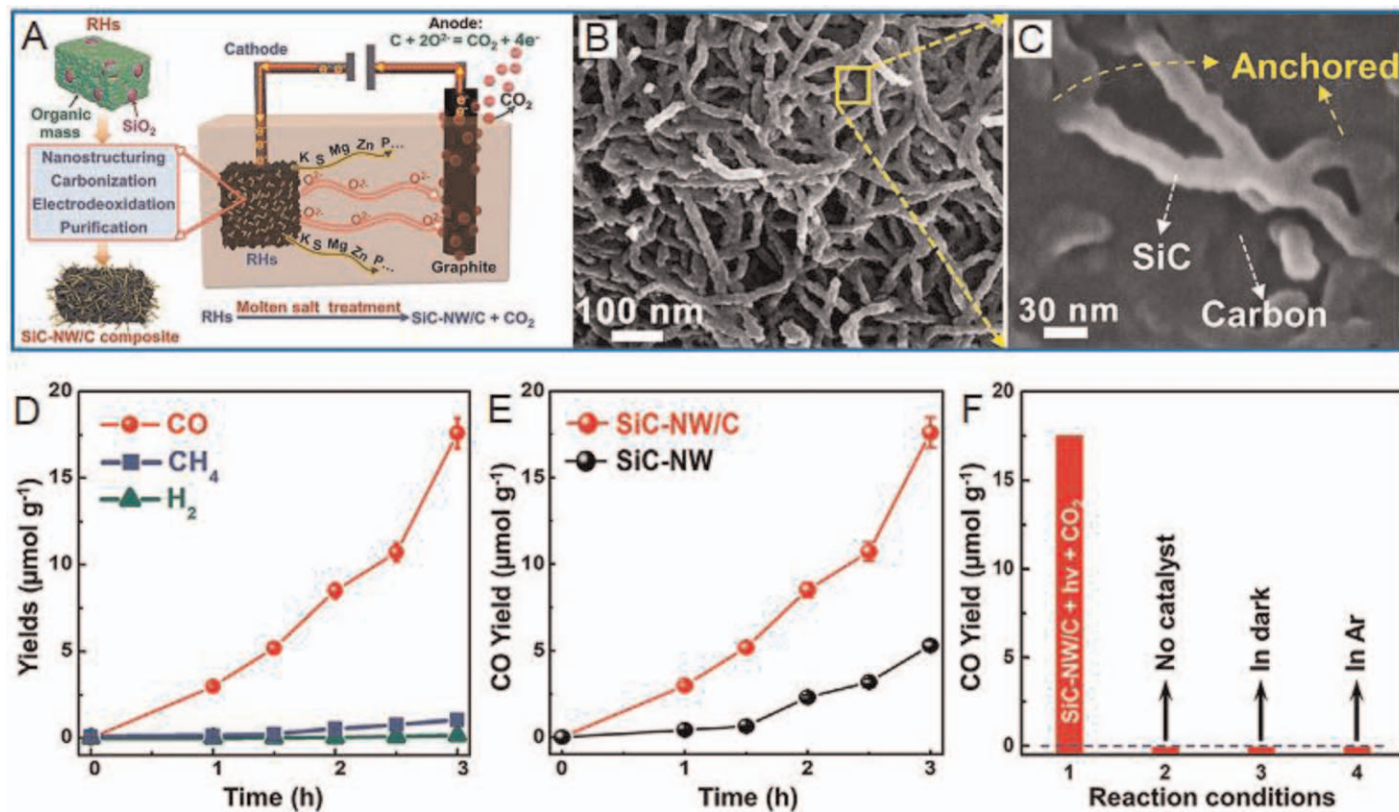
To substantially improve photocatalytic performance, ternary hybridized systems containing g-C<sub>3</sub>N<sub>4</sub> have been developed frequently. For instance, a Pt@CeO<sub>2</sub>/g-C<sub>3</sub>N<sub>4</sub> heterojunction was prepared by using the calcination method and photoreduction technology, which showed better photocatalytic performance for reducing CO<sub>2</sub> to CO or CH<sub>4</sub>.<sup>98</sup> The maximum photocatalytic activity values of 4.69 and 3.03 μmol h<sup>-1</sup> g<sup>-1</sup> toward CO and CH<sub>4</sub>, respectively, under irradiation with UV light were obtained and the reduction activity did not decrease significantly after five cycles. The improved photoreduction of CO<sub>2</sub> can be ascribed to the cooperation effect of the oxygen vacancies in CeO<sub>2</sub> for CO<sub>2</sub> activation and heterojunction for electron separation. Besides, Pt nanoparticles can further promote the transfer of electrons, leading to higher photocatalytic ability. In another work, a graphene-mediated ZnV<sub>2</sub>O<sub>6</sub>/g-C<sub>3</sub>N<sub>4</sub> sheet nanocomposite with Z-scheme electronic transportation was synthesized through a one-step solvothermal reaction and utilized in the photocatalytic reduction of CO<sub>2</sub> in the presence of visible light.<sup>99</sup> The highest CH<sub>3</sub>OH yield of 3488 μmol g<sub>cat</sub><sup>-1</sup> was achieved by using the ZnV<sub>2</sub>O<sub>6</sub>/rGO/g-C<sub>3</sub>N<sub>4</sub> nanocomposite, 1.02 and 1.25 times higher compared to ZnV<sub>2</sub>O<sub>6</sub>/rGO and ZnV<sub>2</sub>O<sub>6</sub>/g-C<sub>3</sub>N<sub>4</sub> materials, respectively. This improved performance was attributed to the well-contacted ternary heterostructures with hierarchical shape and effective charge separation by rGO. Interestingly, CH<sub>3</sub>OH production was further increased *via* the introduction of rGO/g-C<sub>3</sub>N<sub>4</sub> as an electron pool, which resulted in a 1.07 times higher production than that of using rGO alone. The stability of hybrid catalysts was tested with the continuous CH<sub>3</sub>OH generation for 32 h. The above result revealed that the ternary ZnV<sub>2</sub>O<sub>6</sub>/RGO/g-C<sub>3</sub>N<sub>4</sub> nanocomposite in the 2D structure had a larger absorbing capability for visible light, accelerated charge separation, and increased photocatalytic activity by using rGO/g-C<sub>3</sub>N<sub>4</sub> as a multiple mediator. More interestingly, a magnetically recoverable biochar-supported ternary g-C<sub>3</sub>N<sub>4</sub>/Bi<sub>2</sub>O<sub>2</sub>CO<sub>3</sub>/CoFe<sub>2</sub>O<sub>4</sub> (BCBF) heterojunction was fabricated, which showed high visible light photoactivity.<sup>100</sup> Ternary band structure efficiently reduced the charge recombination rate and promoted spectral activity, and the ternary junction showed a high visible light-powered conversion of CO<sub>2</sub>, producing CH<sub>4</sub> (~119 μmol g<sup>-1</sup>), CO (~131 μmol g<sup>-1</sup>), and O<sub>2</sub> (~242 μmol g<sup>-1</sup>) with a high rate constant at 13.05 × 10<sup>-3</sup> s<sup>-1</sup>.

**Other Carbon-containing Nanomaterials:** As a new metal-free photocatalyst, the ternary semiconductor of boron carbon nitride (BCN) has recently been synthesized and utilized in the visible light-driven conversion of CO<sub>2</sub>. As reported, the CO<sub>2</sub> photoreduction property of bulky BCN crystals can be significantly enhanced *via* the surface grafting of CdS spheres.<sup>101</sup> Compared to individual BCN samples, the CdS/BCN hybrid photocatalysts exhibited a 10-fold-enhanced CO<sub>2</sub> conversion activity and high stability, resulting in a great CO yield rate of 12.5 μmol h<sup>-1</sup> (*i.e.* 250 μmol g<sup>-1</sup> h<sup>-1</sup>) when triethanolamine (TEOA) was used as the reducing precursor. The improved photocatalytic

performance for reducing CO<sub>2</sub> was majorly attributed to the greatly increased visible light-harvesting capability and the greatly promoted separation/transfer kinetics of photoproduced electron–hole pairs. In Lou's work,<sup>102</sup> the SiC nanowires/C (SiC-NW/C) composites were synthesized from rice husks (RHs) through a molten salt-involved electrochemical reaction (see Figure 3.12). The SiC-NW/C nanostructures enabled efficient CO<sub>2</sub> capture and rapid separation and transportation of charges. Owing to the structural and compositional advantages, the SiCNW/C composites showed excellent photocatalytic ability for reducing CO<sub>2</sub> into CO.

### 3.3.5 Metal–Organic Frameworks

MOFs are an emerging type of functional nanomaterials having porous structures that show extraordinary specific surface area and tuned surface reaction; thus, they exhibit a promising potential as a photocatalyst for CO<sub>2</sub> reduction.<sup>103–105</sup> For achieving excellent-performance MOFs, a series of Zr–porphyrin MOF/ultrathin g-C<sub>3</sub>N<sub>4</sub> (ZPUCN) photocatalysts were synthesized through an *in situ* hydrothermal reaction combined with a self-assembly approach, which were utilized as stable and efficient catalysts for photocatalytically reducing CO<sub>2</sub>.<sup>106</sup> The hollow Zr-MOF tubes were surrounded with ultrathin g-C<sub>3</sub>N<sub>4</sub> sheets to form an interface through covalent linkages of the unsaturated metal atoms and organic functional groups of Zr-MOFs onto g-C<sub>3</sub>N<sub>4</sub> sheets. The interfacial heterojunction provided a platform for g-C<sub>3</sub>N<sub>4</sub> sheets as conductors to migrate electrons or as donors to move electrons into Zr–O nanocluster to react with CO<sub>2</sub>, significantly accelerating the spatial separation of charge carriers and inhibiting the photoproduced electron–hole pair annihilation. Owing to the strong synergetic effects of the well-contacted structures and chemical modification, the resulting ZPUCN nanocomposite not only exhibited a high CO production yield (5.05 mmol g<sup>-1</sup> h<sup>-1</sup>), 2.2 times and 3.2 times higher as compared to individual Zr-MOFs and g-C<sub>3</sub>N<sub>4</sub>, respectively, but also displayed good stability to undertake a continual photoreaction for 96 h. In Luo's work,<sup>107</sup> MOF-like hierarchical nanoflowers were developed from a bifunctional Ru-MOF, which acted as a stable and efficient photocatalyst for the visible light-responsive catalytic reduction of CO<sub>2</sub>. The resultant flowered nanostructures significantly enhanced the photocatalytic ability, which was about 150% higher than that of bulk particles. Moreover, the hierarchical structures also greatly improved the photostability of the bifunctional Ru-MOFs for their recycled use in photocatalysis. For reducing the photocorrosion of CdS, CdS/ZIF-8 composites with core–shell structures were prepared to not only improve the photostability of CdS but also enhance its CO<sub>2</sub> adsorption capacity without impairing its light-harvesting ability.<sup>108</sup> The CdS/ZIF-8 catalyst showed higher efficiency and better selectivity than unmodified CdS in the photocatalytic conversion of CO<sub>2</sub> to CO, which was attributed to its higher CO<sub>2</sub> adsorption capability. Recently, cobalt-containing zeolitic imidazolate frameworks (Co-ZIF-9) have been reported as emerging imidazolate motifs for CO<sub>2</sub> capture and utilization. In Xu's work,<sup>109</sup> a Co-ZIF-9/TiO<sub>2</sub> (ZIFx/T) nanocomposite was



**Figure 3.12** (A) Reaction process of molten salt–assisted electrochemical conversion of RHs to SiC-NW/C for CO<sub>2</sub> photoreduction. (B,C) SEM images of SiC-NW/C nanostructure. (D) CO<sub>2</sub> photoreduction performance of SiC-NW/C. (E) Time-dependent CO yields of SiC-NW/C and SiC-NW. (F) Activity of reaction system under various conditions. Reproduced from ref. 102 with permission from John Wiley & Sons, Copyright © 2020 WILEY-VCH Verlag GmbH & Co. KGaA, Weinheim.

fabricated by an *in situ* preparation process, in which TiO<sub>2</sub> and Co-ZIF-9 were strongly bound with each other to accelerate the separation of charge carriers. As a result, 8.79 mmol of CO, 0.99 mmol of CH<sub>4</sub>, and 1.30 mmol of H<sub>2</sub> were achieved after the photocatalysis of CO<sub>2</sub> for 10 h by using ZIF0.03/T, and the total used photoelectron number (28.17 mmol) was ~2.1 times more than that of bare TiO<sub>2</sub>. As revealed, Co-ZIF-9 can efficiently activate the CO<sub>2</sub> molecules and positively move the onset potential of CO<sub>2</sub> conversion. Both easier CO<sub>2</sub> activation and more rapid charge separation contributed to the excellent performance of the well-synthesized ZIFx/T nanostructures. In another work, a MOF-involved ternary nano hybrid was fabricated by the self-assembly of TiO<sub>2</sub>/Cu<sub>2</sub>O heterostructures in a microdroplet-based system and the subsequent formation of Cu<sub>3</sub>(BTC)<sub>2</sub> (BTC = 1,3,5-benzenetricarboxylate).<sup>110</sup> Benefiting from the high density of charge carriers and efficient activation of CO<sub>2</sub> molecules, the ternary hybridized nanocomposites exhibited an excellent efficiency for converting CO<sub>2</sub> and a preferential generation of CH<sub>4</sub>.

With superb optoelectronic features, perovskite CsPbBr<sub>3</sub> QDs have been utilized for developing perovskite solar cell and LED devices, but there are few works that focus on photochemical CO<sub>2</sub> reduction because of their poor stability in moisture atmosphere. For that, the CsPbBr<sub>3</sub> QDs/Uio-66(NH<sub>2</sub>) nanocomposites were specially exploited to reduce CO<sub>2</sub> to chemical fuels in a nonaqueous environment.<sup>111</sup> The resulting hybrid nanocomposite exhibited substantially increased photocatalytic activity and the yield amount of CO can reach 98.57 μmol g<sup>-1</sup> when CsPbBr<sub>3</sub> QDs concentration was 15 wt%. The outstanding photocatalytic ability could be attributed to the accelerated electron extraction and transportation between Uio-66(NH<sub>2</sub>) and CsPbBr<sub>3</sub>, larger accessible specific surface area, and higher absorbing capacity for visible light. Meanwhile, the nano hybrid showed good reusability for photocatalytically reducing CO<sub>2</sub>. Similarly, Yang's group demonstrated a MOF-loaded photocatalyst that had increased CO<sub>2</sub> reduction ability and reuse stability (see Figure 3.13).<sup>112</sup> For preventing dimerization to deactivation, a cocatalyst, ReI(CO)<sub>3</sub>(BPYDC)Cl (BPYDC = 2,2'-bipyridine-5,5'-dicarboxylate), was covalently linked onto a zirconium MOF, Uio-67 (Ren-MOF), for readily achieving CO<sub>2</sub>-to-CO transformation. By rationally manipulating its density in the hybrid, the best photocatalytic performance was measured by using Re<sub>3</sub>-MOF. Referring to the activity-structure relationship of Re<sub>n</sub>-MOFs, Re<sub>3</sub>-MOF was further loaded onto Ag nanocubes (Ag ⊂ Re<sub>3</sub>-MOF), which spatially confined active Re sites to the intensified near-surface electric fields at the surface of Ag nanocubes, leading to a sevenfold improvement in the conversion of CO<sub>2</sub> to CO under visible light with long-term stability for continual use for 48 h.

Recently, Ye's group successfully realized the solar-driven CO<sub>2</sub> reduction into CO by utilizing a MOF-hybridized Fe@C nanocatalyst, which contained an iron core with a size of <10 nm and an outer thin carbon layer.<sup>113</sup> Compared to naked iron nanoparticles, the carbon layer-shelled iron catalysts showed an enhanced catalytic activity in the solar-induced CO<sub>2</sub> reduction with H<sub>2</sub>. Importantly, it provided a more stable CO<sub>2</sub> reduction speed

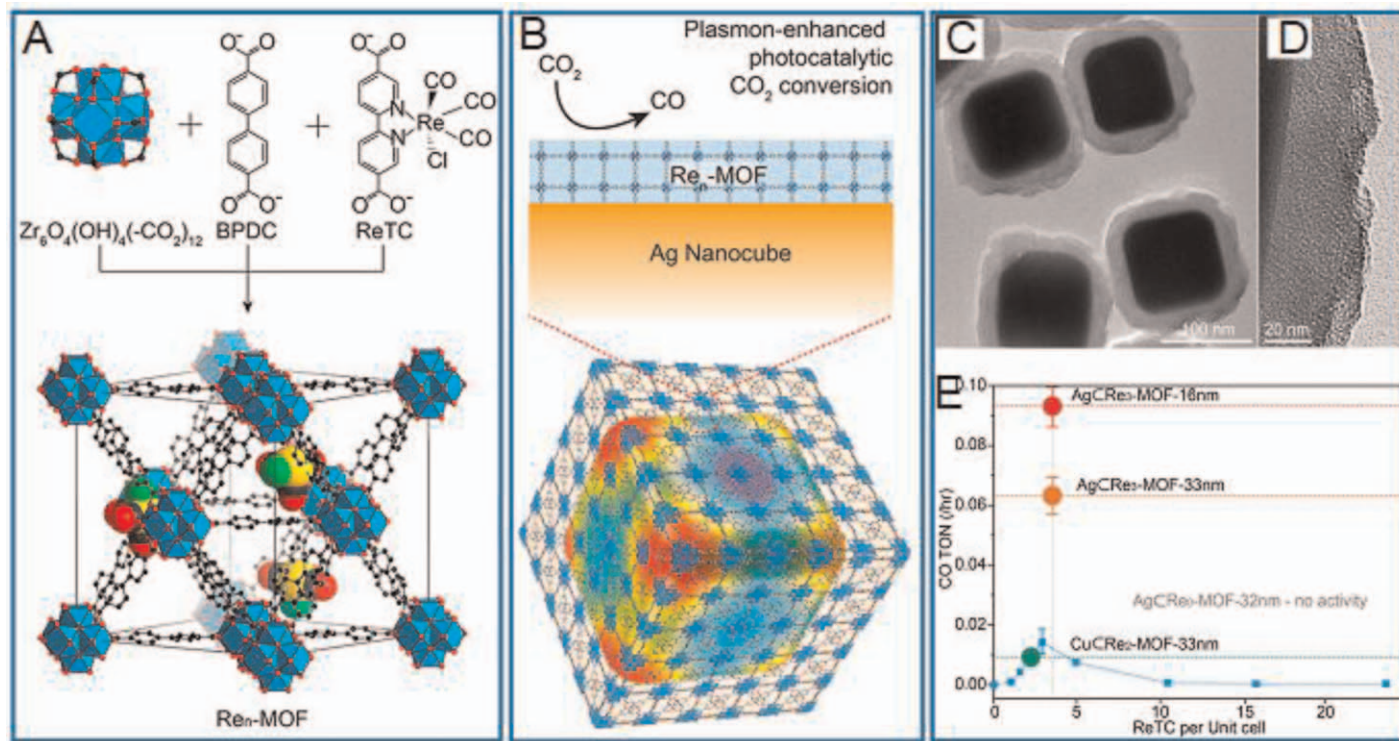
and higher selectivity to produce CO. The strong adsorbing capacity for visible and infrared light caused a significant thermal effect to promote the catalytic reaction. UV-driven LSPR from iron particles was revealed to have a high ability to activate CO<sub>2</sub> at high temperatures. As indicated, the plasmon-photon coupling effect was significantly amplified on the surface of the iron nanoparticles, resulting in the increased production of energetic hot electrons for activating CO<sub>2</sub>. The few-layered carbon shell at the iron nanocrystals can significantly stimulate the desorption of the yielded CO from the photocatalyst's surface and thus increase the production selectivity for CO. This work can be recognized as a combination of photo- and thermocatalytic reactions that will bring a new research field for exploiting more conversion paths of CO<sub>2</sub>.

### 3.4 Electrochemical Reduction of CO<sub>2</sub> With Nanostructured Materials

Besides the above-demonstrated photocatalytic reductions, electrocatalytic conversion also offers a talented avenue for reducing CO<sub>2</sub> into useful fuels and chemicals.<sup>114</sup> The electrocatalytic reduction of CO<sub>2</sub>, with water as a hydrogen source, has been attracting numerous research interests, benefiting from its outstanding performance for recycling carbon and utilizing renewable electric energy. However, the large-scale commercial use of electrochemical CO<sub>2</sub> reduction systems is hindered by poor electrocatalyst activity, large overpotential, low energy conversion efficiency, and product selectivity in reducing CO<sub>2</sub>.<sup>5</sup> Thus, there is an urgent requirement to rationally design highly efficient, stable, and scalable electrocatalysts to overcome the above constraints.<sup>22</sup> In early 1873, Brodie first demonstrated the electrocatalytic reduction of CO<sub>2</sub> with low efficiency and poor selectivity toward reducing products.<sup>115</sup> Due to the extensive utilization of nanotechnology and rapid development of characterization techniques for nanostructure and features, lots of successes have been achieved for highly efficiently converting CO<sub>2</sub> by using nanostructured electrocatalysts.<sup>116</sup> Therefore, this section overviews those great efforts for improving the electrocatalytic activity in CO<sub>2</sub> conversion by using nanostructured catalysts and highlights the new trends in advancing the electrochemical reduction of CO<sub>2</sub>.

#### 3.4.1 Nanostructured Monometal Electrocatalysts

**Gold Nanomaterials:** The nanostructured engineering of catalytic materials is an effective and promising method to improve their performance, which can create new active surfaces for significantly enhancing the catalytic ability and durability. Particularly, gold nanocrystal-involved nanomaterials exhibit various promising properties in the electrochemical reduction of CO<sub>2</sub> into fuels. To fully explain the exceptional enhancement in the electrocatalytic activity and understanding the electrochemical mechanism for CO<sub>2</sub> reduction, the length of the Au–Au bond and low work function at the Au



**Figure 3.13** Structures of (A)  $\text{Re}_n\text{-MOF}$  and (B)  $\text{Ag}\subset\text{Re}_n\text{-MOF}$  for the plasmon-improved photocatalysis of  $\text{CO}_2$ . (C) TEM image and (D) magnified TEM image of  $\text{Ag}\subset\text{Re}_3\text{-MOF}$ . (E) Photocatalytic activities of different samples for realizing  $\text{CO}_2$ -to- $\text{CO}$  conversion. Reproduced from ref. 112 with permission from American Chemical Society, Copyright 2017.

surface were investigated and proved to enhance electrocatalytic CO<sub>2</sub> conversion.<sup>117</sup> For studying the enhanced mechanism of electrocatalysis, Jin's group reported two kinds of Au<sub>25</sub> nanoclusters with different morphologies (*i.e.* sphere and rod) for electrocatalytic CO<sub>2</sub> reduction.<sup>118</sup> The Au<sub>25</sub> spheres exhibited higher Faradaic efficiency for producing CO and production rate relative to the Au<sub>25</sub> rods. Referring to the fact that the degradation rate of CO<sub>2</sub> and product selectivity of this reaction are highly sensitive to the surface structures of electrocatalysts, 4H Au nanostructures were employed as advanced electrocatalysts for highly active and selective conversion of CO<sub>2</sub> into CO. Au nanoribbons in the pure 4H phase, Au nanorods in the hybrid 4H/fcc phase, and those in the fcc phase were comparatively studied for the electroreduction of CO<sub>2</sub>.<sup>119</sup> Both the activity and selectivity for CO production were found to exhibit the order trend of 4H-nanoribbons > 4H/fcc-nanorods > fcc-nanorods, with the 4H-nanoribbons achieving >90% Faradaic efficiency toward CO. The combination of crystal phase and shape control gave rise to the preferential exposure of undercoordinated sites with high reactivity. In Gracias's work,<sup>120</sup> with the assistance of a prestrained polymer, they compressed a 60 nm thick gold film along uniaxial and biaxial directions to fabricate a nanofolded catalyst for electrochemical CO<sub>2</sub> conversion. In those two types of folds, the ratio from loose to tight was tuned by controlling the content of prestrain in those polymers. In the experiment, grain reorientation and coarsening effect were observed in the nanofolded Au nanocrystals and an enhanced Faradaic efficiency for producing CO was measured over the biaxially compressed folded electrocatalyst by a factor of nine compared with the flat electrocatalyst. It was demonstrated that the nanofolded structures can substantially optimize their grain features, mass transport, and electrocatalytic activity. Alternatively, Oh *et al.* reported the fabrication of Au nanocrystals through the electrochemical reduction of anodic Au(OH)<sub>3</sub> for selectively producing CO in an electrocatalytic conversion of CO<sub>2</sub>.<sup>121</sup> After adjusting the anodic potential and current density for reduction, the Au morphology can be changed into either pore- or pillar-like nanostructures. This unique shape was determined by the electric field-driven transportation of Au<sup>3+</sup> across the Au(OH)<sub>3</sub>/Au interfaces. Both Au nanocrystals exhibited remarkably higher CO selectivity compared to the untreated Au films, which can be attributed to the high density of grain boundaries (GBs) for more rapid stabilization of the CO<sub>2</sub><sup>•-</sup> intermediate. Particularly, the porous Au nanocrystals had a higher CO selectivity than the pillar-like ones at low overpotentials, whereas at high overpotentials, the pillar-like Au nanocrystals had a higher selectivity for CO.

**Silver Nanomaterials:** Jiao's group explored the electrochemical mechanism of CO<sub>2</sub> reduction over Ag nanocrystals in an aqueous electrolyte.<sup>122</sup> Compared with bulky Ag materials, both Ag nanoparticles and porous Ag nanocrystals showed increased activity for reducing the activation energy of CO<sub>2</sub> to COOH intermediates *via* the low-coordinated surface Ag atoms, suggesting an interesting conversion mechanism, including a fast first electron/proton transportation and then a slow second proton migration.

Luo's group unraveled the structure effects of ultras-small Ag nanocubes (NCs) with lengths below 25 and 70 nm (L25- and L70-Ag-NCs) covered completely by the (100) plane for an efficient CO<sub>2</sub> reduction to CO.<sup>123</sup> As a result, the L25-Ag-NCs delivered an extraordinarily larger current density, a significantly higher Faradaic efficiency of near-unity, an excellent energy conversion of 64.0%, and a higher stability of up to 18 h. In another one of their works, fivefold twinned Ag wires with diameters less than 25 (D-25) and 100 nm (D-100) were synthesized *via* a bromide-mediated polyol approach.<sup>124</sup> Relative to D-100 Ag nanowires and Ag particles, D-25 Ag nanowires possessed significantly increased current density, as well as greatly enhanced Faradaic efficiency and energy utilization efficiency and achieved maximum values of 99.3% and 61.3%, respectively. The enhanced electrocatalytic activity originated from the increased ratio of the active sites due to both diameter and length effects and the unique fivefold twinned structure completely covered by energetically favorable planes for CO<sub>2</sub> reduction. In Sun's work,<sup>125</sup> silver nanostructures with hierarchical porosities of multiple length scales were synthesized through the electrochemical reduction of silver benzenethiolate nanoboxes to exhibit superior electrocatalytic performance toward the electroreduction of CO<sub>2</sub>. The Faradaic efficiency of reducing CO<sub>2</sub> to CO can be close to 100% at high cathodic potentials, benefiting from the readsorbed benzenethiolate ions on the Ag surface that can inhibit the hydrogen generation effect. As revealed, the disfavored H binding on the benzenethiolate-modified Ag surface was responsible for inhibiting the hydrogen evolution reaction. The mass-specific activity of CO<sub>2</sub> reduction can be over 500 Ag<sup>-1</sup> because the multiple-scale porosities maximized the diffusion of reactive species to and away from the Ag surface. In Zhang's study,<sup>126</sup> Ag nanocrystals were synthesized *via* the electrochemical deposition of Ag with the assistance of a Keggin-type polyoxometalate, [PMo<sub>12</sub>O<sub>40</sub>]<sup>3-</sup> (PMo). The binding of PMo at the surface of the newly generated Ag lowered its surface energy to stabilize the resultant nanostructures. The electrochemical activity of the Ag-PMo nanocomposites for reducing CO<sub>2</sub> was estimated in a CO<sub>2</sub>-saturated dimethylformamide medium with 0.1 M [*n*-Bu<sub>4</sub>N]PF<sub>6</sub> and 0.5% (v/v) additive H<sub>2</sub>O. The experimental results showed that the Ag-PMo nanocomposites can catalytically reduce CO<sub>2</sub> to CO with an onset potential of -1.70 V, which was only 0.29 V more negative compared to the reversible potential for the identical process and 0.70 V more positive compared to that using bulky Ag powder. A high Faradaic efficiency of ~90% was achieved at a wide range of applied potentials, which suggested that the fast generation of CO<sub>2</sub><sup>•-</sup> was followed by the rate-dependent protonation process.

**Copper Nanomaterials:** For substantially improving the selectivity and stability of Cu catalysts, Xia's group demonstrated that controlling the surface oxidation of Cu nanowires can greatly improve their C<sub>2+</sub> selectivity and stability.<sup>127</sup> Specifically, a Faradaic efficiency of 57.7 and 52.0% for ethylene was achieved when the Cu nanowires were oxidized by the O<sub>2</sub> from air and aqueous H<sub>2</sub>O<sub>2</sub>, respectively, and both of them showed hydrogen selectivity below 12%. The high yields of C<sub>2+</sub> products can be majorly ascribed to the



increment in surface roughness and the generation of defects and cavities during the electrochemical reduction of the oxide layer. Similarly, MacFarlane's group reported the electrocatalytic reduction of CO<sub>2</sub> based on Cu wire array, which showed a much higher current density than polycrystalline Cu.<sup>128</sup> Through sputter loading an Au thin film on the Cu wires, the Faradaic efficiency of CO could reach 30%. Under an overpotential of 540 mV with respect to the production of CO, the electrode comprised of Cu/Au core-shell wire arrays catalytically produced a syngas with a stable CO/H<sub>2</sub> ratio. In Nilsson's work,<sup>129</sup> a nanostructured Cu surface possessing a cubic structure was synthesized *in situ* during the electroreduction of CO<sub>2</sub> to provide high selectivity for ethylene production from electrocatalytic CO<sub>2</sub> conversion. The cubic nanocrystals were capable of strongly favoring the production of multicarbon products from CO<sub>2</sub>, which was a unique property of this surface and was a critical step for developing an electrocatalyst that had specific selectivity for multicarbon products. Agapie's group reported nanostructured copper electrodes by using *N,N'*-ethylene-phenanthroline dibromide as an additive agent.<sup>130</sup> A selectivity of 70% for C<sub>≥2</sub> products was measured within 40 h without observed evolution on the surface morphology. In addition, Wang's group reported a novel 3D Cu-based nanostructure as an advanced catalyst for electrocatalytic CO<sub>2</sub> reduction.<sup>131</sup> With the assistance of thermal oxidation, CuO nanowire and/or porous nanostructures were loaded onto Cu foams with 3D frameworks. The resulting Cu-containing hierarchical nanosystem demonstrated high electrocatalytic activity and good selectivity for CO<sub>2</sub> reduction, resulting in >80% Faradaic efficiency and an almost three-times increment in the CO<sub>2</sub> reduction rate as compared to the Cu nanowires synthesized on planar substrates.

**Other Metals:** Tuning surface strains is recognized as a good way to improve the electrocatalytic activity of heterostructured nanocatalysts *via* optimizing the electronic structures. In Yang's work,<sup>132</sup> the strain effect on the electrocatalytic conversion of CO<sub>2</sub> was studied by employing Pd octahedra and icosahedra as a well-manipulated platform. The Pd icosahedra/C hybrid catalysts showed a maximum Faradaic efficiency for producing CO of 91.1% at -0.8 V, 1.7-fold higher than with Pd octahedra/C electrocatalysts at -0.7 V. This comparison revealed that the tensile strain at the surface of icosahedra boosted the electrocatalytic function by moving up the d-band center and so strengthening the adsorption of the main intermediate COOH\*. Alternatively, a surface-reconstructed process from (111) facets to active (100) sites was found at a defect-rich Pd thin sheet for CO<sub>2</sub> electroreduction.<sup>133</sup> Because the reconstruction increased the concentration of active sites and reduced the CO binding force at the Pd surface, the conversion of CO<sub>2</sub> to CO was significantly promoted to achieve a high CO Faradaic efficiency of 93%.

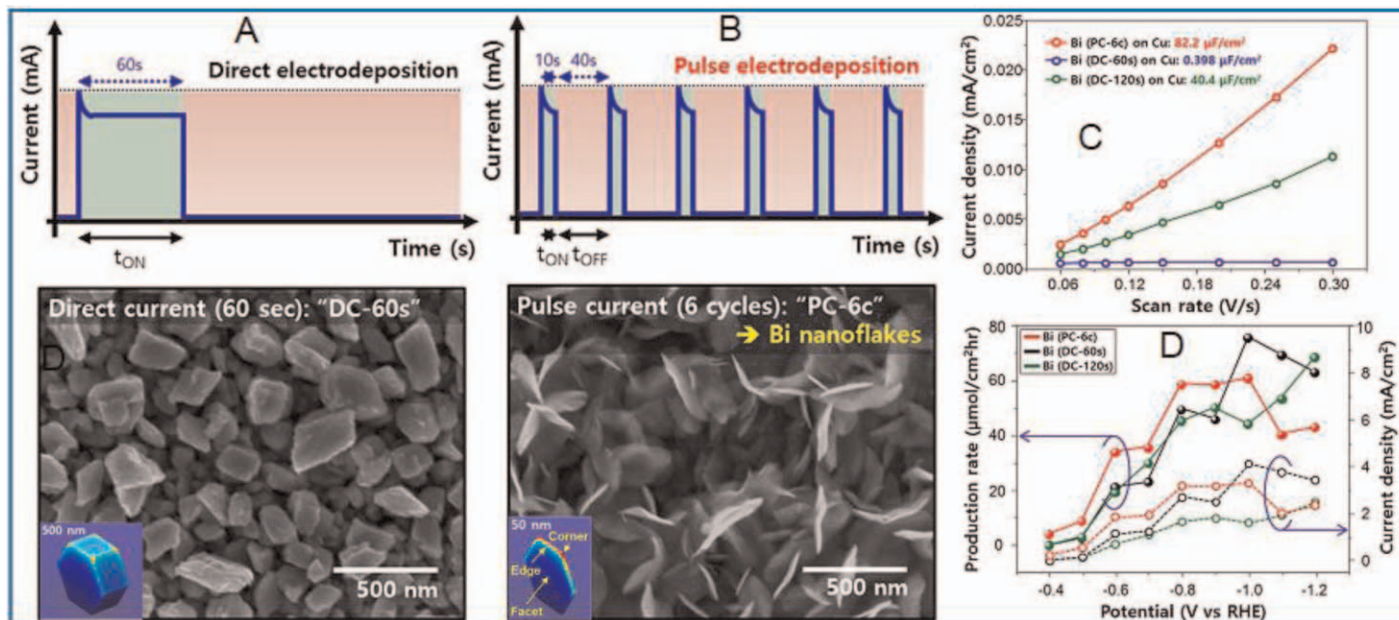
Bismuth (Bi) has recently been exploited to develop ideal electrocatalytic materials for CO<sub>2</sub> conversion and utilization. For improving its selectivity, a one-step reducing process was employed to fabricate novel Bi nanostructures in water, which exhibited outstanding electrocatalytic activity for CO<sub>2</sub> reduction with a high Faradaic efficiency of 92% toward formate at a potential

of  $-0.9$  V, benefiting from increased active sites and more exposed crystalline facets.<sup>134</sup> The theoretical calculation confirmed that the high-index Bi facets were beneficial for the production of intermediate \*OCHO that is subsequently converted to formate. In a similar work, ultrathin Bi nanosheets with a single crystalline structure and increased surface areas were synthesized *via* an *in situ* topotactic evolution of bismuth oxyiodide sheets, which afforded superb catalytic activity for the electrochemical conversion of CO<sub>2</sub> to formate.<sup>135</sup> Almost 100% selectivity, large current density, and good durability, more than 10 h, were achieved over a wide potential. Alternatively, nanostructured Bi flakes were directly synthesized onto Cu substrates by using a pulse electrodeposition approach (see Figure 3.14).<sup>136</sup> Compared to Bi films electrodeposited with direct current, the novel Bi flakes had considerably sharp edge and corner sites, which formed strong local electric fields for boosting electrocatalytic activity in the conversion of CO<sub>2</sub>. As demonstrated, the Bi flakes exhibited a high HCOO<sup>-</sup> Faradaic efficiency of 79.5% at a low potential of  $-0.4$  V and a nearly 100% Faradaic efficiency at  $-0.6$  V, signifying that the morphological manipulation of Bi catalysts was really an efficient strategy for reducing the feeding of electrical power in HCOO<sup>-</sup> generation.

### 3.4.2 Hybridization of Different Metals

With the electronic coupling and complementary geometry, bimetallic nanostructures are usually more outstanding than the monometallic counterpart in various catalytic reactions. In Shao's study,<sup>137</sup> Au-Pd core-shell microspheres comprised of an Au-Pd alloy core and an ultrathin Pd shell were fabricated *via* a one-pot preparation strategy and were further estimated in the electrocatalytic reduction of CO<sub>2</sub> to CO. A greatly enhanced CO selectivity can be achieved by using the resulting Au-Pd microspheres with a maximum Faradaic efficiency of 96.7% at  $-0.6$  V. Under an overpotential of 390 mV, the Au<sub>9.4</sub>Pd<sub>6</sub> nanocatalyst showed an ultrahigh mass activity of up to 99.8 A g<sub>Pd-Au</sub><sup>-1</sup> in CO generation from CO<sub>2</sub> reduction. In another one of their works, twisted Pd-Au wires were fabricated to exhibit a core-shell and GB-rich structure.<sup>138</sup> Compared to individual Pd particles, the core-shell wires had a greatly enhanced CO selectivity to result in a maximum CO Faradaic efficiency of 94.3% at  $-0.6$  V. At an extremely low overpotential of 90 mV, a Faradaic efficiency of 8.5% for CO production was measured on Pd<sub>0.8</sub>Au wires that also showed superb specific and mass activity. As revealed, surface CO could be more readily formed at a lower overpotential over metal wires as compared to that over metal spheres.

Similar to Au-based alloys, Ag-containing alloys have also been used for the electrocatalytic reduction of CO<sub>2</sub>. Typically, Jin and coworkers reported the preparation of self-supported Ag-Cu bimetallic catalysts with continuous nanoporous geometries and adjustable compositions through an electrochemical anodizing/dealloying process of Ag<sub>52</sub>Cu<sub>39</sub>Sn<sub>9</sub> alloy foil to exploit their performances in electrocatalytic CO<sub>2</sub> reduction.<sup>139</sup> By changing the

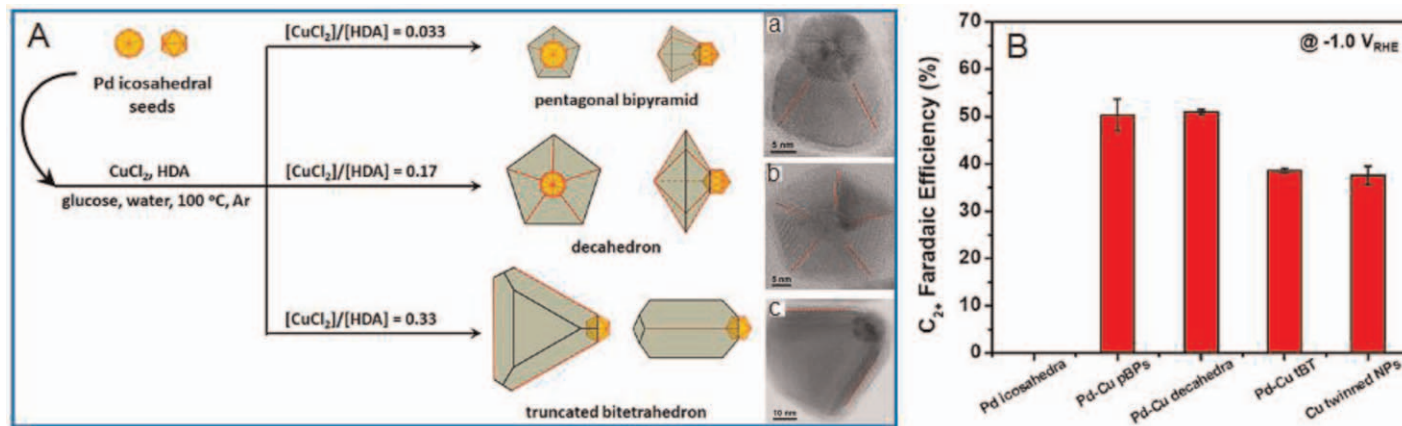


**Figure 3.14** (A,B) Transient current curves and SEM images of electrodeposited Bi films achieved by (A) direct-current 60 s and (B) pulse-current six cycles. (C) Electrochemical  $\text{CO}_2$  reduction measured by current density at different cyclic voltammetry (CV) scan rates. (D) Generation rate of  $\text{HCOO}^-$  and current density in  $\text{CO}_2$ -purged 0.1 M  $\text{KHCO}_3$  electrolyte. Reproduced from ref. 136 with permission from Elsevier, Copyright 2017.

compositions from Ag<sub>91</sub>Cu<sub>9</sub> to Ag<sub>65</sub>Cu<sub>35</sub>, the variations in atomic arrangement and electronic structure around the active sites bring a synergistic effect on the binding forces of different reaction intermediate products, realizing tunable product selectivity from CO to formate at high Faradaic efficiencies. Alternatively, a variety of core-shell Ag/(amorphous-Sn(IV)) (Ag/(A-Sn(IV))) particles were synthesized as highly active and selective nanocatalysts for electrochemical reduction.<sup>140</sup> The thin amorphous nanoshell not only effectively inhibited the generation of hydrogen to enhance the electrocatalytic ability but also realized the ready conversion of CO to HCOOH with the continual increment of applied voltages. As a result, the Ag<sub>75</sub>/(A-Sn(IV))<sub>25</sub> nanoparticles showed excellent performances with a CO Faradaic efficiency of 88.0% at a partial current density of 7.9 mA cm<sup>-2</sup> at -0.7 V and an HCOOH Faradaic efficiency of 75.1% at a partial current density of 13.4 mA cm<sup>-2</sup> at -0.9 V. As revealed by theoretical simulations, the manipulation on the shell thickness significantly suppressed the hydrogen evolution reaction and improved the electrochemical activities for CO<sub>2</sub> reduction.

As shown in Figure 3.15, Xia's group reported a facile preparation of Pd-Cu Janus nanostructures with controlled morphology, which was achieved in the direction of active sites *via* the glucose-driven reduction of Cu(II) precursor in the solution of hexadecylamine and icosahedral Pd seeds.<sup>141</sup> At a slow reducing speed, the Cu ions nucleated and grew from one vertex of the Pd seed to fabricate a pentatwinned Janus nanostructure like a pentagonal bipyramid or decahedron. In comparison, the Cu ions were directly reduced onto the edge of the Pd seed at a fast reduction speed to generate a singly twinned Janus nanostructure like a truncated bitetrahedron. The arrangement of Pd/Cu and the twin boundaries on the interfaces made these Janus nanostructures efficient electrocatalysts for the chemical conversion of CO<sub>2</sub>. At an onset potential of -1.0 V, the C<sub>2+</sub> products were obtained in 0.5 M KHCO<sub>3</sub> solution to exhibit a Faradaic efficiency approaching 51.0%. Similarly, novel mesoporous Pd-Cu bimetallic catalysts were reported to exhibit superb ability and high Faradaic efficiencies.<sup>142</sup> The mesoporous nanostructure provided a rough surface with plentiful active sites and promoted selectivity to producing CO, which suggested that surface Pd atoms served as active centers for highly selective CO generation benefiting from the geometric and electronic functions in the Pd-Cu alloys.

Besides Pd-Cu nanocatalysts, other metals have been reported in hybrids with Cu for developing electrocatalytic nanomaterials. For instance, an *in situ* growth of porous Zn-Cu alloys was achieved by simply annealing a brass foil at 500 °C in air, in which Zn first melted and then moved out of the alloy framework to synthesize a thin ZnO film on its surface and subsequently the further electrochemical reduction fabricated porous Zn-rich surface.<sup>143</sup> As indicated, the Zn content was increased from 36% to 50% within 10 min to 81% after 3 h and to 87% after 12 h of annealing process while the pore size decreased from 290 nm to 120 nm upon increasing the annealing time from 1 h to 12 h. Compared to untreated brass foils, the Faradaic efficiencies of CO<sub>2</sub> conversion to CO and HCOOH increased nearly 4 and 6 times, respectively.



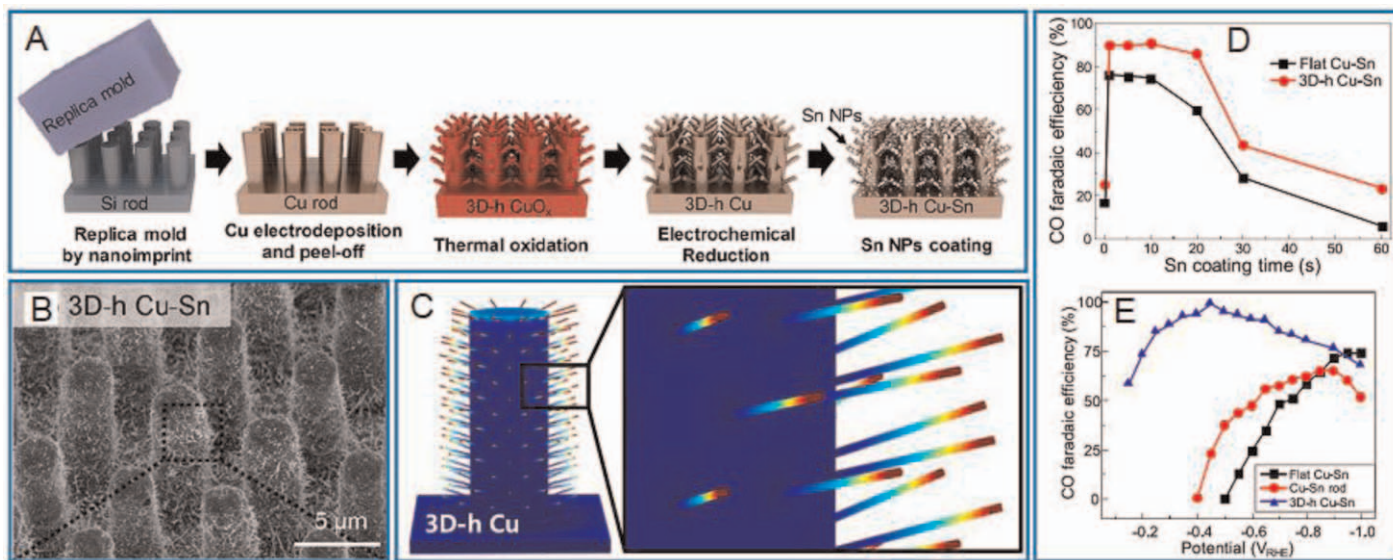
**Figure 3.15** (A) Different experimental conditions and processes for forming Pd – Cu Janus structures with three distinctive morphologies (a–c are the corresponding TEM images). (B) Faradaic efficiencies of C<sub>2+</sub> products at –1.0 V by using different crystals as the electrocatalysts. Reproduced from ref. 141 with permission from American Chemical Society, Copyright 2021.

Moreover, the porous Zn–Cu nanocatalyst produced a stable ratio of CO/H<sub>2</sub> and a steady working current density in a continuous electrocatalysis for 18 h. For understanding the compositional and geometrical functions of bimetallic nanocatalysts on high selectivity, Lee's group fabricated 3D hierarchical (3D-h) Cu nanostructures and coated them with Sn nanospheres for studying the factors on electrocatalytic activity (see Figure 3.16).<sup>144</sup> With increasing the coating time from 1 to 60 s, larger Sn nanoparticles were loaded on the 3D-h Cu in a higher surface density to significantly decrease the atomic ratio of Cu/Sn at surfaces. Under a low potential of  $-0.6$  V, the compositional change undesirably decreased Faradaic efficiency for CO from 90.0 to 23.4%. However, the 3D-h Cu–Sn exhibited the maximum Faradaic efficiency of CO of 98.6% at  $-0.45$  V, much higher than flat and rods. These results and comparison revealed that the composition and nanostructured geometry can be optimized for significantly improving the electrochemical conversion of CO<sub>2</sub>. Similarly, Cu–In nanoalloys were also reported to exhibit an excellent performance for selectively reducing CO<sub>2</sub> to CO in electrochemical catalysis.<sup>145</sup> In the experiment, the Cu–In alloys were prepared *via* the *in situ* reaction of CuInO<sub>2</sub> and In<sub>2</sub>O<sub>3</sub>-supported Cu particles, whose structure evolved substantially over electrochemical cycles to increase their catalytic activity and selectivity for CO formation. As reported, the content of In(OH)<sub>3</sub> in these heterostructures determined the performance of the hybrid electrocatalysts, which indicated that In(OH)<sub>3</sub> played a critical function in optimizing the formation of CO using Cu–In catalysts.

Recently, Lee's group reported the fabrication of monolithic porous In–Sn alloy nanostructures driven by the electrochemical reduction of indium tin oxide branches.<sup>146</sup> The electrochemical reaction created a local electric field at the tip of alloy materials, resulting in a current-induced joule-heating effect to achieve a porous In–Sn alloyed structure. The pore size of In–Sn alloys could be tuned from 1176 to 65 nm by controlling the electrochemical reduction conditions such as applied potential and the reaction time. At the optimized conditions, Faradaic efficiency for formate was increased from 42.4% to 78.6%, and current density at  $-1.2$  V was raised from  $-6.6$  to  $-9.6$  mA cm<sup>-2</sup> to result in the highest HCOO<sup>-</sup> generation yield of 75.9 μmol h<sup>-1</sup> cm<sup>-2</sup>.

### 3.4.3 Metal Oxides and Their Hybrids

To combine the catalytic oxidation of organic contaminants with the electrochemical reduction of CO<sub>2</sub>, Luo's group combined the electrochemical catalysis and SO<sub>4</sub><sup>•-</sup>-based oxidation technology for the rapid degradation of 4-nitrophenol on a hexagonal Co<sub>3</sub>O<sub>4</sub> anode.<sup>147</sup> In this process, 4-nitrophenol was oxidized into CO<sub>2</sub>, and then the produced CO<sub>2</sub> gas was catalytically reduced to CH<sub>3</sub>OH and C<sub>2</sub>H<sub>5</sub>OH by electrochemical reduction on a flowered CuO cathode. The production amounts of CH<sub>3</sub>OH and C<sub>2</sub>H<sub>5</sub>OH were measured as 98.29 mmol L<sup>-1</sup> and 40.95 mmol L<sup>-1</sup>, respectively, representing that 41.8% of 4-nitrophenol was successfully converted into liquid fuels. In another work, an *in situ* gas-involved synthetic method was demonstrated to



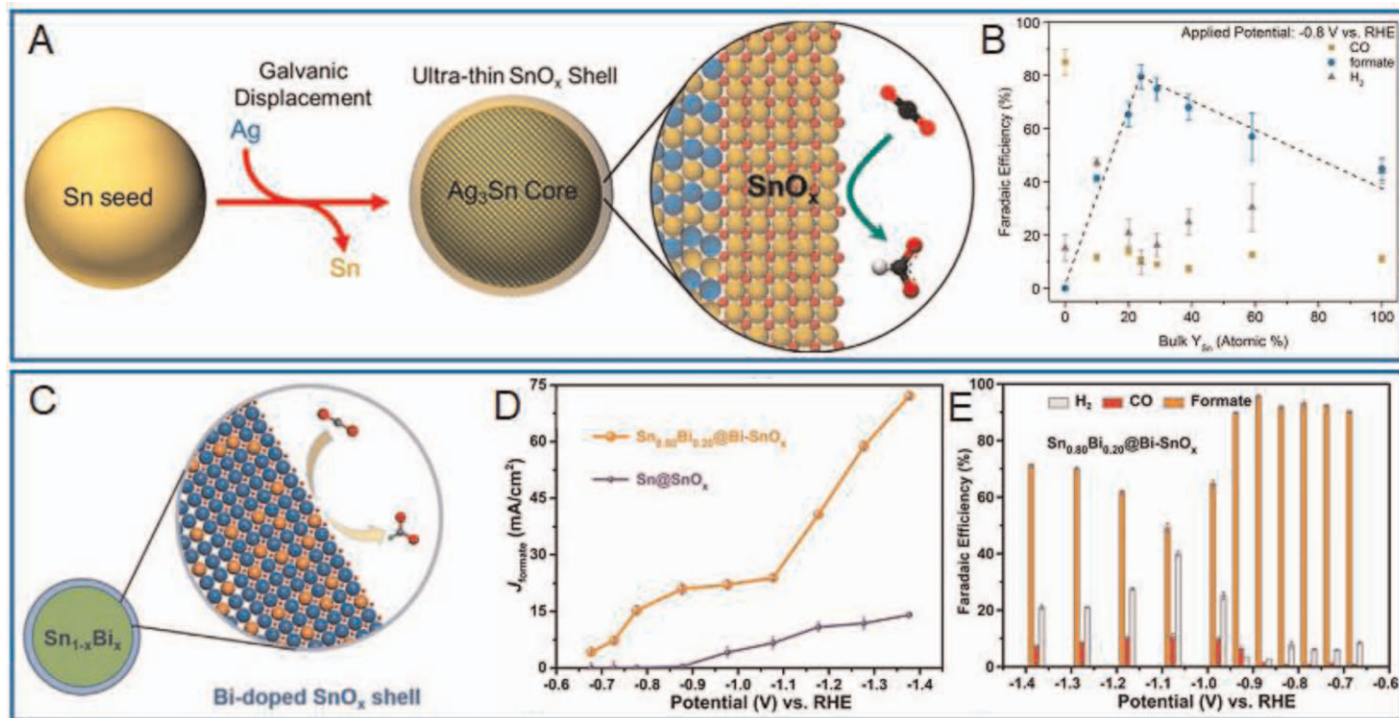
**Figure 3.16** (A) Schematic for fabricating 3D hierarchical (3D-h) Cu–Sn nanocatalysts: template-assisted pattern transfer of the Cu rod, thermal oxidation, electroreduction to 3D-h Cu, and chemical deposition of Sn spheres. (B) SEM image of 3D-h Cu–Sn nanocatalysts. (C) Calculated electric field distribution of 3D-h Cu. (D) Measured CO Faradaic efficiency of different samples with  $t_c$  change from 0 to 60 s. (E) Electrocatalytic reduction of CO<sub>2</sub> via measuring CO Faradaic efficiency in CO<sub>2</sub>-purged 0.1 M KHCO<sub>3</sub> at a scan rate of 50 mV s<sup>-1</sup>. Reproduced from ref. 144 with permission from American Chemical Society, Copyright 2020.

form Mn-incorporated SnO<sub>2</sub> nanosheets for the highly efficient reduction of CO<sub>2</sub> in the electrochemical reaction.<sup>148</sup> Relative to the commercial SnO<sub>2</sub> sample, Mn-SnO<sub>2</sub> exhibited various improved performances in the electrochemical production of formic acid, such as a higher current density of ~21.2 mA cm<sup>-2</sup>, higher Faradaic efficiency of ~85% at a lower overpotential of 240 mV, and total Faradaic efficiency of ~91.6%. As revealed, the ultrathin nanosheets not only featured a narrower bandgap for electron excitation but also exposed more surface reactive sites for catalytic conversion. Moreover, the introduction of Mn modulated the electronic structure of SnO<sub>2</sub> and generated numerous oxygen vacancies, which significantly reduced the energy barrier of electron transfer during the CO<sub>2</sub> reduction.

With a lower activation energy barrier, first-row transition metals are a promising alternative to develop electrochemical nanocatalysts for the easy conversion of CO<sub>2</sub>. Because these types of metals have a high affinity with oxygen so as to be easily oxidized to greatly compromise their catalytic performances, a strategy was proposed to fabricate Ag-Sn catalysts that contained a bimetallic core with high electronic conductivity and a partially oxidized shell for electrocatalytic CO<sub>2</sub> degradation (see Figure 3.17A).<sup>149</sup> When the SnO<sub>x</sub> shell was controlled at ~1.7 nm, the core-shell nanocatalyst demonstrated a formate Faradaic efficiency up to ~80% and a partial current density of ~16 mA cm<sup>-2</sup> at -0.8 V. In Quan's work,<sup>150</sup> homogeneous Sn<sub>1-x</sub>Bi<sub>x</sub> particles were synthesized and coated with Bi-incorporated SnO<sub>x</sub> nanoshells for the highly efficient electrochemical reduction of CO<sub>2</sub> (see Figure 3.17B). The Bi-SnO<sub>x</sub> shells boosted the production of formate with high Faradaic efficiencies of >90% over a broad potential range (-0.67 to -0.92 V). In particular, the Bi-SnO<sub>x</sub> shells obtained from Sn<sub>0.80</sub>Bi<sub>0.20</sub> alloys exhibited a higher partial current density of 74.6 mA cm<sup>-2</sup> and Faradaic efficiency of 95.8%, indicating that the doping of Bi atom into Sn nanocrystal facilitated formate production by inhibiting the generation of H<sub>2</sub> and CO. For evaluating the electrocatalytic performance of oxide-containing metal structures for CO<sub>2</sub> conversion at a low overpotential, Xie's group synthesized pure cobalt and the coexisting areas of cobalt/cobalt oxide to reveal the function of varied catalytic sites.<sup>151</sup> As confirmed, cobalt as an atomically thin layer majorly produced formate in the electrochemical reduction of CO<sub>2</sub>, suggesting that the surface cobalt atoms on the ultrathin layer had higher intrinsic activity and selectivity for formate generation than cobalt atoms in the bulky system at lower overpotentials. Partially oxidized cobalt layers further increased the catalytic activity to achieve a stable current density of 10 mA cm<sup>-2</sup> for 40 h, with ~90% selectivity for producing formate at an overpotential of only 0.24 V. It can be seen that the morphological optimization and controlled oxidized state can deliver a noncatalytic system into an active catalyst.

Based on the finding that GBs have more highly reactive sites and can optimize the selectivity toward special products through the enhanced stabilization of intermediate products, a hybrid of Bi spheres/Bi<sub>2</sub>O<sub>3</sub> sheets with plentiful GBs was fabricated *via* a hydrothermal reduction method.<sup>152</sup> The as-synthesized hybrid exhibited a large partial current density (24.4 mA cm<sup>-2</sup>), high selectivity





**Figure 3.17** (A) Preparation of partially oxidized tin oxide shells for CO<sub>2</sub> electrocatalytic reduction. (B) Faradaic efficiencies of the CO<sub>2</sub> electroreduction of AgSn/SnO<sub>x</sub> nanocatalysts. Reproduced from ref. 149 with permission from American Chemical Society, Copyright 2017. (C) The structural features of Bi-loaded SnO<sub>x</sub> electrocatalyst for CO<sub>2</sub> reduction. (D) Partial current densities of Sn@SnO<sub>x</sub> and Sn<sub>0.80</sub>Bi<sub>0.20</sub>@Bi-SnO<sub>x</sub> nanocatalysts. (E) Faradaic efficiencies of Sn<sub>0.80</sub>Bi<sub>0.20</sub>@Bi-SnO<sub>x</sub> nanocatalysts for producing H<sub>2</sub>, CO, and formate. Reproduced from ref. 150 with permission from John Wiley & Sons, Copyright © 2020 WILEY-VCH Verlag GmbH & Co. KGaA, Weinheim.

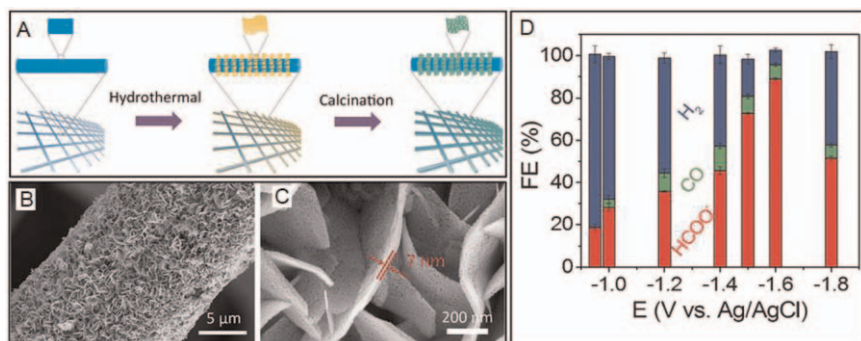
(~100%), and good durability (>24 h) for electrocatalytically reducing CO<sub>2</sub> to formate. It was confirmed that the microstructures of Bi resulting from chemical reduction relative to electrochemical reduction played a main role in enhancing their electrocatalytic activity in CO<sub>2</sub> reduction. Similarly, Qiu *et al.* studied a morphology-dependent electrocatalytic reduction of CO<sub>2</sub> into formate over Bi<sub>2</sub>O<sub>3</sub> electrode in 0.5 M KHCO<sub>3</sub> electrolyte.<sup>153</sup> Compared to Bi nanoparticles synthesized using Bi<sub>2</sub>O<sub>3</sub> rods (Bi<sub>2</sub>O<sub>3</sub>-R) electrode, the nanoflowered Bi *in situ* synthesized through the reduction of etched Bi<sub>2</sub>O<sub>3</sub> rods (Bi<sub>2</sub>O<sub>3</sub>-E) demonstrated a greatly enhanced catalytic ability for the electrochemical reduction of CO<sub>2</sub> to formate. A low overpotential of 530 mV was measured on the Bi<sub>2</sub>O<sub>3</sub>-E electrode for producing formate, and the maximum Faradaic efficiency of 99.2% was realized at -1.5 V when operating at a current density of 7.5 mA cm<sup>-2</sup>, which was much better than that of Bi<sub>2</sub>O<sub>3</sub>-R (~67.9%). The reaction durability on the Bi<sub>2</sub>O<sub>3</sub>-E electrode was at least 20 h under continuous electrocatalysis, while there is a negligible change in Faradaic efficiency and current density. The excellent properties indicate that the reactive surface area and catalytic ability mainly resulted from the flowered nanostructure with plentiful edge sites. In Hu's work,<sup>154</sup> Bi sheets were uniformly synthesized on flow-through Cu hollow fiber gas diffusion electrodes (HFGDEs) for utilizing the unique morphology and plentiful reactive surface area. Pulse electrodeposition was employed to fill Bi<sup>3+</sup> ions into the adjacency of HFGDEs for uniformly synthesizing Bi sheets. Then, the thermal oxidation process significantly increased the reactive sites, improved surface wettability, and enhanced formate generation due to the formation of Bi/Bi<sub>2</sub>O<sub>3</sub> heterojunctions.

### 3.4.4 Other Interesting Electrocatalytic Systems

In the electrocatalytic reduction of CO<sub>2</sub> to other chemicals, a main challenge is the ready activation of CO<sub>2</sub> into CO<sub>2</sub><sup>•-</sup> or other intermediate products, which was critically dependent on the used catalysts and/or electrolyte additives. For instance, Yu's group synthesized a CdS-nanostructured material by using a microwave heating method for efficiently catalyzing CO<sub>2</sub> conversion into CO in electrochemical reduction.<sup>155</sup> The CdS needle arrays exhibited an extraordinary current density of 212 mA cm<sup>-2</sup> with 95.5% CO Faraday efficiency at -1.2 V. The high-curvature CdS nanocatalyst had an enhanced proximity effect to give rise to a strong electric field, which can enrich alkali metal cations to increase CO<sub>2</sub> reduction efficiency. In Fontecave's work,<sup>156</sup> a CNT-gold nanohybrid was employed as an efficient electrochemical catalyst for the conversion of CO<sub>2</sub> in 0.5 M NaHCO<sub>3</sub> solution. The hybridized nanomaterial exhibited outstanding catalytic activity with a current density of 10 mA cm<sup>-2</sup> at -0.55 V, which produced a stable CO yield rate of 0.52 mmol s<sup>-1</sup> after 4 h electrochemical catalysis. In this work, monodispersed Au spheres loaded on CNTs in a layer-by-layer manner allowed very little Au content to minimize the cost of electrode preparation. Its mass activity was up to 100 Ag<sup>-1</sup> at -0.55 V, 33 times higher than that of pure Au particles. Alternatively, mesoporous carbon nanoframes were prepared by using Fe-doped MOF as precursors to have a hierarchical

distribution of pore size and atomically dispersed Fe-N<sub>x</sub> reactive sites.<sup>157</sup> The existence of numerous mesopores in the carbon frames enhanced the accessibility of single-atom reactive sites and boosted mass and charge transportation. Such a unique structure resulted in outstanding catalytic properties for reducing oxygen at a more positive onset potential (1.01 V vs. 0.97 V) and half-wave potential (0.89 V vs. 0.82 V) relative to the commercial Pt/C.

To exploit Sn and its hybrids as selective catalysts for CO<sub>2</sub> reduction, Zheng's group synthesized ~5 nm SnO<sub>2</sub> particle-modified hollow carbon (SnO<sub>2</sub>/C) microspheres for electrocatalytically reducing CO<sub>2</sub> in an efficient manner.<sup>158</sup> Relative to the plain SnO<sub>x</sub> materials, aggregated SnO<sub>x</sub> particles, and hollow carbon microspheres, SnO<sub>2</sub>/C catalysts resulted in higher Faradaic efficiency and improved electrocatalytic stability, which were ascribed to the Sn-O-C bonds between SnO<sub>2</sub> and the carbon microspheres, and increased CO<sub>2</sub> chemisorption, electron transferring speed, and number of reactive sites. For further improving energy efficiency, selectivity, and stability, mesoporous SnO<sub>2</sub> sheets were loaded on carbon cloth to fabricate 3D hierarchical nanostructure (see Figure 3.18).<sup>159</sup> The resultant electrode exhibited an extraordinary current density of ~45 mA cm<sup>-2</sup> at a small overpotential (0.88 V) with high Faradaic efficiency (87 ± 2%) for the electrochemical reduction of CO<sub>2</sub> into formate. Similarly, 3D Bi<sub>2</sub>O<sub>3</sub> fractal structures (f-Bi<sub>2</sub>O<sub>3</sub>) were successfully loaded onto carbon fiber papers (CFPs) *via* a scalable hot-aerosol preparation approach.<sup>160</sup> The resulting f-Bi<sub>2</sub>O<sub>3</sub> electrode demonstrated superb reduction capability in the electrocatalytic conversion of CO<sub>2</sub> to formate (HCOO<sup>-</sup>) at low onset overpotential and a high Faradaic efficiency of 87% at the applied potential of -1.2 V. Moreover, a high mass-specific partial current density for formate was measured at



**Figure 3.18** (A) The process for synthesizing porous SnO<sub>2</sub> sheets on carbon cloth (CC) by hydrothermal method and subsequent calcination in air atmosphere. (B,C) SEM images of porous SnO<sub>2</sub> sheets on carbon cloth. (D) Faradaic efficiency of the SnO<sub>2</sub>/CC catalyst in CO<sub>2</sub>-saturated 0.5 M NaHCO<sub>3</sub> solution for producing formate, CO, and H<sub>2</sub> at various applied potentials. Reproduced from ref. 159 with permission from John Wiley & Sons, Copyright © 2017 Wiley-VCH Verlag GmbH & Co. KGaA, Weinheim.

–52.2 mA mg<sup>-1</sup>, which was about three times higher than that of the drop-fabricated Bi<sub>2</sub>O<sub>3</sub> electrocatalyst.

### 3.5 Summary and Outlook

The excess emission of CO<sub>2</sub> into the atmosphere leads to global warming and the energy crisis due to the greenhouse effect, which has become one of the biggest environmental challenges. Therefore, to effectively reduce atmospheric CO<sub>2</sub> has been attracting more and more research interests for maintaining human sustainability and Earth's life cycle. Among them, the capture technique can immediately remove CO<sub>2</sub> after its emission *via* physical adsorption, selective separation, or chemical fixation on substrates, while the catalytic conversion technique can ideally recycle CO<sub>2</sub> into some usable fuels by using catalysts. It can be seen that for each strategy, the development of materials is essential for achieving good performance in removing CO<sub>2</sub> gas. Compared to bulk counterparts, the nanostructured systems possess a larger surface area for adsorbing CO<sub>2</sub> and more active sites for their catalytic conversation, so nanomaterials are very promising to be utilized in the capture, storage, and conversion of CO<sub>2</sub>. With the wide exploitation of varied nanotechnologies and advanced characterized means, diversified nanostructured materials with a greatly improved performance have been facilely synthesized *via* structural design, surface modification, and nanohybridization. In this chapter, the important advances and related breakthroughs are representatively overviewed to demonstrate the outstanding functions of nanostructured materials and their promising applications in CO<sub>2</sub> cycling, including the capture of CO<sub>2</sub> by nanostructured materials, photocatalytic CO<sub>2</sub> reduction over nanostructures, and electrochemical reduction of CO<sub>2</sub> with nanostructured materials.

A variety of nanomaterials have been investigated to exhibit unprecedented advantages for reducing CO<sub>2</sub> content in the air atmosphere. Nevertheless, the development of efficient and stable nanostructures for long-time operation remains a great challenge. In the catalytic conversion of CO<sub>2</sub>, capture/activation of CO<sub>2</sub> on the catalyst surface are critical aspects, which should be studied more deeply to essentially improve their performances from all-around features. Furthermore, the types of intermediate and final products are mainly determined by different reactive factors but the estimated condition is not fully identical, so it is difficult to clearly clarify the catalytic mechanisms. In addition, typical computational works are still lacking, which hinders the rational development of catalytic CO<sub>2</sub> conversion, such as the simulation of energy states and prediction of occurring reaction steps. Therefore, it requires the normalization of experimental conditions and the introduction of computational models to study the catalytic reduction of CO<sub>2</sub>. In the future, with more efforts being contributed to the exploitation of nanomaterials, there will be more perfect nanostructured systems to be produced for the treatment of excess CO<sub>2</sub>, with improved physical/chemical stability, environmental compatibility, efficiency, energy-saving properties, and recycling performance.

## References

1. J. K. Stolarczyk, S. Bhattacharyya, L. Polavarapu and J. Feldmann, *ACS Catal.*, 2018, **8**, 3602.
2. R. K. Pachauri, M. R. Allen, V. R. Barros, J. Broome, W. Cramer, R. Christ, J. A. Church, L. Clarke, Q. Dahe, P. Dasgupta and N. K. Dubash. in *Climate Change 2014: Synthesis Report. Contribution of Working Groups I, II and III to the Fifth Assessment Report of the Intergovernmental Panel on Climate Change*, IPCC, 2014, p. 151.
3. H. M. Al-Maamary, H. A. Kazem and M. T. Chaichan, *Renewable Sustainable Energy Rev.*, 2017, **76**, 555.
4. E. Dlugokencky and P. Tans, NOAA/ESRL, <http://www.esrl.noaa.gov/gmd/ccgg/trends/>, (accessed: April 2021).
5. T. Ouyang, S. Huang, X. Wang and Z. Liu, *Chem. – Eur. J.*, 2020, **26**, 14024.
6. N. N. Vu, S. Kaliaguine and T. O. Do, *Adv. Funct. Mater.*, 2019, **29**, 1901825.
7. H. Liu, Y. Zhu, J. Ma, Z. Zhang and W. Hu, *Adv. Funct. Mater.*, 2020, **30**, 1910534.
8. T. F. Hurst, T. T. Cockerill and N. H. Florin, *Energy Environ. Sci.*, 2012, **5**, 7132.
9. S. Shit, I. Shown, R. Paul, K. H. Chen, J. Mondal and L. C. Chen, *Nanoscale*, 2020, **12**, 23301.
10. J. Wu, Y. Huang, W. Ye and Y. Li, *Adv. Sci.*, 2017, **4**, 1700194.
11. C. Liu, B. C. Colón, M. Ziesack, P. A. Silver and D. G. Nocera, *Science*, 2016, **352**, 1210.
12. Q. Lu, J. Rosen and F. Jiao, *ChemCatChem*, 2015, **7**, 38.
13. V. Castagnola, J. Cookman, J. M. de Araújo, E. Polo, Q. Cai, C. P. Silveira, Y. Krpetić, L. Yan, Boselli and K. A. Dawson, *Nanoscale Horiz.*, 2017, **2**, 187.
14. A. A. Olajire, *J. CO2 Util.*, 2018, **24**, 522.
15. M. N. Anwar, A. Fayyaz, N. F. Sohail, M. F. Khokhar, M. Baqar, W. D. Khan, K. Rasool, M. Rehan and A. S. Nizami, *J. Environ. Manage.*, 2018, **226**, 131.
16. A. Alonso, J. Moral-Vico, A. A. Markeb, M. Busquets-Fité, D. Komilis, V. Puentes, A. Sánchez and X. Font, *Sci. Total Environ.*, 2017, **595**, 51.
17. Q. Shao, P. Wang, S. Liu and X. Huang, *J. Mater. Chem. A*, 2019, **7**, 20478.
18. J. Yang, Y. Guo, W. Lu, R. Jiang and J. Wang, *Adv. Mater.*, 2018, **30**, 1802227.
19. Z. L. Wang, C. Li and Y. Yamauchi, *Nano Today*, 2016, **11**, 373.
20. S. Wang, Y. Wang, S. Q. Zang and X. W. Lou, *Small Methods*, 2020, **4**, 1900586.
21. C. Hiragond, S. Ali, S. Sorcar and S. I. In, *Catalysts*, 2019, **9**, 370.
22. D. Gao, H. Zhou, F. Cai, J. Wang, G. Wang and X. Bao, *ACS Catal.*, 2018, **8**, 1510.

23. A. E. Creamer and B. Gao, *Environ. Sci. Technol.*, 2016, **50**, 7276.
24. K. Rahimi, S. Riahi, M. Abbasi and Z. Fakhroueian, *J. Environ. Manage.*, 2019, **242**, 81.
25. M. Nabipour, P. Keshavarz and S. Raeissi, *Int. J. Refrig.*, 2017, **73**, 1.
26. E. S. Muckley, T. Aytug, R. Mayes, A. R. Lupini, J. Y. Carrillo, M. Goswami, B. G. Sumpter and I. N. Ivanov, *ACS Appl. Mater. Interfaces*, 2019, **11**, 48466.
27. J. Wang, L. Huang, Q. Zheng, Y. Qiao and Q. Wang, *J. Ind. Eng. Chem.*, 2016, **36**, 255.
28. V. K. Yadav, S. H. Mir and J. K. Singh, *Appl. Surf. Sci.*, 2020, **527**, 146445.
29. C. Goel, H. Bhunia and P. K. Bajpai, *J. Environ. Sci.*, 2015, **32**, 238.
30. A. F. M. El-Mahdy, T. E. Liu and S. W. Kuo, *J. Hazard. Mater.*, 2020, **391**, 122163.
31. T. Shi, Y. Zheng, T. Wang, P. Li, Y. Wang and D. Yao, *ChemPhysChem*, 2018, **19**, 130.
32. G. Sargazi, D. Afzali, A. Mostafavi and S. Y. Ebrahimipour, *J. Solid State Chem.*, 2017, **250**, 32.
33. Q. Li, J. Guo, H. Zhu and F. Yan, *Small*, 2019, **15**, 1804874.
34. Q. Fu, J. Kim, P. A. Gurr, J. M. P. Scofield, S. E. Kentish and G. G. Qiao, *Energy Environ. Sci.*, 2016, **9**, 434.
35. J. Kim, Q. Fu, J. M. Scofield, S. E. Kentish and G. G. Qiao, *Nanoscale*, 2016, **8**, 8312.
36. H. Sehaqui, M. E. Galvez, V. Becatinni, Y. Ng, A. Steinfeld, T. Zimmermann and P. Tingaut, *Environ. Sci. Technol.*, 2015, **49**, 3167.
37. J. Y. Lim, J. K. Kim, C. S. Lee, J. M. Lee and J. H. Kim, *Chem. Eng. J.*, 2017, **322**, 254.
38. A. Naderi, A. A. Tashvigh and T. S. Chung, *J. Membr. Sci.*, 2019, **572**, 343.
39. Z. Dai, L. Ansaloni, J. J. Ryan, R. J. Spontak and L. Deng, *Green Chem.*, 2018, **20**, 1391.
40. L. Zhu, M. T. Swihart and H. Lin, *J. Mater. Chem. A*, 2017, **5**, 19914.
41. M. Benitez-Guerrero, J. M. Valverde, P. E. Sanchez-Jimenez, A. Perejon and L. A. Perez-Maqueda, *Chem. Eng. J.*, 2018, **334**, 2343.
42. F. Yan, J. Jiang, K. Li, N. Liu, X. Chen, Y. Gao and S. Tian, *Environ. Sci. Technol.*, 2017, **51**, 7606.
43. T. Zhao, B. Guo, F. Zhang, F. Sha, Q. Li and J. Zhang, *ACS Appl. Mater. Interfaces*, 2015, **7**, 15918.
44. A. H. Chowdhury, P. Bhanja, N. Salam, A. Bhaumik and S. M. Islam, *Mol. Catal.*, 2018, **450**, 46.
45. D. Prasad, K. N. Patil, R. B. Dateer, H. Kim, B. M. Nagaraja and A. H. Jadhav, *Chem. Eng. J.*, 2021, **405**, 126907.
46. Z. Li, J. Chu, D. Meng, Y. Wen, X. Xing, H. Miao, M. Hu, C. Yu, Z. Wei, Y. Yang and Y. Li, *ACS Catal.*, 2019, **9**, 8659.
47. A. J. Bard and M. A. Fox, *Acc. Chem. Res.*, 1995, **28**, 141.
48. M. Aresta and A. Dibenedetto, *Dalton Trans.*, 2007, 2975.
49. M. Halmann, *Nature*, 1978, **275**, 115.
50. A. Pichon, Energy Materials: A Stretch to Save the World 2010, <http://www.natureasia.com/en/nchina/article/10.1038/nchina.2010.126>.

51. W. Tu, Y. Zhou and Z. Zou, *Adv. Mater.*, 2014, **26**, 4607.
52. S. Xie, Q. Zhang, G. Liu and Y. Wang, *Chem. Commun.*, 2016, **52**, 35.
53. H. Song, X. Meng, T. D. Dao, W. Zhou, H. Liu, L. Shi, H. Zhang, T. Nagao, T. Kako and J. Ye, *ACS Appl. Mater. Interfaces*, 2018, **10**, 408.
54. X. Cai, F. Wang, R. Wang, Y. Xi, A. Wang, J. Wang, B. Teng and S. Bai, *J. Mater. Chem. A*, 2020, **8**, 7350.
55. C. Huang, R. Guo, W. Pan, J. Tang, W. Zhou, X. Liu, H. Qin and P. Jia, *Appl. Surf. Sci.*, 2019, **464**, 534.
56. M. Cheng, S. Yang, R. Chen, X. Zhu, Q. Liao and Y. Huang, *Int. J. Hydrogen Energy*, 2017, **42**, 9722.
57. A. Wang, S. Wu, J. Dong, R. Wang, J. Wang, J. Zhang, S. Zhong and S. Bai, *Chem. Eng. J.*, 2021, **404**, 127145.
58. A. Pougine, G. Dodekatos, M. Dilla, H. Tuysuz and J. Strunk, *Chem. – Eur. J.*, 2018, **24**, 12416.
59. C. Xu, W. Huang, Z. Li, B. Deng, Y. Zhang, M. Ni and K. Cen, *ACS Catal.*, 2018, **8**, 6582.
60. B. Fang, Y. Xing, A. Bonakdarpour, S. Zhang and D. P. Wilkinson, *ACS Sustainable Chem. Eng.*, 2015, **3**, 2381.
61. M. Cheng, S. Yang, R. Chen, X. Zhu, Q. Liao and Y. Huang, *Mol. Catal.*, 2018, **448**, 185.
62. F. Xu, B. Zhu, B. Cheng, J. Yu and J. Xu, *Adv. Opt. Mater.*, 2018, **6**, 1800911.
63. M. Zubair, H. Kim, A. Razzaq, C. A. Grimes and S. I. In, *J. CO<sub>2</sub> Util.*, 2018, **26**, 70.
64. M. Tahir, B. Tahir and N. S. Amin, *Mater. Res. Bull.*, 2015, **63**, 13.
65. M. Iqbal, Y. Wang, H. Hu, M. He, A. H. Shah, L. Lin, P. Li, K. Shao, A. Reda Woldu and T. He, *Appl. Surf. Sci.*, 2018, **443**, 209.
66. H. Huo, D. Liu, H. Feng, Z. Tian, X. Liu and A. Li, *Nanoscale*, 2020, **12**, 13912.
67. H. Wang, H. Rong, D. Wang, X. Li, E. Zhang, X. Wan, B. Bai, M. Xu, J. Liu, J. Liu, W. Chen and J. Zhang, *Small*, 2020, **16**, 2000426.
68. H. Robotjazi, H. Zhao, D. F. Swearer, N. J. Hogan, L. Zhou, A. Alabastri, M. J. McClain, P. Nordlander and N. J. Halas, *Nat. Commun.*, 2017, **8**, 27.
69. J. Jia, P. G. O'Brien, L. He, Q. Qiao, T. Fei, L. M. Reyes, T. E. Burrow, Y. Dong, K. Liao, M. Varela, S. J. Pennycook, M. Hmadeh, A. S. Helmy, N. P. Kherani, D. D. Perovic and G. A. Ozin, *Adv. Sci.*, 2016, **3**, 1600189.
70. F. You, J. Wan, J. Qi, D. Mao, N. Yang, Q. Zhang, L. Gu and D. Wang, *Angew. Chem., Int. Ed.*, 2020, **59**, 721.
71. P. K. Prajapati, H. Singh, R. Yadav, A. K. Sinha, S. Szunerits, R. Boukherroub and S. L. Jain, *Appl. Surf. Sci.*, 2019, **467–468**, 370.
72. S. Yan, Y. Yu and Y. Cao, *Appl. Surf. Sci.*, 2019, **465**, 383.
73. M. Wang, Q. Han, L. Li, L. Tang, H. Li, Y. Zhou and Z. Zou, *Nanotechnology*, 2017, **28**, 274002.
74. J. Bian, J. Feng, Z. Zhang, Z. Li, Y. Zhang, Y. Liu, S. Ali, Y. Qu, L. Bai, J. Xie, D. Tang, X. Li, F. Bai, J. Tang and L. Jing, *Angew. Chem., Int. Ed.*, 2019, **58**, 10873.

75. Y. Cao, L. Guo, M. Dan, D. E. Doronkin, C. Han, Z. Rao, Y. Liu, J. Meng, Z. Huang, K. Zheng, P. Chen, F. Dong and Y. Zhou, *Nat. Commun.*, 2021, **12**, 1675.
76. A. P. Rangappa, D. Praveen Kumar, Y. Hong, S. Jeong, D. A. Reddy, J. K. Song and T. K. Kim, *ACS Appl. Energy Mater.*, 2020, **3**, 10533.
77. B. Khan, F. Raziq, M. B. Faheem, M. U. Farooq, S. Hussain, F. Ali, A. Ullah, A. Mavlonov, Y. Zhao, Z. Liu, H. Tian, H. Shen, X. Zu, S. Li, H. Xiao, X. Xiang and L. Qiao, *J. Hazard. Mater.*, 2020, **381**, 120972.
78. J. S. DuChene, G. Tagliabue, A. J. Welch, W. H. Cheng and H. A. Atwater, *Nano Lett.*, 2018, **18**, 2545.
79. J. F. Liao, Y. T. Cai, J. Y. Li, Y. Jiang, X. D. Wang, H. Y. Chen and D. B. Kuang, *J. Energy Chem.*, 2021, **53**, 309.
80. W. J. Ong, L. K. Putri and A. R. Mohamed, *Chem. – Eur. J.*, 2020, **26**, 9710.
81. X. Lin, S. Wang, W. Tu, H. Wang, Y. Hou, W. Dai and R. Xu, *ACS Appl. Energy Mater.*, 2019, **2**, 7670.
82. S. Liu, T. Jiang, M. Fan, G. Tan, S. Cui and X. Shen, *J. Alloys Compd.*, 2021, **861**, 158598.
83. Y. Rambabu, U. Kumar, N. Singhal, M. Kaushal, M. Jaiswal, S. L. Jain and S. C. Roy, *Appl. Surf. Sci.*, 2019, **485**, 48.
84. L. Kuai, Y. Zhou, W. Tu, P. Li, H. Li, Q. Xu, L. Tang, X. Wang, M. Xiao and Z. Zou, *RSC Adv.*, 2015, **5**, 88409.
85. M. Biswas, A. Ali, K. Y. Cho and W. C. Oh, *Ultrason. Sonochem.*, 2018, **42**, 738.
86. X. Zhang, P. Yang and S. P. Jiang, *Nanotechnology*, 2021, **32**, 175401.
87. Z. Mo, X. Zhu, Z. Jiang, Y. Song, D. Liu, H. Li, X. Yang, Y. She, Y. Lei, S. Yuan, H. Li, L. Song, Q. Yan and H. Xu, *Appl. Catal., B*, 2019, **256**, 117854.
88. J. Fu, B. Zhu, C. Jiang, B. Cheng, W. You and J. Yu, *Small*, 2017, **13**, 1603938.
89. J. Qin, S. Wang, H. Ren, Y. Hou and X. Wang, *Appl. Catal., B*, 2015, **179**, 1.
90. W. J. Ong, L. L. Tan, S. P. Chai and S. T. Yong, *Dalton Trans.*, 2015, **44**, 1249.
91. Q. Wang, L. Zhang, Y. Guo, M. Shen, M. Wang, B. Li and J. Shi, *Chem. Eng. J.*, 2020, **396**, 125347.
92. M. Liang, T. Borjigin, Y. Zhang, B. Liu, H. Liu and H. Guo, *Appl. Catal., B*, 2019, **243**, 566.
93. R. Guo, X. Liu, H. Qin, Z. Wang, X. Shi, W. Pan, Z. Fu, J. Tang, P. Jia, Y. Miao and J. Gu, *Appl. Surf. Sci.*, 2020, **500**, 144059.
94. S. Liu, F. Chen, S. Li, X. Peng and Y. Xiong, *Appl. Catal., B*, 2017, **211**, 1.
95. W. J. Ong, L. L. Tan, S. P. Chai and S. T. Yong, *Chem. Commun.*, 2015, **51**, 858.
96. W. J. Ong, L. L. Tan, S. P. Chai, S. T. Yong and A. R. Mohamed, *Nano Energy*, 2015, **13**, 757.
97. Y. Huo, J. Zhang, Z. Wang, K. Dai, C. Pan and C. Liang, *J. Colloid Interface Sci.*, 2021, **585**, 684.



98. X. Zhao, J. Guan, J. Li, X. Li, H. Wang, P. Huo and Y. Yan, *Appl. Surf. Sci.*, 2021, **537**, 147891.
99. A. Bafaqeer, M. Tahir, A. A. Khan and N. A. S. Amin, *Ind. Eng. Chem. Res.*, 2019, **58**, 8612.
100. A. Kumar, A. Kumar, G. Sharma, A. A. H. Al-Muhtaseb, M. Naushad, A. A. Ghfar, C. Guo and F. J. Stadler, *Chem. Eng. J.*, 2018, **339**, 393.
101. M. Zhou, S. Wang, P. Yang, C. Huang and X. Wang, *ACS Catal.*, 2018, **8**, 4928.
102. W. Weng, S. Wang, W. Xiao and X. W. D. Lou, *Adv. Mater.*, 2020, **32**, 2001560.
103. L. Y. Wu, Y. F. Mu, X. X. Guo, W. Zhang, Z. M. Zhang, M. Zhang and T. B. Lu, *Angew. Chem., Int. Ed.*, 2019, **58**, 9491.
104. M. Y. Masoomi, A. Morsali, A. Dhakshinamoorthy and H. Garcia, *Angew. Chem., Int. Ed.*, 2019, **58**, 15188.
105. C. V. Reddy, K. R. Reddy, V. V. N. Harish, J. Shim, M. V. Shankar, N. P. Shetti and T. M. Aminabhavi, *Int. J. Hydrogen Energy*, 2020, **45**, 7656.
106. Y. Wang, W. Zhen, Y. Zeng, S. Wan, H. Guo, S. Zhang and Q. Zhong, *J. Mater. Chem. A*, 2020, **8**, 6034.
107. S. Zhang, L. Li, S. Zhao, Z. Sun, M. Hong and J. Luo, *J. Mater. Chem. A*, 2015, **3**, 15764.
108. Y. Liu, L. Deng, J. Sheng, F. Tang, K. Zeng, L. Wang, K. Liang, H. Hu and Y. N. Liu, *Appl. Surf. Sci.*, 2019, **498**, 143899.
109. S. Yan, S. Ouyang, H. Xu, M. Zhao, X. Zhang and J. Ye, *J. Mater. Chem. A*, 2016, **4**, 15126.
110. X. He and W. N. Wang, *J. Mater. Chem. A*, 2018, **6**, 932.
111. S. Wan, M. Ou, Q. Zhong and X. Wang, *Chem. Eng. J.*, 2019, **358**, 1287.
112. K. M. Choi, D. Kim, B. Rungtaweeworant, C. A. Trickett, J. T. Barmanbek, A. S. Alshammari, P. Yang and O. M. Yaghi, *J. Am. Chem. Soc.*, 2017, **139**, 356.
113. H. Zhang, T. Wang, J. Wang, H. Liu, T. D. Dao, M. Li, G. Liu, X. Meng, K. Chang, L. Shi, T. Nagao and J. Ye, *Adv. Mater.*, 2016, **28**, 3703.
114. A. S. Varela, W. Ju and P. Strasser, *Adv. Energy Mater.*, 2018, **8**, 1703614.
115. B. C. Brodie, *Proc. R. Soc. London*, 1873, **21**, 245.
116. L. Zhang, Z. J. Zhao, T. Wang and J. Gong, *Chem. Soc. Rev.*, 2018, **47**, 5423.
117. H. Kim, H. S. Jeon, M. S. Jee, E. B. Nursanto, J. P. Singh, K. Chae, Y. J. Hwang and B. K. Min, *ChemSusChem*, 2016, **9**, 2097.
118. S. Zhao, N. Austin, M. Li, Y. Song, S. D. House, S. Bernhard, J. C. Yang, G. Mpourmpakis and R. Jin, *ACS Catal.*, 2018, **8**, 4996.
119. Y. Wang, C. Li, Z. Fan, Y. Chen, X. Li, L. Cao, C. Wang, L. Wang, D. Su, H. Zhang, T. Mueller and C. Wang, *Nano Lett.*, 2020, **20**, 8074.
120. K. S. Kwok, Y. Wang, M. C. Cao, H. Shen, Z. He, G. Poirier, B. E. McCandless, K. J. Livi, D. A. Muller, C. Wang and D. H. Gracias, *Nano Lett.*, 2019, **19**, 9154.
121. J. Kim, J. T. Song, H. Ryoo, J. G. Kim, S. Y. Chung and J. Oh, *J. Mater. Chem. A*, 2018, **6**, 5119.

122. J. Rosen, G. S. Hutchings, Q. Lu, S. Rivera, Y. Zhou, D. G. Vlachos and F. Jiao, *ACS Catal.*, 2015, **5**, 4293.
123. S. Liu, C. Sun, J. Xiao and J. L. Luo, *ACS Catal.*, 2020, **10**, 3158.
124. S. Liu, X. Z. Wang, H. Tao, T. Li, Q. Liu, Z. Xu, X. Z. Fu and J. L. Luo, *Nano Energy*, 2018, **45**, 456.
125. S. C. Abeyewera, J. Yu, J. P. Perdew, Q. Yan and Y. Sun, *Nano Lett.*, 2020, **20**, 2806.
126. S. X. Guo, F. Li, L. Chen, D. R. MacFarlane and J. Zhang, *ACS Appl. Mater. Interfaces*, 2018, **10**, 12690.
127. Z. Lyu, S. Zhu, M. Xie, Y. Zhang, Z. Chen, R. Chen, M. Tian, M. Chi, M. Shao and Y. Xia, *Angew. Chem., Int. Ed.*, 2021, **60**, 1909.
128. K. Chen, X. Zhang, T. Williams, L. Bourgeois and D. R. MacFarlane, *Electrochim. Acta*, 2017, **239**, 84.
129. F. S. Roberts, K. P. Kuhl and A. Nilsson, *Angew. Chem., Int. Ed.*, 2015, **54**, 5179.
130. A. Thevenon, A. Rosas-Hernandez, J. C. Peters and T. Agapie, *Angew. Chem., Int. Ed.*, 2019, **58**, 16952.
131. D. Raciti, Y. Wang, J. H. Park and C. Wang, *ACS Appl. Energy Mater.*, 2018, **1**, 2392.
132. H. Huang, H. Jia, Z. Liu, P. Gao, J. Zhao, Z. Luo, J. Yang and J. Zeng, *Angew. Chem., Int. Ed.*, 2017, **56**, 3594.
133. Y. Zhao, X. Tan, W. Yang, C. Jia, X. Chen, W. Ren, S. C. Smith and C. Zhao, *Angew. Chem., Int. Ed.*, 2020, **59**, 21493.
134. P. Lu, D. Gao, H. He, Q. Wang, Z. Liu, S. Dipazir, M. Yuan, W. Zu and G. Zhang, *Nanoscale*, 2019, **11**, 7805.
135. N. Han, Y. Wang, H. Yang, J. Deng, J. Wu, Y. Li and Y. Li, *Nat. Commun.*, 2018, **9**, 1320.
136. S. Kim, W. J. Dong, S. Gim, W. Sohn, J. Y. Park, C. J. Yoo, H. W. Jang and J. L. Lee, *Nano Energy*, 2017, **39**, 44.
137. S. Zhu, X. Qin, Q. Wang, T. Li, R. Tao, M. Gu and M. Shao, *J. Mater. Chem. A*, 2019, **7**, 16954.
138. S. Zhu, Q. Wang, X. Qin, M. Gu, R. Tao, B. P. Lee, L. Zhang, Y. Yao, T. Li and M. Shao, *Adv. Energy Mater.*, 2018, **8**, 1802238.
139. W. Zhang, C. Xu, Y. Hu, S. Yang, L. Ma, L. Wang, P. Zhao, C. Wang, J. Ma and Z. Jin, *Nano Energy*, 2020, **73**, 104796.
140. J. Zhang, M. Qiao, Y. Li, Q. Shao and X. Huang, *ACS Appl. Mater. Interfaces*, 2019, **11**, 39722.
141. Z. Lyu, S. Zhu, L. Xu, Z. Chen, Y. Zhang, M. Xie, T. Li, S. Zhou, J. Liu, M. Chi, M. Shao, M. Mavrikakis and Y. Xia, *J. Am. Chem. Soc.*, 2021, **143**, 149.
142. M. Li, J. Wang, P. Li, K. Chang, C. Li, T. Wang, B. Jiang, H. Zhang, H. Liu, Y. Yamauchi, N. Umezawa and J. Ye, *J. Mater. Chem. A*, 2016, **4**, 4776.
143. H. Hu, Y. Tang, Q. Hu, P. Wan, L. Dai and X. J. Yang, *Appl. Surf. Sci.*, 2018, **445**, 281.
144. C. J. Yoo, W. J. Dong, J. Y. Park, J. W. Lim, S. Kim, K. S. Choi, F. O. Odongo Ngame, S. Y. Choi and J. L. Lee, *ACS Appl. Energy Mater.*, 2020, **3**, 4466.

145. G. O. Larrazábal, A. J. Martín, S. Mitchell, R. Hauert and J. Pérez-Ramírez, *ACS Catal.*, 2016, **6**, 6265.
146. W. J. Dong, C. J. Yoo and J. L. Lee, *ACS Appl. Mater. Interfaces*, 2017, **9**, 43575.
147. J. P. Zou, Y. Chen, S. S. Liu, Q. J. Xing, W. H. Dong, X. B. Luo, W. L. Dai, X. Xiao, J. M. Luo and J. Crittenden, *Water Res.*, 2019, **150**, 330.
148. Y. Wei, J. Liu, F. Cheng and J. Chen, *J. Mater. Chem. A*, 2019, **7**, 19651.
149. W. Luc, C. Collins, S. Wang, H. Xin, K. He, Y. Kang and F. Jiao, *J. Am. Chem. Soc.*, 2017, **139**, 1885.
150. Q. Yang, Q. Wu, Y. Liu, S. Luo, X. Wu, X. Zhao, H. Zou, B. Long, W. Chen, Y. Liao, L. Li, P. K. Shen, L. Duan and Z. Quan, *Adv. Mater.*, 2020, **32**, 2002822.
151. S. Gao, Y. Lin, X. Jiao, Y. Sun, Q. Luo, W. Zhang, D. Li, J. Yang and Y. Xie, *Nature*, 2016, **529**, 68.
152. L. Li, D. K. Ma, F. Qi, W. Chen and S. Huang, *Electrochim. Acta*, 2019, **298**, 580.
153. Y. Qiu, J. Du, C. Dai, W. Dong and C. Tao, *J. Electrochem. Soc.*, 2018, **165**, H594.
154. H. Rabiee, L. Ge, X. Zhang, S. Hu, M. Li, S. Smart, Z. Zhu and Z. Yuan, *Appl. Catal., B*, 2021, **286**, 119945.
155. F. Y. Gao, S. J. Hu, X. L. Zhang, Y. R. Zheng, H. J. Wang, Z. Z. Niu, P. P. Yang, R. C. Bao, T. Ma, Z. Dang, Y. Guan, X. S. Zheng, X. Zheng, J. F. Zhu, M. R. Gao and S. H. Yu, *Angew. Chem., Int. Ed.*, 2020, **59**, 8706.
156. T. N. Huan, P. Prakash, P. Simon, G. Rousse, X. Xu, V. Artero, E. Gravel, E. Doris and M. Fontecave, *ChemSusChem*, 2016, **9**, 2317.
157. X. Chen, D. D. Ma, B. Chen, K. Zhang, R. Zou, X. T. Wu and Q. L. Zhu, *Appl. Catal., B*, 2020, **267**, 118720.
158. Y. Yiliguma, Z. Wang, C. Yang, A. Guan, L. Shang, A. M. Al-Enizi, L. Zhang and G. Zheng, *J. Mater. Chem. A*, 2018, **6**, 20121.
159. F. Li, L. Chen, G. P. Knowles, D. R. MacFarlane and J. Zhang, *Angew. Chem., Int. Ed.*, 2017, **56**, 505.
160. T. Tran-Phu, R. Daiyan, Z. Fusco, Z. Ma, R. Amal and A. Tricoli, *Adv. Funct. Mater.*, 2020, **30**, 1906478.

## CHAPTER 4

# *Nanotechnology for the Remediation of Plastic Wastes*

Y. ZHENG,<sup>a</sup> C. MAO,<sup>b</sup> Z. ZHANG,<sup>a</sup> R. LIU\*<sup>a</sup> AND B. YAN<sup>a,b</sup>

<sup>a</sup> Institute of Environmental Research at Greater Bay Area, Key Laboratory for Water Quality and Conservation of the Pearl River Delta, Ministry of Education, Guangzhou University, Guangzhou 510006, China; <sup>b</sup> School of Environmental Science and Engineering, Shandong University, Qingdao 266237, China

\*Email: liurr@gzhu.edu.cn

## 4.1 Introduction

Plastics have been widely used in industrial production and daily life for several decades due to their advantageous properties in terms of durability, lightness, stability, and low cost.<sup>1,2</sup> They are increasingly applied in various fields such as packaging, manufacturing, construction, and cosmetics and occupy a large section of the materials market.<sup>3–5</sup> According to statistics, around 322 million tons of plastics were produced globally in 2015, with an increase of 40% compared to 5 years ago.<sup>6</sup> In 2018, global production and consumption had reached 359 million tons and 385 million tons, respectively.<sup>7</sup> Enormous quantities of plastics were produced and consumed every year. However, it is reported that only 173 million tons of total waste were recycled and landfilled. A large amount of unmanaged plastic waste has been improperly treated and leaches into the ecological environment and landscapes<sup>4,7–9</sup> (see Figure 4.1). Additionally, the accumulated plastics in the environment gradually decompose into small pieces, forming microplastics and nanoplastics (NPLs), which are more persistent and harmful, posing significant risks to living organisms and humans.<sup>10–14</sup>

---

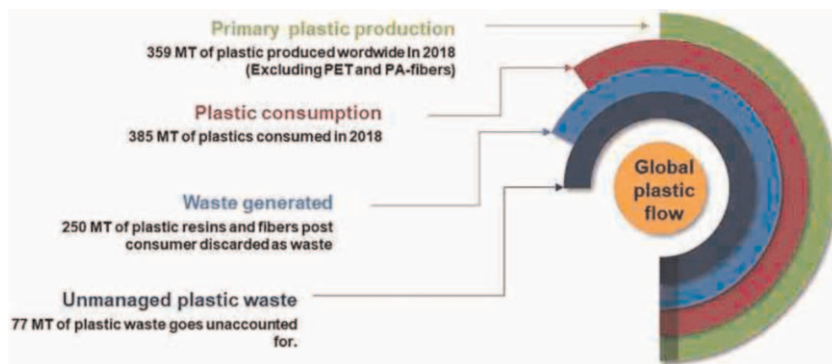
Nanoscience & Nanotechnology Series No. 57

Sustainable Nanotechnology

Edited by Zibiao Li, Jie Zheng and Enyi Ye

© The Royal Society of Chemistry 2022

Published by the Royal Society of Chemistry, www.rsc.org

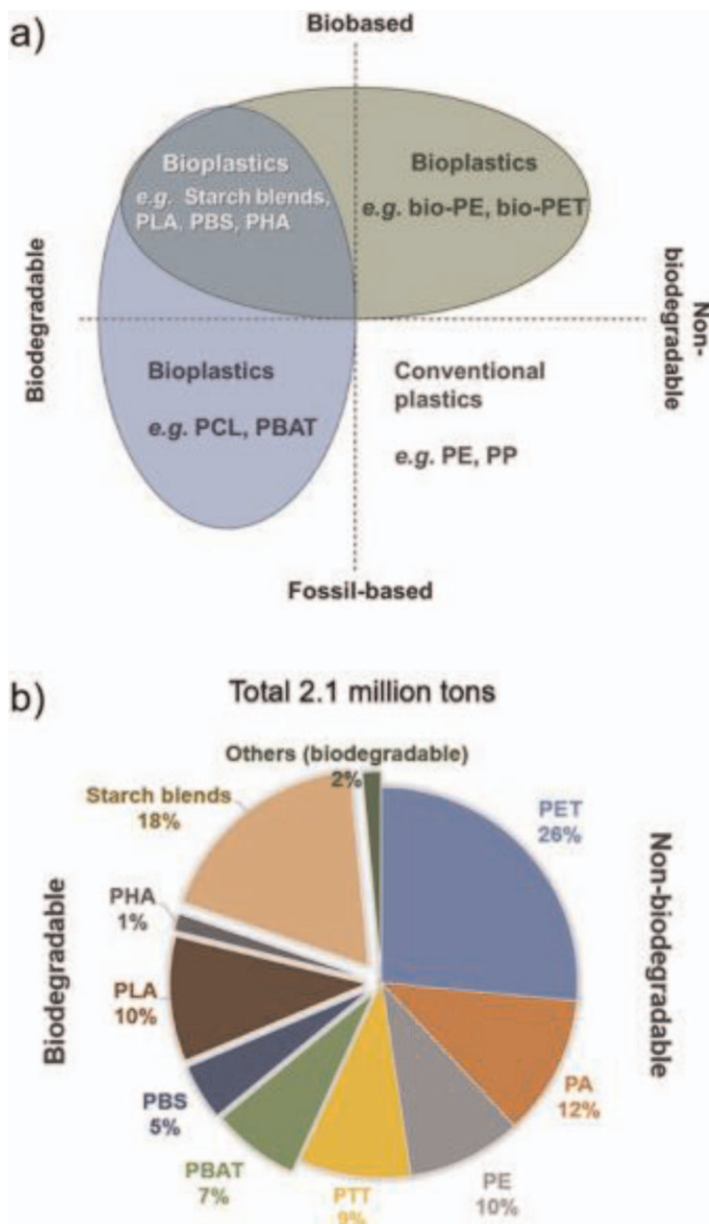


**Figure 4.1** Global flow of plastic material in 2018. Reproduced from ref. 9 with permission from Elsevier, Copyright 2021.

Therefore, considerable attention has been paid to finding promising solutions to the burdening issue of global plastic pollution.

Regarding plastic waste disposal and its environmental risks, there are several treatment methods, including incineration, sanitary landfill, and recycling (chemical recovery, energy recovery, remanufacturing, *etc.*). Pyrolysis is one of the management methods. It is a thermochemical treatment technology that thermally degrades long-chain organics in an inert atmosphere. Long chains of organic materials break down into short and simple chains under heat flow and pressure.<sup>3,15</sup> Meanwhile, the available energy can be recycled. Some researchers have successfully recovered energy from the pyrolysis of plastic bags and rice straw.<sup>16</sup> Compared with other treatment methods, pyrolysis can reduce the emission of greenhouse gases and does not produce carcinogenic dioxin.<sup>3,17</sup> However, it produces highly toxic volatile substances such as methane, aldehydes, and ketones.<sup>18,19</sup> The burning of plastic wastes could produce a large amount of dust, toxic smoke, and irritant gases, while landfill may produce leachate, which potentially pollutes groundwater and soil. How to treat plastic waste in a more effective and environmentally friendly way is an urgent problem that needs to be faced.

Bioplastics with synthetically or naturally derived polymers offer a solution to the remediation of plastic wastes and can be a suitable alternative to conventional fossil-based plastics such as polyethylene (PE), polypropylene (PP), and polyvinyl chloride (PVC).<sup>20</sup> They can be partially or completely degraded in the natural environment and have great potential for recycling. In general, the term bioplastics usually refers to plastics that are biobased or biodegradable, or both<sup>21</sup> (see Figure 4.2). Biobased plastics are derived from renewable resources such as biomass rather than fossil materials.<sup>22–28</sup> They are not necessarily biodegradable. Since biobased plastics are based on natural materials, their decompositions in principle induce zero net-carbon emission. Biodegradable plastics (BPs) are usually degraded through the enzymatic activities of microorganisms to carbon dioxide, methane, water, biomass, humic matter, and other natural substances.<sup>29</sup> Although biodegradable polymers are environmentally friendly, they may not demonstrate comparable mechanical and physical properties to



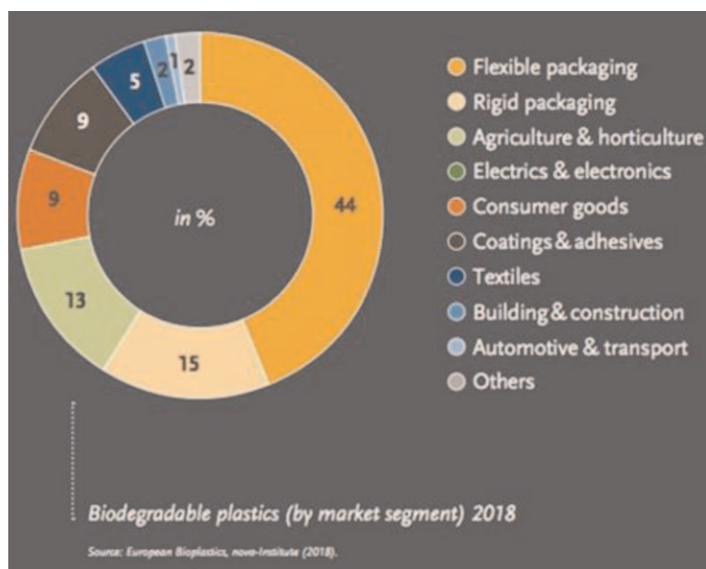
**Figure 4.2** The classifications of plastics (a) and global production of bioplastics (b). Reproduced from ref. 21 with permission from Elsevier, Copyright 2020.

conventional polymers, which restricts their wide applications.<sup>30–33</sup> Herein, the development of smart BPs in recent years and their improved properties with nanomaterials addition are comprehensively reviewed. Nanotechnology for decomposing plastic wastes into valuable substances is also highlighted. It offers a great promising solution for the reuse and recycling of plastic waste.

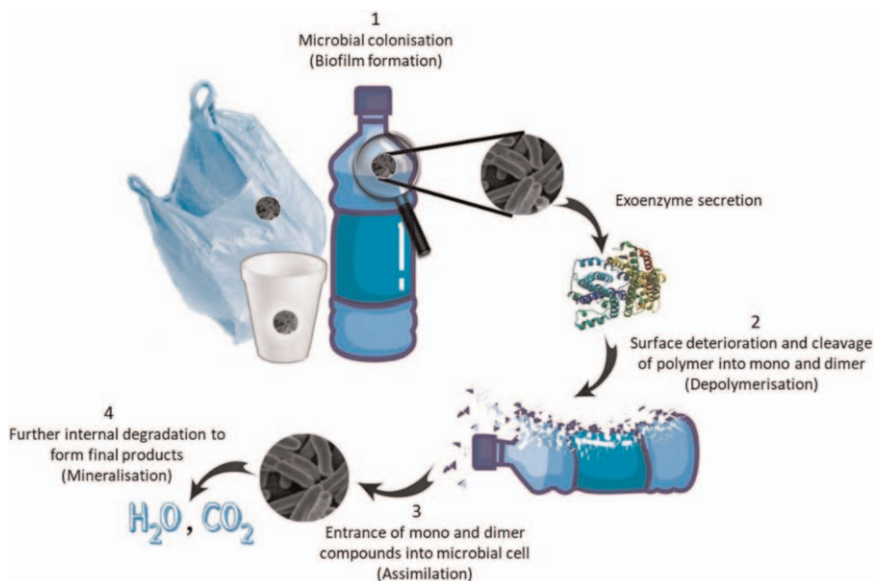
## 4.2 Biodegradable Plastics

BPs, defined as plastics that are degraded by microorganisms (bacteria, fungi, algae, *etc.*) existing in the natural environment such as marine waters, soil, and compost could be ultimately decomposed to carbon dioxide (CO<sub>2</sub>), methane (CH<sub>4</sub>), water (H<sub>2</sub>O), elements of mineralized inorganic salts, and biomass.<sup>34–37</sup> The ideal BP has excellent performance for applications and can be slowly biodegraded in nature, eventually entering the global carbon cycles. With the increasing awareness of risks from plastic waste, the need for and application of degradable plastics have greatly increased today. According to the data published, BPs have been widely used in various fields and packaging is its major application area. Flexible and rigid packaging accounted for about 60% of their market in 2018<sup>38</sup> (see Figure 4.3). People have also applied BPs in high-performance and high-end markets with great potential.

BPs are a type of polymer material with complex chemical structures, long carbon chains, and high molecular weights. In general, the biodegradation process usually goes through four steps: biodeterioration, biopolymerization, bioassimilation, and mineralization<sup>39</sup> (see Figure 4.4). In the first step, the microbial biofilms are formed, leading to surface degradation and polymer fragmentation. The fragmented polymer chains are further depolymerized to oligomers, dimers, or monomers by the extracellular enzymes secreted by microorganisms. In the bioassimilation process, small



**Figure 4.3** Market proportion of biodegradable plastics. Reproduced from ref. 38, <https://doi.org/10.1002/open.201900272>, under the terms of the CC BY 4.0 license <https://creativecommons.org/licenses/by/4.0/>.



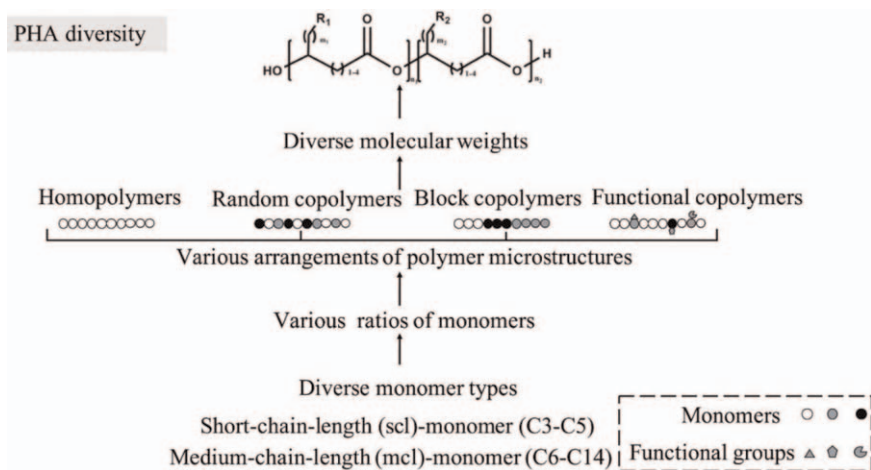
**Figure 4.4** The biodegradation process of polymer by microorganisms. Reproduced from ref. 39 with permission from Elsevier, Copyright 2021.

molecules are taken by microbial cells and primary/secondary metabolites are generated. Finally, metabolites are mineralized, releasing  $CO_2$ ,  $CH_4$ ,  $H_2O$ ,  $N_2$ , *etc.*, into the environment.

At present, there are many types of biodegradable polymers, including poly(lactic acid) (PLA), starch blends, polyhydroxyalkanoates (PHAs), poly(butylene succinate) (PBS), and poly(butylene adipate terephthalate) (PBAT).<sup>33,40,41</sup> According to the degree and nature of biodegradation, BPs are generally divided into two categories: fully degradable plastics and destructive degradable plastics.<sup>42–44</sup> The first category is completely biodegradable, which is made of natural polymers such as starch, cellulose, chitin, or agricultural and sideline products. They can be degraded through microbial fermentation or synthesis. The second category is a natural polymer such as starch combined with a synthetic polymer, which is not completely biodegradable. It achieves degradation by destroying the structure of the natural components in the copolymer.

Among biodegradable polymers, PHA and PLA are the two most common ones. PHAs are environmentally friendly bioplastics with excellent performance owing to their hydrophobic properties and extensive flexibility in mechanical properties, coupled with good biocompatibility and biodegradability. They are thermoprocessible, elastomeric, and nontoxic. PHA has been used in many forms, such as films, foams, fibers, and food additives. PHA have varied properties due to diverse monomer types and different arrangements of microstructures. A monomer with a 3–5 carbon chain length is usually called a short-chain-length (scl) monomer, and that with a





**Figure 4.5** Influencing factors of PHA diversity, including monomer structures, molecular weights, polymer chain structures, functionalization, and all the combinations. Reproduced from ref. 45 with permission from Elsevier, Copyright 2020.

6–14 carbon chain length is called a medium-chain-length (mcl) monomer<sup>45</sup> (see Figure 4.5). Generally, scl-PHAs are highly crystalline and have poor tensile strength, while mcl-PHAs are amorphous and have high elasticity with low melting points. Copolymers with different ratios of scl and mcl could exhibit diverse elasticities and tensile strengths.

PLA is another type of biodegradable engineering plastic popular due to its advantageous characteristics, such as ease of processing and high mechanical strength. More importantly, the half-life of PLA is generally 30 weeks, and the *L*- or *D*-chirality of the PLA will greatly affect the degradation rates and adjust its half-life to meet various clinical needs<sup>46,47</sup> (see Table 4.1). Choosing *L*-chirality over *D*-chirality will determine the biodegradability and mechanical properties of the polymer, as well as whether the polymer is semicrystalline or amorphous.<sup>47</sup>

Although biodegradable polymers have reduced environmental risks compared with traditional plastics, they have certain disadvantages in terms of thermal and mechanical properties, processing cost, and application fields.<sup>48–50</sup> For example, PLA is hard and brittle in nature, which is not conducive for processing. Starch-based plastics are usually not resistant to high temperatures, causing products to be easily deformed and torn. In addition, the cost issue has always been one of the key factors that plague the development of the BP industry. In order to give full play to the potential of BPs and expand their use scale, it is necessary to improve their performance or develop novel properties that can meet specific applications. To this end, nanotechnologies provide a very promising and effective strategy for improving the physicochemical properties and mechanical properties of BPs.

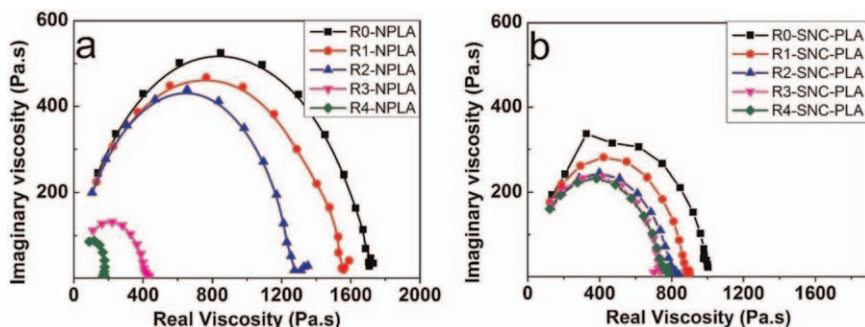
**Table 4.1** PLA composition and degradation profiles.

PLA composition	Chirality	Degradation conditions	Degradation time	Usage
PLA	D,L	<i>In vitro</i> : 0.13 M phosphate buffer, pH 7.4, 37 °C	Plates: 11 weeks; Films: 25 weeks	Size-dependence degradation testing
PLA films	L	<i>In vitro</i> : 0.2 M citrate buffer, pH 7, 37 °C	10% Weight loss over 16 weeks	Materials in surgery
PLA sheet	No indication	<i>In vivo</i> : transplantation in the infraorbital rim of macaque monkeys	Remnants found at the surgical site 38 weeks postimplantation	PLA bone implants
PLA plates	D,L	<i>In vivo</i> : subperiosteal in rabbits	70% Loss of molecular weight after 42 days	PLA bone implants
PLA implant	L	<i>In vivo</i> : transplantation to rats	14% Weight loss after 3 months	Implants
PLA fibers	No indication	<i>In vivo</i> : rat oral tissue	Full degradation between 42 and 70 days	Sutures
PLA-Zn 0.05% (98% L)	D,L	<i>In vitro</i> : 0.13 M phosphate buffer, pH 7.4, 37 °C	9% Weight loss after 12 months	PLA screws
PLA microcapsules	D,L	<i>In vivo</i> : Intramuscular injection to rats	Breakdown first observed after 150 days and total erosion after 420 days	Drug delivery
PLA microspheres	L	<i>In vivo</i> : injection to rats' livers	Implant conserved its geometrical form 14 months after injection	Drug delivery
PLA films-initial intrinsic viscosity of 3.24 dL/g	D,L	<i>In vivo</i> : subdermal implantation in rabbits	58% Weight loss over 60 weeks	Experimental degradation rate study

### 4.2.1 Nanomaterials for Improving the Performance of Plastics

Graphene is a well-known carbon nanomaterial, possessing excellent characteristics and good biocompatibility. Some researchers studied to add graphene to biobased plastics such as PLA to improve plastics' recyclable performance. After being added to PLA, graphene dramatically increased the number of producing cycles of the composite.<sup>51</sup> Tesfaye *et al.* studied the effect of silk nanocrystals (SNCs) on the thermal rheological properties of PLA during the repeated extrusion process. The results showed that SNCs promoted the crystallization process of the PLA matrix and slowed down its thermal degradation rate<sup>52,53</sup> (see Figure 4.6). Pantani *et al.* melted and incorporated ZnO rod-shaped nanoparticles with PLA with a composition range of 0.5% to 3% to form a new type of PLA-ZnO nanocomposite film.<sup>54</sup> ZnO in this film presented good dispersibility, which retained excellent molecular and mechanical properties of film. The nanocomposite containing ZnO also exhibited good antibacterial activity against tested Gram-positive and Gram-negative bacteria. The performance-in-one materials have the potential to replace traditional plastics.

Fortunati reported that doped PLA-based plastics with cellulose nanocrystals and silver nanoparticles modified by surfactants could improve the overall crystallinity of the composite material and produce an effective barrier effect.<sup>55</sup> Jaroslav reported a study of adding carbon black to PLA/PHB to prepare aluminum foil. Its aging and structural changes were studied, and it was found that it can improve the photochemical stability of aluminum foil, prevent crystallization during the aging process, and delay the deterioration of its mechanical properties. Catalysts are also very popular in the catalytic cracking of polyolefins. When conventional zeolite and amorphous silica-alumina are used as catalysts, they often affect the catalytic cracking effect *via* several factors such as conversion rate, selectivity, and deactivation. It will create space and diffusion barriers to bulky polymer molecules. New materials with highly



**Figure 4.6** Cole-Cole plots of neat PLA (a) and SNC-PLA composite (b) for different recycle times. Reproduced from ref. 53 with permission from Elsevier, Copyright 2017.

accessible active sites, such as hierarchical zeolite, super-large pore zeolite, and layered zeolite, can achieve higher activity and required selectivity to achieve a more ideal plastic cracking effect.<sup>56</sup>

Mdletshe *et al.* successfully enhanced the properties of polycaprolactone (PCL) by adding silicon carbide (SiC) nanoparticles to PCL using a melt mixing method. Although SiC improves the performance of PCL, the problem is that the biodegradation process of PCL in the soil environment is delayed in the presence of SiC, which is not conducive to the protection of the ecological environment, so further improvements are needed.<sup>57</sup> Karina *et al.* used acetic acid and chloroform with *N,N*-dimethylformamide (DMF) to further enhance the advantages of PCL and TiO<sub>2</sub> NPs composite membranes. They found that the composite membrane refined with chloroform-DMF has better surface homogeneity than the composite membrane refined with acetic acid. This study broadens the practical application of PCL-based material blends in BPs.<sup>58</sup>

Starch is a kind of high molecular polymer with abundant sources in nature. It is renewable and can be widely used to produce starch-based plastics through modification and plasticization. However, starch-based plastics are brittle and water sensitive and have low barrier properties. Wang *et al.* incorporated Bi<sub>2</sub>WO<sub>6</sub>-TiO<sub>2</sub> (BT) nanoparticles into starch film by casting method. The incorporation of BT nanomaterials improves the tensile strength of the film and also increases the opacity of the film. In addition, it also solves the problem of photocatalyst recovery and fixation, and the developed BT/starch film shows high photocatalytic activity when decomposing C<sub>2</sub>H<sub>4</sub> under visible light ( $\lambda > 420$  nm).<sup>59</sup> Goudarzi *et al.* used nano TiO<sub>2</sub> to modify the starch film. The performance of the prepared starch/TiO<sub>2</sub> nanocomposite is significantly improved compared to starch film, and it can also effectively protect products from ultraviolet rays. This starch film can be used as an environmentally friendly and antiultraviolet food packaging material.<sup>60</sup>

### 4.2.2 Biodegradability of Plastics

Although BP is a promising alternative to traditional plastics, it is necessary to thoroughly evaluate its degradation products to ensure that they can be degraded without the emission of secondary pollutants into the environment. It has been reported that biodegradable polymers can be biodegraded by biological agents only under certain conditions and within a certain period of time. The conditions are not always reliable in the natural environment, which means it is difficult to evaluate the biodegradability of BPs under standardized laboratory conditions to reflect the changing actual natural environment. The biodegradation rate depends on the characteristics of the polymer itself, the choice of service life, and external physical and chemical conditions, such as ambient temperature, oxygen, light, water content, pH value, and the presence of specific microorganisms.

Biodegradable polymers with complex chemical structures will require extra enzymes or complex coenzymes for degradation. In general, the shorter

the polymer chain, the higher its biodegradation rate. When polymers contain functional groups such as ester bond, hydroxyl group, and carboxyl group and have flexible active sites, their biodegradation rate will be higher since the active groups bind to enzyme sites much faster than rigid groups.<sup>61</sup>

Naba *et al.* mixed PLA, PCL, and microcrystalline cellulose (MCC) at different concentrations to evaluate their biodegradability. It was found that PLA-based multiblends can degrade 60–90% within 100–140 days, which helps better predict the biodegradability of PLA/PCL/MCC hybrid fibers under composting conditions and may open new doors for the manufacture and use of degradable bioplastics.<sup>62</sup>

Narancic *et al.* conducted biodegradation tests with commonly used BPs and their mixtures in three managed environments, namely, domestic composting, anaerobic digestion, and industrial composting, and four unmanaged environments, namely, freshwater, marine, soil, and water anaerobic digestion.<sup>63</sup> They observed that the degradation rate of PLA in the soil was very slow. Based on this result, it is estimated that the biodegradation of PLA in the soil will even take more than 30 years. Except for PHA and thermoplastic starch, the others were not degraded in the aquatic environment. It is worth noting that most of the polymers and their mixtures tested in this study did not meet ASTM and ISO biodegradability standards, and some did not show any biodegradability.

In order to evaluate the impact of BP mulch on groundwater and soil quality, Sintim *et al.* conducted field trials for four consecutive years from 2015 to 2018 in two locations with different climates, covering the vegetable production process with BPs; among them, PE mulch, and cellulose paper mulch and no mulch were used as control treatments, and then the water quality and the characteristics of the soil leachate were analyzed. Results showed that compared with no covering, the use of BP mulch increases the water permeability by 10–12%, reduces the penetration of nitrate and nitrite into groundwater, and increases soil aggregate stability by 6–16%. In addition to the explosive reduction of microbial respiration, the BP mulch has a positive effect on groundwater quality and soil overall. In this experiment, the BP mulch seems to be a viable alternative to conventional plastic mulch.<sup>64</sup>

Sintim *et al.* composted the two biodegradable mulch films of BioAgri<sup>®</sup> and PLA/PHA and conventional PE mulch films for 18 weeks and evaluated their degradation.<sup>65</sup> The experimental results proved that BioAgri<sup>®</sup> and PLA/PHA had been degraded, but the micron- and nanosized particles still remain on the nylon fiber. In addition, during the degradation of plastics, plastic additives such as carbon black were released. Long-term use of such plastic mulch may lead to the accumulation of additives in soil and other ecological environments, which may cause long-term harm to the environment.

González-Pleiter *et al.* studied the released secondary PHB-NPLs from PHB-microplastics through nonbiodegradable methods and then studied the effects of secondary PHB-NPLs (~200 nm) on three representative aquatic organisms: filamentous cyanobacterium *Anabaena*, crustacean *Daphnia magna*, and *Chlamydomonas reinhardtii*.<sup>66</sup> The experiment ruled out

the influence of toxic chemicals on PHB-microplastics and proved that secondary PHB-NPLs are highly toxic to these three freshwater organisms, which can cause their growth inhibition and even death. PHB-NPLs can increase the amount of cellular reactive oxygen species (ROS) formed, which in turn destroys the integrity of the cell plasma membrane and changes its permeability, resulting in impaired mitochondrial function.

These biodegradability tests of plastics conducted in real environments clearly indicate that due to the natural differences of environmental types, the development of BPs is still facing considerable challenges. When we intentionally or unintentionally release plastics into land or aquatic environments, biodegradability is an advantage over conventional plastics. However, for plastics that can only be biodegraded in a narrow or partial environment, the research and development of BPs need to pay more attention to their biodegradable conditions, making BPs more suitable for the title of green environmental protection.

## 4.3 Nanotechnologies for the Remediation of Plastics

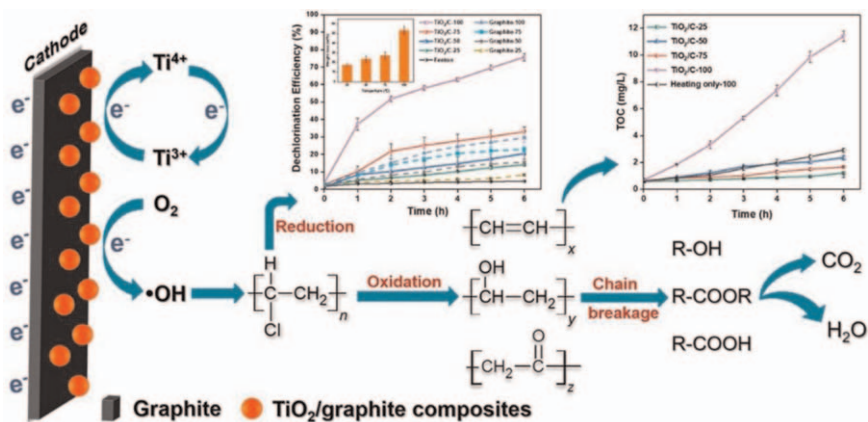
### 4.3.1 Nanofiller

Hydrophilic nanoscale additives as fillers can increase the interface-specific surface area and area/volume ratio, thereby significantly improving the performance of plastic, including mechanical properties, dimensional stability, barrier properties, and gas permeability. Compared with traditional microscale fillers, a very small amount of nanoscale fillers is sufficient to obtain excellent performance without dramatically affecting the density, light transmittance, or cost of the basic polymer.<sup>67–69</sup> With nanomaterials addition, the performance of plastics was improved, and a composite that was lightweight, easy to process, and low in cost was obtained. Therefore, small amounts of nanoscale fillers can be used to improve polymer performance without affecting its density, light transmittance, and cost. They are widely used in aerospace, automotive, construction, and other engineering fields.<sup>70</sup> Scientists have also carried out a large number of experiments to explore polymers with better performance, wider application, and better recycle management.

Clay, the most commonly used nanomaterial on the market, is cheap and nontoxic. Some researchers used layered silicate (nanoscale clay) as a filler to modify plastics and optimize the amount of clay added. They added compatibilizers or modified clays to increase the compatibility of the composite or control the synthesis methods and conditions to adjust the properties of the resulting mixture.<sup>67,69,71–73</sup> The nanoscale clay with ethylene-glycidyl methacrylate (E-GMA) compatibilizer was added to the rHDPE/rPET blend, and the nanocomposite prepared *via* the melt blending method exhibited high compatibility and flexural performance. The result shows that with the increase of nanoscale clay content, the plastics' bending resistance, dispersibility, thermal stability, and flame retardancy were all improved.<sup>73</sup>

Titanium dioxide is another one of the commonly used nanofillers for mixing polymers. Low-density polyethylene (LDPE) is a nondegradable plastic. Its degradability can be improved with nanomaterial additives. Functionally modified titanium dioxide nanoparticles were extruded and combined with LDPE and then subjected to photocatalytic degradation. It was found that the functionalized particles have better dispersibility, but due to the limited space where the chain scission process occurs, the polymer only undergoes heterogeneous degradation.<sup>74</sup> Photodegradation of polymer nanocomposite with TiO<sub>2</sub> instead of landfill and incineration could greatly reduce the generation of toxic by-products such as dioxins.<sup>75</sup> Additionally, Miao *et al.* presented a high dechlorination efficiency (75%) of PVC microplastics *via* an electro-Fenton-like system based on a TiO<sub>2</sub>/graphite cathode.<sup>76</sup> The dechlorination reaction of PVC was initiated by the reduction reaction on the cathode and the oxidation of hydroxyl radical under heating, which leads to the oxidation of the PVC backbone. Then, the long chain of PVC was further broken down into small molecules and eventually decomposed to CO<sub>2</sub> and H<sub>2</sub>O<sup>76</sup> (see Figure 4.7). This work provides an eco-friendly approach to microplastics treatment.

Nanosilica mixed with a kind of compatibilizer called PP grafted with maleic anhydride can fine-tune the shape of a blend of 80% PP and 20% polyamide. It was found that using PP/PA6 blends stabilized with nanosilica particles has good mechanical and barrier properties.<sup>77</sup> With adding maleic anhydride-grafted-polypropylene (MA-*g*-PP), the structure and properties of isotactic polypropylene (PP)/Cloisite 15A (5 wt%) nanocomposites were studied, and it is found that it can be recycled up to 4 times, but as the number of cycles increases, the morphology of the composite material changes significantly. The viscosity is significantly reduced, and even if it can be reused, the recyclability of the product after reprocessing cycles is



**Figure 4.7** The proposed degradation mechanism of polyvinyl chloride microplastics and dechlorination efficiencies. Reproduced from ref. 76 with permission from Elsevier, Copyright 2020.

reduced.<sup>78</sup> Mixing wood plastic board waste and fresh material at a ratio of 30 : 70 was not found to affect the mechanical properties of the wood–plastic board produced.<sup>79</sup> Maleic anhydride was used to functionalize post-consumer plastic to compatibilized materials and increase its extensibility, which improved the compatibility of polyolefins and the dispersibility of nanofillers in plastic composites.<sup>70</sup>

Graphene oxide modified with melamine terephthaldehyde (MTR–GO) was used as a nanofiller to prepare a PVC nanocomposite. The results showed that MTR–GO could significantly increase the thermal stability time of PVC with 10 wt% nanofiller, and the incorporation of MTR–GO significantly improved the performance of the PVC matrix, for example, in terms of corrosion resistance and hot hydrochloric acid release ability.<sup>80</sup>

Amigo *et al.* added starch nanoparticles with a diameter of 70 nm to the PE matrix for the preparation of high-density PE composites *via in situ* polymerization. Starch nanoparticles were employed as nucleating agents to increase the relative proportion without disturbing the crystallization mechanism. The results showed that the addition of starch nanocrystals improved not only the thermal stability of the matrix but also the photodegradability of PE. The temperature required for thermal degradation of PE composites prepared by *in situ* polymerization with nanostarch was decreased, and the crystallinity was higher than pure PE at the same temperature. The photodegradation rate was increased as well.<sup>81</sup>

### 4.3.2 Photodegradation of Plastics

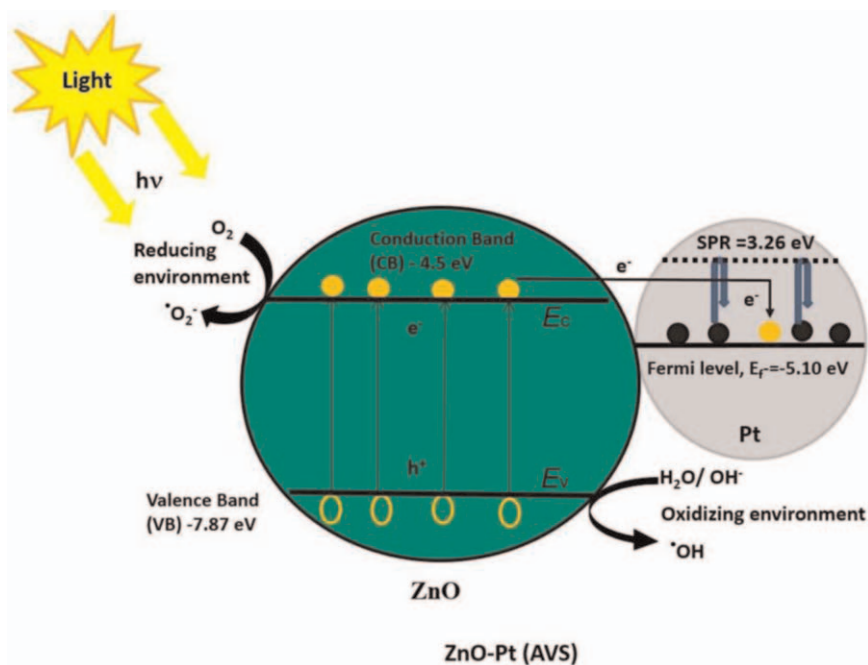
Photodegradable plastic refers to the use of the light-induced effect of plastic under the sun causing the chemical bond of the plastic to break, destroying the integrity of the plastic structure, and finally oxidizing the plastic into carbon dioxide and water. Photodegradable plastics are mainly copolymer plastics and additive plastics. The difference between the two is that the former refers to the introduction of suitable photosensitive groups, while the latter changes the composition of the polymer by adding photocatalysts or photosensitizers so that the polymer structure is destroyed by light and thus degraded. Using nanomaterials as photocatalysts can not only improve the photocatalytic effect and degradation efficiency but also has the characteristics of low cost and simple process flow and thus is a method with great application potential. In recent years, photocatalytic research on plastic waste has provided new ideas and vitality for plastic degradation.

Maria *et al.* used protein-derived C/N–TiO<sub>2</sub> semiconductors to photodegrade HDPE MP at different pH levels and temperatures. The study found that a low pH (pH = 3) is conducive to the formation of hydroperoxide during photo-oxidation. and low temperature (0 °C) increases the surface area of MP. Temperature and pH have comprehensive effects on the degradation of microplastics. Adjusting these can accelerate and enhance the degradation of HDPE MP.<sup>82</sup> One study demonstrated the degradation of microplastics, particularly LDPE film, through visible light-induced plasmonic photocatalyst.



The photocatalyst was composed of platinum nanoparticles deposited onto zinc oxide nanorods (ZnO-Pt). Attributing to the plasmonic effects, the nanocomposite photocatalyst exhibited better degradation kinetics and effectively degraded microplastic fragments. It provides a clean and green route for the degradation of microplastics in the ecosystem using sunlight<sup>83</sup> (see Figure 4.8).

In order to make plastic waste more environmentally friendly after degradation, researchers are trying to degrade plastics with zinc oxide photocatalysts with higher activity. Tofa *et al.* used heterogeneous ZnO nanorods as a catalyst and used visible light to stimulate the degradation of LDPE microplastic residues.<sup>84</sup> Bandara *et al.* compared the photodegradation catalytic ability of  $ZrO_2$  and  $TiO_2$  on PE and PP plastics under the two treatment conditions of using a solar simulator and real sunlight. The study found that, with 95% confidence, nano- $ZrO_2$  can cause higher photocatalytic degradation of PE and PP plastics than nano- $TiO_2$ .<sup>85</sup> Xu *et al.* prepared mesoporous titanium dioxide (M- $TiO_2$ ) nanoparticles through the hydrothermal method, modified them with polyaniline (PANI) of different contents as a composite catalyst, and then combined M- $TiO_2$  particles, and PANI/M- $TiO_2$  is introduced into the matrix of LDPE to improve its non-biodegradability. The results show that PANI-modified M- $TiO_2$  has a higher photocatalytic ability for LDPE degradation under ultraviolet light.<sup>86</sup>



**Figure 4.8** Mechanism of enhanced photocatalytic activities with platinum/zinc oxide nanorod (energy levels: Absolute vacuum scale [AVS]). Reproduced from ref. 83 with permission from MDPI, Copyright 2019.

### 4.3.3 Nanotechnology in Flexible Plastics

With the increasing use of flexible packaging, their recycling, sorting, resource utilization, and other aspects have also obtained a lot of research focus. In order to improve the performance of plastic films, people will also use nanofillers as additives in the polymerization process to prepare composite films to improve the ductility so that people reuse and reproduce them more often. After the spectroscopic and rheological analysis of the blend of plastic film and copolyamide (CoPA), it is proved that the copolyamide and the film have good compatibility. Adding copolyamide and organically modified sepiolite to the film, the nanocomposite obtained has good dispersibility and the rigidity and strength are unchanged, but the elongation is significantly improved by 10 times.<sup>87</sup>

The PE film is loaded with nano-zinc oxide wrapped in starch, which has a bactericidal effect and can make the film more environmentally friendly.<sup>88</sup> Ordered mesoporous carbon (OMC) is used as a nanofiller for film production and silica as a template. Under the protection of inert gas, the carbon precursor is infiltrated into the mesoporous silica for pyrolysis, OMCs are synthesized, and then hydrofluoric acid is used. After removing the silicon template, it was found that 5% loading of hydrophilic OMCs (H-OMCs) improved the surface hydrophilicity, wettability, and pure water permeability of the membrane.<sup>89</sup>

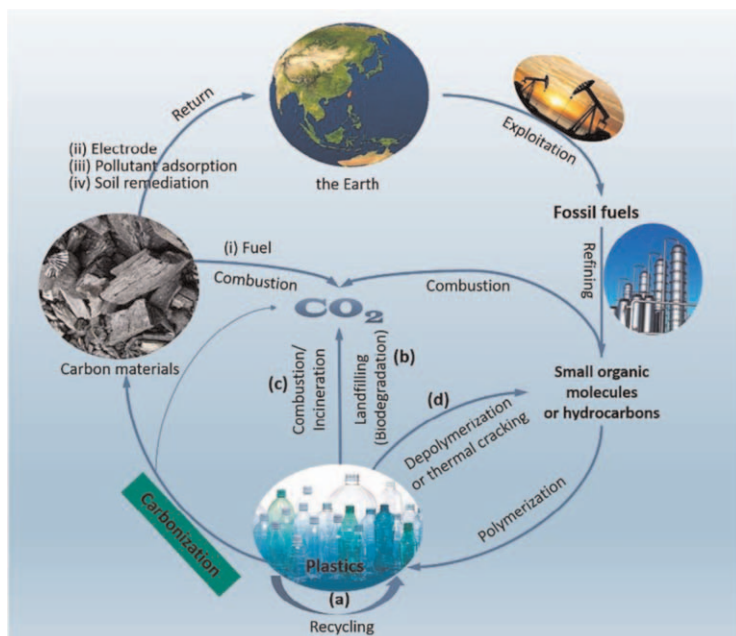
Plastics are also widely used in the food field. Multilayer silicate/polyamide composites are commonly used as oxygen barriers, and LDPE is used as a moisture-proof and sealing layer in food packaging, but its safety issues and industrial-scale use need to be improved. Researchers have used copolyimide as the polymer matrix and selected two organically modified layered silicates as nanofillers. The results show that this composite polymer has better barrier and mechanical properties than PA/PE commercial films. Not only is it compatible, but it is also an environmentally friendly material.<sup>90</sup>

### 4.3.4 Nanotechnology in the Carbonization of Plastics

Carbonization of plastic under the action of a catalyst is also an effective way to use plastic waste.<sup>91-93</sup> The collected plastic can be directly carbonized without processing. The hydrogen and part of the carbon atoms in it will be oxidized to release a lot of heat. The method of the catalytic carbonization of plastic waste not only simplifies the process and can reduce the production cost of raw carbonaceous materials but also reduces energy consumption. The method of generating carbon nanotubes *via* the catalytic carbonization of plastic waste can be divided into two types according to the reactor: the one-pot method and the stepwise method. No matter what kind of reactor is used, it mainly includes two processes: first, the plastic is decomposed in the liquid or gas phase, and then the resulting decomposition product is used as the carbon raw material to grow into carbon nanotubes under the action of a catalyst. As the intermediate proton acid site of plastic, solid acid is the place where the active intermediate of carbon ion degrades plastic.

The carbonization of plastics enriches and fixes the carbon atoms in plastics to form carbon materials, which can be stored for thousands of years, while also reducing greenhouse gas emissions.<sup>93,94</sup> The carbon material formed by the carbonization of plastic waste can be used as fuel, such as biomass charcoal; it can also be used as an adsorbent to adsorb environmental pollutants, such as organic matter and heavy metals;<sup>95–98</sup> good biocompatibility is conducive to the reproduction of microorganisms, so it can also be used for soil repair and its fertility;<sup>99</sup> and excellent conductivity makes it useful as an electrode material, such as batteries and supercapacitors.<sup>95,96,100–102</sup> As the development of supercapacitors is hindered by cost, the development of active materials from plastic waste is a very promising direction.<sup>103</sup> Especially, the carbon materials produced through the conversion of polytetrafluoroethylene have a high surface area and large pore volume, as well as the excellent electrochemical performance of supercapacitor electrode materials.<sup>104</sup> The conventional carbon cycle routes during the production and disposal of plastics are shown in Figure 4.9.<sup>94</sup>

Duan *et al.* used PE waste as a carbon source and nickel acetate tetrahydrate as a catalyst to synthesize carbon nanotubes containing 20% nickel nanoparticles. As the content of palladium nanoparticles increases, the electrocatalytic performance of carbon nanotubes is also enhanced.



**Figure 4.9** Schematic diagram of conventional carbon cycle routes during the production and disposal of plastics. Reproduced from ref. 94 with permission from Elsevier, Copyright 2020.

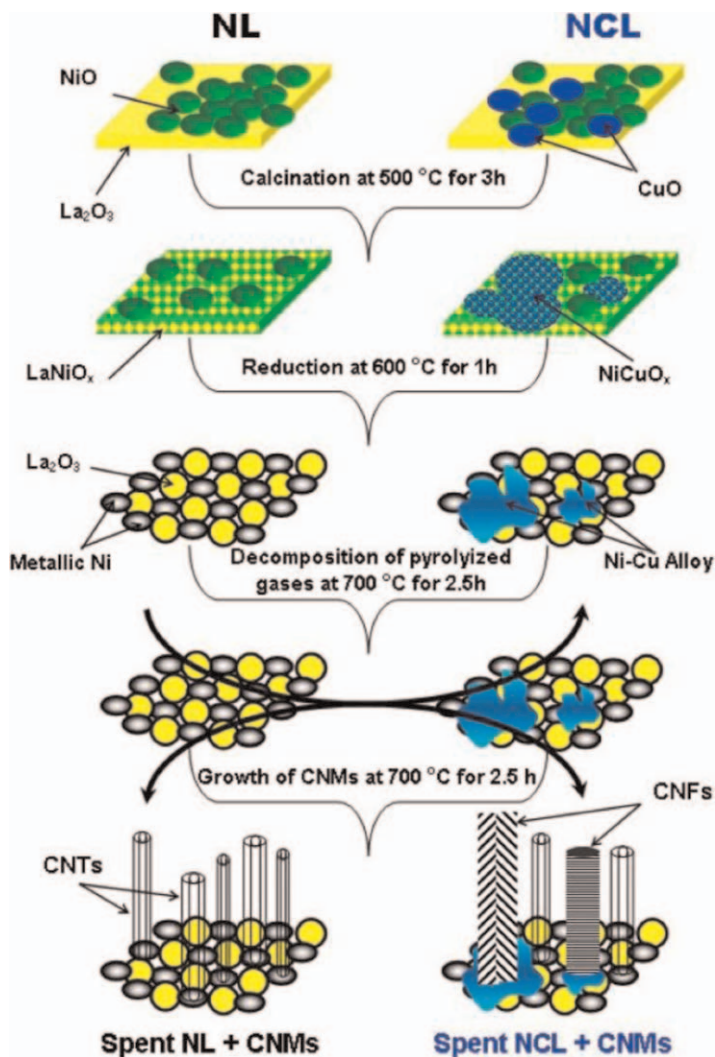
It provides a direction for the production of carbonaceous materials from plastic wastes.<sup>105</sup> Han *et al.* proposed a strategy to effectively convert waste plastic and rust into high-quality Fe@C NPs. The step of converting this waste into usable materials is a simple one-step calcination, which utilizes plastic waste as a carbon source. The use of composite materials provides an economical and sustainable strategy for reusing plastic wastes.<sup>106</sup> Ateyya *et al.* synthesized large-scale, high-quality carbon nanofibers and nanotubes by using PP plastic waste as raw material and lanthanum oxide ( $\text{La}_2\text{O}_3$ ) loaded Ni or Ni-Cu as catalysts. Higher temperature is conducive to obtaining carbon nanomaterials with better performance<sup>107</sup> (see Figure 4.10).

Yang *et al.* established a two-stage fluidized catalytic bed reactor system for the continuous coproduction of CNT and hydrogen from the gasification of waste plastic PP and low-density PE<sup>108</sup> (see Figure 4.11). The Ni/Al-SBA-15 catalyst can promote the degradation of waste plastics in the first stage and produce hydrocarbons as a source of carbon nanotube synthesis. When the reaction temperature of the two stages of the reactor is controlled to 600 °C and 800 °C, respectively (ER 0.1), a higher fraction of CNTs will be obtained. Masato Tominaga *et al.* synthesized a Pt/nano-ZrO<sub>2</sub>-SO<sub>4</sub> bifunctional metal acid catalyst and then used it to convert LDPE waste into high-value hydrocarbons, which improved the catalytic activity and stability of LDPE hydrocracking.<sup>109</sup>

### 4.3.5 Nanotechnology for the Transformation of Plastics to High-value Products

Common household wastes, such as plastic bottles, can also be an ingredient for turning wastes into usable materials. Zander *et al.* used recycled bottle-grade polyethylene terephthalate, polystyrene, and PP to form fibers from the melt and studied and compared the morphology and chemical, and thermal properties of the blend fibers.<sup>110</sup> The results showed that ethylene terephthalate fiber has the highest tensile strength, and its mechanical properties can be improved by adding it into polymers. This research provides a new idea for the recycling of a large number of low-cost raw materials and plastics produced from households.

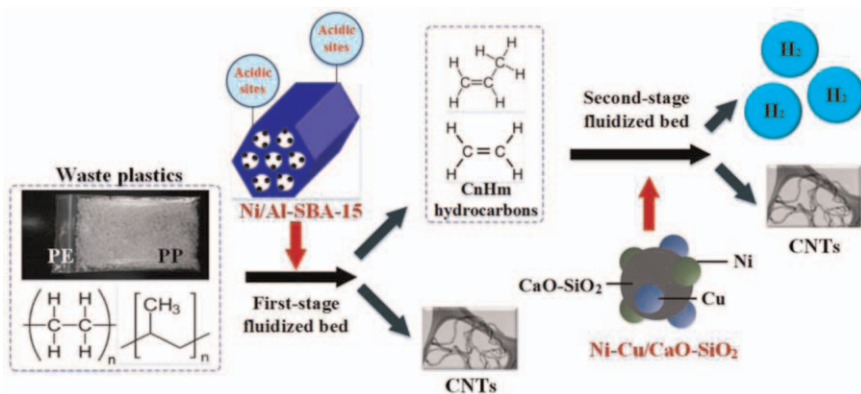
Tam's team used cellulose nanoparticles with hydroxyl groups on the surface to improve the performance of poly(3-hydroxybutyrate-co-3-hydroxyvalerate) (PHBV).<sup>111</sup> They studied the degradation rate by modulating hydrogen-bonding interactions between PHBV and cellulose nanoparticles. The results showed that the degradability of nanocomposite can be increased with more hydroxyl groups, and thermal stability during the degradation process has also been reinforced. They proposed the possible degradation mechanism of this nanocomposite in different degradation processes.<sup>111</sup> For the thermal degradation, the interactions of hydrogen bonds at the interface hindered the formation of the six-membered ester ring on PHBV, which may improve thermal stability during the degradation process. The microorganisms in the soil can degrade and digest the



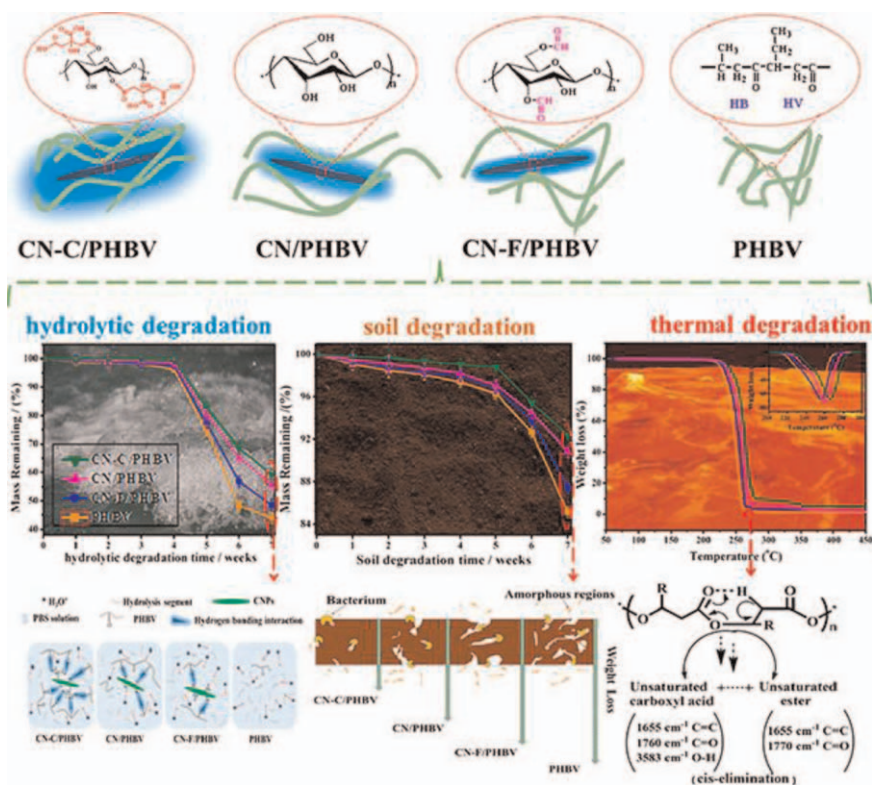
**Figure 4.10** Schematic diagram showing the growth mechanism of carbon nanomaterials (CNMs) over 50%Ni/La<sub>2</sub>O<sub>3</sub> (NL) and 40%Ni10%Cu/La<sub>2</sub>O<sub>3</sub> catalysts (NCL) catalysts. Reproduced from ref. 107 with permission from Elsevier, Copyright 2019.

amorphous domains of the nanocomposite in the degradation process (see Figure 4.12). With manipulated degradation rates, the nanocomposites can be suitable for wider applications.

Researchers have developed many green methods for plastic waste conversion. The Rodrigo J. de Oliveira team used thermally induced phase separation to convert waste industrial granular polystyrene foam into nanofoam and used the tin dioxide produced as a photocatalyst to catalyze the



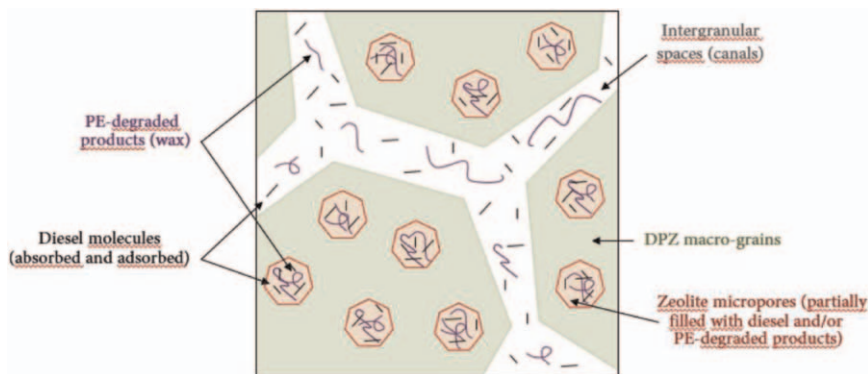
**Figure 4.11** Schematic diagram of the catalytic process and mechanism for CNTs and hydrogen coproduction in a two-stage fluidized-bed system. Reproduced from ref. 108 with permission from Elsevier, Copyright 2020.



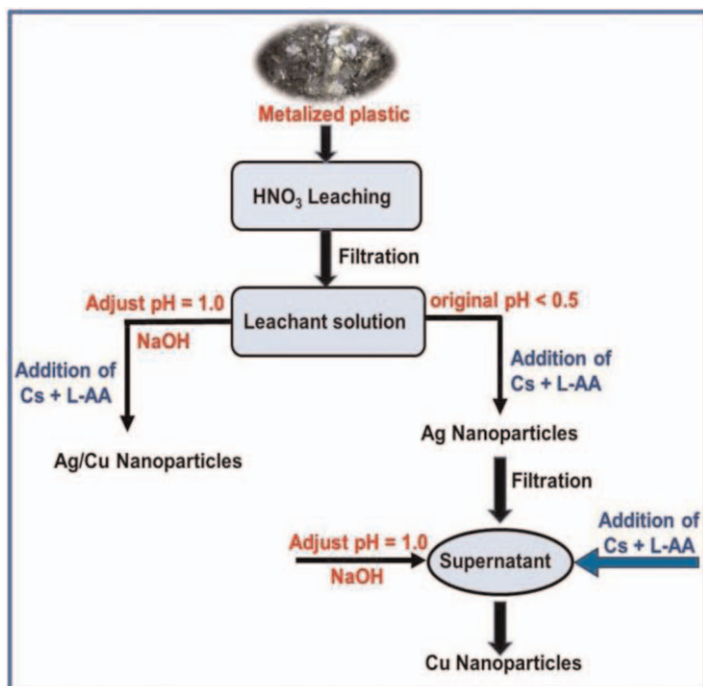
**Figure 4.12** Schematic diagram of structural changes of CNP/PHBV nanocomposites after hydrolytic degradation, soil degradation, and thermal degradation. Reproduced from ref. 111 with permission from American Chemical Society, Copyright 2019.

removal of pollutants in wastewater and underground books.<sup>112</sup> After blending LDPE and zeolite, the porous composite adsorbent obtained after partial degradation at 200 °C has good thermodynamic and adsorption properties, and the efficiency of removing diesel from water is as high as 39%<sup>113</sup> (see Figure 4.13). The mixed plastic waste with PS is converted into porous carbon nanosheets with high specific surface area, high adsorption capacity, and rich functional groups. It is a promising adsorbent that can be used in environmental remediation, energy storage, catalysis, *etc.*<sup>114</sup> There are also some studies using formaldehyde dimethyl acetal (FDA) as an external crosslinking agent and ferric chloride ( $\text{FeCl}_3$ ) as a catalyst to obtain nanoporous hyper-cross-linked polymers (HCPs) from polystyrene foam waste. HCPs can effectively and selectively adsorb  $\text{CO}_2$  in the flue gas mixture; remove methylene blue (MB), rhodamine B (RB), neutral red (NR), uniblue A (UA), methyl orange (MO), and other organic dyes; and can adsorb As(v) from aqueous solution. These excellent removal capabilities are even comparable to commercial products and the most advanced nanoporous materials.<sup>115</sup>

Acrylonitrile-butadiene styrene (ABS) plastic has good mechanical and physical properties, which has become an ideal choice for electroplating. The electroplating decoration makes ABS plastic products valuable. They have become high-end products with a nice metal appearance and excellent plastic properties. However, the recycling of metalized plastic parts is a challenge. Elsayed *et al.* immersed metalized ABS plastic samples in 3.2 M nitric acid, which can dissolve more than 92% Cu and 87% Ag, using chitosan as a stabilizer and ascorbic acid as a reducing agent.<sup>116</sup> Ag and Ag/Cu nanoparticles with a size of less than 60 nm can be obtained at a temperature of 60 °C. The nanoparticles obtained in this study exhibited suitable antibacterial activities against both Gram-positive and Gram-negative bacteria<sup>116</sup> (see Figure 4.14).



**Figure 4.13** The structure and absorption/adsorption mechanism of degraded polyethylene with zeolite. Reproduced from ref. 113 with permission from Academic Press Inc., Copyright 2020.



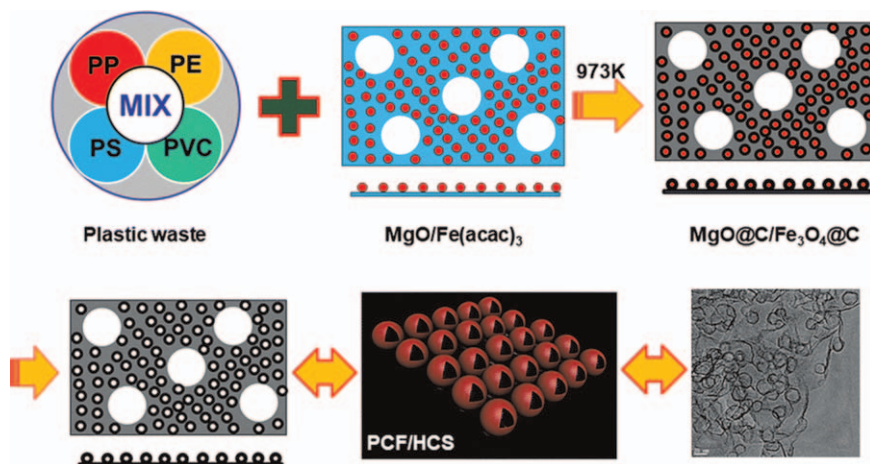
**Figure 4.14** The overall method flow diagram of preparing Ag, Cu, and Ag/Cu nanoparticles from metalized plastic waste. Reproduced from ref. 116 with permission from Elsevier, Copyright 2020.

Min *et al.* developed a catalyst template to prepare a three-dimensional hollow carbon sphere/porous carbon flake (HCS-PCF) hybrid nanostructure from plastic wastes. Mixed plastic wastes can be carbonized through magnesium oxide and iron(III) acetylacetonate with high conversion yields (>70 wt%)<sup>117</sup> (see Figure 4.15). This approach can not only be used for hydrocarbon polymers but also for halogen-containing polymers. Moreover, the prepared 3D advanced carbon structure exhibited excellent electrochemical performance and can be used as an anode material in lithium-ion batteries. Thereby, plastic wastes can be upcycled into high-value products. It will be a promising approach and a sustainable green way for plastic waste disposal.

#### 4.4 Conclusion and Outlook

With increasing global plastic production and consumption, people are highly aware of the environmental problems of plastic waste. The fate of plastic wastes has been the global concern and countless approaches have been developed to improve their recycling rate. Meanwhile, scientists have racked their brains to develop new methods to improve the performance of plastics. Although current measures have been taken to recycle and reduce





**Figure 4.15** Schematic illustration of the synthesis process of 3D porous carbon flake/hollow carbon sphere nanomaterials with catalyst. Reproduced from ref. 117 with permission from the Royal Society of Chemistry.

plastic usage, the effectiveness is still limited to some extent. Looking forward, biodegradable polymers could be promising alternatives to conventional plastics and may bring less plastic pollution to the environment. However, their biodegradability is limited to industrial composting systems and dependent on the surrounding environments. Some biobased plastics have negligible biodegradability. Therefore, it is necessary to consider the key factors for biodegradation when designing and selecting polymers for certain usage. Furthermore, with the development of nanotechnologies, more and more plastic wastes will be converted and recycled through effective ways, which will greatly facilitate the remediation of plastic waste for a more sustainable future. One thought-provoking question was raised in *Science* in 2021: “How to manage the world’s plastic waste better? Is it possible to create a recyclable material that replaces plastic?”<sup>118</sup> We still have a long way to go to find eco-friendly solutions for the problem of plastic accumulation in the environment. Great efforts are needed to manage plastic wastes effectively and change the habits of plastic disposal.

## References

1. R. Ganesh Saratale, S. K. Cho, G. Dattatraya Saratale, A. A. Kadam, G. S. Ghodake, M. Kumar, R. Naresh Bharagava, G. Kumar, D. Su Kim, S. I. Mulla and H. Seung Shin, *Bioresour. Technol.*, 2021, **325**, 124685.
2. S. M. Al-Salem, A. Antelava, A. Constantinou, G. Manos and A. Dutta, *J. Environ. Manage.*, 2017, **197**, 177–198.
3. O. P. Abioye, A. A. Abioye, S. A. Afolalu and S. O. Ongbali, *Int. J. Mech. Eng. Technol.*, 2018, **9**, 1172–1185.

4. B. Luijsterburg and H. Goossens, *Resour. Conserv. Recycl.*, 2014, **85**, 88–97.
5. D. Mahanta, S. A. Dayanidhi, S. Mohanty and S. K. Nayak, *Polym. Compos.*, 2012, **33**, 2114–2124.
6. N. Ahmad, M. Nasibullah, F. Hassan, S. A. K, P. D. K, K. A. R and M. Rahman, *Int. Res. J. Environ. Sci.*, 2012, **1**(4), 32–36.
7. P. Rai, S. Mehrotra, S. Priya, E. Gnansounou and S. K. Sharma, *Bioresour. Technol.*, 2021, **325**, 124739.
8. T. Degnan and S. L. Shinde, *MRS Bull.*, 2019, **44**, 436–437.
9. S. B. Borrelle, J. Ringma, K. L. Law, C. C. Monnahan, L. Lebreton, A. McGivern, E. Murphy, J. Jambeck, G. H. Leonard, M. A. Hilleary, M. Eriksen, H. P. Possingham, H. De Frond, L. R. Gerber, B. Polidoro, A. Tahir, M. Bernard, N. Mallos, M. Barnes and C. M. Rochman, *Science*, 2020, **369**, 1515–1518.
10. D. K. Barnes, F. Galgani, R. C. Thompson and M. Barlaz, *Philos. Trans. R. Soc., B*, 2009, **364**, 1985–1998.
11. T. Kogel, O. Bjoroy, B. Toto, A. M. Bienfait and M. Sanden, *Sci. Total Environ.*, 2020, **709**, 136050.
12. A. Wahl, C. Le Juge, M. Davranche, H. El Hadri, B. Grassl, S. Reynaud and J. Gigault, *Chemosphere*, 2021, **262**, 127784.
13. Z. Sobhani, X. Zhang, C. Gibson, R. Naidu, M. Megharaj and C. Fang, *Water Res.*, 2020, **174**, 115658.
14. X. Wang, N. Bolan, D. C. W. Tsang, B. Sarkar, L. Bradney and Y. Li, *J. Hazard. Mater.*, 2021, **402**, 123496.
15. H. Qinglan, W. Chang, L. Dingqiang, W. Yao, L. Dan and L. Guiju, *Int. J. Hydrogen Energy*, 2010, **35**, 8884–8890.
16. O. Alarm, M. Billah and D. Yajie, *Resour., Conserv. Recycl.*, 2018, **132**, 121–129.
17. M. Kanniche, R. Gros-Bonnivard, P. Jaud, J. Valle-Marcos, J.-M. Amann and C. Bouallou, *Appl. Therm. Eng.*, 2010, **30**, 53–62.
18. B. Andričić, T. Kovačić and I. Klarić, *Polym. Eng. Sci.*, 2008, **48**, 572–577.
19. R. T. Thomas, V. Nair and N. Sandhyarani, *Colloids Surf., A*, 2013, **422**, 1–9.
20. T. Ahmed, M. Shahid, F. Azeem, I. Rasul, A. A. Shah, M. Noman, A. Hameed, N. Manzoor, I. Manzoor and S. Muhammad, *Environ. Sci. Pollut. Res. Int.*, 2018, **25**, 7287–7298.
21. X. Chen and N. Yan, *Mater. Today Sustain.*, 2020, **7–8**, 100031.
22. Y. Wang, S. Furukawa and N. Yan, *ACS Catal.*, 2019, **9**, 6681–6691.
23. J. Kang, G. Lee, Y.-W. Suh and J. Jung, *J. Nanosci. Nanotechnol.*, 2017, **17**, 8242–8247.
24. S. Yu, E. Kim, S. Park, I. K. Song and J. C. Jung, *Catal. Commun.*, 2012, **29**, 63–67.
25. G. Lee, Y. Jeong, A. Takagaki and J. C. Jung, *J. Mol. Catal. A: Chem.*, 2014, **393**, 289–295.
26. D. Wang, B. Ma, B. Wang, C. Zhao and P. Wu, *Chem. Commun.*, 2015, **51**, 15102–15105.

27. G. Xu, A. Wang, J. Pang, X. Zhao, J. Xu, N. Lei, J. Wang, M. Zheng, J. Yin and T. Zhang, *ChemSusChem*, 2017, **10**, 1390–1394.
28. G. Liang, A. Wang, L. Li, G. Xu, N. Yan and T. Zhang, *Angew. Chem. Int. Ed. Engl.*, 2017, **129**, 3096–3100.
29. X. Zhao, Z. Li, Y. Chen, L. Shi and Y. Zhu, *Appl. Surf. Sci.*, 2008, **254**, 1825–1829.
30. M. Bishai, S. De, B. Adhikari and R. Banerjee, *Food Sci. Biotechnol.*, 2013, **22**, 73–77.
31. P. Ma, D. G. Hristova-Bogaerds, J. G. P. Goossens, A. B. Spoelstra, Y. Zhang and P. J. Lemstra, *Eur. Polym. J.*, 2012, **48**, 146–154.
32. P. Ma, A. B. Spoelstra, P. Schmit and P. J. Lemstra, *Eur. Polym. J.*, 2013, **49**, 1523–1531.
33. R. Zhang, C. Cai, Q. Liu and S. Hu, *J. Polym. Environ.*, 2016, **25**, 1335–1341.
34. L. Filiciotto and G. Rothenberg, *ChemSusChem*, 2021, **14**, 56–72.
35. S. M. Emadian, T. T. Onay and B. Demirel, *Waste Manage.*, 2017, **59**, 526–536.
36. J. P. Eubeler, S. Zok, M. Bernhard and T. P. Knepper, *TrAC, Trends Anal. Chem.*, 2009, **28**, 1057–1072.
37. M. Karamanlioglu, A. Houlden and G. D. Robson, *Int. Biodeterior. Biodegrad.*, 2014, **95**, 301–310.
38. R. Ciriminna and M. Pagliaro, *ChemistryOpen*, 2020, **9**, 8–13.
39. N. Taghavi, I. A. Udugama, W. Q. Zhuang and S. Baroutian, *Biotechnol. Adv.*, 2021, **49**, 107731.
40. F. G. Torres, S. Rodriguez and A. C. Saavedra, *J. Polym. Environ.*, 2019, **27**, 2651–2673.
41. A. Anstey, S. Muniyasamy, M. M. Reddy, M. Misra and A. Mohanty, *J. Polym. Environ.*, 2014, **22**, 209–218.
42. H. A. EI-Shafei, N. H. Abd El-Nasser, A. L. Kansoh and A. M. Ali, *Polym. Degrad. Stab.*, 1998, **62**, 361–365.
43. I. Jakubowicz, *Polym. Degrad. Stab.*, 2003, **80**, 39–43.
44. E. Chiellini, A. Corti and S. D'Antone, *Polym. Degrad. Stab.*, 2007, **92**, 1378–1383.
45. Y. Zheng, J. C. Chen, Y. M. Ma and G. Q. Chen, *Metab. Eng.*, 2020, **58**, 82–93.
46. D. da Silva, M. Kaduri, M. Poley, O. Adir, N. Krinsky, J. Shainsky-Roitman and A. Schroeder, *Chem. Eng. J.*, 2018, **340**, 9–14.
47. J. Nilsen-Nygaard, E. N. Fernandez, T. Radusin, B. T. Rotabakk, J. Sarfraz, N. Sharmin, M. Sivertsvik, I. Sone and M. K. Pettersen, *Compr. Rev. Food Sci. Food Saf.*, 2021, **20**, 1333–1380.
48. L. Zhang, S. H. Goh and S. Y. Lee, *Polymer*, 1998, **39**, 4841–4847.
49. C. L. Simões, J. C. Viana and A. M. Cunha, *J. Appl. Polym. Sci.*, 2009, **112**, 345–352.
50. N. I. Akos, M. U. Wahit, R. Mohamed and A. A. Yussuf, *Polym. Compos.*, 2013, **34**, 763–768.
51. L. Botta, R. Scaffaro, F. Suter and M. C. Mistretta, *Polymers*, 2018, **10**, 18.

52. R. K. Bharadwaj, A. R. Mehrabi, C. Hamilton, C. Trujillo, M. Murga, R. Fan, A. Chavira and A. K. Thompson, *Polymer*, 2002, **43**, 3699–3705.
53. M. Tesfaye, R. Patwa, A. Gupta, M. J. Kashyap and V. Katiyar, *Int. J. Biol. Macromol.*, 2017, **101**, 580–594.
54. R. Pantani, G. Gorrasi, G. Vigliotta, M. Murariu and P. Dubois, *Eur. Polym. J.*, 2013, **49**, 3471–3482.
55. E. Fortunati, M. Peltzer, I. Armentano, A. Jiménez and J. M. Kenny, *J. Food Eng.*, 2013, **118**, 117–124.
56. D. P. Serrano, J. Aguado and J. M. Escola, *ACS Catal.*, 2012, **2**, 1924–1941.
57. T. S. Mdletshe, S. B. Mishra and A. K. Mishra, *J. Appl. Polym. Sci.*, 2015, **132**, 42145.
58. K. Del Angel-Sanchez, C. I. Borbolla-Torres, L. M. Palacios-Pineda, N. A. Ulloa-Castillo and A. Elias-Zuniga, *Polymers*, 2019, **11**, 1955.
59. H. Wang, L. Wang, S. Ye and X. Song, *Food Hydrocolloids*, 2019, **88**, 92–100.
60. V. Goudarzi, I. Shahabi-Ghahfarrokhi and A. Babaei-Ghazvini, *Int. J. Biol. Macromol.*, 2017, **95**, 306–313.
61. T. Narancic and K. E. O'Connor, *Microbiology*, 2019, **165**, 129–137.
62. N. K. Kalita, S. M. Bhasney, C. Mudenur, A. Kalamdhad and V. Katiyar, *Chemosphere*, 2020, **247**, 125875.
63. T. Narancic, S. Verstichel, S. Reddy Chaganti, L. Morales-Gamez, S. T. Kenny, B. De Wilde, R. Babu Padamati and K. E. O'Connor, *Environ. Sci. Technol.*, 2018, **52**, 10441–10452.
64. H. Y. Sintim, S. Bandopadhyay, M. E. English, A. Bary, J. E. Liquey y González, J. M. DeBruyn, S. M. Schaeffer, C. A. Miles and M. Flury, *Geoderma*,
65. H. Y. Sintim, A. I. Bary, D. G. Hayes, M. E. English, S. M. Schaeffer, C. A. Miles, A. Zelenyuk, K. Suski and M. Flury, *Sci. Total Environ.*, 2019, **675**, 686–693.
66. M. González-Pleiter, M. Tamayo-Belda, G. Pulido-Reyes, G. Amariei, F. Leganés, R. Rosal and F. Fernández-Piñas, *Environ. Sci.: Nano*, 2019, **6**, 1382–1392.
67. B. Alexandre, D. Langevin, P. Médéric, T. Aubry, H. Couderc, Q. T. Nguyen, A. Saiter and S. Marais, *J. Membr. Sci.*, 2009, **328**, 186–204.
68. Y. Zare, *Waste Manage.*, 2013, **33**, 598–604.
69. R. David, S. P. Tambe, S. K. Singh, V. S. Raja and D. Kumar, *Surf. Coat. Technol.*, 2011, **205**, 5470–5477.
70. E. Garofalo, L. Di Maio, P. Scarfato, F. Di Gregorio and L. Incarnato, *Polym. Degrad. Stab.*, 2018, **152**, 52–63.
71. M. Entezam, H. A. Khonakdar, A. A. Yousefi, S. H. Jafari, U. Wagenknecht and G. Heinrich, *Mater. Des.*, 2013, **45**, 110–117.
72. M. Biswal, S. Mohanty and S. K. Nayak, *J. Appl. Polym. Sci.*, 2012, **125**, E432–E443.
73. R. S. Chen, S. Ahmad and S. Gan, *Composites, Part B*, 2017, **131**, 91–99.
74. J. Alvarado, G. Acosta and F. Perez, *Polym. Degrad. Stab.*, 2016, **134**, 376–382.

75. S. H. Kim, S.-Y. Kwak and T. Suzuki, *Polymer*, 2006, **47**, 3005–3016.
76. F. Miao, Y. Liu, M. Gao, X. Yu, P. Xiao, M. Wang, S. Wang and X. Wang, *J. Hazard. Mater.*, 2020, **399**, 123023.
77. J. K. Palacios, A. Sangroniz, J. I. Eguiazabal, A. Etxeberria and A. J. Müller, *Eur. Polym. J.*, 2016, **85**, 532–552.
78. N. Touati, M. Kaci, S. Bruzard and Y. Grohens, *Polym. Degrad. Stab.*, 2011, **96**, 1064–1073.
79. N. Petchwattana, S. Covavisaruch and J. Sanetuntikul, *Constr. Build. Mater.*, 2012, **28**, 557–560.
80. M. Khaleghi, K. Didehban and M. Shabanian, *Ultrason. Sonochem.*, 2018, **43**, 275–284.
81. N. Amigo, H. Palza, D. Canales, F. Sepúlveda, D. A. Vasco, F. Sepúlveda and P. A. Zapata, *Composites, Part B*, 2019, **174**, 106979.
82. M. C. Ariza-Tarazona, J. F. Villarreal-Chiu, J. M. Hernandez-Lopez, J. Rivera De la Rosa, V. Barbieri, C. Siligardi and E. I. Cedillo-Gonzalez, *J. Hazard. Mater.*, 2020, **395**, 122632.
83. T. S. Tofa, F. Ye, K. L. Kunjali and J. Dutta, *Catalysts*, 2019, **9**, 819.
84. T. S. Tofa, K. L. Kunjali, S. Paul and J. Dutta, *Environ. Chem. Lett.*, 2019, **17**, 1341–1346.
85. W. R. L. N. Bandara, R. M. de Silva, K. M. N. de Silva, D. Dahanayake, S. Gunasekara and K. Thanabalasingam, *RSC Adv.*, 2017, **7**, 46155–46163.
86. J. Xu, X. Wang, X. Yuan, J. Tao, S. Peng, W. Yang, X. Dong, C. Zhang and Y. Luo, *Polym. Int.*, 2019, **68**, 1332–1340.
87. E. Garofalo, L. Di Maio, P. Scarfato, F. Di Gregorio and L. Incarnato, *Polymers*, 2019, **11**, 830.
88. R. Tankhiwale and S. K. Bajpai, *Colloids Surf., B*, 2012, **90**, 16–20.
89. E.-S. Kim and B. Deng, *J. Membr. Sci.*, 2011, **375**, 46–54.
90. E. Garofalo, P. Scarfato, L. Di Maio and L. Incarnato, *Polym. Compos.*, 2018, **39**, 3157–3167.
91. Y. Shen, *Biomass Bioenergy*, 2020, **134**, 105479.
92. L. Dai, N. Zhou, Y. Lv, Y. Cheng, Y. Wang, Y. Liu, K. Cobb, P. Chen, H. Lei and R. Ruan, *Sci. Total Environ.*, 2021, **782**, 146897.
93. V. G. Pol, *Environ. Sci. Technol.*, 2010, **44**, 4753–4759.
94. S. Chen, Z. Liu, S. Jiang and H. Hou, *Sci. Total Environ.*, 2020, **710**, 136250.
95. J. Gong, X. Chen and T. Tang, *Prog. Polym. Sci.*, 2019, **94**, 1–32.
96. Q. Ma, Y. Yu, M. Sindoro, A. G. Fane, R. Wang and H. Zhang, *Adv. Mater.*, 2017, **29**, 1605361.
97. J. L. Jiang Gong, X. Chen, Z. Jiang, X. Wen, E. Mijowska and T. Tang, *J. Mater. Chem. A*, 2015, **3**, 341–351.
98. L. Gonsalvesh, S. P. Marinov, G. Gryglewicz, R. Carleer and J. Yperman, *Fuel Process. Technol.*, 2016, **149**, 75–85.
99. L. Beesley, E. Moreno-Jimenez, J. L. Gomez-Eyles, E. Harris, B. Robinson and T. Sizmur, *Environ. Pollut.*, 2011, **159**, 3269–3282.
100. M. Maharjan, A. Bhattarai, M. Ulaganathan, N. Wai, M. O. Oo, J.-Y. Wang and T. M. Lim, *J. Power Sources*, 2017, **362**, 50–56.

101. W. S. Fonseca, X. Meng and D. Deng, *ACS Sustainable Chem. Eng.*, 2015, **3**, 2153–2159.
102. Z. W. Ying Bai, C. Wu, R. Xu, F. Wu, Y. Liu, H. Li, Y. Li, J. Lu and K. Amine, *ACS Appl. Mater. Interfaces*, 2015, **7**, 5598–5604.
103. W. Utetiwabo, L. Yang, M. K. Tufail, L. Zhou, R. Chen, Y. Lian and W. Yang, *Chin. Chem. Lett.*, 2020, **31**, 1474–1489.
104. X. Y. Chen, L. X. Cheng, X. Deng, L. Zhang and Z. J. Zhang, *Ind. Eng. Chem. Res.*, 2014, **53**, 6990–6997.
105. L. Gao, F. Zhou, Q. Chen and G. Duan, *ChemistrySelect*, 2018, **3**, 5321–5325.
106. H. Zhang, Y. Liu, T. Meng, L. Ma, J. Zhu, M. Xu, C. M. Li, W. Zhou and J. Jiang, *ACS Sustainable Chem. Eng.*, 2019, **7**, 10995–11003.
107. A. A. Aboul-Enein and A. E. Awadallah, *Polym. Degrad. Stab.*, 2019, **167**, 157–169.
108. R.-X. Yang, S.-L. Wu, K.-H. Chuang and M.-Y. Wey, *Renewable Energy*, 2020, **159**, 10–22.
109. M. Utami, W. Trisunaryanti, K. Shida, M. Tsushida, H. Kawakita, K. Ohto, K. Wijaya and M. Tominaga, *RSC Adv.*, 2019, **9**, 41392–41401.
110. N. E. Zander, M. Gillan and D. Sweetser, *Materials*, 2017, **10**, 1044.
111. J. Zhu, Y. Chen, H.-Y. Yu, Y. Guan, Y. Zhou, X. Yang, Z.-Y. Zou and K. C. Tam, *ACS Sustainable Chem. Eng.*, 2019, **7**, 15537–15547.
112. G. C. de Assis, E. Skovroinski, V. D. Leite, M. O. Rodrigues, A. Galembeck, M. C. F. Alves, J. Eastoe and R. J. de Oliveira, *ACS Appl. Mater. Interfaces*, 2018, **10**, 8077–8085.
113. S. Molina Flores, M. Dumon, P. Elizondo Martinez and M. G. Sanchez Anguiano, *J. Environ. Manage.*, 2020, **271**, 110939.
114. J. Gong, J. Liu, X. Chen, Z. Jiang, X. Wen, E. Mijowska and T. Tang, *J. Mater. Chem. A*, 2015, **3**, 341–351.
115. X. Dong, A. Akram, B. Comesaña-Gándara, X. Dong, Q. Ge, K. Wang, S.-P. Sun, B. Jin and C. H. Lau, *ACS Appl. Polym. Mater.*, 2020, **2**, 2586–2593.
116. D. M. Elsayed, S. M. Abdelbasir, H. M. Abdel-Ghafar, B. A. Salah and S. A. Sayed, *J. Environ. Chem. Eng.*, 2020, **8**, 103826.
117. J. Min, X. Wen, T. Tang, X. Chen, K. Huo, J. Gong, J. Azadmanjiri, C. He and E. Mijowska, *Chem. Commun.*, 2020, **56**, 9142–9145.
118. A. G. Levine, *125 Questions: Exploration and Discovery*, 2021.

## CHAPTER 5

# *Sustainable Nanomaterials for Pollutant Treatment*

VAN-PHUC DINH,<sup>\*a,b</sup> ZIBIAO LI<sup>c,d</sup> AND ENYI YE<sup>c</sup>

<sup>a</sup> Future Materials & Devices Laboratory, Institute of Fundamental and Applied Sciences, Duy Tan University, Ho Chi Minh City 700000, Viet Nam; <sup>b</sup> Faculty of Natural Sciences, Duy Tan University, Da Nang, 550000, Vietnam; <sup>c</sup> Institute of Materials Research and Engineering, Agency for Science, Technology & Research, 2 Fusionopolis Way, Singapore 138634, Singapore; <sup>d</sup> Department of Materials Science and Engineering, National University of Singapore, 9 Engineering Drive 1, Singapore 117576, Singapore  
\*Email: dinhvanphuc@duytan.edu.vn

## 5.1 Introduction

In recent years, industrialization has led to many pressing environmental issues, especially organic compound and heavy toxic metal pollution derived from refining industries, various chemical industries, and the burning of waste containing them. The content of these toxic chemicals over the limited concentration can cause human health problems and living organisms in water. According to the United States Environmental Protection Agency (US EPA) and the International Agency for Research on Cancer (IARC), heavy toxic metals such as arsenic, cadmium, chromium, lead, and mercury at high concentrations are human carcinogens.<sup>1</sup> Therefore, there are different ways for eliminating heavy metals from the environment, including solvent extraction,<sup>2</sup> membrane separation,<sup>3,4</sup> adsorption,<sup>5-8</sup> coagulation,<sup>9-11</sup> ion exchange,<sup>12,13</sup> electrodeposition,<sup>14</sup> and reverse osmosis.<sup>15</sup> Among them, adsorption is well known as a promising method owing to its advantages over

other processes, for example, simple operation, low cost, and a huge number of adsorbents.<sup>16</sup> The adsorbents may be sourced from natural minerals,<sup>17–19</sup> industrial by-products,<sup>20,21</sup> agricultural wastes,<sup>22–26</sup> biomass,<sup>27,28</sup> or nanomaterials.<sup>29–34</sup> Table 5.1 shows a variety of adsorbents used to remove heavy toxic metals and organic compounds from wastewater.

In recent years, nanomaterials have attracted scientists in many areas, especially the treatment of wastewater due to their unique properties. One of the research areas in the field of nanotechnology is increasing their affinity,

**Table 5.1** Maximum adsorption capacities of several adsorbents from different resources.

Material	Adsorbent	Heavy metals/ organic compounds	Maximum capacity (mg g <sup>-1</sup> )	Ref.
Natural minerals	Natural bentonite	Pb(II), Zn(II)	8.55, 7.90	19
	Natural mesoporous goethite	Cr(VI)	0.569	36
	Sodium polyacrylate modified bentonite	Pb(II)	60.79	17
Industrial by- products	Carbonaceous from carbon slurry of fertilizer industry	Ethyl orange, metanil yellow, and acid blue 113	198, 211, and 219	20
Agricultural wastes	Steel slag, iron filings	Phosphate	2.40, 5.37	21
	Pomelo fruit peel	Pb(II), Cd(II), Cr(III), and methylene blue	47.18, 13.35, 11.3, and 218.5	24,25
	Grapefruit ( <i>Citrus paradisi</i> L.)	Cd(II)	52.63	37
Biomass	Activated biomass from cassava peels, groundnut shell, yam peel	Pb(II)	50.1, 46.6, 38.5	27
	Biomass-derived porous carbon from lignin	Pb(II), Cd(II)	250.5, 126.4	28
Metal oxide- based nanomaterials	$\alpha$ -MnO <sub>2</sub> nanoparticles	Pb(II), Fe(III)	124.9, 30.83	38
	$\gamma$ -MnO <sub>2</sub> nanoparticles	Pb(II), Fe(III)	200, 127.6	39
	MnO <sub>2</sub> /chitosan nanocomposites	Zn(II), Pb(II), Cr(VI)	24.21, 126.1, 61.56	32–34
	ZnO nanorods	As(III)	52.63	40
	ZnO nanoparticles	Malachite green; acid fuchsin, and Congo red	2963, 3307, and 1554	41
		Methylene blue	7918.02–9197.70	42
	ZnO and SnO <sub>2</sub> nanoparticles	Malachite Green Oxalate	310.50, 216.90	43
	Fe <sub>2</sub> O <sub>3</sub> , CoO, and NiO nanoparticles	Methylene Blue	1124.70, 5501.93, and 10585	44
	Fe <sub>3</sub> O <sub>4</sub> nanoparticles	Methylene Blue	42.35	30
	MgO nanoparticles	As(III) and F	540.9 and 290.67	45



capacity, and selectivity for heavy metals and other contaminants. In comparison with traditional adsorbents, nanomaterials have much higher efficiencies and faster uptake rates in water treatment due to their high surface area.<sup>35</sup>

## 5.2 Heavy Metals in Wastewater

Mercury, arsenic, lead, cadmium, and chromium are heavy toxic metals, which can contaminate the environment and threaten creatures and humans owing to their toxicity. Effects of these metals on human health have been widely studied and regularly reviewed by the World Health Organization (WHO) and other international environmental organizations.

Arsenic (As), known as the king of poisons, is found in food, water, and environment and exists in various forms: metalloid ( $\text{As}^0$ ), inorganic ( $\text{As}^{3+}$  and  $\text{As}^{5+}$ ), and organic.<sup>46,47</sup> The toxicity of As compounds decreases in the order of inorganic ( $\text{As}^{3+}$  and  $\text{As}^{5+}$ ) > metalloid ( $\text{As}^0$ ) > organic arsenicals.<sup>48</sup> Among them, inorganic arsenic  $\text{As}^{3+}$  is the most toxic species because of its binding to thiol groups of biologically active proteins, with its acute toxicity being attributed to the inhibition of metabolic enzymes. According to the WHO, the limit of the concentration of arsenic in drinking water is  $10 \mu\text{g L}^{-1}$ . The excess of limited concentration causes acute effects, including vomiting, abdominal pain, and diarrhea, and long-term effects, such as cancers of the skin, bladder, and lungs. In particular, it is mutagenic, carcinogenic, and teratogenic.<sup>47</sup>

Mercury (Hg) can exist in air, water, and soil and is present in three forms: elemental or metallic mercury ( $\text{Hg}^0$ ), inorganic mercury ( $\text{Hg}^+$ ,  $\text{Hg}^{2+}$ ), and organic mercury (commonly methyl or ethyl mercury). The toxicity of mercury compounds decreases in the order of organic mercury > inorganic mercury > metallic mercury.<sup>49</sup> According to the WHO, the limit of the total concentration of mercury in water is  $1 \mu\text{g L}^{-1}$ .

Lead ( $\text{Pb(II)}$ ) is a naturally toxic metal found in the Earth's crust and generated by industrial activities, such as metal plating, metal processing, ceramic and glass industries, petroleum refining, battery manufacture, tetraethyl lead manufacturing, and leather tanning.<sup>50</sup> According to the WHO, the limit of the concentration of  $\text{Pb(II)}$  in water is  $0.01 \text{ mg L}^{-1}$ .  $\text{Pb(II)}$  causes serious illnesses, such as anemia, encephalopathy, and hepatitis.<sup>33</sup>

Cadmium( $\text{II}$ ) is generated by both natural and human activities, such as volcanic activity, tobacco smoking, mining, smelting, manufacture of phosphate fertilizers, and recycling of cadmium-plated steel scrap and electric and electronic waste.<sup>51</sup> According to the WHO, the limit of the concentration of cadmium( $\text{II}$ ) in drinking water is  $0.003 \text{ mg L}^{-1}$ . An excess of this concentration causes diseases such as renal disturbances, bone lesions, lung insufficiency, hypertension, cancer, anemia, encephalopathy, and hepatitis in humans.<sup>33,37,52-54</sup>

Chromium is used in various industries, including chrome plating, leather tanning, electroplating, and manufacture of pigments and paints,<sup>55,56</sup>

leading to the release of a large amount of this metal into the environment. Despite the existence of both chromium(vi) and chromium(iii) compounds in aqueous solution, Cr(iii) is less poisonous than Cr(vi) due to its physical and biochemical properties.<sup>57</sup> Chromium(vi) has high toxicity and is a strong oxidizing agent that moves easily through soils and aquatic environments and is absorbed through the skin. According to the WHO, the limit of the concentration of Cr(vi) in drinking water is  $0.05 \text{ mg L}^{-1}$ . A superabundance of chromium(vi) causes acute effects, including gastrointestinal disorders, hemorrhagic diathesis, and convulsions, and it is carcinogenic to humans.<sup>58</sup>

## 5.3 Mechanisms of the Adsorption of Contaminants From Wastewater Using Nanomaterials

### 5.3.1 Isotherm Adsorption Models

Commonly, in order to understand the adsorption of contaminants in nature, Langmuir and Freundlich isotherm models have been applied. Langmuir isotherm describes the equilibrium between adsorbate and adsorbent systems, where the adsorbate adsorption is limited to one molecular layer (also called monolayer adsorption). It means that the adsorption is homogeneous, and all sites possess an equal affinity for the adsorbates. In addition, there is no interaction between all adsorbates. In contrast, Freundlich isotherm describes non-ideal and reversible adsorption, and it is not restricted to the formation of a monolayer (also called multi-layer adsorption). This model refers a heterogeneous adsorption. These models are given as follows as non-linear equations:

Langmuir non-linear isotherm:<sup>59,60</sup>

$$Q_e = \frac{Q_m \cdot K_L \cdot C_e}{1 + K_L \cdot C_e}, \quad (5.1)$$

Freundlich non-linear isotherm:<sup>60,61</sup>

$$Q_e = K_F \cdot C_e^{1/n} \quad (5.2)$$

Here,  $Q_e$  ( $\text{mg g}^{-1}$ ) is the amount of adsorbate in the adsorbent at equilibrium and  $Q_m$  ( $\text{mg g}^{-1}$ ) is the maximum monolayer adsorption capacity;  $K_L$  ( $\text{L mg}^{-1}$ ) is the Langmuir isotherm constant;  $K_F$  [ $(\text{mg g}^{-1}) (\text{L mg}^{-1})^{1/n}$ ] is the Freundlich isotherm constant; and  $n$  is the heterogeneity factor.

Notably, to investigate the isotherm adsorption, a range of experiments with different concentrations from low to high are carried out. This restricted the application of these models because the Langmuir model is suitable for high concentrations, whereas the Freundlich model is satisfied with a low concentration.<sup>62</sup> Therefore, the Sips model, which was formed by combining Langmuir and Freundlich models, circumvents this limitation. This isotherm is presented as:

Sips non-linear isotherm:<sup>60,63</sup>

$$Q_e = \frac{Q_s \cdot C_e^{\beta_s}}{1 + \alpha_s \cdot C_e^{\beta_s}}, \quad (5.3)$$

where  $Q_s$  ( $\text{L g}^{-1}$ ) and  $\alpha_s$  ( $\text{L mg}^{-1}$ ) are the Sips isotherm model constants and  $\beta_s$  is the Sips isotherm model exponent.

### 5.3.2 Kinetic Adsorption Models

Kinetic studies play an essential role in giving information related to adsorption pathways and the probable mechanisms involved. Some commonly used kinetic models are pseudo-first-order, pseudo-second-order, and intra-diffusion models.<sup>25,64</sup>

#### 5.3.2.1 Pseudo-first-order Kinetic Model

This model is applied to determine the adsorption rate of a sorbent onto a sorbate and its non-linear form is written as follows:

$$Q_t = Q_e (1 - e^{-k_1 t}), \quad (5.4)$$

where  $Q_t$  ( $\text{mg g}^{-1}$ ) and  $Q_e$  ( $\text{mg g}^{-1}$ ) are the adsorption capacity at time  $t$  (min) and at the equilibrium, respectively.  $k_1$  ( $\text{min}^{-1}$ ) is the equilibrium rate constant in the pseudo-first-order model.

#### 5.3.2.2 Pseudo-second-order Kinetic Model

This model suggests that the rate-limiting step is chemisorption, and the uptake rate is dependent on adsorption capacity without the concentration of adsorbate. The non-linear form of this model is written as follows:

$$Q_t = \frac{Q_e^2 \cdot k_2 \cdot t}{1 + k_2 \cdot Q_e \cdot t}, \quad (5.5)$$

where  $k_2$  ( $\text{min}^{-1}$ ) is the equilibrium rate constant of the pseudo-second-order model.

#### 5.3.2.3 Weber and Morris Kinetic Model

In order to determine the diffusion mechanism in the adsorption, Weber and Morris proposed the intra-diffusion model, the equation of which is presented as follows:

$$Q_t = k_d t^{1/2} + C, \quad (5.6)$$

where  $k_d$  ( $\text{mg g}^{-1} \text{min}^{-1/2}$ ) is the intraparticle diffusion rate constant. The  $C$  ( $\text{mg g}^{-1}$ ) value, providing information about the thickness of the boundary

layer, is evaluated from the slope and intercept of the regression line. If the  $C$  value differs from zero, this plot of  $Q_t$  versus  $t$  does not pass through the origin. This indicates that the adsorption is affected by various mechanisms.

### 5.3.3 Data Analysis

Since the isotherm and kinetic models used are non-linear forms, mathematical error functions as the RMSE (root mean square error) and chi-square  $\chi^2$  are used to predict the correlation between experimental data and theoretical models. These values are calculated by using the following equations:<sup>62</sup>

$$\text{RMSE} = \sqrt{\frac{1}{(n-1)} \sum_{n=1}^n (Q_{e,\text{meas}} - Q_{e,\text{calc}})^2}, \quad (5.7)$$

$$\chi^2 = \sum_{n=1}^n \frac{(Q_{e,\text{meas}} - Q_{e,\text{calc}})^2}{Q_{e,\text{calc}}}, \quad (5.8)$$

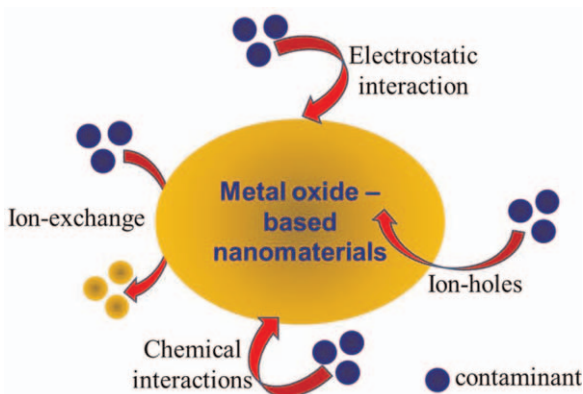
in which  $Q_{e,\text{meas}}$  ( $\text{mg g}^{-1}$ ) is the experimental adsorption capacity and  $Q_{e,\text{calc}}$  ( $\text{mg g}^{-1}$ ) is the theoretical adsorption capacity. To determine these values, the least-squares method is applied based on the solver add-in function in Microsoft Excel. In addition, using the calculated RMSE and  $\chi^2$  values, we can indicate the best suitable model, namely, the model that gives the best fit with experimental data when the RMSE and  $\chi^2$  values are the smallest.

### 5.3.4 Spectroscopy Methods

During adsorption, the uptake of contaminants occurs in four stages:<sup>65,66</sup> (1) adsorbates are transferred from the bulk solution to the boundary film surrounding the nanomaterials (called bulk diffusion); (2) adsorbates diffuse from the boundary layer to the external surface (called external transfer); (3) during the first two stages, the adsorbates transfer to the material's surface *via* van der Waals interactions,<sup>67,68</sup> but in the third stage, the diffusion of adsorbates to the pores of the nanomaterials occurs (called internal transfer); (4) in the last stage, the adsorbates interact with active adsorption sites *via* physical and/or chemical interactions, as shown in Figure 5.1.

#### 5.3.4.1 Electrostatic Interaction

It occurs between a negative surface of nanomaterials and heavy metal cations when the point of zero charge ( $\text{pH}_{\text{PZC}}$ ) of nanomaterials is smaller than the pH of heavy ion solutions. In a study by Zhang *et al.*<sup>42</sup> about the adsorption of methylene blue (MB) on ZnO nanoparticles, the  $\text{pH}_{\text{PZC}}$  of this material was  $10.1 \pm 0.6$ . The surface of ZnO nanoparticles was charged positively when pH of solution was smaller than  $\text{pH}_{\text{PZC}}$ . This led to the



**Figure 5.1** Proposed mechanisms of the adsorption of heavy metals using nanomaterials.

formation of the electrostatic force between ZnO and MB that was favorable to the adsorption of MB.

#### 5.3.4.2 Ion Exchange

This mechanism is formed between unwanted dissolved ions in water and wastewater with other similarly charged ions. Metal oxide nanomaterials include hydroxyl groups ( $\text{OH}^-$ ) on the surface that are easily exchanged with anions. By using Fourier transform infrared [FT-IR] and X-ray photoelectron spectroscopy (XPS) analyses, Du *et al.*<sup>69</sup> confirmed that ion exchange between hydroxyl groups ( $\text{OH}^-$ ) on the surface of  $\text{MnO}_2$  nanoparticles and Cr(vi) or As(v) species ( $\text{Cr}_2\text{O}_7^{2-}$ ,  $\text{HCrO}_4^-$ ,  $\text{H}_2\text{AsO}_4^-$ , or  $\text{HAsO}_4^{2-}$ ) was through the Cr(vi) or As(v) adsorption mechanism.

#### 5.3.2.4 Chemical Interactions

Metal oxide nanoparticles can interact with contaminants *via* chemical bonds, such as ionic bonding or complexation. By using XPS analysis, Zhang *et al.*<sup>42</sup> demonstrated that the ionic bonding was mainly considered as the interaction between  $\text{Zn}^{2+}$  in  $\text{Zn}(\text{OH})^+$  and sulfonic groups ( $-\text{SO}_3^-$ ) in MB. In another research, Zhang *et al.*<sup>41</sup> reported that the primary mechanism of the malachite green (MG) removal of ZnO nanoparticles was the chemical precipitation generated from the interaction between  $\text{Zn}(\text{OH})^+$  and MG, whereas ionic bonding played an instrumental role in the adsorption of acid fuchsin (AF) anionic dye onto ZnO nanoparticles. These findings were confirmed by FT-IR and XPS analyses.

#### 5.3.2.5 Ion Holes

Many metal oxide nanomaterials have many defects, porous structures, tunnels, or frameworks in their structures. These are beneficial for

absorbing heavy metals or organic compounds having smaller diameters or sizes because these contaminants can fall into them. This mechanism can be confirmed using positron lifetime spectroscopy.<sup>33,70–73</sup>

In order to confirm the proposed mechanisms above, FT-IR, thermogravimetry and differential scanning calorimetry (TG-DSC), and X-ray diffraction (XRD) methods have been applied.

### 5.3.2.6 FT-IR Spectroscopy

FT-IR applies the mathematical Fourier transform to translate raw data (interferogram) into an actual spectrum. The FT-IR technique is utilized to identify the occurrence of different functional groups present in a sample. An FT-IR spectrum is a resultant signal obtained at the detector from 4000 to 400  $\text{cm}^{-1}$  for mid-IR region wavelength. The FT-IR spectra of oxide nanomaterials present some common vibration bands, which present different functional groups of materials. Namely, the bands in the regions of 3800–3200  $\text{cm}^{-1}$  and 1700–1600  $\text{cm}^{-1}$  are related to the –OH groups in adsorbed water molecules,<sup>74</sup> whereas peaks located in the region of 1000–400  $\text{cm}^{-1}$  correspond with the metal–oxygen bonds. Table 5.2 presents characteristic peaks of some metal oxide nanoparticles.

Comparison of the FT-IR spectra of oxide nanomaterials before and after the adsorption of heavy metals can reveal information about the adsorption mechanisms. If there is a change in the intensity of characteristic vibrations with or without a small shift of wavenumbers, the adsorption follows physical mechanisms. Herein, the electrostatic interaction plays an instrumental role. In contrast, if there is a significant shift of wavenumbers or a formation of new peaks after the uptake, chemical mechanisms, such as surface precipitation or ion exchange or complexation, control the adsorption. For instance, Yuvaraja *et al.*<sup>40</sup> found that after the As(III) adsorption onto ZnO, the intensity of peak at 3415  $\text{cm}^{-1}$  related with –OH and –NH<sub>2</sub> stretching vibrations increased due to the electrostatic interaction between the negative surface of ZnO nanoparticles at  $\text{pH}_{\text{solution}} = 7.0$  higher than  $\text{pH}_{\text{PZC}} = 6.5$  and As(III) cations. Furthermore, the shift of peaks concerned with –NH<sub>2</sub> bending and C–O stretching vibrations from 1659  $\text{cm}^{-1}$  and 1019  $\text{cm}^{-1}$  to 1618  $\text{cm}^{-1}$  and 1032  $\text{cm}^{-1}$ , respectively, suggested the involvement of these functional groups in binding As(III). Another example is that Gao *et al.* ascertained the formations of As–O and Mg–F bonds after As(III) and F removal by a MgO nanomaterial because their related new peaks were observed at the wavenumbers of 820  $\text{cm}^{-1}$  and 530  $\text{cm}^{-1}$  in the FT-IR spectra.

### 5.3.2.7 TG–DSC Analysis

DSC and thermogravimetric analysis (TGA) are two common thermal analysis techniques, which are used to understand thermal phenomena associated with nanomaterials when they are heated under predetermined heating rate and temperature conditions. DSC provides qualitative and

**Table 5.2** Specific FT-IR peaks of metal oxide nanoparticles.

Metal oxide nanoparticles	-OH groups in adsorbed water molecules ( $\text{cm}^{-1}$ )		Metal-oxygen bonds ( $\text{cm}^{-1}$ )	Ref.
MgO	3450	1634; 1012	836; 652	75
	3420	1450	426	76
	3438	1644	424	45
	3697		854	77
	3434	1430	520	78
ZnO			750; 520	41
	3449	1615	460	79
	3435	1630	507; 423	80
$\delta$ -MnO <sub>2</sub>	3410	1628	518	81
Birnessite-type MnO <sub>2</sub>	3433	1635	517; 487	82
MnO nanorods	3442	1636	630; 525	83
FeFe <sub>2</sub> O <sub>4</sub>	3138	1637	838; 796; 618	30
Fe <sub>3</sub> O <sub>4</sub>	3160–3430	1652	570–585	84
$\alpha$ -Fe <sub>2</sub> O <sub>3</sub>	3431	1631	577; 631	85
	3400		536; 450	86
		1670	602; 545; 465	87
TiO <sub>2</sub>	3240	1620	500; 430	88
	3424	1641	679; 518	89
	3354	1628	1024; 493	90
	3450		696	91
$\gamma$ -Al <sub>2</sub> O <sub>3</sub>	3200–3700	1638; 1470	873; 435	92
	3451	1630	881; 757; 558	93
$\alpha$ -Al <sub>2</sub> O <sub>3</sub>	3447	1617	811	93
			577	94

quantitative information regarding the thermal properties of solid materials, such as the melting and degradation temperatures, glass transition temperature, melt and crystallization enthalpy, specific and latent heats, polymorphism, and purity of the materials, whereas TGA is applied for determining the mass loss when a sample is heated, cooled, or kept at a constant temperature in a controlled atmosphere.<sup>95</sup> Observation of the change in TGA–DSC curves before and after the uptake of contaminants can determine the adsorption mechanisms. For instance, Sabela *et al.*<sup>96</sup> investigated the Cu(II) adsorption mechanism of activated carbon (AC) by using the TG–DSC method. Obviously, the loss of weight after the adsorption (40.38%) was higher than before the adsorption (16.08%). In addition, an exothermic peak before the adsorption at the temperature range from 600 to 800 °C was shifted to a higher temperature range of from 800 to 1000 °C, caused by the formation of CuO onto the AC surface.

## 5.4 Metal Oxide Nanomaterials

Metal oxide nanomaterials used as adsorbents have attracted much attention from researchers, owing to their large specific surface; high adsorption capacity; catalytic activity; and magnetic, optical, and thermal properties.<sup>29,42,97,98</sup> Recently, several metal-oxide nanomaterials have been studied for the

treatment of heavy metals and organic compounds from aqueous solutions, such as manganese dioxide, iron oxide, zinc oxide, and magnesium oxide nanomaterials.

### 5.4.1 MnO<sub>2</sub> Nanomaterials

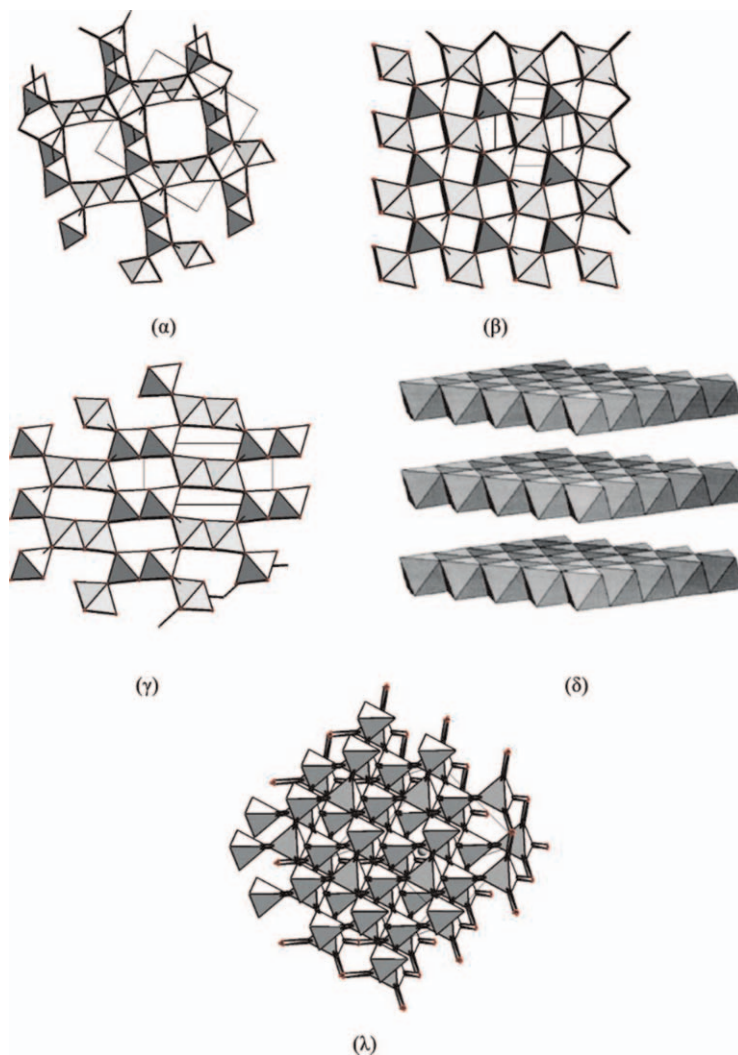
MnO<sub>2</sub> nanomaterials are identified as promising materials owing to their low cost, high stability, environmental compatibility, and abundant availability. MnO<sub>2</sub> has a variety of structures including tunnel structures ( $\alpha$ ,  $\beta$ ,  $\gamma$ , and  $\delta$ ) and layer structure ( $\lambda$ ), as presented in Figure 5.2.<sup>99</sup> According to the tunnel structure, the difference between these structural forms is the dimension of tunnels surrounded by chains of [MnO<sub>6</sub>] octahedral.  $\alpha$ -MnO<sub>2</sub> includes both (2×2) and (1×1) tunnels, and  $\beta$ -MnO<sub>2</sub> displays (1×1) tunnels, while  $\gamma$ -MnO<sub>2</sub> consists of a mixture of (1×1) and (1×2) tunnels. The large tunnels, for example, in a (2×2) tunnel of  $\alpha$ -MnO<sub>2</sub>, can offer sites for the intercalation of large ions (Ba<sup>2+</sup>, K<sup>+</sup>, Pb<sup>2+</sup>, Ca<sup>2+</sup>, Na<sup>+</sup>) and water molecules, whereas small tunnels can be occupied by small cations such as H<sup>+</sup> or Li<sup>+</sup>, for instance, a (1×1) tunnel in  $\beta$ -MnO<sub>2</sub>.<sup>100</sup> Therefore, MnO<sub>2</sub> nanomaterials have been applied to remove many contaminants from wastewater.

Pb(II), Fe(III), Cu(II), and Co(II) are common heavy metals in wastewater. Dinh *et al.* successfully synthesized  $\gamma$ - and  $\alpha$ -MnO<sub>2</sub> nanomaterials and applied them to remove these metals from aqueous solution.<sup>31,38,39</sup> The obtained results showed that  $\gamma$ -MnO<sub>2</sub> nanomaterials adsorbed these metals better than  $\alpha$ -MnO<sub>2</sub> nanomaterials because of their higher surface area. The order of increase in maximum adsorption capacities is  $83.33 < 90.91 < 127.6 < 200 \text{ mg g}^{-1}$  for Cu(II) < Co(II) < Fe(III) < Pb(II), respectively. Adsorption isotherm and kinetic studies presented that the experimental data gave the best fit with the Sips isotherm model and the uptakes of these metals were controlled by the pseudo-second-order model. However, the  $C$  values calculated from intra-diffusion models being different from zero suggested that the uptake of Pb(II), Fe(III), Cu(II), and Co(II) onto  $\gamma$ - and  $\alpha$ -MnO<sub>2</sub> nanomaterials followed different mechanisms.

Generally, electrostatic interaction is usually involved in the adsorption of heavy metal ions on MnO<sub>2</sub> nanomaterials. However, in these studies above reported by Dinh *et al.*,<sup>31,38,39</sup> this mechanism could not occur because of the material's surface charged positively similar to cations at pH<sub>solution</sub> smaller than pH<sub>PZC</sub>. Therefore, a new mechanism (called “ion-holes”) was proposed in another report by Dinh *et al.*,<sup>33</sup> where  $\gamma$ -MnO<sub>2</sub> includes many tunnels and porous holes that are bigger than the average radius of these cations, leading to those cations falling into the holes, as in Figure 5.3. This mechanism was demonstrated by using positron lifetime measurements.

In another report, Wang *et al.*<sup>101</sup> used  $\delta$ -MnO<sub>2</sub> to remove As(V). The uptake of this metal was simulated by the Freundlich model with a high correlation coefficient ( $R^2 = 0.983$ ). The maximum adsorption capacity of  $\delta$ -MnO<sub>2</sub> toward As(V) as calculated from the Langmuir models was  $213.2 \text{ mg g}^{-1}$  at pH 7.0 and 298 K. The As(V) adsorption mechanisms were confirmed using

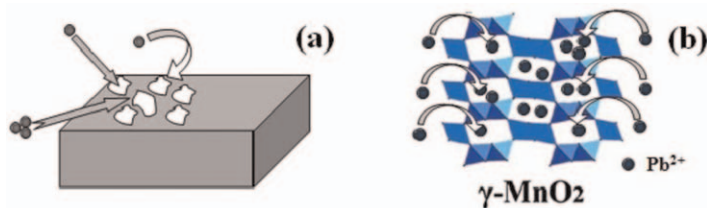




**Figure 5.2** Various Crystallographic Structures of  $\text{MnO}_2$  nanomaterials. Reproduced from ref. 99 with permission from American Chemical Society, Copyright 2008.

FT-IR and XPS analyses. The results indicated that  $\text{As(V)}$  strongly interacts with the Mn-O lattice due to the disappearance of two peaks at  $520$  and  $460\text{ cm}^{-1}$  and the formation of a new peak at  $902\text{ cm}^{-1}$  in the FT-IR spectrum. This finding was consistent with XPS analysis.

The organic adsorption ability of  $\text{MnO}_2$  nanoparticles has been investigated by many researchers.  $\text{MnO}_2$  microspheres used by Chen *et al.*<sup>102</sup> to remove MB from aqueous solution at  $80\text{ }^\circ\text{C}$  displayed the highest adsorption capacity at  $259.2\text{ mg g}^{-1}$ . In a comparative study of MB removal from aqueous solution, Dinh *et al.*<sup>29</sup> showed that the maximum adsorption



**Figure 5.3** “Ion-holes” mechanism for removing  $\text{Pb}^{2+}$ . Reproduced from ref. 33 with permission from Elsevier, Copyright 2018.

capacity of  $\gamma\text{-MnO}_2$  was nearly triple that of  $\alpha\text{-MnO}_2$  nanoparticles. Hu *et al.*<sup>103</sup> utilized  $\text{MnO}_2$  hollow spheres as a potential adsorbent to effectively remove methyl orange (MO) from wastewater with  $1677.14 \text{ mg g}^{-1}$  of maximum adsorption capacity at the optimal condition.

Recently, in order to enhance the potential application of  $\text{MnO}_2$  nanomaterials for the treatment of contaminants from wastewater, these materials have been modified with AC or organic compounds, such as poly(3,4-propylenedioxythiophene),<sup>16</sup> chitosan,<sup>32–34,104</sup> powder AC or nanocarbon,<sup>105–107</sup> biochar,<sup>108,109</sup> polydopamine/ $\text{Fe}_3\text{O}_4$ ,<sup>110</sup> and poly(vinyl alcohol).<sup>111</sup> From the obtained results, it can be observed that the adsorption capacities were clearly increased after the modification. For example, the maximum adsorption capacity of  $\text{MnO}_2$ -biochar composites for  $\text{Cu(II)}$  was  $142.02 \text{ mg g}^{-1}$ , which was greater than that of  $\text{MnO}_2$  nanoparticles ( $93.91 \text{ mg g}^{-1}$ ).<sup>108</sup>

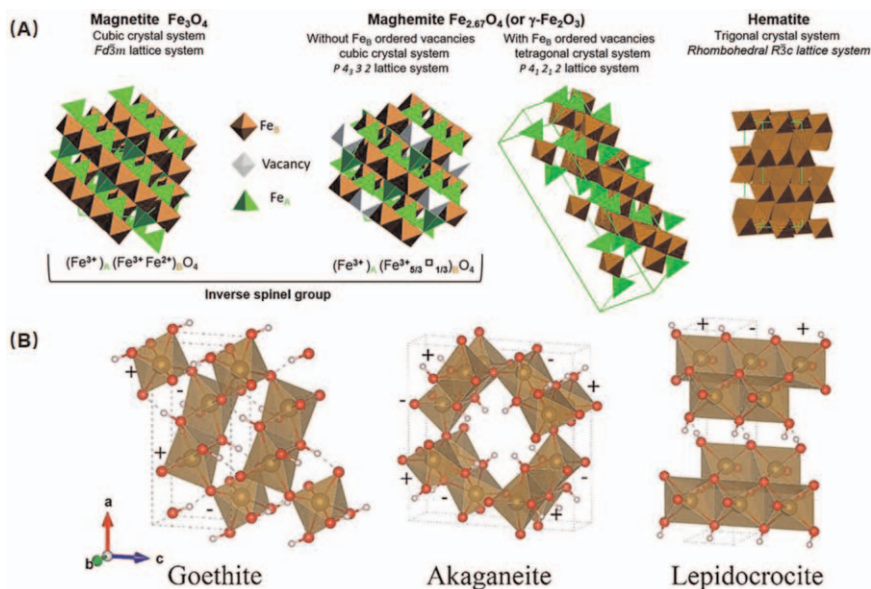
## 5.4.2 Iron Oxide Nanomaterials

Many different forms of iron oxide, such as goethite, magnetite, and hematite (as shown in Figure 5.4),<sup>112,113</sup> have been used as adsorbents by many researchers for the removal of metallic pollutants from aqueous solutions and industrial effluents. Among them, magnetic iron oxide nanomaterial has been considered one of the potential materials because of its magnetic properties, high surface area, chemical stability, easy synthesis, and low toxicity.<sup>84</sup>

In a study, Rajput *et al.*<sup>84</sup> used  $\text{Fe}_3\text{O}_4$  nanoparticles to remove  $\text{Cr(VI)}$  and  $\text{Pb(II)}$  from aqueous solution. The experimental data gave the best fit with the Langmuir and Sips models and the uptakes of both metals followed the pseudo-second-order kinetic model. The maximum Langmuir adsorption capacities were  $34.87 \text{ mg g}^{-1}$  for  $\text{Cr(VI)}$  and  $53.11 \text{ mg g}^{-1}$  for  $\text{Pb(II)}$  at  $45^\circ\text{C}$ .

In another report, Zhang *et al.*<sup>114</sup> also used this material to remove a mixed solution containing coexistent  $\text{Cr(VI)}$  and  $\text{Cu(II)}$ . The maximum adsorption capacities were  $8.67 \text{ mg g}^{-1}$  and  $18.61 \text{ mg g}^{-1}$  for  $\text{Cr(VI)}$  and  $\text{Cu(II)}$ , respectively, under the investigated conditions.

In a study about the removal of  $\text{As(V)}$  and  $\text{Cu(II)}$ , Iconaru *et al.*<sup>115</sup> compared the two metal's adsorption ability of commercial analogous  $\text{Fe}_3\text{O}_4\text{-CA}$  and  $\text{Fe}_3\text{O}_4$  nanoparticles. Obtained results showed that  $\text{Fe}_3\text{O}_4\text{-NPs}$  remove  $\text{As(V)}$  better than  $\text{Fe}_3\text{O}_4\text{-CA}$  by approximately two times, while the  $\text{As(V)}$



**Figure 5.4** The different phases of iron oxyhydroxides, (A) Reproduced from ref. 112 with permission from the Royal Society of Chemistry, and (B) Reproduced from ref. 113 with permission from Elsevier, Copyright 2019.

maximum adsorption capacity of  $\text{Fe}_3\text{O}_4$ -NPs is similar to that of  $\text{Fe}_3\text{O}_4$ -CA. Spectroscopic methods (FT-IR, Raman) were employed to confirm the mechanisms of As(v) and Cu(II) onto the  $\text{Fe}_3\text{O}_4$ -NPs surface.

Furthermore, magnetic iron oxide nanomaterial has been applied to remove dye effectively. For example, Dinh *et al.*<sup>30</sup> employed  $\text{FeFe}_2\text{O}_4$  nanoparticles to treat methylene blue (MB) with  $42.35 \text{ mg g}^{-1}$  of the maximum adsorption capacity at  $\text{pH} = 10$  and adsorption time =  $80^\circ \text{C}$  at room temperature. The MB adsorption mechanisms of this material were discussed based on theoretical models and spectroscopies (FT-IR and TGA-DSC). Meanwhile, Damasceno *et al.*<sup>116</sup> compared the removal of indigo carmine (IC) dye on commercial magnetite nanoparticles (NP-COM) and superparamagnetic magnetite nanoparticles (NP-SYN). Results showed that NP-SYN adsorbed IC better than NP-COM by roughly three times with the same conditions ( $6.12 \text{ mg g}^{-1}$  for NP-COM and  $14.45 \text{ mg g}^{-1}$  for NP-SYN).

### 5.4.3 Zinc Oxide Nanomaterials

Recently, zinc oxide nanomaterials have been receiving attention due to their large surface area and high catalytic activity. The adsorption behavior and mechanism of methylene blue (MB) on zinc oxide nanoparticles were reported by Fan *et al.*<sup>42</sup> The studied results revealed the potential application of this material due to the highest MB adsorption capacity of  $10.70 \pm 0.8 \text{ mmol g}^{-1}$ . The adsorption mechanisms of MB were proposed

based on the combination of isotherm and kinetic models and the XPS method. The results proved that  $\text{Zn}^{2+}$  in  $\text{Zn}(\text{OH})^+$  and sulfonic ( $-\text{SO}_3^-$ ) groups in MB were the major functional groups, and ionic bonding played the main role in the uptake mechanism of MB.

In a different study, Fan *et al.*<sup>41</sup> showed the high adsorption capability and selectivity of ZnO nanoparticles for three dyes, namely, MG, AF, and Congo red (CR). The maximum adsorption capacities were 2963, 3307, and 1554  $\text{mg g}^{-1}$  for MG, AF, and CR, respectively. Studying adsorption mechanisms indicated the uptake of these dyes controlled by chemical precipitation, electrostatic attraction, and hydrogen bonding.

## 5.5 Conclusions

In this chapter, the use of metal oxide nanomaterials, especially  $\text{MnO}_2$ ,  $\text{Fe}_3\text{O}_4$ , and ZnO nanoparticles, as novel adsorbents to remove contaminants from aqueous solution has been discussed. From the obtained results, it is clear that metal oxide nanomaterials are potential and promising adsorbents for the treatment of heavy toxic metals as well as organic compounds from wastewater. Furthermore, the adsorption mechanisms are discussed in detail by the combination of isotherm and kinetic models and spectroscopy methods.

## References

1. P. B. Tchounwou, C. G. Yedjou, A. K. Patlolla and D. J. Sutton, *Exper. Suppl.*, 2012, **101**, 133–164.
2. J. H. Luo, J. Li, Y. B. Qi and Y. Q. Cao, *Desalin. Water Treat.*, 2013, **51**, 2130–2134.
3. S. K. Mondal and P. Saha, *Chem. Eng. Res. Des.*, 2018, **132**, 564–583.
4. J. Wang, Z. Wu, T. Li, J. Ye, L. Shen, Z. She and F. Liu, *Chem. Eng. J.*, 2018, **334**, 579–586.
5. S. O. Owalude and A. C. Tella, *Beni-Suef University J. Basic Appl. Sci.*, 2016, **5**, 377–388.
6. A. Ali, K. Saeed and F. Mabood, *Alexandria Eng. J.*, 2016, **55**, 2933–2942.
7. M. A. Khan, Z. A. Alothman, M. Naushad, M. R. Khan and M. Luqman, *Desalin. Water Treat.*, 2015, **53**, 515–523.
8. E. Altıntig, H. Altundag, M. Tuzen and A. Sari, *Chem. Eng. Res. Des.*, 2017, **122**, 151–163.
9. G. Qin, M. J. McGuire, N. K. Blute, C. Seidel and L. Fong, *Environ. Sci. Technol.*, 2005, **39**, 6321–6327.
10. A. Esmaili, E. Hejazi and A. H. Hassani, *Water, Air, Soil Pollut.*, 2014, **225**, 2140.
11. N. W. Zainon Najib, F. M. Ridwan, A. M. Syakirah and B. S. Lim, *Study of Methylene Blue Color Removal Effectiveness by Moringa Oleifera and Alum*, 2012.
12. S. Rengaraj, K.-H. Yeon and S.-H. Moon, *J. Hazard. Mater.*, 2001, **87**, 273–287.

13. L. Rafati, A. H. Mahvi, A. R. Asgari and S. S. Hosseini, *Int. J. Environ. Sci. Technol.*, 2010, **7**, 147–156.
14. R. Giovanardi and G. Orlando, *Surf. Coat. Technol.*, 2011, **205**, 3947–3955.
15. A. Çimen, *Russ. J. Phys. Chem. A*, 2015, **89**, 1238–1243.
16. R. Jamal, L. Zhang, M. Wang, Q. Zhao and T. Abdiryim, *Prog. Nat. Sci.: Mater. Int.*, 2016, **26**, 32–40.
17. Y.-G. Chen, R.-P. Liao, C. Yu and X. Yu, *Adv. Powder Technol.*, 2020, **31**, 3274–3286.
18. M. Zbair, Z. Anfar and H. A. Ahsaine, *RSC Adv.*, 2019, **9**, 5756–5769.
19. A. Esmaeili and H. Eslami, *MethodsX*, 2019, **6**, 1979–1985.
20. A. K. Jain, V. K. Gupta, A. Bhatnagar and Suhas, *J. Hazard. Mater.*, 2003, **101**, 31–42.
21. B. M. Sellner, G. Hua, L. M. Ahiablame, T. P. Trooien, C. H. Hay and J. Kjaersgaard, *Environ. Technol.*, 2019, **40**, 756–767.
22. J. Anwar, U. Shafique, Z. Waheeduz, M. Salman, A. Dar and S. Anwar, *Bioresour. Technol.*, 2010, **101**, 1752–1755.
23. S. S. Ahluwalia and D. Goyal, *Eng. Life Sci.*, 2005, **5**, 158–162.
24. V.-P. Dinh, T. D. Xuan, N. Q. Hung, T.-T. Luu, T.-T.-T. Do, T. D. Nguyen, V.-D. Nguyen, T. T. K. Anh and N. Q. Tran, *Environ. Sci. Pollut. Res.*, 2021, **28**, 63504–63515.
25. V.-P. Dinh, T.-D.-T. Huynh, H. M. Le, V.-D. Nguyen, V.-A. Dao, N. Q. Hung, L. A. Tuyen, S. Lee, J. Yi, T. D. Nguyen and L. V. Tan, *RSC Adv.*, 2019, **9**, 25847–25860.
26. A. Herrera, C. Tejada-Tovar and Á. D. González-Delgado, *ACS Omega*, 2020, **5**, 23645–23653.
27. C. O. Thompson, A. O. Ndukwe and C. O. Asadu, *Emerging Contam.*, 2020, **6**, 259–267.
28. A. Wang, Z. Zheng, R. Li, D. Hu, Y. Lu, H. Luo and K. Yan, *Green Energy Environ.*, 2019, **4**, 414–423.
29. V.-P. Dinh, T.-H. Ho, T.-T. Luu, H.-N. Vo, T.-T.-T. Do, T.-H. Trinh and H.-B.-S.-L. Nguyen, *Desalin. Water Treat.*, 2019, **144**, 384–392.
30. V.-P. Dinh, N. Q. Tran, N.-Q.-T. Le, Q.-H. Tran, T. D. Nguyen and V. T. Le, *Prog. Nat. Sci.: Mater. Int.*, 2019, **29**, 648–654.
31. V.-P. Dinh, N.-C. Le, T.-D. Le, T.-A. Bui and N.-T. Nguyen, *J. Electron. Mater.*, 2017, **46**, 3681–3688.
32. V.-P. Dinh, M.-D. Nguyen, Q. H. Nguyen, T.-T.-T. Do, T.-T. Luu, A. T. Luu, T. D. Tap, T.-H. Ho, T. P. Phan, T. D. Nguyen and L. V. Tan, *Chemosphere*, 2020, **257**, 127147.
33. V.-P. Dinh, N.-C. Le, L. A. Tuyen, N. Q. Hung, V.-D. Nguyen and N.-T. Nguyen, *Mater. Chem. Phys.*, 2018, **207**, 294–302.
34. V.-P. Dinh, N.-C. Le, V.-D. Nguyen and N.-T. Nguyen, *Desalin. Water Treat.*, 2017, **58**, 427–434.
35. H. Sadegh, G. A. M. Ali, V. K. Gupta, A. S. H. Makhlof, R. Shahryari-ghoshekandi, M. N. Nadagouda, M. Sillanpää and E. Megiel, *J. Nanos-struct. Chem.*, 2017, **7**, 1–14.

36. S. Kar and S. M. Equeenuddin, *Groundwater Sustainable Dev.*, 2019, **9**, 100250.
37. J. Bayo, G. Esteban and J. Castillo, *Environ. Technol.*, 2012, **33**, 761–772.
38. V.-P. Dinh, N.-C. Le, T.-P.-T. Nguyen and N.-T. Nguyen, *J. Chem.*, 2016, **2016**, 8285717.
39. N. C. Le and D. Van Phuc, *Adv. Nat. Sci.: Nanosci. Nanotechnol.*, 2015, **6**, 025014.
40. G. Yuvaraja, C. Prasad, Y. Vijaya and M. V. Subbaiah, *Int. J. Indus. Chem.*, 2018, **9**, 17–25.
41. F. Zhang, X. Chen, F. Wu and Y. Ji, *Colloids Surf., A*, 2016, **509**, 474–483.
42. F. Zhang, J. Lan, Y. Yang, T. Wei, R. Tan and W. Song, *J. Nanopart. Res.*, 2013, **15**, 2034.
43. K. Y. Kumar, H. B. Muralidhara, Y. A. Nayaka, J. Balasubramanyam and H. Hanumanthappa, *Powder Technol.*, 2013, **246**, 125–136.
44. L. H. Li, J. Xiao, P. Liu and G. W. Yang, *Sci. Rep.*, 2015, **5**, 9028.
45. P. Gao, X. Tian, C. Yang, Z. Zhou, Y. Li, Y. Wang and S. Komarneni, *Environ. Sci.: Nano*, 2016, **3**, 1416–1424.
46. A. Q. Shah, T. G. Kazi, J. A. Baig, M. B. Arain, H. I. Afridi, G. A. Kandhro, S. K. Wadhwa and N. F. Kolachi, *Food Chem.*, 2010, **119**, 840–844.
47. D. K. Gupta, S. Tiwari, B. H. N. Razafindrabe and S. Chatterjee, in *Arsenic Contamination in the Environment: The Issues and Solutions*, ed. D. K. Gupta and S. Chatterjee, Springer International Publishing, Cham, 2017, pp. 1–12.
48. M. Balali-Mood, K. Naseri, Z. Tahergorabi, M. R. Khazdair and M. Sadeghi, *Front. Pharmacol.*, 2021, **12**, 643972.
49. A. Kungolos, I. Aoyama and S. Muramoto, *Ecotoxicol. Environ. Saf.*, 1999, **43**, 149–155.
50. World Health Organization, *Lead in Drinking-water: Background Document for Development of WHO Guidelines for Drinking-water Quality*, World Health Organization, 2003.
51. World Health Organization (WHO), *Journal*, 2010.
52. A. A. Al-Homaidan, J. A. Alabdullatif, A. A. Al-Hazzani, A. A. Al-Ghanayem and A. F. Alabbad, *Saudi J. Biol. Sci.*, 2015, **22**, 795–800.
53. M. M. Ghoneim, H. S. El-Desoky, K. M. El-Moselhy, A. Amer, E. H. Abou El-Naga, L. I. Mohamedein and A. E. Al-Prol, *Egypt. J. Aquat. Res.*, 2014, **40**, 235–242.
54. V. K. Gupta and A. Rastogi, *J. Hazard. Mater.*, 2008, **153**, 759–766.
55. H. Liu, F. Zhang and Z. Peng, *Sci. Rep.*, 2019, **9**, 3663.
56. C. Namasivayam and R. T. Yamuna, *Chemosphere*, 1995, **30**, 561–578.
57. S. Mishra and R. N. Bharagava, *J. Environ. Sci. Health, Part C*, 2016, **34**, 1–32.
58. World Health Organization, *Chromium in Drinking-water*, World Health Organization, 2020.
59. I. Langmuir, *J. Am. Chem. Soc.*, 1918, **40**, 1361–1403.
60. M. A. Al-Ghouthi and D. A. Da'ana, *J. Hazard. Mater.*, 2020, **393**, 122383.
61. H. M. F. Freundlich, *J. Phys. Chem.*, 1906, **57**, 385–471.

62. K. Y. Foo and B. H. Hameed, *Chem. Eng. J.*, 2010, **156**, 2–10.
63. R. Sips, *J. Chem. Phys.*, 1948, **16**, 490–495.
64. Z. H. Khan, M. Gao, W. Qiu, M. S. Islam and Z. Song, *Chemosphere*, 2020, **246**, 125701.
65. M. E. Argun, S. Dursun, C. Ozdemir and M. Karatas, *J. Hazard. Mater.*, 2007, **141**, 77–85.
66. Y. S. Ho, D. A. J. Wase and C. F. Forster, *Environ. Technol.*, 1996, **17**, 71–77.
67. P. O. Bedolla, G. Feldbauer, M. Wolloch, S. J. Eder, N. Dörr, P. Mohn, J. Redinger and A. Vernes, *J. Phys. Chem. C*, 2014, **118**, 17608–17615.
68. R. H. S. Winterton, *Contemp. Phys.*, 1970, **11**, 559–574.
69. Y. Du, G. Zheng, J. Wang, L. Wang, J. Wu and H. Dai, *Microporous Mesoporous Mater.*, 2014, **200**, 27–34.
70. G. Consolati, M. Mariani, R. Millini and F. Quasso, *Nuclear Instruments and Methods in Physics Research B*, 2009, **267**, 2550–2553.
71. K. Sato, K. Fujimoto, M. Nakata and N. Shikazono, *IOP Conf. Ser.: Mater. Sci. Eng.*, 2010, **15**, 012006.
72. A. T. T. Pham, T. A. Luu, N. K. Pham, H. K. T. Ta, T. H. Nguyen, D. Van Hoang, H. T. Lai, V. C. Tran, J.-H. Park, J.-K. Lee, S. Park, O. Michitaka, S.-D. Park, H. Q. Nguyen and T. B. Phan, *Ceram. Int.*, 2020, **46**, 10748–10758.
73. L. A. Tuyen, T. Dong Xuan, H. A. Tuan Kiet, L. Chi Cuong, P. Trong Phuc, T. Duy Tap, D.-V. Phuc, L. L. Nguyen, N. T. Ngoc Hue, P. Thi Hue, L. Thai Son, D. Van Hoang, N. Hoang Long and N. Quang Hung, *Radiat. Phys. Chem.*, 2020, **172**, 108867.
74. M. R. Derrick, D. Stulik and J. M. Landry, *Infrared Spectroscopy in Conservation Science*, Getty Publications, 2000.
75. A. Ansari, A. Ali, M. Asif and Shamsuzzaman, *New J. Chem.*, 2018, **42**, 184–197.
76. R. Mahadevaiah, H. S. Lalithamba, S. Shekarappa and R. Hanumanaika, *Sci. Iran.*, 2017, **24**, 3002–3013.
77. M. H. Zahir, M. M. Rahman, K. Irshad and M. M. Rahman, *Nanomaterials (Basel)*, 2019, **9**, 1773.
78. M. R. M. Shafiee, M. Kargar and M. Ghashang, *Green Processing and Synthesis*, 2018, **7**, 248–254.
79. M. Zare, K. Namratha, S. Alghamdi, Y. H. E. Mohammad, A. Hezam, M. Zare, Q. A. Drmosh, K. Byrappa, B. N. Chandrashekar, S. Ramakrishna and X. Zhang, *Sci. Rep.*, 2019, **9**, 8303.
80. A. Anžlovar, Z. Crnjak Orel, K. Kogej and M. Žigon, *J. Nanomater.*, 2012, **2012**, 760872.
81. X. Chen, S. Yan, N. Wang, S. Peng, C. Wang, Q. Hong, X. Zhang and S. Dai, *RSC Adv.*, 2017, **7**, 55734–55740.
82. M. Huang, Y. Zhang, F. Li, L. Zhang, R. S. Ruoff, Z. Wen and Q. Liu, *Sci. Rep.*, 2014, **4**, 3878.
83. M. Zheng, H. Zhang, X. Gong, R. Xu, Y. Xiao, H. Dong, X. Liu and Y. Liu, *Nanoscale Res. Lett.*, 2013, **8**, 166.

84. S. Rajput, C. U. Pittman and D. Mohan, *J. Colloid Interface Sci.*, 2016, **468**, 334–346.
85. S. Hwang, A. Umar, G. Dar, S. Kim and R. Badran, *Sens. Lett.*, 2014, **12**, 97–101.
86. A. A. Jahagirdar, N. Dhananjaya, D. L. Monika, C. R. Kesavulu, H. Nagabhushana, S. C. Sharma, B. M. Nagabhushana, C. Shivakumara, J. L. Rao and R. P. S. Chakradhar, *Spectrochim. Acta, Part A*, 2013, **104**, 512–518.
87. A. Rufus, N. Sreeju and D. Philip, *RSC Adv.*, 2016, **6**, 94206–94217.
88. Y. Gao, Y. Masuda, W.-S. Seo, H. Ohta and K. Koumoto, *Ceram. Int.*, 2004, **30**, 1365–1368.
89. G. Gohari, A. Mohammadi, A. Akbari, S. Panahirad, M. R. Dadpour, V. Fotopoulos and S. Kimura, *Sci. Rep.*, 2020, **10**, 912.
90. N. K. Sethy, Z. Arif, P. K. Mishra and P. Kumar, *Green Processing and Synthesis*, 2020, **9**, 171–181.
91. B. Jaleh, E. Zare, S. Azizian, O. Qanati, M. Nasrollahzadeh and R. S. Varma, *J. Inorg. Organomet. Polym. Mater.*, 2020, **30**, 2213–2223.
92. R. Romero Toledo, V. Ruiz Santoyo, C. D. Moncada Sánchez and M. Martínez Rosales, *Nova Sci.*, 2018, **10**, 83–99.
93. K. Atrak, A. Ramazani and S. Taghavi Fardood, *J. Mater. Sci.: Mater. Electron.*, 2018, **29**, 8347–8353.
94. P. A. Prashanth, R. S. Raveendra, R. Hari Krishna, S. Ananda, N. P. Bhagya, B. M. Nagabhushana, K. Lingaraju and H. Raja Naika, *J. Asian Ceram. Soc.*, 2015, **3**, 345–351.
95. C. Leyva-Porras, P. Cruz-Alcantar, V. Espinosa-Solís, E. Martínez-Guerra, C. I. Piñón-Balderrama, I. Compean Martínez and M. Z. Saavedra-Leos, *Polymers*, 2020, **12**, 5.
96. M. I. Sabela, K. Kunene, S. Kanchi, N. M. Xhakaza, A. Bathinapatla, P. Mdluli, D. Sharma and K. Bisetty, *Arabian J. Chem.*, 2019, **12**, 4331–4339.
97. J. T. Hernandez, A. A. Muriel, J. Tabares, G. P. Alcázar and A. Bolaños, *Journal of Physics: Conference Series*, 2015, **64**, 012007.
98. N. Prabha and M. Vennila, *J. Appl. Sci. Eng. Methodol.*, 2016, **2**, 388–393.
99. S. Devaraj and N. Munichandraiah, *J. Phys. Chem. C*, 2008, **112**, 4406–4417.
100. S. M. Husnain, U. Asim, A. Yaqub, F. Shahzad and N. Abbas, *New J. Chem.*, 2020, **44**, 6096–6120.
101. H. Wang, Y.-N. Wang, Y. Sun, X. Pan, D. Zhang and Y. F. Tsang, *Process Saf. Environ. Prot.*, 2018, **113**, 40–47.
102. R. Chen, J. Yu and W. Xiao, *J. Mater. Chem. A*, 2013, **1**, 11682–11690.
103. X. Hu, F. Zhang, H. Wang, X. Zhang and L. Zhang, *J. Nanomater.*, 2019, **2019**, 7430687.
104. S. Mallakpour and M. Madani, *Carbohydr. Polym.*, 2016, **147**, 53–59.
105. H. Cui, Q. Li, Y. Qian, Q. Zhang and J. Zhai, *Environ. Technol.*, 2012, **33**, 2049–2056.



106. S. Pathan, N. Pandita and N. Kishore, *Arabian J. Chem.*, 2019, **12**, 5200–5211.
107. S. E. A. S. El-Deen, S. I. Moussa, Z. A. Mekawy, M. K. K. Shehata, S. A. Sadeek and H. H. Someda, *Radiochim. Acta*, 2017, **105**, 43–55.
108. L. Zhou, Y. Huang, W. Qiu, Z. Sun, Z. Liu and Z. Song, *Molecules*, 2017, **22**, 173.
109. H. Zhang, F. Xu, J. Xue, S. Chen, J. Wang and Y. Yang, *Sci. Rep.*, 2020, **10**, 6067.
110. S. Shi, C. Xu, Q. Dong, Y. Wang, S. Zhu, X. Zhang, Y. Tak Chow, X. Wang, L. Zhu, G. Zhang and D. Xu, *Appl. Surf. Sci.*, 2021, **541**, 148379.
111. S. Mallakpour and F. Motirasoul, *J. Cleaner Prod.*, 2019, **224**, 592–602.
112. Z. Li, C. Chanéac, G. Berger, S. Delaunay, A. Graff and G. Lefèvre, *RSC Adv.*, 2019, **9**, 33633–33642.
113. Z. Huang, F. Han, M. Li, Z. Zhou, X. Guan and L. Guo, *Comput. Mater. Sci.*, 2019, **169**, 109110.
114. J. Zhang, S. Lin, M. Han, Q. Su, L. Xia and Z. Hui, *Water*, 2020, **12**, 446.
115. S. L. Iconaru, R. Guégan, C. L. Popa, M. Motelica-Heino, C. S. Ciobanu and D. Predoi, *Appl. Clay Sci.*, 2016, **134**, 128–135.
116. B. S. Damasceno, A. F. V. da Silva and A. C. V. de Araújo, *J. Environ. Chem. Eng.*, 2020, **8**, 103994.

CHAPTER 6

# *The Application of Nanomaterials in the Built Environment*

PIN JIN ONG, MING HUI CHUA, SOO XIANG YUN DEBBIE  
AND QIANG ZHU\*

Institute of Materials Research and Engineering, Agency for Science,  
Technology and Research (A\*STAR), 2 Fusionopolis Way, Innovis, #08-03,  
Singapore 138634, Singapore

\*Email: zhuq@imre.a-star.edu.sg

## **6.1 Introduction**

For the past 30 years, scientists have been turning to nanotechnology to solve issues in areas like medicine, ecology and computer science.<sup>1-6</sup> Pollution control, in particular, has seen new and better techniques being developed as nanomaterials push the capabilities and limits of technology. For example, nanomaterials have been developed to capture air pollutants,<sup>7</sup> remove toxic pollutants from water and degrade harmful pollutants into harmless products.<sup>8-11</sup> Even though nanomaterials hold much potential for pollution control, high cost is an obstacle for mass commercialization and replacing present-day technologies completely.

The application of nanomaterials in the construction industry is a recent initiative that emerged at the end of the last century. The common building materials used in today's construction are concrete, steel, glass, brick, wood, stones, timber, *etc.* The most popular application of nanomaterials is the

---

Nanoscience & Nanotechnology Series No. 57

Sustainable Nanotechnology

Edited by Zibiao Li, Jie Zheng and Enyi Ye

© The Royal Society of Chemistry 2022

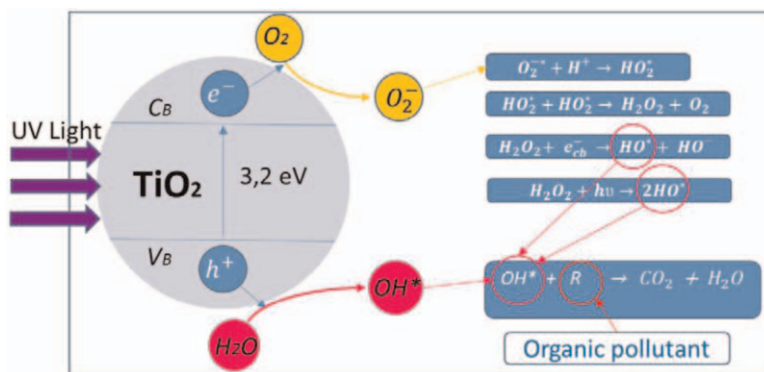
Published by the Royal Society of Chemistry, [www.rsc.org](http://www.rsc.org)

photocatalytic capacity of semiconductor materials.<sup>12–16</sup> Several semiconductor materials, such as titanium dioxide ( $\text{TiO}_2$ ), cadmium selenide ( $\text{CdSe}$ ), iron(III) oxide ( $\text{Fe}_2\text{O}_3$ ) and zinc oxide ( $\text{ZnO}$ ), possess photocatalytic capacity.<sup>17</sup> However,  $\text{TiO}_2$  is the most commonly used because of its chemical stability, compatibility with traditional construction materials, high catalysis efficiency and low toxicity.<sup>18</sup>  $\text{TiO}_2$  can crystallize in three different forms: rutile, brookite and anatase. The rutile form is the most stable form and is also the most widely available. It is often used as an additive in the painting industry. The brookite and anatase forms are meta-stable and can be changed into the rutile form with thermal treatment.  $\text{TiO}_2$  has a bandgap of 3.2 eV. When it is being irradiated with ultraviolet (UV) rays (320–400 nm), electrons and holes will be produced in the valence band and conduction band, respectively, as shown in the equation below:



Electrons can react with oxygen molecules to produce superoxide radicals ( $\text{O}_2^{\bullet -}$ ), while the holes will react with the surrounding water molecules to produce hydroxyl radicals ( $\text{OH}^{\bullet}$ ). These highly reactive compounds will disintegrate inorganic compounds and dirt into water ( $\text{H}_2\text{O}$ ) and carbon dioxide ( $\text{CO}_2$ ).

The photocatalytic mechanism of  $\text{TiO}_2$  is shown in Figure 6.1. Photocatalysis of  $\text{TiO}_2$  also plays a part in reducing the contact angle between a given surface and water droplets. This results in super-hydrophilic or super-hydrophobic surfaces, which makes the removal of pollutants easier. Its self-cleaning properties have been applied in many building elements, such as glasses, mortars, concrete pavements and ceramic tiles.<sup>20–24</sup> This chapter therefore shall discuss current studies and findings related to the use of nanomaterials such as  $\text{TiO}_2$  in building components and how they can be applied in order to achieve pollution control.



**Figure 6.1** Photocatalytic mechanism of  $\text{TiO}_2$ . Reproduced from ref. 19 with permission from IOP Publishing, Copyright 2018.

## 6.2 Nanomaterial in Building Components

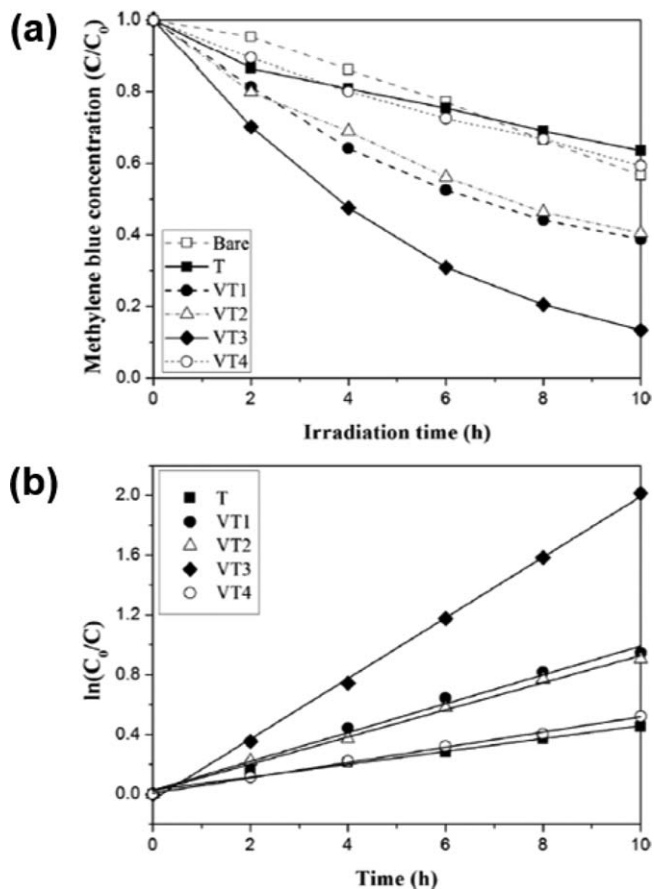
### 6.2.1 Glass

Glass is often used on the exterior of buildings and it is therefore imperative that these large glass facades be kept clean so as to maintain the building's esthetics. Solutions to solving the problem of constant accretion of dirt and pollutants are either to degrade them on the surface or to prevent them from adhering to the surface. Self-cleaning glasses not only reduce maintenance cost but also avoid the need for cleaning in areas that are difficult to access. Glass coatings have been studied and are currently employed since the second half of the 19th century. The impact of glass coatings in the building industry is ever-increasing in popularity as the annual production of glass of about  $10^9$  m<sup>2</sup> was made up of 70% of glass with coatings.<sup>25</sup> The potential of these self-cleaning glasses has led to the development and commercialization of such products by many companies.

In 2001, the British company Pilkington was the first company to come up with self-cleaning windows, named Pilkington Activ™. In the months to follow, other major glass companies announced similar products as well, including the Pittsburgh Plate Glass (PPG) company's SunClean® and Saint-Gobain's Bioclean®. The common characteristic of these windows is that they are coated with a thin transparent layer of TiO<sub>2</sub>. The TiO<sub>2</sub> absorbs the UV component of sunlight to produce strongly oxidizing free radicals in the presence of moisture, which will then clean the glass surface. In addition, hydrophilicity attributed to TiO<sub>2</sub> will cause water to spread across the surface instead of in droplets form, which facilitates the washing off of dirt from the surface.

Chen *et al.* evaluated the photocatalytic activities of a vanadium-doped (V-doped) TiO<sub>2</sub> thin film by studying the degradation of methylene blue (MB) under UV light irradiation.<sup>26</sup> The V-doped TiO<sub>2</sub> sols were prepared using the sol-gel method with four different NH<sub>4</sub>VO<sub>3</sub>-to-TiO<sub>2</sub> weight ratios, namely, 1:100, 2:100, 3:100 and 4:100, denoted as VT1, VT2, VT3 and VT4, respectively. The V-TiO<sub>2</sub> thin film was coated on soda lime glass substrates through dip coating with a total coating surface area of 35 cm<sup>2</sup> for each glass substrate. To conduct the photocatalytic test, the coated glass substrates were dipped into a quartz cell containing 10 mg L<sup>-1</sup> concentration of MB for 12 h, with a UVC lamp at the top. Figure 6.2 shows the resultant photocatalytic activity under UV light irradiation.

As shown in Figure 6.2, V-doped TiO<sub>2</sub> films exhibit better photodegradation efficiencies of MB as compared to undoped TiO<sub>2</sub>. V doping has been found to significantly reduce the bandgap energy and produce more photogenerated electrons and holes, thus improving photocatalytic activity. However, if the concentration of V doping exceeds the optimum concentration (determined to be 3%), the photoinduced electrons or holes might recombine before migrating to the surface, leading to a low photocatalytic activity.

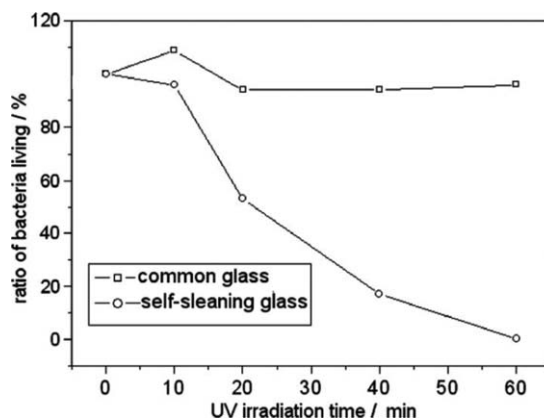


**Figure 6.2** Photocatalytic degradation of MB under UV light irradiation by plotting (a)  $C/C_0$  versus time (h). (b)  $\ln(C_0/C)$  versus time (h). Reproduced from ref. 26 with permission from Elsevier, Copyright 2015.

Zhao *et al.* studied the anti-bacterial effects between common glass and self-cleaning glass *via* UV light irradiation.<sup>27</sup> The results showed that glass coated with  $\text{TiO}_2$  film displayed remarkable anti-bacterial properties (Figure 6.3). Since  $\text{TiO}_2$  films do not display much anti-bacterial effect without UV irradiation, a silver (Ag)-doped (0.1%)  $\text{TiO}_2$  film was prepared for the study of anti-bacterial properties using two different strains of bacteria (*Staphylococcus aureus* ATCC 6538 and *Escherichia coli* ATCC 25922) without UV light irradiation. The results summarized in Table 6.1 clearly show that doping enhanced the anti-bacterial properties of the  $\text{TiO}_2$  film.

### 6.2.2 Brick

Clay building facades are susceptible to visible stains, which compromises the esthetic properties of the building. Flores-Colen *et al.* reported that 36%



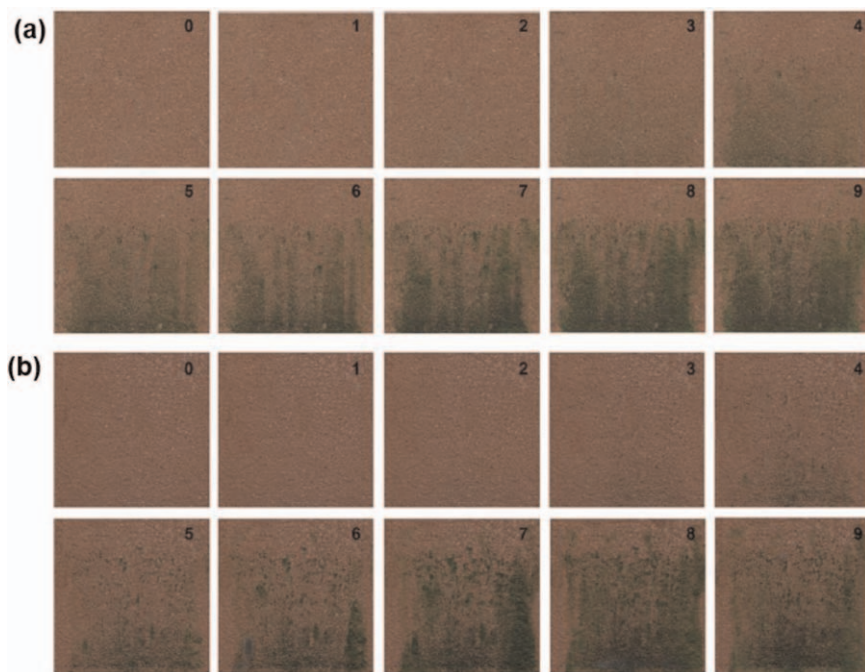
**Figure 6.3** Anti-bacterial effect of self-cleaning glass. Experimental conditions: 15 W 365 nm UV lamp by Cole-Parmer Instrument Co., average power  $1000 \pm 30 \mu\text{W cm}^{-2}$ ; bacteria: *E. coli* DH5a; concentration:  $1 \times 10^6 \text{ CFC cm}^{-3}$ ; temp.:  $25 \pm 1 \text{ }^\circ\text{C}$ ; humidity: 75%. Reproduced from ref. 27 with permission from Elsevier, Copyright 2007.

**Table 6.1** Anti-bacterial effect of self-cleaning glass without UV irradiation at room temperature  $25 \pm 1 \text{ }^\circ\text{C}$ . Reproduced from ref. 27 with permission from Elsevier, Copyright 2007.

Time of action (h)	Bacteria	Bacteria content ( $\text{CFU cm}^{-2}$ )	Ratio (%)
1	<i>Staphylococcus aureus</i> ATCC 6538	$1.9 \times 10^5$	92.63
24	<i>Staphylococcus aureus</i> ATCC 6538	$1.9 \times 10^5$	99.99
24	<i>Escherichia coli</i> ATCC 25922	$9.0 \times 10^4$	98.00

of buildings inspected during a study had stains on them.<sup>28</sup> When foreign materials such as atmospheric aerosol pollutants accumulate on clay surfaces, they can penetrate into the pores *via* absorption when they are dissolved in water. The literature shows that the intrinsic properties of substrata, such as moisture content, texture, roughness and porosity, influence the growth of microorganisms.<sup>29–33</sup>

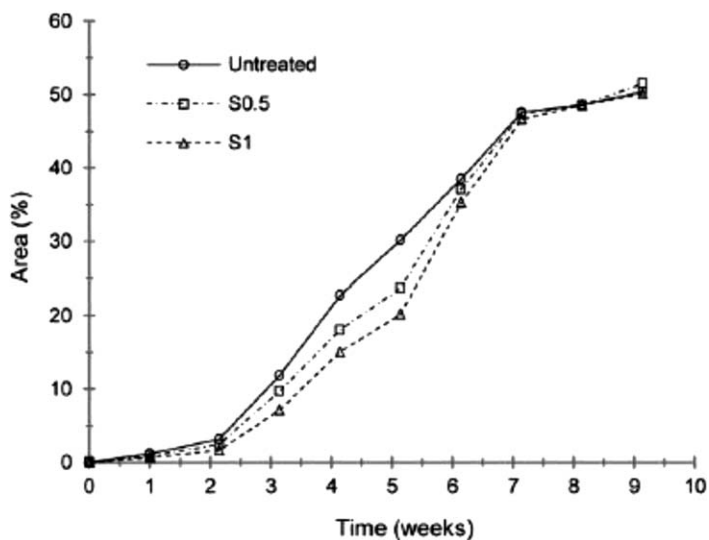
Graziani *et al.*<sup>28</sup> studied the biocidal effect of  $\text{TiO}_2$  coatings on two different types of microorganisms: cyanobacteria species *Chroococcidiopsis fissurarum* and green alga *Chlorella mirabilis* that were applied on clay brick facades under weak UV radiation over a period of 9 weeks. A total of 12 clay brick specimens were prepared: eight treated specimens and four untreated (control) specimens. Commercial  $\text{TiO}_2$  (nanocrystalline anatase form) samples, S1 and S2, were deposited<sup>35–37</sup> on four of the clay brick specimens, respectively, with S1 having a  $\text{TiO}_2$  concentration of 1% w/v and S2 having a  $\text{TiO}_2$  concentration of 0.5% w/v. All eight specimens were then dried at  $60 \text{ }^\circ\text{C}$  for 1 h in order to speed up the drying process and a water run-off test was carried out to accelerate the growth of the test strains. Figure 6.4 shows the results of the



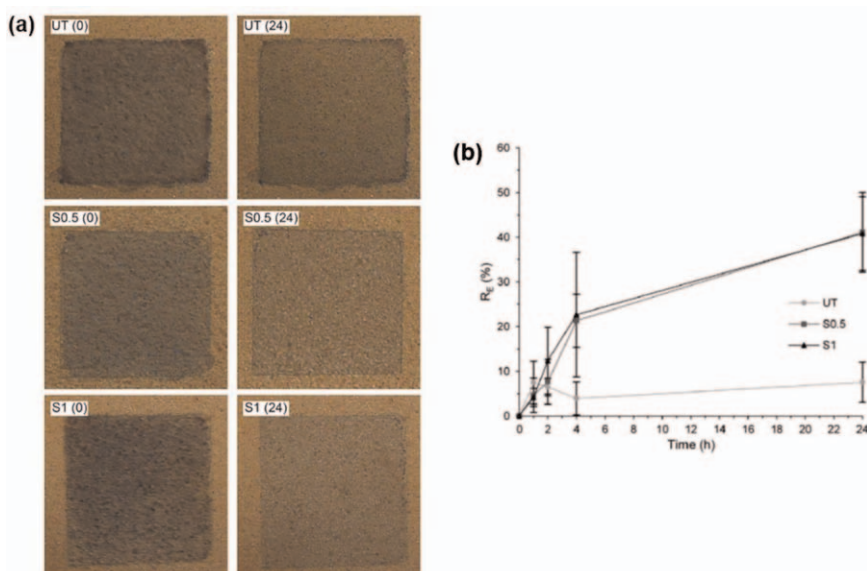
**Figure 6.4** Fouling on (a) untreated specimens and (b) treated specimens. Numbers indicate week progression. Images are representative of four specimens for each treatment. Reproduced from ref. 34 with permission from Elsevier, Copyright 2013.

accelerated growth test, while Figure 6.5 shows the percentages of the area covered by the  $\text{TiO}_2$  nanofilm during the water run-off test. While both figures have shown that  $\text{TiO}_2$  was not able to completely inhibit the growth of the test strains at the end of the 9 weeks, the photocatalytic effect of  $\text{TiO}_2$  was observed to cause an inhibition on the growth of the test strains from week 3 onward due to exposure to sufficient UV irradiation for successful photocatalysis activation. In addition, it was noted that S1 has a slower growth rate of the test strains than S2, which proved that a higher loading of  $\text{TiO}_2$  does result in a higher efficiency of inhibitory effect.

Graziani *et al.*<sup>38</sup> also investigated the self-cleaning ability of  $\text{TiO}_2$  by evaluating the degradation of MB on fired clay brick facades using a test method from the literature.<sup>39,40</sup> Similar to the preparation process mentioned earlier, a total of 12 brick specimens (4 untreated and 8 treated) were prepared with two different concentrations of commercial  $\text{TiO}_2$  water solution: S0.5 (0.5% w/v) and S1 (1% w/v) applied on the specimens. A 0.5 mL MB aqueous solution ( $100 \mu\text{mol L}^{-1}$ ) was used, and the self-cleaning test was conducted for 24 h. Figures 6.6a shows the results of the self-cleaning test after 24 h. For the untreated specimens, a slight discoloration was observed and this was due to the fact that MB is affected by UV radiation that causes self-degradation. The results of the test, as shown in Figure 6.6b, indicated



**Figure 6.5** Percentages of area covered by the biofilm during the water run-off test. Mean value ( $n=4$ ). Reproduced from ref. 34 with permission from Elsevier, Copyright 2013.



**Figure 6.6** (a) Degradation of MB: sample surfaces for each type of treatment at the beginning of test (0) and after 24 h of UV illumination (24). Samples in the figure are representative of four samples for each type. (b) Degradation efficiency of TiO<sub>2</sub> ( $R_E$ ) assessed by color variation between tested specimens and original color of clay brick surface. Reproduced from ref. 38 with permission from Elsevier, Copyright 2013.

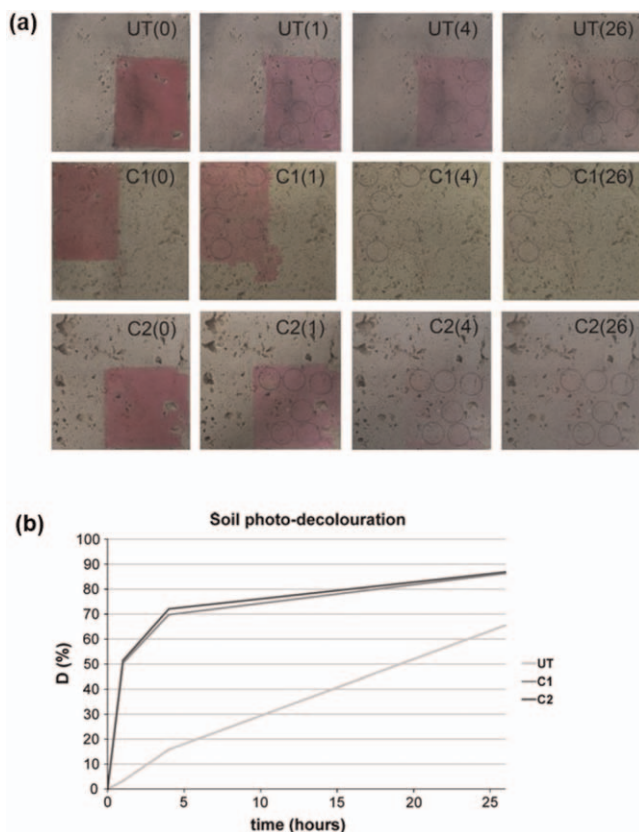


that treated specimens are able to decompose MB. The efficiency reached about 22% in the first 4 h and increased to about 42% by the hour 24. On the other hand, the degradation efficiency of untreated specimens appeared low and was about eight times lower than the treated specimens.

### 6.2.3 Stone

Since ancient times, stone has been one of the most commonly used materials for building applications. Like all other building materials, when stones are exposed to different elements in the environment over a long period of time, they are susceptible to structural and esthetical deterioration. For example, stone decay might occur when fine particulates or pollutants in the environment cause disaggregation of the material. Other factors like natural weathering, growth of microorganisms, humidity,<sup>41–43</sup> or even the characteristics of stone itself will affect its esthetic appearance.<sup>44,45</sup> Stony materials, being porous and owing to their high level of bioreceptivity, tend to be favorable for the growth of living organisms like algae and bacteria.<sup>46,47</sup> There are ways to clean the stone in buildings but they may bring about adverse effects like surface etching, salt formation, staining, bleaching and surface changes.<sup>48,49</sup> Therefore, in order to minimize or reduce the frequency of cleaning, it is imperative to protect the surface from pollutants attack and prevent the formation of soiling. Nanotreatments applied on building stones were found to be helpful in fending off biological agents from attacking the surface, slowing down the rate of soil formation while maintaining the esthetic properties of buildings.<sup>50</sup>

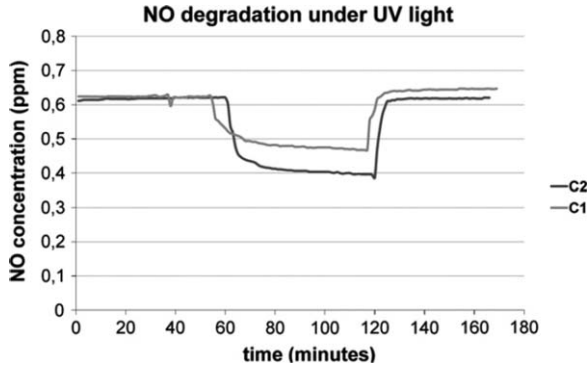
Quagliarini *et al.*<sup>36</sup> investigated the de-pollution and self-cleaning properties of a transparent TiO<sub>2</sub> coating by studying the decoloration of rhodamine B and degradation of nitrogen oxide (NO<sub>x</sub>) on travertine. Travertine is a natural limestone that is widely used in architectural, monumental and historical buildings. TiO<sub>2</sub> nanoparticles are synthesized in water *via* polyol synthesis.<sup>51</sup> The TiO<sub>2</sub>-based suspension was spray-coated on travertine samples (8.0×8.0×1.5 cm<sup>3</sup>) with both a single layer (C1) (25 mL m<sup>-2</sup>) and three layers (C2) (70 mL m<sup>-2</sup>). To evaluate the de-pollution capability of TiO<sub>2</sub>, travertine samples were first stained with rhodamine B solution (0.05 ± 0.005 g L<sup>-1</sup>, 0.5 mL of solution per sample), and the applied soil was dried for 24 h and then treated under UVA light (irradiance value: 3.75 ± 0.25 W m<sup>-2</sup>). The decolorization of rhodamine B was monitored before UV irradiation and also after exposure times of 1, 4 and 26 h. Figure 6.7 shows the results of the photodecoloration of soiling based on the rhodamine B test. It can be seen from Figure 6.7b that after 1 and 4 h, there is a larger extent of degradation of rhodamine B for the treated surfaces, C1 and C2, as compared to the untreated (UT) one. Even though the differences between C1, C2 and UT become smaller as the test proceeds, at the end of 26 h, C1 and C2 surfaces are still about 30% better than the untreated one. Figure 6.8 shows the results of the photodegradation test of NO<sub>x</sub> and it shows that C2 has a higher efficiency of 35% as compared to



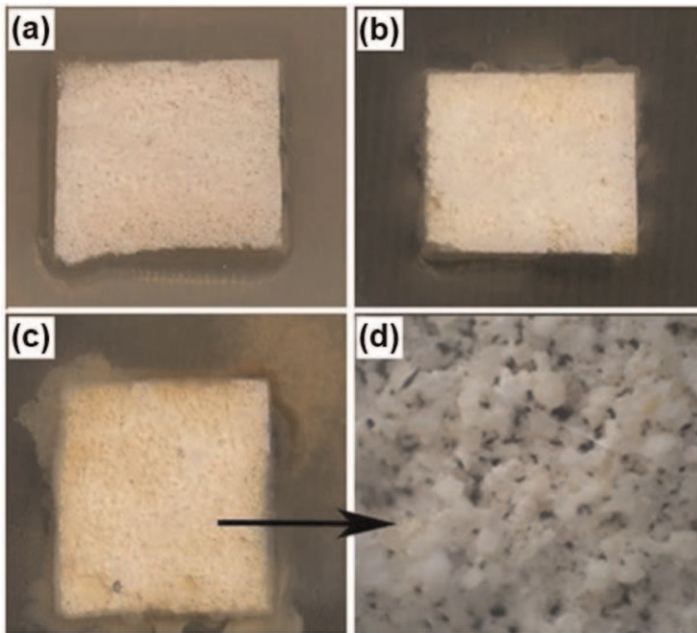
**Figure 6.7** (a) Rhodamine B test: sample surfaces at the beginning of the test (UT(0), C1(0), C2(0)) before UV exposure and after 1, 4 and 26 h of UV illumination. (b) Rhodamine B test results: decoloration  $D^*$  during time of UV exposure. Reproduced from ref. 36 with permission from Elsevier, Copyright 2012.

25% for C1. Even though both tests have proven that a higher content of  $\text{TiO}_2$  does lead to greater photocatalytic activity, the correlation was not proportional and hence having many layers of coating might not be a viable short-term solution.

Russa *et al.*<sup>52</sup> studied the biocidal and self-cleaning properties of  $\text{TiO}_2$  by monitoring the growth of *Aspergillus niger* and carrying out an MB degradation test on limestone. Fosbuild FBLE 200, a commercial nanopowdered  $\text{TiO}_2$  of anatase phase with a mean diameter of 20 nm dispersed in an aqueous suspension of acrylic polymer (polymer 4 wt%,  $\text{TiO}_2$  0.3 wt%), was brushed on limestone samples with two different concentrations:  $20 \text{ g m}^{-2}$  (CL) and  $40 \text{ g m}^{-2}$  (CH). *A. niger* was applied on limestone samples ( $2 \text{ cm} \times 2 \text{ cm} \times 1 \text{ cm}$ ) and they were left for 12 days in an outdoor environment. To quantify the microbial growth of the fungal species, the biological



**Figure 6.8** NO degradation under UV irradiation. Reproduced from ref. 36 with permission from Elsevier, Copyright 2012.

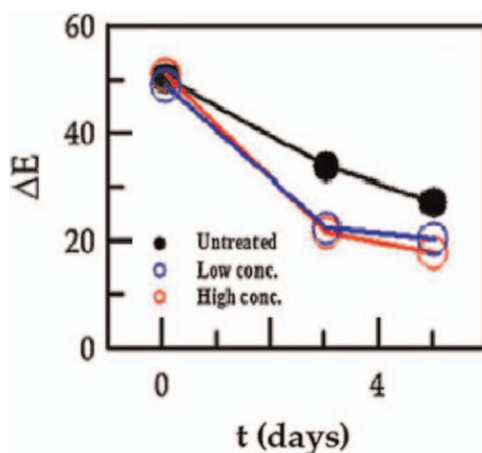


**Figure 6.9** Fungal colonization on stone samples. (a) Treated limestone sample after one day since inoculation. (b) Treated and (c) untreated limestone samples after 8 days. (d) Microphotograph of the colonized limestone surface. Reproduced from ref. 52 with permission from Elsevier, Copyright 2011.

colonization was categorized into four different levels: 1 = no colonization; 2 = start of appearance of colonization; 3 = colonization occupying less than half of the petri dish; 4 = high degree of colonization. For the MB degradation test, the dye was stained ( $2 \text{ g m}^{-2}$  and  $4 \text{ g m}^{-2}$ ) on limestone samples, and both treated and untreated samples were irradiated with UVA light

**Table 6.2** Temporal evolution of *A. niger* growth. After 5 days, a diffuse growth of colonies on untreated specimens of limestone can be observed. Reproduced from ref. 52 with permission from Elsevier, Copyright 2011.

Time (days)	Limestone untreated	CL	CH
1	1	1	1
2	2	2	2
5	4	2	2
8	4	2	2
12	4	2	2



**Figure 6.10** Color variation values measured on stained surface during the time. Reproduced from ref. 52 with permission from Elsevier, Copyright 2011.

( $2 \text{ W cm}^{-2}$ ) for 5 days. Figure 6.9 and Table 6.2 show the results of the *A. niger* growth test. For the untreated samples, the growth of the fungal species seemed to proliferate after 5 days, whereas both the CH and CL treated samples seemed to contain the growth rate even after 12 days. Interestingly, it was noted that a higher  $\text{TiO}_2$  content does not correlate to a higher biocidal efficiency.

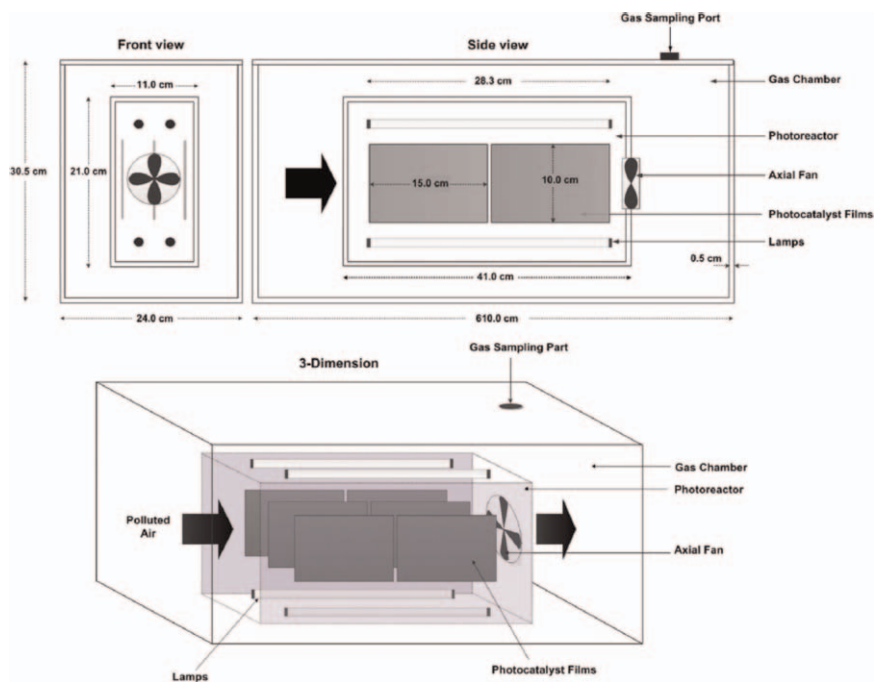
Figure 6.10 shows the color variation of MB with time on the treated and untreated samples and it indicated that both the treated samples degrade MB at a faster rate.

#### 6.2.4 Indoor Air Treatment

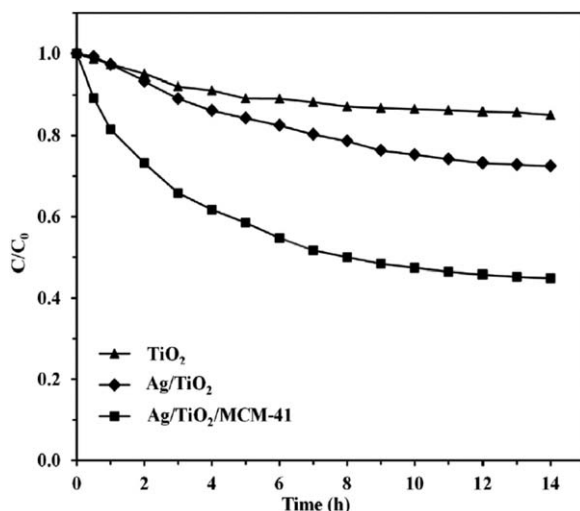
Indoor air pollution has raised serious health concerns as air pollutants in buildings arise not only from building materials but also as a result of human activities. They are reported to have an impact on human health related to long-term health risks.<sup>53-55</sup> The World Health Organization (WHO) has listed the following as air pollutants: polycyclic aromatic hydrocarbons, benzene, carbon monoxide, particulate matter and several

others.<sup>56</sup> In this section, the removal of benzene and particulate matter using nanotechnology will be discussed.

Tongon *et al.*<sup>57</sup> investigated the effect of Ag/TiO<sub>2</sub>/MCM-41 nanocomposite film for the removal of gaseous benzene in a simulated indoor air system. Benzene can be found in office and residential buildings and this is attributed to different sources such as solvents, fuels, paints, glues and lubricants.<sup>56</sup> Benzene is carcinogenic and it can cause a slew of health risks, which include leukemia, anemia, excessive bleeding and even death.<sup>58,59</sup> Photocatalytic oxidation is one of the most viable options to treat air pollutants as it can convert these organic pollutants into harmless compounds like CO<sub>2</sub> and H<sub>2</sub>O. Despite the numerous advantages that TiO<sub>2</sub> offers, it suffers from a charge recombination effect and low specific surface area. To alleviate the effect of charge recombination and improve the photocatalytic reactivity of TiO<sub>2</sub> under visible light, Ag nanoparticles have been introduced as a dopant.<sup>60–62</sup> However, the surface area of TiO<sub>2</sub> will be drastically reduced as a result. To overcome this, porous and mesoporous silica (MCM-41) was added to increase the overall porosity. To synthesize the Ag/TiO<sub>2</sub>/MCM-41 nanocomposite film, a microwave-assisted sol-gel technique was used.<sup>63</sup> A simulated indoor air system (Figure 6.11) was used to conduct the photocatalytic treatment of benzene gas (50 ppm) using visible light on three different types of nanocomposite films: TiO<sub>2</sub>, Ag/TiO<sub>2</sub> and Ag/TiO<sub>2</sub>/MCM-41.



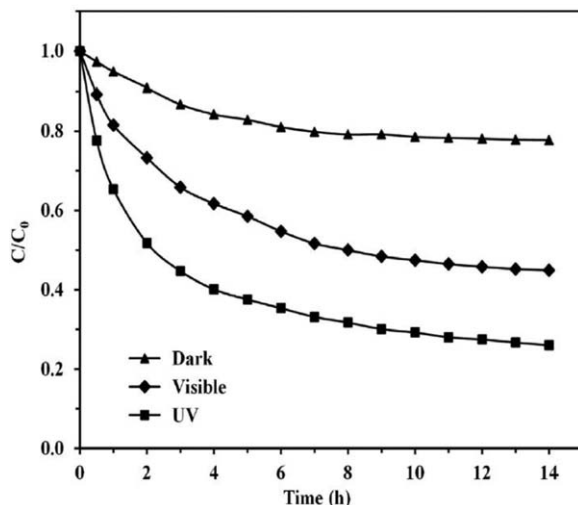
**Figure 6.11** Schematic diagram of the simulated indoor air system. Reproduced from ref. 57 with permission from Elsevier, Copyright 2014.



**Figure 6.12** The photocatalytic degradation of gaseous benzene by different films under visible light irradiation. Reproduced from ref. 57 with permission from Elsevier, Copyright 2014.

In addition, the removal of gaseous benzene was also conducted under three different conditions for the Ag/TiO<sub>2</sub>/MCM-41 nanocomposite film: in the dark, under UV and under visible light irradiation. Figure 6.12 shows the results of the photocatalytic activity of the three films under visible light irradiation. The TiO<sub>2</sub>, Ag/TiO<sub>2</sub> and Ag/TiO<sub>2</sub>/MCM-41 films have photodegradation efficiencies of 15%, 28% and 55% respectively. During the photocatalytic treatment, gaseous benzene is adsorbed onto the film surface. Superoxides and hydroxyl ions produced due to the surface plasmon resonance of Ag oxidize benzene to form phenol, hydroquinone and 1,4-benzoquinone.<sup>64</sup> The photodegradation of benzene under dark (adsorption), UV and visible light (photocatalytic) conditions was determined and is shown in Figure 6.13. In the dark, adsorption equilibrium was attained within 8 h, while on the other hand, UV and visible light irradiation led to an increase in photodegradation efficiencies to 74% and 55%, respectively.

Shi *et al.*<sup>65</sup> developed two nanofiber filters and evaluated the potential of these filters as window screens to filter out outdoor PM<sub>2.5</sub> (particulate matter with a diameter less than 2.5 μm) in residential buildings. The ways in which PM<sub>2.5</sub> can get into the indoor environment include ventilation and infiltration.<sup>66–68</sup> Long-term exposure to ambient PM<sub>2.5</sub> has been reported to cause several health issues such as asthma, reduced lung function and increased rates of chronic bronchitis. In this study, polyimide and silk nanofiber filters were put to the test, respectively, under two different scenarios: utilizing the filters throughout the year (S1) and using them only when the outdoor PM<sub>2.5</sub> concentration is higher than the national standard of China (S2), which is 75 μg m<sup>-3</sup>. Two different sets of data were collected, namely, the reduction of indoor PM<sub>2.5</sub> (C<sub>in</sub>) of outdoor origin and the effect that these filters have on



**Figure 6.13** Removal of gaseous benzene by adsorption (in the dark) and photocatalytic activity of Ag/TiO<sub>2</sub>/MCM-41 films under UV and visible light irradiation. Reproduced from ref. 57 with permission from Elsevier, Copyright 2014.

natural ventilation. To account for the variations of PM<sub>2.5</sub> reduction and natural ventilation rates among different residences, the Monte Carlo method was used. The results obtained showed that for S1, the annual average of particulate matter concentration dropped from  $49.0 \pm 6.65 \mu\text{g m}^{-3}$  to  $17.5 \pm 8.08 \mu\text{g m}^{-3}$  for the polyimide nanofiber and  $17.1 \pm 7.09 \mu\text{g m}^{-3}$  for the silk nanofiber. However, the air resistance that arose from the window screens caused the annual average residential exchange rate to plummet from  $2.34 \pm 0.11$  to  $0.42 \pm 0.09 \text{ h}^{-1}$  and  $0.36 \pm 0.08 \text{ h}^{-1}$  for polyimide nanofiber and silk nanofiber, respectively, which is about 58–64% lower than the national standard of residential air exchange rate in China of  $1 \text{ h}^{-1}$ . Similarly, even though the polyimide and silk nanofiber for S2 reduced the annual average  $C_{\text{in}}$  to  $25.1 \pm 7.07$  and  $25.2 \pm 7.66 \mu\text{g m}^{-3}$ , respectively, the annual average residential exchange rate also decreased to  $0.78 \pm 0.14$  and  $0.69 \pm 0.14 \text{ h}^{-1}$ , respectively. Therefore, lowering the air resistance of the nanofibers will be necessary for improving the performance of these nanofibers.

### 6.2.5 Wood

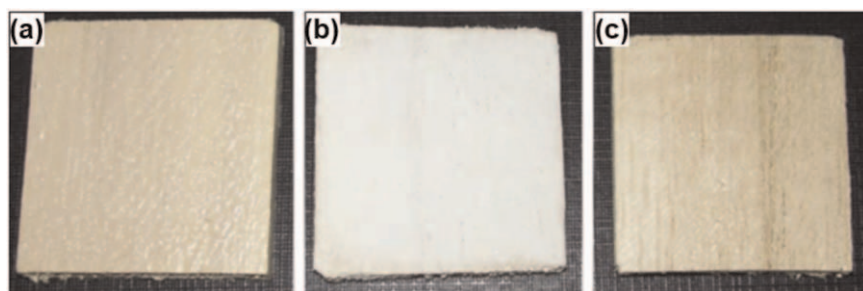
Wood is a material that is widely used in the construction industry all over the world. It is vulnerable to attacks, especially by insects and fungi.<sup>46</sup> Mold fungi are typically detected in water-damaged buildings<sup>69</sup> and cause deterioration of the internal structure<sup>70–72</sup> and affect the esthetics of buildings. It was found that 27–36% of residences in North America suffer from mold attacks. Exposure to mold has been reported to be related to respiratory symptoms,<sup>73–79</sup> asthma<sup>80</sup> and allergies and can be detrimental to people who

have suppressed immune systems.<sup>81</sup> Some of the ways to limit the growth of fungal are controlling the amount of moisture in buildings or rapidly drying the various wetted components in them. However, it is not possible to eliminate the growth of fungal entirely. Fungal decay is a result of an infection caused by fungal spores and comprises a few stages. Firstly, in the initial colonization stage, there will be slight changes in the wood texture and color. Next, significant changes in the texture, strength and color of the wood will follow, and lastly the wood structure will be vastly compromised.

Chen *et al.*<sup>82</sup> studied the antifungal activity of TiO<sub>2</sub> film photocatalytic reaction against mold fungi *A. niger* (AS 3.316) on moist wood boards. Two commercially available TiO<sub>2</sub> products with different nanophase types were used for this study: a pure anatase phase with an average particle size of 6 nm named TiO<sub>2</sub> #1 and another with a mixed phase comprising 80% anatase and 20% rutile named TiO<sub>2</sub> #2 or Degussa P25. Both TiO<sub>2</sub> #1 and #2 were sonicated in deionized water for 30 min to disperse the particles uniformly. *Paulownia* (25 mm×25 mm×2 mm) was used as the substrate and the TiO<sub>2</sub> film (1.5 mg cm<sup>-2</sup>) was applied to the substrate using dip coating. Figure 6.14 shows the photographs of the as-prepared substrates. The substrates were placed in air-tight boxes for 20 days, and each box contained either two 8 W UVA light lamps (black lamp, emission 365 nm peak) or no lamps (to facilitate indoor natural light condition).

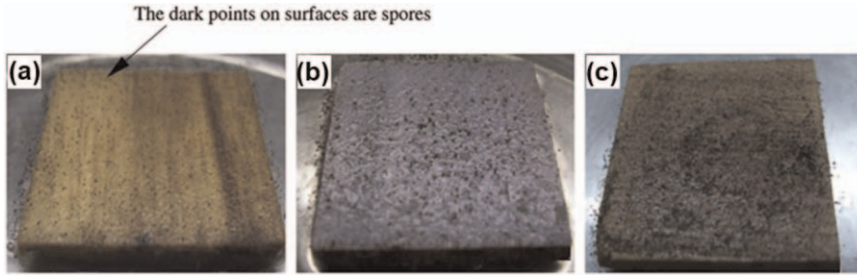
Figure 6.15 shows the different substrates that were cultured in indoor natural light conditions after 20 days. It can be seen that the growth of *A. niger* on all three surfaces is almost the same as indoor natural light cannot induce TiO<sub>2</sub> photocatalytic oxidation to inhibit fungal growth. On the contrary, when there is irradiation of UVA light on the wood surfaces, the growth of *A. niger* is completely inhibited, as shown in Figure 6.16. It was also reported that recovery and re-growth of *A. niger* occurred once the irradiation stopped for the TiO<sub>2</sub>-treated wood boards, so further studies are required to explore the potential of photocatalytic deactivation of fungi.

Goffredo *et al.*<sup>83</sup> also evaluated the biocidal ability of photocatalytic TiO<sub>2</sub> in combination with Ag and copper (Cu) nanoparticles on the growth of

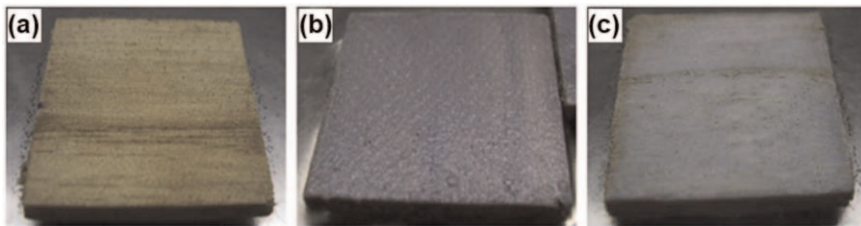


**Figure 6.14** Photograph of TiO<sub>2</sub> thin film on wood surface. (a) TiO<sub>2</sub> #1. (b) TiO<sub>2</sub> #2. (c) Absence of TiO<sub>2</sub>. Reproduced from ref. 82 with permission from Elsevier, Copyright 2008.





**Figure 6.15** *A. niger* growth degree on different coated surfaces with indoor natural light (cultivated for 20 days). (a) Untreated surface wetted by sterilized water. (b) TiO<sub>2</sub> #1-coated surface wetted by sterilized water. (c) TiO<sub>2</sub> #2-coated surface wetted by sterilized water. Reproduced from ref. 82 with permission from Elsevier, Copyright 2008.



**Figure 6.16** Effect of TiO<sub>2</sub> photocatalytic reaction on *A. niger* with UVA irradiation for 20 days: (a) untreated surface; (b) TiO<sub>2</sub> #1; and (c) TiO<sub>2</sub> #2. Reproduced from ref. 82 with permission from Elsevier, Copyright 2008.

*A. niger* (F18). Two different wood species were selected for this study, namely, beech (*Fagus sylvatica* L.) and pine (*Pinus sylvestris* L.), whereas five different nano-compounds were prepared: a pure TiO<sub>2</sub> aqueous solution, two sols containing both TiO<sub>2</sub> and Ag nanoparticles with different Ag contents and two sols containing both TiO<sub>2</sub> and Cu nanoparticles with different Cu content. The nanocompounds were applied on the wood surfaces, which were then irradiated with UVA light (350–400 nm) for 24 h to activate the biocidal ability of TiO<sub>2</sub> before inoculating and incubating the fungi for four weeks. It was concluded that the nanocompounds are able to inhibit the growth of *A. niger*, solely due to TiO<sub>2</sub>, while the addition of metallic nanoparticles did not necessarily increase the biocidal efficiency.

### 6.3 Risk of Nanomaterials

The use of nanomaterials in construction is becoming increasingly common as they have brought about new construction products with incredibly innovative and promising properties. It is estimated that by 2025, about half of our building materials may contain nanomaterials, which is attributed to technological advances that allow us to manipulate matter at the atomic

level. However, issues have been raised regarding their potential toxicity when exposed to these nanomaterials.

The toxicity of nanomaterials arises due to many factors. The two main factors influencing the toxicity are the size and shape of the nanomaterials. Due to the small dimensions of the nanomaterials (two- or three-dimensional nanorods or nanoparticles), their electronic properties behave differently as a result and this is reflected by their chemical reactivity, where they are more aggressive toward the normal functions of the human body. It has been reported that nanomaterials agglomerate or bind more efficiently to certain parts of the human body that disable normal functionality or induce more pronounced inflammatory effects (*via* oxidative stress). The significantly high reactivity is also due to their small size, where their surface area is relatively enlarged with respect to their particle volume. Besides the size of the nanomaterials, the specific shape of nanoparticles is also a key factor contributing to the toxicity. For example, particles can be relatively non-toxic but nanorods, which are needle like, can perforate human tissue. Other factors that play an important role in determining the hazard of the nanoparticles are agglomeration and aggregation of the material, the morphology (crystalline or amorphous) that do affect the chance of getting exposed to the material, the solubility and the intensity of the potential hazard related to the material.

Although there is still much to be understood with regard to the toxicity of nanomaterials, carbon nanotubes (CNTs), TiO<sub>2</sub>, silicon dioxide (SiO<sub>2</sub>) and Ag are among the ones best studied to date. Toxicity studies have indicated that CNTs exhibit asbestos-like behavior in lung tissue.<sup>84,85</sup> The toxicity depends on the agglomeration state, length/diameter ratio, surface characteristics and the presence of small impurities of metal catalysts.<sup>86,87</sup> TiO<sub>2</sub> used for photocatalytic applications can be in the anatase or rutile form, with the former being the most toxic form.<sup>88</sup> Long-term exposure to anatase TiO<sub>2</sub> may cause DNA damage,<sup>89</sup> affects the central nervous system of the fetus and has carcinogenic effects and also the possibility of reprotoxic effects in humans.<sup>90</sup> Grassian *et al.*<sup>91</sup> reported that the inhalation of TiO<sub>2</sub> particles of primary particle sizes between 2 and 5 nm with a concentration of 8.8 mg m<sup>-3</sup> resulted in lung inflammation. Similar findings have also been reported by others.<sup>92,93</sup> SiO<sub>2</sub> can be crystalline or amorphous. According to Merget *et al.*,<sup>94</sup> synthetic amorphous nano-SiO<sub>2</sub> is non-toxic and water soluble and the toxicity is usually regarded as the same as non-nano amorphous silica dust in terms of human risk factors. Nevertheless, amorphous SiO<sub>2</sub> may be contaminated with crystalline SiO<sub>2</sub>, which is very toxic and is known to cause silicosis upon exposure. Wijnhoven *et al.*<sup>95</sup> reported that while Ag might be relatively non-toxic, ingested or inhaled nano-Ag can enter the bloodstream and have adverse effects on the central nervous system. This could be due to the large surface area of the nanoparticles, which leads to a relatively higher concentration of dissolved Ag ions.

The risks of nanomaterials in building materials have still not been entirely well studied at the moment. More studies and research are required to

understand the likelihood of workers being exposed to these nanomaterials, the type of nanomaterials involved and whether there are significant health risks involved. With this current knowledge, it might be difficult for companies to advise what kind of precautions their workers need to take to protect themselves but the fact remains that there are many existing risks known to us that these nanomaterials can bring about. The prevalence of nanomaterials in the built environment will undoubtedly continue to rise. Therefore, it is important for companies to emphasize the importance of good practice in health risk management to their workers so that these nanomaterials will be a boon to us and at the same time not at the expense of people's health.

## 6.4 Conclusion

While there are many advantages to using nanomaterials in the built environment, such as pollution control and cutting down on wastes, the production of these materials does require a lot of energy. More importantly, some of them are toxic and people's lives are at risk. This creates an environmental challenge to the construction industry as well. Environmental and sustainability issues that stem from growing economic development have since garnered worldwide attention. The impact that the construction industry has on the environment is significant since it consumes a huge amount of resources and is also heavily involved in economic development. As such, it is crucial to ensure that the regulations and practices in the construction industry are sustainable. In order to achieve sustainable nanotechnology in the long run, more research and practice efforts are required with planning and smart design. It is important to establish a system to identify environmentally friendly and non-harmful construction nanomaterials so that construction projects can not only eliminate unnecessary wastage of resources but also save energy and be made sustainable.

## References

1. P. Hassanzadeh, F. Atyabi and R. Dinarvand, *Life Sci.*, 2017, **182**, 93–103.
2. A. Tan, R. Chawla, G. Natasha, S. Mahdibeiraghdar, R. Jeyaraj, J. Rajadas, M. R. Hamblin and A. M. Seifalian, *J. Plast. Reconstr. Aesthet. Surg.*, 2016, **69**, 1–13.
3. S. Tyagi, D. Rawtani, N. Khatri and M. Tharmavaram, *J. Water Process Eng.*, 2018, **21**, 84–95.
4. S. Y. Rhee, K. D. Bimbaum and D. W. Ehrhardt, *Trends Plant Sci.*, 2019, **24**, 303–310.
5. A. Mubarakali, J. Ramakrishnan, D. Mavaluru, A. Elsir, O. Elsier and K. Wakil, *Nano Commun. Networks*, 2019, **21**, 100252.
6. L. Fu, L. Cao, Y. Liu and D. Zhu, *Adv. Colloid Interface Sci.*, 2004, **111**, 133–157.
7. M. Nischk, P. Mazierski, M. Gazda and A. Zaleska, *Appl. Catal., B*, 2014, **144**, 674–685.

8. J. Chen, G. Li, Z. He and T. An, *J. Hazard. Mater.*, 2011, **190**, 416–423.
9. W. Dong, Y. Sun, Q. Ma, L. Zhu, W. Hua, X. Lu, G. Zhuang, S. Zhang, Z. Guo and D. Zhao, *J. Hazard. Mater.*, 2012, **229–230**, 307–320.
10. F. Tang and X. Yang, *Build. Environ.*, 2012, **56**, 329–334.
11. F. Thevenet, C. Guillard and A. Rousseau, *Chem. Eng. J.*, 2014, **244**, 50–58.
12. K. Pirkanniemi and M. Sillanpää, *Chemosphere*, 2002, **48**, 1047–1060.
13. A. Mills and S. L. Hunte, *J. Photochem. Photobiol., A*, 1997, **108**, 1–35.
14. D. S. Bhatkhande, V. G. Pangarkar and A. ACM Beenackers, *J. Chem. Technol. Biotechnol.*, 2001, **77**, 102–116.
15. J. K. Reddy, K. Lalitha, V. D. Kumari and M. Subrahmanyam, *Catal. Lett.*, 2008, **121**, 131–136.
16. S. A. Ruffolo, M. F. La Russa, M. Malagodi, C. O. Rossi, A. M. Palermo and G. M. Crisci, *Appl. Phys. A: Mater. Sci. Process.*, 2010, **100**, 829–834.
17. A. Makowski and W. Wardas, *Curr. Top. Biophys.*, 2001, **25**, 19–25.
18. K. Djebbar and T. Sehili, *J. Pestic. Sci.*, 1998, **54**, 269–276.
19. Nasikhudin, M. Diantoro, A. Kusumaatmaja and K. Triyana, presented in part at International Conference on Theoretical and Applied Physics (ICTAP), Yogyakarta, Indonesia, September, 2017.
20. J. Chen and C. Poon, *Build. Environ.*, 2009, **44**, 1899–1906.
21. J. Zhao and X. Yang, *Build. Environ.*, 2003, **38**, 645–654.
22. M. V. Diamanti, M. Ormellese and M. Pedferri, *Cem. Concr. Res.*, 2008, **38**, 1349–1353.
23. M. F. Brunella, M. V. Diamanti, M. P. Pedferri, F. Di Fonzo, C. S. Casari and A. Li Bassi, *Thin Solid Films*, 2007, **515**, 6309–6313.
24. F. Bondioli, R. Taurino and A. M. Ferrari, *J. Colloid Interface Sci.*, 2009, **334**, 195–201.
25. L. Martinu and D. Poitras, *J. Vac. Sci. Technol., A*, 2000, **18**, 2619–2645.
26. Y. Chen, J. Chang and B. Moongraksathum, *J. Taiwan Inst. Chem. Eng.*, 2015, **52**, 140–146.
27. X. Zhao, Q. Zhao, J. Yu and B. Liu, *J. Non-Cryst. Solids*, 2008, **354**, 1424–1430.
28. I. Flores-Colen, J. de Brito and V. P. de Freitas, *Constr. Build. Mater.*, 2008, **22**, 211–221.
29. H. Barberousse, B. Ruot, C. Yéprémian and G. Boulon, *Build. Environ.*, 2007, **42**, 2555–2561.
30. M. D’Orazio, G. Cursio, L. Graziani, L. Aquilanti, A. Osimani, F. Clementi, C. Yéprémian, V. Lariccia and S. Amoroso, *Build. Environ.*, 2014, **77**, 20–28.
31. H. Barberousse, R. J. Lombardo, G. Tell and A. Couté, *Biofouling*, 2006, **22**, 69–77.
32. J. J. Ortega-Calvo, X. Ariño, M. Hernandez-Marine and C. Saiz-Jimenez, *Sci. Total Environ.*, 1995, **167**, 329–341.
33. S. Johansson, L. Wadsö and K. Sandin, *Build. Environ.*, 2010, **45**, 1153–1160.
34. L. Graziani, E. Quagliarini, A. Osimani, L. Aquilanti, F. Clementi, C. Yéprémian, V. Lariccia, S. Amoroso and M. D’Orazio, *Build. Environ.*, 2013, **64**, 38–45.

35. E. Quagliarini, F. Bondioli, G. B. Goffredo, A. Licciulli and P. Munafò, *J. Cult. Heritage*, 2012, **13**, 204–209.
36. E. Quagliarini, F. Bondioli, G. B. Goffredo, C. Cordoni and P. Munafò, *Constr. Build. Mater.*, 2012, **37**, 51–57.
37. E. Quagliarini, F. Bondioli, G. B. Goffredo, A. Licciulli and P. Munafò, *J. Cult. Heritage*, 2013, **14**, 1–7.
38. L. Graziani, E. Quagliarini, F. Bondioli and M. D'Orazio, *Build. Environ.*, 2014, **71**, 193–203.
39. ISO 10678:2010. Fine ceramics (advanced ceramics, advanced technical ceramics), determination of photocatalytic activity of surfaces in an aqueous medium by degradation of methylene blue. International Standards Organization; 2010.
40. UNI 11259:2008. Determination of the photocatalytic activity of hydraulic binders – Rodamina test method. Ente nazionale italiano di unificazione; 2008.
41. M. Urosevic, A. Yebra-Rodriguez, E. Sebastián and C. Cardell, *Sci. Total Environ.*, 2012, **414**, 564–575.
42. C. Saiz-Jimenez, *Int. Biodeterior. Biodegrad.*, 1997, **40**, 225–232.
43. A. Jain, S. Bhadauria, V. Kumar and R. S. Chauhan, *Build. Environ.*, 2009, **44**, 1276–1284.
44. P. J. Creighton, P. J. Liroy, F. H. Haynie, T. J. Lemmons, J. L. Miller and J. Gerhart, *J. Air Waste Manage. Assoc.*, 2012, **40**, 1285–1289.
45. C. M. Grossi, R. M. Esbert, F. Díaz-Pache and F. J. Alonso, *Build. Environ.*, 2003, **38**, 147–159.
46. C. Gaylarde, M. R. Silva and Th. Warscheid, *Mater. Struct.*, 2003, **36**, 342–352.
47. C. C. Gaylarde and P. M. Gaylarde, *Int. Biodeterior. Biodegrad.*, 2005, **55**, 131–139.
48. M. E. Young, D. C. M. Urquhart and R. A. Laing, *Build. Environ.*, 2003, **38**, 1125–1131.
49. C. M. Grossi, P. Brimblecombe, R. M. Esbert and F. J. Alonso, *Color Res. Appl.*, 2007, **32**, 320–331.
50. P. Brimblecombe and C. M. Grossi, *Sci. Total Environ.*, 2005, **349**, 175–189.
51. S. Albonetti, G. Baldi, A. Barzanti, A. L. Costa, J. E. Mengou, F. Trifirò and A. Vaccari, *Appl. Catal., A*, 2007, **325**, 309–315.
52. M. F. La Russa, S. A. Ruffolo, N. Rovella, C. M. Belfiore, A. M. Palermo, M. T. Guzzi and G. M. Crisci, *Prog. Org. Coat.*, 2012, **74**, 186–191.
53. G. Xiao, A. Huang, H. Su and T. Tan, *Build. Environ.*, 2013, **65**, 215–221.
54. C. A. Pope III, R. T. Burnett, M. J. Thun, E. E. Calle, D. Krewski, K. Ito and G. D. Thurston, *JAMA*, 2002, **287**, 1132–1141.
55. O. Yu, L. Sheppard, T. Lumley, J. Q. Koenig and G. G. Shapiro, *Environ. Health Perspect.*, 2000, **108**, 1209–1214.
56. World Health Organization. *WHO guidelines for indoor air quality: selected pollutants*. Copenhagen2010: E-Publishing Inc; p. 15–54.
57. W. Tongon, C. Chawengkijwanich and S. Chiarakorn, *Build. Environ.*, 2014, **82**, 481–489.

58. J. Lelieveld, J. S. Evans, M. Fnais, D. Giannadaki and A. Pozzer, *Nature*, 2015, **525**, 367–384.
59. Y. Shang, Z. Sun, J. Cao, X. Wang, L. Zhong, X. Bi, H. Li, W. Liu, T. Zhu and W. Huang, *Environ. Int.*, 2013, **54**, 100–111.
60. P. Peerakiatkhajorn, C. Chawengkijwanich, W. Onreabroy and S. Chiarakorn, *Mater. Sci. Forum*, 2012, **712**, 133–145.
61. M. M. Viana, N. D. S. Mohallem, D. R. Miquita, K. Balzuweit and E. Silva-Pinto, *Appl. Surf. Sci.*, 2013, **265**, 130–136.
62. M. F. Brugnera, M. Miyata, C. Q. F. Leite and M. V. B. Zanoni, *J. Photochem. Photobiol., A*, 2014, **278**, 1–8.
63. W. Tongon, C. Chawengkijwanich and S. Chiarakorn, *Superlattices Microstruct.*, 2014, **69**, 108–121.
64. O. d’Hennezel, P. Pichat and D. F. Ollis, *J. Photochem. Photobiol., A*, 1998, **118**, 197–204.
65. S. Shi and C. Chen, *Procedia Eng.*, 2017, **205**, 2386–2392.
66. C. Chen, B. Zhao, W. Zhou, X. Jiang and Z. Tan, *Build. Environ.*, 2012, **47**, 339–348.
67. C. Chen, B. Zhao and C. J. Weschler, *Epidemiology*, 2012, **23**, 870–878.
68. T. Xia and C. Chen, *Build. Environ.*, 2019, **147**, 528–539.
69. M. A. Andersson, M. Nikulin, U. Köljalg, M. C. Andersson, F. Rainey, K. Reijula, E. L. Hintikka and M. Salkinoja-Salonen, *Appl. Environ. Microbiol.*, 1997, **63**, 387–393.
70. I. M. Ezeonu, D. L. Price, R. B. Simmons, A. Crow and D. G. Ahearn, *Appl. Environ. Microbiol.*, 1994, **60**, 4172–4173.
71. T. Murtoniemi, M. R. Hirvonen, A. Nevalainen and M. Suutari, *Indoor Air*, 2003, **13**, 65–73.
72. T. Lee, S. A. Grinshpun, D. Martuzevicius, A. Adhikari, C. M. Crawford, J. Luo and T. Reponen, *Indoor Air*, 2006, **16**, 37–47.
73. M. H. Garrett, P. R. Rayment, M. A. Hooper, M. J. Abramson and B. M. Hopper, *Clin. Exp. Allergy*, 1998, **28**, 459–467.
74. B. Jacob, B. Ritz, U. Gehring, A. Koch, W. Bischof, H. E. Wichmann and J. Heinrich, *Environ. Health Perspect.*, 2002, **110**, 647–653.
75. R. L. Górný, T. Reponen, K. Willeke, D. Schmechel, E. Robine, M. Boissier and S. A. Grinshpun, *Appl. Environ. Microbiol.*, 2002, **68**, 3522–3531.
76. D. M. Kuhn and M. A. Ghannoum, *Clin. Microbiol. Rev.*, 2003, **16**, 44–172.
77. K. F. Martinez, C. Y. Rao and N. C. Burton, *Grana*, 2004, **43**, 193–208.
78. L. D. Stetzenbach, M. P. Buttner and P. Cruz, *Curr. Opin. Biotechnol.*, 2004, **15**, 170–174.
79. M. Simoni, E. Lombardi, G. Berti, F. Rusconi, S. L. Grutta, S. Piffer, M. G. Petronio, C. Galassi, F. Forastiere and G. Viegi, *Occup. Environ. Med.*, 2005, **62**, 616–622.
80. G. Richardson, S. Eick and R. Jones, *J. Adv. Nurs.*, 2005, **52**, 328–339.
81. C. A. Clausen and V. W. Yang, *Int. Biodeterior. Biodegrad.*, 2005, **55**, 99–102.
82. F. Chen, X. Yang and Q. Wu, *Build. Environ.*, 2009, **44**, 1088–1093.
83. G. B. Goffredo, B. Citterio, F. Biavasco, F. Stazi, S. Barcelli and P. Munafò, *J. Cult. Heritage*, 2017, **27**, 125–136.

84. C. A. Poland, R. Duffin, I. Kinloch, A. Maynard, W. A. H. Wallace, A. Seaton, V. Stone, S. Brown, W. MacNee and K. Donaldson, *Nat. Nanotechnol.*, 2008, **3**, 423–428.
85. M. Pacurari, X. J. Yin, J. Zhao, M. Ding, S. S. Leonard, D. Schwegler-Berry, B. S. Ducatman, D. Sbarra, M. D. Hoover, V. Castranova and V. Vallyathan, *Environ. Health Perspect.*, 2008, **116**, 1211–1217.
86. K. Pulskamp, S. Diabaté and H. Krug, *Toxicol. Lett.*, 2007, **168**, 58–74.
87. P. Wick, P. Manser, L. K. Limbach, U. Dettlaff-Weglikowska, F. Krumeich, S. Roth, W. J. Stark and A. Brunink, *Toxicol. Lett.*, 2007, **168**, 121–131.
88. C. M. Sayes, R. Wahi, P. A. Kurian, Y. Liu, J. L. West, K. D. Ausman, D. B. Warheit and V. L. Colvin, *Toxicol. Sci.*, 2006, **92**, 174–185.
89. N. Singh, B. Manshian, G. J. S. Jenkins, S. M. Griffiths, P. M. Williams, T. G. G. Maffei, C. J. Wright and S. H. Doak, *Biomaterials*, 2009, **30**, 3891–3914.
90. M. Shimizu, H. Tainaka, T. Oba, K. Mizuo, M. Umezawa and K. Takeda, *Part. Fibre Toxicol.*, 2009, **6**, 20–27.
91. V. H. Grassian, P. T. O’Shaughnessy, A. Adamcakova-Dodd, J. M. Pettibone and P. S. Thorne, *Environ. Health Perspect.*, 2007, **115**, 397–402.
92. Y. Yu, Q. Zhang, Q. Mu, B. Zhang and B. Yan, *Nanoscale Res. Lett.*, 2008, **3**, 271–277.
93. A. Liu, K. Sun, J. Yang and D. Zhao, *J. Nanopart. Res.*, 2008, **10**, 1303–1307.
94. R. Merget, T. Bauer, H. U. Küpper, S. Philippou, H. D. Bauer, R. Breitstadt and T. Bruening, *Arch. Toxicol.*, 2002, **75**, 625–634.
95. S. W. P. Wijnhoven, W. Peijnenburg and C. Herberts, *et al.*, *Nanotoxicology*, 2009, **3**, 109–138.

## CHAPTER 7

# *Nanotechnology for Energy Storage and Efficiency*

JIE XUAN,<sup>a</sup> GUIJIAN GUAN,<sup>\*a</sup> YONG YU,<sup>\*b</sup> ENYI YE<sup>b</sup> AND ZIBIAO LI<sup>b,c</sup>

<sup>a</sup> Institute of Molecular Plus, Tianjin University, Tianjin 300072, P.R. China; <sup>b</sup> Institute of Materials Research and Engineering, Agency for Science, Technology and Research (A\*STAR), 2 Fusionopolis Way, Innovis #08-03, Singapore 138634, Singapore, yuy@imre.a-star.edu.sg;

<sup>c</sup> Department of Materials Science and Engineering, National University of Singapore, Singapore 117574, Singapore

\*Emails: gujianguan@tju.edu.cn; yuy@imre.a-star.edu.sg

## 7.1 Introduction

Nanotechnology has been playing a critical function in all aspects of the energy industry, such as acquiring, conversion, storage, and usage.<sup>1-4</sup> Nanotechnology relates to manipulating materials at the nanometer size range of 1–100 nm for practical applications. Being at the same scale as atoms, molecules, and supramolecular structures, these nm-sized materials (*i.e.*, nanomaterials) possess a high percentage of surface atoms, high surface energies, and therefore unique physicochemical properties distinctively different from bulk materials.<sup>5-7</sup> Moreover, their properties are greatly dependent on their sizes, shapes, compositions, and assembled hierarchical configuration.<sup>8</sup> Due to their small size in at least one dimension and a high percentage of surface atoms, nanomaterials are superior to conventional bulk materials in energy-related applications due to higher efficiency (*e.g.*, turnover rate per atom or molecule). The past few decades have witnessed

---

Nanoscience & Nanotechnology Series No. 57

Sustainable Nanotechnology

Edited by Zibiao Li, Jie Zheng and Enyi Ye

© The Royal Society of Chemistry 2022

Published by the Royal Society of Chemistry, www.rsc.org

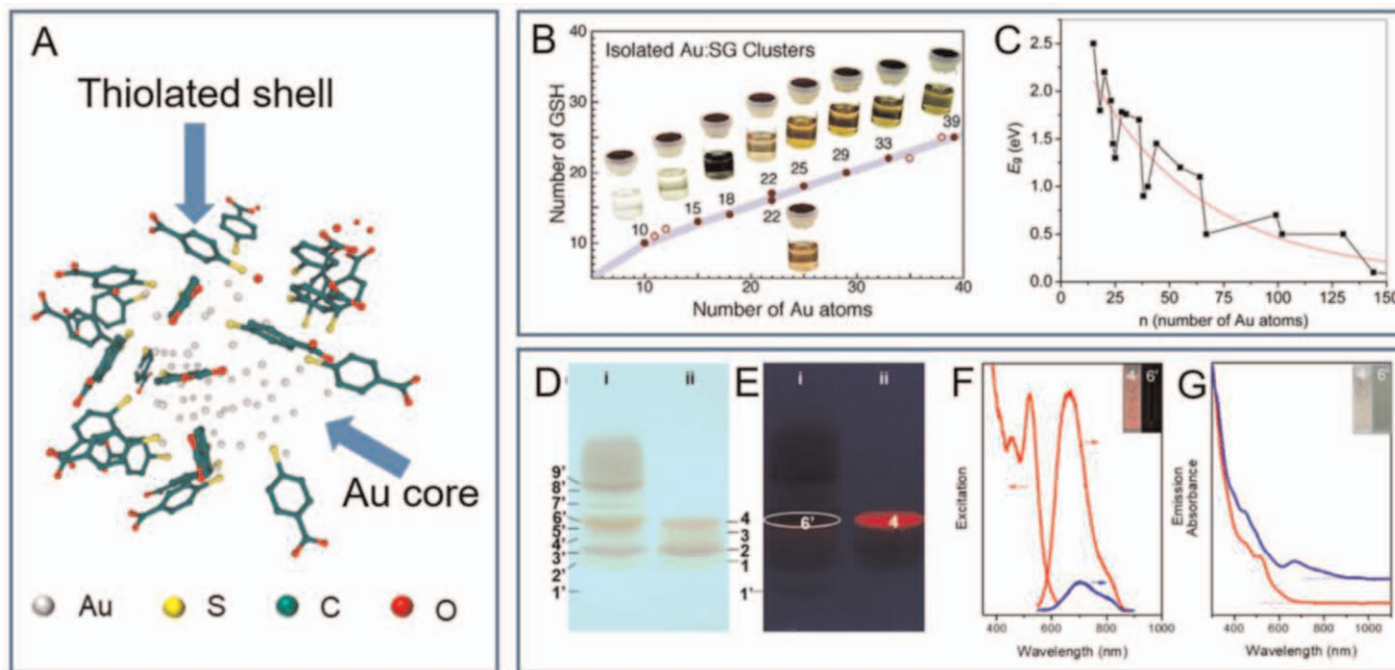


the thrusting progress of nanotechnology, including nanomaterials' synthesis, characterization, manipulation, and translational applications.<sup>9–12</sup> In this short chapter, a special type of nanomaterials, namely, thiolate-protected metal nanoclusters (NCs), are selected as a representative example to discuss how nanotechnology evolves in energy-related fields, such as conversion, storage, and utilization.

Thiolate-protected metal NCs can be regarded as aggregates containing a few to a hundred metal atoms (particularly noble metals such as gold and silver) that are linked with a surface thiolate (RSH) layer.<sup>1</sup> The thiolate-linked Au/Ag NCs are therefore represented as  $Au_n(SR)_m$  or  $Ag_n(SR)_m$ , in which  $n$  and  $m$  refer to the number of Au or Ag atoms and the thiolate ligand in one NC, respectively. In recent years, thiolate-protected Au/Ag NCs have been receiving more and more research attention due to their ultrasmall scale and unique properties such as quantized electronic states,<sup>13–15</sup> optical chirality,<sup>16–18</sup> magnetism,<sup>19</sup> and luminescence.<sup>20–22</sup> Such interesting properties make thiolate-protected Au/Ag NCs attractive not only in fundamental research but also in a wide spectrum of practical applications.<sup>20–25</sup>

Thiolate-stabilized Au/Ag NCs can be regarded as a special nanoparticle adopting a core–shell configuration in which Au or Ag atoms constitute the metal core and the thiolate group forms the shell layer. Figure 7.1A is a crystal structure of  $Au_{102}(SR)_{44}$  reported in 2007, which depicts the core comprising 102 Au atoms and the surface layer formed by  $-SR-(Au-SR)_n-$  staple motifs.<sup>4</sup> This scheme clearly outlines various attributes that are responsible for the physical property of a thiolate-protected Au or Ag NC, *e.g.*, the core size (or  $n$  value), the surface ligand amount and property, the interface formed between the organic stabilizer and the metal core and the resulting electron/energy transfer, and the replacement of certain amount of core metal with a second foreign metal. As a thiolate-protected Au/Ag NC generally contains only several to tens of atoms, the size of the metal core is very small (<2 nm) and is thus influenced by a strong quantum confinement effect, which results in unique molecular-like absorption and emission.<sup>26</sup> When thiolate-protected Au or Ag NCs are employed in energy-related devices, they are expected to be more efficient. Moreover, their well-defined formula also renders it amendable to control the core size, surface, composition, and photoluminescence property.

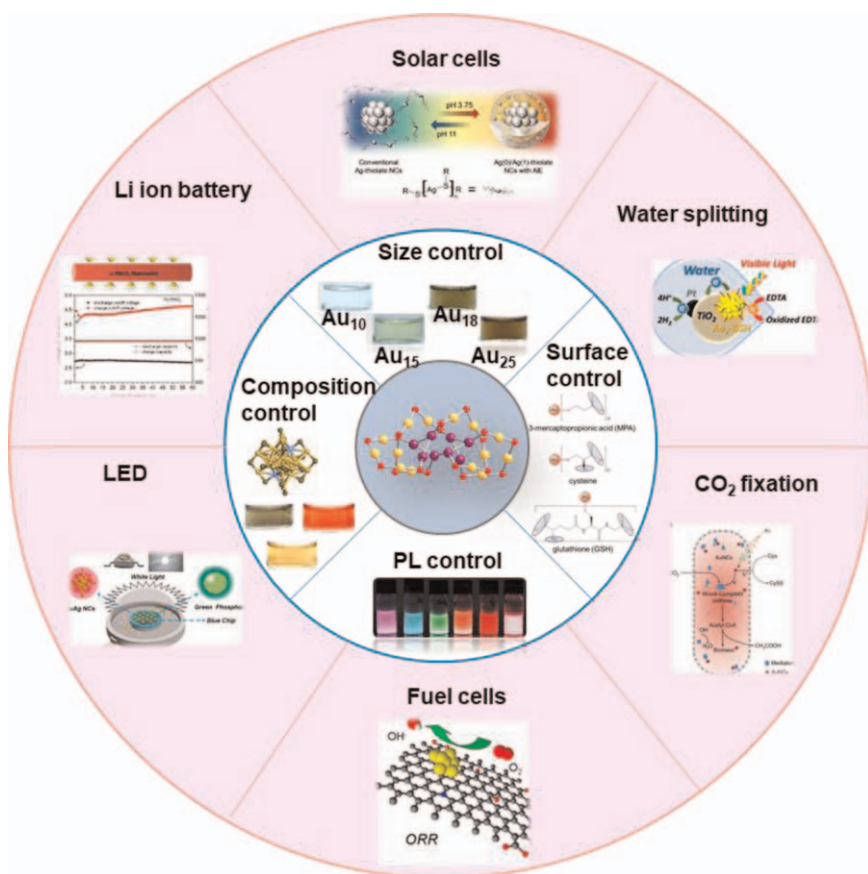
More importantly, the physicochemical behaviors of thiolate-coated Au/Ag NCs are greatly size tunable.<sup>27</sup> For example, a series of PAGE (polyacrylamide gel electrophoresis)–separated  $Au_n(SG)_m$  NCs ( $n$  and  $m$  are 10–39 and 10–24, respectively; GSH represents  $\gamma$ -glutathione, a naturally occurring tripeptide) exhibit different colors in aqueous solutions (as well as resulting in different optical absorption spectra) irrespective of only a small difference in the number of Au atoms to form NCs (Figure 7.1B).<sup>28</sup> Similarly, the bandgap energies of a spectrum of known thiolate-protected Au NCs show a general trend of size-dependent decrease with the increment of their core size (*i.e.*, the number of metal atoms in the core) (Figure 7.1C).<sup>29</sup> In the trend, some zig-zags imply the uniqueness of the atomic packing mode of each cluster, which may serve as a critical factor for determining their bandgap energies.



**Figure 7.1** Typical structure of thiolate-protected metal nanoclusters and their size- and component-dependent properties. (A) X-ray crystal structure of the  $\text{Au}_{102}(\text{SR})_{44}$  cluster.<sup>16</sup> (B) Images of a series of PAGE-separated Au NCs dissolved in water. Reproduced from ref. 28 with permission from American Chemical Society, Copyright 2005. (C) Bandgaps of Au NCs as a function of sizes. Reproduced from ref. 29 with permission from the Royal Society of Chemistry. (D-G) Comparison of a red-emissive  $\text{Au}_{22}(\text{SG})_{18}$  with  $\text{Au}_{25}(\text{SG})_{18}$ : (D,E) PAGE gels showing the two clusters migrate at a similar speed under daylight and UV light; (F) photoemission spectra and (G) UV-Vis absorption spectra of  $\text{Au}_{25}(\text{SG})_{18}$  (red line) and  $\text{Au}_{22}(\text{SG})_{18}$  (blue line) ( $\lambda_{\text{ex}} = 520$  nm). Reproduced from ref. 30 with permission from American Chemical Society, Copyright 2014.

Furthermore, the extreme sensitivity of Au NCs in size was not just observed for their appearance under daylight but also their photoluminescence property.<sup>30</sup> As shown in Figure 7.1D–G, two atomically precise Au clusters, namely,  $\text{Au}_{25}(\text{SG})_{18}$  (band 6' in lane i of the gel image) and  $\text{Au}_{22}(\text{SG})_{18}$  (band 4 in lane ii of the gel image), have the same type and number of surface ligand and only three atoms difference in core size. They migrate at a close speed in the electrophoresis but show very different UV–Vis spectra (Figure 7.1G) and luminescent properties (Figure 7.1F).  $\text{Au}_{25}(\text{SG})_{18}$  shows a negligible luminescence under UV light irradiation with photoluminescence quantum yield (PLQY) of 0.2%, while  $\text{Au}_{22}(\text{SG})_{18}$  shows bright red emission with a PLQY of 8%. As the first report of atomically precise thiolate-protected Au NCs showing strong photoluminescence, the high thiolate-to-Au ratio as an indication of the existence of a long Au–thiolate motif is ascribed to its strong photoluminescence.

The overall structure of this chapter is presented below (Figure 7.2). After a demonstration of the general synthesis strategies of thiolate-coated



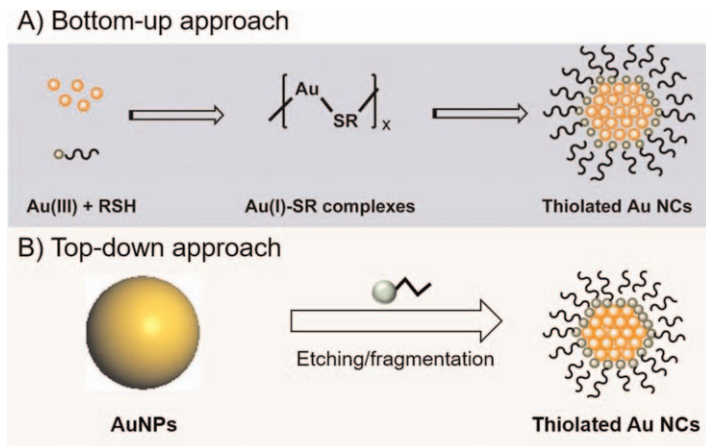
**Figure 7.2** Diagram depicting engineering size, surface, composition, and photoluminescence of ligand-protected metal nanoclusters toward diverse applications in energy conversion and efficiency.

Au/Ag NCs, progresses in engineering the size, surface, composition, and photoluminescence of thiolate-protected Au/Ag NCs are presented. Special emphases are placed on the mechanisms of controlling the size of thiolate-coated Au/Ag NC with accuracy in atomic number and giving out high luminescent yield, as various important applications of the thiolate-coated Au/Ag NCs in energy conversion and storage are governed by these two properties. Following the summary, the applications of thiolate-coated Au/Ag NCs in different fields of energy-related applications will be discussed, including solar cells (solar energy to electricity), water splitting (solar energy to fuels), CO<sub>2</sub> fixation (also solar energy to fuels), fuel cells (chemical fuels to electricity), white light-emitting devices (WLEDs) (electricity to light), and lithium-ion batteries (electricity storage). It should be mentioned that there is much excellent work on utilizing thiolate-protected Au/Ag NCs in energy-related applications. This chapter is not intended to be as comprehensive as possible. Rather, only a few typical and exemplary papers are discussed to make the chapter easy to read. Hopefully, this chapter serves as a tutorial guide for anyone who is keen to develop the application of thiolate-stabilized Au or Ag NCs for energy conversion and storage disciplines. Interested readers can refer to many good review articles discussing each related topic in more detail.<sup>31,32</sup>

## 7.2 Engineering Core Size, Surface Property, Composition, and Photoluminescence of Thiolate-coated Au or Ag NCs

Two basic strategies are employed to synthesize thiolate-coated Au/Ag NCs, namely, the top-down and bottom-up approaches, as demonstrated in Figure 7.3. In a classical top-down approach, large-sized nanoparticles having a wide distribution in size, some of which are relatively large and even in the micrometer size range, are subjected to a reaction solution containing a thiol as an etching agent. Through a series of reactions such as size reduction and/or structure reorganization effected by the strong metal–thiolate interactions, monodisperse thiolate-protected Au/Ag NCs can be synthesized (Figure 7.3B).<sup>33</sup> Sometimes, a two-phase system is also introduced to allow for the separation of monodisperse clusters from the initial polydisperse precursors to improve the size monodispersity of the final product.<sup>34,35</sup>

Alternatively, a typical bottom-up strategy involves a metal salt precursor as the source of metal element, a reducing agent that reduces the metal salt to its metallic form, and a protecting agent that prevents the aggregation of the formed metal NCs into large polydispersed metal nanoparticles. Figure 7.3A depicts the general process of synthesizing thiolate-protected Au NCs *via* a bottom-up approach. A thiol molecule (denoted as R-SH) usually reacts with an Au(III) salt first (typically gold trichloride hydrochloride) to form a polymeric Au(I)–thiolate complex, which is sequentially reduced with



**Figure 7.3** Schematic diagram for synthesizing thiolate-protected Au NCs *via* (A) bottom-up and (B) top-down approaches. Reproduced from ref. 23 with permission from the Royal Society of Chemistry.

the assistance of a reductive ligand and gradually forms thiolate-coated Au NCs. Many research efforts have been contributed to controlling the reaction kinetics of the formation of thiolate-protected Au NCs, including delicate control over the reaction temperature and the stirring speed during the formation of Au–thiolate complexes,<sup>36,37</sup> selection of a proper reducing agent to deliver a mild reducing power,<sup>38,39</sup> or purposely decreasing the reducing power of commonly used reducing agents (*e.g.*, sodium borohydride).<sup>40,41</sup> Due to the flexibility in controlling the reaction kinetics, a bottom-up approach has been widely adopted to control the core size, surface property, composition, and photoluminescence performance of thiolate-coated Au/Ag NCs.

### 7.2.1 Synthesis Strategies for Size Control

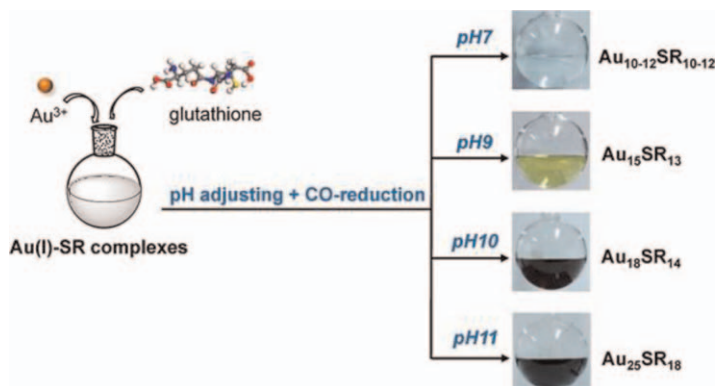
As discussed in the Introduction section, the physical and chemical behaviors of thiolate-protected Au/Ag NCs are critically dependent on their core size, *i.e.*, the  $n$  value of the general denotation of  $\text{Au}_n(\text{SR})_m$ . Therefore, size control at atomic precision is the first pivotal step in the synthesis of thiolate-protected Au/Ag NCs toward realizing real applications. Many strategies have been developed to manipulate the size of thiolate-coated Au/Ag NCs in recent years' progress of thiolate-protected Au/Ag NCs.<sup>42,43</sup> Kinetic control, size focusing, and size transformation induced by ligand exchange are three of the most effective strategies developed thus far that have proven their capability in the production of thiolate-coated Au NCs with controllable sizes. A few typical works are discussed below in detail for each strategy.

### 7.2.1.1 Size Control by Kinetic Control

A bottom-up method for producing thiolate-coated Au or Ag NCs outlines two key factors that dictate the dimension of Au or Ag NCs, which are respectively the polymerization degree/size of the Au(I)-SR complex and the reductive ability of the used reducing substrate. When the Au(III) salt is mixed with a thiol molecule, it is first reduced by the -SH group to link Au(I). The resultant Au(I) then binds strongly with thiolate to form Au(I)-SR complexes. It is easy to reach the hypothesis that the polymerization degree/configuration of the Au(I)-SR complex sets a barrier for the complexes to be reduced. On the other hand, the reducing capability of the reducing agent drives the reduction of the complexes toward the formation of Au NCs. A balance of the two competing forces thus determines the size of the final product in a dynamic way.

The size effect of the Au(I)-SR complex on the thiolate-protected Au NCs was studied by Zhu *et al.*<sup>36</sup> It has been observed that a polymeric Au(I)-SR complex with a size range of 100–400 nm obtained by adjusting the reaction temperature at 0 °C and the stirring speed at ~30 rpm led to Au<sub>25</sub> with a higher yield upon reductive decomposition. Alternatively, the Au(I)-SR complex formed at room temperature showed multiple sizes, including the sizes of <2 nm, 100–400 nm, and >1 μm, even larger aggregates (i.e., polydispersed Au NCs). The configuration of the Au(I)-SR complexes also plays a great function in tuning the size of Au NCs. As demonstrated by Yuan *et al.*, surfactants such as cetyltrimethylammonium bromide (CTAB) were used to form a protecting shell on Au(I)-SR complexes through electrostatic interactions between CTA<sup>+</sup> and COO<sup>-</sup> of the thiolate ligands.<sup>44</sup> The CTAB-protected Au(I)-SR complexes were able to create a unique microenvironment through the formation of well-defined inverse micelles in toluene. High-quality Au<sub>25</sub>(SR)<sub>18</sub> was synthesized in as fast as 10 min.

On the other hand, controlling the reducing power of the reducing agent is a widely adopted approach to realize the atomically precise control of thiolate-coated Au/Ag NCs. Sodium borohydride (NaBH<sub>4</sub>) is a reducing agent frequently used to produce thiolate-coated Au or Ag NCs. However, its reductive capability is relatively strong to control the reaction kinetics. Ways to control the reducing power of NaBH<sub>4</sub> include reducing its concentration, limiting its diffusion by adopting a solid-state synthesis, or dissolving it in diluted alkaline solutions.<sup>37,45,46</sup> Borane-based reducing agents such as borane-*tert*-butylamine complex and sodium cyanoborohydride are good alternatives to NaBH<sub>4</sub> as they possess a weaker reducing power. Good examples of using borane-based reductive agents include the production of thiolate-protected Au NCs of small core sizes, such as Au<sub>15</sub>(SR)<sub>13</sub>, Au<sub>18</sub>(SR)<sub>14</sub>, and Au<sub>19</sub>(SR)<sub>13</sub> NCs, as reported by several different researchers.<sup>38,39,47</sup> Gaseous reductants such as CO have also emerged as important reductants for NC synthesis in recent years. It not only provides a mild reduction environment but also improves the synthesis quality due to its coordination ability. For example, the authors' group developed a



**Figure 7.4** Synthesis of different-sized Au NCs by implementing a facile CO reduction method. Reproduced from ref. 48 with permission from American Chemical Society, Copyright 2013.

CO-based strategy for versatily controlling the size of thiolate-coated Au NCs. Through changing the pH of the Au(I)–SR complexes solution before CO reduction, various Au NCs with precision on atomic number, namely,  $\text{Au}_{10-12}(\text{SR})_{10-12}$ ,  $\text{Au}_{15}(\text{SR})_{13}$ ,  $\text{Au}_{18}(\text{SR})_{14}$ , and  $\text{Au}_{25}(\text{SR})_{18}$ , were obtained in large quantities (scalable to hundreds of milligrams) (Figure 7.4).<sup>48</sup> By extending this method in a methanol–water mixed solvent system, the production of  $\text{Au}_{29}(\text{SR})_{20}$  was also achieved at a large scale.<sup>49</sup>

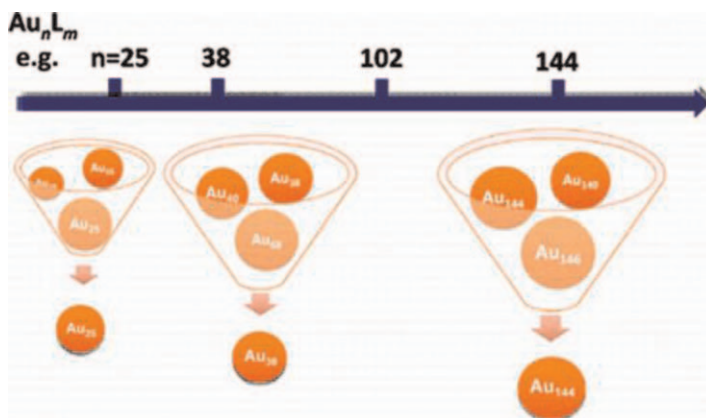
### 7.2.1.2 Size Control by Size Focusing

Size focusing is another important method developed by Jin *et al.* to prepare thiolate-coated Au or Ag NCs having tunable sizes.<sup>50</sup> Size focusing refers to a phenomenon that  $\text{Au}_n(\text{SR})_m$  NCs with certain sizes always survive selectively from a harsh environment (*e.g.*, thiol as etching agents). The underlying principle for the size focusing method is based on the great difference in the stability of thiolate-protected Au or Ag NCs of varied sizes. For example, Shichibu *et al.* applied thiol etching to a series of glutathione-protected  $\text{Au}_n$  NCs ( $n = 10-39$ ) and found that  $\text{Au}_{25}(\text{SG})_{18}$  exhibited extreme stability against thiol etching.<sup>51</sup> A facile synthesis method of  $\text{Au}_{25}(\text{SG})_{18}$  was therefore developed by treating polydispersed Au NCs in glutathione solution at an elevated temperature.<sup>52</sup> The extreme stability of  $\text{Au}_{25}(\text{SR})_{18}$  was also found in other research works. The size change during the size focusing process was monitored *via* UV–Vis absorbance spectra and matrix-assisted desorption ionization mass spectra.<sup>53–55</sup>

In general, the process of size focusing is a rather common phenomenon among various-sized Au NCs. Another interesting work is the preparation of  $\text{Au}_{38}(\text{SR})_{24}$ . Qian and coworker reported a two-step synthesis procedure for  $\text{Au}_{38}(\text{SR})_{24}$ .<sup>56</sup> In this first step, polymeric complexes formed by reacting Au salts with glutathione in acetone were reduced by  $\text{NaBH}_4$  to form

polydispersed  $Au_n$  ( $38 \leq n \leq 102$ ) NCs. In the second step, the polydispersed  $Au_n$  ( $38 \leq n \leq 102$ ) NCs were treated by a different thiol (2-phenylethanethiol or  $PhC_2H_4SH$ ) in the solvent of toluene and the reaction at  $80^\circ C$  for 40 h led to the production of  $Au_{38}(SR)_{24}$  at a high yield (25%). In addition, the production of  $Au_{144}(SR)_{60}$  is another atomic precise cluster synthesized by using size focusing.<sup>56</sup> It also involves two steps similar to the synthesis of  $Au_{38}$  but with some modifications. The first step adopted a revised Brust-Schiffrin method to synthesize polydispersed Au clusters. Specifically, Au chloride salts were dissolved in methanol with the assistance of a surfactant tetraoctylammonium bromide (TOAB), while  $NaBH_4$  was prepared in deionized water. The mixture solvent promotes the precipitation of polydispersed Au NCs upon reduction. These Au NC precipitates were then subjected to thiol etching to yield  $Au_{144}$  and  $Au_{25}$  as the major products. As  $Au_{25}$  is soluble in acetone while  $Au_{144}$  is insoluble,  $Au_{144}$  was harvested by washing the mixture with acetone.

In summary, size focusing has been demonstrated to be a versatile method for the size-controlled production of thiolate-coated Au NCs (Figure 7.5). The critical step of this method is described as the achievement of a correct size distribution of the polydispersed Au NCs, which is carried out before the thiol-mediated size focusing reaction. Typically, in the preparation of  $Au_{38}$  discussed earlier, the preselection of Au NCs with a desired size distribution ( $38 \leq n \leq 102$ ) is the key for the generation of  $Au_{38}(SR)_{24}$  as  $Au_{25}$  and  $Au_{102}$  seem more stable over  $Au_{38}$ .<sup>16,50</sup> Time course characterizations such as UV-Vis absorbance spectra and mass spectrometry are powerful techniques to monitor the size evolution in the course of size focusing.



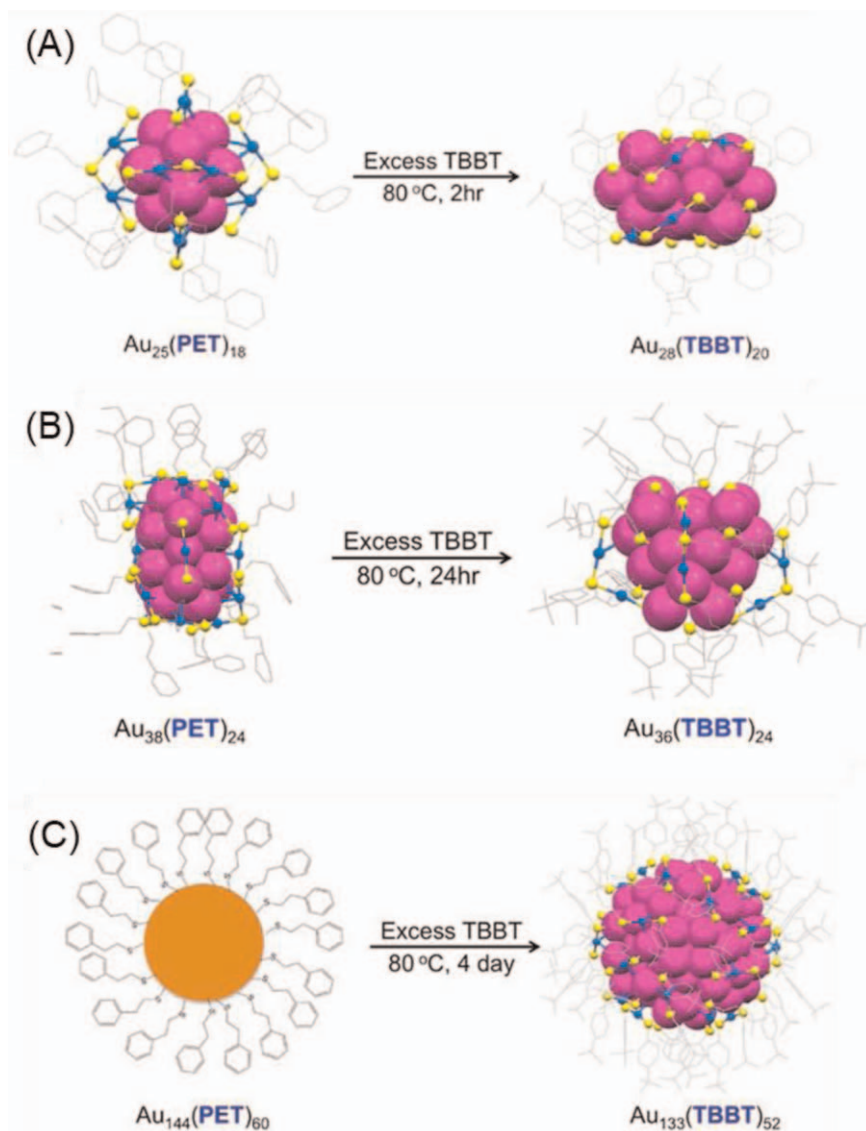
**Figure 7.5** Selective syntheses of atomically precise Au NCs using the size focusing method. Reproduced from ref. 50 with permission from American Chemical Society, Copyright 2010.



### 7.2.1.3 Size Alteration During Ligand Exchange

In more recent years, the alteration of Au NCs from one size to another one has been an interesting research topic in the community of NC development. Thanks to the availability of various Au NCs in different sizes synthesized by either kinetic control or size focusing, it has become much easier to expand the universe of different-sized Au NCs with the development of a strategy called ligand exchange-induced size transformation.<sup>57</sup>

Although previously developed size focusing methods have resulted in a stable range of sizes, these “from bottom to up” compositions are like still a “trial-and-error” process in many cases. To address this issue, Zeng *et al.* recently demonstrated a new method for inducing the alternation of NCs in size and structure by exchanging their surface ligands, thereby obtaining new  $\text{Au}_n(\text{SR})_m$  NCs.<sup>57</sup> As shown in Figure 7.6A, the  $\text{Au}_{25}(\text{PET})_{18}$  ( $\text{PET}=\text{SCH}_2\text{CH}_2\text{Ph}$ ) cluster undergoes a ligand exchange and gradually evolves into other stable NCs that are formulated as  $\text{Au}_{28}(\text{TBBT})_{20}$ .<sup>58</sup> In detail, the transformation kinetics can be carefully tuned to trigger the thermal reaction of  $\text{Au}_{25}(\text{PET})_{18}$  with excess TBBT thiol *via* increasing the reaction temperature to 80 °C so that the size/structure transformation from ligand exchanging becomes faster; after a reaction period of ~2 h, all the  $\text{Au}_{25}(\text{PET})_{18}$  clusters were characterized to be completely converted into  $\text{Au}_{28}(\text{TBBT})_{20}$  with a high yield of >90%. Through studying the crystal structure of  $\text{Au}_{28}(\text{TBBT})_{20}$ , it is revealed that the  $\text{Au}_{28}(\text{TBBT})_{20}$  structure is also greatly different from that of the starting  $\text{Au}_{25}(\text{PET})_{18}$ , which has a core of icosahedral  $\text{Au}_{13}$  kernel and six surface-protective  $\text{Au}_2(\text{SR})_3$  dimeric staple motifs. Alternatively, they successfully used mercaptan for the first time in the mercaptan heat exchange between molecular pure  $\text{Au}_{38}(\text{PET})_{24}$  clusters and 4-*tert*-butylbenzenethiol (TBBT). As shown in Figure 7.6,<sup>59</sup>  $\text{Au}_{38}(\text{PET})_{24}$  NCs react in the presence of TBBT at 80 °C for more than 12 h. TBBT and PET were introduced on the  $\text{Au}_{38}$  cluster at a mole ratio of 160:1, which was a much higher value in various ligand exchange experiments. By clean mass spectrometry and thermogravimetric analysis, the process was confirmed to yield a new  $\text{Au}_{36}(\text{TBBT})_{24}$  cluster with a high yield of >90% (gold atomic base) and high purity at the molecular scale. Interestingly, the  $\text{Au}_{36}(\text{TBBT})_{24}$  cluster has a face-centered cubic (FCC) crystalline structure, greatly different from the initial  $\text{Au}_{38}(\text{PET})_{24}$  NC, although they were only performed at different temperatures and times. The FCC configuration was supposed to be unstable at a smaller size, and gold atoms exhibited the FCC atomic stacking pattern only when the size was larger than a critical value.  $\text{Au}_{36}(\text{TBBT})_{24}$  is the first example to exhibit FCC crystal observed in  $\text{Au}_n(\text{SR})_m$  clusters. This discussion shows that surface ligand indeed plays a key function in stabilizing  $\text{Au}_{36}$  cluster FCC kernel. Furthermore, Zeng *et al.* successfully converted  $\text{Au}_{144}(\text{PET})_{60}$  clusters into  $\text{Au}_{133}(\text{TBBT})_{52}$  NCs (Figure 7.6C), which was carried out by the thermal treatment of pure  $\text{Au}_{144}(\text{PET})_{60}$  in the presence of excess TBBT (the mole ratio of TBBT and PET was set as 370:1) at 80 °C for 4 days.<sup>60</sup> Therefore, this transformation chemistry also has an impact on the efficiency of larger NCs.



**Figure 7.6** Synthesis of atomically precise Au NCs by a ligand exchange–induced transformation method. Reproduced from ref. 57 with permission from American Chemical Society, Copyright 2015.

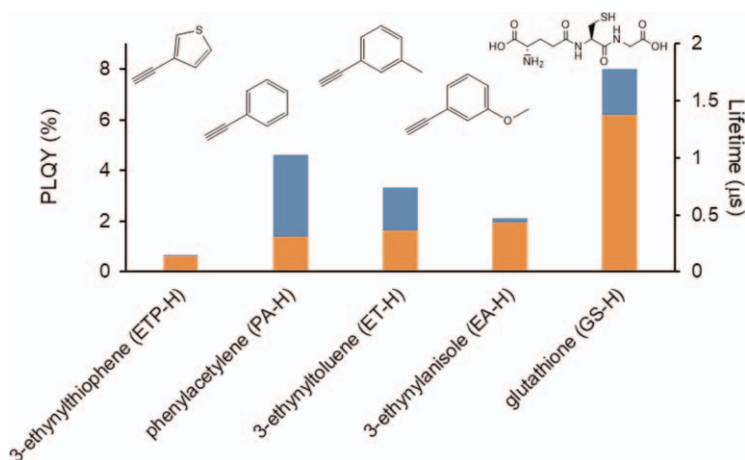
Combined with the size focusing method, other sized stable  $\text{Au}_n(\text{SR})_m$  clusters were synthesized *via* ligand exchange in future research, whose basis is the varied stability of different-sized  $\text{Au}_n(\text{SR})_m$  clusters. In contrast to the size-focusing production of metal NCs, ligand exchange for inducing size/structure optimization is a simpler reaction, because the size-focusing

synthesis usually undergoes complicated procedures like reduction, nucleation, growth, and etching, and fine-tuning of each reaction step is required for achieving a high uniformity on cluster size. Therefore, the size focusing approach needs much effort to optimize the reaction conditions for obtaining the pure single-sized clusters. Whereas the ligand exchange strategy is simply started from pure clusters at a specific size (*e.g.*, Au<sub>38</sub>) and can exclusively lead to the production of the highly stable clusters with close sizes as the starting clusters (*e.g.*, Au<sub>36</sub>). In previous works, it was clearly revealed that the simple strategy of ligand exchange significantly benefits realizing the generation of new magic sizes.

However, the ligand exchange process is first dependent on the production of pure magic sizes, which can be achieved *via* the size focusing approach. Moreover, not all types of thiolate ligands can be successfully utilized in the size transformation process. For instance, the thiolate ligands having very bulky carbon groups and weak affinity onto gold (*e.g.*, bulky adamantanethiol) would be reluctant in the ligand exchange process, which can quench the ligand exchange at the early stage. In addition, the ligand exchange process often resulted in a mixed-ligand shell on clusters due to an incomplete exchange between one ligand and another. As revealed, the type of ligand can determine the magic-sized NCs and the geometric configuration of the ligand played a more important function in determining the crystalline structure compared to the electronic effect. It can be concluded that the ligand exchange reaction can become an effective method to fabricate interesting NCs with new magic sizes and offer many insights for understanding the nanoscale transformation in chemistry. It is thus reasonable to say the ligand exchange preparation may be a good research topic for obtaining atomically precise clusters.

## 7.2.2 Surface Control

Other than controlling the core size of Au NCs at atomic precision, the surface features of Au NCs can also be modified by using different protecting agents while keeping the core size unchanged. An interesting case is the synthesis of Au<sub>22</sub>L<sub>18</sub>. Yu *et al.* discovered a bright red-emissive Au NC in a CO reduction method, which was identified as Au<sub>22</sub>(SG)<sub>18</sub> through electrospray ionization mass spectrometry (ESI-MS).<sup>30</sup> With a size close to the well-known Au<sub>25</sub>(SG)<sub>18</sub>, its property is distinctively different. In a separate study later, a series of alkynyl ligands were used as protecting agents for the synthesis of Au<sub>22</sub>(C=CR)<sub>18</sub> NCs.<sup>61</sup> While only the Au<sub>22</sub>(ETP)<sub>18</sub> NC (ETP=3-ethynylthiophene) was crystallized to resolve its structure, which contains a bitetrahedral Au<sub>7</sub> core coated by three oligomers of Au<sub>3</sub>(ETP)<sub>4</sub> and one ring of Au<sub>6</sub>(ETP)<sub>6</sub>, UV-Vis and 1H NMR spectroscopy clearly reveal that the four clusters adopt the same geometric and electronic structures. Interestingly, the photoluminescence property is strongly influenced by the R group. Figure 7.7 summarizes the PLQY and lifetime of the five Au<sub>22</sub>R<sub>18</sub> clusters reported thus far with different protecting ligands (see inset for the molecular structure



**Figure 7.7** Comparing PLQY and lifetime of  $\text{Au}_{22}$  cluster protected by two different types of ligand.<sup>30,61</sup>

of each ligand). The photoluminescence QY follows the sequence of  $\text{Au}_{22}(\text{SG})_{18} > \text{Au}_{22}(\text{PA})_{18} > \text{Au}_{22}(\text{ET})_{18} > \text{Au}_{22}(\text{EA})_{18} > \text{Au}_{22}(\text{ETP})_{18}$ , while the lifetime follows the sequence of  $\text{Au}_{22}(\text{SG})_{18} > \text{Au}_{22}(\text{EA})_{18} > \text{Au}_{22}(\text{ET})_{18} > \text{Au}_{22}(\text{PA})_{18} > \text{Au}_{22}(\text{ETP})_{18}$ .

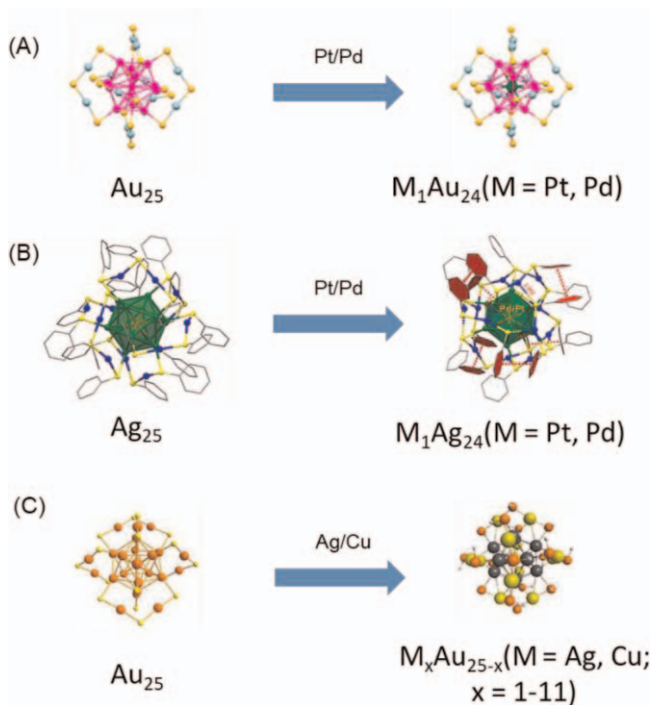
### 7.2.3 Composition Control

Over the past decades, various great developments in the production, isolation, characterization, and crystalline structure of a remarkable number of gold species have been made,<sup>62–64</sup> but similar advances have only been made for a few species of silver.<sup>65–69</sup> Based on current research, the reported silver NCs cannot match their gold NC analogs, which makes it difficult and challenging to directly compare gold and silver NCs. The research efforts have started to achieve the doping of silver atoms into gold NCs, although the amount of dopant did not equal the total gold atoms due to the fact that there are only limited accessible positions within gold NCs for keeping the original crystal structure. For example, when doping Ag into the  $\text{Au}_{25}$  cluster, there are 12 exchangeable sites in  $\text{Au}_{25}$  for maintaining the structural integrity of NCs.<sup>70</sup> Further increment of the dopant amount resulted in the decomposition of NC, which may be because of the instability of Ag NCs. As revealed, Au NCs with the same ligand can exhibit various sizes; in contrast, Ag NCs exhibit a much stronger relationship between size and ligand type.<sup>71–73</sup>

With the development of Ag-doped Au NCs, other metals are also used as dopants to extend the types of noble metal NCs. Typically, Murray's group synthesized monopalladium-contained  $\text{Pd}_1\text{Au}_{24}(\text{SC}_2\text{H}_4\text{Ph})_{18}$  clusters in the presence of other clusters such as  $\text{Au}_{25}(\text{SC}_2\text{H}_4\text{Ph})_{18}$ , which was characterized by mass spectrometry.<sup>74</sup> Negishi's group utilized solvent fractionation together with high-performance liquid chromatography to achieve the

successful isolation of pure  $\text{Pd}_1\text{Au}_{24}(\text{SC}_{12}\text{H}_{25})_{18}$ , in which Pd atom was located at the place of the central Au atom in  $\text{Au}_{25}(\text{SR})_{18}$ .<sup>75</sup> Similarly, two approaches were demonstrated by Qian *et al.* for synthesizing  $\text{Pd}_1\text{Au}_{24}(\text{SC}_2\text{H}_4\text{Ph})_{18}$  clusters (Figure 7.8A), which were successfully isolated for being identified from the atomic structure by using the fragmentation pattern in mass spectroscopy.<sup>76</sup> Interestingly, the synthesized doped NCs exhibited a continuous blueshift in absorbance and fluorescence peaks with an increment of Ag atoms in  $\text{Ag}_x\text{Au}_{25-x}(\text{SR})_{18}$ .<sup>77</sup> In theory, beyond Pd and Ag, there are still 14 elements in groups 1, 2, and 10–14, that can be used as dopants for replacing the central Au of  $\text{Au}_{25}(\text{SR})_{18}$  while maintaining the electronic and crystal structures.<sup>78,79</sup> Among various doped NCs, the monoplatinum-contained  $\text{Pt}_1\text{Au}_{24}(\text{SR})_{18}$  NC was confirmed to have the strongest interaction between the central atom and the surrounding  $\text{Au}_{24}(\text{SR})_{18}$  shell. In Qian's work,  $\text{Pt}_1\text{Au}_{24}(\text{SC}_2\text{H}_4\text{Ph})_{18}$  clusters were successfully synthesized and isolated to exhibit a similar structure to  $\text{Au}_{25}(\text{SR})_{18}$  – only Pt atom replaced the central Au atom in new NC.<sup>80</sup>

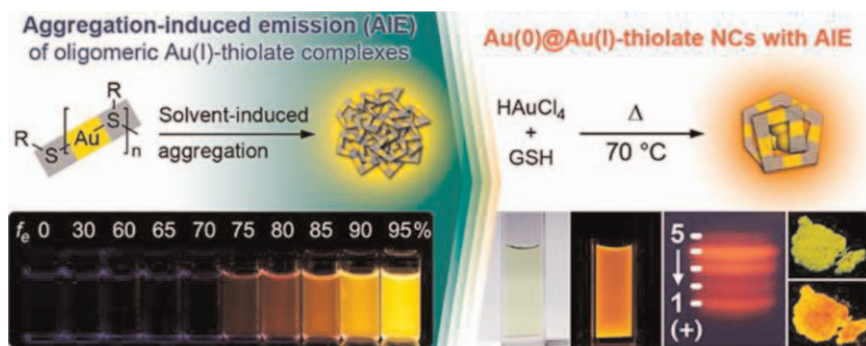
After doping Pd or Pt atoms, Yan *et al.* successfully prepared thiol-rich  $\text{Ag}_{25}$ -metal atom NCs for the first time and characterized their structures



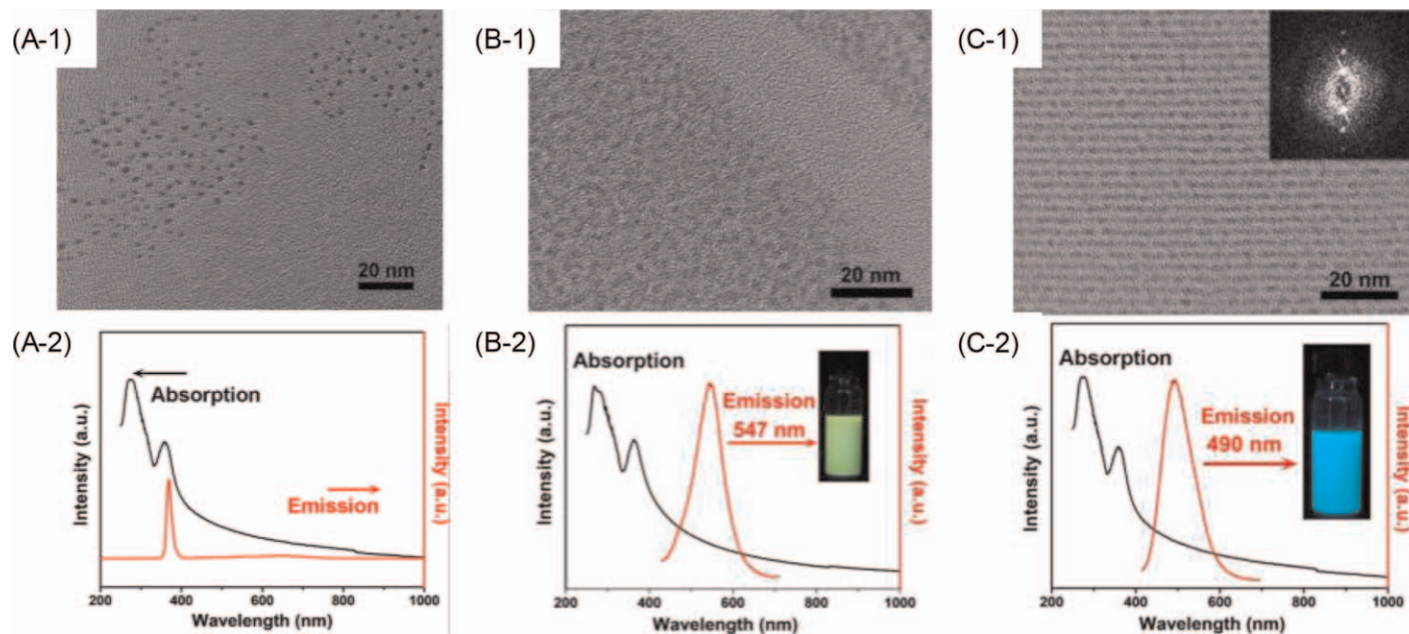
**Figure 7.8** Scheme showing the doping of a foreign metal into Au or Ag cluster to form bimetallic alloy clusters. Reproduced from ref. 80–82 from American Chemical Society, Copyright 2012 and 2015.

(Figure 7.8B).<sup>71,81</sup> 25-metal-atom NCs composed of  $[\text{PdAg}_{24}(\text{SR})_{18}]^{2-}$  or  $[\text{PtAg}_{24}(\text{SR})_{18}]^{2-}$  have a frame structure like the widely studied  $\text{Au}_{25}(\text{SR})_{18}$ . In those two types of NCs, the  $\text{M@Ag}_{12}$  (M refers to the metal dopant) core was covered with six twisted dimeric  $-\text{RS}-\text{Ag}-\text{SR}-\text{Ag}-\text{SR}-$  units. Different from that structure, the silver-thiolate overburden produces geometric chirality with the variance of  $\text{Au}_{25}(\text{SR})_{18}$ . The change in electronic structure was also investigated after being doped with other metals by measuring their UV-Vis absorbance spectra and theoretically simulating their configuration using density functional theory. As suggested, the modulation of the electronic structure by changing the metal dopant can offer an effective approach to control the electronic behaviors of thiolate-protected metal clusters, such as optical, chemical, and catalytic properties.

Guidez *et al.* studied the  $\text{Au}_{25-n}\text{Ag}_n(\text{SH})_{18}^-$  ( $n = 1, 2, 4, 6, 8, 10, 12$ ) system through density functional theory (Figure 7.10C) and studied the effect of silver doping on the  $\text{Au}_{25}(\text{SH})_{18}^-$  system.<sup>82</sup> When one silver atom was doped, the icosahedral shells of metal nuclei were more energetically favorable compared with the incorporation of metal-thiolate units or core centers. When the doped silver atoms are equal to or more than two, only the doping of silver happens on the core surface, and when the silver dopant is near, the favorable degree of the arrangement is slightly lower. However, the difference in energy is small so that all doped NCs are reachable by optimizing the experimental conditions, which exhibited similar characteristics in the excitation spectra to the undoped  $\text{Au}_{25}(\text{SH})_{18}^-$ . A main difference is that the blueshift was observed for the low-energy HOMO-LUMO ( $1\text{P} \rightarrow 1\text{D}$ ) (HOMO = Highest Occupied Molecular Orbital; LUMO = Lowest Unoccupied Molecular Orbital) peaks and the peak's intensity at 2.5 eV increased with the increase in the number of doped silver atoms. The doping of silver reduces the energy of ligand orbitals and promotes the transition between superatomic orbitals. The silver-incorporated system exhibits a wider excitation spectrum because it breaks the symmetry of the superatomic orbitals.



**Figure 7.9** Schematic illustration of synthesis highly luminescent Au NCs *via* an aggregation-induced emission (AIE) mechanism. Reproduced from ref. 83 with permission from American Chemical Society, Copyright 2012.



**Figure 7.10** Converting nonfluorescent Cu NCs to strongly emissive ones *via* self-assembly into different structures (yellow for sheets while cyan for ribbons). Reproduced from ref. 84 with permission from American Chemical Society, Copyright 2015.

## 7.2.4 Photoluminescence Control

Charge transfer from ligand to metal usually signifies poor QY because of the efficient pathways of nonradiative relaxation *via* surface–ligand vibrations and rotations. So, ways to suppress the surface–ligand motions and decrease the charge transfer interactions may be helpful to enhance the photoluminescence of Au NCs. Until now, approaches to enhance photoluminescence (PL) include aggregation-induced emission, ligand rigidification, doping with foreign atoms, host–guest interaction of the ligand shell, and matrix confinement.

### 7.2.4.1 Aggregation-induced Emission Enhancement

In contrast with small dyes that face aggregation-caused quenching problems, the photoluminescence of metal NCs can be enhanced through the phenomenon of aggregation-induced emission (AIE), which significantly restricts the stretching and rotation motion of surface ligand and suppresses the nonradiative relaxation pathways. Generally, the aggregation of metal NCs can be induced by the introduction of pure solvents and cations that screen off the negatively charged metal NCs. Luo *et al.* generated strong fluorescence with the assistance of the AIE mechanism. Then, a one-pot strategy was developed to produce highly fluorescent gold-thiolate clusters possessing a QY of ~15% by using the AIE properties of the complex (Figure 7.9).<sup>83</sup>

In addition, the assembly of metal NCs to periodical micrometer-sized structures or crystallization also helps with the photoluminescence enhancement of metal NCs. Yang *et al.* demonstrated a great increment in fluorescence intensity for 1-dodecanethiol (DT)-covered Cu NCs after the self-assembly process.<sup>84</sup> As revealed, the formation of a compact and ordered structure made the original nonluminescent NCs emit strong fluorescence.

Cu NCs for the study of assembly-induced luminescence enhancement were first synthesized at 0 °C in dibenzyl ether by utilizing DT as a protective and reducing agent. The transmission electron microscope (TEM) image shows that the resultant Cu NCs are quasispherical structures with an average size of  $1.9 \pm 0.2$  nm (Figure 7.10A-1). There was no fluorescence in the visible range to be observed by excitation at 365 nm, indicating a low fluorescence efficiency of single Cu NCs (Figure 7.10A-2). To further illustrate the increase in emission intensity induced by self-assembly, self-assembled copper nanocrystals with loose aggregation structures were fabricated. Sheet formation takes place at a lower annealing temperature (*i.e.*, 20 °C) compared to thin strips, but for a long treatment time of 24 h. The condition of low temperature inhibits the fluidity of the DT alkyl chain and thus inhibits DT entanglement on adjacent NCs, resulting in a loose assembly configuration. TEM image shows the loose arrangement of Cu NCs in plates (Figure 7.10B-1). It is worth noting that when the fluorescence intensity decreased, the generation of thin slices with low-density NCs arrangement causes the emission spectrum to redshift to 547 nm, with

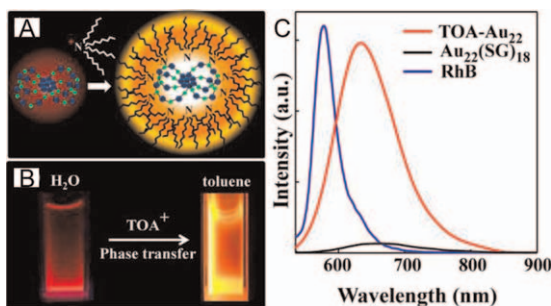


a half-width of about 84 nm (Figure 7.10B-2), and the apparent emission color turns yellow.

Further, Cu NCs were self-assembled into bands by annealing the di-benzyl ether solution of Cu NCs at 128 °C. After 3 h, the annealing process promoted the dynamic migration of the DT alkyl chain on the NCs, allowing a two-dimensional directional self-assembly of the NCs through dipole-driven van der Waals gravity in an asymmetric format. The progress of self-assembly was characteristic of nanoscale metal NCs and was determined by the metal types. The morphology of self-assembled structures depends largely on the type of metal by changing the coordinating interaction of weak interactions between different NCs. Cu produces a stronger NCs interdipole attraction. Therefore, copper nanocrystals tend to generate self-assembly bands at a one-dimensional orientation. As shown in the TEM image, the ribbon is composed of single NCs rather than Cu nanocrystal, and the Cu NCs show a highly ordered structure within the ribbon region (Figure 7.10C-1). Although the size, composition, structure, and optical properties of Cu NCs remained unchanged, it was found that the NC emission intensity increased significantly after self-assembly. The NCs component shows a blue-green fluorescent color and a high fluorescent peak centered at 490 nm, having a half-height width of about 86 nm (Figure 7.10C-2). As revealed, assembly-driven fluorescence increment was assigned to two factors. Firstly, the enhanced inter- and intra-NCs cuprophilic interactions greatly contribute to the excited-state relaxation dynamics in a radiative way. Secondly, the intramolecular vibration and rotation of the coating ligand were restricted to reduce the nonradiative relaxation of the excited state. These two processes significantly increase the fluorescent intensity of the self-assembled NCs.

#### 7.2.4.2 Ligand Rigidification

Fluorescent nanostructured materials have been attracting more research interest for a long time because they provide outstanding performance for being utilized in organic/inorganic light-emitting displays, optoelectronics, optical sensing, biological imaging, and fast diagnostics.<sup>85</sup> As demonstrated, core-shell Au NCs at atomic precision presented a good prospect for achieving high fluorescence emission. Using Au<sub>22</sub>(SG)<sub>18</sub> NCs as starting materials, Kyunglim Pyo *et al.* produced Au NCs to exhibit a luminescent QY greater than 60% by curing the gold shell with tetraoctylammonium (TOA) cations.<sup>85</sup> Time-resolved and temperature-dependent optical observations showed that the Au<sub>22</sub>(SG)<sub>18</sub> had a high fluorescent QY in the visible range below freezing, suggesting that the shell rigidity significantly enhanced the fluorescence quantum efficiency. In this work, Au<sub>22</sub>(SG)<sub>18</sub> NCs were bound with bulky TOA for achieving high rigidity of the gold shell, resulting in a QY higher than 60% at room temperature. This work provided an effective method to increase the luminescence efficiencies of Au NCs by rigidifying the shell of Au(I)-thiolate.



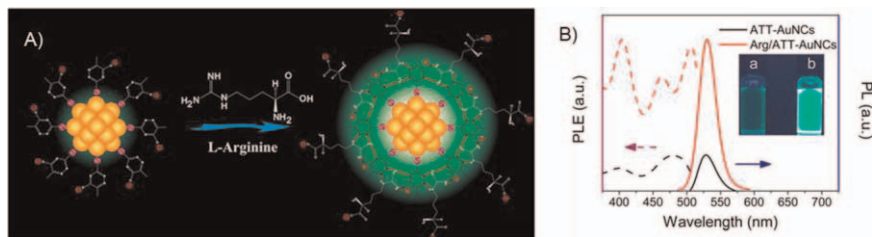
**Figure 7.11** PL enhancement by rigidifying the Au(I)-thiolate shell of Au<sub>22</sub>SG<sub>18</sub> NC via phase transfer. Reproduced from ref. 85 with permission from American Chemical Society, Copyright 2015.

Kyunglim Pyo and coworkers believed that there were remarkable intramolecular interactions between the alkyl chains of TOA cations, resulting in a hard shell of Au(I)-thioether, as shown in Figure 7.11A.<sup>49</sup> The electrostatic affinity between the carboxylate anions of the Au<sub>22</sub>(SG)<sub>18</sub> NC in the aqueous phase and the TOA cation in toluene was very strong, and thus, the TOA-linked Au<sub>22</sub> cluster was easily transferred into the toluene phase after a few minutes. Moreover, the TOA-linked Au<sub>22</sub> NCs (TOA-Au<sub>22</sub>) were observed to be very stable in the toluene phase and can be dissolved in many other organic solvents. After TOA pairing, the luminescence intensity was significantly enhanced, as shown in Figure 7.11B. In toluene, the strength of the TOA-Au<sub>22</sub> cluster increased by nearly nine times, with a QY of 62%. At the same time, as shown in Figure 7.11C, the luminescence maximum shifted to higher energies (~630 nm), indicating that the binding of the Au shell with TOA changed the luminescent triplet state. It is also worth noting that these properties significantly differ from the observed AIE process of Au(I)-thiolate complexes, which resulted in the ubiquity of TOA-Au<sub>22</sub> NC.

#### 7.2.4.3 Doping with Foreign Atoms

Rod-like Au<sub>25</sub> NCs have a poor photoluminescent ability (QY ≈ 0.1%) and therefore have no real utilization in biological imaging and related fields. Wang *et al.* showed that substituting gold atoms with silver atoms for the 25-atom matrix can significantly increase photoluminescent intensity.<sup>86</sup> The resulting Ag<sub>x</sub>Au<sub>25-x</sub> ( $x = 1-13$ ) clusters showed a higher QY (QY = 40.1%), in sharp contrast to the usually weakly fluorescent Ag<sub>x</sub>Au<sub>25-x</sub> clusters (QY = 0.21%).

First, Au<sub>25</sub> and silver-doped I and II NCs used the same biicosahedral configuration. Since [Ag<sub>x</sub>Au<sub>25-x</sub>(PPh<sub>3</sub>)<sub>10</sub>(SC<sub>2</sub>H<sub>4</sub>Ph)<sub>5</sub>Cl<sub>2</sub>]<sup>2+</sup> clusters contained different amounts of Ag atoms and X-ray crystallography only gives a map of average electron density, partial occupation analysis (POA) was further performed to reveal the special locations of Ag dopants in the double icosahedral configuration. The POA result shows that in samples I and II, the top and bottom vertex places are mostly occupied by silver atoms, compared to

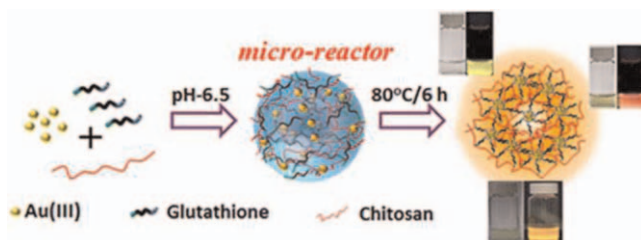


**Figure 7.12** Photoluminescence enhancement of Au NCs *via* host-guest recognition. (A) Diagram of photoluminescence enhancement of a 6-aza-2-thiothymine-protected Au NCs (ATT-Au NCs) using L-arginine as a guest molecule. (B) Photoexcitation (dashed curves) and photoemission (solid curves) spectra of the ATT-Au NCs (item a and black curves) and Arg/ATT-Au NCs (item b and red curves). Reproduced from ref. 87 with permission from American Chemical Society, Copyright 2017.

the Au vertex positions in pure Au<sub>25</sub> NCs. This is because these two vertex positions bound to Cl and Ag have a stronger interaction for halogens than Au. In sample I, a series of Ag<sub>x</sub>Au<sub>25-x</sub> clusters ( $x < 12$ ) have the same biicosahedral geometry. The POA showed that the metal atoms at the “waist” part were randomly occupied with Au and Ag atoms having a roughly equal probability (silver occupancy was about 45%, an average value for all Ag<sub>x</sub>Au<sub>25-x</sub> NCs in the nanocrystal), and the double icosahedral center was randomly occupied by Au and Ag, with Ag accounting for 65%. In sample II, gold atoms at the waist were replaced with silver atoms to exhibit more probability (about 80%), including at the center (about 76% silver occupancy). This difference greatly affects the luminescence of samples I and II.

#### 7.2.4.4 Host-Guest Interaction of the Ligand Shell

Metal NCs have made little progress in the preparation of water-soluble, homogeneous, and ultra-bright metal NCs. Deng *et al.* synthesized gold nanoparticles with up to 65% photoluminescence QY in water through a simple blending method.<sup>87</sup> Their attempt to uncover the origin of PL-enhanced 6-aza-2-thiothymine-protected Au NCs (ATT-Au NCs) induction parameters is described in Figure 7.12A. During excitation by light, the excited state is quickly relaxed by the first singlet excited state (S1) *via* an internal conversion effect. The S1 state exhibited a clear difference in transfer characteristics, and the intramolecular vibration and rotation of ATT in the shell led to an effective nonradiative relaxation. After the addition of Arg, the intense host-object interaction between ATT-Au NCs and Arg hardened the coating ligand. Then, the vibration and rotation of ATT were significantly inhibited to reduce the level of nonradiative relaxation of the excited state, resulting in a significant increment in the luminescent QY of ATT-Au NCs. Figure 7.13B shows the excitation and emission spectra of ATT-Au NCs in an aqueous solution. Two excitation extremes appear at 400 nm and 480 nm. The maximum emission wavelength is 528 nm. Neither pure ATT nor



**Figure 7.13** Preparation of emission-tunable thiolate-protected Au NCs by spatial confinement in nanogels. Reproduced from ref. 88 with permission from American Chemical Society, Copyright 2016.

$\text{HAuCl}_4$  emitted light by using the same conditions, indicating that the observed luminescence came from the generated ATT–Au NCs complex. The yellow aqueous solution of ATT–Au NCs emits a weak green fluorescence under ultraviolet light.

Deng *et al.* enhanced the luminescence of ATT–Au NCs by hardening their ligand shell *via* host–guest interaction.<sup>87</sup> The supramolecular host–guest combination that existed between ATT and arginine guanidine on gold nucleus effectively inhibited the vibration and rotation of ATT occurring at intramolecular places and inhibited the energy loss process on the NCs surface to a large extent, resulting in a high QY. This experiment not only revealed the luminescence mechanism of metal NCs but also provided a new way for synthesizing metal NCs with high fluorescence QY.

#### 7.2.4.5 Matrix Confinement

Although there are many ways to improve the luminescence efficiency, the existing types of fluorescent metal NCs exhibit some disadvantages, including<sup>61</sup> (i) lower fluorescence QY (about 0.1%) for more mature chromophores such as organic dyes and semiconductor quantum dots; (ii) the mechanistic origin of the fluorescence emission remaining controversial; and (iii) poor surface function resulting in a low accumulation of these NCs at the target sites when utilized in imaging and therapy. Moreover, the applicability of these emerging fluorescent materials is limited due to the lack of efficient synthesis strategies that do not need any stimulating agents and/or organic solvents. For example, most of the fluorescence-increased approaches previously used for metal NCs are not directly applicable to biomedical fields because they are either stabilized in a solid matrix or phase-transferred into detrimental organic solvents. An effective strategy is to “spatially confine” these luminescent metal NCs in biocompatible nanogels.<sup>88</sup>

By “spatially limiting” Au(I)–thiolate complexes in the presence of cationic polymer chitosan with biocompatible and biodegradable features, Nirmal Goswami *et al.* obtained highly fluorescent gold sulfide NCs in the form of nanohydrogels.<sup>88</sup> In their synthesis scheme, GSH was selected as the

thiol-ligand and temperature-driven preparation of fluorescent Au NCs was selected as the model process to produce the so-called Au(0)@Au(I)-SG NCs, as shown in Figure 7.13. Chitosan was added into a solution of the polymer Au(I)-SG complex in the gel pH range (between the  $pK_a$  and GSH of chitosan), where the negative charge of the carboxyl group in the GSH ligand on the Au(I)-SG complex was readily neutralized with the positively charged amine group of chitosan, followed by self-assembly in aqueous solution. Through the gelation process, Au(I)-SG complexes were spatially constrained but evenly distributed in these self-assembled structures. The spatial limit of the Au(I)-SG complex in nanogels also promoted the fast formation of highly fluorescent Au(0)@Au(I)-SG NCs in gel solutions.

This gel platform accelerates the formation of AIE-type luminescent gold nanocrystals to a large extent. The spatial limitation of impregnated gold nanogels also inhibits the nonradiative decay pathway to a large extent, leading to enhanced photoluminescence in the nanogels. In addition to other remarkable properties, including high solubility, good water stability, nontoxicity, and excellent biocompatibility, the resulting nanogel-based gold nanocomposites have a wide application prospect in the biomedical field.<sup>89,90</sup>

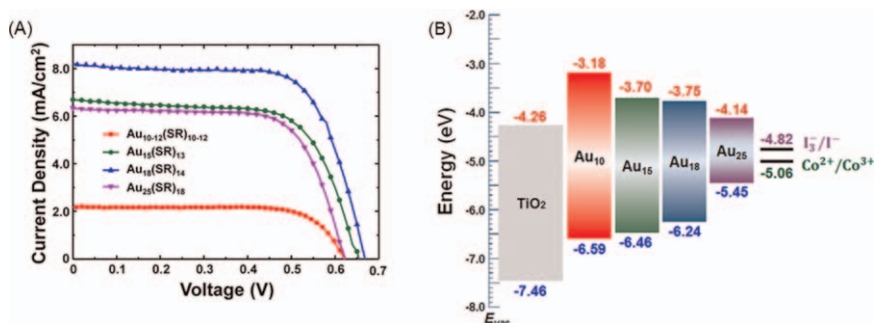
## 7.3 Energy Conversion Applications

As demonstrated above, noble metal NCs with a smaller size than 2 nm have been receiving more and more attention benefiting from the unique physical properties, which are distinguished from the nanomaterials having a size of  $>5$  nm through the existence of separated energy levels caused by quantum confinement effects.<sup>91</sup> Unlike precious metal nanostructures that exhibit light absorption through the cooscillation of charge to form the surface plasma, the absorption of photons by the NCs is because of the movement of electrons from the ground state to the excited state. The molecule-like performance of NCs has attracted a great amount of interest for its promising applications such as ‘light to electricity’, ‘light to chemicals’, and ‘chemical to electric’, which are classified into solar cells, water splitting, CO<sub>2</sub> fixation, and so on.

### 7.3.1 Solar Cells

The plasmonic enhancement effect of large gold nanoparticles was investigated recently and used for organic solar cells, which formed a hole-transporting nanolayer (HTL) after being mixed with a certain amount of Au QDs.<sup>92</sup> Au NCs emitting different colors (blue, green, and red) were studied. It was reported that organic solar cells constituted by green-emitting Au QD layers and Au NPs-based HTL show the highest enhancement of up to 13.0% in power conversion efficiency.<sup>93</sup>

Figure 7.14A shows the  $J-V$  characteristics of different Au NCs. It can be seen from the figure that the voltage of open circuit ( $V_{OC}$ ), current density of



**Figure 7.14** (A) Summary of solar cell parameters of different-sized Au NC-sensitized solar cells. (B) Energy diagrams of different-sized Au NC-sensitized solar cells. Reproduced from ref. 93 with permission from American Chemical Society, Copyright 2016.

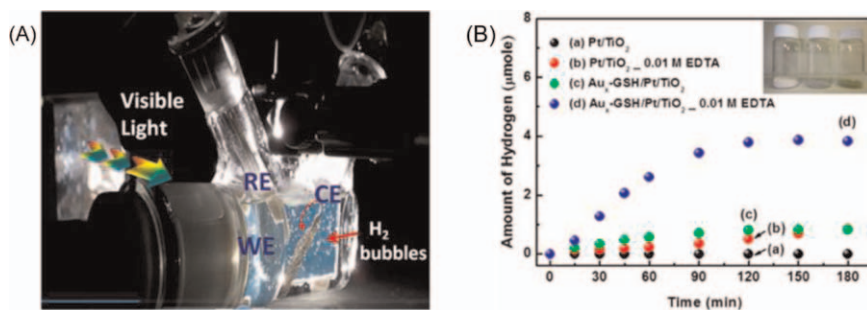
short circuit ( $J_{SC}$ ), and fill factor (FF) of all Au nanocluster solar cells are 0.6–0.7 V, 2–8 mA cm<sup>-2</sup>, and more than 0.7, respectively.  $J_{SC}$  of Au<sub>18</sub>(SR)<sub>14</sub>-involved cells was higher by 22% than that of the ones containing Au<sub>15</sub>(SR)<sub>13</sub> rather than Au<sub>18</sub>(SR)<sub>14</sub>. And the  $J_{SC}$  increase was almost four times higher compared to the cells involving Au<sub>10-12</sub>(SR)<sub>10-12</sub>. Moreover, the Au<sub>18</sub>(SR)<sub>14</sub>-based cells were the most volatile as well, although all cells showed similar FFs. Notably, the size-varied dependence in performance is in accord with the size-determined charge transfer properties of gold nanoclusters, which was recently studied by femtosecond transient absorption spectroscopy using methyl viologen as a probe. As demonstrated, Au<sub>18</sub>(SR)<sub>14</sub> clusters were the most sensitive agent, having the best potential benefiting from their excellent electron transfer kinetics and high collection ability for visible light. The energy levels of Au NC simulated by theoretical calculation are shown in Figure 7.14B. The HOMO–LUMO level of TiO<sub>2</sub> and redox potential of electrolyte were shown together with Au NCs. Compared to the reported experimental measurements of the HOMO–LUMO levels of GSH-protected Au NCs, their calculations yielded a close match of energy levels. These similarities and the close matching of UV–Vis absorbance spectra ensured the validity and reliability of theoretical simulations. From this energy diagram, photoinduced electron transfer from gold nanocluster to titanium dioxide was feasible at any size. Moreover, the redox potential of the electrolyte helps to clear the holes, so Au NCs can be produced again rather than through photodegradation under light irradiation. The corollary signified that all gold nanoclusters can be used as sensitizers for titanium dioxide solar cells.

### 7.3.2 Water Splitting

Hydrogen is widely regarded as a clean fuel for future developments. To achieve the production of hydrogen, it is significantly required to exploit effective technologies to deliver hydrogen after utilizing some renewable

energy materials. Photodriven catalytic decomposition of water on semiconductor photocatalysts has been considered a feasible option.<sup>54</sup> As reported, semiconductors with large bandgaps, such as  $\text{TiO}_2$ , were confirmed to be very efficient, although they are not responsive to visible light, while semiconductors with a smaller bandgap, such as CdS and CdSe, are able to produce hydrogen from water only in the presence of a sacrificial electron donor. Furthermore, other visible light-driven semiconductors like  $\alpha\text{-Fe}_2\text{O}_3$  need external bias of up to 1.0 V. When used as independent systems, they are not active in water cracking. Glutathione-capped metal NCs ( $\text{Au}_x\text{GS}$  NCs) have molecular properties and can be used as photosensitizers to generate hydrogen in photoelectrochemical cells (PECs) and photodriven catalytic slurry reactors.

Using  $\text{Au}_x\text{-GS}$  NCs as a sensitizer in a mesoscopic  $\text{TiO}_2$  film that served as the photoanode and Pt as the counter electrode in a pH 7 solution, Chen *et al.* observed remarkable photocurrent property under irradiation of visible light (400–500 nm).<sup>94</sup> Alternatively, the three-electrode PEC system was also constructed and tested, in which the operating electrode of the cell was maintained at a bias voltage of 0.4 V to RHE (Reversible Hydrogen Electrode), and the result is similar to that of a dual-electrode cell, but the hydrogen production was relatively high. Figure 7.15A shows an image of hydrogen production from the three-electrode cell by using an aqueous solution (pH = 7.0) as the electrolyte. The direct correlation between photochemistry converting light into electrical energy and chemical energy (hydrogen generation) showed the effectiveness of  $\text{Au}_x\text{GS}$  NC as an ideal sensitizer under visible light to generate solar fuel. The photocatalytic slurry experiment was first carried out in deionized water (pH = 7.0, controlled with a dilute NaOH solution) in the presence of visible light with an excitation wavelength of 420 nm. The headspace of reactive cells was periodically sampled and introduced in gas chromatography to analyze the production of  $\text{H}_2$ . Figure 7.15B demonstrates the generation of  $\text{H}_2$  after  $\text{Au}_x\text{-GS}$  NCs



**Figure 7.15** (A) Image showing hydrogen evolution near the Pt mesh counter electrode in a photoelectrochemical cell. (B) Time course hydrogen evolution following the visible light illumination of an aqueous suspension containing various different catalysts. Reproduced from ref. 94 with permission from American Chemical Society, Copyright 2014.

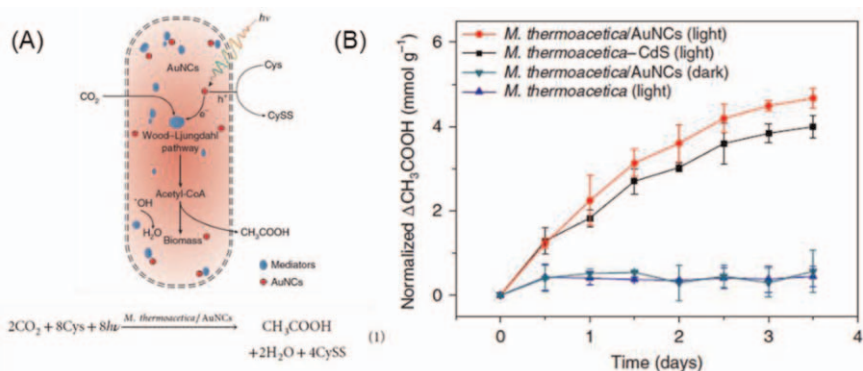
deposition on Pt/TiO<sub>2</sub> nanoparticles as photocatalytic materials. During the first 90 min of illumination, a linear increase in hydrogen precipitation was observed. By performing a similar experimental process (curve 'a' in Figure 7.15B), no hydrogen was produced on the electrode of Pt/TiO<sub>2</sub> nanoparticles, confirming that Au<sub>x</sub>GS NCs were helpful in finally generating hydrogen. The hydrogen evolution speed in the first 60 min was 0.3 mmol h<sup>-1</sup> g<sup>-1</sup> for Au<sub>x</sub>GS NCs. To prolong illumination time to 120 min and longer, the generation of hydrogen was reduced and eventually stopped, suggesting that prolonged illumination may inactivate Au<sub>x</sub>GSH NCs. Of note, after 0.01 M ethylenediaminetetraacetic acid (EDTA) was added to the reaction solution as a sacrificial electron donor, the hydrogen production rate was significantly increased (1.4 mmol h<sup>-1</sup> g<sup>-1</sup> Au<sub>x</sub>GS NCs). As before, with the extension of illumination time (>120 min), hydrogen precipitation stopped. Through the assistance of EDTA, however, Au<sub>x</sub>GSH NCs did not retain reactive ability over a long period of time. The apparent quantum yield (AQY) was measured under monochromatic illumination at 395 nm (wide band). The hydrogen yields of the Pt/TiO<sub>2</sub> nanoparticles sensitized by water (pH = 7) and 0.01 M EDTA were 0.05% and 0.13%, respectively.

Joya *et al.* demonstrated an example of a highly efficient nanocrystalline electrocatalytic system for water oxidation using well-studied Ni clusters, Ni<sub>4</sub>(PET)<sub>8</sub>, and Ni<sub>6</sub>(PET)<sub>12</sub> for anodic oxygen generation.<sup>95</sup> The development of synthetic nickel nanocrystals involves coating the thin film on the electrode surface by simple injection. These atomically precise monodisperse nickel nanocrystals have been investigated *via* UV-Vis absorbance spectroscopy, single-crystal X-ray diffraction, and mass spectrometry. The obtained results show that the molecular compositions of the Ni clusters are Ni<sub>4</sub>(PET)<sub>8</sub> and Ni<sub>6</sub>(PET)<sub>12</sub>. It is a highly active oxygen production electrocatalyst in the absence of any pretreatment. As demonstrated, Ni<sub>4</sub>(PET)<sub>8</sub> is a better catalyst compared to Ni<sub>6</sub>(PET)<sub>12</sub>, initiating oxygen production at a surprisingly low overpotential of ~1.51 V.

### 7.3.3 CO<sub>2</sub> Fixation

The ultrabright photoluminescence of Au<sub>22</sub>(SG)<sub>18</sub> NCs was used in culturing genetically engineered bacteria for CO<sub>2</sub> fixation.<sup>96</sup> As shown in Figure 7.16, Au<sub>22</sub>(SG)<sub>18</sub> is water soluble and highly fluorescent, a marker of daylighting, and a prime candidate for microbial photosensitization. Images of Au NCs in the cell of *Moorella thermoacetica* at different focal planes suggested that Au NCs were incorporated into and dispersed throughout the cells. Moreover, the use of Au<sub>22</sub>(SG)<sub>18</sub> as a sensitizer can improve cell viability and intracellular penetration to result in the generation of acetic acid at a higher rate (Figure 7.16B). When the time for constant photoproduction was set as 4 days, the amount of obtained acetic acid in the *M. thermoacetica*-Au<sub>22</sub>(SG)<sub>18</sub> system was higher than in the *M. thermoacetica*-CdS one.<sup>48</sup> Thus, Au NCs served as a powerful second-generation photosensitizer for photoproduction in cells.





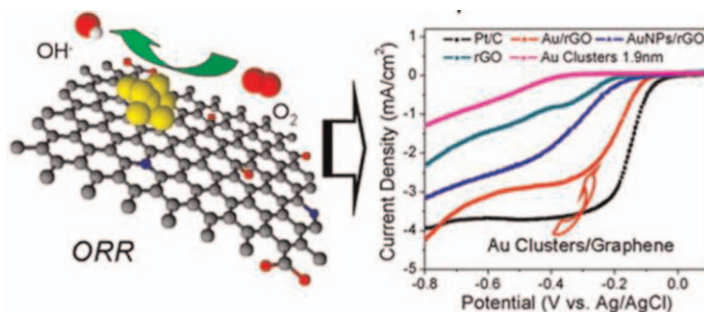
**Figure 7.16** (A) Schematic illustration of the conversion of solar energy to acetate using engineered *M. thermoacetica*-Au<sub>22</sub>(SG)<sub>18</sub>. (B) Normalized acetate production using different *M. thermoacetica*-nanoparticle systems. Reproduced from ref. 96 with permission from the Royal Society of Chemistry.

In short, photosensitive microbes offer a ground-breaking way to use solar energy to convert carbon dioxide into upgradable hydrocarbons. The biological hybridization utilizes the replication, self-healing, and specificity of bacteria that immobilizes carbon dioxide, as well as the excellent solar capture of semiconductor materials. The intracellular interface, especially on the Au NCs structure, bypasses the slow dynamics that were related to extracellular charge uptake. Advances in the development of protective agents for cells will allow this technology to be used.

### 7.3.4 Fuel Cells

Nonplatinum noble metal clusters such as Au NCs are considered high-performance catalytic agents in the cathodic oxygen reduction reaction (ORR) of fuel cells.<sup>97–99</sup> However, there are still great problems in the catalytic reaction process, such as the existence of a large number of coating ligands at their surface, which are prone to be dissolved or induce aggregation. To address the disadvantages, Yin *et al.* proposed a new general approach to prepare ultrafine Au NCs and other metal NCs onto reduced graphene oxide (rGO) nanosheets in the absence of any additional protective molecules and reducing agents.<sup>100</sup>

By measuring the corresponding Rotating disk electrode (RDE) curve of ORR (1600 RPM), the electrocatalytic activity of currently widely used catalysts, including commercial Pt/C, rGO tablets, Au NP/rGO complexes (Au NP/rGO), and mercaptan-terminated Au NCs with the same size, was compared to that of Au/rGO complexes. It is clear from Figure 7.17 that the ORR initial potential of Au/rGO complex (−0.10V) was higher than that of the Au NP/rGO complex (−0.20V), rGO sheet (−0.22V), and thiol-capped Au NCs (−0.32V). And, the current density in the ORR reaction of Au/rGO hybrids (4.11 mA cm<sup>−2</sup>) at −0.8 V



**Figure 7.17** (A) Schematic illustration of oxygen reduction reaction on the Au/rGO hybrids. (B) RDE curves using different catalyst systems. Reproduced from ref. 100 with permission from American Chemical Society, Copyright 2012.

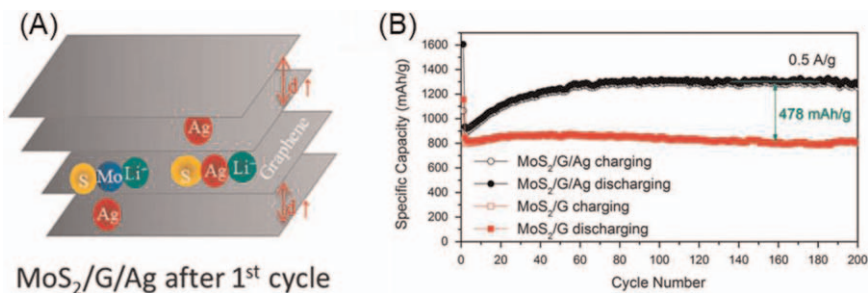
vs. Ag/AgCl was also greatly higher than that of Au NP/rGO hybrid ( $2.96 \text{ mA cm}^{-2}$ ), rGO sheet ( $2.14 \text{ mA cm}^{-2}$ ), and sulfur-labeled Au NCs ( $1.27 \text{ mA cm}^{-2}$ ). A possible reason for the excellent ORR ability of the Au/rGO complexes can be the fact that the small size effect of Au NCs is favorable to activate oxygen molecules (Au/rGO and Au NP/rGO complexes). The weakened coordinating property of gold and the decreased electrophilicity of small NCs lead to an inevitable compromise on the activating energy of O<sub>2</sub> dissociation chemisorption, which correspondingly promotes the 4-electron reduction of the O<sub>2</sub> molecule, resulting in a positive initial potential.

Compared to the currently widely used nanostructured catalysts such as commercial Pt/C, rGO tablets, Au NP/rGO complexes, and sulfhydryl-terminated Au NCs with the same size), the produced Au NC/rGO complexes show remarkable electrocatalytic properties for ORR, such as high initial potential, excellent methanol tolerance, and good stability.

### 7.3.5 Lithium-ion Batteries

In the field of lithium-ion batteries, two-dimensional layered nanomaterials are effective structures for the reversible storage of lithium ion. Common graphite anodes are a good example.<sup>101</sup> The disadvantage of graphite, however, is that its capacity is limited by LiC<sub>6</sub> stoichiometry ( $372 \text{ mAh g}^{-1}$ ). Therefore, there is a strong incentive to find high-capacity graphite alternatives.

Ge Ji *et al.* developed graphene, MoS<sub>2</sub> nanosheets, and Ag NCs (1 wt%) to form MoS<sub>2</sub>/G/Ag composites (Figure 7.18A).<sup>101</sup> The existence of a small amount of Ag NCs increased the lithium storage ability of MoS<sub>2</sub> by 60% ( $\sim 1300 \text{ mAh g}^{-1}$  discharge capacity at  $0.5 \text{ Ag}^{-1}$ , compared to  $800\text{--}850 \text{ mAh g}^{-1}$  discharge capacity of MoS<sub>2</sub>/graphene [MoS<sub>2</sub>/G] composites in the absence of Ag NCs). MoS<sub>2</sub>/G/Ag composites also exhibit excellent rate properties: discharge capacities of  $1040$  and  $850 \text{ mAh g}^{-1}$  at extremely high current densities of  $1$  and  $5 \text{ Ag}^{-1}$ , respectively; correspondingly, the values



**Figure 7.18** (A) A schematic of MoS<sub>2</sub>/G/Ag composite structure after the first cycle. (B) Comparison of the cycling performance of MoS<sub>2</sub>/G and MoS<sub>2</sub>/G/Ag. Reproduced from ref. 101, <https://doi.org/10.1038/am.2016.21>, under the terms of the CC BY 4.0 license <https://creativecommons.org/licenses/by/4.0/>.

for MoS<sub>2</sub>/G in the absence of Ag NCs are 790 and 580 mAh g<sup>-1</sup>, respectively. Ag NCs were chosen for a number of reasons, including (1) the strong binding between Ag and S, (2) the larger surface area of NCs than the nanoparticles being able to reduce the use of Ag, and (3) the fact that the smaller size of Ag NCs may enable them to be inserted into the corridor space between MoS<sub>2</sub> layer and the graphene layer. The results of the high capacity and high magnification performance test of the MoS<sub>2</sub>/G/Ag composites properly prove the effectiveness of NC modification in improving the properties of transition metal dichalcogenides-based lithium-ion battery (LIB) anode materials. Ag NC enhancement effects (as shown in Figure 7.18B) include the immobilization of S, binding of Li, and an increase in distance between graphene sheets.

In another work, Lu *et al.* used Au and Ag NCs-modified  $\alpha$ -MnO<sub>2</sub> nanowires as a mixed oxygen electrocatalyst oxygen battery with nonaqueous lithium.<sup>102</sup> The performance of Au-MnO<sub>2</sub> and Ag-MnO<sub>2</sub> nanohybrids exceeds the original  $\alpha$ -MnO<sub>2</sub> wires in the full battery test, following the order of Au-MnO<sub>2</sub> > Ag-MnO<sub>2</sub> > original  $\alpha$ -MnO<sub>2</sub>. Cells containing the Au-MnO<sub>2</sub> nanocatalyst can decrease the discharge/charge overpotentials at 100 mA g<sup>-1</sup> to 0.23/1.02 V with discharge/charge capacities of 5784/5020 mAh g<sup>-1</sup>. They can also be used for more than 60 cycles at a discharge depth of 1000 mAh g<sup>-1</sup>. The excellent property of the whole cell demonstrates the effectiveness of Au/Ag NCs to promote oxygen electrochemical catalysis on  $\alpha$ -MnO<sub>2</sub> for forming discharge samples having more reactive forms.

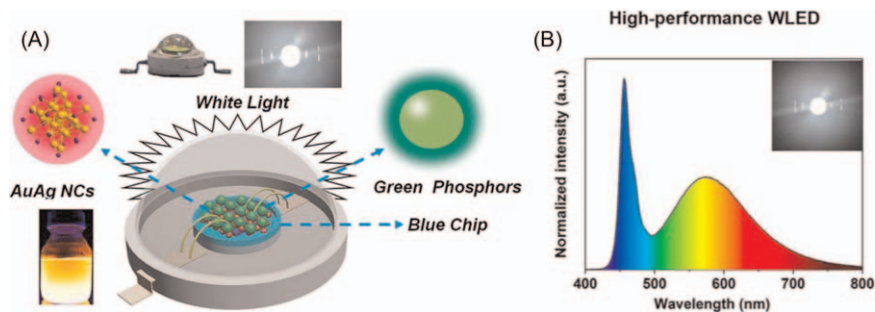
### 7.3.6 Light-driven Emitting Diodes

A light-emitting diode (LED) can be claimed as a light source of semiconductors to convert electricity to light. LEDs have been widely applied in indoor lighting and backlight displays due to their high efficiency (emitting more lumens per watt), small size, long lifetime, good monochrome, and very low heat radiation. For instance, Aires's work presented an *in situ*

preparation and stabilization of luminescent Au NCs with different sizes by utilizing engineered scaffolds of protein in water.<sup>103</sup> The protein-caged Au NC hybrid exhibits dual emission at 450 and 700 nm with a recorded luminescence QY of up to 20%. These properties enable them to be applied as biohybrid LEDs (*i.e.*, color down-conversion filters or biophosphors): effective white emission with a coordinated 0.31/0.29 for  $x/y$  CIE color and stability over 800 h. This represents an increment of two orders of magnitude compared to the existing technology. In addition to excellent properties, the protein matrix is also inferred to have special anisotropic emission characteristics, which has been a proof of concept for developing single-point illumination and display of high interest.

As an emerging nanomaterial for developing solid-state phosphors, Cu NCs have attracted more and more research interest in the aspect of WLEDs.<sup>103</sup> However, their practical uses are limited, owing to the low QY for luminescence and poor tunability for the emission color of Cu NCs. Interestingly, Deng *et al.* reported the facile preparation of a new type of Cu NCs that can emit cyan and orange fluorescence and eventually serve as color conversion phosphors in WLEDs *via* the combination of different fluorescence.<sup>104</sup> In the experiment, the Cu NCs with cyan and orange emission were produced by utilizing 2-mercapto-1-methylimidazole (MMI) and *N*-acetyl-L-cysteine (NAC) as stabilizing and reducing agents, respectively. The solutions of MMI-Cu NCs and NAC-Cu NCs exhibited weak fluorescence emission. However, when drying into powders, they both showed ultrahigh PLQYs (*i.e.*, 45.2% for MMI-CuNCs and 64.6% for NAC-CuNCs), which should be attributed to the process of aggregation-induced emission. Based on the surprising phenomenon, all-Cu NC constructed WLEDs were then designed and fabricated employing powdered MMI-Cu NC and NAC-Cu NC products together with commercially available 365 nm GaN LED substrates, which displayed acceptable white light emission with a coordinate value and color rendering index of (0.26, 0.30) and 83, respectively.

In terms of color rendering index (CRI) and luminous efficiency, Wang *et al.* fabricated Cu NC-based WLED and achieved a CRI of 92 but low luminous efficiency.<sup>105</sup> Yin *et al.* reported a fabrication of a good-performance WLED with high CRI (80.6), high luminous efficiency (LE) ( $91.9 \text{ lm W}^{-1}$ ), and nonchromaticity parameter drift after employing an AIE-characteristic fluorescent bimetallic AuAg NCs as a red label. As shown in Figure 7.19, down-conversion WLED was prepared by combining ultrabright orange AuAg NCs with commercially available green phosphors. The ultra-small-sized AuAg NCs ensure a good mixture with green phosphors. The NCs-based WLED showed good CRI (80.6) and high LE ( $91.9 \text{ lm W}^{-1}$ ) with no chroma parameter drift. As reported, this is the highest CRI record based on NC WLEDs, which matches the requirements of the WLEDs in high-end lighting emission. The research is interesting because it not only shows the power of NC but also offers a feasible approach to solve the low CRI and chroma parameter drift problems of LEDs through the development of novel functional nanomaterials. In addition, Huang *et al.* prepared



**Figure 7.19** (A) Schematic illustration and (B) electroluminescence spectrum of a WLED constructed by combining an AIE type orange-emissive Au/AgNC with commercially available green phosphors on a blue chip. Reproduced from ref. 106 with permission from American Chemical Society, Copyright 2020.

zinc-coordinated GSH-Au NCs assembly through a simple postprocessing method.<sup>106</sup> These Zn-GSH-Au NCs exhibit a high solid PLQY of  $40 \pm 5\%$  even in the aggregation state. This effect could be attributed to the great inhibition of nonradiative relaxation and an increment in charge transfer interactions, as demonstrated by time-resolved PL and X-ray photoelectron spectroscopy (XPS) observations. Moreover, fluorescent emission is relatively stable under practical environmental conditions and does not exhibit aggregation-induced self-quenching process and reabsorption losses from large Stokes shifts.<sup>107</sup>

Over the past decade, precious metal NCs (Au and Ag) have achieved impressive development. Copper is an abundant and cheap metallic element on Earth that comes from the same group of elements as Au and Ag in the periodic table and has become the hot topic of numerical control investigations. Wang *et al.* wrote a review focusing on the wet chemical preparation of Cu NCs, introducing their optical characterization and some emerging exploitations of copper nanoparticles.<sup>53</sup> Since the surface protection template/ligand plays a critical function in optimizing the stability and performances of copper NCs, they classified the synthesis strategies according to the properties of the coating agent. The optical features of copper NCs are also introduced in terms of the effects of metal cores, surface ligands, and environmental conditions (solvent and aggregation) on the emission properties of copper NCs. The application of light-emitting copper nanotubes in biosystem imaging and light-emitting devices is discussed as well.<sup>108</sup>

## 7.4 Summary

In summary, thiolate-protected metal NCs were used as representatives to discuss the controllable factors in the synthesis process, including size control, surface control, composition control, and photoluminescence control. Noble metal NCs exhibit various outstanding properties for their

improved uses in energy conversion. Because of its good electron transfer kinetics and strong visible light collection ability, it is the best sensitizer used in solar cells. Because of its molecular properties, it can be used as a photosensitizer to generate hydrogen in PEC and photocatalytic slurry reactors and has great application value in water decomposition and new energy. At the same time, it is a water-soluble molecule with high fluorescence intensity and is a marker of sunlight. It is a major candidate for microbial photosensitivity and can be used in carbon dioxide fixation. It offers a ground-breaking way to use solar energy to convert carbon dioxide into upgradeable hydrocarbons. The biological hybridization utilizes the replication, self-repair, and specificity provided by special bacteria to fix carbon dioxide, as well as extraordinary solar energy to capture semiconductor nanoparticles. Metal NCs have also been used as fuel cells. Compared with the currently widely used nanocatalysts, the synthesized gold clusters/rGO complexes show remarkable electrocatalytic properties for ORR, such as high initial potential, excellent methanol tolerance, and good stability. When metal NCs composite materials are applied to lithium batteries, the excellent performance of the whole battery indicates that the oxygen electrocatalysis of Au/Ag NCs can promote the formation of more reactive discharge products. As an emerging type of solid phosphor, metal NCs have been attracting extensive attention for developing light-emitting devices with white light.

## References

1. A. K. Hussein, *Renewable Sustainable Energy Rev.*, 2015, **42**, 460.
2. Z. L. Wang and W. Z. Wu, *Angew. Chem. Int. Ed.*, 2012, **51**, 11700.
3. J. Lu, Z. H. Chen, Z. F. Ma, F. Pan, L. A. Curtiss and K. Amine, *Nat. Nanotechnol.*, 2016, **11**, 1031.
4. L. M. Dai, D. W. Chang, J. B. Baek and W. Lu, *Small*, 2012, **8**, 1130.
5. M. A. Gattoo, S. Naseem, M. Y. Arfat, A. M. Dar, K. Qasim and S. Zubair, *BioMed Res. Int.*, 2014, **2014**, 498420.
6. A. W. Carpenter, C. F. de Lannoy and M. R. Wiesner, *Environ. Sci. Technol.*, 2015, **49**, 5277.
7. A. Jain, S. Ranjan, N. Dasgupta and C. Ramalingam, *Crit. Rev. Food Sci. Nutr.*, 2018, **58**, 297.
8. P. B. Liu, M. Y. Yang, S. H. Zhou, Y. Huang and Y. D. Zhu, *Electrochim. Acta*, 2019, **294**, 383.
9. P. Singh, Y. J. Kim, D. B. Zhang and D. C. Yang, *Trends Biotechnol.*, 2016, **34**, 588.
10. I. Malkiel, M. Mrejen, A. Nagler, U. Arieli, L. Wolf and H. Suchowski, *Light: Sci. Appl.*, 2018, **7**, 60.
11. K. Ariga, J. B. Li, J. B. Fei, Q. M. Ji and J. P. Hill, *Adv. Mater.*, 2016, **28**, 1251.
12. X. F. Zhang, Z. G. Liu, W. Shen and S. Gurunathan, *Int. J. Mol. Sci.*, 2016, **17**, 1534.

13. R. W. Murray, *Chem. Rev.*, 2008, **108**, 2688.
14. M. Zhu, C. M. Aikens, F. J. Hollander, G. C. Schatz and R. Jin, *J. Am. Chem. Soc.*, 2008, **130**, 5883.
15. Y. Li, G. Galli and F. Gygi, *ACS Nano*, 2008, **2**, 1896.
16. P. D. Jadzinsky, G. Calero, C. J. Ackerson, D. A. Bushnell and R. D. Kornberg, *Science*, 2007, **318**, 430.
17. M. Zhu, H. Qian, X. Meng, S. Jin, Z. Wu and R. Jin, *Nano Lett.*, 2011, **11**, 3963.
18. H. Qian, W. T. Eckenhoff, Y. Zhu, T. Pintauer and R. Jin, *J. Am. Chem. Soc.*, 2010, **132**, 8280.
19. M. Zhu, C. M. Aikens, M. P. Hendrich, R. Gupta, H. Qian, G. C. Schatz and R. Jin, *J. Am. Chem. Soc.*, 2009, **131**, 2490.
20. Y. Lu and W. Chen, *Chem. Soc. Rev.*, 2012, **41**, 3594.
21. L. Shang, S. J. Dong and G. U. Nienhaus, *Nano Today*, 2011, **6**, 401.
22. J. Zheng, C. Zhou, M. Yu and J. Liu, *Nanoscale*, 2012, **4**, 4073.
23. Y. Yu, Q. Yao, Z. Luo, X. Yuan, J. Y. Lee and J. Xie, *Nanoscale*, 2013, **5**, 4606.
24. X. Yuan, Z. Luo, Y. Yu, Q. Yao and J. Xie, *Chem. – Asian J.*, 2013, **8**, 858.
25. Y. Zhu, H. Qian and R. Jin, *J. Mater. Chem.*, 2011, **21**, 6793.
26. Q. F. Yao, Z. N. Wu, Z. H. Liu, Y. Z. Lin, X. Yuan and J. P. Xie, *Chem. Sci.*, 2021, **12**, 99.
27. K. Kwak and D. Lee, *Acc. Chem. Res.*, 2019, **52**, 12.
28. Y. Negishi, K. Nobusada and T. Tsukuda, *J. Am. Chem. Soc.*, 2005, **127**, 5261.
29. R. Jin, *Nanoscale*, 2015, **7**, 1549.
30. Y. Yu, Z. Luo, D. M. Chevrier, D. T. Leong, P. Zhang, D. E. Jiang and J. Xie, *J. Am. Chem. Soc.*, 2014, **136**, 1246.
31. Q. F. Yao, T. K. Chen, X. Yuan and J. P. Xie, *Acc. Chem. Res.*, 2018, **51**, 1338.
32. X. Yuan, B. Zhang, Z. T. Luo, Q. F. Yao, D. T. Leong, N. Yan and J. P. Xie, *Angew. Chem., Int. Ed.*, 2014, **53**, 4623.
33. C.-A. J. Lin, T.-Y. Yang, C.-H. Lee, S. H. Huang, R. A. Sperling, M. Zanella, J. K. Li, J.-L. Shen, H.-H. Wang, H.-I. Yeh, W. J. Parak and W. H. Chang, *ACS Nano*, 2009, **3**, 395.
34. H. Qian, Y. Zhu and R. Jin, *Proc. Natl. Acad. Sci. U. S. A.*, 2012, **109**, 696.
35. C. Kumara, X. Zuo, J. Ilavsky, K. W. Chapman, D. A. Cullen and A. Dass, *J. Am. Chem. Soc.*, 2014, **136**, 7410.
36. M. Zhu, E. Lanni, N. Garg, M. E. Bier and R. Jin, *J. Am. Chem. Soc.*, 2008, **130**, 1138.
37. X. Yuan, M. I. Setyawati, A. S. Tan, C. N. Ong, D. T. Leong and J. Xie, *NPG Asia Mater.*, 2013, **5**, e39.
38. A. Ghosh, T. Udayabhaskararao and T. Pradeep, *J. Phys. Chem. Lett.*, 2012, **3**, 1997.
39. Q. Yao, Y. Yu, X. Yuan, Y. Yu, J. Xie and J. Y. Lee, *Small*, 2013, **9**, 2696.
40. X. Yuan, Y. Yu, Q. Yao, Q. Zhang and J. Xie, *J. Phys. Chem. Lett.*, 2012, **3**, 2310.

41. Y. Yu, J. Geng, E. Y. X. Ong, V. Chellappan and Y. N. Tan, *Adv. Healthcare Mater.*, 2016, **5**, 2528.
42. K. Y. Zheng, X. Yuan, N. Goswami, Q. B. Zhang and J. P. Xie, *RSC Adv.*, 2014, **4**, 60581.
43. Q. F. Yao, X. Yuan, T. K. Chen, D. T. Leong and J. P. Xie, *Adv. Mater.*, 2018, **30**, 1802751.
44. X. Yuan, Y. Yu, Q. Yao, Q. Zhang and J. Xie, *J. Phys. Chem. Lett.*, 2012, **3**, 2310.
45. M. Zhu, H. Qian and R. Jin, *J. Phys. Chem. Lett.*, 2010, **1**, 1003.
46. T. U. B. Rao, B. Nataraju and T. Pradeep, *J. Am. Chem. Soc.*, 2010, **132**, 16304.
47. Z. Wu, M. A. MacDonald, J. Chen, P. Zhang and R. Jin, *J. Am. Chem. Soc.*, 2011, **133**, 9670.
48. Y. Yu, X. Chen, Q. Yao, Y. Yu, N. Yan and J. Xie, *Chem. Mater.*, 2013, **25**, 946.
49. Y. Yu, Q. Yao, K. Cheng, X. Yuan, Z. Luo and J. Xie, *Part. Part. Syst. Charact.*, 2014, **31**, 652.
50. R. Jin, H. Qian, Z. Wu, Y. Zhu, M. Zhu, A. Mohanty and N. Garg, *J. Phys. Chem. Lett.*, 2010, **1**, 2903.
51. Y. Shichibu, Y. Negishi, H. Tsunoyama, M. Kanehara, T. Teranishi and T. Tsukuda, *Small*, 2007, **3**, 835.
52. M. A. Habeeb Muhammed and T. Pradeep, *Small*, 2011, **7**, 204.
53. A. C. Dharmaratne, T. Krick and A. Dass, *J. Am. Chem. Soc.*, 2009, **131**, 13604.
54. Z. Wu, J. Suhan and R. Jin, *J. Mater. Chem.*, 2009, **19**, 622.
55. Z. Luo, V. Nachammai, B. Zhang, N. Yan, D. T. Leong, D. E. Jiang and J. Xie, *J. Am. Chem. Soc.*, 2014, **136**, 10577.
56. H. Qian and R. Jin, *Chem. Mater.*, 2011, **23**, 2209.
57. C. Zeng, Y. Chen, A. Das and R. Jin, *J. Phys. Chem. Lett.*, 2015, **6**, 2976.
58. C. Zeng, T. Li, A. Das, N. L. Rosi and R. Jin, *J. Am. Chem. Soc.*, 2013, **135**, 10011.
59. C. J. Zeng, H. F. Qian, T. Li, G. Li, N. L. Rosi, B. Yoon, R. N. Barnett, R. L. Whetten, U. Landman and R. Jin, *Angew. Chem., Int. Ed.*, 2012, **51**, 13114.
60. C. Zeng, Y. Chen, K. Kirschbaum, K. Appavoo, M. Y. Sfeir and R. Jin, *Sci. Adv.*, 2015, **1**, e1500045.
61. S. Ito, S. Takano and T. Tsukuda, *J. Phys. Chem. Lett.*, 2019, **10**, 6892.
62. R. Jin, *Nanoscale*, 2015, **7**, 1549.
63. M. Zhu, C. M. Aikens, F. J. Hollander, G. C. Schatz and R. Jin, *J. Am. Chem. Soc.*, 2008, **130**, 5883.
64. M. W. Heaven, A. Dass, P. S. White, K. M. Holt and R. W. Murray, *J. Am. Chem. Soc.*, 2008, **130**, 3754.
65. K. Zheng, X. Yuan, N. Goswami, Q. Zhang and J. Xie, *RSC Adv.*, 2014, **4**, 60581.



66. A. Desireddy, B. E. Conn, J. Guo, B. Yoon, R. N. Barnett, B. M. Monahan, K. Kirschbaum, W. P. Griffith, R. L. Whetten, U. Landman and T. P. Bigioni, *Nature*, 2013, **501**, 399.
67. H. Yang, Y. Wang, H. Huang, L. Gell, L. Lehtovaara, S. Malola, H. Häkkinen and N. Zheng, *Nat. Commun.*, 2013, **4**, 2422.
68. R. S. Dhayal, J. H. Liao, Y. C. Liu, M. H. Chiang, S. Kahlal, J. Y. Saillard and C. W. Liu, *Angew. Chem., Int. Ed.*, 2015, **54**, 3702.
69. L. G. AbdulHalim, M. S. Bootharaju, Q. Tang, S. del Gobbo, R. G. AbdulHalim, M. Eddaoudi, D. E. Jiang and O. M. Bakr, *J. Am. Chem. Soc.*, 2015, **137**, 11970.
70. C. Kumara, C. M. Aikens and A. J. Dass, *Phys. Chem. Lett.*, 2014, **5**, 461.
71. C. P. Joshi, M. S. Bootharaju, M. J. Alhilaly and O. M. Bakr, *J. Am. Chem. Soc.*, 2015, **137**, 11578.
72. M. W. Heaven, A. Dass, P. S. White, K. M. Holt and R. W. Murray, *J. Am. Chem. Soc.*, 2008, **130**, 3754.
73. M. Zhu, C. M. Aikens, F. J. Hollander, G. C. Schatz and R. Jin, *J. Am. Chem. Soc.*, 2008, **130**, 5883.
74. C. A. Fields-Zinna, M. C. Crowe, A. Dass, J. E. F. Weaver and R. W. Murray, *Langmuir*, 2009, **25**, 7704.
75. Y. Negishi, W. Kurashige, Y. Niihori, T. Iwasa and K. Nobusada, *Phys. Chem. Chem. Phys.*, 2010, **12**, 6219.
76. H. Qian, E. Barry, Y. Zhu and R. Jin, *Acta Phys. Chim. Sin.*, 2011, **27**, 513.
77. Y. Negishi, T. Iwai and M. Ide, *Chem. Commun.*, 2010, **46**, 4713.
78. D. Jiang and S. Dai, *Inorg. Chem.*, 2009, **48**, 2720.
79. D. Jiang and R. L. Whetten, *Phys. Rev. B*, 2009, **80**, 115402.
80. H. Qian, D. E. Jiang, G. Li, C. Gayathri, A. Das, R. R. Gil and R. Jin, *J. Am. Chem. Soc.*, 2012, **134**, 16159.
81. J. Yan, H. Su, H. Yang, S. Malola, S. Lin, H. Häkkinen and N. Zheng, *J. Am. Chem. Soc.*, 2015, **137**, 11880.
82. E. B. Guidez, V. Mäkinen, H. Häkkinen and C. M. Aikens, *J. Am. Chem. Soc. C*, 2012, **116**, 20617.
83. Z. Luo, X. Yuan, Y. Yu, Q. Zhang, D. T. Leong, J. Y. Lee and J. Xie, *J. Am. Chem. Soc.*, 2012, **134**, 16662.
84. Z. Wu, J. Liu, Y. Gao, H. Liu, T. Li, H. Zou, Z. Wang, K. Zhang, Y. Wang, H. Zhang and B. Yang, *J. Am. Chem. Soc.*, 2015, **137**, 12906.
85. K. Pyo, V. D. Thanthirige, K. Kwak, P. Pandurangan, G. Ramakrishna and D. Lee, *J. Am. Chem. Soc.*, 2015, **137**, 8244.
86. S. Wang, X. Meng, A. Das, T. Li, Y. Song, T. Cao, X. Zhu, M. Zhu and R. Jin, *Angew. Chem., Int. Ed.*, 2014, **53**, 2376.
87. H. H. Deng, X. Q. Shi, F. F. Wang, H. P. Peng, A. L. Liu, X. H. Xia and W. Chen, *Chem. Mater.*, 2017, **29**, 1362.
88. N. Goswami, F. Lin, Y. Liu, D. T. Leong and J. Xie, *Chem. Mater.*, 2016, **28**, 4009.
89. Z. T. Luo, K. Y. Zheng and J. P. Xie, *Chem. Commun.*, 2014, **50**, 5143.
90. E. N. Zare, P. Makvandi, B. Ashtari, F. Rossi, A. Motahari and G. Perale, *J. Med. Chem.*, 2020, **63**, 1.

91. T. K. Sau, A. L. Rogach, F. Jackel, T. A. Klar and J. Feldmann, *Adv. Mater.*, 2010, **22**, 1805.
92. M. Notarianni, K. Vernon, A. Chou, M. Aljada, J. Z. Liu and N. Motta, *Sol. Energy*, 2014, **106**, 23.
93. M. A. Abbas, T. Y. Kim, S. U. Lee, Y. S. Kang and J. H. Bang, *J. Am. Chem. Soc.*, 2016, **13**, 390.
94. Y. S. Chen and P. V. Kamat, *J. Am. Chem. Soc.*, 2014, **136**, 6075.
95. K. S. Joya, L. Sinatra, L. G. AbdulHalim, C. P. Joshi, M. N. Hedhili, O. M. Bakr and I. Hussain, *Nanoscale*, 2016, **8**, 9695.
96. S. Cestellos-Blanco, H. Zhang and P. Yang, *Faraday Discuss.*, 2019, **215**, 54.
97. H. A. Gasteiger, S. S. Kocha, B. Sompalli and F. T. Wagner, *Appl. Catal., B*, 2005, **56**, 9.
98. A. A. Gewirth and M. S. Thorum, *Inorg. Chem.*, 2010, **49**, 3557.
99. M. K. Debe, *Nature*, 2012, **486**, 43.
100. H. Yin, H. Tang, D. Wang, Y. Gao and Z. Tang, *ACS Nano*, 2012, **6**, 8288.
101. G. Ji, Y. Yu, Q. Yao, B. Qu, D. Chen, W. Chen, J. Xie and J. Y. Lee, *NPG Asia Mater.*, 2016, **8**, e247.
102. M. Lu, J. Qu, Q. Yao, C. Xu, Y. Zhan, J. Xie and J. Y. Lee, *ACS Appl. Mater. Interfaces*, 2015, **7**, 5488.
103. A. Aires, V. Fernández-Luna, J. Fernández-Cestau, R. D. Costa and A. L. Cortajarena, *Nano Lett.*, 2020, **20**, 2710.
104. H. H. Deng, Q. Q. Zhuang, K. Y. Huang, P. Balasubramanian, Z. Lin, H. P. Peng, X. H. Xia and W. Chen, *Nanoscale*, 2020, **12**, 15791.
105. Z. Wang, B. Chen, A. S. Susha, W. Wang, C. J. Reckmeier, R. Chen, H. Zhong and A. L. Rogach, *Adv. Sci.*, 2016, **3**, 1600182.
106. Z. Yin, Z. Wang, X. Dai, N. Liu, S. Wang, G. Li, F. Du and X. Yuan, *ACS Sustainable Chem. Eng.*, 2020, **8**, 15336.
107. H. Y. Huang, K. B. Cai, M. J. Talite, W. C. Chou, P. W. Chen and C. T. Yuan, *Sci. Rep.*, 2019, **9**, 4053.
108. Z. Wang, B. Chen and A. L. Rogach, *Nanoscale Horiz.*, 2017, **2**, 135.

## CHAPTER 8

# *Nanocatalysis With Sustainability*

LILI ZHOU,<sup>a</sup> JIE ZHENG,<sup>b</sup> ENYI YE,<sup>b</sup> ZIBIAO LI<sup>\*a,b</sup> AND CHAOBIN HE<sup>\*a,b</sup>

<sup>a</sup> Department of Materials Science and Engineering, National University of Singapore, 9 Engineering Drive 1, Singapore 117576, Singapore; <sup>b</sup> Institute of Materials Research and Engineering, A\*STAR (Agency for Science, Technology and Research), 2 Fusionopolis Way, Innovis, #08-03, Singapore 138634, Singapore,

\*Emails: lizb@imre.a-star.edu.sg; msehc@nus.edu.sg

## 8.1 Introduction

Catalysis plays an increasingly important role in various fields, *i.e.*, agriculture, energy, and the environment.<sup>1–4</sup> Due to wide applications, a lot of efforts have been devoted to developing different kinds of catalysts.<sup>5–8</sup> The catalytic systems can be generally classified into homogeneous and heterogeneous depending on whether they are miscible with reactant systems.<sup>9–11</sup> As for homogeneous catalysts, they stay in the same phase, with the reactants generally exhibiting high catalytic efficiency due to sufficient contact.<sup>12–14</sup> However, trace amounts of them often remain in the solution or in the end product, which makes it difficult to obtain high-purity products. In the industrial process, the homogeneous catalysts are commonly recovered by using biphasic systems, which will further generate other wastes. Compared with homogeneous catalysts, heterogeneous catalysts have attracted much attention because of their easy separation from the reaction mixtures through filtration.<sup>15–17</sup> The advancement of nanoscience helps to

---

Nanoscience & Nanotechnology Series No. 57

Sustainable Nanotechnology

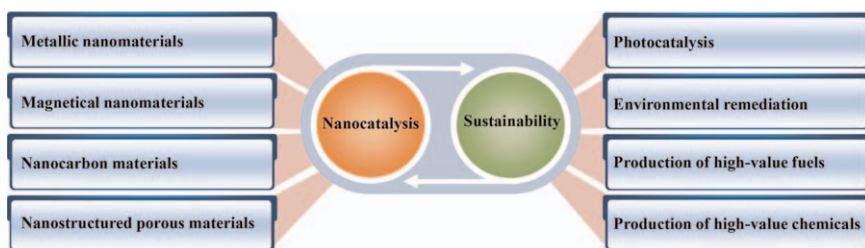
Edited by Zibiao Li, Jie Zheng and Enyi Ye

© The Royal Society of Chemistry 2022

Published by the Royal Society of Chemistry, www.rsc.org

develop catalytically active nanocatalysts that bridge homogeneous and heterogeneous catalysis. The catalysts of nano-size combine the activity and selectivity of homogeneous catalysts and the stability/separability of heterogeneous counterparts.<sup>18–20</sup> Their typical insolubility allows them to be easily recovered and reused. In fact, the nanomaterials show unique physiochemical properties in contrast to bulk material, thus enhancing catalytic activity and selectivity because of the small size effect and quantum tunneling effect. In particular, nano-sized materials often have large surface-to-volume ratios and sizes, which further increase the intimate contact between reactants and active sites. Besides, the changes in size and morphology can induce different catalytic properties, including activity, selectivity, and stability.<sup>21,22</sup> Various kinds of nanocatalysts with different surface energies and morphologies have been synthesized through physical, chemical, and biological methods or surface characterization to improve their properties.

Anthropological development has improved the quality of our life in the past centuries; however, it has also given rise to an enormous number of global challenges, such as associated climate change, depletion of traditional feedstocks, and continuous increase of energy demands. The current and anticipated challenges indicate a frustrating future unless sustainable solutions are developed. Promising methodologies and novel technologies for the rational design and fabrication of catalytic systems with sustainability, durability, recycling, and cost-effectiveness are expected to solve these issues, which has become the ultimate goal of catalysis research.<sup>23–26</sup> The proper utilization of renewable resources and preparation of highly efficient and sustainable nanocatalysts with minimized by-product generation undoubtedly require much attention. Thus, the scarcity, high cost, or potential bio- and eco-toxicity related to materials in industrial processes could be improved by using more sustainable alternatives. The energy demands call for cleaner, more efficient, and green fossil resources, which can be realized by converting coal into natural gases, chemicals, liquid fuels, and other renewable energy sources.<sup>27,28</sup> It is particularly expected to utilize alternative feedstocks like wastes from industries and eco-friendly materials to obtain the desired chemicals.<sup>29–31</sup> The present chapter presents recent developments in the area of nanocatalysis and explores its applications to



**Figure 8.1** Schematic representation of different types of nanocatalysts and their sustainable applications.

overcome the challenges related to the chemistry, energy, and environment sectors. Figure 8.1 presents different types of nanocatalysts and their sustainable applications.

## 8.2 Nanocatalysis Materials

A large number of nanocatalysts have been developed in recent decades. Among them, metal nanoparticles have been most widely used with respect to the classic nanocatalytic systems. The magnetically recyclable nanocatalysts, carbon nanoparticles, and nanostructured porous materials are also exhibiting improvements in the catalytic field. The following text summarizes the research of different types of nanocatalysts.

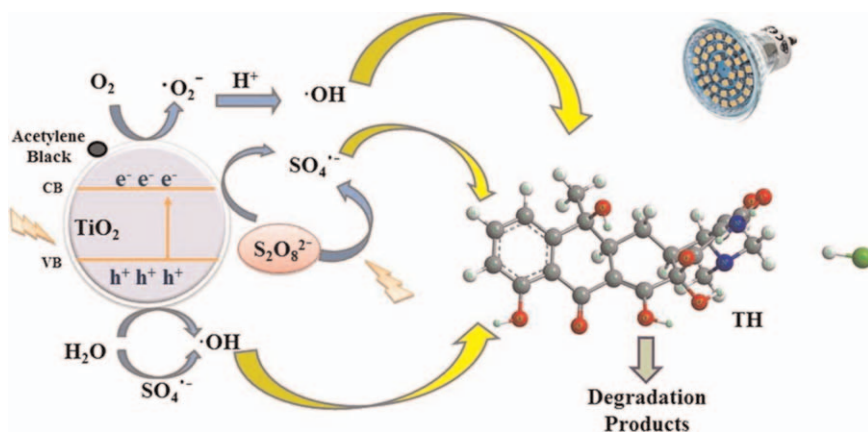
### 8.2.1 Metallic Nanoparticles

In recent decades, many significant achievements have been made in metallic nanomaterials, mainly including metals, their oxides, and bimetallic composites at the nanoscale, as heterogeneous catalysts.<sup>32–34</sup> Since the reactions occur on the surface of the metal particles and/or the metal–support interfaces, the morphology, size, and surface property of the catalysts all have a great effect on the catalytic performance. It is generally acknowledged that these structural features are closely linked with unsaturated coordinated active sites, which are further related to catalytic activity. Careful tuning of the structure can lead to higher stability and activity. Some nanomaterials exhibit high catalytic activity and selectivity for certain reactions.<sup>35–38</sup> Metallic nanoparticles with a high surface area are extensively used for energy storage and conversion in electrocatalysis, particularly for oxygen reduction and evolution reactions. For example, Pt is often used as oxygen reduction catalysts, while Ir and Ru usually act as oxygen evolution catalysts. The metallic nanoparticles are also often dispersed on some supports to avoid sintering and fast deactivation. Generally, early transition metals, including Ti, Zr, Nb, Mn, V, Cr, Mo, and W, with their weak hydrogenation ability, could be applied in certain hydrogenation reactions; Fe, Co, and Ni are widely used in typical reactions, including hydrogenation, hydrosilation, oxidation, and C–C coupling reactions; Cu, Ag, and Au often exhibit excellent redox ability; noble metals, including Ru, Rh, Pt, Pd, and Ir, with their excellent hydrogenation ability, are commonly used for hydrogenation reactions.<sup>39–43</sup>

Metal nanoparticles have been used in large-scale industrial processes due to their well-known excellent catalytic activities in a large number of reactions.<sup>1</sup> Generally, Pd is regarded as the best catalyst to synthesize  $\text{H}_2\text{O}_2$  from  $\text{H}_2$  and  $\text{O}_2$  directly due to its remarkable activity and selectivity.<sup>44</sup> Growing concerns about the harmful effects of CO on the environment and health have also been deeply explored. The Au nanoparticles exhibit remarkably high activity toward CO oxidation.<sup>45,46</sup> Besides, they can selectively catalyze the reduction of functionalized nitro groups with  $\text{H}_2$  under mild

reaction conditions.<sup>47</sup> Apart from the above points, Au nanoparticles also present high catalytic activity for ethylene hydrogenation, additions to multiple C–C bonds, and so on.<sup>48,49</sup> Due to the scarcity, toxicity, and high cost of noble metal catalysts, base metals have been extensively investigated in nanocatalysis areas due to their versatile, abundant, economical, less harmful, and environmentally benign features. For example, the well-established Pd-catalyzed cross-coupling reactions are studied with Ni-based catalysts.<sup>50</sup> Sharma *et al.*<sup>51</sup> prepared silica-based Ni nanocatalysts for Suzuki coupling reactions by substituting expensive palladium. The catalyst keeps high catalytic performance over six cycles and can be recovered through magnetic forces. The base metals commonly show weak hydrogenation ability and can be used in hydrogenation reactions.

Metal oxide nanoparticles also emerge as good alternatives for nanocatalysts. Compared with metallic-state, the metal oxides with nano-size have lower surface energy and exhibit higher structural stabilities.<sup>37,52</sup> Among them, TiO<sub>2</sub> has been one of the most widely used photocatalysts in various fields, including photocatalytic H<sub>2</sub> production by water splitting, degradation of contaminants, organic transformations, and CO<sub>2</sub> reduction.<sup>53</sup> Zhang *et al.*<sup>54</sup> utilized TiO<sub>2</sub> nanomaterials to degrade tetracycline hydrochloride under visible light (Figure 8.2). The TiO<sub>2</sub> is doped with acetylene black to further improve the adsorption capacity of solar energy. And the persulfate generates reactive hydroxyl radicals and sulfate to degrade organic contaminants. The degradation efficiency is still above 85% over five cycles. The oxides of Mn, V, Cr, and Mo are widely used in alkane oxidation reactions.<sup>37</sup> The CO oxidation is also catalyzed by Co<sub>3</sub>O<sub>4</sub> nanorods at temperatures as low as –77 °C.<sup>55</sup> The nanorod morphology of Co<sub>3</sub>O<sub>4</sub> sufficiently exposes their planes with active Co<sup>3+</sup> species at the surface. Besides, the catalyst remains stable in feed gases containing large amounts of H<sub>2</sub>O and



**Figure 8.2** The mechanism of tetracycline hydrochloride photodegradation. Reproduced from ref. 54 with permission from Elsevier, Copyright 2020.

CO<sub>2</sub> at high temperatures. The catalysis of metal oxide nanoparticles is an area worthy of research efforts in the future.

Bimetallic nanomaterials have also been investigated in depth for their synergistic catalytic properties. Pt/Fe, Pt/Pd, Pd/Ni, Pd/Au, Au/Fe, and Cu/Au are the most representative bimetallic nanomaterials.<sup>39</sup> The biggest advancement of the Pt/Pd catalytic converter for green chemistry applications lies in the car exhaust system. When the engine is started for a few minutes, the temperature, as high as 200 °C, causes the oxidation of CO. Bimetallic composites, composed of two different metal elements, show enhanced catalytic performance than original monometallic ones, as well as possess new properties because of the synergy in the heterostructural constitution. For instance, Schroter *et al.*<sup>56</sup> found that ZnO surface decorated with Cu nanoparticles has high catalytic activity for methanol synthesis from CO and H<sub>2</sub>, whereas Cu nanoparticles alone are completely inactive. Especially, the noble–nonnoble composites are an ideal candidate, in which the nonnoble metals are used as substrates to form metal composites with noble metal nanoparticles. Sun *et al.*<sup>57</sup> prepared Cu nanowires–Ag composite, which exhibited remarkable performance for the reduction of 4-nitrophenol resulting from the surface effect and synergistic effect of their heterostructures.

### 8.2.2 Magnetically Recyclable Nanocatalysts

Magnetic nanoparticles have attracted a great deal of interest as a new type of recyclable nanocatalysts due to their excellent applications in catalytic areas.<sup>58–60</sup> For economic and environmental concerns, the efficient recovery and reusability of expensive catalysts from the reaction medium after catalytic reaction in large-scale syntheses without loss of activity are the pivotal factors for industrial applications and sustainable development.<sup>61–63</sup> Anchoring catalysts on magnetic nanoparticles is a good choice to achieve these goals. These catalysts can be immobilized on the magnetic nanoparticles and well dispersed in a reaction solution to make intimate contact between active sites on the magnetic nanoparticles and substrate molecules, just like the other nanoparticles. Moreover, catalysts can be separated easily from the mixtures by a simple magnetic field and they can be reused again without losing their activity after many cycles. Compared with other common separation methods, such as filtration and centrifugation, magnetic separation is a more innovative and environmentally friendly process for the easy isolation of catalysts.<sup>64</sup> In fact, magnetically separable catalysis is an effective strategy to bridge the split between heterogeneous and homogeneous catalysis.

The typical magnetic nanoparticles are classified into the following types. (1) Metal magnetic nanomaterials: metals such as Fe, Co, and Ni are used. The Fe-based magnetic nanoparticle is one of the most representative nanostructures. (2) Metal alloy nanomaterials: for metal alloy nanoparticles, FePd and FePt are widely used due to their chemical stability and high magnetocrystalline anisotropy. (3) Metallic oxides: metallic oxides–based

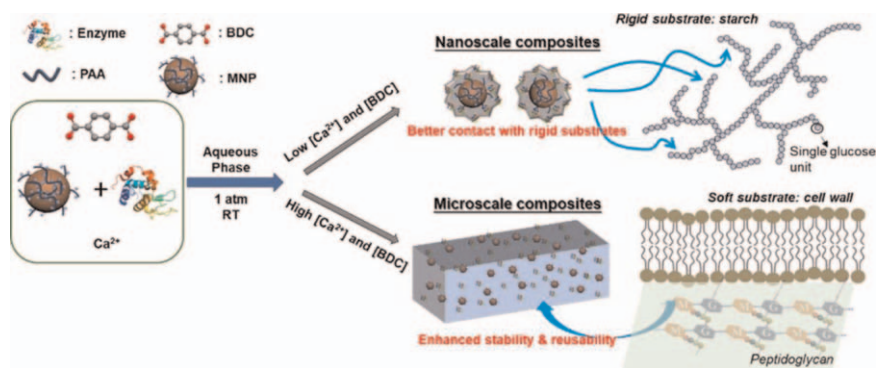
magnetic nanomaterials like chromium dioxide ( $\text{CrO}_2$ ), cobalt ferrite ( $\text{Fe}_2\text{CoO}_4$ ), maghemite ( $\text{Fe}_2\text{O}_3$ ,  $\gamma\text{-Fe}_2\text{O}_3$ ), and magnetite ( $\text{Fe}_3\text{O}_4$ ) have also been widely applied due to their better long-term operation stability. Among them, Fe-based oxides are the most widely exploited because of their better magnetic properties and lower cost, including ferric chloride ( $\text{FeCl}_3$ ), ferrous oxide ( $\text{Fe}_2\text{O}_3$ ), ferric oxide ( $\text{Fe}_3\text{O}_4$ ), ferrous sulfate ( $\text{FeSO}_4$ ), and ferric nitrate ( $\text{Fe}(\text{NO}_3)_3$ ). (4) Metal carbides: iron carbides, such as  $\text{Fe}_5\text{C}_2$ ,  $\text{Fe}_3\text{C}$ , and  $\text{Fe}_2\text{C}$ , can also be used for magnetic separation. Compared with the oxides, their carbides show higher stability and magnetic saturation. However, the relative difficulty of synthesis limits their further application. (5) Multi-component magnetic nanomaterials: they exhibit multifunctional properties because of their diverse composition, which combine magnetic properties with additional fangled functions.<sup>65–67</sup> In  $\text{FePt-Au}$ ,  $\text{FePt}$  provides excellent magnetic properties, whereas  $\text{Au}$  presents outstanding catalytic activity. Core@shell heterostructures have also been widely investigated due to the synergistic effects of composites and the protection function of the shell.<sup>68–70</sup> These superparamagnetic nanoparticles have attracted much attention as catalysts or supports in the catalytic area.

Magnetite nanoparticles have intrinsic catalytic activity in some cases. Among them,  $\text{Fe}_3\text{O}_4$ , with highly efficient and cost-effective advantages, is the most widely used nanomaterial for catalytic application.<sup>71</sup> Gao *et al.*<sup>72</sup> found that recyclable superparamagnetic nanoparticles own intrinsic peroxidase-like catalytic activity. A catalytic amount of  $\text{Fe}_3\text{O}_4$  nanoparticles catalyzes substrates such as 3,3,5,5-tetramethylbenzidine, diazoaminobenzene, and *o*-phenylenediamine with typical Michaelis–Menten kinetics. Besides, they have a higher binding affinity with substrates, which leads to a 40-fold higher catalytic activity than natural peroxidases. Furthermore,  $\text{Fe}_3\text{O}_4$  nanoparticles are easily separated from the reaction mixtures and recovered for recycling. The activity of natural enzymes is often inactivated upon exposure to extreme environments. Compared with natural peroxidases,  $\text{Fe}_3\text{O}_4$  nanoparticles is a more robust and effective, as well as economical, catalyst. Mojtahedi *et al.*<sup>73</sup> reported that  $\text{Fe}_3\text{O}_4$  nanoparticles can efficiently catalyze the thiolysis of epoxides at room temperature. These  $\text{Fe}_3\text{O}_4$  nanoparticles realize highly efficient ring-opening of epoxides with thiols to hydroxy sulfides without solvent, as well as offer enhanced separation efficiency and reusability.

The magnetic nanoparticles are more commonly used as supports than catalysts.<sup>74–77</sup> As supports, these magnetic nanoparticles can be either uncoated or coated with a layer of silica or carbon.<sup>78</sup> Uncoated magnetic nanoparticles can be easily synthesized and functionalized. However, most magnetic nanomaterials are not stable enough and easily oxidized under an air atmosphere, which may change their magnetic properties. In particular, zero-valence metals or magnetite exhibit low stability in an acidic medium. For example, pure  $\text{Fe}$  nanoparticles can only be used under inert conditions. Alloys like  $\text{FePt}$  with superparamagnetic properties are more stable but expensive and laborious to obtain. Compared with zero-valence magnetic



materials, iron oxide nanoparticles are easier to prepare and handle.<sup>79</sup> Co and Ni nanoparticles can also be used both as catalysts and supports in a similar way. However, they also face the same problems of easy oxidation. Besides, their oxide nanoparticles possess lower magnetization than metallic Ni and Co.<sup>80,81</sup> Therefore, iron oxides are more attractive catalyst supports due to their low toxicity, low cost, and easy preparation. Uncoated magnetic nanoparticles can also affect the catalytic activity of the supported catalysts. Lee *et al.*<sup>82</sup> found that the dumbbell-like heterostructures of Au-Fe<sub>3</sub>O<sub>4</sub> nanoparticles show a synergetic effect for H<sub>2</sub>O<sub>2</sub> reduction. Au-Fe<sub>3</sub>O<sub>4</sub> nanoparticles are more active than individual Au and Fe<sub>3</sub>O<sub>4</sub> nanoparticles with the same structure. The polarization effect at the heterostructure interface makes Fe<sub>3</sub>O<sub>4</sub> more active to further enhance the activity. Magnetic nanomaterials coated with other materials, including silica, carbon, polymer, and metal, have received a great deal of attention in catalysis. The magnetic nanoparticles are coated to protect the inner magnetic core from contacting with other agents. The protective shells provide an effective barrier against adverse contact and oxidation. Besides, the coating layers of magnetic nanomaterials improve chemical and thermal stability.<sup>83</sup> The dispersion can also be controlled reversibly in reactions when the catalysts are loaded onto magnetic supports. Li *et al.*<sup>84</sup> prepared the metal-organic framework (MOF) by using Ca<sup>2+</sup> and terephthalic acid (BDC) encapsulating enzymes coated on Fe<sub>3</sub>O<sub>4</sub> magnetic nanoparticles under mild conditions in the aqueous phase by one-pot synthesis for biocatalysis (Figure 8.3). And the sizes of the composites can be tuned from the range of sub- $\mu\text{m}$  to tens of  $\mu\text{m}$ , which will satisfy various needs for different sizes of enzymes. The composites are separated easily from the reaction media and reused after many cycles without losing their activity. This method can also be used to immobilize other enzymes with high stability and recyclability in biocatalysis. Gupta *et al.*<sup>85</sup> synthesized bioactive 3,3-di(indolyl)indolin-2-ones by using a silica-coated magnetic nanoparticle-supported 1,4-diazabicyclo[2.2.2]octane

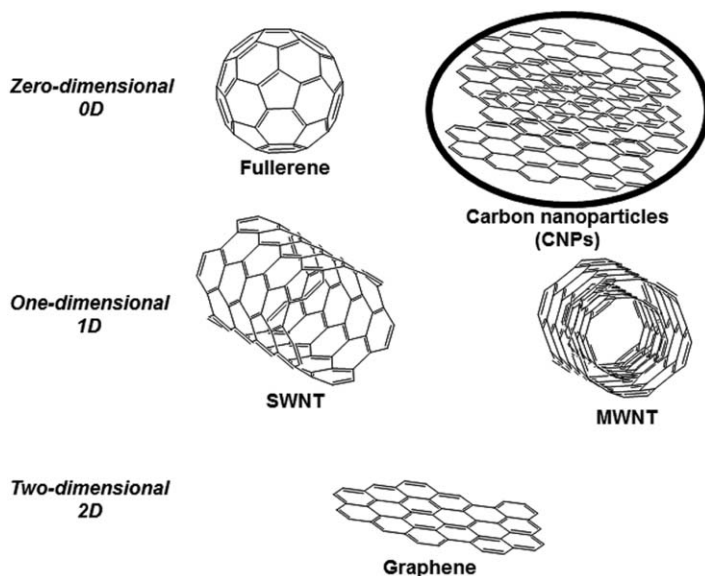


**Figure 8.3** Schematic illustration of the composites with different sizes for tuning the catalytic activity. Reproduced from ref. 84 with permission from American Chemical Society, Copyright 2020.

(DABCO)-derived and an acid-functionalized ionic liquid as the catalyst. A library of indolinones is obtained in excellent yields under mild reaction conditions. Similarly, the catalyst is easily recovered from the reaction mixture through an external magnet and reused without losing catalytic activity after eight consecutive cycles.

### 8.2.3 Nanocarbon Materials

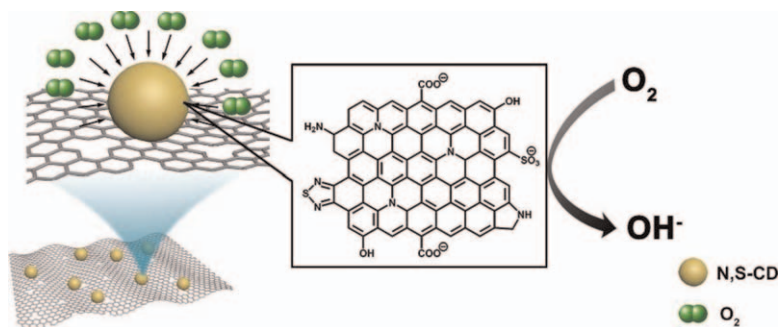
Conventional metal nanocatalysts are frequently limited because of their high cost, toxicity, and environmental issues. Nanocarbon materials, as metal-free green heterogeneous catalysts, possess great potential to replace metal catalysts or supporting materials for improving the performance of catalysts.<sup>86–90</sup> Nanocarbon materials refer to a wide class of organic nanomaterials based on carbon atoms in different hybrids ( $sp^1$ ,  $sp^2$ ,  $sp^3$ ).<sup>91–94</sup> Their allotropic structures, based on their geometric dimensions, can be normally classified into zero-dimensional structures (fullerene, nanodiamonds, and carbon nanoparticles), one-dimensional structures (carbon nanotubes), two-dimensional structures (graphene), and three-dimensional structures (mesoporous carbons) (Figure 8.4). Due to the different orientations of orbitals in these hybrids, these multiform allotropes exhibit markedly different properties. Compared with other nanoparticles, such as metal nanoparticles, nanocarbon materials are excellent candidates for the “next generation” of nanocatalysts due to their low cost, nontoxicity,



**Figure 8.4** Nanocarbon materials. Reproduced from ref. 101 with permission from the Royal Society of Chemistry.

sustainability, and relatively easy functionalization.<sup>95–98</sup> Further, carbon nanomaterials are often decorated with many functional groups, or coupled to inorganic materials, to add significant versatility and improve desired functionalities.<sup>99,100</sup> In this respect, the unique properties of nanocarbon materials as metal-free catalysts make them the most promising nanomaterials for the development of sustainable nanocatalysts.

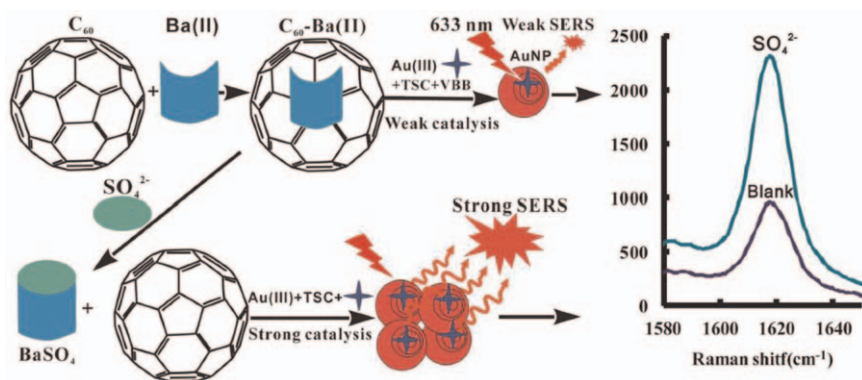
Carbon nanoparticles, also called carbon quantum dots, are a new kind of quasispherical nanoparticles formed by amorphous carbon or graphite sheets with a diameter range of 2–10 nm.<sup>101–103</sup> Compared with other nanocarbon materials, carbon nanoparticles can be easily and cheaply synthesized on a large scale *via* many methods, including hydrothermal carbonization, electrolysis, and pyrolysis.<sup>104</sup> They also show advantages in terms of high stability, biocompatibility, and abundance. The carbon nanoparticles are often used as excellent photosensitizers for photocatalytic applications, which show a broad absorption band in the UV and visible region.<sup>105–107</sup> Li *et al.*<sup>108</sup> decorated carbon quantum dots with hydrogen sulfate groups with a diameter of 2–9 nm, which catalyze ring-opening reactions of epoxides with high conversion values at room temperature under visible light irradiation. This system also presents photoswitchable acidity resulting from photoexcitation and charge separation in carbon quantum dots, which leads to an electron-withdrawing effect in acidic groups. The photoirradiation of carbon quantum dots makes the protons easily released from the sulfate groups, leading to a stronger acid photocatalyst. Besides, the catalyst can be easily separated by filtration and is recyclable without loss of efficiency. Zhang *et al.*<sup>109</sup> prepared a carbon-based electrocatalyst in oxygen reduction reactions by N,S-codoped carbon quantum dots anchored onto reduced graphene oxide (Figure 8.5). Because of abundant edges/defects on carbon nanoparticle surfaces, the system shows better performance than reduced graphene oxide. Compared with individual dopants, the codoped samples exhibit higher catalytic activity due to more electron transfer pathways.



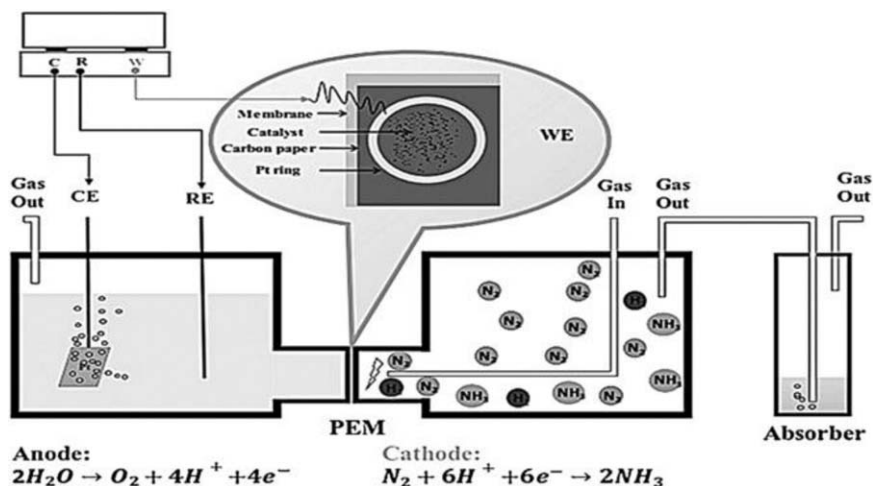
**Figure 8.5** Schematic illustration of heteroatom-doped carbon dots for oxygen reduction. Reproduced from ref. 109 with permission from Elsevier, Copyright 2019.

Fullerenes are another important carbon class of nanostructures that are broadly applied in the areas of solar energy conversion and catalysis.<sup>110–112</sup> In C<sub>60</sub> molecules, all carbon atoms are sp<sup>2</sup> hybrids, which makes them efficient charge acceptors. Due to their strong electron-withdrawing ability, fullerenes especially play an important role in radical reaction and surface functionalization. Besides, they are often modified with other chemical species in order to possess high chemical reactivities. Vidal *et al.*<sup>113</sup> modified fullerenes with highly active metal atom Ir to catalyze hydrogen transfer reactions, including reduction of ketone and *N*-alkylation with alcohols. They exhibit a high catalytic ability and can be easily separated from the reaction medium and reused several times without loss of catalytic efficiency. Li *et al.*<sup>114</sup> successfully used fullerene as a catalyst to establish a new quantitative analysis method for SO<sub>4</sub><sup>2-</sup> in serum samples (Figure 8.6). Fullerenes show strong catalysis for redox reaction of HAuCl<sub>4</sub>-trisodium citrate to obtain gold nanoplasmonic detection, which gives a strong surface-enhanced Raman scattering signal. Upon the addition of Ba<sup>2+</sup>, Ba<sup>2+</sup> adsorbs on the fullerene surface to inhibit the nanocatalysis. Then analyte SO<sub>4</sub><sup>2-</sup> could form stable BaSO<sub>4</sub> precipitate with Ba<sup>2+</sup> to release free fullerene, which causes the catalytic ability of fullerene to recover and signal peak to increase. Thus, a new and sensitive way is developed for the detection of sulfate by fullerene catalytic reaction.

Carbon nanotubes with high-impact nanostructures are also widely utilized in catalytic areas. They can be seen as rolled cylindrical graphitic sheets, but the presence of curvature endows them with different electronic properties.<sup>115–119</sup> The high surface area, excellent electrical properties, and super thermal stability make carbon nanotubes competitive candidates in electrocatalytic fields.<sup>120–122</sup> Gong *et al.*<sup>123</sup> reported N-doped carbon nanotube arrays with a length of 8 mm and a diameter of 25 nm for oxygen reduction in alkaline fuel cells (Figure 8.7). A steady-state output potential of -80 mV and a current density of 4.1 mA cm<sup>-2</sup> at -0.22 V are obtained in the



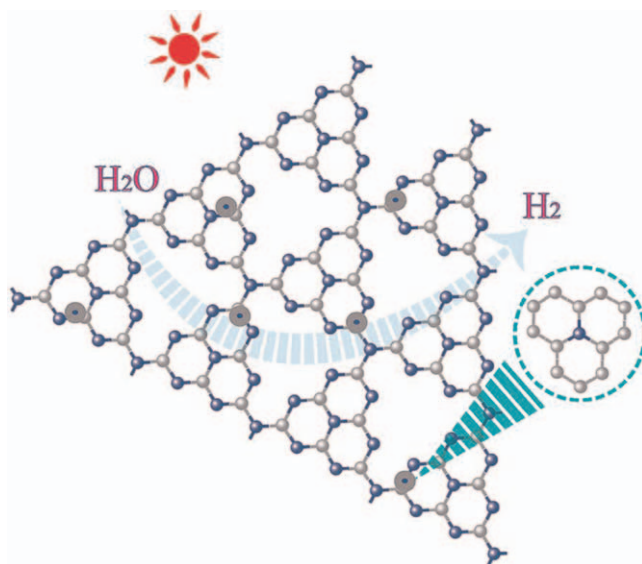
**Figure 8.6** Quantitative analysis method for sulfate combined BaSO<sub>4</sub> reaction using fullerene as the nanocatalyst. Reproduced from ref. 114 with permission from MDPI, Copyright 2018.



**Figure 8.7** Electrocatalytic synthesis of ammonia at room temperature and atmospheric pressure from water and nitrogen on a carbon nanotube-based electrocatalyst. Reproduced from ref. 124 with permission from John Wiley & Sons, Copyright © 2017 Wiley-VCH Verlag GmbH & Co. KGaA, Weinheim.

air-saturated 0.1 M KOH electrolyte. Compared with Pt-based electrodes, carbon nanotube performs a four-electron pathway with a smaller crossover effect, higher electrocatalytic activity and stability, and better long-term operation. Chen *et al.*<sup>124</sup> utilized Fe nanoparticles supported on carbon nanotubes as an electrocatalyst to synthesize  $\text{NH}_3$  from water and  $\text{N}_2$  at room temperature and atmospheric pressure. The rate of  $\text{NH}_3$  formation is as high as  $2.2 \times 10^{-3} \text{ g}_{\text{NH}_3} \text{ m}^{-2} \text{ h}^{-1}$  and the electrocatalyst keeps stable catalytic capabilities of more than 60 h in this half-cell.

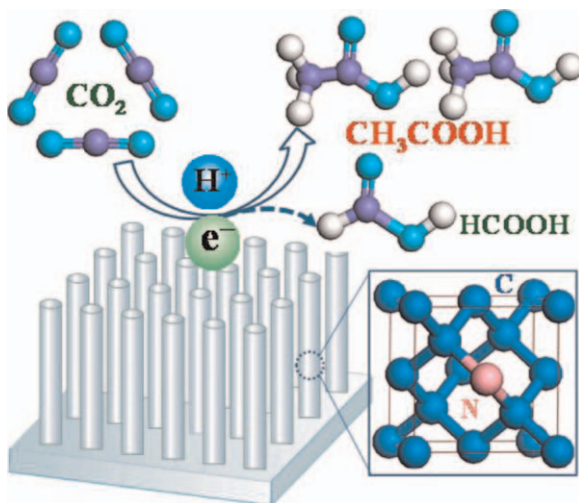
Graphene is a two-dimensional and  $\text{sp}^2$ -hybridized single atomic carbon sheet. Both the covalent  $\sigma$ -bond in plane and  $\pi$ -bond out of plane exist in graphene, which facilitates electron delocalization over graphene sheets.<sup>125–128</sup> Because of the large surface area and great adsorptive capacity, these 2D carbon systems can also be further modified by attaching nanoparticles as an excellent catalysis support material.<sup>129–131</sup> Especially, graphene has emerged as a new photocatalyst and electrocatalyst owing to its outstanding electrical, optical, and thermal conductivity.<sup>132–134</sup> Zhou *et al.*<sup>135</sup> reported N-doped graphitic carbon-incorporated  $\text{g-C}_3\text{N}_4$  photocatalysts for significantly enhanced  $\text{H}_2$  evolution rate by water splitting under visible light (Figure 8.8). N-doped graphitic carbon promotes visible light-harvesting enhancement and prevents charge carrier recombination, as well as remarkably extends and delocalizes the aromatic  $\pi$ -conjugated system of  $\text{g-C}_3\text{N}_4$ . The  $\text{H}_2$  evolution rate on the composites reaches as high as  $64 \mu\text{mol h}^{-1}$ , which is three times higher than that on pure  $\text{g-C}_3\text{N}_4$ . Moreover, these special capabilities of graphene molecules, including facile decoration, easy electron conduction, and tunable bandgap, make them a



**Figure 8.8** Schematic illustration of N-doped graphitic carbon-incorporated  $g\text{-C}_3\text{N}_4$  for photocatalytic  $\text{H}_2$  evolution under visible light. Reproduced from ref. 135 with permission from Elsevier, Copyright 2016.

perfect candidate for the development of metal-free catalyst systems. Nanographene and its derivatives also have been applied in various chemical transformations, including oxidation, addition, esterification, hydration, and C–C coupling.<sup>136</sup> Qi *et al.*<sup>137</sup> used graphene as a nonmetal catalyst for [2 + 3]cycloaddition of nitriles and sodium azide. Its unique electrical and magnetic properties facilitate electron transfer and reactant aggregation, elevating the catalytic performance. Besides, this catalyst can be easily separated *via* centrifugation from the reaction medium and reused.

Nanodiamond is a relatively new class of nanostructured carbon catalysts. In nanodiamonds, carbon atoms are  $sp^2/sp^3$  hybrids, resulting in a tetrahedral orientation, which gives the diamond superior chemical stability, high thermal conductivity, and surface energy.<sup>138,139</sup> The  $sp^2/sp^3$  hybrid configuration in nanodiamond helps understand the effect of molecular structure and surface chemistry on catalytic performance.<sup>140–143</sup> Especially, strain and defect sites of N-doped nanodiamond inducing a reduced energy barrier provide active sites for electrochemical reaction.<sup>144–146</sup> Liu *et al.*<sup>147</sup> prepared an N-doped nanodiamond/Si rod array electrode as a high-efficiency electrocatalyst for the reduction of  $\text{CO}_2$  to acetate (Figure 8.9). It prefers to obtain acetate over formate, and the formation rate of acetate is 1.65–1.90 times higher than that of formate. Besides, the remarkable current efficiency of 91% at  $-0.8$  to  $-1.0$  V for  $\text{CO}_2$  reduction has been achieved. The same group further developed a B- and N-codoped nanodiamond for the electrochemical reduction of  $\text{CO}_2$  to high-heating-value ethanol.<sup>148</sup> The codoped nanodiamond exhibits high selectivity and activity that ethanol



**Figure 8.9** Electrochemical reduction of  $\text{CO}_2$  to acetate catalyzed by N-doped nanodiamond. Reproduced from ref. 147 with permission from American Chemical Society, Copyright 2015.

production rate is much higher than that of minor products. Compared with B- or N-doped nanodiamond, the codoped nanodiamond with a significant modulation of the electrical structure prefers to form defect-induced sites. This results in a more negative  $\text{H}_2$  evolution potential which, in turn, remarkably enhances its photocatalytic performance for  $\text{CO}_2$  evolution. The synergistic effect of B and N codoping makes it easier for  $\text{CO}_2$  reduction with a current efficiency as high as 93.2% for ethanol.

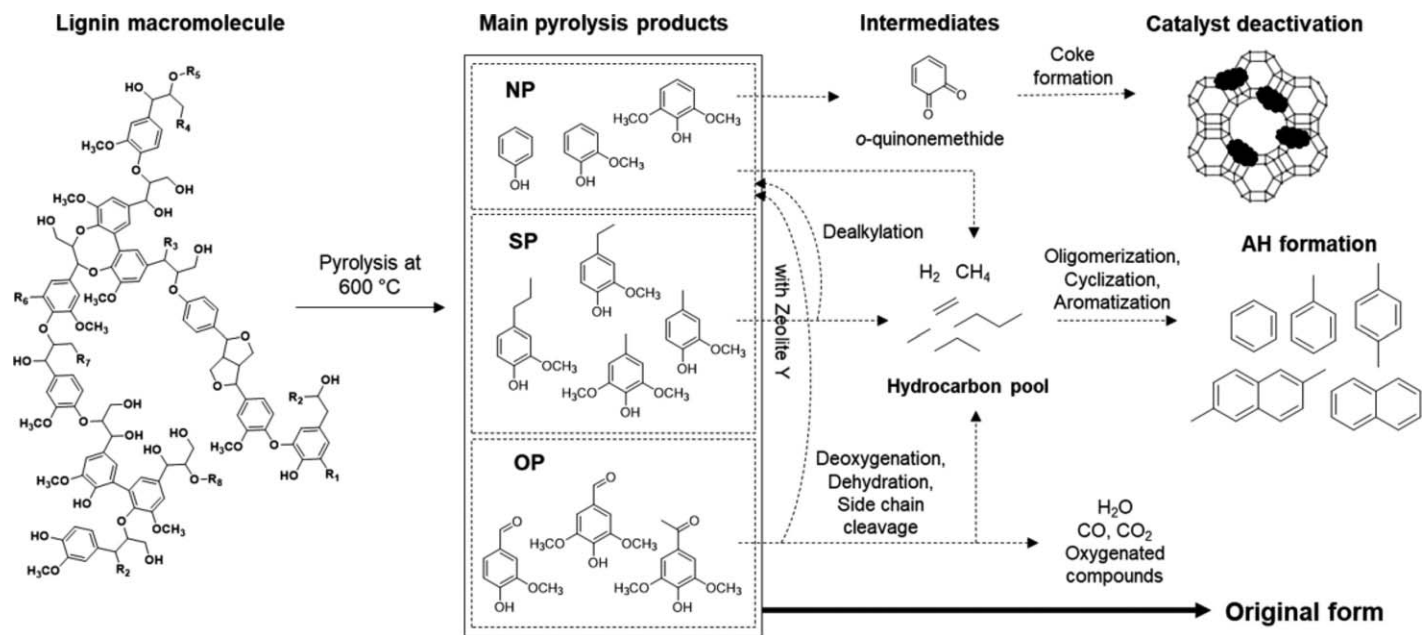
### 8.2.4 Nanostructured Porous Materials

After these years of exploration, porous nanomaterials for ethanol become one of the most popular catalytic systems extended from traditional zeolites and inorganic mesoporous silica to present MOFs and covalent organic frameworks (COFs).<sup>149–151</sup> Zeolites and MOFs possess crystalline porous structures, while mesoporous silica is a kind of amorphous pore material. These porous materials have a big difference in terms of pore size. Zeolites usually have pore sizes smaller than 1 nm, and mesoporous silica has pore sizes of about a few nanometers, whereas MOFs or COFs have cavities ranging from the ultramicropore to mesopore range.<sup>152–155</sup> Besides, mesoporous silica and MOFs with large pore sizes can also be used as supporting materials for other catalysts.<sup>156–158</sup> They exhibit unique features, including uniform pore volume, abundant active sites, and high adsorption ability.<sup>159,160</sup> These strengths favor the diffusion of the reactants and desorption of the products, which endow them with higher selectivity and catalytic activity.

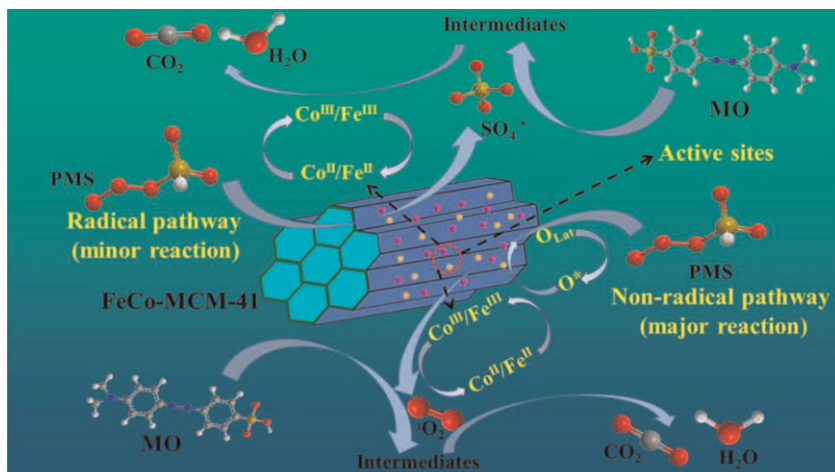
Zeolites are crystalline aluminosilicates and an important class of porous materials that have large-scale commercial applications in industrial and environmental catalysis.<sup>161–164</sup> Hundreds of zeolite systems with different sizes, shapes, and channels have been reported, such as zeolite Y, ZSM-5, ferrierite, and mordenite.<sup>165–168</sup> Zeolites exhibit pronounced thermal and hydrothermal stability, and some zeolites even remain stable up to 800 °C or higher. Therefore, zeolite frameworks are specially serviced as ideal catalysts for gas-phase reactions, which are generally performed at high temperatures.<sup>169–171</sup> It should be noted that the adsorption of products or by-products poses problems of deactivation for many heterogeneous catalysts after several catalytic cycles. But zeolites can be easily reactivated by pyrolysis or combustion.<sup>172</sup> Kim *et al.*<sup>173</sup> reported the conversion of phenol intermediates into aromatic hydrocarbons in lignin pyrolysis by using various zeolites (Figure 8.10). The lignin-derived phenols are pyrolyzed by three zeolite catalysts (Y, BETA, and ZSM-5) to offer benzene, toluene, xylenes, and naphthalene as the main products at high temperatures. The yield of aromatic hydrocarbons is about 30–140  $\mu\text{g mg}^{-1}$ . Y-type zeolite shows good performance in producing monocyclic aromatic hydrocarbons because of its suitable pore size and high surface area. Notably, BETA provides high efficiency in the production of naphthalene. Kowalska-Kuś *et al.*<sup>174</sup> utilized zeolites to convert crude glycerol with acetone into solketal through a continuous flow process. BEA zeolite and hierarchical zeolite of MFI show excellent catalytic behavior that offers nearly 85% conversion and 98% selectivity to solketal only after 1 h.

Silica-based mesoporous materials turned out to be one promising class of catalysts. Their high specific surface area (800–1400  $\text{m}^2 \text{g}^{-1}$ ) and relatively large pore diameter (2–50 nm) make them excellent nanostructured catalysts and adsorbents in heterogeneous catalysis.<sup>175–178</sup> The silanol groups on the internal surface of silica nanomaterials lead to a wide variety of functional groups to be easily immobilized and effectively functionalized due to the presence of hydrogen bonding or covalent bonding. They are often easily derivatized with acids, amines, carboxylic acids, or metallic complexes to improve their versatility and performance.<sup>155,179,180</sup> Although mesoporous silica shows the long-range ordered structure, their amorphous nature leads to lower thermal stability than those of zeolites. Porous silica nanomaterials especially show excellent catalytic activity in the field of acid catalysis, hydrogenation catalysis, and photocatalysis.<sup>181–185</sup> In particular, popular mesoporous silica support materials including MCM-41, MCM-48, SBA-15, and HMS show widespread applications in nanocatalysis.<sup>186–189</sup> Sun *et al.*<sup>190</sup> used Fe–Co bimetal-doped MCM-41 *via* peroxymonosulfate activation to degrade organic contaminant methyl orange in wastewater (Figure 8.11). The co-doping of iron helps promote the cycle of  $\text{Co}^{2+}/\text{Co}^{3+}$ . The metals are well dispersed in MCM-41, which exhibit high activity and low leaching during the degradation process. Bregante *et al.*<sup>191</sup> compared alkene epoxidation on catalysts composed of Ti atoms in zeolite BEA (Ti–BEA) and Ti atoms grafted to mesoporous SBA-15 (Ti–SBA-15). The reaction rates are strongly





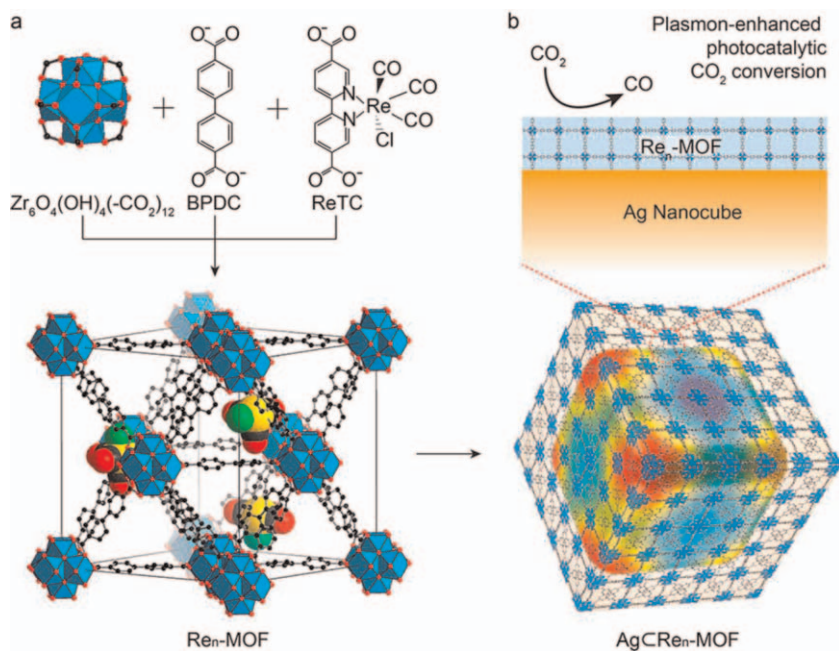
**Figure 8.10** The conversion of phenol intermediates into aromatic hydrocarbons from lignin with zeolite Y catalyst. Reproduced from ref. 173 with permission from Elsevier, Copyright 2020.



**Figure 8.11** Efficient degradation of methyl orange by Fe–Co bimetal-doped MCM-41 as peroxydisulfate activator. Reproduced from ref. 190 with permission from Elsevier, Copyright 2020.

dependent on the morphology of the catalysts as evident from the higher oxidation rates in Ti–BEA-12.5 than in TiSBA-15. Compared with the micropores of Ti–BEA-12.5, the mesopores of TiSBA-15 allow transition states to access conformations that lower the free energy and are less sensitive to epoxidation rates with larger pore sizes. This work reveals how to tune catalyst rates by tuning the shape and size of the pore.

MOFs, also called porous coordination polymer particles, are a novel class of crystalline materials that comprise secondary building units, metal cations, and organic linkers.<sup>192–194</sup> Different from purely inorganic materials like zeolite or mesoporous silica, their structure and function are flexibly tuned through a rational selection of metal, organic linkers, or postsynthetic modification. MOFs possess ultrahigh surface areas compared to zeolites, which are as high as  $10\,400\text{ m}^2\text{ g}^{-1}$ .<sup>195–197</sup> Compared with traditional heterogeneous nanocatalysts, MOFs afford a perfectly defined cavity, allowing the selective introduction of substrates. Nowadays, MOF-derived nanomaterials also focus on using abundant noble metal-free catalysts instead of noble metals. Due to high surface areas, ordered porous structure, and uniform channel sizes (0.5 to 9.8 nm), MOF nanocatalysis has been effectively applied in organic reactions, electrocatalysis, and photocatalysis.<sup>198–201</sup> Apart from guest nanocatalyst encapsulated inside the cavity, the MOF itself including metal centers and organic linkers also provides synergistic catalytic effects, leading to considerable catalytic improvements. Chen *et al.*<sup>202</sup> reported PdAg alloy nanoparticles located in an MOF MIL-101 as a multifunctional catalyst in one-pot cascade reactions for the synthesis of secondary arylamines. This system exhibits excellent catalytic activity and selectivity due to multiple active sites that the MOF structure offers as Lewis acid sites, and Pd affords hydrogenation activity while Ag improves



**Figure 8.12** Photocatalytic CO<sub>2</sub> conversion within MOF under visible light. Reproduced from ref. 203 with permission from American Chemical Society, Copyright 2017.

selectivity. The host-guest cooperation and bimetallic synergy exert respective functions in catalysis. Choi *et al.*<sup>203</sup> attached sensitizer ReI(CO)<sub>3</sub>(BPYDC)Cl to a zirconium MOF as a photocatalyst for CO<sub>2</sub> reduction under visible light (Figure 8.12). The MOF successfully prevents the dimerization and deactivation of the catalyst. When the Re<sub>3</sub>-MOF is coated onto Ag nanocubes, the catalytic centers are confined within the enhanced electromagnetic field surrounding the surface of the nanocubes, resulting in a sevenfold enhancement in CO<sub>2</sub> photocatalytic conversion to CO. Besides, the catalyst activity is maintained up to 48 h.

COFs are another class of porous crystalline materials that are connected *via* covalent bonds.<sup>204,205</sup> Similar to MOF, the large surface area and tunable porous size make the COF an ideal candidate for next-generation catalysts.<sup>206–208</sup> However, COFs usually present poorer crystallinity with more disordered structures when compared with MOFs.<sup>209–211</sup> Due to the main organic skeletal structure, COFs show poor thermal stability in comparison with inorganic crystalline zeolite materials. On the other side, metal-free and strong covalent bonds in COFs possess much greater bond dissociation energy than the coordinative bond in MOFs, and thus COFs are more stable in aqueous solution, organic solvents, or other harsh conditions.<sup>212–214</sup> Some catalysts exhibit better catalytic function when incorporated into COFs. Lin *et al.*<sup>215</sup> reported that the COF comprising Co

porphyrin exhibits efficient catalysis for the electrochemical reduction of  $\text{CO}_2$  to CO in an aqueous solution. The skeletal structure of COF influences the electronic properties of Co-active centers directly, which improves the selectivity and activity. The Faradaic efficiency for CO production is as high as 90% and turnover numbers up to 290 000 have been achieved with an overpotential of  $-0.55$  V. The system exhibits a 26-fold improvement in efficiency compared with the parent molecular precursor and maintains catalytic activity for 24 h. Wang *et al.*<sup>216</sup> constructed COFs based on a benzobis(benzothiophene sulfone) moiety for photocatalytic hydrogen evolution from water. The crystalline COF shows a much higher catalytic activity than its amorphous or semicrystalline solids. The strong light absorption and hydrophilic mesopores cause the catalyst to show high quantum efficiencies for water splitting. The dye-sensitized COF material also keeps stable for at least 50 h under visible light and gives photocatalytic hydrogen evolution rates of up to  $16.3 \text{ mmol g}^{-1} \text{ h}^{-1}$ .

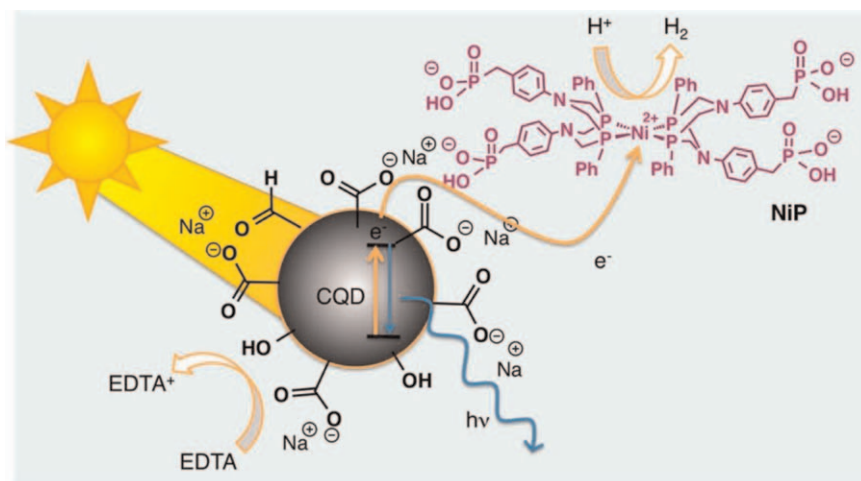
## 8.3 Nanocatalysis With Sustainability

The continuous increase in environmental and energy problems demands sustainable development. Nanocatalysts play very significant roles in organic transformations/synthesis, energy-related systems, environmental protection, and so on. Researchers are focusing on more sustainable development and green chemistry using clean resources like hydrogen energy and solar energy for a future society. The sustainable applications of nanocatalysts range from environmental remediation to the production of high-value chemicals and fuels, which are introduced as follows.

### 8.3.1 Photocatalysis

For over a century, light has been considered a viable alternative energy source for replacing fossil burning. In particular, tremendous developments have been achieved in the field of photocatalysis over the past decades. Photocatalysis has also gained much attention in the area of nanocatalysis due to its sustainability, simplicity, and relatively low cost.<sup>217–219</sup> In the 1970s, Fujishima and Honda used the photoexcited semiconductor  $\text{TiO}_2$  for splitting water into  $\text{H}_2$  and  $\text{O}_2$  in a photoelectrochemical solar cell, which has further promoted numerous applications for photocatalytic technology in the environment and energy sectors.<sup>220,221</sup> Light-driven catalytic technologies provide a sustainable way for energy injection in green chemistry. When photocatalysts absorb solar energy larger than the energy gap, they are excited to electron-donating or electron-accepting sites to produce electron–hole pairs with a higher energy level and release such absorbed energy to substrates, inducing oxidation–reduction reactions.<sup>222–224</sup> Most photocatalysts are metal oxide semiconductors, such as  $\text{TiO}_2$ , ZnS, or CdS. Among them,  $\text{TiO}_2$  is the most widely used photocatalyst due to its ease of preparation, high stability, and activity.<sup>225–227</sup> The reduction of  $\text{N}_2$  to  $\text{NH}_3$  is very

important in the field of the chemical industry. Zhao *et al.*<sup>228</sup> prepared ultrathin TiO<sub>2</sub> nanosheets by using the facile copper-doping method. Defect-rich TiO<sub>2</sub> nanosheets show excellent performance toward the photocatalytic reduction of N<sub>2</sub> to NH<sub>3</sub> in water under light irradiation *via* a promising and sustainable route. The TiO<sub>2</sub> nanosheets show a wide solar absorption range, which can be extended up to 700 nm with NH<sub>3</sub> evolution rates of 0.72 μmol g<sup>-1</sup> h<sup>-1</sup>. The abundant oxygen vacancies and strain effect synergistically promote the adsorption and activation of N<sub>2</sub>, which facilitates fast electron-hole pairs separation, leading to high rates of NH<sub>3</sub> evolution under visible-light irradiation. In addition to TiO<sub>2</sub>, CDs are a new kind of effective, stable, and adjustable photocatalyst for energy conversion applications. Muthulingam *et al.*<sup>229</sup> synthesized CDs doped with N and ZnO. These nanoparticles effectively degrade industrial commercial dyes, including malachite green, methylene blue, and fluorescein, within about 30–45 min by using solar light. Besides, they maintain excellent photocatalytic activity even after being reused four times. The applications of photocatalysis range from the degradation of pollutants to renewable energy production. The CDs can act as photosensitizers that are abundant, inexpensive, biologically inert, stable, and sustainably synthesized on a large scale. Martindale *et al.*<sup>230</sup> combined CDs as a photosensitizer with Ni-bis-(diphosphine) to catalyze H<sub>2</sub> production in water under solar light irradiation (Figure 8.13). These CDs covered by carboxylic groups on their surface show good solubility in water. These CDs absorb solar light and directly transfer photoexcited electrons to the catalyst NiP, which subsequently reduces aqueous protons. Ethylenediaminetetraacetic acid (EDTA) acts as an electron donor to quench photoinduced holes in CDs. A maximum activity of



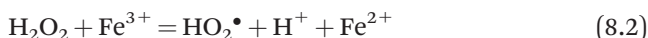
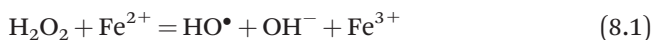
**Figure 8.13** CDs as a photosensitizer for H<sub>2</sub> production in water under solar light irradiation. Reproduced from ref. 230 with permission from American Chemical Society, Copyright 2015.

398  $\mu\text{mol}_{\text{H}_2}(\text{g}_{\text{CQD}})^{-1}\text{h}^{-1}$  and a turnover frequency of 41  $\text{h}^{-1}$  are achieved for solar light-driven  $\text{H}_2$  production.

### 8.3.2 Environmental Remediation

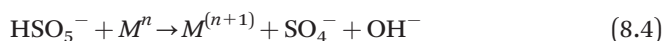
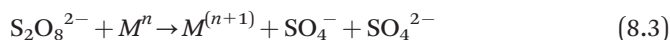
The advanced oxidation process is an efficient, powerful, and environmentally friendly method to degrade contaminants and reduce or eliminate pollutants from soils and wastewaters.<sup>231</sup> In environmental remediation, nanomaterials can principally activate and catalyst peroxides including  $\text{H}_2\text{O}_2$ ,  $\text{O}_3$ , and persulfates (peroxymonosulfate and peroxydisulfate) to produce reactive oxygen species in an aqueous phase for the oxidative degradation of organic pollutants during the purification of contaminated soil or water.<sup>232,233</sup> The structure, oxidative states, and defects of nanomaterials significantly affect the activation process.

To date, Fenton reactions are typically used operations that are intensively applied for the remediation of persistently contaminated soils, sediments, or groundwater. In classical Fenton reactions,  $\text{Fe(II)}$  catalytically decomposes  $\text{H}_2\text{O}_2$  by breaking up the peroxide bonds to produce hydroxyl radical ( $\bullet\text{OH}$ ) for further degrading organic contaminants (eqn (8.1)–(8.2)).



Indeed, a lot of researchers have applied Fenton's reagent to degrade a wide range of refractory toxic compounds, such as 2,4,6-trinitrotoluene, 2,4-dinitrophenol, chlorophenols, chlorobenzenes, tetrachloroethylene, and haloalkanes.<sup>234–236</sup> For example, as a Fenton-type catalyst, hierarchical manganese silicate hollow nanotubes exhibit high performance toward discoloring industrial dyes.<sup>237</sup> Nearly 98% methylene blue is degraded within 45 min at room temperature. Upon increasing the temperature to 60 °C, a 530% higher kinetic constant is obtained in only 2 min. The Fenton process is a facile and flexible method for the generation of powerful oxidizing agents to degrade pollutants. However, it is rather risky to store and transport  $\text{H}_2\text{O}_2$ . Besides, iron sludge needs to be removed, and the solution needs to be neutralized at the end of the treatment.  $\text{O}_3$  has also been applied for remediation because of its strong oxidation ability and low environmental adverse effect.  $\text{O}_3$  is activated to produce highly reactive species  $\bullet\text{OH}$ ,  $\text{O}_2\bullet^-$ , and  $^1\text{O}_2$ , which exhibit prominent decomposition efficiency toward organic contaminants.<sup>232,238,239</sup> Because  $\text{SO}_4\bullet^-$  can possess high oxidation potential (2.5–3.1 V) and keep stable over a wide pH range, sulfate radical-based advanced oxidation processes are particularly thought of as efficient methods for environmental remediation. Persulfates, including peroxymonosulfate and peroxydisulfate, can be activated to produce reactive  $\text{SO}_4\bullet^-$  and exhibit higher chemical stability in transport and storage (eqn (8.3)–(8.5)).<sup>232</sup> The cobalt oxides/peroxymonosulfate system is considered the most promising catalytic system that can form  $\text{SO}_4\bullet^-$  as major

oxidizing species.<sup>240–242</sup> Due to its toxic nature, researchers have tried to replace cobalt oxides with other transition metal oxides.



### 8.3.3 Production of High-value Fuels

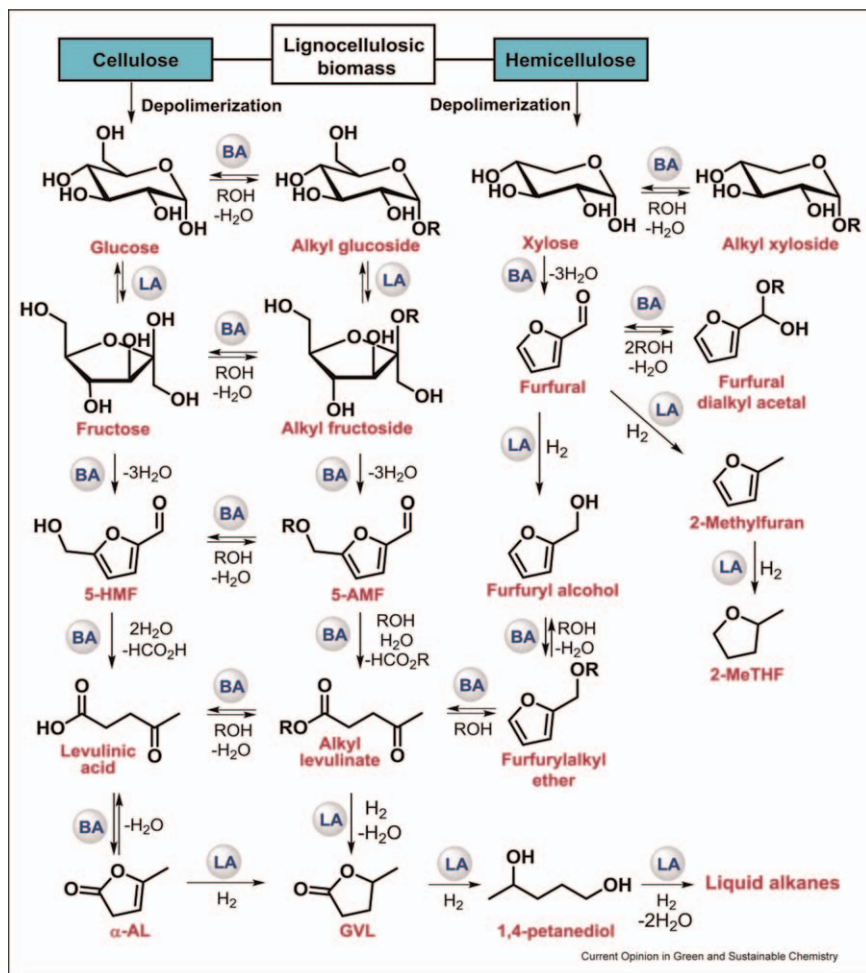
The majority of fuel energy used in today's industries is often obtained either via large-scale fuel synthesis or crude petrochemical refining. Only a small part of the energy comes from renewable resources. Excessive consumption of petroleum resources is the major contributor to greenhouse gas emissions, and the fast depletion of petroleum reserves leads to an energy crisis. Thus, the energy policy tends to utilize alternative renewable fuels. Due to technological advancements, a promising and futuristic alternative is to apply nanocatalysis for the fabrication of valuable fuels from a variety of feedstock.<sup>243–245</sup> Biomass is recognized as a renewable source of carbon for the production of fuels to replace petroleum-derived fuels. Biofuels such as biodiesel and bioethanol are absolutely renewable liquid fuels bringing benefits from the energy and environmental viewpoints.<sup>246–249</sup> Ghalandari *et al.*<sup>250</sup> synthesized a nano-sized magnetic core-mesoporous shell ( $\text{Fe}_3\text{O}_4@g\text{-Al}_2\text{O}_3$ ) as support loaded with KOH on the surface as an active component to catalyze the transesterification of canola oil in the presence of methanol to methyl esters. The yield of biodiesel achieved is as high as 97.4%. Similarly, Prabu *et al.*<sup>251</sup> prepared Mg/Al/Zn hydrotalcite/SBA-15 composite material as a nanocatalyst for the transesterification of vegetable oil with methanol to biofuel. By incorporating hydrotalcite into SBA-15 pore channels, the catalytic performance and stability of the nanocomposite is improved significantly. A yield of approximately 90% under mild conditions are observed and that this high catalytic activity performance continues for more than 200 h without deactivation. Global energy consumption leads to increasing  $\text{CO}_2$  emissions that could be mitigated by the use of sustainable and green products.  $\text{H}_2$  is an important renewable and clean energy source that is obtained through water splitting, thermochemical conversion of fossil fuels, or biological processes.<sup>252–254</sup> Besides, hydrogen production using photocatalysis or photoelectrochemical cells in water-splitting technologies is an environmentally safe process and sustainable development strategy.<sup>255–257</sup> Wan *et al.*<sup>258</sup> designed a 2D porous nitrogen-linked COF for visible light-driven photocatalytic water splitting with an energy conversion efficiency of over 20.6%. The 2D COFs with a widely tunable electronic bandgap (1.92–3.23 eV) that well matches the chemical reaction potential of  $\text{H}_2/\text{H}^+$  and  $\text{O}_2/\text{H}_2\text{O}$  split water into  $\text{H}_2$  and  $\text{O}_2$  under visible light. Luo *et al.*<sup>259</sup> used Ru-doped  $\text{ZnIn}_2\text{S}_4$  as a photocatalyst for the coproduction of  $\text{H}_2$  and diesel fuel precursors from lignocellulose-derived methylfurans through

dehydrogenative C – C coupling with a quantum yield of 15.2% under visible light. Then 1.04 g  $g_{\text{catalyst}}^{-1} \text{h}^{-1}$  of diesel fuel precursors and 6.0 mmol  $g_{\text{catalyst}}^{-1} \text{h}^{-1}$  of  $\text{H}_2$  were produced. The desired diesel fuels consisting of  $\sim\text{C}_{10}\text{--}\text{C}_{18}$  straight- and branched-chain alkanes were obtained. Ru dopants can improve light harvesting and charge separation efficiency, thus promoting C – H activation for the coproduction of  $\text{H}_2$  and diesel fuel precursors.

### 8.3.4 Production of High-value Chemicals

The use of nanocatalysis for the preparation of key-value chemicals from wastes gives much hope to develop the concept of sustainable synthesis in the field of green chemistry. The strategies for obtaining high-value chemicals and materials starting from a suitable depolymerization of biomass through downstream processing help lower greenhouse gas emissions and protect our environment. Researchers have concentrated on the potential applications of nanocatalysts for the selective conversion and further modification of biomass-derived feedstock, such as cellulose, hemicellulose, and lignin, into important chemicals and valuable products.<sup>260–262</sup> For example, glucose and xylose can be depolymerized from cellulose and hemicellulose, respectively. These monomeric sugars are dehydrated in acid medium into products such as aldehydes furfural and 5-hydroxymethyl furfural, which can be further converted to value-added products such as levulinic acid, alkyl levulinates, and  $\gamma$ -valerolactone (Figure 8.14).<sup>263</sup> The  $\text{N}_2$  fixation reaction is also an important chemical process in nature and industry. Because of the strong nonpolar bond and high N–N bond energy of  $940.95 \text{ kJ mol}^{-1}$ , it is still a challenge for efficient nitrogen fixation.<sup>264–266</sup>  $\text{NH}_3$  is the main product of  $\text{N}_2$  fixation and is used as a raw material for the synthesis of fertilizers in industry. Being one of the most important scientific discoveries in the 20th century, the Haber–Bosch process ( $\text{N}_2 + 3\text{H}_2 \rightarrow 2\text{NH}_3$ ) performed at  $400\text{--}600 \text{ }^\circ\text{C}$  and  $20\text{--}40 \text{ MPa}$  is still widely used now.<sup>267</sup> Due to the extreme energy dependency of the Haber–Bosch reaction, it is strongly expected to develop an appropriate nanostructured catalyst for efficient  $\text{N}_2$  fixation that strongly interacts with  $\text{N}_2$  to promote adsorption and activation and lower the energy barrier of  $\text{N}_2$  fixation, as well as react in a relatively mild reaction. Gong *et al.*<sup>268</sup> successfully revealed a ternary intermetallic material LaCoSi as a highly effective and stable catalyst for  $\text{N}_2$  fixation under mild conditions. The negatively charged cobalt atoms facilitate the initial adsorption of  $\text{N}_2$  and effectively tune electron transfer from lanthanum to  $\text{N}_2$ , which greatly reduces the activation energy of  $\text{N}_2$  dissociation. The specific configuration and electronic property of LaCoSi enhance  $\text{N}_2$  adsorption capabilities with a strongly exothermic process and further lower the activation barrier of  $\text{N}_2$  dissociation. Especially, LaCoSi shows robust stability and high catalytic activity ( $1250 \mu\text{mol g}^{-1} \text{h}^{-1}$ ) under mild reaction conditions ( $400 \text{ }^\circ\text{C}$ ,  $0.1 \text{ MPa}$ ).  $\text{CO}_2$  reduction reaction provides a valuable approach to remove excess  $\text{CO}_2$  from the atmosphere and transform it into





**Figure 8.14** Schematic representation of value-added chemicals *via* conversion of biomass-derived carbohydrate. Reproduced from ref. 263 with permission from Elsevier, Copyright 2019.

high-value chemicals, such as HCOOH, CO, HCHO, CH<sub>3</sub>OH, and CH<sub>4</sub>, which integrates carbon capture, utilization, and storage in carbon cycles with no further addition of atmospheric CO<sub>2</sub>.<sup>269–271</sup> Weng *et al.*<sup>272</sup> reported metallic copper nanoclusters in copper(II) phthalocyanine as active sites for electrochemical CO<sub>2</sub> reduction. Copper(II) phthalocyanine shows high activity and selectivity in CO<sub>2</sub>-to-CH<sub>4</sub> conversion with a partial current density of 13 mA cm<sup>-2</sup> and a Faradaic efficiency of 66% at the potential of -1.06 V *versus* the reversible hydrogen electrode, and copper(II) phthalocyanine restructured to about 2 nm metallic copper nanoclusters under the working conditions and then reversibly turned back to the original structure and oxidation state upon the release of the negative electrode potential.

Additionally, effectively reducing CO<sub>2</sub> into other high-value chemicals *via* photocatalysis is considered to mimic natural photosynthesis. Cui *et al.*<sup>273</sup> developed visible-light photocatalytic nanomaterials for solar-driven CO<sub>2</sub> reduction. Au nanoclusters simultaneously absorb solar energy. Then various metal cations as catalytic active sites are modified onto the surface of Au nanoclusters through ligand grafting with L-cysteine for photocatalytic CO<sub>2</sub> reduction. The bonding bridge facilitates photogenerated electrons to transfer from Au nanoclusters to metal cations. And the process of CO<sub>2</sub> reduction could be tuned by simply changing the grafted metal cations with varied D-band centers and binding energies with CO<sub>2</sub>. The Au nanoclusters grafted with Co<sup>2+</sup> offer a rate of 3.54 μmol g<sub>cat</sub><sup>-1</sup> h<sup>-1</sup> and a selectivity up to 65.2% for CO production.

## 8.4 Conclusion

Although nanocatalysis has already been studied for decades, it is still a very active area due to its important applications in improving sustainability. Here, we have summarized different types of nanocatalysts and their sustainable applications in various fields. It is expected to give a comprehensive understanding of nanocatalysis and help researchers in this area reasonably design and synthesize appropriate nanomaterials. It is undeniable that a lot of achievements have been obtained in the area of nanocatalysis. Nevertheless, it still requires significant efforts to overcome some challenges for the further development of nanocatalysts. Firstly, as nanocatalytic materials, it is very important to develop novel systems on the nanometer scale for use in various reactions. Although a lot of guidelines for design strategies of nanocatalysts have been provided, it is still difficult to precisely predict its properties over a broad range of parameters in terms of catalytic activity, including the nanomaterial's crystal surface, morphology, and valence state. In particular, building a better structure–property relationship is still a major challenge. Hopefully, instrumentation and computational methods are expected to guide material design, predict nanocatalytic properties, and discuss catalytic mechanisms. Secondly, there are only limited nanomaterials applied to industry, and it is quite difficult to achieve industrial applications with many developed products. Additionally, a compatible combination of other materials with nanocatalysts is another ideal method to produce desired properties but it demands interdisciplinary efforts. Thirdly, the replacement of industrial processes requiring expensive noble metallic nanomaterials *via* metal-free, sustainable, and greener processes hopes to be achieved in the near future. For economic efficiency, it is also quite important to solve the recyclability of catalysts and maintain high catalytic activity to avoid poisoning. Lastly, the sustainable application scopes of nanocatalysts are still relatively narrow, and it will be of great importance to broaden the breadth and sophistication of their applications. It is expected that the efforts of researchers will provide a window to future sustainable possibilities in the fascinating world of nanocatalysts.

## References

1. L. Filiciotto and R. Luque, *Encyclopedia of Sustainability Science and Technology*, Springer-Verlag, New York, 2018, pp. 1–28.
2. C. K. Prier, D. A. Rankic and D. W. MacMillan, *Chem. Rev.*, 2013, **113**, 5322–5363.
3. Z. W. Seh, J. Kibsgaard, C. F. Dickens, I. Chorkendorff, J. K. Nørskov and T. F. Jaramillo, *Science*, 2017, **355**, 146.
4. S. Basumatary, B. Nath, B. Das, P. Kalita and B. Basumatary, *Fuel*, 2021, **286**, 119357.
5. C. G. Morales-Guio, L. A. Stern and X. Hu, *Chem. Soc. Rev.*, 2014, **43**, 6555–6569.
6. D. Deng, K. S. Novoselov, Q. Fu, N. Zheng, Z. Tian and X. Bao, *Nat. Nanotechnol.*, 2016, **11**, 218–230.
7. Y. B. Huang, J. Liang, X. S. Wang and R. Cao, *Chem. Soc. Rev.*, 2017, **46**, 126–157.
8. X. Li, S. Zhao, X. Duan, H. Zhang, S. Yang, P. Zhang, S. P. Jiang, S. Liu, H. Sun and S. Wang, *Appl. Catal., B*, 2021, **283**, 119660.
9. L. Liu and A. Corma, *Chem. Rev.*, 2018, **118**, 4981–5079.
10. S. Fukuzumi and D. Hong, *Eur. J. Inorg. Chem.*, 2014, **2014**, 645–659.
11. F. Chen, X. Jiang, L. Zhang, R. Lang and B. Qiao, *Chin. J. Catal.*, 2018, **39**, 893–898.
12. D. J. Cole-Hamilton, *Science*, 2003, **299**, 1702–1706.
13. A. Kumar and C. Gao, *ChemCatChem*, 2020, **12**, 1–31.
14. N. Sugisawa, H. Nakamura and S. Fuse, *Catalysts*, 2020, **10**, 1321.
15. N. Oger and F.-X. Felpin, *ChemCatChem*, 2016, **8**, 1998–2009.
16. X. Li, L. Zhang, S. Wang and Y. Wu, *Front. Chem.*, 2019, **7**, 948.
17. M. Tamura, Y. Nakagawa and K. Tomishige, *Asian J. Org. Chem.*, 2020, **9**, 126–143.
18. R. Ricciardi, J. Huskens and W. Verboom, *ChemSusChem*, 2015, **8**, 2586–2605.
19. Y. Yang, A. C. Reber, S. E. Gilliland, C. E. Castano, B. F. Gupton and S. N. Khanna, *J. Catal.*, 2018, **360**, 20–26.
20. A. Zuliani, F. Ivars and R. Luque, *ChemCatChem*, 2018, **10**, 1968–1981.
21. N. Ta, J. Liu and W. Shen, *Chin. J. Catal.*, 2013, **34**, 838–850.
22. F. Yang, D. Deng, X. Pan, Q. Fu and X. Bao, *Natl. Sci. Rev.*, 2015, **2**, 183–201.
23. V. Polshettiwar and R. S. Varma, *Green Chem.*, 2010, **12**, 743–754.
24. V. I. Parvulescu and I. Fecete, *Catal. Today*, 2018, **306**, 1.
25. G. E. M. Crisenza and P. Melchiorre, *Nat. Commun.*, 2020, **11**, 803.
26. R. S. Varma, *Curr. Opin. Green Sustainable Chem.*, 2019, **15**, 1–3.
27. W. Chen, T. Lin, Y. Dai, Y. An, F. Yu, L. Zhong, S. Li and Y. Sun, *Catal. Today*, 2018, **311**, 8–22.
28. F. Liu, G. Yu, D. Yu, S. Chen, J. Han, X. Yu and J. Wu, *Fuel*, 2021, **287**, 128952.
29. P. Fantke and N. Illner, *Curr. Opin. Green Sustainable Chem.*, 2019, **15**, 91–97.

30. J. E. Forman and C. M. Timperley, *Curr. Opin. Green Sustainable Chem.*, 2019, **15**, 103–114.
31. S. B. Kalidindi and B. R. Jagirdar, *ChemSusChem*, 2012, **5**, 65–75.
32. Z. B. Shifrina, V. G. Matveeva and L. M. Bronstein, *Chem. Rev.*, 2019, **120**, 1350–1396.
33. Y. Zhou, C. Jin, Y. Li and W. Shen, *Nano Today*, 2018, **20**, 101–120.
34. J. Wang and H. Gu, *Molecules*, 2015, **20**, 17070–17092.
35. M. Nasrollahzadeh, N. Motahharifar, F. Ghorbannezhad, N. S. Soheili Bidgoli, T. Baran and R. S. Varma, *Mol. Catal.*, 2020, **480**, 110492.
36. M. Nasrollahzadeh, M. Sajjadi, M. Shokouhimehr and R. S. Varma, *Coord. Chem. Rev.*, 2019, **397**, 54–75.
37. C. Gadipelly and L. K. Mannepalli, *Curr. Opin. Green Sustainable Chem.*, 2019, **15**, 20–26.
38. P. K. Verma, M. L. Shegavi, S. K. Bose and K. Geetharani, *Org. Biomol. Chem.*, 2018, **16**, 857–873.
39. N. Yan, C. Xiao and Y. Kou, *Coord. Chem. Rev.*, 2010, **254**, 1179–1218.
40. C. Rivera-Cárcamo and P. Serp, *ChemCatChem*, 2018, **10**, 5058–5091.
41. S. Zhao, F. Han, J. Li, X. Meng, W. Huang, D. Cao, G. Zhang, R. Sun and C. P. Wong, *Small*, 2018, **14**, e1800047.
42. S. Rawalekar and T. Mokari, *Adv. Energy Mater.*, 2013, **3**, 12–27.
43. N. Narayan, A. Meiyazhagan and R. Vajtai, *Materials*, 2019, **12**, 3602.
44. R. Arrigo, M. E. Schuster, S. Abate, G. Giorgianni, G. Centi, S. Perathoner, S. Wrabetz, V. Pfeifer, M. Antonietti and R. Schlögl, *ACS Catal.*, 2016, **6**, 6959–6966.
45. H. Koga, K. Sakata, Y. Ato, A. Hayashi, K. Tada and M. Okumura, *Chin. J. Catal.*, 2016, **37**, 1588–1593.
46. K. Sun, *Chin. J. Catal.*, 2016, **37**, 1608–1618.
47. A. Corma and P. Serna, *Science*, 2006, **21**, 332–334.
48. T. Ishida, T. Murayama, A. Taketoshi and M. Haruta, *Chem. Rev.*, 2020, **120**, 464–525.
49. Y. Zhang, X. Cui, F. Shi and Y. Deng, *Chem. Rev.*, 2012, **112**, 2467–2505.
50. M. Yadav and R. K. Sharma, *Curr. Opin. Green Sustainable Chem.*, 2019, **15**, 47–59.
51. R. K. Sharma, M. Yadav, R. Gaur, Y. Monga and A. Adholeya, *Catal.: Sci. Technol.*, 2015, **5**, 2728–2740.
52. Z. Fu, G. Zhang, Z. Tang and H. Zhang, *Catal. Surv. Asia*, 2019, **24**, 38–58.
53. J. Wen, X. Li, W. Liu, Y. Fang, J. Xie and Y. Xu, *Chin. J. Catal.*, 2015, **36**, 2049–2070.
54. T. Zhang, Y. Liu, Y. Rao, X. Li, D. Yuan, S. Tang and Q. Zhao, *Chem. Eng. J.*, 2020, **384**, 123350.
55. X. Xie, Y. Li, Z. Q. Liu, M. Haruta and W. Shen, *Nature*, 2009, **458**, 746–749.
56. M. K. Schroter, L. Khodeir, M. W. van den Berg, T. Hikov, M. Cokoja, S. Miao, W. Grunert, M. Muhler and R. A. Fischer, *Chem. Commun.*, 2006, 2498–2500.

57. Y. Sun, F. Zhang, L. Xu, Z. Yin and X. Song, *J. Mater. Chem. A*, 2014, **2**, 18583–18592.
58. C. W. Lim and I. S. Lee, *Nano Today*, 2010, **5**, 412–434.
59. M. Kazemi and M. Mohammadi, *Appl. Organomet. Chem.*, 2019, **34**, 5400.
60. T. Cheng, D. Zhang, H. Li and G. Liu, *Green Chem.*, 2014, **16**, 3401–3427.
61. R. B. Baig and R. S. Varma, *Chem. Commun.*, 2013, **49**, 752–770.
62. J. Govan and Y. K. Gun'ko, *Nanomaterials*, 2014, **4**, 222–241.
63. L. Wu, A. Mendoza-Garcia, Q. Li and S. Sun, *Chem. Rev.*, 2016, **116**, 10473–10512.
64. L. M. Rossi, N. J. S. Costa, F. P. Silva and R. Wojcieszak, *Green Chem.*, 2014, **16**, 2906–2933.
65. K. Zhu, Y. Ju, J. Xu, Z. Yang, S. Gao and Y. Hou, *Acc. Chem. Res.*, 2018, **51**, 404–413.
66. Q. Zhang, X. Yang and J. Guan, *ACS Appl. Nano Mater.*, 2019, **2**, 4681–4697.
67. Y. Zhang, X. Wang, C. Chu, Z. Zhou, B. Chen, X. Pang, G. Lin, H. Lin, Y. Guo, E. Ren, P. Lv, Y. Shi, Q. Zheng, X. Yan, X. Chen and G. Liu, *Nat. Commun.*, 2020, **11**, 5421.
68. K. Xu, J. Wu, Q. Fang, L. Bai, J. Duan, J. Li, H. Xu, A. Hui, L. Hao and S. Xuan, *Chem. Eng. J.*, 2020, **398**, 125571.
69. M. B. Gawande, A. Goswami, T. Asefa, H. Guo, A. V. Biradar, D. L. Peng, R. Zboril and R. S. Varma, *Chem. Soc. Rev.*, 2015, **44**, 7540–7590.
70. B. Liu and Z. Zhang, *ACS Catal.*, 2015, **6**, 326–338.
71. R. K. Sharma, S. Dutta, S. Sharma, R. Zboril, R. S. Varma and M. B. Gawande, *Green Chem.*, 2016, **18**, 3184–3209.
72. L. Gao, J. Zhuang, L. Nie, J. Zhang, Y. Zhang, N. Gu, T. Wang, J. Feng, D. Yang, S. Perrett and X. Yan, *Nat. Nanotechnol.*, 2007, **2**, 577–583.
73. M. M. Mojtahedi, M. S. Abaee, A. Rajabi, P. Mahmoodi and S. Bagherpoor, *J. Mol. Catal. A: Chem.*, 2012, **361–362**, 68–71.
74. M. Aqeel Ashraf, Z. Liu, Y. Yang and D. Zhang, *Synth. Commun.*, 2020, **50**, 2885–2905.
75. M. Ghobadi, P. Pourmoghaddam Qhazvini, M. Eslami and M. Kazemi, *Synth. Commun.*, 2020, 1–26.
76. I. Guerrero, A. Saha, J. A. M. Xavier, C. Vinas, I. Romero and F. Teixidor, *ACS Appl. Mater. Interfaces*, 2020, **12**, 56372–56384.
77. M. Kazemi, *Synth. Commun.*, 2020, **50**, 2079–2094.
78. M. B. Gawande, Y. Monga, R. Zboril and R. K. Sharma, *Coord. Chem. Rev.*, 2015, **288**, 118–143.
79. I. Khan, A. Khalil, F. Khanday, A. M. Shemsi, A. Qurashi and K. S. Siddiqui, *Arabian J. Sci. Eng.*, 2017, **43**, 43–61.
80. R. Dalpozzo, *Green Chem.*, 2015, **17**, 3671–3686.
81. M. Duan, J. G. Shapter, W. Qi, S. Yang and G. Gao, *Nanotechnology*, 2018, **29**, 452001.
82. Y. Lee, M. A. Garcia, N. A. Frey Huls and S. Sun, *Angew. Chem., Int. Ed.*, 2010, **49**, 1271–1274.

83. B. Zuo, W. Li, X. Wu, S. Wang, Q. Deng and M. Huang, *Chem. – Asian J.*, 2020, **15**, 1248–1265.
84. Q. Li, Y. Pan, H. Li, L. Alhalhooly, Y. Li, B. Chen, Y. Choi and Z. Yang, *ACS Appl. Mater. Interfaces*, 2020, **12**, 41794–41801.
85. R. Gupta, M. Yadav, R. Gaur, G. Arora, P. Rana, P. Yadav, A. Adholeya and R. K. Sharma, *ACS Omega*, 2019, **4**, 21529–21539.
86. X. Duan, J. Xu, Z. Wei, J. Ma, S. Guo, S. Wang, H. Liu and S. Dou, *Adv. Mater.*, 2017, **29**, 1701784.
87. J. Kang, L. Zhou, X. Duan, H. Sun and S. Wang, *Catal. Today*, 2020, **357**, 341–349.
88. P. Yang, R. Wang, H. Zhuzhang, M.-M. Titirici and X. Wang, *ACS Catal.*, 2020, **10**, 12706–12715.
89. X. Sun, R. Wang and D. Su, *Chin. J. Catal.*, 2013, **34**, 508–523.
90. Y. Zhai, Z. Zhu and S. Dong, *ChemCatChem*, 2015, **7**, 2806–2815.
91. G. Speranza, *C. J. Carbon Res.*, 2019, **5**, 84.
92. K. Itami and T. Maekawa, *Nano Lett.*, 2020, **20**, 4718–4720.
93. Y. Segawa, H. Ito and K. Itami, *Nat. Rev. Mater.*, 2016, **1**, 1–14.
94. N. Panwar, A. M. Soehartono, K. K. Chan, S. Zeng, G. Xu, J. Qu, P. Coquet, K. T. Yong and X. Chen, *Chem. Rev.*, 2019, **119**, 9559–9656.
95. D. S. Su, G. Wen, S. Wu, F. Peng and R. Schlogl, *Angew. Chem., Int. Ed.*, 2017, **56**, 936–964.
96. X. Lu, D. Wang, K. H. Wu, X. Guo and W. Qi, *J. Colloid Interface Sci.*, 2020, **573**, 376–383.
97. R. Sekiya and T. Haino, *Chem. – Asian J.*, 2020, **15**, 2316–2328.
98. Z. Wu, S. Shen, L. Li, M. Sun and J. Yang, *Catalysts*, 2016, **6**, 111.
99. P. Yan, B. Zhang, K.-H. Wu, D. Su and W. Qi, *Carbon*, 2019, **143**, 915–936.
100. L. H. Zhang, Y. Shi, Y. Wang and N. R. Shiju, *Adv. Sci.*, 2020, **7**, 1902126.
101. C. Testa, A. Zammataro, A. Pappalardo and G. Trusso Sfrazzetto, *RSC Adv.*, 2019, **9**, 27659–27664.
102. L. Tian, Z. Li, P. Wang, X. Zhai, X. Wang and T. Li, *J. Energy Chem.*, 2021, **55**, 279–294.
103. X. T. Zheng, A. Ananthanarayanan, K. Q. Luo and P. Chen, *Small*, 2015, **11**, 1620–1636.
104. R. Das, R. Bandyopadhyay and P. Pramanik, *Mater. Today Chem.*, 2018, **8**, 96–109.
105. K. A. Fernando, S. Sahu, Y. Liu, W. K. Lewis, E. A. Guliants, A. Jafariyan, P. Wang, C. E. Bunker and Y. P. Sun, *ACS Appl. Mater. Interfaces*, 2015, **7**, 8363–8376.
106. V. N. Rao, N. L. Reddy, M. M. Kumari, K. K. Cheralathan, P. Ravi, M. Sathish, B. Neppolian, K. R. Reddy, N. P. Shetti, P. Prathap, T. M. Aminabhavi and M. V. Shankar, *J. Environ. Manage.*, 2019, **248**, 109246.
107. Z. Zhang, G. Yi, P. Li, X. Zhang, H. Fan, Y. Zhang, X. Wang and C. Zhang, *Nanoscale*, 2020, **12**, 13899–13906.

108. H. Li, C. Sun, M. Ali, F. Zhou, X. Zhang and D. R. MacFarlane, *Angew. Chem., Int. Ed.*, 2015, **54**, 8420–8424.
109. P. Zhang, J. S. Wei, X. B. Chen and H. M. Xiong, *J. Colloid Interface Sci.*, 2019, **537**, 716–724.
110. N. F. Goldshleger, *Fullerene Sci. Technol.*, 2001, **9**, 255–280.
111. J. Lopez-Andarias, A. Frontera and S. Matile, *J. Am. Chem. Soc.*, 2017, **139**, 13296–13299.
112. Z. Felfli, K. Suggs, N. Nicholas and A. Z. Msezane, *Int. J. Mol. Sci.*, 2020, **21**, 3159.
113. S. Vidal, J. Marco-Martinez, S. Filippone and N. Martin, *Chem. Commun.*, 2017, **53**, 4842–4844.
114. C. Li, L. Wang, Y. Luo, A. Liang, G. Wen and Z. Jiang, *Nanomaterials*, 2018, **8**, 277.
115. Y. Yan, J. Miao, Z. Yang, F. X. Xiao, H. B. Yang, B. Liu and Y. Yang, *Chem. Soc. Rev.*, 2015, **44**, 3295–3346.
116. Z. Yang, Z. Liu, H. Zhang, B. Yu, Y. Zhao, H. Wang, G. Ji, Y. Chen, X. Liu and Z. Liu, *Chem. Commun.*, 2017, **53**, 929–932.
117. A. B. Bornhof, M. Vazquez-Nakagawa, L. Rodriguez-Perez, M. Angeles Herranz, N. Sakai, N. Martin, S. Matile and J. Lopez-Andarias, *Angew. Chem., Int. Ed.*, 2019, **58**, 16097–16100.
118. Y. Wang, C. Pan, W. Chu, A. K. Vipin and L. Sun, *Nanomaterials*, 2019, **9**, 439.
119. B. Ye, S.-I. Kim, M. Lee, M. Ezazi, H.-D. Kim, G. Kwon and D. H. Lee, *RSC Adv.*, 2020, **10**, 16700–16708.
120. G. Chen, Y. Xu, L. Huang, A. I. Douka and B. Y. Xia, *J. Energy Chem.*, 2021, **55**, 183–189.
121. K. Kisand, A. Sarapuu, D. Danilian, A. Kikas, V. Kisand, M. Rahn, A. Treshchalov, M. Kaarik, M. Merisalu, P. Paiste, J. Aruvali, J. Leis, V. Sammelselg, S. Holdcroft and K. Tammeveski, *J. Colloid Interface Sci.*, 2021, **584**, 263–274.
122. F. Liu, X. Zhang, X. Zhang, L. Wang, M. Liu and J. Zhang, *J. Colloid Interface Sci.*, 2021, **581**, 523–532.
123. K. Gong, F. Du, Z. Xia, M. Durstock and L. Dai, *Science*, 2009, **323**, 760–764.
124. S. Chen, S. Perathoner, C. Ampelli, C. Mebrahtu, D. Su and G. Centi, *Angew. Chem., Int. Ed.*, 2017, **56**, 2699–2703.
125. L. Qu, Y. Liu, J. Baek and L. Dai, *Acs Nano*, 2010, **4**, 1321–1326.
126. X. Tong, Q. Wei, X. Zhan, G. Zhang and S. Sun, *Catalysts*, 2016, **7**, 1.
127. T. Sattar, *Top Curr. Chem.*, 2019, **377**, 10.
128. N. Zhang, J. Wu, T. Yu, J. Lv, H. Liu and X. Xu, *Front. Phys.*, 2021, **16**, 23201.
129. M. Adeel, M. Bilal, T. Rasheed, A. Sharma and H. M. N. Iqbal, *Int. J. Biol. Macromol.*, 2018, **120**, 1430–1440.
130. X. Li, J. Yu, S. Wageh, A. A. Al-Ghamdi and J. Xie, *Small*, 2016, **12**, 6640–6696.

131. F. Limosani, R. Kaur, A. Cataldo, S. Bellucci, F. Micciulla, R. Zaroni, A. Lembo, B. Wang, R. Pizzoferrato, D. M. Guldi and P. Tagliatesta, *Angew. Chem., Int. Ed.*, 2020, **59**, 23706–23715.
132. D. Higgins, P. Zamani, A. Yu and Z. Chen, *Energy Environ. Sci.*, 2016, **9**, 357–390.
133. N. Zhang, Y. Zhang and Y. J. Xu, *Nanoscale*, 2012, **4**, 5792–5813.
134. S. B. Singh and C. M. Hussain, *ChemistrySelect*, 2018, **3**, 9533–9544.
135. Y. Zhou, L. Zhang, W. Huang, Q. Kong, X. Fan, M. Wang and J. Shi, *Carbon*, 2016, **99**, 111–117.
136. C. Wang and D. Astruc, *Prog. Mater. Sci.*, 2018, **94**, 306–383.
137. G. Qi, W. Zhang and Y. Dai, *Res. Chem. Intermed.*, 2013, **41**, 1149–1155.
138. V. N. Mochalin, O. Shenderova, D. Ho and Y. Gogotsi, *Nat. Nanotechnol.*, 2011, **7**, 11–23.
139. X. Duan, W. Tian, H. Zhang, H. Sun, Z. Ao, Z. Shao and S. Wang, *ACS Catal.*, 2019, **9**, 7494–7519.
140. Y. Lin, X. Sun, D. S. Su, G. Centi and S. Perathoner, *Chem. Soc. Rev.*, 2018, **47**, 8438–8473.
141. P. Du, X. X. Zhang, S. Zhang, Y. Zhao, L. Zhang, B. Zhang and B. Yang, *ChemCatChem*, 2020, **13**, 610–616.
142. X. Duan, C. Su, L. Zhou, H. Sun, A. Suvorova, T. Odedairo, Z. Zhu, Z. Shao and S. Wang, *Appl. Catal., B*, 2016, **194**, 7–15.
143. Y. Lin, Z. Feng, L. Yu, Q. Gu, S. Wu and D. S. Su, *Chem. Commun.*, 2017, **53**, 4834–4837.
144. S. A. Shaik, A. Goswami, R. S. Varma and M. B. Gawande, *Curr. Opin. Green Sustain. Chem.*, 2019, **15**, 67–76.
145. M. Chen, L. Wang, H. Yang, S. Zhao, H. Xu and G. Wu, *J. Power Sources*, 2018, **375**, 277–290.
146. X. Duan, Z. Ao, D. Li, H. Sun, L. Zhou, A. Suvorova, M. Saunders, G. Wang and S. Wang, *Carbon*, 2016, **103**, 404–411.
147. Y. Liu, S. Chen, X. Quan and H. Yu, *J. Am. Chem. Soc.*, 2015, **137**, 11631–11636.
148. Y. Liu, Y. Zhang, K. Cheng, X. Quan, X. Fan, Y. Su, S. Chen, H. Zhao, Y. Zhang, H. Yu and M. R. Hoffmann, *Angew. Chem., Int. Ed.*, 2017, **56**, 15607–15611.
149. S. Dutta, K. C. W. Wu and T. Kimura, *Chem. Mater.*, 2015, **27**, 6918–6928.
150. P. Bhanja and A. Bhaumik, *Fuel*, 2016, **185**, 432–441.
151. P. Bhanja and A. Bhaumik, *J. Nanosci. Nanotechnol.*, 2016, **16**, 9050–9062.
152. P. Bhanja, A. Modak and A. Bhaumik, *Chem. – Eur. J.*, 2018, **24**, 7278–7297.
153. Q. Jiang, C. Zhou, H. Meng, Y. Han, X. Shi, C. Zhan and R. Zhang, *J. Mater. Chem. A*, 2020, **8**, 15271–15301.
154. Y. S. Wei, M. Zhang, R. Zou and Q. Xu, *Chem. Rev.*, 2020, **120**, 12089–12174.



155. P. Verma, Y. Kuwahara, K. Mori, R. Raja and H. Yamashita, *Nanoscale*, 2020, **12**, 11333–11363.
156. C. Fang, L. Liu, J. Weng, S. Zhang, X. Zhang, Z. Ren, Y. Shen, F. Meng, B. Zheng, S. Li, J. Wu, W. Shi, S. Lee, W. Zhang and F. Huo, *Angew. Chem., Int. Ed.*, 2021, **60**, 976–982.
157. J. Wei, L. Zou, Y. Li and X. Zhang, *New J. Chem.*, 2019, **43**, 5833–5838.
158. B. Singh, J. Na, M. Konarova, T. Wakihara, Y. Yamauchi, C. Salomon and M. B. Gawande, *Bull. Chem. Soc. Jpn.*, 2020, **93**, 1459–1496.
159. J. Liang, Z. Liang, R. Zou and Y. Zhao, *Adv. Mater.*, 2017, **29**, 1701139.
160. Q. Zhang, Q. Wang and S. Wang, *Chem. Phys. Lett.*, 2020, **753**, 137598.
161. K. Li, J. Valla and J. Garcia-Martinez, *ChemCatChem*, 2014, **6**, 46–66.
162. K. Na and G. A. Somorjai, *Catal. Lett.*, 2014, **145**, 193–213.
163. B. M. Weckhuysen and J. Yu, *Chem. Soc. Rev.*, 2015, **44**, 7022–7024.
164. Y. Chai, W. Shang, W. Li, G. Wu, W. Dai, N. Guan and L. Li, *Adv. Sci.*, 2019, **6**, 1900299.
165. H. Dai, Y. Shen, T. Yang, C. Lee, D. Fu, A. Agarwal, T. T. Le, M. Tsapatsis, J. C. Palmer, B. M. Weckhuysen, P. J. Dauenhauer, X. Zou and J. D. Rimer, *Nat. Mater.*, 2020, **19**, 1074–1080.
166. W. Dai, C. Wang, B. Tang, G. Wu, N. Guan, Z. Xie, M. Hunger and L. Li, *ACS Catal.*, 2016, **6**, 2955–2964.
167. E. Catizzzone, A. Aloise, E. Giglio, G. Ferrarelli, M. Bianco, M. Migliori and G. Giordano, *Catal. Commun.*, 2021, **149**, 106214.
168. G. Feng, Z.-H. Wen, J. Wang, Z.-H. Lu, J. Zhou and R. Zhang, *Microporous Mesoporous Mater.*, 2021, **312**, 110810.
169. Y. Yan, X. Guo, Y. Zhang and Y. Tang, *Catal. Sci. Technol.*, 2015, **5**, 772–785.
170. S. Abate, K. Barbera, G. Centi, P. Lanzafame and S. Perathoner, *Catal. Sci. Technol.*, 2016, **6**, 2485–2501.
171. A. D. Chowdhury and J. Gascon, *Angew. Chem., Int. Ed.*, 2018, **57**, 14982–14985.
172. A. Martin, *Catalysts*, 2016, **6**, 118.
173. J.-Y. Kim, J. Moon, J. H. Lee, X. Jin and J. W. Choi, *Fuel*, 2020, **279**, 118484.
174. J. Kowalska-Kuś, A. Held and K. Nowińska, *Chem. Eng. J.*, 2020, **401**, 126143.
175. G. Martínez-Edo, A. Balmori, I. Pontón, A. Martí del Rio and D. Sánchez-García, *Catalysts*, 2018, **8**, 617.
176. T. Cheng, Q. Zhao, D. Zhang and G. Liu, *Green Chem.*, 2015, **17**, 2100–2122.
177. X. Fang, X. Zhao, W. Fang, C. Chen and N. Zheng, *Nanoscale*, 2013, **5**, 2205–2218.
178. A. Maity and V. Polshettiwar, *ChemSusChem*, 2017, **10**, 3866–3913.
179. L. Fu, S. Li, Z. Han, H. Liu and H. yang, *Chem. Commun.*, 2014, **50**, 10045–10048.
180. B. Sun, G. Zhou and H. Zhang, *Prog. Solid State Chem.*, 2016, **44**, 1–19.

181. N. Sharma, H. Ojha, A. Bharadwaj, D. P. Pathak and R. K. Sharma, *RSC Adv.*, 2015, **5**, 53381–53403.
182. Z. Nasresfahani and M. Z. Kassaei, *Catal. Commun.*, 2015, **60**, 100–104.
183. J. Li, L.-S. Li and L. Xu, *Mater. Lett.*, 2017, **193**, 67–69.
184. K. Motokura, M. Ikeda, M. Nambo, W.-J. Chun, K. Nakajima and S. Tanaka, *ChemCatChem*, 2017, **9**, 2924–2929.
185. R. Jin, D. Zheng, R. Liu and G. Liu, *ChemCatChem*, 2018, **10**, 1739–1752.
186. J. Špačková, E. Svobodová, T. Hartman, I. Stibor, J. Kopecká, J. Cibulková, J. Chudoba and R. Cibulka, *ChemCatChem*, 2017, **9**, 1177–1181.
187. M. Davidson, Y. Ji, G. J. Leong, N. C. Kovach, B. G. Trewyn and R. M. Richards, *ACS Appl. Nano Mater.*, 2018, **1**, 4386–4400.
188. M. Eslami, M. G. Dekamin, L. Motlagh and A. Maleki, *Green Chem. Lett. Rev.*, 2018, **11**, 36–46.
189. J. Ying, C. Janiak, Y. X. Xiao, H. Wei, X. Y. Yang and B. L. Su, *Chem. – Asian J.*, 2018, **13**, 31–34.
190. X. Sun, D. Xu, P. Dai, X. Liu, F. Tan and Q. Guo, *Chem. Eng. J.*, 2020, **402**, 125881.
191. D. T. Bregante, J. Z. Tan, R. L. Schultz, E. Z. Ayla, D. S. Potts, C. Torres and D. W. Flaherty, *ACS Catal.*, 2020, **10**, 10169–10184.
192. J. Liu, L. Chen, H. Cui, J. Zhang, L. Zhang and C. Y. Su, *Chem. Soc. Rev.*, 2014, **43**, 6011–6061.
193. Y. V. Kaneti, J. Tang, R. R. Salunkhe, X. Jiang, A. Yu, K. C. Wu and Y. Yamauchi, *Adv. Mater.*, 2017, **29**, 1604898.
194. Y. Qin, X. Han, Y. Li, A. Han, W. Liu, H. Xu and J. Liu, *ACS Catal.*, 2020, **10**, 5973–5978.
195. H. D. Mai, K. Rafiq and H. Yoo, *Chem. – Eur. J.*, 2017, **23**, 5631–5651.
196. C. Wang, B. An and W. Lin, *ACS Catal.*, 2018, **9**, 130–146.
197. L. Wang, S. R. Li, Y. Z. Chen and H. L. Jiang, *Small*, 2021, 2004481.
198. A. Majedi, F. Davar and A. R. Abbasi, *Int. J. Nano Dimens*, 2016, **7**, 1–14.
199. Q. Wang and D. Astruc, *Chem. Rev.*, 2020, **120**, 1438–1511.
200. Y.-Z. Chen, R. Zhang, L. Jiao and H.-L. Jiang, *Coord. Chem. Rev.*, 2018, **362**, 1–23.
201. M. J. Kalmutzki, C. S. Diercks and O. M. Yaghi, *Adv. Mater.*, 2018, **30**, e1704304.
202. Y.-Z. Chen, Y.-X. Zhou, H. Wang, J. Lu, T. Uchida, Q. Xu, S.-H. Yu and H.-L. Jiang, *ACS Catal.*, 2015, **5**, 2062–2069.
203. K. M. Choi, D. Kim, B. Rungtaweeworant, C. A. Trickett, J. T. Barmanbek, A. S. Alshammari, P. Yang and O. M. Yaghi, *J. Am. Chem. Soc.*, 2017, **139**, 356–362.
204. D. Ma, Y. Wang, A. Liu, S. Li, C. Lu and C. Chen, *Catalysts*, 2018, **8**, 404.
205. Y. Meng, Y. Luo, J. L. Shi, H. Ding, X. Lang, W. Chen, A. Zheng, J. Sun and C. Wang, *Angew. Chem., Int. Ed.*, 2020, **59**, 3624–3629.
206. R. S. B. Gonçalves, A. B. V. deOliveira, H. C. Sindra, B. S. Archanjo, M. E. Mendoza, L. S. A. Carneiro, C. D. Buarque and P. M. Esteves, *ChemCatChem*, 2016, **8**, 743–750.

207. Q. Sun, B. Aguila and S. Ma, *Mater. Chem. Front.*, 2017, **1**, 1310–1316.
208. H. Li, X. Feng, P. Shao, J. Chen, C. Li, S. Jayakumar and Q. Yang, *J. Mater. Chem. A*, 2019, **7**, 5482–5492.
209. S. Y. Ding and W. Wang, *Chem. Soc. Rev.*, 2013, **42**, 548–568.
210. G. Lin, H. Ding, D. Yuan, B. Wang and C. Wang, *J. Am. Chem. Soc.*, 2016, **138**, 3302–3305.
211. G. Lin, H. Ding, R. Chen, Z. Peng, B. Wang and C. Wang, *J. Am. Chem. Soc.*, 2017, **139**, 8705–8709.
212. Y. X. Ma, Z. J. Li, L. Wei, S. Y. Ding, Y. B. Zhang and W. Wang, *J. Am. Chem. Soc.*, 2017, **139**, 4995–4998.
213. I. Romero-Muniz, A. Mavrandonakis, P. Albacete, A. Vega, V. Briois, F. Zamora and A. E. Platero-Prats, *Angew. Chem., Int. Ed.*, 2020, **59**, 13013–13020.
214. Y. Shi, X. Zhang, H. Liu, J. Han, Z. Yang, L. Gu and Z. Tang, *Small*, 2020, **16**, e2001998.
215. S. Lin, C. S. Diercks, Y.-B. Zhang, N. Kornienko, E. M. Nichols, Y. Zhao, A. R. Paris, D. Kim, P. Yang, O. M. Yaghi and C. J. Chang, *Science*, 2015, **349**, 1208–1213.
216. X. Wang, W.-H. Zhu, L. Chen, S. Y. Chong, M. A. Little, Y. Wu, R. Clowes, Y. Yan and A. I. Cooper, *Nat. Chem.*, 2018, **10**, 1180–1189.
217. C. Xu, P. Ravi Anusuyadevi, C. Aymonier, R. Luque and S. Marre, *Chem. Soc. Rev.*, 2019, **48**, 3868–3902.
218. X. Meng, L. Liu, S. Ouyang, H. Xu, D. Wang, N. Zhao and J. Ye, *Adv. Mater.*, 2016, **28**, 6781–6803.
219. B. Ohtani, *Front. Chem.*, 2017, **5**, 79.
220. A. Fujishima and K. Honda, *Nature*, 1972, **238**, 37–38.
221. T. Hisatomi, J. Kubota and K. Domen, *Chem. Soc. Rev.*, 2014, **43**, 7520–7535.
222. A. Gelle, T. Jin, L. de la Garza, G. D. Price, L. V. Besteiro and A. Moores, *Chem. Rev.*, 2020, **120**, 986–1041.
223. P. V. Kamat and S. Jin, *ACS Energy Lett.*, 2018, **3**, 622–623.
224. X. Wang, K. Faungnawakij and M. Chareonpanich, *ChemCatChem*, 2019, **11**, 5838–5841.
225. Q. Guo, C. Zhou, Z. Ma and X. Yang, *Adv. Mater.*, 2019, **31**, e1901997.
226. S. Kohtani, A. Kawashima and H. Miyabe, *Front. Chem.*, 2019, **7**, 630.
227. B. Liu, H. Wu and I. P. Parkin, *ACS Omega*, 2020, **5**, 14847–14856.
228. Y. Zhao, Y. Zhao, R. Shi, B. Wang, G. I. N. Waterhouse, L. Z. Wu, C. H. Tung and T. Zhang, *Adv. Mater.*, 2019, **31**, e1806482.
229. S. Muthulingam, I. H. Lee and P. Uthirakumar, *J. Colloid Interface Sci.*, 2015, **455**, 101–109.
230. B. C. Martindale, G. A. Hutton, C. A. Caputo and E. Reisner, *J. Am. Chem. Soc.*, 2015, **137**, 6018–6025.
231. D. Rodríguez-Padrón, A. R. Puente-Santiago, A. M. Balu, M. J. Muñoz-Batista and R. Luque, *ChemCatChem*, 2018, **11**, 18–38.
232. S. Zhu, S.-H. Ho, C. Jin, X. Duan and S. Wang, *Environ. Sci. Nano*, 2020, **7**, 368–396.

233. X. Duan, H. Sun, Z. Shao and S. Wang, *Appl. Catal., B*, 2018, **224**, 973–982.
234. M. A. Oturan and J.-J. Aaron, *Crit. Rev. Environ. Sci. Technol.*, 2014, **44**, 2577–2641.
235. V. Poza-Nogueiras, E. Rosales, M. Pazos and M. A. Sanroman, *Chemosphere*, 2018, **201**, 399–416.
236. A. K. Mishra, K. V. Lakshmi and L. Huang, *Sci Rep*, 2015, **5**, 15718.
237. S.-M. Hao, J. Qu, Z.-S. Zhu, X.-Y. Zhang, Q.-Q. Wang and Z.-Z. Yu, *Adv. Funct. Mater.*, 2016, **26**, 7334–7342.
238. X. Liu, Y. Wu, R. He, H. L. Jiang and C. Wang, *Environ. Technol.*, 2018, **39**, 1697–1704.
239. A. Tamadoni and F. Qaderi, *Ozone: Sci. Eng.*, 2019, **41**, 454–472.
240. X. Chen, J. Chen, X. Qiao, D. Wang and X. Cai, *Appl. Catal., B*, 2008, **80**, 116–121.
241. Z. Zhou, X. Liu, K. Sun, C. Lin, J. Ma, M. He and W. Ouyang, *Chem. Eng. J.*, 2019, **372**, 836–851.
242. D. Zhi, Y. Lin, L. Jiang, Y. Zhou, A. Huang, J. Yang and L. Luo, *J. Environ. Manage.*, 2020, **260**, 110125.
243. M. J. Climent, A. Corma and S. Iborra, *Green Chem.*, 2014, **16**, 516–547.
244. W. J. Ong, L. L. Tan, Y. H. Ng, S. T. Yong and S. P. Chai, *Chem. Rev.*, 2016, **116**, 7159–7329.
245. Y. An, Y. Zhao, F. Yu, T. Lin, Y. Lu, S. Li, Z. Li, Y. Dai, X. Wang, H. Wang, L. Zhong and Y. Sun, *J. Catal.*, 2018, **366**, 289–299.
246. A. P. Ingle, A. K. Chandel, R. Philippini, S. E. Martiniano and S. S. da Silva, *Symmetry*, 2020, **12**, 256.
247. B. Thangaraj, P. R. Solomon, B. Muniyandi, S. Ranganathan and L. Lin, *Clean Energy*, 2019, **3**, 2–23.
248. G. Baskar and R. Aiswarya, *Renewable Sustainable Energy Rev.*, 2016, **57**, 496–504.
249. A. Mudhoo, P. C. Torres-Mayanga, T. Forster-Carneiro, P. Sivagurunathan, G. Kumar, D. Komilis and A. Sanchez, *J. Waste Manage*, 2018, **79**, 580–594.
250. A. Ghalandari, M. Taghizadeh and M. Rahmani, *Chem. Eng. Technol.*, 2019, **42**, 89–99.
251. M. Prabu, M. Manikandan, P. Kandasamy, P. R. Kalaivani, N. Rajendiran and T. Raja, *ACS Omega*, 2019, **4**, 3500–3507.
252. D. Zhao, Z. Zhuang, X. Cao, C. Zhang, Q. Peng, C. Chen and Y. Li, *Chem. Soc. Rev.*, 2020, **49**, 2215–2264.
253. C. V. Reddy, K. R. Reddy, N. P. Shetti, J. Shim, T. M. Aminabhavi and D. D. Dionysiou, *Int. J. Hydrogen Energy*, 2020, **45**, 18331–18347.
254. Z. Abdin, A. Zafaranloo, A. Rafiee, W. Mérida, W. Lipiński and K. R. Khalilpour, *Renewable Sustainable Energy Rev.*, 2020, **120**, 109620.
255. B. J. Ng, L. K. Putri, X. Y. Kong, Y. W. Teh, P. Pasbakhsh and S. P. Chai, *Adv. Sci.*, 2020, **7**, 1903171.
256. Q. Wang and K. Domen, *Chem. Rev.*, 2020, **120**, 919–985.

257. L. Ju, J. Shang, X. Tang and L. Kou, *J. Am. Chem. Soc.*, 2020, **142**, 1492–1500.
258. S. Li, L. Li, Y. Li, L. Dai, C. Liu, Y. Liu, J. Li, J. Lv, P. Li and B. Wang, *ACS Catal.*, 2020, **10**, 8717–8726.
259. N. Luo, T. Montini, J. Zhang, P. Fornasiero, E. Fonda, T. Hou, W. Nie, J. Lu, J. Liu, M. Heggen, L. Lin, C. Ma, M. Wang, F. Fan, S. Jin and F. Wang, *Nat. Energy*, 2019, **4**, 575–584.
260. R. S. Varma, *ACS Sustainable Chem. Eng.*, 2019, **7**, 6458–6470.
261. Z. Zhang, M. Sadakane, N. Hiyoshi, A. Yoshida, M. Hara and W. Ueda, *Angew. Chem., Int. Ed.*, 2016, **55**, 10234–10238.
262. A. D. Lalsare, B. Leonard, B. Robinson, A. C. Sivri, R. Vukmanovich, C. Dumitrescu, W. Rogers and J. Hu, *Appl. Catal., B*, 2021, **282**, 119537.
263. C. G. S. Lima, E. Y. C. Jorge, L. G. S. Batinga, T. d. M. Lima and M. W. Paixão, *Curr. Opin. Green Sustainable Chem.*, 2019, **15**, 13–19.
264. N. Cherkasov, A. O. Ibhadon and P. Fitzpatrick, *Chem. Eng. Process*, 2015, **90**, 24–33.
265. S. Wang, F. Ichihara, H. Pang, H. Chen and J. Ye, *Adv. Funct. Mater.*, 2018, **28**, 1803309.
266. R. Shi, X. Zhang, G. I. N. Waterhouse, Y. Zhao and T. Zhang, *Adv. Energy Mater.*, 2020, **10**, 2000659.
267. S. Licht, B. Cui, B. Wang, F.-F. Li, J. Lau and S. Liu, *Science*, 2013, **345**, 637–640.
268. Y. Gong, J. Wu, M. Kitano, J. Wang, T.-N. Ye, J. Li, Y. Kobayashi, K. Kishida, H. Abe, Y. Niwa, H. Yang, T. Tada and H. Hosono, *Nat. Catal.*, 2018, **1**, 178–185.
269. S. Zhang, Q. Fan, R. Xia and T. J. Meyer, *Acc. Chem. Res.*, 2020, **53**, 255–264.
270. L. Wang, W. Chen, D. Zhang, Y. Du, R. Amal, S. Qiao, J. Wu and Z. Yin, *Chem. Soc. Rev.*, 2019, **48**, 5310–5349.
271. R. Guil-Lopez, N. Mota, J. Llorente, E. Millan, B. Pawelec, J. L. G. Fierro and R. M. Navarro, *Materials*, 2019, **12**, 3902.
272. Z. Weng, Y. Wu, M. Wang, J. Jiang, K. Yang, S. Huo, X. F. Wang, Q. Ma, G. W. Brudvig, V. S. Batista, Y. Liang, Z. Feng and H. Wang, *Nat. Commun.*, 2018, **9**, 415.
273. X. Cui, J. Wang, B. Liu, S. Ling, R. Long and Y. Xiong, *J. Am. Chem. Soc.*, 2018, **140**, 16514–16520.

CHAPTER 9

# *Bio-refining Through Nanotechnology*

FENG LIU, YI REN, MING HUI CHUA AND HUI ZHOU\*

Institute of Materials Research and Engineering, Agency for Science, Technology and Research (A\*STAR), 2 Fusionopolis Way, Innovis, #08-03, Singapore 138634, Singapore

\*Email: zhouh@imre.a-star.edu.sg

## 9.1 Introduction

The 2012 revision of the official United Nations population estimated that the global population would have increased from 7.2 billion (2013) to 8.1 billion by 2025.<sup>1</sup> The continuously increasing consumption of resources would not be sustained by fossil sources alone, because of their limited storage and devastating effects on Earth's environment. The CO<sub>2</sub> mainly generated from fossil fuels is regarded as a greenhouse gas for global warming.<sup>2</sup> The Keeling Curve, which was started in the 1950s for the accurate recording of CO<sub>2</sub> concentration, showed that the concentration of CO<sub>2</sub> gas was 400 ppm in 2013, which possibly increases global warming by 2 °C.<sup>3</sup> Thus, the growing energy and environmental protection needs have pushed the fundamental change of fossil fuels in the global energy pattern. To target this issue, renewable technology for sustainable energy and materials plays an irreplaceable role in academic, industrial and policy developments.<sup>4</sup> The replacement of fossil fuel with biomass is regarded as carbon neutral, in which the produced CO<sub>2</sub> output could be effectively neutralized by CO<sub>2</sub> fixation *via* the photosynthesis of plants. Biomass contributes almost 10% of the primary energy supply in the world and is the fourth largest

---

Nanoscience & Nanotechnology Series No. 57

Sustainable Nanotechnology

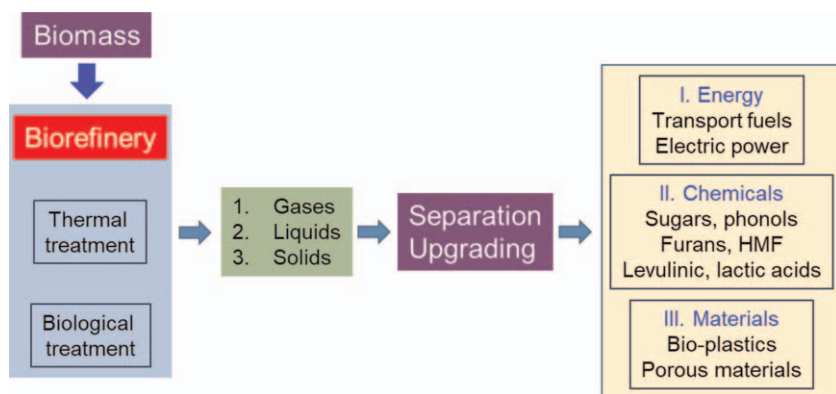
Edited by Zibiao Li, Jie Zheng and Enyi Ye

© The Royal Society of Chemistry 2022

Published by the Royal Society of Chemistry, www.rsc.org

energy source globally, following fuel oil, coal and natural gas. The global primary energy supply from biomass had reached an approximate 55 EJ in 2012.<sup>5</sup> In order to reduce the emission of CO<sub>2</sub>, a White Paper published by the European Commission in 1997 required all EU member states to use more bio-renewables to produce 20% of all energy by 2020.<sup>6,7</sup>

The use of biomass for energy sources and chemical materials has existed for several centuries. However, research dedicated to renewable resources has been taking place only over the last two decades.<sup>8</sup> Industry has been developing “bio-refinery technology”, which shows similar functions to modern petroleum refineries, *e.g.* conversion of raw materials (biomass or bio-derived feedstock) into energy, chemicals and materials (Figure 9.1).<sup>9</sup> The output of these methods after processing the waste feedstock would be majorly classified into two types: (1) low-value, high-volume products, *e.g.* fuels, and (2) high-value, low-volume chemicals, *e.g.* waxes and glycerol. Among them, high-value, low-volume chemicals are widely used as starting compounds for the materials and pharmaceutical industries.<sup>10,11</sup> Bio-refineries also conduct various processes, including extraction, biological treatment and thermal treatment, with the purposes of retaining the flexibility to process different types of biomass feedstocks.<sup>12–14</sup> The first-generation bio-refining mainly produced liquid fuels from industrially available energy crops and food crops,<sup>15,16</sup> introducing huge pressure to agriculture and the food supply chain.<sup>17</sup> In order to solve this issue, second-generation bio-refineries had been improved to process non-food biomass, *e.g.* lignocellulosic materials, waste food and waste biomass. However, the conversion of non-food biomass, *e.g.* non-food lignocellulosic biomaterials, to valuable materials in a continuous way is very challenging, due to their complex structure with inserted components like crystalline cellulose.<sup>18</sup> In addition, the current processing technologies of the second-generation bio-refineries are not cheap enough for large-scale industrial applications. Therefore, the development of new technologies is urgently required to overcome significant scientific and engineering challenges.<sup>19</sup> In other



**Figure 9.1** Illustration of the bio-refinery concept.

words, when compared with the first-generation bio-refineries, the second-generation bio-refineries can process more different types of raw biomass, *e.g.* forestry, non-food lignocellulosic biomass, agricultural wastes and food wastes.<sup>20–22</sup> Moreover, the second-generation bio-refineries can convert hemicellulose and cellulose to fermentable sugars,<sup>23–25</sup> which can be conveniently converted to alcohols.

The biological treatment is an energy-efficient process despite being time consuming and producing lignin as waste. The thermal treatment uses heat to break down the raw materials in order to produce various chemicals and fuels.<sup>26,27</sup> However, the thermal treatment has several drawbacks, *e.g.* huge energy requirements, high capital input and high operational costs. Currently, products based on pyrolysis also face difficulties in fuel applications due to their strong acidity and high water and alkali metal contents.<sup>27</sup> Nonetheless, when compared to the biological treatment, the thermal treatment shows a significant advantage of less restriction on the type of feedstock, although its selectivity is poor in producing final products.<sup>28–30</sup> An ideal treatment would be to combine the two different strategies into one continuous process with low temperature requirements, in which both the product types and their individual yields would be optimized. To achieve this, it is necessary to involve heterogeneous catalysts in the process. Previous research has demonstrated that nanoparticles can be used as efficient catalysts for the treatment of biomass, leading to treatments with better performance.<sup>31,32</sup>

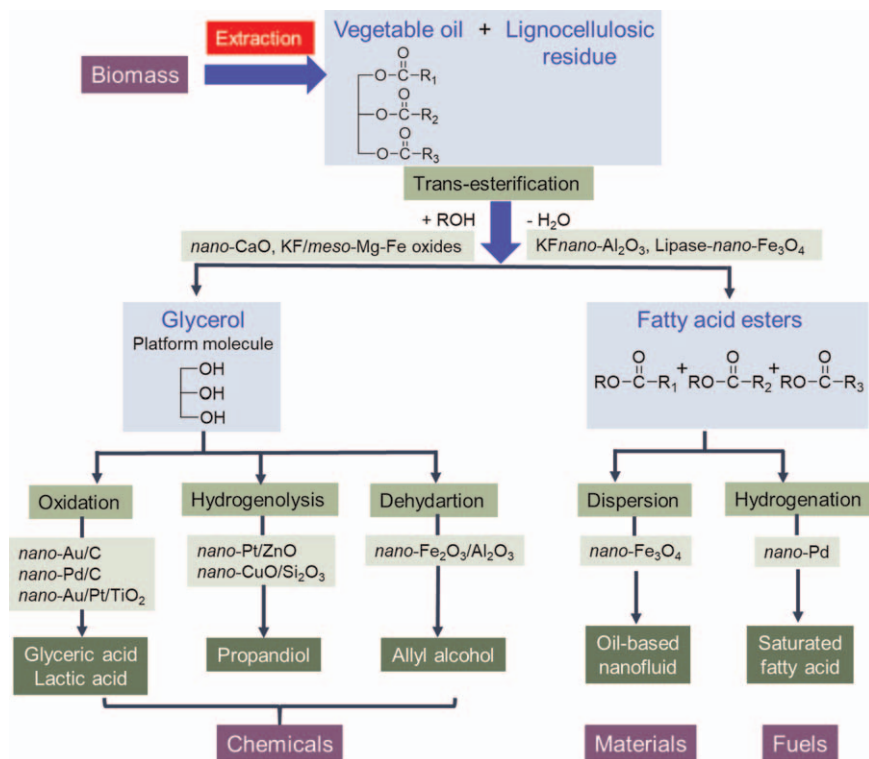
Here, we will mainly focus on the latest developments in nanoparticles as heterogeneous catalysts in the bio-refining process and their advantages, including yield, catalysts lifetime and selectivity. The chapter will also present the concept of employing plant-synthesized nanoparticles for catalyzed bio-refinery, which has great potential in generating a greener and more sustainable bio-refinery process.

## 9.2 First Generation Bio-refineries Based on Nano-catalysts

### 9.2.1 Biodiesel Production

Because of triglycerides' relatively high molecular weight, the resulting low volatility and high viscosity limit their direct use in diesel engines. As shown in Figure 9.2, these problems would be partially resolved through the catalyzed transesterification of triglycerides to fatty acid methyl esters (FAMES) with short-chain alcohols, *e.g.* methanol. Several environmentally safe biofuels have been produced with reduced viscosity.<sup>33</sup> Base catalysts, *e.g.* hydroxides and alkoxides of sodium and potassium, are preferred for industrial application.<sup>34</sup> However, the significant amount of free fatty acids (FFAs) existing in triglyceride sources will neutralize some of the base catalysts, leading to an increased need for more of the base catalyst and more methanol to generate high-quality bio-diesel.<sup>35</sup> Thus, a

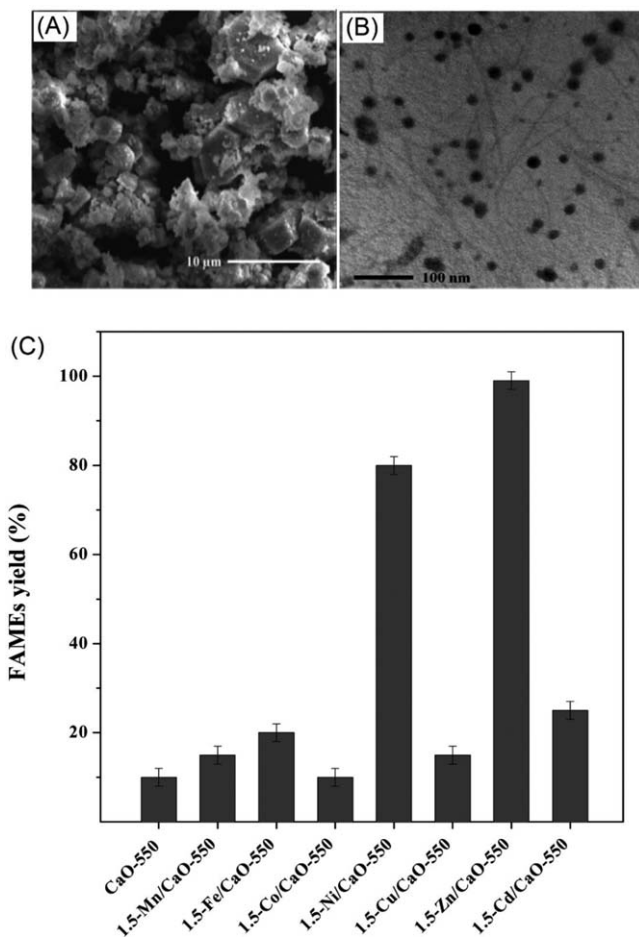




**Figure 9.2** Examples of nano-catalysts used in the production of biodiesel.

pre-esterification of raw feedstock by acid catalysts is always necessitated.<sup>36</sup> In addition, a single acid catalyst for these two transformations is also applicable. Acid catalysts show less activity in the transesterification step than base catalysts. The heterogeneous catalysts in solid state not only display better performance as substitutes for both acid and base catalysts but also exhibit more advantages for green and simple downstream processing.<sup>37,38</sup> Various types of catalysts and methods have been reported, *e.g.* alkali metal oxides and hydrocarbonates, but their industrial applications are rarely reported.

Nanotechnology may provide some new route for further development in the bio-refinery area. For example, CaO in nano-crystalline states could produce biodiesel from triglyceride with 99% conversion. In contrast, common CaO is hardly active in the conversion of triglyceride to biodiesel (Figure 9.3).<sup>39</sup> This type of nano-catalyst also shows good stability and could retain activity after five catalytic cycles. The activity of a CaO nano-catalyst would be partially deactivated by trace organic impurities and/or enolation *via*  $\alpha$ -carbon deprotonation of the carboxyl group in the triglyceride or FAMES. Nano-sized  $\gamma$ -Al<sub>2</sub>O<sub>3</sub> incorporated with KF (15 wt%) shows good activity to give methyl ester with yields of 97.7%, due to the integration of the



**Figure 9.3** (A) Scanning electron microscope (SEM) image and (B) Transmission electron microscopy (TEM) image of 1.5-Zn/CaO-550. (C) The catalytic activity of catalysts loaded with different transition metal ions.<sup>39</sup> Adapted from ref. 39 with permission from American Chemical Society, Copyright 2013.

catalyst's highly basic surface ( $1.68 \text{ mmol g}^{-1}$ ) and  $\gamma\text{-Al}_2\text{O}_3$  nanoparticle's high surface/volume ratio.<sup>40</sup> A similar efficiency would be achieved by introducing KF onto the mesoporous surface of Mg-Fe or Ca-Al bi-metal oxides.<sup>41,42</sup> In addition, enzyme catalysts are successfully used for the transesterification of vegetable oil.<sup>43,44</sup> The transesterification reaction would be catalyzed under very mild conditions by immobilizing enzymes on nanoparticles. For example, by grafting lipase onto the surface of magnetic  $\text{Fe}_3\text{O}_4$  nanoparticles *via* a 1-ethyl-3-(3-dimethylaminopropyl)carbodiimide linkage, the resulting lipase-grafted nanoparticles show a yield of 94% in the methyl ester reaction, indicating similar catalytic activity to the original lipase.<sup>45</sup> Lipase would be

immobilized on the superparamagnetic nanoparticles, which also display high catalytic activity in the methyl ester reaction.<sup>46</sup>

Soybean oil is one of the most widely used raw materials to produce biodiesel in Brazil and the United States. The huge amounts of unsaturated fatty acids in soybean oil are easily affected by auto-oxidative degradation. Thus, many scientists have aimed to improve the anti-oxidation of biodiesel derived from soybean oil, *e.g.* through the hydrogenation of soybean oil. In order to control the fluidity and produce high-quality biodiesel, the unsaturated fatty acids in soybean oil are usually hydrogenated to monosaturated compounds. Recently, the palladium (Pd) nanoparticles formed in ionic liquids have shown high efficiency in selective hydrogenating methyl ester groups in soybean oil. The catalyst can keep its catalytic activity after three cycles.<sup>47</sup> Pd/C displays good catalytic activity for converting saturated fatty acids to saturated hydrocarbons.<sup>48,49</sup> Interestingly, the bio-oil could be used as a medium to prepare and disperse nanoparticles. Li *et al.* report a green method in which Fe<sub>3</sub>O<sub>4</sub> nanoparticles would be well dispersed in vegetable oil to prepare high-quality nano-fluids.<sup>50</sup>

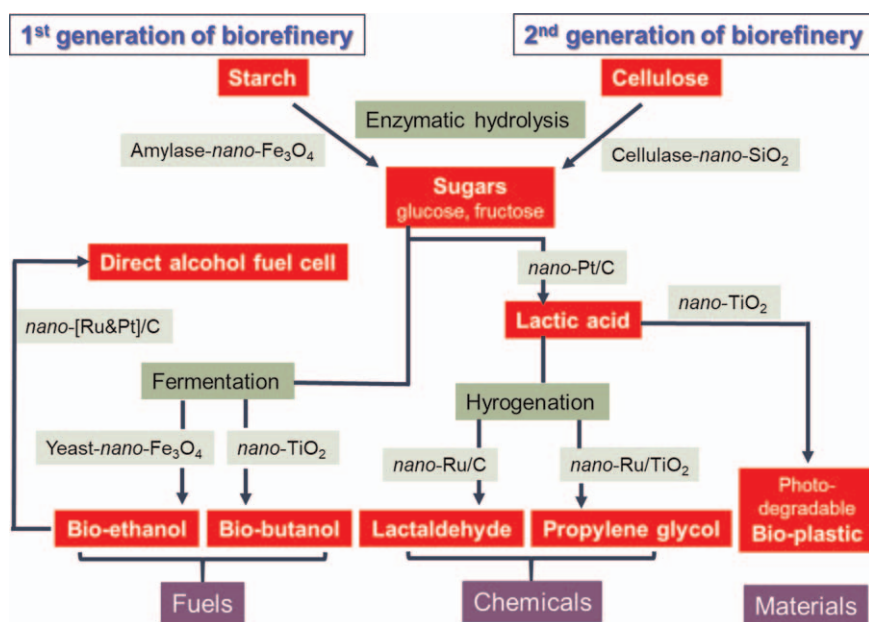
### 9.2.2 High-value Chemicals from Glycerol

Glycerol is one of the major side products of the biodiesel industry. The supply of glycerol as a sustainable raw material is growing steadily because of the increasing need for greener biodiesel. The three hydroxyl groups in glycerol make it versatile and highly reactive, which makes glycerol a good and abundant source for the microbiology industry.<sup>51,52</sup> However, there are only a few efficient catalysts developed for glycerol application, in which some nano-catalysts have displayed high potential (Figure 9.2). The glycerol could be selectively converted to glyceric acid (GLYA) under the catalysts of Pd and Pt nanoparticles.<sup>53–55</sup> In the abovementioned examples, the activity of the catalyst is significantly affected by the nanoparticles' size. The selectivity to GLYA production of those metallic nanoparticles can be further enhanced by loading them on graphite or activated carbon.<sup>53,56</sup> For instance, when 1 wt% Au/graphite is applied, the glycerol can be converted to GYLA in 54% conversion yield with 100% selectivity.<sup>57</sup> Lactic acid is another key product from glycerol conversion (Figure 9.2), which would be further converted to high-value compounds, *e.g.* lactaldehyde (LAL), propylene glycol (PG) and polylactic acid (PLA).<sup>58</sup> An important method to convert glycerol to lactic acid was obtained under O<sub>2</sub> (1 atm) at 90 °C through a catalyst system, which combined an Au–Pt/TiO<sub>2</sub> catalyst with NaOH.<sup>58</sup> A similar performance would be achieved by utilizing Rh/ZnO and Pt/ZnO in quantitatively oxidizing glycerol to 1,2-propanediol (PG) and lactic acid with a ratio of 30% to 70%.<sup>59</sup> In contrast, a higher selectivity of 99% to PG from glycerol would be obtained through using highly dispersed silica-supported copper nanoparticles, but the conversion yield is still as low as 19% and is required to be improved.<sup>60</sup> Moreover, glycerol would be converted to allyl alcohol *via* dehydration and continue hydrogen transfer by using iron oxides as catalysts,

demonstrating the potential by employing low-cost metals catalysts to convert biomass to high-value chemicals without using expensive Pd- and Pt-related catalysts.<sup>61</sup>

### 9.2.3 Conversion of Starch-rich Biomass to Bio-ethanol

Currently, bio-ethanol is one of the most widely used sustainable fuels for transportation. Bio-ethanol is generally produced *via* the enzymatic fermentation of glucose, which is commonly generated through the starch hydrolysis of crops (Figure 9.4). By 2014, the global annual sales of amylolytic enzymes for fermentation had increased to US\$225 million.<sup>62</sup> In addition, lactic acid and biobutanol are another two important compounds that would be produced from sugar fermentation, in which bio-butanol is an alternative fuel product<sup>63</sup> and lactic acid is a monomer material for bio-plastics manufacturing (Figure 9.4).<sup>64</sup> As widely applied in biodiesel production, the enzyme's immobilization onto the nanoparticle surface is a common methodology for the catalytic reactions due to straightforward processes such as catalyst recovery and reaction system clean-up. Taking  $\alpha$ -amylases as an example, immobilization is most widely used in the industrial route. By immobilizing  $\alpha$ -amylase on magnetic nanoparticles ( $\text{Fe}_3\text{O}_4$  or  $\text{Fe}_2\text{O}_3$ ), the resulting catalysts can be efficiently recovered due to their magnetic properties.<sup>65-67</sup> Moreover, the related catalysts display 83% catalytic activity after eight consecutive cycles, when compared with freshly prepared catalysts.



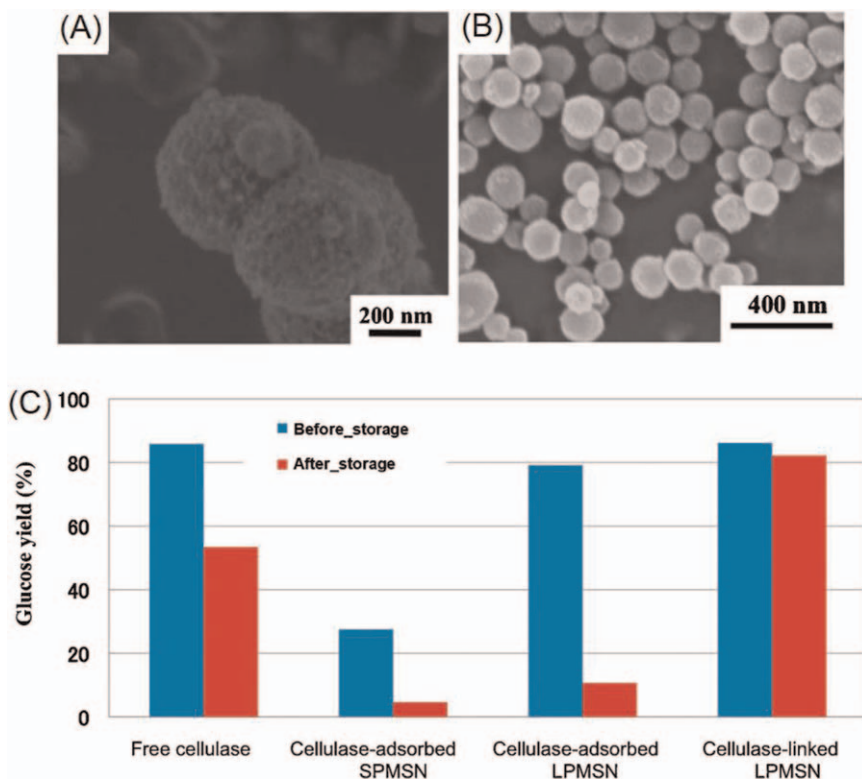
**Figure 9.4** Nanoparticles as catalysts in the conversion of polysaccharides to fuels, chemicals and materials.

## 9.3 Second Generation Bio-refineries Based on Nano-catalysts

### 9.3.1 Bio-ethanol Derived From Lignocellulosic Biomass

Cellulose is a bio-polymer derived from the condensation of D-glucose units, which are connected *via*  $\beta$ -1,4-glycosidic linkers. In addition, the van der Waals forces and molecular hydrogen bonds within the cellulose strands generate a stable structure with a crystalline fibrous morphology, leading to a strong tensile strength.<sup>68</sup> The hydrolysis of cellulose has displayed high potential in converting biomass to valuable compounds.<sup>69</sup> However, cellulose hydrolysis would be affected by various environmental factors, *e.g.* temperature, leading to several issues for their industrial applications. The use of solid-supported catalysts would offer a better stability for cellulose heterogenization, resulting in improved catalytic activity.<sup>70</sup> Through the immobilization of cellulase enzyme onto mesoporous silica nanoparticles *via* physisorption and covalent bonding, the immobilized catalyst shows stable catalytic efficiency at 80% glucose conversion yields, which is comparable to that of free cellulase enzyme (Figure 9.4).<sup>71</sup> However, the catalytic activity of free cellulase enzyme could be significantly reduced after being stored for a longer time (23 days) when compared to covalently bonded cellulase enzyme on mesoporous silica nanoparticles (Figure 9.5). Finally, the physisorbed cellulase enzyme lost most of its activity after a prolonged storage time. Lupoi *et al.* studied the catalytic activity of nanoparticle-immobilized cellulase enzyme to continually saccharify and ferment cellulose.<sup>70</sup> The ethanol yields can be nearly doubled when cellulase enzyme is physically absorbed on silica nanoparticles when compared to the reaction using enzyme without nanoparticles. The major use of glucose from enzymatic hydrolysis is to produce bio-ethanol (Figure 9.4), which is one of the most commonly used biofuels. In 2010, 120 billion liters (bnl) of biofuel for transport were produced, including 100 bnl bio-ethanol and 20 bnl biodiesel. Global biofuel production was predicted to increase to 200 bnl by 2020, including 155 bnl bio-ethanol and 45 bnl bio-diesel. The increasing requirement for new biofuel accelerates the development of new biofuel production technologies at the commercial scale, *e.g.* second-generation bio-refinery.<sup>72</sup> When compared to batch processes, the fermentation systems that process in continuous mode provide many advantages, leading to improved productivity, smaller bioreactors and less investment/operational costs.<sup>73</sup> In addition, the sustained processes would be advanced by cell immobilization techniques to maintain the high cell densities in the reactors. Ivanova *et al.* reported continuous ethanol fermentation processes involving nanotechnology, in which *Saccharomyces cerevisiae* cells were retained in an alginate mixture with dispersed nanoparticles with magnetic properties.<sup>74</sup>

When compared to bio-ethanol, biobutanol is another important biofuel owing to its advantages such as higher hydrophobicity, higher blending



**Figure 9.5** TEM images of (A) large pore mesoporous silicananoparticles (LPMSN) and (B) small pore mesoporous silicananoparticles (SPMSN). (C) Glucose yields produced from free cellulase, cellulase-adsorbed SPMSN, cellulase-adsorbed LPMSN and cellulase-linked LPMSN. “Before\_storage” means freshly prepared catalysts were used for the reaction. “After\_storage” means that the aged catalysts were used for the reaction.<sup>71</sup> Adapted from ref. 71 with permission from the Royal Society of Chemistry.

capacity, lower vapor pressure and higher energy content.<sup>75</sup> Over the past decades, bio-butanol fermentation has received more attention for the industrial manufacturing of 1-butanol and other liquid fuels. However, the low concentration of butanol in the fermentation mixture (normally 1–2%, w/v) increases the cost of recovery methods for solvents, *e.g.* distillation.<sup>76</sup> Among those recovery methods, pervaporation (PV) by employing functional membranes is regarded as a cost-effective technology, because of its high energy efficiency and convenience to produce highly concentrated 1-butanol.<sup>77</sup> Organo-philic polymers are the most widely used PV membranes for butanol recovery, *e.g.* poly(1-trimethylsilyl-1-propyne) (PTMSP), poly(ether-*block*-amide) (PEBA) and polydimethylsiloxane (PDMS).<sup>78</sup> Inorganic fillers would often be introduced into polymers to form mixed matrix membranes, leading to polymer membranes with enhanced pervaporation performance.<sup>79</sup>

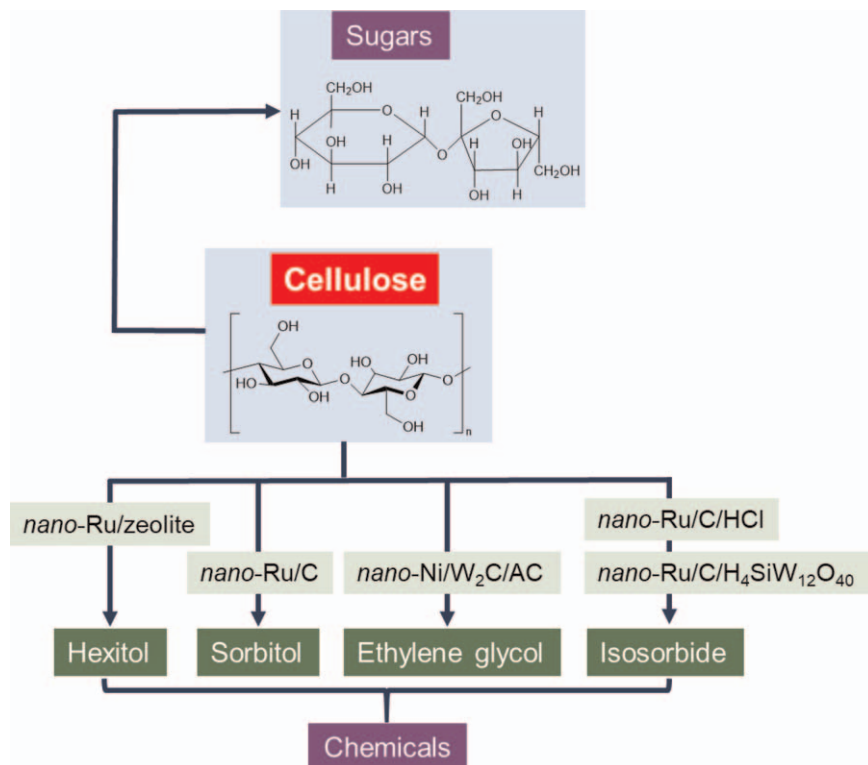
Chung *et al.* used nanotechnology in 1-butanol recovery by incorporating organosilanes-functionalized SiO<sub>2</sub> nanoparticles into polymer membranes, leading to significantly improved selectivity toward 1-butanol *via* increasing the aqueous 1-butanol sorption coefficient.<sup>80</sup> Moreover, nanotechnology has been used to fabricate electrodes of fuel cells, which can convert chemical energy (*e.g.* butanol) to electrical power with higher efficiency and lower pollutants.<sup>81</sup>

### 9.3.2 Lactic Acid and Chemicals Derived From Glucose

A chemical process that combines alkaline degradation and air oxidation of D-glucose into lactic acid has been developed by employing activated carbon-supported Pt nanoparticles (Pt/C), resulting in lactic acid with a yield of 45%.<sup>82</sup> The resultant lactic acid could then be converted into various types of chemicals. Lactic acid could be hydrogenated to PG by ruthenium nanoparticles (size: 2–30 nm) supported by titanium oxide (Ru/TiO<sub>2</sub>) with a yield of 95%, and its reaction speed is almost three times higher than that using ruthenium bulk metal.<sup>83</sup> Interestingly, using activated carbon supporting ruthenium (Ru/C) under mild conditions (70 °C; ambient pressure), the main product of lactic acid electro-hydrogenation is LAL, which is not commercially available in pure state. This process thus provides a green, convenient and efficient method to prepare LAL.<sup>84</sup> Wang *et al.* reported a technology in which lactic acid could be dehydrated to lactide through using nano-sized lanthanum–titanium composite oxides as the catalyst.<sup>56,85</sup> Lactide then would be easily polymerized to produce PLA.<sup>86</sup> Sun *et al.* proposed a convenient method to synthesize photodegradable PLA, in which a PLA/TiO<sub>2</sub> photodegradable sample was prepared *in situ* through a condensation reaction of lactic acid using TiO<sub>2</sub> nanoparticles.<sup>87</sup>

### 9.3.3 Chemicals Derived From Cellulose

Scientists and engineers have paid significant attention to the direct conversion of cellulose to valuable chemicals, including hexitol, ethylene glycol and isosorbide (Figure 9.6). Recently, more efforts have been put into the application of nanoparticles for the abovementioned conversion in order to achieve better performance. Through the combination of Ru-loaded zeolites and trace amounts of mineral acid, the catalyst system would completely convert cellulose to hexitols with a 90% yield.<sup>88,89</sup> By applying Ru/carbon nanotubes catalysts, cellulose would be converted to sorbitol.<sup>89</sup> In addition, cellulose can also be one-pot converted to ethylene glycol in the presence of catalysts based on tungsten.<sup>90,91</sup> Microcrystalline cellulose would be hydrogenated to produce isosorbide with 50% yield using a Ru/C catalyst with dilute hydrochloric acid.<sup>92</sup> Moreover, a better efficient method to produce isosorbide is developed through the combination of H<sub>4</sub>SiW<sub>12</sub>O<sub>40</sub> and Ru/C, in which isosorbide can be achieved from fibrillar cellulose with a yield of 63%.<sup>93</sup>



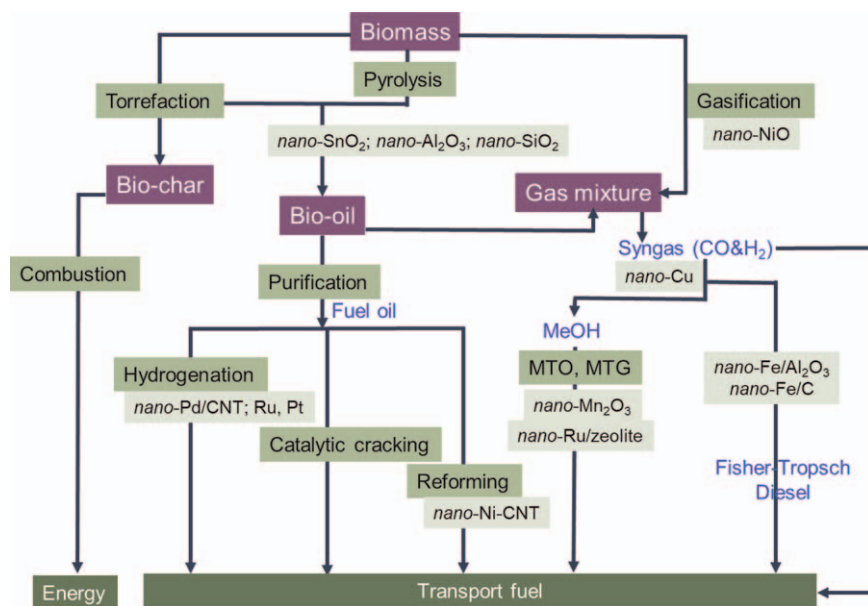
**Figure 9.6** Catalytic conversion of cellulose to chemicals by nanoparticles.

### 9.3.4 Pyrolysis of Lignocellulosic Biomass

Pyrolysis can be dated back to Egyptian times, in which tar for caulking boats and certain embalming agents was obtained. There are three major thermal processes, namely, gasification,<sup>94</sup> pyrolysis<sup>27</sup> and torrefaction,<sup>95</sup> which are always applied to convert biomass to valuable products, *e.g.* char, bio-gas and bio-oil. Figure 9.7 summarizes the different routes and downstream conversions.

The thermal decomposition of biomass is a highly multi-skilled process in which different types of products (*e.g.* bio-gas, bio-oil and char) could be conveniently controlled by adjusting the process parameters, including heating speed, temperature and heating time (Table 9.1). The torrefaction process increases the product's density and specific heating value while reducing its moisture content. In addition, the hydrophobic nature of torrefied biomass excludes the moisture penetration during the storage time, thus eliminating the fungal degradation of the product. Therefore, torrefied biomass exhibits an important advantage to maintain the quality of products.<sup>96–98</sup> Current studies are trying to figure out the relationship between nanoparticle catalyst and biomass gasification, which majorly focus on the





**Figure 9.7** Conversion of biomass to energy and chemicals through thermochemical treatment. MTO: methanol to olefin; MTG: methanol to gasoline.

**Table 9.1** The effect of thermal process parameters on the product.

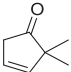
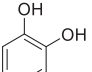
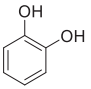
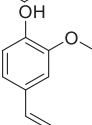
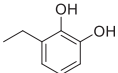
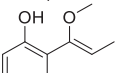
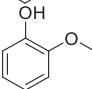

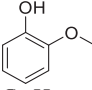
Code	Type of pyrolysis	Temperature (°C)	Heating speed (°C min <sup>-1</sup> )	Major product
1	Torrefaction	200–350	< 50	Bio-char
2	Fast pyrolysis	400–550	100–10 000	Bio-oil
3	Gasification	550–1000	100–10 000	Bio-gas

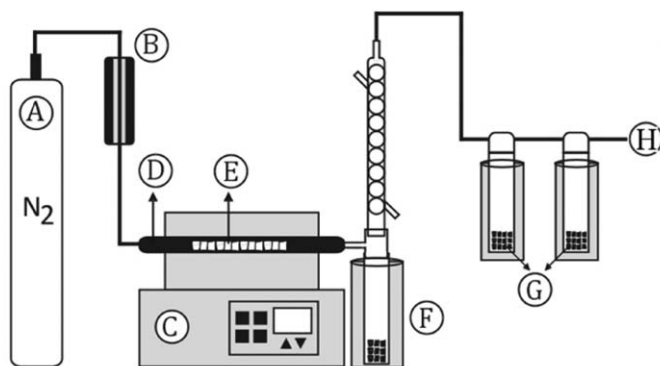
development of solid-supported nano-catalysts for tar removal during biomass gasification/pyrolysis, and quality improvement of generated gases.  $\gamma$ - $\text{Al}_2\text{O}_3$  supported nano-NiO displays good catalytic activity for the pyrolysis of biomass at 800 °C, in which the tar removal efficiency is as high as 99% and the gas yield is significantly increased.<sup>99</sup> Additionally, the addition of catalyst significantly changes the composition of the produced gas, where more valuable  $\text{H}_2$  and CO are generated than less-value  $\text{CO}_2$  and  $\text{CH}_4$  derived from the catalyst-free system. Catalysts based on nanoparticles are also successfully used for the anaerobic digestion of biomass.<sup>100</sup> The influence of the hematite nanoparticles' concentration (0–1600 mg L<sup>-1</sup>) and the starting pH (4.0–10.0) on  $\text{H}_2$  produce are studied. This process involves sucrose and anaerobic bacteria in batch reaction at 35 °C, in which the optimized condition is 200 mg L<sup>-1</sup> at pH 8.48, leading to an optimized  $\text{H}_2$  efficiency of 3.21 mol  $\text{H}_2$  per mol sucrose (increased by 32% when compared to the blank test).

Generally, bio-oil is a liquid with dark brown color at room temperature, and its compositions are greatly affected by the nature of the original

biomass. The bio-oil is commonly composed of various chemicals, including acids, aldehydes, furans, phenols, mono-saccharides, anhydro-sugars and oligo/polymers (Table 9.2). The abovementioned components directly originate from the dehydration and breakdown of cellulose and lignin in biomass, while a huge volume of water (15–50 wt%) is generated during the process.<sup>30</sup> Nanoparticles have shown the potential to catalyze and affect the pyrolysis processes, finally changing the properties of bio-oil and its content distribution. There are also studies using nanoparticles as catalysts in pyrolysis and gasification of biomass.<sup>101,102</sup> Gokdai *et al.* studied the catalytic behaviors of nano-SnO<sub>2</sub> in the hazelnut shell pyrolysis process.<sup>101</sup> Figure 9.8 displays the general experimental setup for pyrolysis. The large surface area of SnO<sub>2</sub> nanoparticles could significantly accelerate the primary and secondary decomposition reactions, resulting in improved gas production. In addition, the components of bio-oil are completely changed after the application of nano-SnO<sub>2</sub> particles (Table 9.3). Fabbri *et al.* also studied the catalytic behaviors of nanoparticles (*e.g.* SiO<sub>2</sub>, Al<sub>2</sub>O<sub>3</sub>, MgO, Ti(SO<sub>4</sub>)<sub>2</sub> and Al<sub>2</sub>O<sub>3</sub>-TiO<sub>2</sub>) on the cellulose pyrolysis to anhydro-sugars, in which the Al- and Ti-based nanoparticles would significantly increase the yields of levoglucosan (Table 9.3).<sup>99,102</sup>

**Table 9.2** The comparison of major components in pyrolysis oil derived from hazelnut shell catalyzed with a common catalyst based on SiO<sub>2</sub> and catalyst based on nano-SiO<sub>2</sub>.

Code	Common catalyst based on SiO <sub>2</sub>			Catalyst based on nano-SiO <sub>2</sub>		
	Component	Structure	Peak area (%)	Component	Structure	Peak area (%)
1	2,2-Dimethylcyclopent-3-en-1-one		1.8	1,2-Benzenediol		3.7
2	1,2-Benzenediol		4.8	2-Methoxy-4-vinylphenol		4.1
3	3-Ethylbenzene-1,2-diol		5.2	2-(1-Methoxyprop-1-enyl)phenol		5.3
4	1-Dodecanol	C <sub>9</sub> H <sub>20</sub> O	5.6	2-Methoxy-4-methylphenol		5.5
5	Bicyclo[3.3.1]nonane		6.5	2-Methoxyphenol (guaiacol)		5.8
6	Tetracosane	C <sub>24</sub> H <sub>50</sub>	15.6	Tetrapentacontane	C <sub>54</sub> H <sub>110</sub>	9



- A = N<sub>2</sub> gas  
 B = Flowmeter  
 C = Furnace with temperature control system  
 D = Quartz reactor  
 E = Hazel nut shell powder + catalyst  
 F = Cooling unit  
 G = Traps  
 H Gas exit

**Figure 9.8** Illustration of an experimental setup for pyrolysis.<sup>101</sup> Adapted from ref. 101 with permission from Elsevier, Copyright 2010.

**Table 9.3** Influence of nanoparticles on the product distributions of cellulose pyrolysis.<sup>a</sup>

Code	Nanoparticles	Anhydro-sugar			
		LGO%	LAC%	DGP%	LGA%
1	Without	3.7	1.5	2.6	10.5
2	Al <sub>2</sub> O <sub>3</sub>	7.7	4.5	2.2	9.1
3	MgO	2.2	6.1	3.9	11
4	Si <sub>2</sub> O	0.2	0.2	1.0	2.8
5	Ti <sub>2</sub> (SiO <sub>4</sub> ) <sub>2</sub>	11	4.9	2.1	7.0
6	Al <sub>2</sub> O <sub>3</sub> TiO <sub>2</sub>	19	5.9	1.6	2.3
7	Al <sub>2</sub> O <sub>3</sub> TiO <sub>2</sub>	2.9	1.3	2.1	7.0

<sup>a</sup>Levoglucosone (LGO); 1-Hydroxy, (1R)-3,6-dioxabicyclo[3.2.1]octan-2-one (LAC); 1,4:3,6-Dianhydro- $\alpha$ -D-glucopyranose (DGP); Levoglucosan (LGA).

### 9.3.5 Bio-oil Upgrading

Currently, the use of bio-oil in industry is limited by several drawbacks, *e.g.* poor stability, high viscosity and corrosivity. Bio-oil also cannot be blended with common fossil fuels.<sup>14</sup> Thus, more efforts are required to develop processes capable of bio-oil upgrading, including esterification,<sup>104</sup> hydrogenation,<sup>103</sup> hydrodeoxygenation,<sup>105</sup> steam reforming<sup>106</sup> and emulsification of bio-oil and diesel.<sup>107</sup> However, most of these technologies are not cost efficient, because they often require expensive equipment and complicated procedures and suffer from the catalysts fouling. In order to solve these issues, Crossley *et al.* present a method to stabilize the emulsions of water–oil while catalyzing the hydrodeoxygenation at the liquid–liquid interface *via* applying solid nano-hybrid materials.<sup>108</sup> The catalytic activities of Pd catalysts supported on carbon nanotubes and nano-sized oxides

are studied, in which the turn-over number is similar to that of Pd/C in a homogeneous phase system. The biphasic system displays higher activity than the monophasic system, because of the better dispersion of particles at the liquid–liquid interface for the biphasic system, leading to higher H<sub>2</sub> concentration at the interface due to its higher solubility in the organic phase. Dyson *et al.* reported that the nanoparticles would benefit the hydrogenation of phenols, in which the catalyst composited by Ru, Pd and Pt nanoparticles with an ionic liquid exhibits activities in both hydrogenation and dehydration to convert phenols to cyclohexane.<sup>109</sup> Recently, a method to update bio-oil *via* reformation processes has been proposed, in which Ni nanoparticles supported by carbon nanotubes (CNT) can reform the organic compounds in bio-oil at low temperatures. The yield of H<sub>2</sub> reached 92.5% at 550 °C when the optimized Ni-CNT catalyst was applied (Ni loading value 92.5%) (Figure 9.7).<sup>110</sup>

### 9.3.6 Other Applications

Gasification of biomass and bio-oil to syngas (*e.g.* CO + H<sub>2</sub>) is one of the most popular methods to produce biofuel with high quality, which is carried out under O<sub>2</sub> or by steam assistance at 750–1800 °C.<sup>111</sup> After the upgrading, the syngas would be conveniently transformed into hydrocarbons (C<sub>n</sub>H<sub>2n+2</sub>) *via* the Fischer–Tropsch reaction.<sup>112</sup> However, the improvements of selectivity and efficiency for syngas production are still challenging.<sup>113</sup> Syngas would be converted to C<sub>2</sub>–C<sub>4</sub> olefins with a selective yield of 60 wt% by applying sulfur/sodium-promoted iron nanoparticles on the surface of carbon nanofiber.<sup>114</sup> Tar formation is one of the main problems during the gasification/pyrolysis of biomass (bio-oil). Catalytic cracking of tar at relatively low temperatures provides an efficient method to reduce tar residues. Many research works have studied the application of nanoparticles for tar removal.<sup>8,115,116</sup> The synthesis of methanol from syngas *via* heterogeneously catalytic reaction by a Cu catalyst supported on ZnO/Al<sub>2</sub>O<sub>3</sub> has demonstrated a milestone in the chemical industry. Cu nanoparticle catalyst without any solid support also shows high catalytic activities in the homogeneous synthesis of methanol from syngas.<sup>117</sup> In the past two decades, the technologies for the conversion of methanol-to-propylene (MTP) and MTO have been receiving increasing attention in industry.<sup>118</sup> Recently, Xu *et al.* reported that the nano-crystalline  $\alpha$ -Mn<sub>2</sub>O<sub>3</sub> performs better in the MTO conversion than bulk Mn<sub>2</sub>O<sub>3</sub>, resulting in a higher selectivity to ethylene. This is because the nano  $\alpha$ -Mn<sub>2</sub>O<sub>3</sub> catalyst can adsorb more O<sub>2</sub> than the bulk Mn<sub>2</sub>O<sub>3</sub> catalyst, which is confirmed by the O<sub>2</sub>-Temperature-Programmed Desorption spectrum.<sup>119</sup> Generally, the conversion of methanol to ethylene happens *via* formaldehyde, and nanoparticles have shown improved activities in the conversion step from formaldehyde to ethylene, in which the conversion yield and selectivity can reach 35% and 80%, respectively, at 250 °C. Tang *et al.* reported that zeolite ZSM-supported gold nanoparticles increase the

propylene formation from methanol due to their special ability to catalyze the dehydrogenation of methanol.<sup>120</sup>

## 9.4 Prospects and Outlook

Future bio-refineries will likely include biomass dosed with suitable amounts of nanoparticles to assist and facilitate biomass breakdown. However, the preparation of well-dispersed homogeneous nanoparticles in biomass is very challenging. The traditional catalysts are being consumed at a very high rate, and the recovery of the abovementioned nanoparticle catalysts is also challenging and highly costly.<sup>121–123</sup> The strategy of using all elements in a sustainable way will benefit the future generation of bio-refineries.<sup>124</sup> With a continuously growing middle class in the global population, the need for a higher living standard would also need to be supported by sustainable industry and cleaner energy.<sup>125</sup> Thus, for the application of metal catalysts in biomass conversion, the extraction, reuse and recapture of waste resources should be seriously considered. One green strategy is to utilize natural plants for metal uptake, which will generate a naturally homogeneous distribution of metals in the biomass. In fact, plants naturally have various elements, *e.g.* Si, Al, Fe and Ni, which can catalyze the pyrolysis processes. Among them, the silica content reaches 10 wt% in dry plants.<sup>126</sup> These silica residues mainly exist in the cell walls, which enhance the structural rigidity of plants.<sup>127</sup> The concentration of other inorganic deposits is very low and plants cannot survive under high concentrations of these elements. However, there are some special plants termed hyper-accumulators that have displayed tolerance to high levels of metals.<sup>128</sup>

Hyper-accumulator plants are capable of amassing metal elements with much higher concentrations than non-accumulator plants when growing in the same area.<sup>129</sup> For instance, *Streptanthus polygaloides* and *Berkheya coddii* have shown high uptake capabilities for nickel, where the nickel concentrations reach 1 wt% of the dry weight of the plant. The metal hyper-accumulator species can be defined by the threshold value of uptake metal concentrations, including 10 000 mg kg<sup>-1</sup> for Zn and Mn; 1000 mg kg<sup>-1</sup> for Co, Cu, Ni, As and Se and 100 mg kg<sup>-1</sup> for Cd.<sup>130</sup> The prioritized use of land for food or fuel may be a major factor that limits the application of biomass for burning. However, many areas of land have been contaminated by metals around the world, which are not suitable for food production. It is estimated that 40% of the earth's arable land consists of acidic soil after pollution, which contains a high concentration of aluminum.<sup>131</sup> The high concentration of aluminum in these soils is one of the main factors limiting plant growth, prohibiting those lands from being used for agricultural production.<sup>132</sup> The capability of those metal hyper-accumulator species to uptake metals from soil could add more value to biomass plants, which would be grown in the polluted areas for fuel and chemical purposes, therefore avoiding competition with food production. Additionally, the continual growing and harvesting of plants for a long time will efficiently

reduce the metal concentrations in the contaminated soils, thus reducing their toxicity. However, only a few researchers have focused on metal accumulation by plants. Anderson *et al.* have investigated the metal accumulation capabilities of *Brassica juncea* growing on mine waste, *e.g.* Cu, Ag and Au, the metallic nanoparticles of which are observed in the plants.<sup>133</sup> Moreover, it is confirmed that those nanoparticles are formed spontaneously in the plant during their growth rather than forming in soils and then being adsorbed by the plant roots.<sup>134,135</sup> Lui *et al.* have investigated the bio-oil derived from biomass containing copper, in which the copper-accumulated biomass was able to significantly catalyze the thermal decomposition of biomass, leading to an improved yield and quality of bio-oil when compared to that derived from biomass without copper.<sup>136</sup> Interestingly, the copper would not volatilize to bio-oil during treatment, and all of the copper was retained in the bio-char. More efforts are needed to study whether other metals would not contaminate the bio-oil during the process. Current research at the University of York indicate that the accumulation of metals by plants would provide a feasible method to introduce nanoparticles directly into biomass, generating materials with catalytic activities.<sup>137</sup>

## References

1. World Population Prospects: The 2012 Revision, Key Findings and Advance Tables. Working Paper No. ESA/P/WP.227., United Nations, Department of Economic and Social Affairs, Population Division 2013.
2. P. Falkowski, R. J. Scholes, E. Boyle, J. Canadell, D. Canfield, J. Elser, N. Gruber, K. Hibbard, P. Hogberg, S. Linder, F. T. Mackenzie, B. Moore, T. Pedersen, Y. Rosenthal, S. Seitzinger, V. Smetacek and W. Steffen, *Science*, 2000, **290**, 291–296.
3. The Keeling Curve: A Daily Record of Atmospheric Carbon Dioxide from Scripps Institution of Oceanography at UC San Diego: <http://keelingcurve.ucsd.edu/>.
4. R. A. Sheldon, *Catal. Today*, 2011, **167**, 3–13.
5. REN21. Renewables 2013 Global Status Report, Paris, 2013.
6. M. Mascal and E. B. Nikitin, *Angew. Chem., Int. Ed.*, 2008, **47**, 7924–7926.
7. M. Mascal and E. B. Nikitin, *ChemSusChem*, 2009, **2**, 859–861.
8. M. Brasholz, K. von Kanel, C. H. Hornung, S. Saubern and J. Tsanaktsidis, *Green Chem.*, 2011, **13**, 1114–1117.
9. M. Mascal and E. B. Nikitin, *Green Chem.*, 2010, **12**, 370–373.
10. C. M. Chopko, E. L. Lowden, A. C. Engler, L. G. Griffith and P. T. Hammond, *ACS Macro Lett.*, 2012, **1**, 727.
11. J. Zhang, L. Wu, F. Meng, Z. Wang, C. Deng, H. Liu and Z. Zhong, *Langmuir*, 2012, **28**, 2056.
12. H. Feil, Y. H. Bae, J. Feijen and S. W. Kim, *J. Membr. Sci.*, 1991, **64**, 283.
13. T. Takezawa, Y. Mori and K. Yoshizato, *Biotechnology*, 1990, **8**, 854.
14. F. Liu, G. L. Tao and R. X. Zhuo, *Polym. J.*, 1993, **25**, 561.

15. P. Shi, Q. Li, X. He, S. Li, P. Sun and W. Zhang, *Macromolecules*, 2014, **47**, 7442.
16. *Advances in Interpenetrating Polymer Networks*, ed. D. Klemptner and K. C. Frisch, Technomic, Lancaster, PA, 1994.
17. Z. M. O. Rzaev, S. Dincer and E. Piskin, *Prog. Polym. Sci.*, 2007, **32**, 534.
18. J. Zhang and N. A. Peppas, *J. Appl. Polym. Sci.*, 2001, **82**, 1077.
19. G. Staikos, K. Karayanni and Y. Mylonas, *Macromol. Chem. Phys.*, 1997, **198**, 2905.
20. J. Zhang and N. A. Peppas, *Macromolecules*, 2000, **33**, 102.
21. T. V. Burova, N. V. Grinberg, V. Y. Grinberg, E. V. Kalinina, V. I. Lozinsky, V. O. Aseyev, S. Holappa, H. Tenhu and A. R. Khokhlov, *Macromolecules*, 2005, **38**, 1292.
22. T. Swift, L. Swanson and S. Rimmer, *RSC Adv.*, 2014, **4**, 57991.
23. F. M. Winnik, *Macromolecules*, 1990, **23**, 233.
24. Y. Shiraishi, R. Miyamoto, X. Zhang and T. Hirai, *Org. Lett.*, 2007, **9**, 3921.
25. L. Tang, J. K. Jin, A. Qin, W. Z. Yuan, Y. Mao, J. Mei, J. Z. Sun and B. Z. Tang, *Chem. Commun.*, 2009, 4974.
26. Z. Zhao, S. Chen, J. W. Y. Lam, P. Lu, Y. Zhong, K. S. Wong, H. S. Kwok and B. Z. Tang, *Chem. Commun.*, 2010, **46**, 2221.
27. X. Shen, Y. Shi, B. Peng, K. Li, J. Xiang, G. Zhang, Z. Liu, Y. Cheng and D. Zhang, *Macromol. Biosci.*, 2012, **12**, 1583.
28. F. Mahtab, Y. Yu, J. W. Y. Lam, J. Liu, B. Zhang, P. Lu, X. Zhang and B. Z. Tang, *Adv. Funct. Mater.*, 2011, **21**, 1733.
29. A. Qin, J. W. Y. Lam, L. Tang, C. K. W. Jim, H. Zhao, J. Sun and B. Z. Tang, *Macromolecules*, 2009, **42**, 1421.
30. Z. M. O. Rzaev, S. Dincer and E. Piskin, *Prog. Polym. Sci.*, 2007, **32**, 534.
31. J. L. West and N. J. Halas, *Curr. Opin. Biotechnol.*, 2000, **11**, 215–217.
32. A. M. Balu, B. Baruwati, E. Serrano, J. Cot, J. Garcia-Martinez, R. S. Varma and R. Luque, *Green Chem.*, 2011, **13**, 2750–2758.
33. L. C. Meher, D. V. Sagar and S. N. Naik, *Renewable Sustainable Energy Rev.*, 2006, **10**, 248–268.
34. H. Fukuda, A. Kondo and H. Noda, *J. Biosci. Bioeng.*, 2001, **92**, 405–416.
35. C. V. McNeff, L. C. McNeff, B. Yan, D. T. Nowlan, M. Rasmussen, A. E. Gyberg, B. J. Krohn, R. L. Fedie and T. R. Hoye, *Appl. Catal., A*, 2008, **343**, 39–48.
36. E. Lotero, Y. J. Liu, D. E. Lopez, K. Suwannakarn, D. A. Bruce and J. G. Goodwin, *Ind. Eng. Chem. Res.*, 2005, **44**, 5353–5363.
37. J. F. Gomes, J. F. Puna, J. C. Bordado and M. J. N. Correia, *React. Kinet. Catal. Lett.*, 2008, **95**, 273–279.
38. Z. Helwani, M. R. Othman, N. Aziz, J. Kim and W. J. N. Fernando, *Appl. Catal., A*, 2009, **363**, 1–10.
39. D. Kumar and A. Ali, *Energy Fuels*, 2013, **27**, 3758–3768.
40. H. Tan, J. Zheng, D. Xu, D. Wan, J. Qiu and T. Tang, *J. Phys. Chem. B*, 2014, **118**, 5229–5239.

41. H. Zhou, Q. Ye, W. T. Neo, J. Song, H. Yan, Y. Zong, B. Z. Tang, T. S. A. Hor and J. Xu, *Chem. Commun.*, 2014, **50**, 13785–13788.
42. W. Yuan, T. Shen, X. Liu and J. Ren, *Mater. Lett.*, 2013, **111**, 9–12.
43. S. M. Ramirez, Y. J. Diaz, C. M. Sahagun, M. W. Duff, O. B. Lawal, S. T. Iacono and J. M. Mabry, *Polym. Chem.*, 2013, **4**, 2230–2234.
44. J. Shim, D. G. Kim, J. H. Lee, J. H. Baik and J. C. Lee, *Polym. Chem.*, 2014, **5**, 3432–3442.
45. Z. Li, B. H. Tan, G. Jin, K. Li and C. He, *Polym. Chem.*, 2014, **5**, 6740–6753.
46. A. Pan, S. Yang, L. He and X. Zhao, *RSC Adv.*, 2014, **4**, 27857–27866.
47. S. S. Mahapatra, S. K. Yadav and J. W. Cho, *React. Funct. Polym.*, 2012, **72**, 227–232.
48. R. Sasi kumar and M. Alagar, *RSC Adv.*, 2015, **5**, 33008.
49. A. Lungu, N. M. Şulcă, E. Vasile, N. Badea, C. Pârvu and H. Iovu, *J. Appl. Polym. Sci.*, 2011, **121**, 2919–2926.
50. D. Prządka, J. Jęczalik, E. Andrzejewska, B. Marciniec, M. Dutkiewicz and M. Szłapka, *React. Funct. Polym.*, 2013, **73**, 114–121.
51. R. Bakhshi, A. Darbyshire, J. E. Evans, Z. You, J. Lu and A. M. Seifalian, *Colloids Surf., B*, 2011, **86**, 93–105.
52. Q. H. Zhang, X. Huang, X. L. Wang, X. D. Jia and K. Xi, *Polymer*, 2014, **55**, 1282–1291.
53. H. Lin, X. Wan, X. Jiang, Q. Wnag and J. Yin, *Adv. Funct. Mater.*, 2011, **21**, 2960–2967.
54. X.-F. Lei, M.-T. Qiao, L.-D. Tian, P. Yao, Y. Ma, H.-P. Zhang and Q.-Y. Zhang, *Corros. Sci.*, 2015, **90**, 223–238.
55. S. Duo, H. Ke, T. Liu, M. Song and M. Li, *Nucl. Instrum. Methods Phys. Res., Sect. B*, 2013, **307**, 324–327.
56. N. L. Le and T.-S. Chung, *J. Membr. Sci.*, 2014, **454**, 62–73.
57. Z. Wu, S. Zhang, H. Li, Y. Liang, Z. Qi, Y. Xu, Y. Tang and C. Gong, *J. Power Sources*, 2015, **290**, 42–52.
58. R. Konietzny, T. Koschine, K. Rätzke and C. Staudt, *Sep. Purif. Technol.*, 2014, **123**, 175–182.
59. L. Matějka, I. Amici Kroutilová, J. D. Lichtenhan and T. S. Haddad, *Eur. Polym. J.*, 2014, **52**, 117–126.
60. V. Pistor, B. G. Soares and R. S. Mauler, *Polymer*, 2013, **54**, 2292–2298.
61. L. Wang, C. Zhang and S. Zheng, *J. Mater. Chem.*, 2011, **21**, 19344–19352.
62. K. Sethuraman, P. Prabunathan and M. Alagar, *RSC Adv.*, 2014, **4**, 45433–45441.
63. C. Ni, G. Ni, L. Zhang, J. Mi, B. Yao and C. Zhu, *J. Colloid Interface Sci.*, 2011, **362**, 94–99.
64. L. Matějka, P. Murias and J. Pleštil, *Eur. Polym. J.*, 2012, **48**, 260–274.
65. M. R. Vengatesan, S. Devaraju, K. Dinakaran, J. K. Song and M. Alagar, *Polym. Int.*, 2012, **62**, 127–133.
66. N. Xu, E. J. Stark, P. I. Carver, P. Sharps, J. Hu and C. Hartmann-Thompson, *J. Appl. Polym. Sci.*, 2013, **130**, 3849–3861.
67. M. Selvi, S. Devaraju, M. R. Vengatesan, J. S. Go, M. Kumar and M. Alagar, *RSC Adv.*, 2014, **4**, 8238–8244.



68. K. W. Huang and S. W. Kuo, *Macromol. Chem. Phys.*, 2010, **211**, 2301–2311.
69. Y. C. Wu and S. W. Kuo, *Polymer*, 2010, **51**, 3948–3955.
70. M. C. Tseng and Y. L. Liu, *Polymer*, 2010, **51**, 5567–5575.
71. R. H.-Y. Chang, J. Jang and K. C. W. Wu, *Green Chem.*, 2011, **13**, 2844–2850.
72. J. Mei, Y. Hong, J. W. Y. Lam, A. Qin, Y. Tang and B. Z. Tang, *Adv. Mater.*, 2014, **26**, 5429–5479.
73. B. Z. Tang, X. Zhan, G. Yu, P. P. Sze Lee, Y. Liu and D. Zhu, *J. Mater. Chem.*, 2001, **11**, 2974–2978.
74. M. Wang, G. Zhang, D. Zhang, D. Zhu and B. Z. Tang, *J. Mater. Chem.*, 2010, **20**, 1858–1867.
75. H. Zhou, J. Li, M. H. Chua, H. Yan, B. Z. Tang and J. Xu, *Polym. Chem.*, 2014, **5**, 5628–5637.
76. H. Zhou, X. Wang, T. T. Lin, J. Song, B. Z. Tang and J. Xu, *Polym. Chem.*, 2016, **7**, 6309–6317.
77. J. Luo, K. Song, F. L. Gu and Q. Miao, *Chem. Sci.*, 2011, **2**, 2029–2034.
78. Z. He, L. Shan, J. Mei, H. Wang, J. W. Y. Lam, H. H. Y. Sung, I. D. Williams, X. Gu, Q. Miao and B. Z. Tang, *Chem. Sci.*, 2015, **6**, 3538–3543.
79. R. Hu, C. F. A. Gomez-Duran, J. W. Y. Lam, J. L. Belmonte-Vazquez, C. Deng, S. Chen, R. Ye, E. Pena-Cabrera, Y. Zhong, K. S. Wong and B. Z. Tang, *Chem. Commun.*, 2012, **48**, 10099–10101.
80. G. Feng, R. T. K. Kwok, B. Z. Tang and B. Liu, *Appl. Phys. Rev.*, 2017, **4**, 021307.
81. X. Sun, Y. Liu, G. Shaw, A. Carrier, S. Dey, J. Zhao and Y. Lei, *ACS Appl. Mater. Interfaces*, 2015, **7**, 13189–13197.
82. B. Valeur, *Molecular Fluorescence: Principles and Applications*, Wiley-VCH, Weinheim, 2002.
83. H. Nie, Y. Lv, L. Yao, Y. Pan, Y. Zhao, P. Li, G. Sun, Y. Ma and M. Zhang, *J. Hazard. Mater.*, 2014, **264**, 474–480.
84. Y.-Z. Zhang, X. Xiang, P. Mei, J. Dai, L.-L. Zhang and Y. Liu, *Spectrochim. Acta, Part A*, 2009, **72**, 907–914.
85. J. R. Lakowicz, *Principles of Fluorescence Spectroscopy*, Springer, Singapore, 2006.
86. J. R. Cox, P. Müller and T. M. Swager, *J. Am. Chem. Soc.*, 2011, **133**, 12910–12913.
87. J.-S. Yang and T. M. Swager, *J. Am. Chem. Soc.*, 1998, **120**, 11864–11873.
88. C. Y. K. Chan, J. W. Y. Lam, C. Deng, X. Chen, K. S. Wong and B. Z. Tang, *Macromolecules*, 2015, **48**, 1038–1047.
89. J. Chen, Z. Xie, J. W. Y. Lam, C. C. W. Law and B. Z. Tang, *Macromolecules*, 2003, **36**, 1108–1117.
90. W. Yuan, H. Zhao, X. Shen, F. Mahtab, J. W. Y. Lam, J. Sun and B. Z. Tang, *Macromolecules*, 2009, **42**, 9400–9411.
91. X. Wang, W. Wang, Y. Wang, J. Z. Sun and B. Z. Tang, *Polym. Chem.*, 2017, **8**, 2353–2362.

92. T. Chen, H. Yin, Z.-Q. Chen, G.-F. Zhang, N.-H. Xie, C. Li, W.-L. Gong, B. Z. Tang and M.-Q. Zhu, *Small*, 2016, **12**, 6547–6552.
93. W. Z. Yuan, R. Hu, J. W. Y. Lam, N. Xie, C. K. W. Jim and B. Z. Tang, *Chem. – Eur. J.*, 2012, **18**, 2847–2856.
94. J. Liu, Y. Zhong, J. W. Y. Lam, P. Lu, Y. Hong, Y. Yu, Y. Yue, M. Faisal, H. H. Y. Sung, I. D. Williams, K. S. Wong and B. Z. Tang, *Macromolecules*, 2010, **43**, 4921–4936.
95. R. Hu, J. W. Y. Lam, J. Liu, H. H. Y. Sung, I. D. Williams, Z. Yue, K. S. Wong, M. M. F. Yuen and B. Z. Tang, *Polym. Chem.*, 2012, **3**, 1481–1489.
96. R. Hu, J. W. Y. Lam, M. Li, H. Deng, J. Li and B. Z. Tang, *J. Polym. Sci., Part A: Polym. Chem.*, 2013, **51**, 4752–4764.
97. M. H. Chua, H. Zhou, T. T. Lin, J. Wu and J. W. Xu, *J. Polym. Sci., Part A: Polym. Chem.*, 2017, **55**, 672–681.
98. W. Z. Yuan, H. Zhao, X. Y. Shen, F. Mahtab, J. W. Y. Lam, J. Z. Sun and B. Z. Tang, *Macromolecules*, 2009, **42**, 9400–9411.
99. H. Zhou, Q. Ye, W. T. Neo, J. Song, H. Yan, Y. Zong, B. Z. Tang, T. S. Andy Hor and J. Xu, *Chem. Commun.*, 2014, **50**, 13785–13788.
100. P. Lu, J. W. Y. Lam, J. Liu, C. K. W. Jim, W. Yuan, C. Y. K. Chan, N. Xie, Q. Hu, K. K. L. Cheuk and B. Z. Tang, *Macromolecules*, 2011, **44**, 5977–5986.
101. Z. Gokdai, A. Sinag and T. Yumak, *Biomass Bioenergy*, 2010, **34**, 402–410.
102. W. Yuan, W. Chi, R. Liu, H. Li, Y. Li and B. Z. Tang, *Macromol. Rapid Commun.*, 2017, **38**, 1600745.
103. H. Li, J. Wang, J. Z. Sun, R. Hu, A. Qin and B. Z. Tang, *Polym. Chem.*, 2012, **3**, 1075–1083.
104. Q. Wang, M. Chen, B. Yao, J. Wang, J. Mei, J. Z. Sun, A. Qin and B. Z. Tang, *Macromol. Rapid Commun.*, 2013, **34**, 796–802.
105. Y. Wu, B. He, C. Quan, C. Zheng, H. Deng, R. Hu, Z. Zhao, F. Huang, A. Qin and B. Z. Tang, *Macromol. Rapid Commun.*, 2017, **38**, 1700070.
106. R. Hu, J. W. Y. Lam, Y. Yu, H. H. Y. Sung, I. D. Williams, M. M. F. Yuenc and B. Z. Tang, *Polym. Chem.*, 2013, **4**, 95–105.
107. J. Li, J. Liu, J. W. Y. Lam and B. Z. Tang, *RSC Adv.*, 2013, **3**, 8193–8196.
108. J. Wang, B. Li, D. Xin, R. Hu, Z. Zhao, A. Qin and B. Z. Tang, *Polym. Chem.*, 2017, **8**, 2713–2722.
109. N. Yan, Y. Yuan, R. Dykeman, Y. Kou and P. J. Dyson, *Angew. Chem., Int. Ed.*, 2010, **49**, 5549–5553.
110. Y. Liu, M. Gao, Z. Zhao, J. W. Y. Lam and B. Z. Tang, *Polym. Chem.*, 2016, **7**, 5436–5444.
111. D. Mohan, C. U. Pittman and P. H. Steele, *Energy Fuels*, 2006, **20**, 848–889.
112. K. W. Jun, H. S. Roh, K. S. Kim, J. S. Ryu and K. W. Lee, *Appl. Catal., A*, 2004, **259**, 221–226.
113. M. Asadullah, S. Ito, K. Kunimori, M. Yamada and K. Tomishige, *J. Catal.*, 2002, **208**, 255–259.

114. H. M. T. Galvis, J. H. Bitter, C. B. Khare, M. Ruitenbeek, A. I. Dugulan and K. P. de Jong, *Science*, 2012, **335**, 835–838.
115. J. Li, R. Yan, B. Xiao, D. T. Liang and L. Du, *Environ. Sci. Technol.*, 2008, **42**, 6224–6229.
116. J. Li, R. Yan, B. Xiao, D. T. Liang and D. H. Lee, *Energy Fuels*, 2008, **22**, 16–23.
117. S. Vukojevic, O. Trapp, J. D. Grunwaldt, C. Kiener and F. Schuth, *Angew. Chem., Int. Ed.*, 2005, **44**, 7978–7981.
118. J. F. Haw, W. G. Song, D. M. Marcus and J. B. Nicholas, *Acc. Chem. Res.*, 2003, **36**, 317–326.
119. J. Xu, L. Ouyang, Y. Luo, X. M. Xu, Z. Yang, C. Zhang and J. Gong, *AIChE J.*, 2012, **58**, 3474–3481.
120. L. Wang, L. Sun, C. Tian, T. Tan, G. Mu, H. Zhang and H. Fu, *RSC Adv.*, 2012, **2**, 8359–8367.
121. British Geological Survey <http://www.bgs.ac.uk/research/highlights/2010/peakMetal.html>, Accessed 30 October 2013.
122. House of Commons, Science and Technology Committee, Strategically important metals. House of Commons, Science and Technology Committee, Strategically important metals, Volume I: Report, together with formal minutes, oral and written evidence, 2011.
123. J. R. Dodson, A. J. Hunt, H. L. Parker, Y. Yang and J. H. Clark, *Chem. Eng. Process.*, 2012, **51**, 69–78.
124. A. J. Hunt, T. J. Farmer and J. H. Clark, in *Element Recovery and Sustainability*, 2013, ed. A. J. Hunt, pp. 1–28.
125. S. E. Kesler, *Proceedings for a Workshop on Deposit Modeling, Mineral Resource Assessment, and Their Role in Sustainable Development*, USA, 2007.
126. H. A. Currie and C. C. Perry, *Ann. Bot.*, 2007, **100**, 1383–1389.
127. A. G. Norman, *Adv. Agron.*, 1967, **19.1**, 107–149.
128. S. P. McGrath and F.-J. Zhao, *Curr. Opin. Biotechnol.*, 2003, **14**, 277–282.
129. C. W. N. Anderson, R. R. Brooks, R. B. Stewart and R. Simcock, *Nature*, 1998, **395**, 553–554.
130. C. W. N. Anderson, R. R. Brooks, A. Chiarucci, C. J. LaCoste, M. LeBlanc, B. H. Robinson, R. Simcock and R. B. Stewart, *J. Geochem. Explor.*, 1999, **67**, 407–415.
131. J. F. Ma, P. Ryan and D. Delhaize, *Trends Plant Sci.*, 2001, **6**, 273–278.
132. J. M. De La Fuente, V. Ramirez-Rodriguez, J. L. Cabrera-Ponce and L. Herrera-Estrella, *Science*, 1997, **276**, 1566–1568.
133. C. W. N. Anderson, S. M. Bhatti, J. Gardea-Torresdey and J. Parsons, *ACS Sustainable Chem. Eng.*, 2013, **1**, 640–648.
134. A. T. Harris and R. Bali, *J. Nanopart. Res.*, 2008, **10**, 691–695.
135. R. G. Haverkamp and A. T. Marshall, *J. Nanopart. Res.*, 2009, **11**, 1453–1463.
136. W.-J. Liu, K. Tian, H. Jiang, X.-S. Zhang, H.-S. Ding and H.-Q. Yu, *Environ. Sci. Technol.*, 2012, **46**, 7849–7856.
137. H. L. Parker, PhD thesis, University of York, 2013.

# *Nanotechnology Research for Alternative Renewable Energy*

JIE ZHENG,<sup>\*a,c</sup> CLARIS JIE EE WONG,<sup>b</sup> ENYI YE<sup>a,c</sup> AND ZIBIAO LI<sup>\*a,b,c</sup>

<sup>a</sup> Institute of Materials Research and Engineering, Agency for Science, Technology and Research (A\*STAR), 2 Fusionopolis Way, Innovis, #08-03, Singapore 138634, Singapore; <sup>b</sup> Department of Materials Science and Engineering, National University of Singapore, Singapore 117575, Singapore; <sup>c</sup> Institute of Sustainability for Chemicals, Energy and Environment (ISCE2), A\*STAR, 1 Pesek Road, Jurong Island, Singapore 627833  
\*Emails: zheng\_jie@imre.a-star.edu.sg; lizb@imre.a-star.edu.sg

## **10.1 Introduction**

Fossil-based fuels (such as petroleum, coal, and natural gas) are regarded as the largest contributors to the energy market all over the world (more than 80%).<sup>1,2</sup> However, as we know, the emission of greenhouse gases (for example, CO and CO<sub>2</sub>) that come from the combustion and processing of fossil-based fuels causes disastrous ramifications to the environment and health, such as climate change, air pollution, and respiratory disease.<sup>3</sup> Therefore, the development of new energy sources that are renewable and environmentally friendly is highly desirable for both current society and the next generation.<sup>3-7</sup> Sustainable energy sources, including solar,<sup>8-10</sup> wind,<sup>11,12</sup> geothermal energy,<sup>13,14</sup> and hydrogen,<sup>15-18</sup> are considered promising candidates to replace fossil-based fuels. These green energies show great advantages over traditional fossil fuels, such as reliability, sustainability, and, more importantly, environmental friendliness. Nevertheless,

these green energy sources also have their inevitable constraints, restricting their rapid development in a sustainable society. For example, the supply of solar and wind power is constrained to the weather and climate, whereas geothermal energy is limited to specific geographical regions. Though hydrogen energy is not subjected to natural or geographical restrictions, its growth is still at the early stage with moderate efficiency.

Nanotechnology is an emerging technique attracting great interest due to the unique capability of fabricating structures at the nanometer scale, resulting in materials and devices with novel physical and chemical properties for various applications.<sup>19–21</sup> The combination of nanotechnology and green energy sources has been regarded as one of the ideal solutions for renewable energy development. This strategy enables overcoming the inherent limitations of green energy sources, facilitates the increase of working efficiency, and promotes the implementation of new energy systems.

In this chapter, the application of nanotechnology in the development of alternative renewable energies, including solar energy (Section 10.2), wind power (Section 10.3), geothermal energy (Section 10.4), and hydrogen energy (Section 10.5), will be discussed.

## 10.2 Solar Energy

The energy from the sun (*i.e.* solar energy) represents the most abundant green energy source in the world, with  $430 \times 10^{20}$  J of sunlight energy falling on earth every hour.<sup>9,22</sup> It is assumed by the International Energy Agency that the electricity produced by solar energy allows 27% of the social activities for the whole world. Furthermore, solar energy is also recognized as the most promising candidate to substitute fossil-based fuels and is able to be the leading energy source by the end of 2050. However, solar energy suffers from being inherently intermittent (such as not being available at night or during rainy and cloudy periods), resulting in a mismatch between the energy demand and production. As we know, the energy-demanding period usually does not correspond to the solar resource-sufficient period. Developing efficient energy storage systems is thereby highly sought for the sustainable development of solar energy.

Nowadays, concentrated solar power (CSP)<sup>9,23–29</sup> and photovoltaic (PV)<sup>30–35</sup> serve as the two mainstream technologies for generating solar energy. To begin with, CSP is considered an indirect solar energy-generating strategy. Instead of directly converting solar power to electricity, CSP transforms the sun's energy into high-temperature heat, which subsequently is transformed into electric power. In this system, reflectors are firstly utilized to concentrate the solar energy, which is later used to drive a heat engine as well as an electric generator. In the CSP system, the electricity generated is alternating current, which is easy to distribute on the power network, while PV solar cells are completely distinct from CSP. Unlike the CSP system, which uses solar energy indirectly, PV solar cells directly convert sunlight into electricity. Mechanistically, sunlight is absorbed by a solar PV panel, where the light electrons lose, flow, and directly create a current. The

generated directed current (DC) is subsequently converted into alternating current for distribution.

The application of nanotechnology in the development of solar energy shows remarkable advantages, such as the improvement of working efficiency and energy conversion.

### 10.2.1 Concentrated Solar Power

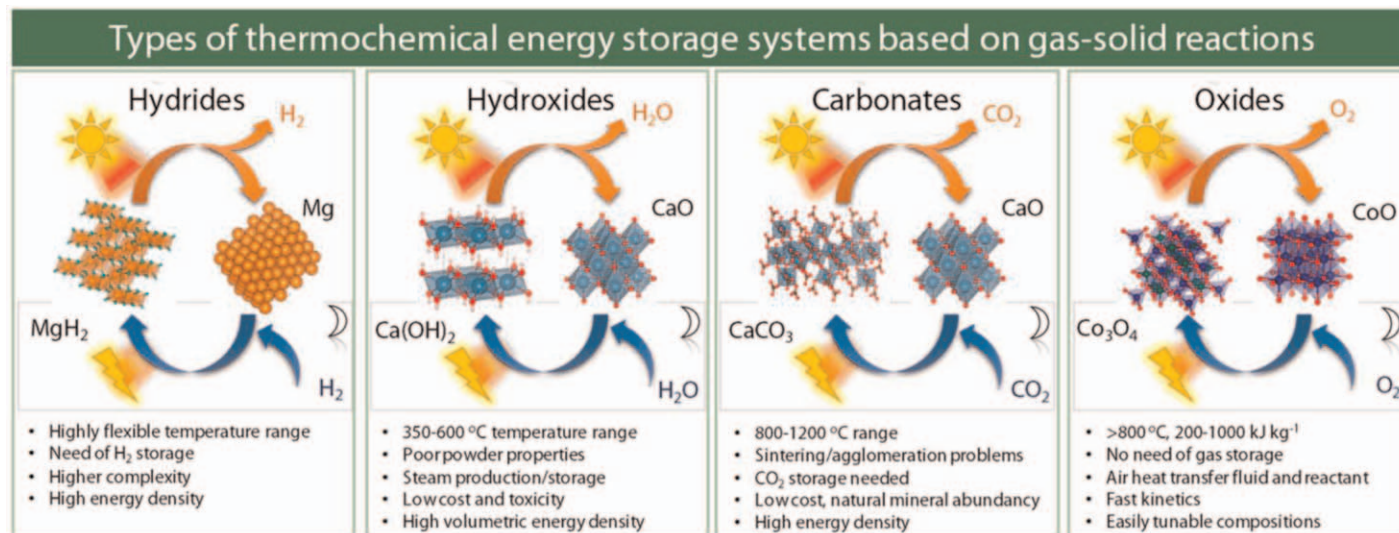
CSP stands out as an excellent solar energy generating strategy, due to its bulk electricity generation capability, overcoming the intermittency of solar resources and enabling generating energy on demand, even during times of insufficient sunlight. Besides, the CSP technology is low in cost, eco-friendly, and reliable. In this system, in the sunlight adequate duration (*i.e.* day cycle), the CSP plant offers solar power for electricity generators as well as the thermal energy storage (TES) system, which next supplies electrical power during the sunlight-inadequate time (*i.e.* night cycle).

There are three main TESs, namely, sensible heat storage (SHS), latent heat storage (LHS), and thermochemical heat storage (TCS). Compared with SHS and LHS, TCS confers benefits such as higher energy storage density, higher flexibility, and no losses of the stored energy for a long period. TCS is based on reversible chemical reactions, in which the charging and discharging process is conducted by carrying out an endothermic and exothermic reaction, respectively. Applying suitable storing materials for thermal storage is one of the key factors in improving the efficiency of TES.

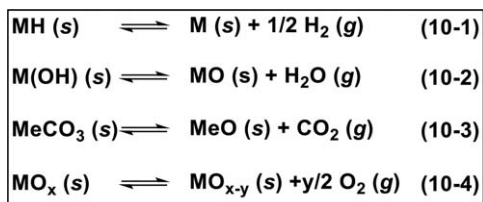
Various storing materials have been used in the TCS system. Figure 10.1 shows four main categories of storing materials, that is, hydrides, hydroxides, metal carbonates, and metal oxides, based on solid–gas reactions, and their reaction schemes, advantages, and disadvantages are summarized as well.<sup>9</sup>

Metal hydrides act as promising candidates for TCS systems because of their outstanding energy storage density.<sup>36</sup> It is calculated that the  $\text{MgH}_2$ -based TES system exhibits an energy storage density of approximately  $2811 \text{ kJ kg}^{-1}$  for each  $100^\circ\text{C}$  of temperature increase. This number is around 20 times higher than the conventional molten salts-based TES system. In this case (eqn (10.1), Scheme 10.1), a metal hydride is dehydrogenated by solar energy, storing solar power in the chemical bonds of the resulting products (*i.e.* solid metal and  $\text{H}_2$ ). The reversed reaction is subsequently conducted to generate energy during the solar energy-insufficient time.

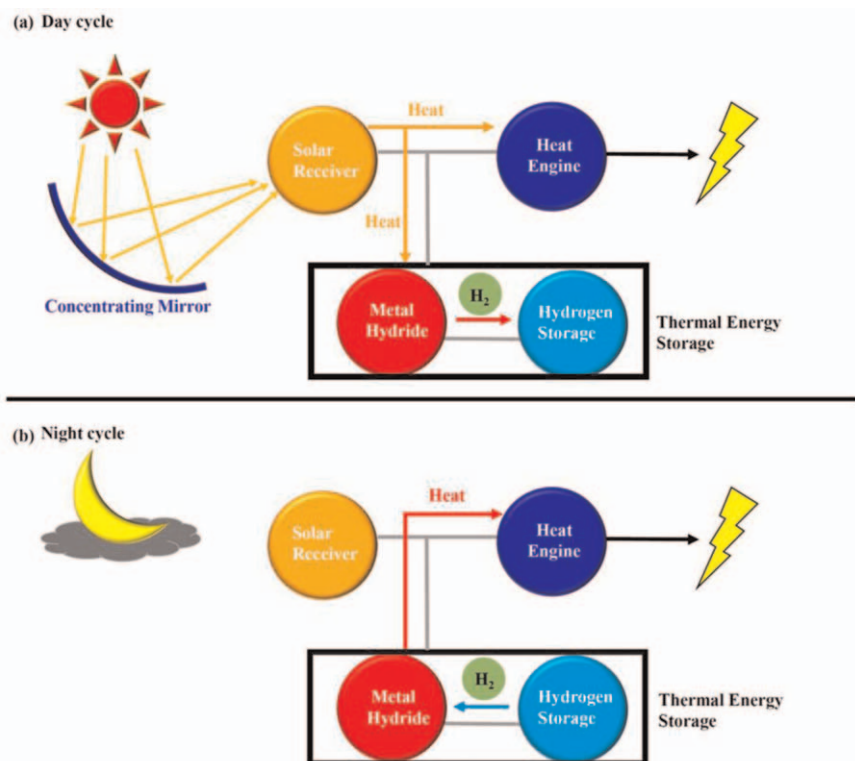
Sheppard and coworkers used underground  $\text{H}_2$  (which is stored in underground salt domes or lines rock caverns) as a component of the metal hydride-based TES system. A series of metal hydrides had been studied for this system, including  $\text{MgH}_2$ ,  $\text{NaH}$ ,  $\text{NaMgH}_3$ ,  $\text{Mg}_2\text{FeH}_6$ , and  $\text{NaMgH}_2\text{F}$ .<sup>37</sup> Owing to the low cost of the underground-stored hydrogen gas, the overall installation cost of this system was reduced to US\$13.7–US\$26.7 per kW h, significantly lower than the cost for the conventional TES system (*i.e.* molten nitrate salts system). Additionally, they also showed that the work efficiency



**Figure 10.1** Summary of the reaction schemes, advantages, and disadvantages of the thermochemical heat storage systems based on gas–solid reactions. Reproduced from ref. 9 with permission from American Chemical Society, Copyright 2019.



**Scheme 10.1** Reaction schemes of hydrides, hydroxides, metal carbonates, and metal oxides.



**Figure 10.2** Schematic diagram of the operation of a CSP system during a) daytime and b) nighttime. Reproduced from ref. 18 with permission from Science and Technology Review Publishing House, Copyright 2021.

of this system could be controlled *via* tuning the reaction conditions of metal hydrides. Apart from the metal hydrides/compressed hydrogen system, the application of two different kinds of metal hydrides in one single TES system has also been studied.<sup>38</sup> In this system, instead of pairing with compressed hydrogen gas, the high-temperature metal hydride ( $\text{MH}_{T_{\text{high}}}$ ) is paired with a low-temperature metal hydride ( $\text{MH}_{T_{\text{low}}}$ ) (Figure 10.2).<sup>18</sup> In the day cycle, solar power is absorbed and stored in  $\text{MH}_{T_{\text{high}}}$ , which releases  $\text{H}_2$  to



promote the generation of  $MH_{T_{low}}$ . The backward reaction –  $H_2$  released from  $MH_{T_{low}}$  into  $MH_{T_{high}}$  – is conducted for energy supply during the night and periods of cloud cover. In such a system, the ideal  $MH_{T_{high}}$  should contain a large ab(de)sorption enthalpy value to enlarge the amount of the heat generated, while  $MH_{T_{low}}$  candidates should be the ones with relatively low ab(de)sorption enthalpy values. Such a low-enthalpy metal hydride in the TES system is beneficial for the reduction of the heat-dissipating amount for both day and night cycles. Moreover, other parameters, including kinetics, thermal conductivity, and cycling stability, need to be considered when choosing metal hydrides for the TES system as well.

Metal hydroxides are another useful material for the TES system. In this system, the dehydration/hydration reactions of metal hydroxides are used for the charging and discharging process (eqn (10.2), Scheme 10.1). In the day cycle, solar energy can be transferred to thermal energy and stored into the metal hydroxide decomposition products (*i.e.* metal oxide and water). In the night cycle, the stored energy can be released on demand *via* the reaction between metal oxide and water. In this system, alkaline earth-based hydroxides, such as  $Mg(OH)_2$ <sup>39–43</sup> and  $Ca(OH)_2$ <sup>44–47</sup> serve as the two most promising candidates, owing to their high energy storage density and low cost.

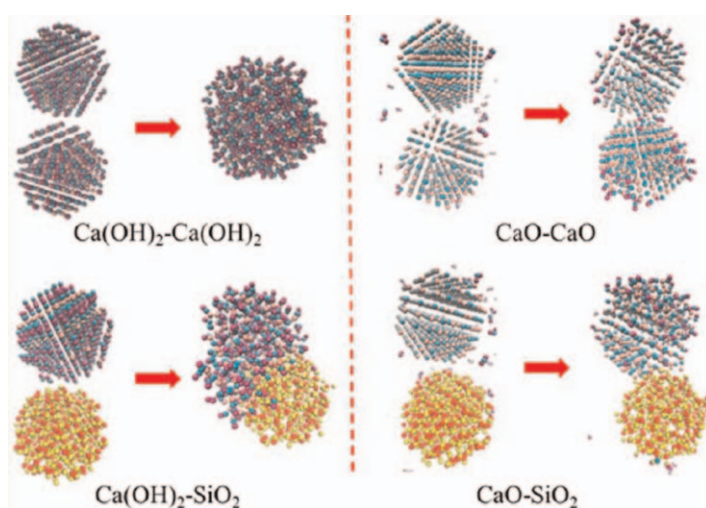
The key challenge in the  $Mg(OH)_2$ -based TES system is the low charging temperature, which significantly restricts its real application implementation. Besides, the backward reaction (hydration) is also conducted under relatively low temperatures (125 °C), and the reaction speed is appreciably slower than dehydration.

Among all strategies proposed to improve the system implementation, the material development approach represented the most propitious one. Mastronardo and coauthors designed a new synthesis approach, termed deposition–precipitation and reverse deposition–precipitation, to improve thermochemical performances.<sup>39</sup> In this case,  $Mg(OH)_2$  was supported by a carbonaceous, such as exfoliated graphite (EG). The resulting hybrid material exhibited good stability and outstanding thermochemical performances. Taking advantage of the smaller particle size,  $Mg(OH)_2$  crystals were able to uniformly disperse over the EG, which in turn facilitated achieving higher dehydration/hydration conversions (84 and 79%, respectively) than for the conventional  $Mg(OH)_2/MgO$  system (52 and 50%). Yu and coworkers reported on  $Mg(OH)_2$  nanosheet-decorated  $MgO$  microbeams for TCS.<sup>40</sup> Through the electron reaction irradiation,  $MgO$  microbeams were generated on the surface of the  $MgO$  pellets, promoting the formation of  $Mg(OH)_2$  on a large scale. Because of the fine powder and no dispersion procedure, this  $MgO/Mg(OH)_2$ -based TES system is expected to be implemented in different TES systems in the future.

Unlike the Mg-based TES system, the calcium-based one possesses the capability of operating at high temperatures (around 400 °C to 600 °C). Besides, the Ca-based system shows a high energy storage density

( $1406 \text{ kJ kg}^{-1}$ ) and is of relatively low cost.  $\text{Ca}(\text{OH})_2$  as a thermochemical energy storage material has been widely studied, from material development to reactor design. The main challenge that remains in this system that needs to be addressed is the cycling instability issue, which is caused by the agglomeration of reactant particles (*i.e.*  $\text{Ca}(\text{OH})_2$  and  $\text{CaO}$ ) during hydration/dehydration reaction cycles. To date, different approaches have been provided to enhance the mechanical stability of the calcium-based materials while simultaneously preserving the high conversion rate of the (de)hydration reaction. Huai and coauthors studied the agglomeration behavior of  $\text{CaO}/\text{Ca}(\text{OH})_2$  particles as a thermochemical energy storage material using molecular dynamics simulations with the reactive force field (Figure 10.3).<sup>45</sup> They revealed that the aggregation of reactant particles caused a negative effect on the cycling stability. In the presence of water, atoms' spatial displacements increased, accelerating the agglomeration rate of  $\text{CaO}$  particles, resulting in the low hydration rate of  $\text{CaO}$ . Moreover, the addition of  $\text{SiO}_2$  particles acted as a barrier to avoid the aggregation of reactant particles during the thermochemical reaction, improving the cycling stability.

Besides, carbonates<sup>23,24,48</sup> and oxides<sup>49–51</sup> have also been extensively studied for use in the TES system. The decarbonation/carbonation reactions are used to absorb/release heat to realize the storage of solar energy (eqn (10.3), Scheme 10.1). The decarbonation temperature of carbonates directly affects the properties of the resulting metal oxide, which in turn influences heat supply. Zhao and coauthors investigated the heat storage/release performance of  $\text{CaCO}_3/\text{CaO}$ -based TES systems with the addition of nanosilica.<sup>48</sup> It was



**Figure 10.3** Agglomeration behavior of calcium hydroxide/calcium oxide as a thermochemical heat storage material using molecular dynamics simulations. Reproduced from ref. 45 with permission from American Chemical Society, Copyright 2017.

concluded that with the doping of nanosilica, the cyclic stability of the  $\text{CaCO}_3/\text{CaO}$  system was increased, and the decarbonation temperature was decreased (between 700 °C and 800 °C). The oxide-based TCS type using reduction–oxidation (redox) reactions of metal oxides (eqn (10.4), Scheme 10.1). In which, reduction (charge) is an endothermic solar-driven process, while oxidation (discharge) is an exothermic process to supply heat.

Notwithstanding the great fundamental achievements that have been obtained, future efforts are still needed to improve the existing technique and/or explore new materials with excellent thermochemical storage performance to deliver high energy storage efficiency for TES systems.

## 10.2.2 Photovoltaic

Because of the presence of the TES system, CSP endows storing solar energy and generating electricity on demand. In contrast to CSP, PV systems only enable producing electricity during the sunlight-sufficient period, without the capability of storing energy. Moreover, the large-scale storage of the generated electricity (for example, in batteries) is also a challenge. To address the limitation of PV systems, solar photovoltaic/thermal (PV/T) systems have been developed, in which solar energy can be converted to electricity and heat, which can be used to supply energy on demand.<sup>20,33,36,52–57</sup>

Rahimi and coauthors studied the cooling performance of channels using Boehmite nanofluid for PV cells.<sup>58</sup> The use of nanofluid leading to the significant reduction in the average PV cell temperature, the recorded reduction temperature (helical channel with 39.7% and the straight channel with 53.8%) was better than that using pure water as a coolant. Xie investigated  $\text{P}_3\text{HT}/\text{CdSe}/\text{CdS}/\text{TiO}_2$  nanorod PV devices with a hybrid layer.<sup>59</sup> In this system, the  $\text{CdS}/\text{CdSe}$  quantum dots improved the light absorption range and created an energy cascade structure that can facilitate charge injection. Mojtabi and colleagues also investigated the cooling of a solar cell by forced convection with an  $\text{Al}_2\text{O}_3/\text{water}$  nanofluid using numerical simulation.<sup>60</sup> They proposed that the used nanofluid enters the cavity at a relatively stable rate at ambient temperature, leading to an improvement in the cooling system. Michael *et al.* used a single rectangular channel to conduct a performance analysis of copper-based PV/T systems by utilizing  $\text{CuO}/\text{water}$  nanofluid.<sup>61</sup> The nanofluid had better performance in terms of cooling and resulted in higher efficiency compared with both  $\text{Cu}/\text{water}$  and pure water systems. Additionally, Al-Shamani and coworkers compared different nanofluids as coolants in the PV/T system, and the one using  $\text{SiC}/\text{water}$  showed the highest efficiency among the tested fluids.<sup>53</sup>

## 10.3 Wind Energy

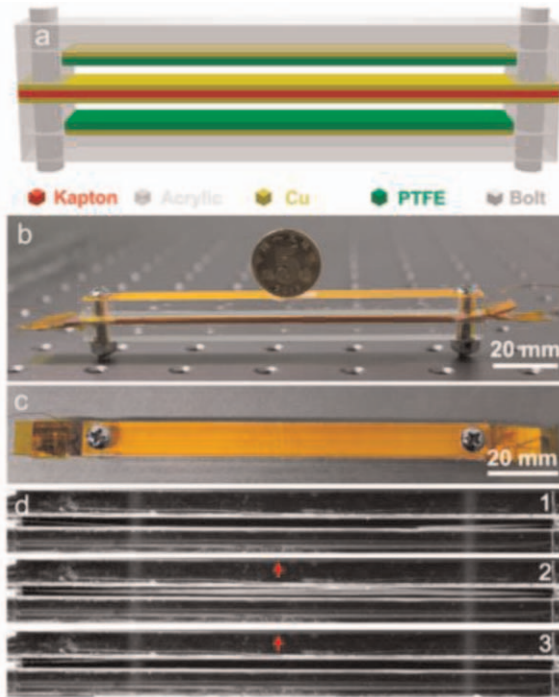
Wind, a clean and widespread type of energy source, has attracted considerable interest and is expected to be one of the electricity suppliers in the future.<sup>62,63</sup> It is assumed that around 4.3% of global electricity was supplied

by wind power technologies by 2015.<sup>64</sup> Exploiting different wind energy harvesters, wind power can be transformed into various available energy forms. For example, wind energy can be converted into electricity by using a wind turbine, while it is transformed into mechanical power using wind-mills.<sup>65</sup> However, similar to solar energy, wind energy system also suffers from serious limitations, including the extra-large size and the high cost of installation, as well as the geographical environment, significantly restraining the widespread use of wind energy generation systems. Thereby, the development of new wind energy collecting systems is essential.

Nanotechnology is extensively applied in wind energy-generating systems to improve wind energy conversion, including for developing new coating materials, lubrication, and high-durability lightweight materials. Also, sensing materials based on nanotechnology can be applied to control the stability or monitor potential damages of wind energy equipment.

Karmouch *et al.* investigated the protective effect of superhydrophobic coating material for a wind turbine blade.<sup>66</sup> This superhydrophobic material was prepared by simply embedding silica nanoparticles into commercial epoxy paint. The resulting coating materials exhibited an outstanding water protection effect with a water contact angle value of about  $152^\circ$ , a hysteresis value less than  $2^\circ$ , and a water drop sliding angle of around  $5^\circ$ . Furthermore, this coating material showed excellent stability under UVC irradiation and water pouring, proving its great potential as a water protection material for various outdoor structures. Polymer-based nanocomposites are widely utilized as protective coating materials for wind blades due to their strong mechanical properties and excellent thermal stability. For example, Ma and coauthors reported on protective coating materials based on carbon nanotubes (CNTs)/polymer nanocomposites for wind blades.<sup>67</sup> The mechanical, electrical, thermal, and barrier properties of the nanocomposite were well investigated. Polyimide/ $\text{Al}_2\text{O}_3$  was examined for use in wind turbine components due to its robust mechanical property and outstanding thermal properties.<sup>68</sup> Polymer-based reinforced composites prepared by the combination of hybrid fibers (*i.e.* carbon, basalt, and glass) and nanopowders (*i.e.* oxides, carbides, and borides) for wind turbine blades were also investigated by Chikhradze's group.<sup>49</sup> Carbon fiber-reinforced polymer based on epoxy/graphene oxide nanocomposites has been utilized in wind turbine blades in order to decrease lightning damages significantly.<sup>69</sup> Additionally, due to the larger radar cross-sections of wind turbines, it appears to be an ongoing threat to radar systems. To address the radar interference issue, Lim and coworkers proposed a stealth wind blade structure, which combines the Salisbury absorbing structure and carbon nanocomposite.<sup>70</sup>

The triboelectric nanogenerator (TENG) features a small scale, low cost, easy fabrication, and portability and has garnered increasing attention in myriad fields.<sup>12,71-74</sup> Notably, various wasted mechanical energies (for example, flowing water, wind, and vibration) can be applied for energy generation *via* changing the TENG structures. The wind-driven triboelectric nanogenerator (WD-TENG) is an emerging technique attracting great



**Figure 10.4** The new wind harvester (triboelectric nanogenerator). Reproduced from ref. 76 with permission from American Chemical Society, Copyright 2015.

attention. WD-TENG acts as a self-supplied sensor, enabling the monitoring of humidity, wind speed, and even the breath-out alcohol concentration.<sup>72</sup> Figure 10.4 clearly shows the comparison between the conventional wind energy harvester (wind turbine) and the new wind energy harvester (WD-TENG) in terms of the mechanism, characteristics, and disadvantages.<sup>12,75,76</sup>

As we know, triboelectrification is a common phenomenon in our life, and almost all materials, from metal, glass, and ceramic to polymers, can generate electrostatic charges through the physical contact between two materials' surfaces. However, collecting and converting such tiny energy into useful energy forms is challenging. Several strategies have been proposed to address this problem, of which modification of the triboelectric materials and structures for fabricating WD-TENG can significantly alter the output performance of WD-TENG.

The triboelectric ability of different materials will vary according to different polarities. Given the WE-TENG requirement (such as durability, toughness, and economic efficiency), metal and artificial polymer are rendered as two competitive candidates to achieve the expected performance. Some reviews and good articles have well illustrated some of the positive and negative materials used to manufacture WD-TENG.<sup>12,77–80</sup>

## 10.4 Geothermal Energy

The heat energy of the earth is termed geothermal energy, which has attracted increased consideration.<sup>14,81</sup> It is estimated that the capacity of the total installed geothermal systems globally significantly increased from 1300 MWe to 10 000 MWe from 1975 to 2007.<sup>82</sup> Geothermal energy can be directly utilized or converted to electricity for use *via* a geothermal power plant system. In a typical geothermal power plant, the heat from hot rocks under the ground can be absorbed through working fluid/water, which subsequently transforms the thermal energy into electricity *via* a steam turbine.

One of the main concerns in the geothermal power plant is the corrosion problem of the heat exchanger, resulting in an increase in cost for installation and maintenance. Taking advantage of nanotechnology, nanocoating has been applied in the geothermal power plant to effectively reduce corrosion. For instance, Sugama prepared a polyphenylene sulfide (PPS)/montmorillonite (MMT) clay nanocomposite coating to prevent carbon steel corrosion.<sup>83</sup> Through a process of octadecylamine (ODA) intercalation to molten PPS co-intercalation to exfoliation, the PPS/MMT nanocomposite was successfully prepared. Exploiting this advanced PPS nanocomposite as a corrosion-preventing coating for carbon steel in a simulated geothermal environment at around 300 °C, a coating of ~150 μm thickness adequately protected the steel against hot brine-caused corrosion. Besides, other nanocoatings, such as nano-ZrO<sub>2</sub>-TiO<sub>2</sub> coatings,<sup>84</sup> polytetrafluoroethylene (PTFE)/carbon nanotube,<sup>84</sup> and SiO<sub>2</sub>-based materials,<sup>85</sup> also exhibit excellent corrosion protecting effects on the geothermal heat exchanger.

## 10.5 Hydrogen Energy

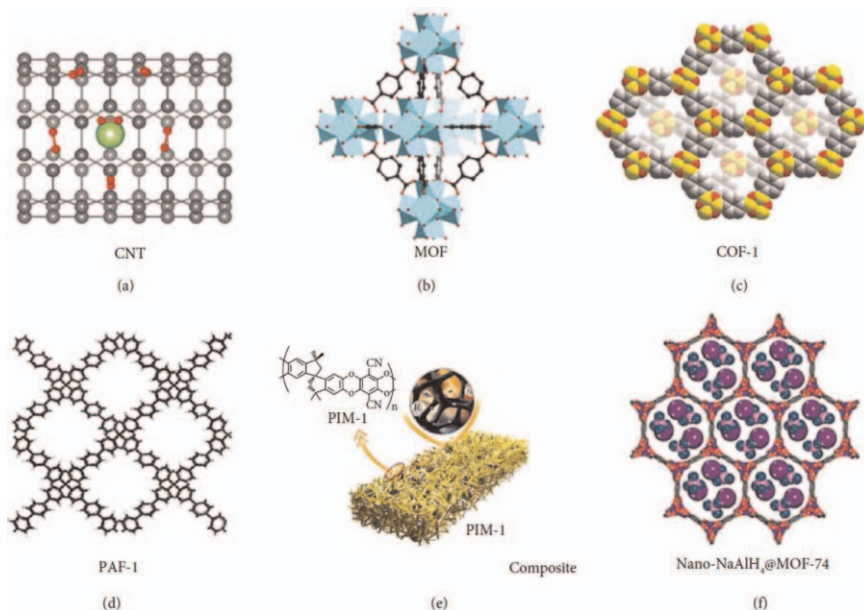
In contrast to previously presented green energy sources (*i.e.* solar energy, wind power, and geothermal energy), with their unavoidable inherent intermittency, hydrogen energy is not subjected to natural or geographical restrictions and is thus considered one of the ideal substitutions for fossil-based fuel. Moreover, hydrogen energy shows environment friendly, renewable, and affordable advantages.<sup>2,15,16,38,86-91</sup>

In the past two decades, hydrogen technology has been a well-developed and fundamental achievement that has been obtained.<sup>17,18,87</sup> The key challenge in the hydrogen energy system is the hydrogen storage problem due to the extremely low volumetric energy density of H<sub>2</sub> (with only 0.01 MJ L<sup>-1</sup> at standard temperature and pressure [STP] – 0 °C and 1 atm). Therefore, effectively storing hydrogen is extremely desired for the development of the sustainable alternative green energy. According to the US Department of Energy (DOE), the ultimate onboard hydrogen storage goal is 0.065 kg H<sub>2</sub> per kg system and 0.050 kg L<sup>-1</sup> for gravimetric and volumetric values, respectively.

In order to realize effective hydrogen storage, various strategies have been proposed. First of all, hydrogen gas was proposed to be stored under high pressure and/or extremely low temperature.<sup>92–95</sup> This is because, under such storage conditions, the density of hydrogen gas can be physically increased, enhancing the storage capacity. For example, the hydrogen density increased from  $0.08988 \text{ g L}^{-1}$  (STP) to  $87 \text{ g L}^{-1}$  (276 bar and 20 K), and a hydrogen storage capacity of 0.058 gravimetric kg H<sub>2</sub> per kg can be achieved. In this case, though relatively high storage capacity has been obtained, various concerns are raised, including the overall initial investment and serious safety issues during the hydrogen storage, operation, and transportation.<sup>90,92,93,96</sup> Converting hydrogen into liquid hydrogen-rich molecules, such as formic acid, methanol, ammonia, and liquid organic hydrogen carriers, has subsequently been widely applied to store hydrogen.<sup>97–101</sup> These liquid hydrogen-rich molecules have low toxicity, are of reasonable cost and are easy to transport. Unfortunately, these liquid molecules suffer from relatively low hydrogen capacity, intricate (de)hydrogenation reactions, and complex purification processes. Besides, another promising hydrogen storage approach is solid hydrogen storage, which involves storing hydrogen in the porous nanomaterials in the solid state.<sup>102–110</sup> In contrast to traditional storage approaches (*i.e.* compressed gas and cryogenic storage), nanomaterial-based hydrogen storage strategies rely on physisorption and/or chemisorption to immobilize and store hydrogen in solid state. The attractive points of this system include but are not limited to high hydrogen capacity, low operational hindrance, safety, transportability, tradability, and release on demand. In this subsection, we will focus on the discussion of hydrogen storage systems based on nanomaterials in the solid state.

To efficiently solve the hydrogen storage problem, nanotechnology was applied to improve the hydrogen storage efficiency in the solid storage system. Due to the high surface areas, porous structures, and adjustable pore size and shape, nanostructured materials have widely been explored for hydrogen storage. Here, six main types of nanomaterials have been discussed (Figure 10.5): nanoporous carbon materials,<sup>18,104,111,112</sup> metal-organic frameworks (MOFs),<sup>106,108,113,114</sup> covalent organic frameworks (COFs),<sup>109,115–118</sup> porous aromatic frameworks (PAFs),<sup>119–123</sup> nanoporous organic polymers,<sup>124–128</sup> and nanoscale hydrides.<sup>129–132</sup>

To begin with, nanoporous carbon materials, including activated carbon (AC), carbon nanofibers (CNFs), and CNTs, are widely applied for hydrogen storage.<sup>99,106,107</sup> These nanoporous carbon materials, with high porosity, low weight, and reasonable price, are one of the ideal hydrogen adsorbents. Dating back to 1997, Heben and coworkers had demonstrated that gas could condense to high density inside single-walled nanotubes (SWNTs) and exhibited great potential as hydrogen storage materials (with up to 5 to 10 wt% hydrogen uptake content).<sup>133</sup> After that, numerous studies have been conducted in this area and great achievements have been attained. For instance, Fuertes and colleagues synthesized a polypyrrole-based carbon material with ultrahigh surface area (3000 to 3500  $\text{m}^2 \text{g}^{-1}$ ), exhibiting excellent hydrogen



**Figure 10.5** Overview and examples of solid hydrogen storage systems. (a) Nanoporous carbon materials (carbon nanotube [CNT],<sup>112</sup> (b) MOF,<sup>114</sup> (c) COF,<sup>118</sup> (d) PAFs,<sup>123</sup> (e) structure of a nanoporous organic polymer [PIM-1] and the composite with a nanoporous filler,<sup>128</sup> and (f) nanohydrides (sodium alanate [NaAlH<sub>4</sub>]) confined in the nanopores of a MOF (MOF-74).<sup>132</sup> Reproduced from ref. 112 with permission from American Chemical Society, Copyright 2019. Reproduced from ref. 114 with permission from John Wiley & Sons, Copyright © 2018 WILEY-VCH Verlag GmbH & Co. KGaA, Weinheim. Reproduced from ref. 118 with permission from American Chemical Society, Copyright 2015. Reproduced from ref. 123 with permission from John Wiley & Sons, Copyright © 2009 WILEY-VCH Verlag GmbH & Co. KGaA, Weinheim. Reproduced from ref. 128, <https://doi.org/10.1007/s10450-019-00065-x>, under the terms of the CC BY 4.0 license <https://creativecommons.org/licenses/by/4.0/>. Reproduced from ref. 132 with permission from Springer Nature, Copyright 2013.

storage performance (*i.e.* hydrogen storage capacity up to 7.03 wt% at 77 K and 20 bar).<sup>134</sup> Besides, Ngadi *et al.* studied the hydrogen storage capacity using the AC produced from empty fruit bunch (EFB).<sup>135</sup> The AC samples were activated using physical and chemical processes, resulting in AC with surface areas of 305–687 m<sup>2</sup> g<sup>-1</sup> and microporous structures up to 94%, respectively. This AC was used to store hydrogen with a maximum hydrogen adsorption capacity of 2.14 wt% at 20 bar.

MOFs are attractive nanomaterials with crystalline porous structures and have extensively been explored for gas storage.<sup>106,108,113,114</sup> Notably, the nanostructures of MOFs, including the framework topology, surface area, and pore size, can be synthetically controlled, leading to adjustable gas



storage capability. Yaghi and coworkers firstly investigated hydrogen storage in MOFs (*i.e.* MOF-5).<sup>136</sup> The designed MOF-5 was prepared by the reaction between zinc salt and 1,4-benzenedicarboxylic acid (BDC) to produce  $\text{Zn}_4\text{O}(\text{BDC})_3$  (MOF-5). The resultant MOF-5 had a cubic 3D crystal structure, with a hydrogen intake value of 4.5 wt% at 78 K and 1 wt% at room temperature and 20 bar. Subsequently, some new MOF materials were developed by introducing new moieties (such as ethynylene units and carboxylic groups) in this MOF-5, obviously enhancing the hydrogen storage performance, regardless of the similar skeletons.<sup>137,138</sup> Besides, Yaghi's group reported another MOF-based hydrogen adsorbent (*i.e.* MOF-210) that exhibited excellent hydrogen intake capacity, as high as 17.6 wt% (77 K and 80 bar), which represented one of the highest hydrogen storage capacities so far.<sup>139</sup> Furthermore, the introduction of active metals (such as sodium (Na), magnesium (Mg), lithium (Li), beryllium (Be), titanium (Ti), copper (Cu), and zinc (Zn)) into MOFs serves as a promising strategy to further improve the hydrogen storage performance. For example, Long and coauthors reported the first Be-based MOF and revealed its application in hydrogen storage.<sup>140</sup> The resulting Be-MOF exhibited an outstanding hydrogen absorption capacity up to 2.3 wt% at 298 K and 95 bar, significantly higher than that with unmodified MOF (for example, MOF-177), which only showed a 0.62 wt% hydrogen uptake at similar conditions.

COFs are porous organic frameworks formed *via* covalent connection and feature large surface areas, associated porosity, low density, structure versatility, low cost, and high stability.<sup>109,115–117</sup> According to the chemical functionalities at the organic building blocks, COFs show different promising applications in various fields, including hydrogen storage. The hydrogen uptake behavior and capacity of three groups of COFs were investigated.<sup>141</sup> According to their structural dimensions and pore sizes, the studied COF candidates were grouped into three types. COF-1 and COF-6 were classified into group 1 with 2D structures and small 1D pores; COF-5, COF-8, and COF-10 were in group 2, containing 2D structures with large 1D pores; and COF-102 and COF-103, consisting of 3D structures and 3D medium-sized pores, were in group 3. The results revealed that group 3 COFs outperformed the ones in groups 1 and 2 and rivaled the best MOFs and other nanomaterials in terms of their gas uptake abilities. For example, the hydrogen uptake capacity of COF-102 reached 7.2 wt% at 77 K and 35 bar and 10.0 wt% at 77 K and 100 bar. Moreover, the hydrogen volumetric uptake of COF-102 achieved was  $40.4 \text{ gL}^{-1}$ , which represented the best performance of these 3D-COFs. Based on COF-102, Froudakis and coworkers designed 3D COFs with enhanced hydrogen uptake ability.<sup>142</sup> According to the simulation result, the gravimetric hydrogen uptake capacity of these designed COFs enabled to exceed 25 wt% at 77 K and 6 wt% at room temperature.

PAFs are another class of interesting porous organic materials with a tetrahedrally diamond-like structure.<sup>119–122,143</sup> PAFs possess similar properties to COFs, such as high porosity, large surface area, and low mass

densities. In contrast to COFs formed by reversible organic condensation reactions, PAFs are generated through irreversible cross-coupling reactions and, therefore, enable PAFs to have robust skeletons and excellent stabilities. Taking advantage of the unique structure and properties, PAFs display great potential in different fields, including hydrogen storage, catalysis, molecular separation, and molecule sensing. In 2009, Zhu's group reported the first PAF (*i.e.* PAF-1) and studied its application in hydrogen storage.<sup>123</sup> The synthesized PAF-1 had a large BET surface area of  $5600 \text{ m}^2 \text{ g}^{-1}$  and a high hydrogen storage capacity of 7.0 wt% at 77 K and 48 bar. Moreover, Sun *et al.* proposed to enhance the hydrogen storage capacity of the PAF with the addition of a lithium tetrazolide group.<sup>144</sup> The prepared PAF-4 showed a hydrogen uptake content of 20.7 wt% (at 77 K and 100 bar) and 4.9 wt% (at 233 K and 100 bar).

Besides, other nanoporous organic polymers, such as hyper-crosslinked polymers (HCPs), conjugated microporous polymers (CMPs), and polymers of intrinsic microporosity (PIMs), have also been widely used as gas storage materials, adsorbents, separation materials, and catalyst carriers.<sup>124–127</sup>

Hydrogen can be stored into nanomaterials *via* not only physical adsorption but also chemical adsorption (*i.e.* hydrides), in which atomic hydrogen chemically bonds with the metal or element.<sup>129–131</sup> Hydrides, including metal hydrides and chemical hydrides, display high hydrogen densities, for example, aluminum hydride ( $\text{AlH}_3$ ) with 10 wt%  $\text{H}_2$ ; magnesium hydride ( $\text{MgH}_2$ ) having 7.6 wt%  $\text{H}_2$ ; and ammonia borane ( $\text{BH}_3 \cdot \text{NH}_3$ , AB) with a hydrogen content as high as 19.6 wt%. However, due to the strong chemical bonding, these hydrides show sluggish kinetics and unacceptable hydrogen desorption temperature, limiting their applications in reversible onboard storage. Several approaches have been proposed, and nanoscale hydrides stand out as an ideal solution to this problem. In contrast to pure hydrides, nanoscale hydrides process a new nanoarchitecture with a higher surface area, additional hydrogen reaction sites, and shorter diffusion distances to conspicuously enhance the kinetics and thermodynamics of hydrogen ab(de)sorption properties.<sup>145–148</sup> For example,  $\text{MgH}_2$ @carbon aerogel microspheres have been used to store hydrogen with significantly enhanced (de)hydrogenation rates.<sup>149</sup> The prepared composite enabled quick uptake of 6.2 wt%  $\text{H}_2$  within 5 min at 275 °C and release of 4.9 wt%  $\text{H}_2$  within 100 min at 350 °C. Besides, the same group also modified  $\text{LiBH}_4$  with 3D porous fluorinated graphene to improve the hydrogen storage performance.<sup>150</sup> The resulting nanohydrides reduced the hydrogen release temperature to 204 °C, which was around 120 °C lower than that of pure  $\text{LiBH}_4$ . Moreover, it allowed the release of 3.45 wt% hydrogen at 400 °C within 1000 s, which was 2.57 times faster than pure  $\text{LiBH}_4$ .

## 10.6 Conclusions and Perspectives

Seeking a substitute for conventional fossil-based energy is imperative due to the grave concerns caused by their combustion. Green energy sources,

such as solar, wind, geothermal, and hydrogen, with cost-attractive, sustainable, and environmentally friendly advantages, are considered ideal candidates for the expected energy system transition. The application of nanotechnology in the development of alternative renewable energy systems is an efficient and economically and environmentally acceptable option to enhance working efficiency, decrease energy systems' dependency on fossil fuels, and overcome their related issues.

Though great advancements have been attained in the development of renewable energies using nanotechnology over the past decade, more efforts are still needed to further improve the efficiency of energy systems, for example, exploring new nanocatalysts, nanoreactors, and/or nanomaterials to facilitate the growth of renewable energies.

## References

1. P. Poizot, J. Gaubicher, S. Renault, L. Dubois, Y. Liang and Y. Yao, *Chem. Rev.*, 2020, **120**, 6490–6557.
2. T. Asefa, K. Koh and C. W. Yoon, *Adv. Energy Mater.*, 2019, **9**, 1901158.
3. M. Shahbaz, C. Raghutla, K. R. Chittedi, Z. Jiao and X. V. Vo, *Energy*, 2020, **207**, 118162.
4. E. Hatipoglu, S. Al Muhanna and B. Efirid, *Russ. J. Econ.*, 2021, **6**, 358–373.
5. L. J. Sonter, M. C. Dade, J. E. M. Watson and R. K. Valenta, *Nat. Commun.*, 2020, **11**, 4174.
6. A. Harjanne and J. M. Korhonen, *Energy Policy*, 2019, **127**, 330–340.
7. H. Wang, Z. Lei, X. Zhang, B. Zhou and J. Peng, *Energy Convers. Manage.*, 2019, **198**, 111799.
8. Z. Jun Wang, H. Song, H. Liu and J. Ye, *Angew. Chem. Int. Ed.*, 2020, **59**, 8016–8035.
9. A. J. Carrillo, J. González-Aguilar, M. Romero and J. M. Coronado, *Chem. Rev.*, 2019, **119**, 4777–4816.
10. S. D. Tilley, *Adv. Energy Mater.*, 2019, **9**, 1802877.
11. S. Boncel, A. Kolanowska, A. W. Kuziel and I. Krzyżewska, *ACS Appl. Nano Mater.*, 2018, **1**, 6542–6555.
12. B. Chen, Y. Yang and Z. L. Wang, *Adv. Energy Mater.*, 2018, **8**, 1702649.
13. S. M. Lu, *Renewable Sustainable Energy Rev.*, 2018, **81**, 2902–2921.
14. L. Zhang, S. Chen and C. Zhang, *Energy Sci. Eng.*, 2019, **7**, 1428–1450.
15. J. Zhu, L. Hu, P. Zhao, L. Y. S. Lee and K. Y. Wong, *Chem. Rev.*, 2020, **120**, 851–918.
16. C. Lang, Y. Jia and X. Yao, *Energy Storage Mater.*, 2020, **26**, 290–312.
17. J. Zheng, H. Zhou, C. G. Wang, E. Ye, J. W. Xu, X. J. Loh and Z. Li, *Energy Storage Mater.*, 2021, **35**, 695–722.
18. J. Zheng, C.-G. Wang, H. Zhou, E. Ye, J. Xu, Z. Li and X. J. Loh, *Research*, 2021, 3750689.
19. S. T. Bryant, K. Straker and C. Wrigley, *J. Cleaner Prod.*, 2020, **244**, 118725.

20. R. Seitz, B. P. Moller, A. Thielmann, A. Sauer, M. Meister, M. Pero, O. Kleine, C. Rohde, A. Bierwisch, M. de Vries and V. Kayser, *Technol. Rep.*, 2013, 1–102.
21. M. Sarno, *Stud. Surf. Sci. Catal.*, 2019, **179**, 431–458.
22. N. S. Lewis and D. G. Nocera, *Proc. Natl. Acad. Sci. U. S. A.*, 2006, **103**, 15729–15735.
23. M. Benitez-Guerrero, J. M. Valverde, P. E. Sanchez-Jimenez, A. Perejon and L. A. Perez-Maqueda, *Sol. Energy*, 2017, **153**, 188–199.
24. M. Benitez-Guerrero, B. Sarrion, A. Perejon, P. E. Sanchez-Jimenez, L. A. Perez-Maqueda and J. Manuel Valverde, *Sol. Energy Mater. Sol. Cells*, 2017, **168**, 14–21.
25. A. Omar, A. Nashed, Q. Li, G. Leslie and R. A. Taylor, *Renewable Sustainable Energy Rev.*, 2020, **119**, 109609.
26. K. Mohammadi, M. Saghafifar, K. Ellingwood and K. Powell, *Desalination*, 2019, **468**, 114083.
27. D. Barley, R. Vidu and P. Stroeve, *Sol. Energy Mater. Sol. Cells*, 2011, **95**, 2703–2725.
28. A. Peinado Gonzalo, A. Pliego Marugán and F. P. García Márquez, *Appl. Energy*, 2019, **255**, 113893.
29. S. Pramanik and R. V. Ravikrishna, *Appl. Therm. Eng.*, 2017, **127**, 602–637.
30. I. Mathews, S. N. Kantareddy, T. Buonassisi and I. M. Peters, *Joule*, 2019, **3**, 1415–1426.
31. P. G. V. Sampaio and M. O. A. González, *Renewable Sustainable Energy Rev.*, 2017, **74**, 590–601.
32. L. Hernández-Callejo, S. Gallardo-Saavedra and V. Alonso-Gómez, *Sol. Energy*, 2019, **188**, 426–440.
33. M. Vinoth, S. Surendhiran, P. R. Senthilmurugan and V. Rajendran, *J. Electron. Mater.*, 2019, **48**, 4589–4597.
34. M. Gul, Y. Kotak and T. Muneer, *Energy Explor. Exploit.*, 2016, **34**, 485–526.
35. A. A. F. Husain, W. Z. W. Hasan, S. Shafie, M. N. Hamidon and S. S. Pandey, *Renewable Sustainable Energy Rev.*, 2018, **94**, 779–791.
36. D. N. Harries, M. Paskevicius, D. A. Sheppard, T. E. C. Price and C. E. Buckley, *Proc. IEEE*, 2012, **100**, 539–549.
37. D. A. Sheppard and C. E. Buckley, *Int. J. Hydrogen Energy*, 2019, **44**, 9143–9163.
38. Q. Lai, M. Paskevicius, D. A. Sheppard, C. E. Buckley, A. W. Thornton, M. R. Hill, Q. Gu, J. Mao, Z. Huang, H. K. Liu, Z. Guo, A. Banerjee, S. Chakraborty, R. Ahuja and K. F. Aguey-Zinsou, *ChemSusChem*, 2015, **8**, 2789–2825.
39. E. Mastronardo, L. Bonaccorsi, Y. Kato, E. Piperopoulos, M. Lanza and C. Milone, *Appl. Therm. Eng.*, 2017, **120**, 626–634.
40. Y. Kim, N. Kim, T. S. Kim, G. J. Park, Y. Kwon and H. K. Yu, *Ceram. Int.*, 2019, **45**, 18908–18913.
41. J. Yan, Z. H. Pan and C. Y. Zhao, *Appl. Energy*, 2020, **275**, 115356.

42. M. Bhourri and I. Bürger, *Int. J. Hydrogen Energy*, 2017, **42**, 16632–16644.
43. E. Piperopoulos, E. Mastronardo, M. Fazio, M. Lanza, S. Galvagno and C. Milone, *Appl. Energy*, 2018, **215**, 512–522.
44. C. M. Valverde-Pizarro, L. Briones, E. Sanz, J. M. Escola, R. Sanz, J. González-Aguilar and M. Romero, *Renew. Energy*, 2020, **162**, 587–595.
45. M. Xu, X. Huai and J. Cai, *J. Phys. Chem. C*, 2017, **121**, 3025–3033.
46. J. Yan, C. Y. Zhao, B. Q. Xia and T. Wang, *Energy*, 2019, **186**, 115837.
47. K. G. Sakellariou, Y. A. Criado, N. I. Tsongidis, G. Karagiannakis and A. G. Konstandopoulos, *Sol. Energy*, 2017, **146**, 65–78.
48. A. A. Khosa and C. Y. Zhao, *Sol. Energy*, 2019, **188**, 619–630.
49. N. M. Chikhradze, F. D. S. Marquis and G. S. Abashidze, *J. Mater. Res. Technol.*, 2015, **4**, 60–67.
50. X. Zhou, M. Mahmood, J. Chen, T. Yang, G. Xiao and M. L. Ferrari, *Appl. Therm. Eng.*, 2019, **159**, 113965.
51. L. André, S. Abanades and L. Cassayre, *J. Solid State Chem.*, 2017, **253**, 6–14.
52. S. S. Joshi and A. S. Dhoble, *Renewable Sustainable Energy Rev.*, 2018, **92**, 848–882.
53. A. N. Al-Shamani, K. Sopian, S. Mat, H. A. Hasan, A. M. Abed and M. H. Ruslan, *Energy Convers. Manage.*, 2016, **124**, 528–542.
54. F. Huide, Z. Xuxin, M. Lei, Z. Tao, W. Qixing and S. Hongyuan, *Energy Convers. Manage.*, 2017, **140**, 1–13.
55. A. H. A. Al-Waeli, K. Sopian, J. H. Yousif, H. A. Kazem, J. Boland and M. T. Chaichan, *Energy Convers. Manage.*, 2019, **186**, 368–379.
56. S. M. Sultan and M. N. Ervina Efzan, *Sol. Energy*, 2018, **173**, 939–954.
57. Y. Jia, G. Alva and G. Fang, *Renewable Sustainable Energy Rev.*, 2019, **102**, 249–265.
58. N. Karami and M. Rahimi, *Energy Convers. Manage.*, 2014, **86**, 275–285.
59. Y. L. Xie, *Electrochim. Acta*, 2013, **105**, 137–141.
60. M. Elmir, R. Mehdaoui and A. Mojtabi, *Energy Procedia*, 2012, **18**, 594–603.
61. J. J. Michael and S. Iniyar, *Sol. Energy*, 2015, **119**, 439–451.
62. S. Chu and A. Majumdar, *Nature*, 2012, **488**, 294–303.
63. G. M. Joselin Herbert, S. Iniyar, E. Sreevalsan and S. Rajapandian, *Renewable Sustainable Energy Rev.*, 2007, **11**, 1117–1145.
64. R. Wiser, K. Jenni, J. Seel, E. Baker, M. Hand, E. Lantz and A. Smith, *Nat. Energy*, 2016, **1**, 1–8.
65. M. H. Ahmadi, M. Ghazvini, M. A. Nazari, M. A. Ahmadi, F. Pourfayaz, G. Lorenzini and T. Ming, *Int. J. Energy Res.*, 2019, **43**, 1387–1410.
66. R. Karmouch and G. G. Ross, *Appl. Surf. Sci.*, 2010, **257**, 665–669.
67. P. C. Ma and Y. Zhang, *Renewable Sustainable Energy Rev.*, 2014, **30**, 651–660.
68. W. Hu, B. X. Du, J. Li, Y. Liu and M. Liu, in *IEEE Innovative Smart Grid Technologies - Asia, ISGT Asia*, 2012, pp. 1–4.
69. O. Vryonis, T. Andritsch, A. S. Vaughan and P. L. Lewin, in *Annual Report - Conference on Electrical Insulation and Dielectric Phenomena, CEIDP*, 2016, pp. 635–638.

70. J. Kim and D. Lim, *Wind Energy*, 2014, **17**, 451–460.
71. Y. Yang and Z. L. Wang, *Nano Energy*, 2014, **14**, 245–256.
72. Z. Wen, J. Chen, M. H. Yeh, H. Guo, Z. Li, X. Fan, T. Zhang, L. Zhu and Z. L. Wang, *Nano Energy*, 2015, **16**, 38–46.
73. T. Quan, X. Wang, Z. L. Wang and Y. Yang, *ACS Nano*, 2015, **9**, 12301–12310.
74. F. R. Fan, Z. Q. Tian and Z. Lin Wang, *Nano Energy*, 2012, **1**, 328–334.
75. S. Wang, X. Wang, Z. L. Wang and Y. Yang, *ACS Nano*, 2016, **10**, 5696–5700.
76. S. Wang, X. Mu, X. Wang, A. Y. Gu, Z. L. Wang and Y. Yang, *ACS Nano*, 2015, **9**, 9554–9563.
77. K. Zhao, Z. L. Wang and Y. Yang, *ACS Nano*, 2016, **10**, 9044–9052.
78. Y. Xie, S. Wang, L. Lin, Q. Jing, Z. H. Lin, S. Niu, Z. Wu and Z. L. Wang, *ACS Nano*, 2013, **7**, 7119–7125.
79. M. L. Seol, J. H. Woo, S. B. Jeon, D. Kim, S. J. Park, J. Hur and Y. K. Choi, *Nano Energy*, 2015, **14**, 201–208.
80. L. Zhang, B. Zhang, J. Chen, L. Jin, W. Deng, J. Tang, H. Zhang, H. Pan, M. Zhu, W. Yang and Z. L. Wang, *Adv. Mater.*, 2016, **28**, 1650–1656.
81. D. Moya, C. Aldás and P. Kaparaju, *Renewable Sustainable Energy Rev.*, 2018, **94**, 889–901.
82. K. H. Williamson, R. P. Gunderson, G. M. L. Gallup and K. Kitz, *Proc. IEEE*, 2001, **89**, 1783–1791.
83. T. Sugama, *Mater. Lett.*, 2006, **60**, 2700–2706.
84. Y. Cai, X. Quan, G. Li and N. Gao, *Ind. Eng. Chem. Res.*, 2016, **55**, 11480–11494.
85. C. Ning, L. Mingyan and Z. Weidong, *Ind. Eng. Chem. Res.* 2012, **51**, 6001–6017.
86. S. Guo, Q. Liu, J. Sun and H. Jin, *Renewable Sustainable Energy Rev.*, 2018, **91**, 1121–1147.
87. A. Midilli, M. Ay, I. Dincer and M. A. Rosen, *Renewable Sustainable Energy Rev.*, 2005, **9**, 255–271.
88. Y. Sun, C. Shen, Q. Lai, W. Liu, D. W. Wang and K. F. Aguey-Zinsou, *Energy Storage Mater.*, 2018, **10**, 168–198.
89. Y. Mao, Y. Gao, W. Dong, H. Wu, Z. Song, X. Zhao, J. Sun and W. Wang, *Appl. Energy*, 2020, **267**, 114860.
90. J. O. Abe, A. P. I. Popoola, E. Ajenifuja and O. M. Popoola, *Int. J. Hydrogen Energy*, 2019, **44**, 15072–15086.
91. A. Pugazhendhi, S. Shobana, D. D. Nguyen, J. R. Banu, P. Sivagurunathan, S. W. Chang, V. K. Ponnusamy and G. Kumar, *Int. J. Hydrogen Energy*, 2019, **44**, 1431–1440.
92. T. Sinigaglia, F. Lewiski, M. E. Santos Martins and J. C. Mairesse Siluk, *Int. J. Hydrogen Energy*, 2017, **42**, 24597–24611.
93. L. Wang, B. Wang, S. Wei, Y. Hong and C. Zheng, *Composites, Part B*, 2016, **97**, 274–281.
94. A. Ozarslan, *Int. J. Hydrogen Energy*, 2012, **37**, 14265–14277.
95. C. J. Webb, *J. Phys. Chem. Solids*, 2015, **84**, 96–106.

96. S. W. Jorgensen, *Curr. Opin. Solid State Mater. Sci.*, 2011, **15**, 39–43.
97. K. Sordakis, C. Tang, L. K. Vogt, H. Junge, P. J. Dyson, M. Beller and G. Laurenczy, *Chem. Rev.*, 2018, **118**, 372–433.
98. H. Zhong, M. Iguchi, M. Chatterjee, Y. Himeda, Q. Xu and H. Kawanami, *Adv. Sustainable Syst.*, 2018, **2**, 1700161.
99. P. Preuster and J. Albert, *Energy Technol.*, 2018, **6**, 501–509.
100. A. Álvarez, A. Bansode, A. Urakawa, A. V. Bavykina, T. A. Wezendonk, M. Makkee, J. Gascon and F. Kapteijn, *Chem. Rev.*, 2017, **117**, 9804–9838.
101. D. A. Bulushev and J. R. H. Ross, *ChemSusChem*, 2018, **11**, 821–836.
102. Z. Sun, X. Lu, F. M. Nyahuma, N. Yan, J. Xiao, S. Su and L. Zhang, *Front. Chem.*, 2020, **8**, 552.
103. A. M. Abioye and F. N. Ani, *Renewable Sustainable Energy Rev.*, 2015, **52**, 1282–1293.
104. S. Peng, L. Li, J. Kong Yoong Lee, L. Tian, M. Srinivasan, S. Adams and S. Ramakrishna, *Nano Energy*, 2016, **22**, 361–395.
105. A. Schoedel, M. Li, D. Li, M. O’Keeffe and O. M. Yaghi, *Chem. Rev.*, 2016, **116**, 12466–12535.
106. H. Wang, Q. L. Zhu, R. Zou and Q. Xu, *Chem*, 2017, **2**, 52–80.
107. L. Jiao, J. Y. R. Seow, W. S. Skinner, Z. U. Wang and H. L. Jiang, *Mater. Today*, 2019, **27**, 43–68.
108. A. J. Howarth, Y. Liu, P. Li, Z. Li, T. C. Wang, J. T. Hupp and O. K. Farha, *Nat. Rev. Mater.*, 2016, **1**, 1–15.
109. S. Cao, B. Li, R. Zhu and H. Pang, *Chem. Eng. J.*, 2019, **355**, 602–623.
110. E. Boateng and A. Chen, *Mater. Today Adv.*, 2020, **6**, 100022.
111. A. Ariharan, B. Viswanathan and V. Nandhakumar, *Int. J. Hydrogen Energy*, 2018, **43**, 5077–5088.
112. E. Anikina, A. Banerjee, V. Beskachko and R. Ahuja, *ACS Appl. Nano Mater.*, 2019, **2**, 3021–3030.
113. A. V. Dighe, R. Y. Nemade and M. R. Singh, *Processes*, 2019, **7**, 527.
114. S. Yuan, L. Feng, K. Wang, J. Pang, M. Bosch, C. Lollar, Y. Sun, J. Qin, X. Yang, P. Zhang, Q. Wang, L. Zou, Y. Zhang, L. Zhang, Y. Fang, J. Li and H. C. Zhou, *Adv. Mater.*, 2018, **30**, 1704303.
115. A. P. Côté, A. I. Benin, N. W. Ockwig, M. O’Keeffe, A. J. Matzger and O. M. Yaghi, *Science*, 2005, **310**, 1166–1170.
116. R. B. Lin, Y. He, P. Li, H. Wang, W. Zhou and B. Chen, *Chem. Soc. Rev.*, 2019, **48**, 1362–1389.
117. J. L. Segura, S. Royuela and M. Mar Ramos, *Chem. Soc. Rev.*, 2019, **48**, 3903–3945.
118. P. J. Waller, F. Gándara and O. M. Yaghi, *Acc. Chem. Res.*, 2015, **48**, 3053–3063.
119. K. Konstas, J. W. Taylor, A. W. Thornton, C. M. Doherty, W. X. Lim, T. J. Bastow, D. F. Kennedy, C. D. Wood, B. J. Cox, J. M. Hill, A. J. Hill and M. R. Hill, *Angew. Chem. Int. Ed.*, 2012, **51**, 6639–6642.
120. L. Wang, Y. Sun and H. Sun, *Faraday Discuss.*, 2011, **151**, 143–156.

121. X. Wu, R. Wang, H. Yang, W. Wang, W. Cai and Q. Li, *J. Mater. Chem. A*, 2015, **3**, 10724–10729.
122. S. Das, P. Heasman, T. Ben and S. Qiu, *Chem. Rev.*, 2017, **117**, 1515–1563.
123. T. Ben, H. Ren, M. Shengqian, D. Cao, J. Lan, X. Jing, W. Wang, J. Xu, F. Deng, J. M. Simmons, S. Qiu and G. Zhu, *Angew. Chem. Int. Ed.*, 2009, **48**, 9457–9460.
124. B. Notario, J. Pinto and M. A. Rodriguez-Perez, *Prog. Mater. Sci.*, 2016, **78**, 93–139.
125. J. Germain, J. M. J. Fréchet and F. Svec, *Small*, 2009, **5**, 1098–1111.
126. L. Tan and B. Tan, *Chem. Soc. Rev.*, 2017, **46**, 3322–3356.
127. J. S. M. Lee and A. I. Cooper, *Chem. Rev.*, 2020, **120**, 2171–2214.
128. M. Tian, S. Rochat, K. Polak-Kraśna, L. T. Holyfield, A. D. Burrows, C. R. Bowen and T. J. Mays, *Adsorption*, 2019, **25**, 889–901.
129. V. A. Yartys, M. V. Lototskyy, E. Akiba, R. Albert, V. E. Antonov, J. R. Ares, M. Baricco, N. Bourgeois, C. E. Buckley, J. M. Bellosta von Colbe, J. C. Crivello, F. Cuevas, R. V. Denys, M. Dornheim, M. Felderhoff, D. M. Grant, B. C. Hauback, T. D. Humphries, I. Jacob, T. R. Jensen, P. E. de Jongh, J. M. Joubert, M. A. Kuzovnikov, M. Latroche, M. Paskevicius, L. Pasquini, L. Popilevsky, V. M. Skripnyuk, E. Rabkin, M. V. Sofianos, A. Stuart, G. Walker, H. Wang, C. J. Webb and M. Zhu, *Int. J. Hydrogen Energy*, 2019, **44**, 7809–7859.
130. U. B. Demirci, *Energies*, 2020, **13**, 3071.
131. J. Bellosta von Colbe, J. R. Ares, J. Barale, M. Baricco, C. Buckley, G. Capurso, N. Gallandat, D. M. Grant, M. N. Guzik, I. Jacob, E. H. Jensen, T. Jensen, J. Jepsen, T. Klassen, M. V. Lototskyy, K. Manickam, A. Montone, J. Puszkiel, S. Sartori, D. A. Sheppard, A. Stuart, G. Walker, C. J. Webb, H. Yang, V. Yartys, A. Züttel and M. Dornheim, *Int. J. Hydrogen Energy*, 2019, **44**, 7780–7808.
132. P. E. De Jongh, M. Allendorf, J. J. Vajo and C. Zlotea, *MRS Bull.*, 2013, **38**, 488–494.
133. A. C. Dillon, K. M. Jones, T. A. Bekkedahl, C. H. Kiang, D. S. Bethune and M. J. Heben, *Nature*, 1997, **386**, 377–379.
134. M. Sevilla, R. Mokaya and A. B. Fuertes, *Energy Environ. Sci.*, 2011, **4**, 2930–2936.
135. S. H. Md Arshad, N. Ngadi, A. A. Aziz, N. S. Amin, M. Jusoh and S. Wong, *J. Energy Storage*, 2016, **8**, 257–261.
136. N. L. Rosi, J. Eckert, M. Eddaoudi, D. T. Vodak, J. Kim, M. O’Keeffe and O. M. Yaghi, *Science*, 2003, **300**, 1127–1129.
137. H. Furukawa, M. A. Miller and O. M. Yaghi, *J. Mater. Chem.*, 2007, **17**, 3197–3204.
138. Y. Li and R. T. Yang, *Langmuir*, 2007, **23**, 12937–12944.
139. H. Furukawa, N. Ko, Y. B. Go, N. Aratani, S. B. Choi, E. Choi, A. Ö. Yazaydin, R. Q. Snurr, M. O’Keeffe, J. Kim and O. M. Yaghi, *Science*, 2010, **329**, 424–428.



140. K. Sumida, M. R. Hill, S. Horike, A. Dailly and J. R. Long, *J. Am. Chem. Soc.*, 2009, **131**, 15120–15121.
141. H. Furukawa and O. M. Yaghi, *J. Am. Chem. Soc.*, 2009, **131**, 8875–8883.
142. E. Klontzas, E. Tylisanakis and G. E. Froudakis, *Nano Lett.*, 2010, **10**, 452–454.
143. Y. Yuan and G. Zhu, *ACS Cent. Sci.*, 2019, **5**, 409–418.
144. Y. Sun, T. Ben, L. Wang, S. Qiu and H. Sun, *J. Phys. Chem. Lett.*, 2010, **1**, 2753–2756.
145. V. Stavila, R. K. Bhakta, T. M. Alam, E. H. Majzoub and M. D. Allendorf, *ACS Nano*, 2012, **6**, 9807–9817.
146. Y. Feng, X. Zhou, J. H. Yang, X. Gao, L. Yin, Y. Zhao and B. Zhang, *ACS Sustainable Chem. Eng.*, 2020, **8**, 2122–2129.
147. K. F. Aguey-Zinsou and J. R. Ares-Fernández, *Chem. Mater.*, 2008, **20**, 376–378.
148. Y. Luo, Q. Wang, J. Li, F. Xu, L. Sun, Y. Zou, H. Chu, B. Li and K. Zhang, *Mater. Today Nano*, 2020, **9**, 100071.
149. D. Peng, Z. Ding, L. Zhang, Y. Fu, J. Wang, Y. Li and S. Han, *Int. J. Hydrogen Energy*, 2018, **43**, 3731–3740.
150. W. Zhang, G. Xu, L. Chen, S. Pan, X. Jing, J. Wang and S. Han, *Int. J. Hydrogen Energy*, 2017, **42**, 15262–15270.

# Subject Index

- ABS. *See* acrylonitrile–butadiene styrene (ABS)
- acetaminophen (ACTP), 47
- acrylonitrile–butadiene styrene (ABS), 136
- ACTP. *See* acetaminophen (ACTP)
- Ag<sub>2</sub>O. *See* silver oxide (Ag<sub>2</sub>O)
- aggregation-induced emission (AIE), 201–202
- AgNPs. *See* silver NPs (AgNPs)
- AIE. *See* aggregation-induced emission (AIE)
- amoxicillin (AMX), 47
- AMX. *See* amoxicillin (AMX)
- apparent quantum yield (AQY), 209
- AQY. *See* apparent quantum yield (AQY)
- Arsenic (As), 146
- Aspergillus niger*, 171
- atom transfer radical polymerization (ATRP), 71
- ATRP. *See* atom transfer radical polymerization (ATRP)
- ATT–Au NCs. *See* 6-aza-2-thiothymine-protected Au NCs (ATT–Au NCs)
- 6-aza-2-thiothymine-protected Au NCs (ATT–Au NCs), 204
- BCN. *See* boron carbon nitride (BCN)
- BDC. *See* 1,4-benzenedicarboxylic acid (BDC)
- 1,4-benzenedicarboxylic acid (BDC), 290
- biodegradable plastics (BPs), 118
- bioassimilation process, 120, 122
- biodegradation process, 120–121
- categories, 121
- disadvantages, 122
- fragmented polymer chains, 120
- graphene, 124
- high-performance, 120
- impact, 126
- metabolites, 121
- microbial biofilms, 120
- nanomaterials, 124–125
- PHA and PLA, 121–123, 126
- polymer material, type of, 120
- short-chain-length (scl) monomer, 121
- starch-based plastics, 122
- types of, 121
- biological synthesis, 12–13
- biomass, 13–14
- biomolecules, 13–14
- bio-refinery, 270–271
- applications, 269–270
- biodiesel production
- acid catalysts, 258
  - CaO, 258
  - heterogeneous catalysts, 258
  - nano-catalyst, 257–258
  - palladium (Pd) nanoparticles, 260
  - soybean oil, 260
- bio-oil upgrading, 268–269
- chemicals derived from cellulose, 264–265

- bio-refinery (*continued*)  
 classification, 256  
 glucose, lactic acid and chemicals derived from, 264  
 glycerol, high-value chemicals from, 260–261  
 lignocellulosic biomass, bio-ethanol derived from, 262–263  
 lignocellulosic biomass, pyrolysis of  
   biomass, thermal decomposition of, 265  
   bio-oil, 266–267  
   nano-SnO<sub>2</sub> particles, 267  
   thermal process parameters, effect of, 265–266  
   torrefaction process, 265  
 modern petroleum refineries, 256  
 starch-rich biomass to bio-ethanol, conversion of, 261  
 boron carbon nitride (BCN), 90  
 BPs. *See* biodegradable plastics (BPs)  
 built environment, 180  
 brick, 166–170  
 glass, 165–166  
 indoor air treatment  
   air pollutants, 173–174  
   gaseous benzene, removal of, 174–176  
   nanocomposite films, types of, 174  
   polyimide nanofiber, 176  
   silk nanofiber, 176  
 nanomaterials, risk of, 178–180  
 stone, 170–173  
 TiO<sub>2</sub>, photocatalytic mechanism of, 164  
 wood  
   *A. niger*, 177–178  
   mold fungi, 176  
   nanocompounds, 178
- CAB. *See* cellulose acetate butyrate (CAB)  
 cadmium(II), 146  
 CAP. *See* continuous assembly of polymers (CAP)  
 carbon dioxide (CO<sub>2</sub>), 109  
   core-shell nanostructures, 67  
   nanostructured materials  
     different metals, hybridization of, 99–103  
     electrocatalytic systems, 107–109  
   Fe<sub>3</sub>O<sub>4</sub> nanoparticles, 69  
   fixation of, 73–74  
   H<sub>2</sub>/CO<sub>2</sub>, 71, 73  
   metal oxides and hybrids, 103–107  
   MOFs, 70–71  
   MWCNTs, 68–69  
   nanostructured mono-metal electrocatalysts, 94–99  
   TBB, 71  
   TiO<sub>2</sub>:Cu<sub>2</sub>O, 69  
 photocatalytic CO<sub>2</sub> reduction, nanostructures  
   Au/Cd<sub>1-x</sub>S, 83  
   Au/p-GaN, 83–85  
   Bi<sub>2</sub>WO<sub>6</sub>/Au/CdS, 82  
   CsPbBr<sub>3</sub>-Au nanocomposite, 84  
   Cu<sub>2</sub>O-based hybrid photocatalysts, 79–80  
   metal-organic frameworks, 91–95  
   metals and alloys, 74, 76  
   MoS<sub>2</sub>, 83  
   Ni/NiO and CoPc, 81  
   RWGS, 81  
   TiO<sub>2</sub>-based photocatalysts, 77–79  
   two-dimensional carbon-containing materials, 84–91  
   ZnMn<sub>2</sub>O<sub>4</sub> microspheres, 81  
   ZnPc/BVNS, 82

- photocatalytic
  - conversion of, 67
  - photosynthesis, 65–66
- carbon fiber papers (CFPs), 108
- carbon nanoparticles (CNPs), 5
- carbon nanotubes (CNTs), 179
- carbon quantum dots (CQDs), 43, 228
- cellulose acetate butyrate (CAB), 49
- CFPs. *See* carbon fiber papers (CFPs)
- chromium, 146–147
- CNPs. *See* carbon nanoparticles (CNPs)
- CNTs. *See* carbon nanotubes (CNTs)
- CO<sub>2</sub>. *See* carbon dioxide (CO<sub>2</sub>)
- cobalt(II) phthalocyanine (CoPc), 81
- COFs. *See* covalent organic frameworks (COFs)
- color rendering index (CRI), 213
- concentrated solar power (CSP), 279–284
- constructive technology assessment (CTA), 21
- continuous assembly of polymers (CAP), 71
- CoPc. *See* cobalt(II) phthalocyanine (CoPc)
- copper, 214
- covalent organic frameworks (COFs), 47, 232
- CQDs. *See* carbon quantum dots (CQDs)
- CRI. *See* color rendering index (CRI)
- CSP. *See* concentrated solar power (CSP)
- CTA. *See* constructive technology assessment (CTA)
- Cu<sub>2</sub>O-based hybrid photocatalysts, 79–80
- DAP. *See* 1,3-diaminopropane (DAP)
- deoxyribonucleic acid (DNA), 14
- DEP. *See* diethylphosphorothioate (DEP)
- Department of Energy (DOE), 287
- 3D-h. *See* 3D hierarchical (3D-h), 103
- 1,3-diaminopropane (DAP), 69
- diethylphosphorothioate (DEP), 41
- DMF. *See* *N,N*-dimethylformamide (DMF)
- DNA. *See* deoxyribonucleic acid (DNA)
- DOE. *See* Department of Energy (DOE)
- ECL. *See* electrogenerated chemiluminescence (ECL)
- EDTA. *See* ethylenediaminetetraacetic acid (EDTA)
- EFB. *See* empty fruit bunch (EFB)
- E-GMA. *See* ethylene-glycidyl methacrylate (E-GMA)
- electrocatalysis, 10–11
- electrochemical biosensors
  - artificial receptors-based
    - “biosensors,” 39
  - biological events, 35
  - characteristics, 35
  - electrochemical biocatalytic biosensors, 38–39
  - future trends, 39–40
  - label-based immunosensors
    - cyanotoxin, 36
    - LOD, 37
    - MC-LR, 37–38
    - QDs, 38
  - sensors, new types of, 36
- electrochemistry, 10–11
- electrogenerated chemiluminescence (ECL), 43
- electronic waste or e-waste, 16
- ELISA. *See* enzyme-linked immunosorbent assay (ELISA)
- empty fruit bunch (EFB), 289
- enzyme-linked immunosorbent assay (ELISA), 39
- Escherichia coli*, 43
- ethylenediaminetetraacetic acid (EDTA), 209, 238
- ethylene-glycidyl methacrylate (E-GMA), 127

- FAMES. *See* fatty acid methyl esters (FAMES)
- fatty acid methyl esters (FAMES), 257
- FDA. *See* formaldehyde dimethyl acetal (FDA)
- FFAs. *See* free fatty acids (FFAs)
- FFV. *See* fractional free volume (FFV)
- flow chemistry, 11–12
- formaldehyde dimethyl acetal (FDA), 136
- fossil-based fuels, 277
- fractional free volume (FFV), 71
- free fatty acids (FFAs), 257
- Freundlich non-linear isotherm, 147
- GLY. *See* glyphosate (GLY)
- glyphosate (GLY), 46
- GQDs. *See* graphene quantum dots (GQDs)
- graphene quantum dots (GQDs), 43, 79
- green nanotechnology, 33–34, 58
  - adsorbing and degrading pollutants in water, nanomaterials for
    - nanophotocatalysts, 47–48
    - nanosorbents, 45–47
  - energy-efficient water purification, thin-film nanocomposite membranes for
    - one-dimensional materials, 55
    - three-dimensional materials, 56–58
    - two-dimensional materials, 55–56
    - zero-dimensional materials, 53–55
  - impurity detection, biosensors and nanoparticles for
    - electrochemical biosensors, 35–40
    - nanoparticles, 40–44
  - removing oil from water
    - nanofibrous membranes, 50–52
    - nanofibrous sorbents, 49–50
    - NFA, 52
- HCS-PCF. *See* hollow carbon sphere/porous carbon flake (HCS-PCF)
- HCSs. *See* hollow carbon spheres (HCSs)
- HDTC. *See* 2-hydroxyethylthiocarbamate (HDTC)
- HFGDEs. *See* hollow fiber gas diffusion electrodes (HFGDEs)
- HNFA. *See* hydrophobic–lipophilic nanofibrous aerogel (HNFA)
- hole-transporting nanolayer (HTL), 206
- hollow carbon sphere/porous carbon flake (HCS-PCF), 137
- hollow carbon spheres (HCSs), 71
- hollow fiber gas diffusion electrodes (HFGDEs), 107
- horseradish peroxidase (HRP), 36
- HRP. *See* horseradish peroxidase (HRP)
- HTL. *See* hole-transporting nanolayer (HTL)
- hydrophobic–lipophilic nanofibrous aerogel (HNFA), 52
- 2-hydroxyethylthiocarbamate (HDTC), 41
- IE. *See* industrial ecology (IE)
- industrial ecology (IE), 18–19
- kinetic adsorption models
  - pseudo-first-order kinetic model, 148
  - pseudo-second-order kinetic model, 148
  - Weber and Morris kinetic model, 148–149
- Langmuir non-linear isotherm, 147
- layered double hydroxides (LDHs), 69

- LCA. *See* life cycle assessment (LCA)
- LDHs. *See* layered double hydroxides (LDHs)
- LDPE. *See* low-density polyethylene (LDPE)
- LE. *See* luminous efficiency (LE)
- lead (Pb(II)), 146
- LED. *See* light-emitting diode (LED)
- life cycle assessment (LCA), 19–20
- light-emitting diode (LED), 212
- limit of detection (LOD), 37
- localized surface plasmon resonance (LSPR), 67
- LOD. *See* limit of detection (LOD)
- low-density polyethylene (LDPE), 128
- LSPR. *See* localized surface plasmon resonance (LSPR)
- luminous efficiency (LE), 213
- MA-g-PP. *See* maleic anhydride-grafted-polypropylene (MA-g-PP)
- maleic anhydride-grafted-polypropylene (MA-g-PP), 128
- material flow analysis (MFA), 19, 21
- MB. *See* methylene blue (MB)
- MCC. *See* microcrystalline cellulose (MCC)
- MC-RR. *See* microcystin-RR (MC-RR)
- mechanochemistry, 7–9
- 2-mercapto-1-methylimidazole (MMI), 213
- mercury (Hg), 146
- metal–organic frameworks (MOFs), 3, 56–58, 70, 226
- metal oxide nanomaterials
- iron oxide, 155–156
  - MnO<sub>2</sub>
    - electrostatic interaction, 153
    - organic adsorption, 154
    - structures, variety of, 153–154
  - zinc oxide, 156–157
- methanol-to-propylene (MTP), 269
- methylene blue (MB), 149, 165
- MF. *See* microfiltration (MF)
- MFA. *See* material flow analysis (MFA)
- microcrystalline cellulose (MCC), 126, 264–265
- microcystin-RR (MC-RR), 37
- microfiltration (MF), 53
- microwave irradiation, 9
- MMI. *See* 2-mercapto-1-methylimidazole (MMI)
- MMT. *See* montmorillonite (MMT)
- MOFs. *See* metal–organic frameworks (MOFs)
- montmorillonite (MMT), 287
- Moorella thermoacetica*, 209
- MTP. *See* methanol-to-propylene (MTP)
- multi-walled carbon nanotubes (MWCNTs), 68
- multi-walled nanotubes (MWNTs), 6
- MWCNTs. *See* multi-walled carbon nanotubes (MWCNTs)
- MWNTs. *See* multi-walled nanotubes (MWNTs)
- NAC. *See* *N*-acetyl-L-cysteine (NAC)
- N*-acetyl-L-cysteine (NAC), 213
- nanocatalysis, 243
- anthropological development, 221
  - environmental remediation, 239–240
  - high-value chemicals, production of, 241–243
  - high-value fuels, production of, 240–241
  - homogeneous and heterogeneous, 220–221
  - magnetically recyclable nanocatalysts
    - classification, 224–225
    - Co and Ni nanoparticles, 226
    - economic and environmental concerns, 224
    - Fe<sub>3</sub>O<sub>4</sub> nanoparticles, 225
    - FePt–Au, 225

- nanocatalysis (*continued*)
    - iron oxides, 226
    - metal alloy
      - nanomaterials, 224
    - metal carbides, 225
    - metallic oxides, 224–225
    - metal magnetic
      - nanomaterials, 224
    - multicomponent magnetic
      - nanomaterials, 225
  - metallic nanoparticles
    - Au nanoparticles, 222–223
    - bimetallic
      - nanomaterials, 224
    - CO oxidation, 223
    - metal oxide
      - nanoparticles, 223
    - oxygen evolution catalysts, 222
    - oxygen reduction catalysts, 222
    - Pd, 222
    - tetracycline hydrochloride
      - photodegradation, 223
    - TiO<sub>2</sub>, 223
    - transition metals, 222
  - nanocarbon materials
    - allotropic structures, 227
    - carbon quantum dots, 228
    - conventional metal nanocatalysts, 227
    - electrocatalytic synthesis, 229–230
    - fullerenes, 229
    - graphene, 230
    - nanodiamond, 231
    - N-codoped nanodiamond, 231–232
    - N-doped graphitic carbon, 230–231
    - NH<sub>3</sub> formation, 230
    - quantitative analysis method, 229
  - nano-sized materials, 221
  - nanostructured porous materials
    - COFs, 236–237
    - lignin-derived phenols, 233
    - MOFs, 232, 235
    - silica-based mesoporous materials, 233
    - zeolites, 232–233
  - photocatalysis, 237–239
  - role, 220
  - types of nanocatalysts, 221
- nanoclusters (NCs), 186
    - ATT–Au, 204–205
    - Au/Ag, 186, 188–191
    - Aux–GS, 208–209
    - Cu, 202
    - thiolate-protected metal, 186
  - nanodiamond, 231
  - nanofiber materials
    - nanofibrous membranes, 50–52
    - nanofibrous sorbents, 49–50
    - NFA, 52
  - nanofibers, 5–6
  - nanofibrous aerogels (NFA), 52
  - nanofiltration (NF), 53
  - nanomaterials
    - graphene, 124
    - in the built environment. *See* built environment
    - types, 34
    - water, adsorbing and degrading pollutants in nanophotocatalysts, 47–49
    - nanosorbents, 45–47
  - nanoparticles (NPs)
    - biosynthesis of, 12
    - bottom-up and top-down approaches, 2–3
    - carbon-based NPs, 5
    - inorganic, 3–4
    - metal oxide nanoparticles, 44
    - organic, 4–5

- QDs
  - cadmium-based QDs, 40
  - classifications, 40
  - CQDs, 43
  - DEP, 41, 43
  - dual-emission, 41
  - E. coli*, 43
  - features, 40
  - fluorescence color of, 41
  - GQDs, 43
  - zinc-based QDs, 41
  - zinc selenide QDs, 43
- TiO<sub>2</sub>, 21
- zero-dimensional materials, 53–55
- nanophotocatalysts, 47–49
- nanoplastics (NPLs), 117
- nanoplates, 6–7
- nanosheets, 55–56
- nanosorbents
  - GLY, 46
  - heavy metal pollutants, removal of, 45–46
  - material synthesizing procedure, 46
  - organic dyes, 45
- nanostructures
  - nanostructured monometal electrocatalysts
    - Au–Pd core–shell microspheres, 99
    - Bi<sub>2</sub>O<sub>3</sub>-E electrode, 107
    - bimetallic nanostructures, 99
    - bismuth (Bi), 98–99
    - Bi-SnO<sub>x</sub> shells, 105
    - CNT-gold nanohybrid, 107
    - CO<sub>2</sub>, electrochemical reduction of, 105, 107
    - copper nanomaterials, 97–98
    - 3D-h Cu, 103–104
    - gold nanomaterials, 94, 96
    - HFGDEs, 107
    - In–Sn alloys, 103
    - Mn–SnO<sub>2</sub>, 105
    - 4-nitrophenol, 103
    - Pd–Cu Janus nanostructures, 101–102
    - silver nanomaterials, 96–97
    - SnO<sub>2</sub>, 108–109
  - photocatalytic CO<sub>2</sub> reduction
    - Au/Cd<sub>1-x</sub>S, 83
    - Au/p-GaN, 83–84
    - Bi<sub>2</sub>WO<sub>6</sub>/Au/CdS, 82
    - CsPbBr<sub>3</sub>-Au nanocomposite, 84
    - Cu<sub>2</sub>O-based hybrid photocatalysts, 79–80
    - metal-organic frameworks, 91–95
    - metals and alloys, 74, 76
    - MoS<sub>2</sub>, 83
    - Ni/NiO and CoPc, 81
    - RWGS, 81
    - TiO<sub>2</sub>-based photocatalysts, 77–79
    - two-dimensional carbon-containing materials, 84–91
    - ZnMn<sub>2</sub>O<sub>4</sub> microspheres, 81
    - ZnPc/BVNS, 82
- nanotechnology, 1–2, 23, 214–215
  - Au/Ag NCs, 186, 189
  - bio-refinery. *See* bio-refinery
  - CO<sub>2</sub>. *See* carbon dioxide (CO<sub>2</sub>)
  - energy conversion applications
    - CO<sub>2</sub> fixation, 209–210
    - fuel cells, 210–211
    - light-driven emitting diodes, 212–214
    - lithium-ion batteries, 211–212
    - solar cells, 206–207
    - water splitting, 207–209
  - environmental impact and life cycle of the environment and human health, 22–23



- nanotechnology (*continued*)  
IE, 18–19  
LCA, 19–20  
MFA and SFA, 21  
technology assessment, 21  
green chemistry and synthetic approaches  
biological synthesis, 12–13  
electrochemistry and electrocatalysis, 10–11  
flow chemistry, 11–12  
mechanochemistry, 7–9  
microwave irradiation, 9  
photochemistry and photocatalysis, 9–10  
nanostructures, types of  
nanofibers, 5–6  
nanoparticles, 2–5  
nanoplates, 6–7  
nanotubes, 6  
plastic wastes, remediation of. *See* plastic wastes, remediation of  
PLQY, 188  
renewable energy. *See* renewable energy  
renewable resources  
biomass and biomolecules, 13–14  
waste, 14–17  
thiolate-coated Au/Ag NCs  
composition control, 197–200  
kinetic control, 191–192  
photoluminescence control, 201–206  
size alteration during ligand exchange, 194–196  
size focusing, 192–193  
surface control, 196–197  
top-down and bottom-up approaches, 189  
thiolate-protected metal NCs, 186  
nanotubes, 6, 55  
National Nanotechnology Initiative (NNI), 1  
NCs. *See* nanoclusters (NCs)  
NF. *See* nanofiltration (NF)  
NFA. *See* nanofibrous aerogels (NFA)  
N-(phosphonomethyl)glycine (PMG), 47  
N,N-dimethylformamide (DMF), 125  
NNI. *See* National Nanotechnology Initiative (NNI)  
NPLs. *See* nanoplastics (NPLs)  
NPs. *See* nanoparticles (NPs)  
octadecylamine (ODA), 287  
ODA. *See* octadecylamine (ODA)  
OFC. *See* oxidized fibrillated cellulose (OFC)  
OMC. *See* ordered mesoporous carbon (OMC)  
ordered mesoporous carbon (OMC), 131  
organic cages, 56–58  
ORR. *See* oxygen reduction reaction (ORR)  
oxidized fibrillated cellulose (OFC), 71  
oxygen reduction reaction (ORR), 210  
PAN. *See* polyacrylonitrile (PAN)  
partial occupation analysis (POA), 203  
PBI. *See* polybenzimidazole (PBI)  
PCL. *See* polycaprolactone (PCL)  
PDMS. *See* polydimethylsiloxane (PDMS)  
PECs. *See* photoelectrochemical cells (PECs)  
PEG. *See* polyethylene glycol (PEG)  
PEI. *See* polyethylenimine (PEI)  
PHB. *See* poly(3-hydroxybutyrate) (PHB)  
PHBV. *See* poly(3-hydroxybutyrate-co-3-hydroxyvalerate) (PHBV)  
photocatalysis, 9–10  
photochemistry, 9–10  
photoelectrochemical cells (PECs), 208  
photoluminescence quantum yield (PLQY), 188

- photovoltaic (PV), 284
- Pittsburgh Plate Glass (PPG), 165
- PLA. *See* poly(lactic acid) (PLA)
- plastics
  - BPs. *See* biodegradable plastics (BPs)
  - NPLs, 117
  - plastic wastes, remediation
    - of. *See* plastic wastes, remediation of
  - plastic wastes, remediation of, 137–138
  - bioplastics, 118
  - BPs, 118
    - bioassimilation process, 120, 122
    - biodegradation process, 120–121
    - categories, 121
    - disadvantages, 122
    - fragmented polymer chains, 120
    - graphene, 124
    - high-performance, 120
    - impact, 126
    - metabolites, 121
    - microbial biofilms, 120
    - nanomaterials, 124–125
    - PHA and PLA, 121–123, 126
    - polymer material, type of, 120
    - short-chain-length (scl) monomer, 121
    - starch-based plastics, 122
    - types of, 121
  - classifications of, 118–119
  - flexible plastics, 131
  - nanofiller
    - hydrophilic nanoscale, 127
    - LDPE, 128
    - MTR-GO, 129
    - nanoscale clay, 127
    - nanosilica, 128
    - PVC, dechlorination reaction of, 128
  - plastics, carbonization of, 131–133
  - plastics, photodegradation of, 129–130
  - plastic waste disposal and environmental risks, 118
  - plastic wastes, burning of, 118
  - transformation of plastics to high-value products
    - ABS plastic, 136
    - household wastes, 133
    - mixed plastic waste, 136–137
    - PHBV, 133
- PLQY. *See* photoluminescence quantum yield (PLQY)
- POA. *See* partial occupation analysis (POA)
- pollutant treatment, sustainable nanomaterials for
  - data analysis, 149
  - isotherm adsorption models, 147–148
  - kinetic adsorption models
    - pseudo-first-order kinetic model, 148
    - pseudo-second-order kinetic model, 148
    - Weber and Morris kinetic model, 148–149
  - metal oxide nanomaterials
    - iron oxide, 155–156
    - MnO<sub>2</sub>, 153–155
    - zinc oxide, 156–157
  - spectroscopy methods
    - chemical interactions, 150
    - electrostatic interaction, 149–150
    - FT-IR spectroscopy, 151–152
    - ion exchange, 150
    - ion holes, 150–151
    - TG-DSC analysis, 151–152
  - wastewater, heavy metals in, 146–147

- polyacrylonitrile (PAN), 71  
polybenzimidazole (PBI), 71  
polycaprolactone (PCL), 125  
polydimethylsiloxane (PDMS), 71  
polyethylene glycol (PEG), 71  
polyethylenimine (PEI), 71  
polynucleotides, 13  
polypeptides, 13  
poly(3-hydroxybutyrate) (PHB), 49  
poly(3-hydroxybutyrate-*co*-3-hydroxyvalerate) (PHBV), 133  
polyphenylene sulfide (PPS), 287  
poly(lactic acid) (PLA), 49  
polysaccharides, 13  
polytetrafluoroethylene (PTFE), 287  
POMs. *See* porous organic materials (POMs)  
porous organic materials (POMs), 56  
PP2A. *See* protein phosphatase 2 (PP2A)  
PPG. *See* Pittsburgh Plate Glass (PPG)  
PPS. *See* polyphenylene sulfide (PPS)  
protein phosphatase 2 (PP2A), 38  
proteins, 13  
pseudo-first-order kinetic model, 148  
pseudo-second-order kinetic model, 148  
PTFE. *See* polytetrafluoroethylene (PTFE)  
pure water permeability (PWP), 53  
PV. *See* photovoltaic (PV)  
PWP. *See* pure water permeability (PWP)
- QDs. *See* quantum dots (QDs)  
quantum dots (QDs), 21, 53–55, 78
- RDE. *See* rotating disk electrode (RDE)  
reactive oxygen species (ROS), 127  
real-time technology assessment (RTTA), 21  
reduced graphene oxide (rGO), 210  
renewable energy, 291–292  
geothermal energy, 287  
hydrogen energy  
COFs, 290–291  
green energy sources, 287  
liquid hydrogen-rich molecules, 288  
MOFs, 289–290  
nanomaterials, types of, 288  
nanoporous carbon materials, 288  
nanoporous organic polymers, 291  
PAFs, 290–291  
storage problem, 287–288  
solar energy, 278–279  
concentrated solar power, 279–284  
photovoltaic, 284  
wind energy, 284–286
- renewable resources  
biomass and biomolecules, 13–14  
waste  
carbon dioxide, 14–15  
electronics recycling, 16–17  
plastic recycling, 15–16
- reverse osmosis (RO), 53  
reverse water gas shift reaction (RWGS), 81  
Reversible Hydrogen Electrode (RHE), 208  
rGO. *See* reduced graphene oxide (rGO)  
RhB. *See* rhodamine B (RhB)  
RHE. *See* Reversible Hydrogen Electrode (RHE)  
rhodamine B (RhB), 47  
ribonucleic acid (RNA), 14  
RO. *See* reverse osmosis (RO)  
ROS. *See* reactive oxygen species (ROS)  
rotating disk electrode (RDE), 210  
RTTA. *See* real-time technology assessment (RTTA)  
RWGS. *See* reverse water gas shift reaction (RWGS)

- SFA. *See* substance flow analysis (SFA)
- SiC. *See* silicon carbide (SiC)
- silicon carbide (SiC), 125
- silk nanocrystals (SNCs), 124
- silver NPs (AgNPs), 17
- silver oxide (Ag<sub>2</sub>O), 44
- single-walled carbon nanohorns (SWNHs), 37
- single-walled nanotubes (SWNTs), 6, 288
- SNCs. *See* silk nanocrystals (SNCs)
- solar energy, 278–279
- CSP
- advantages, and disadvantages, 279–280
  - decarbonation/carbonation reactions, 283
  - metal hydrides, 279, 282
  - Mg(OH)<sub>2</sub>-based TES system, 282
  - MgO microbeams, 282
  - oxide-based TCS, 284
  - TCS, 279
  - TESSs, 279
- photovoltaic, 284
- starch-based plastics, 122, 125
- substance flow analysis (SFA), 19, 21
- SWNHs. *See* single-walled carbon nanohorns (SWNHs)
- SWNTs. *See* single-walled nanotubes (SWNTs)
- TA. *See* technology assessment (TA)
- TBB. *See* 1,3,5-tris(bromomethyl)-benzene (TBB)
- TCS. *See* thermochemical heat storage (TCS)
- technology assessment (TA), 19, 21
- TENG. *See* triboelectric nanogenerator (TENG)
- TES system. *See* thermal energy storage (TES) system
- TFC. *See* thin-film composite (TFC)
- TFN. *See* thin-film nanocomposite (TFN)
- TGA. *See* thermogravimetric analysis (TGA)
- thermal energy storage (TES) system, 279
- thermochemical heat storage (TCS), 279
- thermogravimetric analysis (TGA), 151
- thin-film composite (TFC), 53
- thin-film nanocomposite (TFN), 53
- thiolate-coated Au/Ag NCs
- composition control
    - doped silver atoms, 199
    - gold and silver NCs, 197–198
    - 25-metal-atom NCs, 199
    - Pt<sub>1</sub>Au<sub>24</sub>(SR)<sub>18</sub> NC, 198
  - kinetic control, 191–192
  - photoluminescence control
    - aggregation-induced emission enhancement, 201–202
    - doping with foreign atoms, 203–204
    - ligand rigidification, 202–203
    - ligand shell, host-guest interaction of, 204–205
    - matrix confinement, 205–206
  - size alteration during ligand exchange, 194–196
  - size focusing, 192–193
  - surface control, 196–197
  - top-down and bottom-up approaches, 189
- TiO<sub>2</sub>. *See* titanium dioxide (TiO<sub>2</sub>)
- TiO<sub>2</sub>-based photocatalysts
- Au-TiO<sub>2</sub> hybrid, 77
  - CdS QDs, 78
  - graphene, 79
  - metal oxides and sulfides, 78
  - nanoarrays of MoS<sub>2</sub> sheets, 78–79
  - UV energy, 77
- titanium dioxide (TiO<sub>2</sub>), 21

- triboelectric nanogenerator  
(TENG), 285
- 1,3,5-tris(bromomethyl)benzene  
(TBB), 71
- two-dimensional carbon-containing materials
- BCN, 90
  - graphene and derivatives, 84, 86–87
  - graphitic carbon nitride (g-C<sub>3</sub>N<sub>4</sub>)
    - CeO<sub>2</sub>, 88
    - OCN-tube materials, 87
    - Pt nanoparticles, 88
    - rGO/pCN, 89
    - structural engineering
      - of, 87
    - ZnV<sub>2</sub>O<sub>6</sub>/rGO/g-C<sub>3</sub>N<sub>4</sub> nanocomposite, 90
    - SiC-NW/C nanostructures, 91
- UF. *See* ultrafiltration (UF)
- ultrafiltration (UF), 53
- ultrathin film composite mixed matrix membranes (UTFC-MMMs), 71
- UTFC-MMMs. *See* ultrathin film composite mixed matrix membranes (UTFC-MMMs)
- visible light-driven (VLD), 48
- VLD. *See* visible light-driven (VLD)
- WD-TENG. *See* wind-driven triboelectric nanogenerator (WD-TENG)
- Weber and Morris kinetic model, 148–149
- WHO. *See* World Health Organization (WHO)
- wind-driven triboelectric nanogenerator (WD-TENG), 285–286
- World Health Organization (WHO), 146
- XPS. *See* X-ray photoelectron spectroscopy (XPS)
- X-ray photoelectron spectroscopy (XPS), 214
- zeolitic imidazolate framework-8 (ZIF-8), 89
- ZIF-8. *See* zeolitic imidazolate framework-8 (ZIF-8)
- zinc oxide (ZnO), 44
- ZnO. *See* zinc oxide (ZnO)